Innate Immune Sensing of Virus Infection and Viral Evasion Strategies



A thesis submitted by

Gerissa Fowler

Lady Margaret Hall

For the degree of

Doctor of Philosophy in Medical Sciences

to the

University of Oxford

Michaelmas Term 2024

Words: 44,061

Abstract

Viral infections are a leading cause of death. Recognition of viruses by cellular sensors (such as RIG-I, MDA5, and cGAS) is a crucial step in the initiation of immune responses and therefore is a common target for viral antagonism. Similarly, mutations in these sensor pathway components can cause malfunction and increase susceptibility to severe infection.

At the beginning of my DPhil, I contributed to a study showing that MDA5 was a sensor of SARS-CoV-2 infection. Once activated by viral RNA, MDA5 interacts with MAVS that then induces transcription of IFNs and ISGs. The aggregation of MAVS via its CARD domain is crucial to initiate this signalling cascade. Leaky ribosomal scanning of the *MAVS* transcript causes ribosomes to skip the first AUG start codon. Translation then initiates at one of multiple downstream AUGs, resulting in five N-terminally truncated proteins isoforms of MAVS, all lacking the CARD domain. Truncated MAVS isoforms prevent the aggregation of full-length MAVS and its activation. Single nucleotide polymorphisms (SNPs) in the *MAVS* gene were found to be associated with severe COVID-19. Interestingly, these SNPs are at or near to translation start sites along the *MAVS* transcript. I generated MAVS constructs harbouring these SNPs to determine the effect on MAVS protein translation, activation potential, and its relation to COVID-19 severity. I hypothesized that $MAVS^{C5T}$ results in ribosomal skipping of the first start codon due to a weakened Kozak sequence. Indeed, cells expressing $MAVS^{C5T}$ contained reduced levels of full-length MAVS protein. I showed that HEK293 and Huh7 cells reconstituted with $MAVS^{C5T}$ exhibited reduced ISG and IFN induction after stimulation with RIG-I and MDA5 agonists, while the opposite was true for $MAVS^{G1074C}$, a polymorphism that removes a downstream AUG. Moreover, $MAVS^{C5T}$ expressing cells showed reduced aggregation of MAVS at baseline and after stimulation. In sum, I provide a model explaining how *MAVS* SNPs found in SARS-CoV-2 infected patients contribute to severe COVID-19 by revealing differential MAVS signalling caused by these variants.

In a second line of research, I helped establish that the DNA sensor cGAS was inhibited by varicella-zoster virus's (VZV) ORF9 protein. In uninfected cells, nuclear cGAS is inhibited by binding to the acidic patch of the nucleosome, formed by the H2A-H2B dimer. Interestingly, VZV ORF9 displays sequence similarity to the acidic patch. Viruses often adapt host-like features to disrupt or hijack the host machinery to promote their proliferation. I hypothesized that ORF9 mimics the acidic patch to bind and inhibit cGAS. HEK293T, THP1, and HFF cells were transiently transfected or transduced to express wild-type ORF9 or ORF9 mutants in which negatively charged amino acids in ORF9's putative acidic patch were substituted with positively charged residues. These cells were then stimulated with dsDNA, and cGAS activation was measured by RT-qPCR, cGAMP ELISA and a STING-based FRET assay. Compared to ORF9 WT, which inhibited cGAS, $ORF9^{E211R}$ and $ORF9^{E211R/E227T}$ lost the ability to suppress IFN/ISG induction. In agreement, $ORF9^{E211R}$ and $ORF9^{E211R/E227T}$ did not block cGAMP production. AlphaFold modelling and RMSD values indicate similarities between the tertiary structure of ORF9 and H2A-H2B. Taken together, I propose a novel histone mimicry strategy employed by VZV to inhibit cGAS and downstream cytokine production.

Acknowledgements

Firstly, I would like to thank both past (Dr. Jonny Hertzog, Dr. Natalia Sampaio, Dr. Valerie Odon, Isobel Davis, Dr. Rachel Rigby, and Dr. Henry Blest) and present (Alex Redmond, Dr. Anne Bridgeman, Anna Rozina, Svea Wupper, Lizzie Horton, Aleksandr Fedorov and Dr. Tanja Davis) members of the Rehwinkel laboratory for their troubleshooting, moral support, scientific discussion, festive Christmas decorating and wonderful cake clubs. Particular thanks go to my early program supervisor, Jonny, for training and helping me generate my VZV project. Henry for his endless optimism, unwavering support and for the countless experiments he has helped me troubleshoot. I am very grateful to have supervised Svea Wupper during her MSc placement, an absolutely brilliant student who really didn't require much of my help, and I am happy has decided to join our lab for a DPhil. To the Maelfait lab for their advice and comradery during our lab retreat.

I would like to thank my dear friend Ali Sutherland, who was so greatly supportive during my MSc and after my move to the UK. Her encouragement and advice to apply for the Rothermere fellowship and to the University of Oxford have been some of the best advice I've ever received.

I am truly blessed to have the dearest friends Thatcher Flynn, Amy Rideout, Quinn Durand, Seana Wood, and Blake Colbourne. To the warm support of all my Oxford friends, and my lab mates Lizzie and Isobel who have become some of my most cherished friends.

To Summer, my dog and best friend, who saw me through high school, undergrad, masters and writing of my DPhil thesis. She was the light at the end of every day – I miss her terribly.

To Stephen, my partner, for being so supportive during my countless nights of writing and, despite not being a scientist, has listened to me excitingly ramble on about histone mimicry. His support during my move to a new country during the height of the COVID pandemic got me through an incredibly tough time. His companionship during my DPhil journey has been invaluable to me, I truly could not have done this without him.

To my amazing parents for their unyielding support – which is a lot when you consider 12 years of post-secondary education. I am so incredibly lucky to have them both in my corner. Their advice, love and encouragement are appreciated beyond words – I could not have done this without them. I love you both forever.

To Eileen Parkes and Colin Crump for reviewing my thesis. To Graham Ogg, Ling-Pei Ho, Emily Thornton, and Samana Sanyal for being my Thesis Committee and Transfer of Status examiners.

To Christian Zierhut and Vincente Lebrec for sharing their STING-FRET reporter, which provided exciting data in support of my hypothesis. To Alex for helping me set up and teaching me flow cytometry and FlowJo. To Johnathan Cooper-Knock and Kenneth Baillie for their computational collaboration towards my MAVS project. To Karim Rafie for our exciting ongoing work visualizing ORF9-cGAS. To Kendra Leigh for her generation of ORF9 images in ChimeraX.

To Henry Blest and Shaye Murray for helping me tediously edit my introduction chapter.

To the Rothermere Foundation for their exceeding generous financial support during my DPhil. A fellowship that includes one flight home a year has allowed me to spend Christmas with my family every single year – an otherwise cost-prohibitive venture when you're someone who lives in the sticks of Canada. To the Natural Sciences and Engineering Research Council of Canada for funding my DPhil studies.

Finally, and most importantly, I would like to thank Jan Rehwinkel for his exceptional supervision and supportive work environment. I am eternally grateful for the work and supervision he caters to each of us. I cannot imagine having done my DPhil in any other lab. His support extends beyond my DPhil, as he has already proven to be a supportive mentor for my future scientific journey. It has been an absolute privilege to work with him and I have thoroughly enjoyed my time in his lab.

I would be remiss for not accrediting RedBull in fueling my DPhil and the writing of this thesis.

COVID Statement

I started my DPhil in October 2020, which resulted in disruptions to my introduction to the lab, training, supervision, and mentoring opportunities. The first year of my DPhil was particularly affected as capacity in the lab was reduced to one person per bay to accommodate social distancing (i.e. only 3-4 lab members present at a time), which was managed by a staggered scheduling system. Training was particularly difficult as most members were working from home, and one-on-one training had to take place in advanced PPE. Collaborations and scientific discussions with other labs were all but non-existent at this time. Facilities training was also reduced at this time and operated at reduced capacity. These disruptions resulted in slower progression during my first year, with the end result of less time for data collection. However, I have made significant progress with both my VZV and MAVS projects and plan to continue data collection during my six-month funding extension (Oct 2024 – April 2025) provided by the Rothermere Foundation, towards the end goal of a publication for each project.

Table of Contents

Abstract ..... ***i***

Acknowledgements ..... ***ii***

COVID Statement ..... ***iv***

Acronyms ..... ***v***

Introduction ***1***

1.1 Innate Immunity and Pattern Recognition 1
1.1.1 Sensing cytosolic DNA 3
1.1.1.1 cGAS/STING Signalling Pathway 3
1.1.1.1.1 Regulation of cGAS Activation 6
1.1.1.1.2 cGAS pathologies 9
1.1.1.1.3 Localization of cGAS and Interaction with Nuclear Components 10
1.1.1.1.3.1 Localization of cGAS 10
1.1.1.1.3.2 Nucleosome Inhibition of cGAS 12
1.1.1.1.3.2.1 What happens to nuclear cGAS? 15
1.1.1.2 Other DNA sensors 16
1.1.1.2.1 TLRs 17
1.1.1.2.2 RNA Polymerase III 18
1.1.1.2.3 DNA-PK 18
1.1.1.2.4 IFI16 & AIM2 18
1.1.1.2.5 ZBP1 19
1.1.2 Sensing of Cytosolic RNA 20
1.1.3 Function of IFNs 22
1.1.2.1 Regulation of RNA sensing pathway 24
1.1.2.2 Regulation of MAVS Activation 24
1.1.2.2.1 Post-transcriptional Modifications to *MAVS* 25
1.1.2.2.2 Post-Translational Modifications to MAVS 26
1.1.2.2.2.1 Positive Regulation of MAVS By Post-Translational Modification 27
1.1.2.2.2.2 Negative Regulation of MAVS By Post-Translational Modification 28
1.1.2.2.3 Viral Regulation of MAVS 28

1.3 Research Objectives 30

Materials & Methods ***32***

2. 1 Materials 32
2.1.1 Cells 32
2.1.2 Viruses 34
2.1.3 Plasmids 35
2.1.4 Oligonucleotides 37
2.1.5 TaqMan Probes 38
2.1.6 Antibodies 38
2.1.7 General Reagents 39

2.2 Methods 41
2.2.1 Lentiviral Expression Constructs 41
2.2.2 Lentiviral Production and Transduction 42
2.2.3 IFN Bioassay 43
2.2.4 Dual Luciferase Assay 43
2.2.5 Flow cytometry for STING FRET Assay 44
2.2.6 Western Blotting 44
2.2.7 Immunoprecipitation 45
2.2.8 Recombinant Protein Pull-Down Assays 46
2.2.9 RT-qPCR 47
2.2.10 RLR Stimulations 47
2.2.11 MAVS Aggregation Assay 48

2.2.12 VZV Co-Infection via Co-Culture 48
2.2.14 Conditional Degradation of VZV-ORF9 49
2.2.15 VZV Infection in a Transwell System 49
2.2.16 DNA Stimulation 50
2.2.17 ELISA 50
2.2.17.1 IFNβ and IP-10 ELISA 50
2.2.17.2 cGAMP ELISA 51
2.2.18 STING Stimulations 51
2.2.19 Protein Structure Predictions 52
2.2.20 Data Analysis and Software 52

Polymorphisms Alter Translation and Function of MAVS 53

3.1 SARS-CoV-2 53
3.1.1 Origin story 53
3.1.2 Pathology & Epidemiology 54
3.1.3 The SARS-CoV-2 Genome 56
3.1.4 Replication & Life Cycle 57
3.1.5 Experimental Models of SARS-CoV-2 60
3.1.6 Immune Evasion by SARS-CoV-2 63

3.2 Establishment of MAVS as an Important Component in the Recognition of SARS-Cov-2 Infection 65

3.3 Translation Initiation by Ribosomes 69

3.4 Leaky Ribosomal Scanning of *MAVS* 70

3.5 Single Nucleotide Polymorphism Screen of *MAVS* 72

3.6 SNPs Within MAVS Alter the Ratio of Translated FL Protein 75

3.7 RNA Sensing Ability of *MAVS* Mutants in HEK293 Cells 78
3.7.1 MAVS-C5T Exhibits Reduced Activity in Transfected HEK293 Cells 79
3.7.2 MAVS-C5T Exhibits Reduced Activity in Transduced HEK293 Cells 82

3.8 MAVS Mutants Form Fewer Aggregates Than WT-MAVS 84

3.9 MAVS-C5T Exhibits Reduced Activity in Transduced Huh7 Cells 86

3.10 Discussion 90

Innate Immune Recognition of Varicella Zoster Virus 94

4.1 Introduction 94
4.1.1 Virology & The Genome 94
4.1.2 Pathology & Epidemiology 96
4.1.2.1 Epidemiology 97
4.1.3 Replication & Life Cycle 99
4.1.4 In Vivo Models 102
4.1.5 Immune Response To VZV 103
4.1.5.1 Apoptotic Response 103
4.1.5.2 Innate Response 103
4.1.5.3 Adaptive Response 104
4.1.5.4 Immune Modulation 106
4.1.6 Societal Impact of VZV 107
4.1.7 Summary 108

4.2 Results 109
4.2.1 VZV-ORF9 is Responsible for Inhibition of the cGAS-STING Signalling Axis During Infection 109
4.2.2. Revision Work 112
4.2.2.1 ORF9 Inhibition of IFN Induction Does Not Involve Antagonism of STING 112
4.2.2.2 ORF9 Predicted DNA Binding Region is Dispensable for cGAS Binding 113
4.2.2.3 Conditional Knockout of ORF9 Attenuates cGAS Inhibition 114
4.2.2.4 VZV Infection Prevents Interferon Production in Keratinocyte and Fibroblast Cells 121

4.3 Discussion 124
VZV-ORF9 Acts as a Histone Mimic to Inhibit cGAS 127
5.1 Viral Inhibitors of cGAS 127
5.2 Investigating Histone and ORF9 Similarities. 130
5.3 Mutating ORF9 Residues Homologous to Histones Reduces its Ability to Antagonize cGAS. 133
5.4 ORF9 Mutants Exhibit Reduced cGAS Inhibition in Transduced HFFs. 137
5.5 ORF9 Mutants Exhibit Reduced cGAS Inhibition in Transfected HEK293T Cells as Measured by FRET Assay. 141
5.6 Binding Interactions of ORF9 Mutants with cGAS. 146
5.6.1 cGAS-ORF9 Binding Interactions are Highly Salt Resistant. 147
5.6.2 VZV-ORF9 Forms a Complex with H2A-H2B and cGAS. 148
5.7 ORF9 Protein Structure Predictions. 151
5.8 Discussion 154
Discussion 162
6.1 Objective 1: Importance of MAVS SNPs for Induction of the IFN Response (Chapter 3) 162
6.2 Objective 2: Mechanism of VZV-ORF9 Inhibition of cGAS (Chapters 4 & 5) 165
Bibliography 166
List of Figures 235
Supplemental Figures I
Appendix VI

Acronyms

AA	Amino acid
ACE2	Angiotensin-converting enzyme 2
ADAR1	Adenosine deaminase acting on RNA 1
APCs	Antigen presenting cells
ATP	Adenosine 5’-triphosphate
Bp	Base pairs
BSA	Bovine serum albumin
CARD	Caspase activation and recruitment domain
cGAMP	2'3'-cyclic GMP-AMP
cGAS	Cyclic GMP-AMP synthase
CMV	Cytomegalovirus
COVID-19	2019 novel coronavirus
CTD	Carboxy terminal domain
Cyro-EM	Cryogenic electron microscopy
DAMP	Damage-associated molecular pattern
DC	Dendritic cell
DNA	Deoxyribonucleic acid
DNA-PK	Dependent protein kinase
E	Envelope protein
ecDHFR	*E. coli* dihydrofolate reductase
eIF2α	Eukaryotic translation initiation factor 2A
EMCV	Encephalomyocarditis virus
ENPP1	Ecto-nucleotide pyrophosphatase/phosphodiesterase
EPI	Epiblastin
ER	Endoplasmic reticulum
ERGIC	ER-to-Golgi intermediate compartment
ETI	Effector-triggered immunity
FACS	Fluorescence-activated cell sorting
FCS	Fetal calf serum
FL	Full-length
GTP	Guanosine 5’-triphosphate
hcGAS	Human cGAS
HCV	Hepatitis C virus
HFF	Human foreskin fibroblast
hPAF1C	Human PAF1 transcription elongation complex
HRP	Horseradish peroxidase
HSV-1	Herpes simplex virus 1
HSV-2	Herpes simplex virus 2
IAV	Influenza A virus
IE	Immediate early
IFNAR	IFNα receptors
IFNLR	IFNλ receptors
IKKε	IκB kinase –ε
IP	Immunoprecipitation
iPSCs	Human-induced pluripotent stem cells
IRF3	Interferon regulatory factor 3

IRF9	Interferon regulatory factor 9
ISG	Interferon stimulated Gene
ISRE	Interferon-stimulated response element
IVT	*In vitro* transcribed
KSHV	Kaposi's sarcoma-associated herpesvirus
L-G	L-glutamine
LGP2	Laboratory of genetics and physiology 2
M	Membrane protein
MAVS	Mitochondrial antiviral signalling protein
mcGAS	Murine cGAS
MDA5	Melanoma differentiated-associated protein 5
MEM	Minimal Essential Medium
MERS	Middle East respiratory syndrome coronavirus
MHC-I	Major histocompatibility complex class 1
MOI	Multiplicity of infection
MS	Multiple sclerosis
N	Nucleocapsid protein
NCP	Nucleosome core particle
NFκB	Nuclear factor-κB
NHEJ	Non-homologous end joining
NMR	Nuclear magnetic resonance
NP	Nucleocapsid protein
NS1	Non-structural protein 1
ORF	Open reading frame
PAMP	Pathogen-associated molecular patterns
PARP1	Poly ADP-ribose polymerase 1
PBS	Phosphate buffered saline
PCR	Polymerase chain reaction
pDC	Plasmacytoid dendritic cell
PIC	Preinitiation complex
PKR	Protein kinase R
PMA	Phorbol 12-myristate 13-acetate
pOka	Parental Oka
PRR	Pattern recognition receptors
PTM	Post translation modification
RBD	Receptor binding domain
RIG-I	Retinoic-acid inducible gene
RLRs	Retinoic-acid inducible gene-like receptors
RNA	Ribonucleic acid
RNA Pol III	RNA polymerase III
RPMI	Roswell Park Memorial Institute medium
RSMD	Root mean square deviation
RT-qPCR	Quantitative reverse transcription PCR
RTC	Replication and transcription complex
S	Spike protein
SARS-CoV-1	Severe acute respiratory syndrome coronavirus 1
SARS-CoV-2	Severe acute respiratory syndrome coronavirus 2
SEAP	Secreted embryonic alkaline phosphatase
SeV	Sendai virus

SLE	Systemic lupus erythematosus
SLiMs	Short linear motifs
SMPC	Small-molecule pharmacological chaperones
STING	Stimulator of interferon genes
SUMOylation	Small ubiquitin-like modifier modification
T1D	Type I diabetes
TAF-I	Template-activating factor I
TBK1	TANK-binding protein 1
TCP	TC-P 262
TLR	Toll-like receptor
TM	Transmembrane domain
TMP	Trimethoprim
TREX1	Three prime repair exonuclease 1
TRI	Triamterene
TYK2	Tyrosine kinase 2
UL	Long region
uORF	Upstream open reading frame
US	Short region
UTR	Untranslated region
VACV	Vaccinia virus
VLT	VZV latency-associated transcript
VSV	Vesicular stomatitis virus
VZV	Varicella zoster virus
ZBP1	Z-DNA binding protein 1

Chapter 1

Introduction

1.1 Innate Immunity and Pattern Recognition

In vertebrates, the host is protected from infection by pathogens by two branches of immunity, the innate and adaptive[1–3]. The term 'innate' describes factors belonging to or existing since birth. In the context of immunity, it describes the branch of the immune system a person is born with that does not undergo genetic rearrangement in response to an infection[4–6].

The innate system is composed of physical, chemical and biological barriers. The skin acts as a physical barrier to prevent pathogens from penetrating internal tissues, while antimicrobial peptides, lysozymes and stomach acidity protect the mucosal surfaces[2,6,7]. If these barriers are overcome, the complement system utilizes a series of proteins to lyse invading bacteria and neutralizing antibodies are produced by the adaptive immune system[2,6].

The first critical step in initiating an immune system response is the recognition of foreign material. In 1989, Charles Janeway first hypothesized the existence of germline-encoded pattern recognition receptors (PRRs) that are specialized to detect conserved pathogen-associated molecular patterns (PAMPs)[1,3,5,6,8]. These PRRs recognize fungi, viruses, bacteria, and parasites that often make primary contact with the mucosal surface of the respiratory system[6,9]. PRRs are secreted, embedded in transmembranes or present in the cytoplasm. While some PRRs can directly bind to pathogens, most sense microbe-associated molecular patterns (MAMPs). Nucleic acids can also act as PAMPs to activate specialized PRRs, or as damage-associated molecular patterns (DAMPs) in the context of non-infectious activation, i.e. sterile inflammation.

DNA and RNA originating from bacteria, fungi, viruses or host organelles can be recognized by nucleic acid sensors, which are categorized as PRRs. cGAS is one of the main cytosolic DNA sensors in mammals, while RIG-I and MDA5 detect cytosolic RNA

(Fig. 1, A)[10–14]. These PRRs transmit signals through downstream adaptors to initiate the transcription of type I interferons (IFNs). IFNs bind to receptors on the same and nearby cells to signal for the induction of transcription of interferon-stimulated genes (ISGs). Both IFNs and ISGs have anti-viral functions[10,11,15,16].

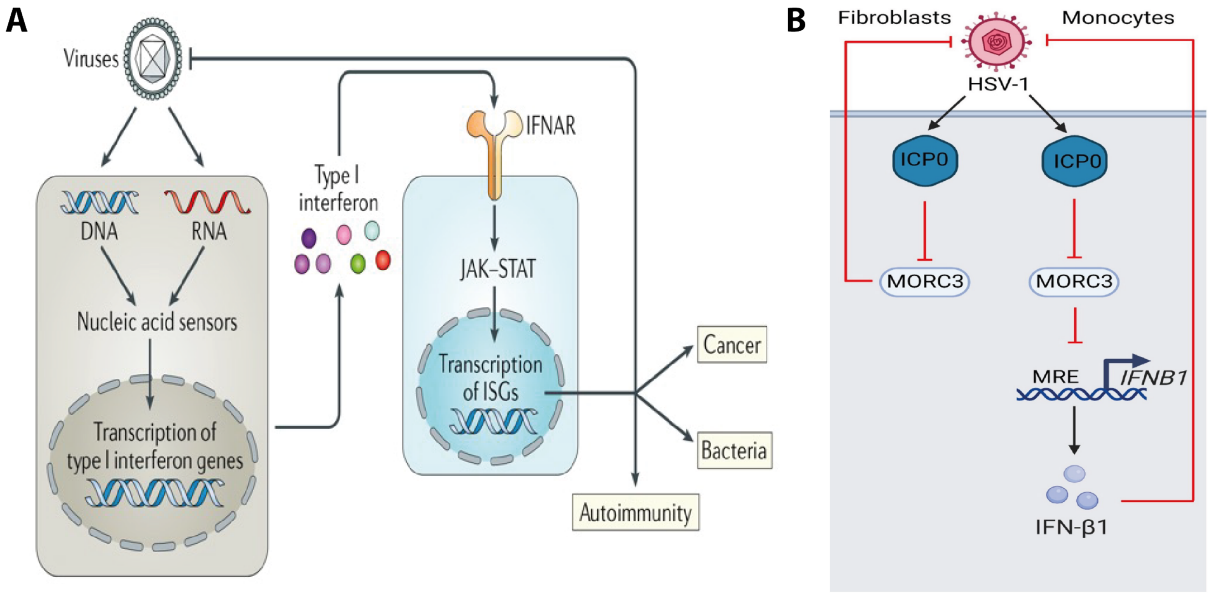


Figure 1: Pathogen Triggered Immunity.
(**A**) PAMP-triggered immune response is triggered by the detection of viral DNA or RNA by pattern recognition receptors (PRRs) in the cytoplasm. The detection by PRRs initiates the transcription of type I interferons (IFNs) which induce bystander cells to transcribe interferon stimulated genes (ISGs). (**B**) HSV-1 encodes an E3- ubiquitin ligase ICP0, which degrades host MORC3. MORC3 regulates *IFNβ1* expression by inhibiting its transcription. MORC3 is targeted for degradation by ICP0 as it has anti-viral functions during HSV-1 infections, however the loss of MORC3 increases *IFNβ1* expression. This system is an example of effector triggered immunity (ETI) as IFNβ1 production is independent of direct HSV-1 detection by PRRs. Panel A is from Rehwinkel & Gack 2020. doi: 10.1038/s41577-020-0288-3. Panel B is from Orzalli & Parameswaran 2022. doi: 10.1016/j.it.2022.10.004.

In contrast to PAMP-triggered immune responses, effector-triggered immunity (ETI) is based on the detection of enzymatic activities of pathogen proteins or the effects of their expression[17,18]. An interesting example of ETI is found during HSV-1 infection in monocytes. HSV-1 encodes an E3 ubiquitin ligase, ICP0, that degrades host MORC3 (Fig. 1, B)[17,19–21]. MORC3 functions to inhibit *IFNβ1*, an anti-viral cytokine. By degrading MORC3, the cell is promoted to produce more anti-viral cytokines, thereby clearing HSV-1 infection, all without directly sensing HSV-1 infection[17,19–21].

The reproductive cycle of viruses necessitates the hijacking of host machinery to successfully replicate; as such evolutionary selection shapes and reshapes mechanisms of anti-viral evasion including PRRs and their signalling pathway components[22].

1.1.1 Sensing cytosolic DNA

1.1.1.1 cGAS/STING Signalling Pathway

Long before Janeway described PRRs, it was shown that viral particles containing viral nucleic acids could induce the production of interferons, thereby priming the immune system. However, particles without nucleic acids could not[15,23] – indicating that it's the presence of viral nucleic acids in the cell that triggers innate immune responses.

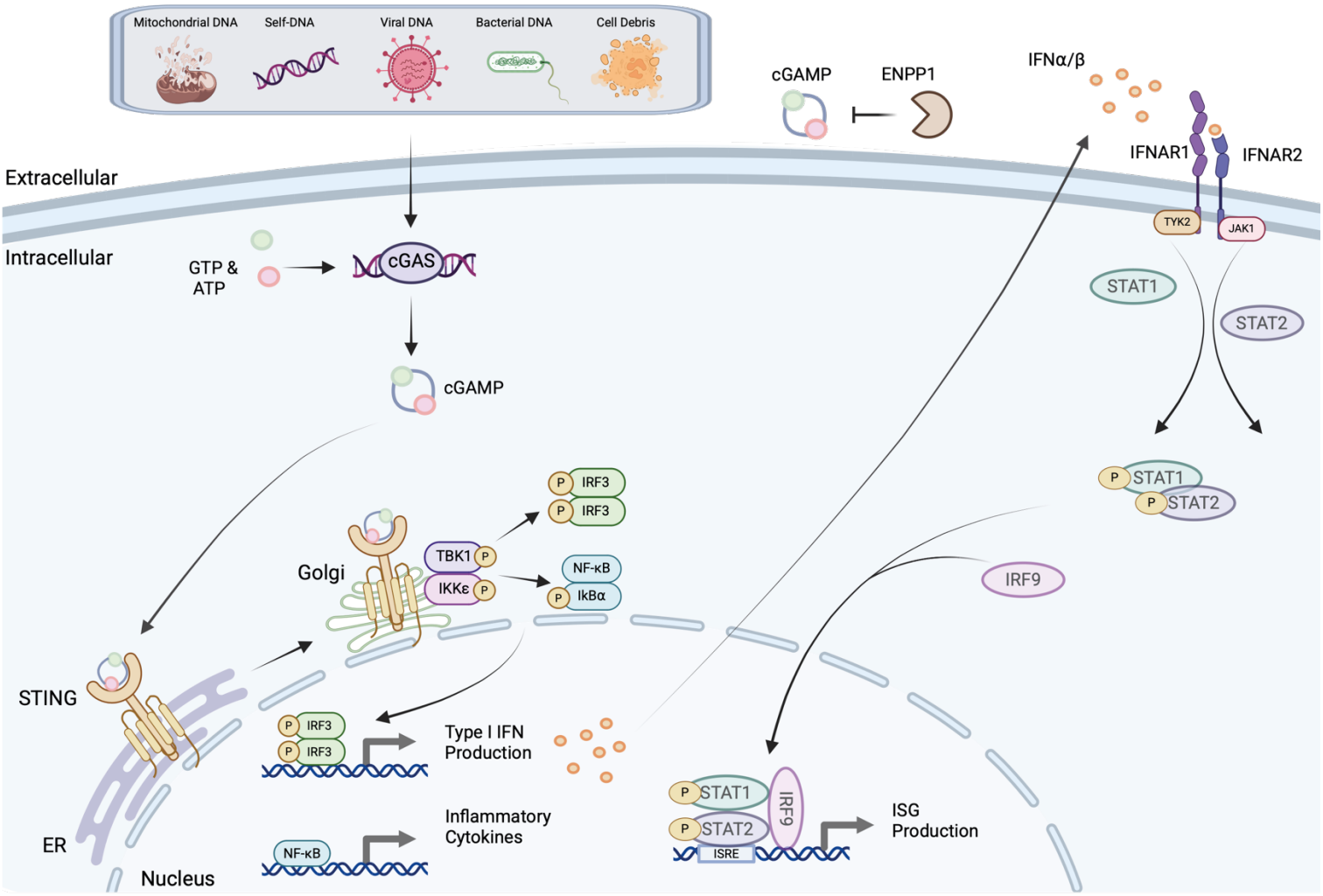


Figure 2: The cGAS-STING Signalling Pathway.
The presence of dsDNA in the cytoplasm binds and activates cGAS, which catalyzes the production of cGAMP. cGAMP binds to STING, which initiates a downstream signalling cascade to ultimately produce IFNs and inflammatory cytokines. These cytokines stimulate the production of ISGs within the cell and bystander cells. Made with BioRender.

In 2013, back-to-back publications by Wu *et al*. and Sun *et al*. ended the race to find the proposed cytosolic DNA sensor - the DNA sensor cyclic GMP-AMP synthase (cGAS)[12,24]. cGAS and its secondary messenger 2'3'-cyclic GMP-AMP (cGAMP) were discovered to be the mediators of type I IFN production after DNA stimulation[12–14,24–27]. cGAS is localized in the cytosol in an autoinhibited state during baseline physiological conditions[6]. It is also localized to the nucleus and inhibited by nucleosomes[28–33]. It is specialized to recognize (sequence-independent) B-form dsDNA with a minimal length of 40bp[34] and when bound to dsDNA, undergoes a conformational change[10,12,35].

Stimulatory dsDNA can be viral, bacterial, or, as a result of cellular damage, nuclear and mitochondrial (Fig. 2). After binding to DNA, cGAS synthesizes 2'3'-cyclic guanosine monophosphate-adenosine monophosphate (2'3'-cGAMP, herein referred to simply as cGAMP) from adenosine 5'-triphosphate (ATP) and guanosine 5'triphosphate (GTP)[6,10,13,25,27]. The DNA-induced rearrangement of the catalytic site allows ATP and GTP to bind and catalyze the synthesis of cGAMP to occur[35]. While dsRNA can bind cGAS, neither it nor ssDNA can induce a conformational change that would allow for cGAMP production[36]. However, DNA:RNA hybrids in the cytoplasm can activate cGAS[37–40]. cGAMP acts as a secondary messenger by binding the stimulator of interferon genes (STING) protein and thereby triggering an antiviral signalling cascade[10,13,25,27].

STING, first discovered in 2008[41,42], is a transmembrane protein primarily localized to the endoplasmic reticulum (ER) in an unstimulated state and undergoes relocation to the Golgi complex after the binding of cGAMP[5]. STING can bind to bacterial cyclic dinucleotide secondary messengers but cGAMP was the first host messenger known to activate this pathway[6]. STING activation and relocation from ER leads to the formation of autophagosomes. After activation of STING by phosphorylation, STING in the Golgi is trafficked into lysosomes for degradation via autophagy[43,44]. One regulatory protein of STING - SRUF4 is an adaptor protein that facilitates retrograde transport of STING from the Golgi back to the ER to prevent activation at steady state[43,45–47], however, there are many other regulators of STING.

Stimulated STING activates the kinases TANK-binding kinase 1 (TBK1) and IκB kinase –ε (IKKε), which recruit and phosphorylate the transcription factors IRF3 and NFκB[10,13,35,41]. Phosphorylated IRF3 forms a dimer and enters the nucleus, where together with NFκB it acts as a transcription factor for the transcription of inflammatory cytokines, type I IFNs and type III IFNs[6,10,35]. The function of type I IFNs and type III IFNs will be discussed in a later section.

1.1.1.1.1 Regulation of cGAS Activation

cGAS activation is at the forefront of the innate immune response and while protective in infectious and malignant diseases, it must be tightly controlled to prevent chronic stimulation in response to self-DNA to prevent autoimmunity. Many mechanisms are in place to control both cGAS and STING signalling. cGAS detects >40bp long dsDNA in the cytosol in a sequence-independent manner, where under physiological conditions dsDNA would not normally be. In virally infected or cancerous cells DNA can leak from the nucleus. Similarly, viral infection can promote the formation of mitochondrial permeability transition pore (mPTP), VDAC pore, and BAX/BAK-mediated pores, which drive mitochondrial outer membrane permeabilization and release mtDNA into the cytosol[48–51]. The dsDNA genomes of DNA viruses such as HIV and HSV-1 are detected by cGAS[52–59]. Therefore, cGAS detects the mislocalization of DNA commonly associated with pathology. dsDNA-cGAS complexes can be composed of as little as 15-20bp, however, >40bp is required for robust cGAS activation[60].

Under physiological conditions, some dsDNA leaks into the cytoplasm but levels are controlled by the exonuclease three prime repair exonuclease 1 (TREX1), which degrades ssDNA in a 3' to 5' direction at baseline[10,61]. Exemplifying the importance of TREX1, mice lacking *Trex1* experience a lethal inflammation phenotype, with an average lifespan of ~110 days. These effects are rescued by the deletion of *cGAS, STING, IRF3* and *IFNAR*[36,62–64]. Interestingly, a single allele knockout of either *cGAS* or *STING* is sufficient to rescue lethality in *Trex1*-KO mice, potentially related to cGAS phase separation (described below). Mutations in *TREX1* are linked to Aicardi-Goutières syndrome (AGS) in humans, which is characterized by early onset of chronic inflammation[36,65]. Molecules will dissolve in solution until reaching their solubility limit, at which point they form non-membrane bound compartments[66], due to liquid-liquid phase separation (LLPS)[67]. LLPS is crucial for the formation of subcellular structures such as heterochromatin, stress granules, membrane receptor clusters and nuclear pore transport channels[67–71]. The separation changes the interaction of nucleic acids and proteins away from predominantly interacting with water molecules to other macromolecules in an energetically favourable process[10,67]. Immunostimulatory DNA

forms liquid-liquid phase separated droplets with cGAS in the cytosol, thereby sequestering DNA from degradation by TREX1[34,72]. AGS causative mutations in *TREX1* mislocalize TREX1 inside cGAS-DNA LLPS condensates, wherein the phase separation droplets suppress TREX1 exonuclease activity[72].

Another mediator of cytoplasmic DNA levels is endosomal DNase II, which mediates the degradation of endocytosed DNA. DNase II deficient mice are embryonically lethal as a result of chronic inflammation[63,73]. The loss of cGAS or STING rescues the phenotype as the host sensing pathway is no longer activated, suggesting an important role for DNase II in the removal of immunostimulatory DNA[36,63,73]. How endosomal dsDNA escapes into the cytosol for detection by cGAS is an important question for future research.

Of note, the stimulation of STING does not only originate from activated cGAS within the same cell. cGAMP is regulated and transported between cells in several ways. Free cGAMP can activate neighbouring cells by transport through gap junctions, cGAMP channels (SLC19A1, SLC46A2, LRRC8A:C, LRRC8A:E and ABCC1), and ATP-regulated pores (P2X7)[74–80]. cGAMP is packaged into virions and transported to neighbouring cells, stimulating STING and downstream anti-viral signalling[81,82]. cGAMP is hydrolyzed by ecto-nucleotide pyrophosphatase/phosphodiesterase (ENPP1) in the extracellular space[83]. Another metazoan cGAMP hydrolase, ENPP3, also degrades extracellular cGAMP; however, it possesses an expression pattern distinct from ENPP1[84]. *ENPP1* and *ENPP3* are expressed in breast and prostate tissues, while *ENPP1* is expressed primarily in the placenta and liver and accounts for the majority of hydrolase activity in mouse plasma[84]. *ENPP3* is predominantly expressed in the small intestine and basophils[84]. Lysates from tissues of mice harbouring a combined missense mutation in ENPP1 and ENPP3$^{-/-}$ show no detectable cGAMP hydrolpase activity, providing evidence that these are the predominant cGAMP hydrolases[84]. Recently a third cGAMP hydrolase was discovered, sphingomyelin phosphodiesterase acid-like 3A (SMPDL3A), however, the enzymatic activity required induction of liver X receptor ligands[85] - potentially indicating enzymatic activity is tissue specific.

Post-translational modifications (PTMs) also regulate the activation of cGAS and STING. TRIM56 and TRIM32 are two E3 ubiquitin ligases that target STING and positively regulate signalling[86–88]. In one study an E3 ubiquitin ligase of cGAS, RNF185, was shown to enhance enzymatic activity during HSV-1 infection [86,89], while another E3 ubiquitin ligase, RNF5, reduced the immune response by targeting STING[90]. Conversely, glutamylation and SUMOylation have been shown to positively and negatively regulate cGAS activity[91–93]. Poly ADP-ribose polymerase 1 (PARP1) attaches negatively charged ADP-ribose to an asparagine on cGAS, thereby preventing DNA binding and negatively regulating both IRF3 and NFκB signalling[94–96]. These examples of cGAS/STING PTM (Fig. 3) regulation are not an exhaustive list of all PTMs. The vast array of mechanisms by which cGAS activation is regulated shows the complexity of innate immune signalling – it also presents a multitude of targets for viral antagonism.

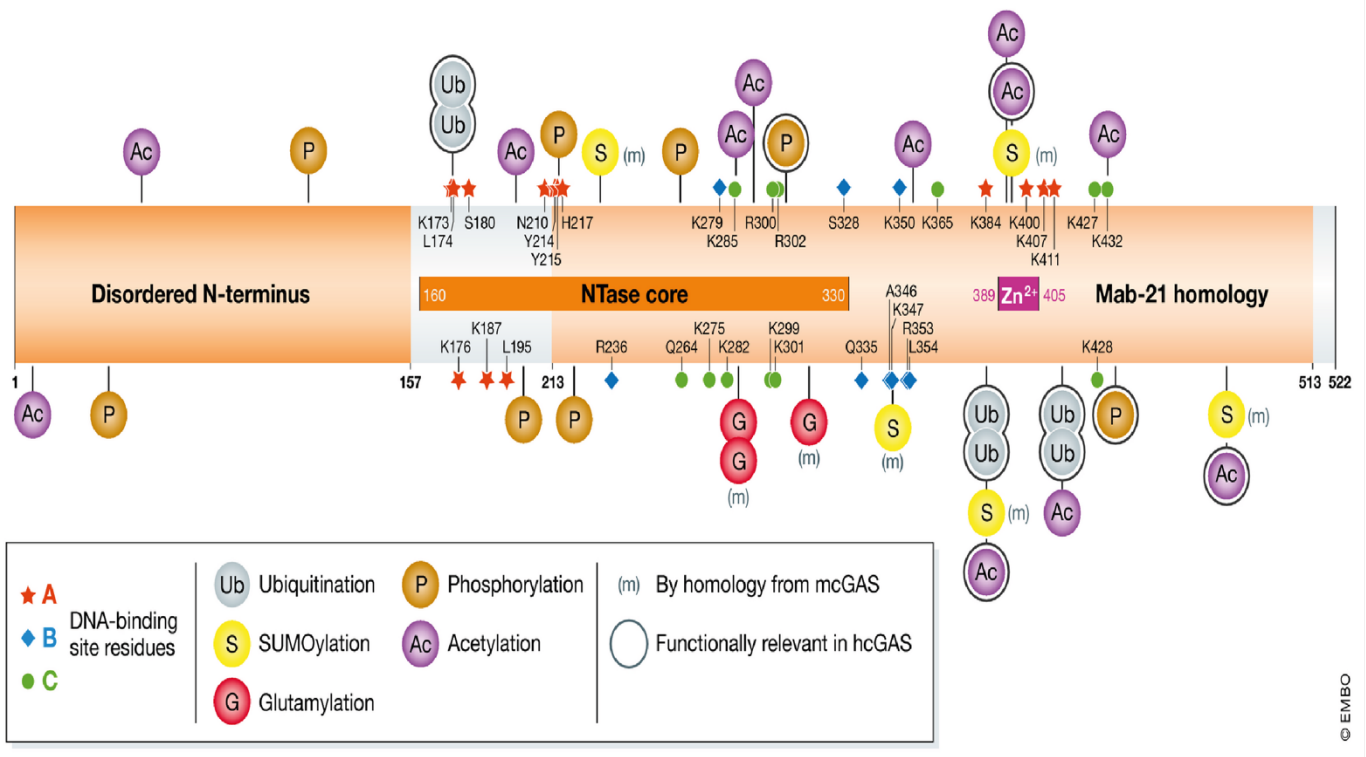


Figure 3: Post-Translational Modification of cGAS.
Numbers indicate amino acids along the cGAS transcript. Residues that contribute to DNA binding are indicated with star, diamond or circle symbols. All post-translational modification sites along cGAS are indicated with a circle - the circles with a border indicate residues with annotated function in human cGAS. Residues with a (m) are post-translational modifications described in mouse cGAS that are predicted at these homologous positions along human cGAS. Figure taken from Hertzog & Rehwinkel 2020. doi: 10.15252/embr.202051345.

1.1.1.1.2 cGAS pathologies

Activation of the cGAS-STING pathway by self-DNA underlies a number of autoimmune, and autoinflammatory diseases, notably several type I interferonopathies[10]. Stimulating cytosolic self-DNA can be nuclear or mitochondrial in origin, but the route to the cytosol varies.

Mutations in *TREX1, RNASEH2A, RNASEH2B, RNASEH2C, LSM11, RNU7-1, SAMHD1,* adenosine deaminase acting on RNA 1 *(ADAR1)*, and *IFIH1* are known to cause AGS and many of which lead to accumulation of DNA to the cytosol, inducing chronic activation of cGAS/STING[97]. AGS is defined by chronically elevated type I IFNs causing progressive encephalopathy, however, the precise clinical manifestations are dependent on the gene affected[10,65,98–101]. Systemic lupus erythematosus (SLE) patients have elevated IFN in their serum and mutations in TREX1 are known to cause SLE phenotypes in some patients, suggesting a role of aberrant cGAS signalling[102,103]. Increased levels of the E3 ubiquitin ligase RNF185 lead to cGAS-STING induction[10,86]. Elevated levels of RNF185 mRNA were found in the serum of SLE patients suggestive of a causative mechanism underlying chronic inflammation[86]. Excessive activation of cGAS-STING is linked to stroke, aging and neurodegenerative diseases including ataxia telangiectasia, Huntington's disease, and Parkinson's disease[104,105].

Type I IFNs have a defined role in controlling anti-tumour responses, including by inducing the expression of pro-apoptotic and anti-proliferative genes[106]. The overactivation of STING triggers T-cells to perform anti-tumour and pro-apoptotic functions[105–112]. Interestingly, transient expression of STING increases anti-tumour immunity by promoting T-cell recruitment and priming. At the same time, chromosomal instability-driven chronic activation of STING drives downstream activation towards pro-tumour pathways such as STAT3 and non-canonical-NF-κB, rather than the canonical anti-tumour IFNAR signalling[106]. cGAS is frequently mutated or silenced in cancer cell lines, suggesting it also has anti-tumour function. Indeed, cGAMP transferred between cells increases anti-tumour responses in bystander cells[83,113].

However, in many types of cancers, cGAS/STING expression is maintained or even increased in tumour tissues, suggesting a pro-tumour role[114–120]. Ultimately, cGAS-STING's role in anti and pro-tumour proliferation is likely cell-type and cancer-specific and requires further study.

1.1.1.1.3 Localization of cGAS and Interaction with Nuclear Components

cGAS is composed of 520 amino acids with an unstructured, basic 160 amino acid flexible N-terminal tail. This is followed by a C-terminal catalytic domain that comprises the Mab-21 domains, and a zing finger thumb[10,12,34]. The DNA length required for cGAS activation is different between human and mouse cGAS; while murine cGAS (mcGAS) can be potently activated by 20bp length DNA, human cGAS (hcGAS) requires at least 40bp[56,60,121,122]. cGAS has three DNA binding sites, termed A, B and C and recognizes dsDNA in a sequence-independent manner through direct interaction with the phosphate sugar backbone of DNA. The catalytic domain contains binding sites A and B, which creates a 2:2 "sandwich" of DNA on cGAS[34] – this configuration is necessary for a stably active complex[35]. The disordered N terminus and binding site C bind DNA to provide stability to higher-order cGAS-DNA oligomers and LLPS condensates[28–30,34,123]. The binding of DNA creates a conformational change in cGAS in the catalytic pocket, allowing for the synthesis of cGAMP. cGAS binds to DNA in a 2:2 quaternary complex, forming a ladder-like network of cGAS dimers[10,29,34,60]. Indeed, this explains why cGAS activation increases with increasing length of DNA.

1.1.1.1.3.1 Localization of cGAS

An important regulatory mechanism of cGAS and STING activation is the spatial separation of ligands and receptors. The former dogma of cGAS's permanent location in the cytosol alluded to its specificity for non-self DNA as it was thought to be compartmentalized away from mitochondrial and nuclear DNA. However, numerous examples exist of misplaced self-DNA eliciting a strong inflammatory response[10,63,64,124]

, which is, in part, due to the breakdown of cellular compartments. This suggests the presence of additional methods of cGAS regulation.

When cGAS was first discovered, it was isolated from the cytosol[24], which shaped our understanding of cGAS localization and its role in the detection of physiologically misplaced DNA. However, in 2019 Volkman *et al.* upended this localization dogma by reporting a highly salt-resistant tight tethering of cGAS to nuclear chromatin[125] and found nucleosomes to be poor agonists of cGAS[126,127]. This provided some explanation why cGAS is not activated during mitosis but the exact mechanism had not yet been resolved.

Nucleosomes are an organizational protein complex on chromatin that functions to package DNA in the nucleus[128–130]. Nucleosomes wind and unwind DNA, to both make it accessible to regulatory proteins and available for transcription[128–134]. Nucleosome core particles (NCPs) are composed of 146bp of DNA which wrap around two copies each of four histone proteins (H2A, H2B, H3 and H4)[128,131]. The positively charged histones form tight bonds with negatively charged phosphates in the sugar backbone of DNA[128–131]. The core components of nucleosomes are highly conserved from yeast through to metazoans[128,130,131]. DNA wrapped around histone cores is protected from nuclease digestion, while linker DNA between nucleosomes remains susceptible to digestion[128].

Nuclear cGAS is found in many cell types, including cancer cells, fibroblasts, keratinocytes and primary immune cells[34,125,127,135,136]. The distribution of cytosolic versus nuclear DNA is dependent on cell type, differentiation and density. For example, primary mouse macrophages have a nuclear cGAS composition of 95% regardless of cell cycle phase, while differentiated THP1s exhibit a more equalized distribution of cGAS[125]. Discovery of nuclear cGAS led to prompt investigation into its precise regulation in the nucleus.

1.1.1.1.3.2 Nucleosome Inhibition of cGAS

As cGAS is a DNA sensor and was initially discovered to sense foreign DNA, our understanding of its role relied on its localization in the cytoplasm. In contrast to the established mechanism of cGAS function, recent reports have described an abundance of cGAS in the nucleus. One would expect the abundance of DNA in the nucleus to potently trigger cGAS activation – potentially to the level of cytokine storm, however, increased innate immune signalling is not observed after nuclear envelope breakdown during mitosis and rapid recruitment of cGAS onto chromatin[53,126]. The observation that synthetic chromatin elicited a strong cGAS-mediated anti-viral response pointed toward a nuclear protein antagonist of cGAS[34,137]. The mechanism of nuclear cGAS inhibition came to light when a collection of six publications with a total of eleven cryo-electron microscopy (cryo EM) structures of cGAS bound to nucleosomes were published in quick succession in 2020[28–34]. Based on previous work by Volkman *et al.*, it is known that truncating cGAS to remove the ~150aa unstructured N-terminal tail does not interfere with nuclear localization or chromatin tethering[34,125], which allowed for necessary stabilization of cGAS required for cryo-EM. These papers describe how cGAS binds to the acidic patch of histone H2A-H2B within the nucleosome. The acidic patch is a conserved region in the H2A-H2B boundary that acts as a docking region for several nucleosome-associated proteins[138,139]. The highly conserved cGAS residue R255, termed arginine anchor (R222 in mcGAS), along with R236 and K254, create strong electrophilic interactions with the acidic patch of H2A with residues E61, E64, D90, and E92[28–30,32–34](Fig. 4, D-F). cGAS binding site A is exposed to exogenous DNA during binding to the NCP. However, the binding of site A to NCPs creates sterical changes that prevent cGAS dimerization, DNA binding and enzymatic activity[29,34] (Fig. 4, A-C). Additionally, mutating binding site A residues did not ablate binding of NCP. Site B directly binds the acidic patch of H2A-H2B, preventing interaction with DNA[28–30,33,34]. cGAS binds distal NCP DNA through binding site C via a KRKR loop (K299, R300, K301, R302) and a KKH loop (K427, K428 and H429). Site C cannot access in trans DNA outside of the NCP complex, which is thought to prevent LLPS of cGAS and DNA[29]. Additionally, while mutation of site C residues retains binding to NCPs, the formation of NCP stack multimers is prevented[29]. Each NCP can bind two

cGAS monomers to form a 2:1 complex but a 2:2 stoichiometry is the most prevalent composition[28–30,32–34]. However, cyro-EM structures of mcGAS and hcGAS show stoichiometries of 1:1, 2:1, 1:2, or 2:2, which may suggest species-specific compositions[34].

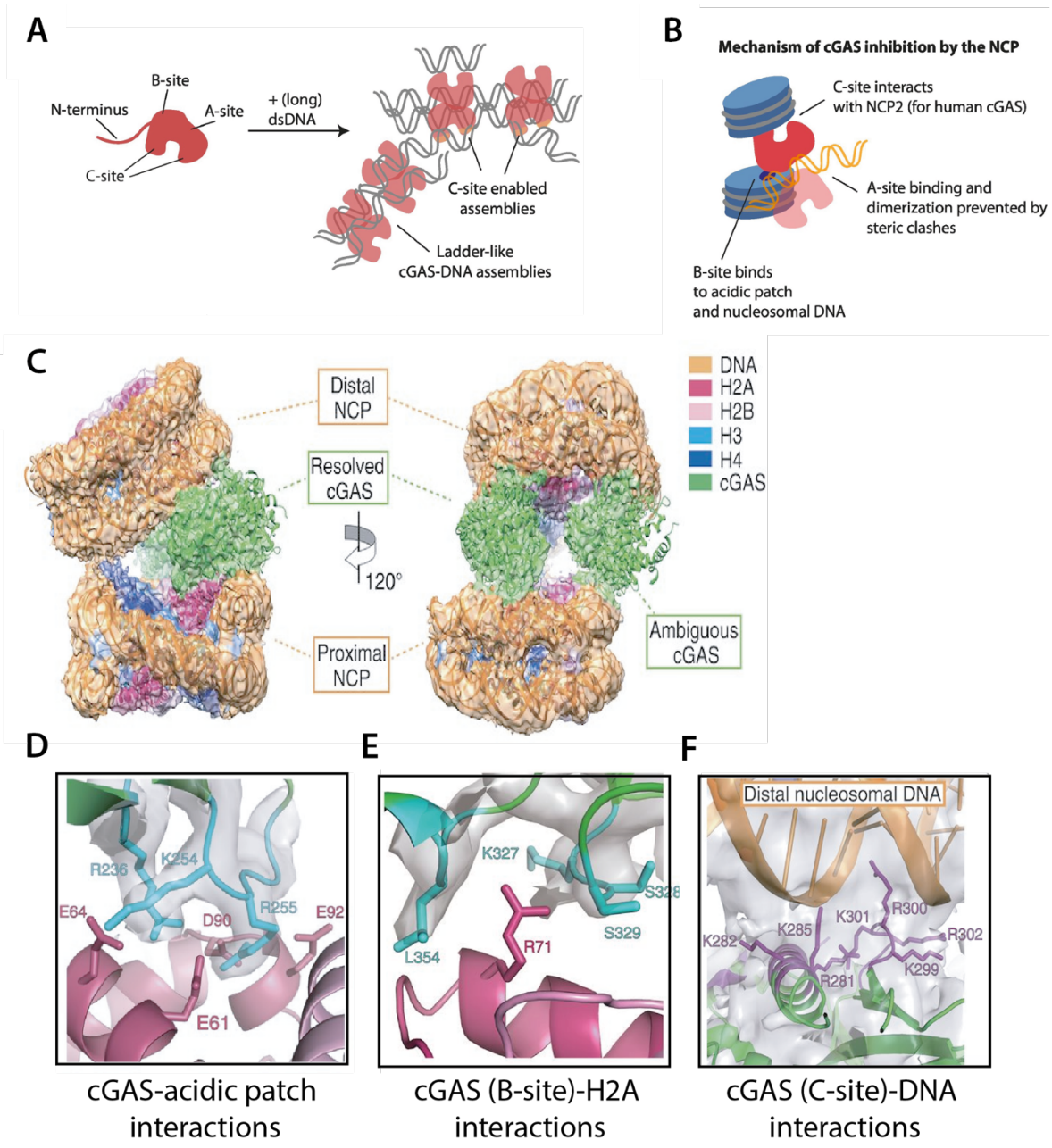


Figure 4: Interaction of cGAS and histones in the nucleus.
(**A**) cGAS binds dsDNA at sites A & B, while site-C mediates cGAS-DNA higher-order ladder-like assemblies. (**B**) cGAS bound to NCP. NCP inhibits DNA binding at the A-site by inducing sterical clashes, at the B-site by binding to the arginine anchor and C-site residues are bound to prevent higher-order structures. (**C**) Cyro-EM structure of cGAS bound to NCP. (**D**) Close up views of cGAS and the acidic patch of H2A. (**E**) cGAS residues in the B-site bound to H2A. (**F**) KRKR loop of cGAS bound to DNA in the distal NCP. (D-E) hcGAS DNA binding site B residues are depicted in cyan, hH2A residues are pink. (F) distal nucleosomal DNA is yellow, cGAS binding site C residues are purple.
Panel A & B from Wischnewski & Ablasser 2021. doi:10.1016/j.tibs.2021.05.011
Panel C-F from Kujirai et al. 2020. doi: 10.1126/science.abd0237.

Together the binding of NCPs to cGAS provides four mechanisms of inhibition.

The NCP binding of cGAS's site A creates steric changes that:

1. Prevent DNA binding by cGAS
2. Prevent cGAS dimerization

The binding of site B:

3. NCPs have a higher binding affinity for binding site B than DNA, therefore outcompeting naked DNA.

The binding of site C:

4. The KRKR and KKH loops residues of cGAS binding site C prevent NCP stacking. However, it is possible this mechanism is species-specific as the KRKR and KKH loops are not conserved between species[29].

Interestingly, mcGAS exhibits different DNA length sensitivity and LLPS characteristics compared to human cGAS (hcGAS), which may be attributed to slightly modified methods of chromatin antagonism[29].

These six publications quite eloquently solved the case of inhibited nuclear cGAS, but it begged the question of what happens to cGAS once it is bound to NCP? NCP have important functions in gene regulation; therefore it is reasonable to assume that if bound to another protein, it may interfere with its regulatory functions.

1.1.1.1.3.2.1 What happens to nuclear cGAS?

Nuclear envelope degradation during mitosis may allow cGAS to interact with DNA and nucleosomes. cGAS activation is controlled by multiple mechanisms of inhibition by NCPs. NCPs have a higher affinity for cGAS than naked DNA, raising the question of if and how cGAS is removed from chromatin and the nucleus. Xu *et al.* showed depletion of nuclear cGAS during interphase of the cell cycle, while cytosolic cGAS remained

unaffected, suggesting a mechanism of nuclear cGAS removal once the nuclear envelope is re-established[140]. The authors found that CRL5-SPSB3 form a ubiquitin ligase protein complex with cGAS to tag it for degradation via the ubiquitin-proteasome system before the next mitotic cycle[140]. This interaction is mediated by the N513 and N514 residues in the C-terminus of cGAS[140]. Additionally, Sun *et al.* reported the nuclear export of cGAS via nuclear pores in response to DNA stimulation. They identified a LEKLKL motif, with L172 being specifically important, as a nuclear export signal in cGAS that is required for exporting nuclear cGAS and mounting an interferon response[141]. Histones are needed to perform their endogenous gene regulation function [128,129]; it is therefore logical to require a mechanism of cGAS removal. Histone tail modifications could potentially disrupt cGAS / NCPs interactions and/or chromatin co-factors known to bind to the acidic patch (e.g. RCC1, LANA, IL-33, SIR3 and HMGN2), could out-compete cGAS binding[34,138,142–146].

This begs the question, is baseline cytosolic cGAS sufficient for stimulation during infection or is nuclear export required for activation in the cytosol?[34] Interestingly, both N-terminal (1-160aa) and C-terminal (161-522aa) cGAS protein fragments localize to the nucleus suggesting two independent nuclear-localization signals[34,127]. A nuclear reservoir of cGAS may regulate cytosolic cGAS available for stimulation and also be a fast way of supplying cGAS to the cytosol during infection[34]. The discovery of nuclear cGAS brings about exciting new directions for future cGAS research.

1.1.1.2 Other DNA sensors

It is worth noting that while we now recognize cGAS as a predominant DNA sensor, several DNA sensors were described before cGAS. cGAS is considered the predominant DNA sensor as knockout studies *in vitro* and *in vivo* clearly show its role in type I and III IFN induction. Additionally, numerous crystallography models of both cGAS alone and in complex with DNA have been generated, depicting the confirmational change upon stimulation, allowing cGAMP synthesis. In addition, I (data not shown) and other researchers have generated cGAMP *in vitro* by providing the raw

reaction components, thereby showing no other co-factors are required for cGAS activation. Over the past decade, various DNA sensors have been proposed with varying degrees of validating evidence. This includes ZBP1, RNA polymerase III (RNA Pol III)[147,148], DNA-PK[149], IFI16[150], DHX9, DHX36, DDX41, DDX60[151,152], MRE11[153], and AIM2[154–156]. Given the evidence for cGAS as a dominant dsDNA sensing PRR, it will be interesting to see what role other DNA sensors play. Many studies rely upon results from knockdown using RNAi as proof of principle, rather than CRISPR-based strategies, putting into question the reliability of these results without full knockdown *in vivo* evidence. Additionally, many sensors have no explained molecular mechanism of DNA binding or defined pathway to IFN induction[157]. It is tempting to ask how these knockdown studies can reveal a role for a sensor of interest required for IFN signalling while so many parallel sensors exist with the same proposed function. However, it is possible that some sensors are tailored to specific cell types or specialized recognition of DNA components yet to be described. Additionally, a multitude of DNA sensors likely exist to create a redundancy system against viral antagonism. While the context of this thesis focuses on viral antagonism of cGAS by VZV, it is worth noting that all of the sensors listed below are antagonized by DNA viruses.

1.1.1.2.1 TLRs

The first toll-like receptor (TLR) identified was TLR4 in 1998[158] – since then nine TLRs have been described in human cells that are divided into two categories, endosomal TLRs that detect nucleic acids (TLR3, TLR7, TLR8 and TLR9), and plasma membrane-anchored TLRs that detect bacterial architecture (TLR1, TLR2, TLR4, TLR5 and TLR6[159–161]. TLR9 was the first dsDNA sensor identified. It resides in endosomes and primarily detects CpG DNA, a component of microbial genomes[161–163]. It is important to note that due to its endosomal localization, TLR9 cannot detect cytosolic DNA.

1.1.1.2.2 RNA Polymerase III

RNA pol III (Pol III) is a housekeeping gene that transcribes tRNA, ribosomal RNA, snRNA, and other stable small RNAs[164,165]. Pol III is a DNA-dependent polymerase that can transcribe viral DNA into 5'-PPP containing immunostimulatory RNAs that are detectable by RIG-I[147,148,166,167]. Pol III was the first to be described foreign DNA sensor in the cytosol[147,148]. Pol III can detect exogenous bacterial and viral infections by *Legionella pneumophila*, *Shigella flexneri*, HSV-1, VZV and Epstein-Barr Virus[147,148,168,169]. Pol III is specialized to detect A:T rich DNA and therefore likely an accessory to other DNA sensors to complement their protection.

1.1.1.2.3 DNA-PK

DNA-dependent protein kinase (DNA-PK) is a protein complex composed of two DNA binding subunits (Ku70 and Ku80) and a catalytic subunit (DNA-PKc), and has a role in the DNA damage response by mediating non-homologous end joining (NHEJ)[170]. In addition to DNA-PK's role in detecting and repairing dsDNA breaks, the Ku70 subunit has been suggested to trigger a STING-dependent type III IFN response (not type I IFNs)[171]. The STING-dependent IFN response by DNA-PK provides further evidence that the cGAS-STING signalling axis is a critical PRR for downstream IFN activation. However, the entire DNA-PK complex induces an IRF3/TBK1-dependent type I IFN response during vaccinia virus (VACV) and HSV-1 infection[149,172,173].

1.1.1.2.4 IFI16 & AIM2

IFI16 detects dsDNA in sequence-independent and cell type-specific manners[150,174]. IFI16 shuttles between the nucleus and cytosol but remains predominantly nuclear at baseline[175]. IFI16 cooperates with cGAS in immortalized human keratinocytes to mount a *full* activation of STING-dependent signalling after infection. It has been proposed that

IFI16 may sense viral RNA, triggering it to bind RNA polymerase II and *RIG-I* promoter, initiating *RIG-I* transcription and activation during infection[176]. IFI16 recognizes KSHV or HIV-1 damaged DNA or DNA in the nucleus and then activates inflammasome formation in the cytosol[174,177–179]. Interestingly, IFI16 is found to be dispensable for the IFN response in primary fibroblasts during human cytomegalovirus infection[180]. Whether this evidence suggests that IFI16 has specialized functions in certain cell types or processes selectively for characteristics of damaged or pathogen DNA is unclear. IFI16 is related to predominantly cytosolic DNA sensor AIM2, which can induce an inflammasome in response, processing interleukins-1β and -18, in response to bacterial, fungal and viral infections[175,181–183]. How AIM2 differentiates host and foreign DNA within the nucleus has not yet been determined.

1.1.1.2.5 ZBP1

Z-DNA binding protein 1 (ZBP1)(previously called DAI) senses both endogenous and exogenous Z-form dsDNA[184–186]. Nucleic acids are primarily in B-form (dsDNA) or A-form (dsRNA) conformations but can switch to the highly unstable Z-form, facilitated by their structural flexibility[184,186]. ZBP1 also senses Z-form RNA during viral infections[184,187,188]. ZBP1 is also suggested to mediate apoptosis[184,188] and necroptosis[189], two regulated cell death pathways and has suggested roles in pyroptosis[185,188]. Doxorubicin, a chemotherapeutic, is found to induce the release of Z-form mtDNA in the cytosol that is subsequently sensed by ZBP1[190]. Interestingly, in this setting ZBP1 binds cGAS in a complex with RIPK1 and RIPK3 in cardiomyocytes to sustain IFN-I signalling. This leads to cancer therapy-associated heart failure in patients, but the cardiotoxic phenotypes are reversed in ZBP1$^{-/-}$, STING$^{-/-}$, or IFNAR$^{-/-}$ mice[190].

1.1.2 Sensing of Cytosolic RNA

Much like dsDNA, RNA can act as a PAMP during viral infections or DAMPs in non-infection settings. Depending on the localization of RNA PAMPs, they can be recognized by and activate multiple signalling responses. Retinoic-acid inducible gene (RIG-I)-like receptors (RLRs) are a family of cytosolic RNA sensors that detect exogenous or self-RNA and encompass three members: RIG-I, melanoma differentiated-associated protein 5 (MDA5) and laboratory of genetics and physiology 2 (LGP2)[11,191–193]. These proteins belong to the SF2 helicase superfamily – RNA helicases play roles in transcription, mRNA processing, translation, and RNA export[193]. A subset of SF2 helicase members are further classified into the subfamily of DExD/H box helicases, which have roles in RNA sensing[193]. Common components of RLRs are their central helicase domain and carboxy-terminal domain (CTD), which are the components necessary for RNA detection[11,192,193]. RIG-I and MDA5 have two amino-terminal caspase activation and recruitment domains (CARD), while their downstream adaptor molecule, mitochondrial antiviral signalling protein (MAVS) has one CARD domain (Fig. 5, A)[11,11,193]. In the absence of stimuli, RIG-I is in an auto-inhibitory confirmation, in which its CARD domain associates with the helicase domain to prevent downstream interaction with MAVS[11,192,193]. When RNA binds to RIG-I, the CARD is released from the repressed state and free for signalling (Fig. 5, B)[193]. The conformational changes of MDA5 upon RNA binding compared to the unstimulated state are less well understood.

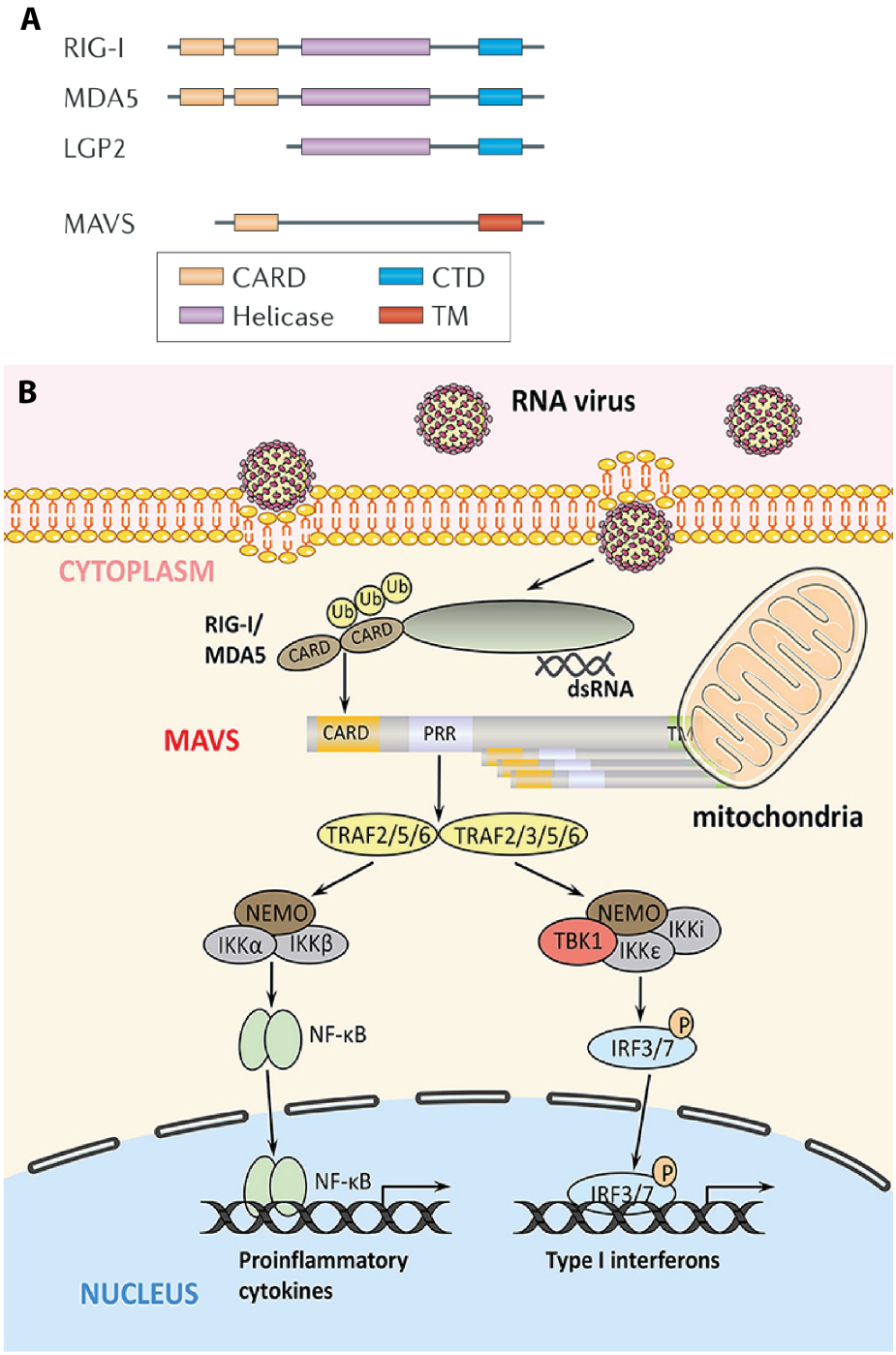


Figure 5: Domain architecture of RLRs and their signalling.
(**A**) RIG-I, MDA5, and LGP2 have a helicase, and CTD domain, while LGP2 lacks a CARD domain. The downstream signalling adaptor MAVS possesses a CARD and TM domain. (**B**) RLR signalling begins with activation of RIG-I or MDA5 via dsRNA that induces interaction of their CARD domains with the CARD of MAVS. MAVS activates IRF3 and NF-kB pathways to induce transcription of type I IFN and inflammatory cytokines. Panel (A) is taken from Rehwinkel & Gack 2020 doi: 10.1038/ s41577-020-0288-3. Panel (B) is taken from Ren et al. 2020 doi: 10.3389/fimmu.2020.01030.

RIG-I binds uncapped 5'triphosphate >19bp dsRNA[194,195], which is a distinct feature of non-self RNA. The vast majority of endogenous RNAs lack free 5'triphosphate groups and are thus not recognized by RIG-I. For example, messenger RNAs possess a 7-methylguanylate cap modified by a 2-O-methyl group, which precludes detection by RIG-I[11,196,197]. MDA5 is known to recognize long (>300bp) dsRNA, however, this data is derived from cell-free experiments and the exact mechanism of activation is still unclear. Interestingly, both RNA and DNA-based viruses of single-stranded and double-stranded composition activate RLRs[11]. Posttranslational modifications of the CARD domains and oligomerization of RIG-I and MDA5 allow them to translocate to and activate MAVS by interacting with its CARD domain[11,192,193]. MAVS is localized to the outer mitochondria membrane, mitochondria-associated membranes of the ER and peroxisomes via its C-terminal transmembrane domain[4,11,193,198]. MAVS then activates TBK1 and IKKε through interaction with tumour necrosis factor receptor-related factors (TRAFs) 2,3,5 and 6, ultimately leading to phosphorylation and homodimerization of IRF3 and IRF7 activation[11,192]. In conjunction with NFκB, the transcription of type I IFNs, type III IFNs and inflammatory cytokines genes are induced[11,192]. Thus, MAVS is the central converging protein of two PRRs and is crucial to antiviral immunity.

1.1.3 Function of IFNs

The downstream signalling response for the cGAS-STING pathway and RLR pathways both include the production of IFNs. Type I IFNs and type III IFNs act in a paracrine and autocrine manner, in that they can signal to neighbouring (bystander) cells or bind receptors on the same cell's surface (Fig. 2). Type I IFNs bind the IFNα/β receptor (IFNAR) while type III IFNs bind the IFNλ receptor (IFNLR)[10,16]. The IFNAR receptor consists of an IFNAR1 and IFNAR2 heterodimer, with intracellular receptor chains bound by the receptor associate Janus kinases TYK2 and JAK1[16,199]. The binding of IFN allows cross-phosphorylation of JAK1 and TYK2, which recruits signal transducer and activator of transcription 1 (STAT1) and STAT2. STAT1 and STAT2 are phosphorylated and dimerize, leading to the formation of the STAT1-STAT2-IRF9 (IFN-regulatory factor 9)

complex, which is also known as ISGF3. ISGF3 traffics to the nucleus where it binds to IFN-stimulated response elements (ISREs) in gene promoters and induces the expression of hundreds of ISGs[16,199].

Despite the multitude of cellular PRRs, particularly nucleic acid sensors, these pathways converge to induce transcription of proinflammatory cytokines, IFNs and ISGs. IFNs are categorized into three groups: type I, type II, and type III IFNs. Human type I IFNs are divided into 17 subtypes; 13 IFNα's, IFNβ, IFNε, IFNκ, and IFNω[11,16,200,201] IFNε is expressed exclusively in female reproductive tissues, IFNκ in keratinocytes, and IFNω in immune cells[202–204]. Type II IFN (the single IFNγ) is only expressed by immune cells including T cells, B cells, APCs and NK cells[205]. It can be stimulated by nucleic acids, cytokines and type I IFNs and predominantly has a role in regulating interactions of lymphocytes and APCs[206]. Type III IFNs (IFNλ1-4) are primarily driven by NFκB but also to a smaller extent by IRF3 and IRF7[207,208], while the opposite is true for type I IFNs. Unlink IFNα, IFNβ possesses a high-affinity interaction with IFNAR1, inducing a potent and distinct ISG response[209–211]. Type III IFNs are structurally dissimilar to type I IFNs, and bind their own receptor (IFNLR) which is mostly expressed on epithelial cells[16,212]. While type I IFNs and type III IFNs induce similar ISGs, type I IFNs are more potent and induce rapid induction of ISG expression compared to type III IFNs[213–215].

Type I IFN and cytokines function to drive ISG production and activate the adaptive immune response. Viruses encode proteins to camouflage, inhibit and degrade host IFN signalling to ensure success of viral entry, replication and production of progeny virus. Viruses antagonize multiple points along innate immune pathways, including ISGs and IFNs, highlighting the need for a wide array and diverse set of ISGs/IFNs to combat viral infections. The primary function of IFNs is anti-viral, accomplishing this by blocking many stages of viral replication, including entry, transcription, translation and release[201,216–219].

1.1.2.1 Regulation of RNA sensing pathway

RIG-I is activated by negative-sense RNA viruses that typically possess a 5' triphosphate group recognized by RIG-I[11]. However, positive-sense RNA viruses such as dengue and Zika viruses also activate RIG-I[11]. Much like the cGAS-STING signalling axis, RIG-I can be activated by host cellular RNAs, however, this is typically a byproduct of viral infection. For example, HSV-1 induces the expression of host pseudogene, *RNA5SP141*, that is recognized by RIG-I as it contains 5'-triphosphate groups, mis-localizes to the cytoplasm and HSV-1's host shut-off function downregulates co-binding proteins of RNA5SP141[11,220].

RIG-I signalling can cross-talk with other signalling pathways, in that the production of type I and III IFN can induce the transcription of RIG-I itself and other PRRs such as cGAS, creating a positive feedback loop[11,192]. Stimulation of RIG-I and MDA5 by type I and III IFNs occurs in most cell types. LGP2 does not have a CARD domain but retains the ability to bind dsRNA and is believed to mediate RIG-I and MDA5 signalling through either competitive RNA binding, competition with IKKε for MAVS, inhibition of oligomerization or interruption of PTMs of RIG-I[192,221–226]. LGP2 positively regulates MDA5 activation by facilitating its oligomerization onto dsDNA[227,228]. ADAR1 acts to control activation of ZBP1, by catalyzing the conversion of adenosine to inosines in dsRNA[185].The editing of RNA by ADAR1 regulates autoimmunity by reducing pattern recognition by MDA5[98,229–231].

1.1.2.2 Regulation of MAVS Activation

Host and viral factors regulate MAVS at both a post-transcriptional and post-translational level, primarily through ubiquitination (Fig. 6). Four main ubiquitin patterns take place in MAVS which positively and negatively regulate its activation – reviewed extensively in REF[232,233].

MAVS is a 540aa protein that is composed of an N-terminal CARD domain, central proline-rich region, and C-terminal transmembrane domain[198,232,234]. During activation of the RIG-I signalling pathway, E3 ligases (TRIM25, RNF125, and/or RIPLET) attach K63-polyubiquitin chains to the CARD of RIG-I or MDA5 which promotes CARD binding to MAVS[232,233]. Interestingly, unanchored K63 ubiquitin chains can act as a potent activating ligand of RIG-I[235]. Once MAVS is activated it forms prion-like aggregates, which creates a cascading effect for other MAVS proteins to aggregate that are crucial for signalling[233,234].

1.1.2.2.1 Post-transcriptional Modifications to *MAVS*

It is common among viruses and bacteria to generate multiple translational products from the same mRNA – known as polycistronic messages – to create protein diversity without the need for alternative splicing[236,237]. Protein translation typically starts from the N-terminal methionine coded by ATG, where ribosomes bind and initiate translation. However, polycistrons produce proteins that begin translation at an internally located methionine, thereby creating truncated protein isoforms[238–241]. MAVS has been found to possess multiple translational start sites within the gene that can result in multiple isoforms of MAVS from one transcript[242,243].

These shortened isoforms of MAVS all lack the N-terminal CARD domain and prevent full-length MAVS from its spontaneous aggregation, thereby inhibiting IFN induction. This mechanism is thought to act as a regulator of antiviral signalling – mainly to prevent inappropriate signalling[242,243]. The post-transcriptional regulation of *MAVS* is expanded upon further in Section 3.3.

1.1.2.2.2 Post-Translational Modifications to MAVS

Four main types of ubiquitination regulate MAVS: K27-linked, K48-linked, K63-linked and small ubiquitin-like modifier modification (SUMOylation)[232].

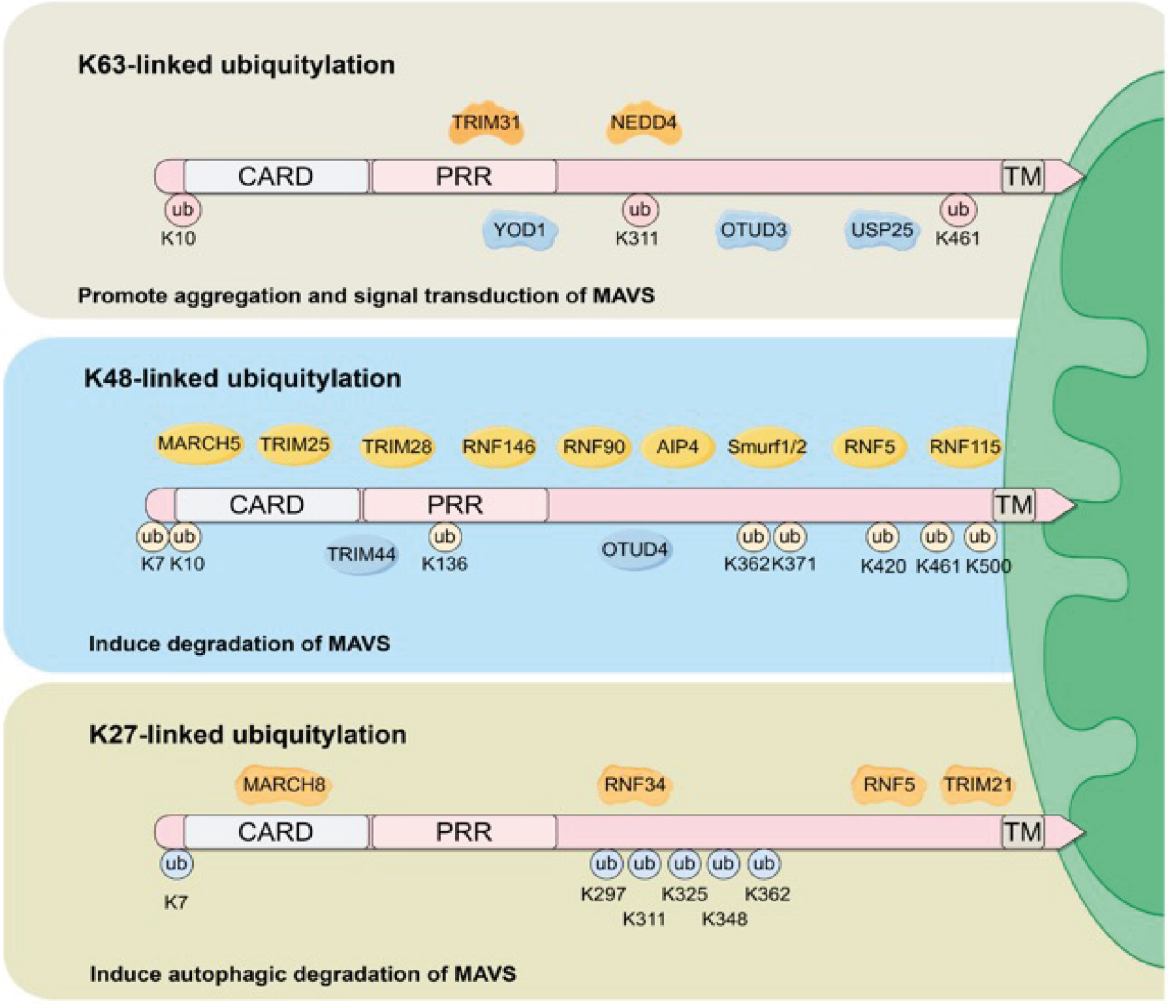


Figure 6: Post-translation modification of MAVS.
MAVS is regulated through the K27, K48 and K63-linked ubiquitylation. The ubiquitylation is mediated by a number of co-factors listed in yellow blobs above the MAVS transcript. Ubiquitin chains are added to the indicated lysine residues. K63-linked ubiquitylation promotes MAVS aggregation and signalling, while K27 and K48-linked ubiquitylation promotes degradation of MAVS. Figure taken from Dong & Shen 2024. doi:10.31083/j.fbl2902072.

1.1.2.2.2.1 Positive Regulation of MAVS By Post-Translational Modification

K63-linked ubiquitination by E3 ligase TRIM31 promotes MAVS signalling by promoting aggregation and interaction with RIG-I[232,233]. This ubiquitination is also thought to recruit TBK1 and IKK[244,245]. The interaction of TBK1 and IKK is also mediated by TRIM21: an E3 ligase mediating K27-linked ubiquitination[233,246].

Viral infection can induce the production of cyclophilin A, a competing protein of TRIM25, to inhibit ubiquitination and degradation of MAVS[233,247].

SUMOylation is a reversible post-translation modification that covalently attaches small ubiquitin-like modifier proteins to specific lysine residues on the substrate[92,248,249]. SARS-CoV-2 increases SUMOylation of MAVS, promoting aggregation and hyperactivating inflammatory signalling. Conversely, SUMO-specific protease 1 hydrolyses poly-SUMO chains from MAVS to inhibit aggregation and IRF3 activation[250]. SUMOylation of MAVS induces phase separation and provides a mechanism for recruiting non-phosphorylated IRF3 to promote the timely activation of innate immune responses[250].

K27-linked ubiquitination by E3 ligase TRIM21 also promotes MAVS signalling and can be hijacked by hepatitis C virus (HCV), Newcastle disease virus, Sendai virus (SeV), and vesicular stomatitis virus (VSV) by inducing the expression of *TRIM21*[233,246]. Autography receptors recognize K27-linked ubiquitinated MAVS, thereby inducing autophagy-mediated degradation.

Sirtuin 3 deacetylates MAVS at lysine residue 7 to promote aggregation and phosphorylation of TBK1 and IRF3. Conversely, desuccinylation of K7 by sirtuin 5 suppresses MAVS signalling[251].

1.1.2.2.2.2 Negative Regulation of MAVS By Post-Translational Modification

Negative regulation of MAVS at the post-translation level is predominantly mediated by the disruption to typical K48-linked ubiquitination, autophagy and apoptosis[233].

K48-linked ubiquitination of MAVS tags it for proteasomal degradation involving a large number of E3 ubiquitin ligases including TRIM25, AIP4, Smurf1, Smurf2, MARCH5, RNF5, OTUD4, and TRIM44[233,252]. Inhibition of TRIM31-mediated K63-linked ubiquitination by host and viral factors suppresses the downstream signalling of MAVS[233].

Lactate, tubulin tyrosine ligase-like protein 12, hexokinase II, protein phosphatase magnesium-dependent 1A, UBX-domain-containing protein 1, and Gpatch domain-containing protein 3 can all independently bind to MAVS to suppress its activity[233,253–257].

If MAVS signalling is unable to be mediated by other mechanisms, induction of apoptosis acts as a final defence to strategically limit misregulation to one cell. Interestingly, a replication-defective SeV promotes apoptosis in tumour cells by inducing the expression of pro-apoptotic genes via RIG-I/MAVS signalling[233,258,259].

1.1.2.2.3 Viral Regulation of MAVS

A prominent strategy of viruses is to inhibit the anti-viral signalling of PRRs and their adaptor proteins through degradation, cleavage or direct inhibition.

HCV cleaves the N-terminal region of MAVS, removing its CARD domain and ablating RIG-I interaction[233,260]. Seneca Valley virus, human rhinovirus C, and coxsackievirus B3 all possess a protease targeting the same G148 residue[233,261–263]. Hepatitis B virus tags MAVS for proteasomal degradation via ubiquitination of its K136 residue[233,264]. The Foot and mouth disease virus structural protein VP3 blocks mRNA expression of *MAVS* and

binds to its transmembrane domain (in a similar manner to lactate mentioned above) preventing aggregation and mitochondrial localization[265].

The H5N1 strain of influenza A virus (IAV) encodes PB1-F2 protein which prevents mitochondrial localization of MAVS by binding its transmembrane domain, while its PB2△ protein induces type I IFN production through MAVS interaction[266,267]. IAV infection leads to the upregulation of miRNAs that bind 3'UTR of MAVS, preventing translation[268].

Severe acute respiratory system disease (SARS) is caused by SARS-CoV-1 that encodes the ORF9b protein which catalyzes the K48-linked ubiquitination of MAVS, tagging it for degradation[233,269]. In SARS-CoV-2 the ORF9b protein interacts with TOM70 on the outer mitochondrial membrane thereby interrupting its canonical function as a MAVS adaptor protein and preventing downstream antiviral responses[270,271]. Additionally, the interaction of ORF9b with TOM70 prevents TOM70-HSP90 binding, which is necessary for the recruitment and phosphorylation of TBK1 and IRF3[271–273]. SARS-CoV-2's nucleocapsid protein (NP), specifically its dimerization domain, induces its LLPS and binding with viral RNA, to promote virion assembly and viral replication[274–281]. Host factors acetylate and deacetylate L375 of NP, reducing its condensation and impact on MAVS activity[282]. Introduction of NP into mice leads to ablated MAVS signalling, higher viral titres and increased mortality[282]. In agreement, transfection of NP into cells blocked *IFNβ* expression during SeV and VSV infection[282,283]. NP disrupted the interaction of MAVS and RIG-I, and RIG-I and TRIM31[282,283]. Additionally, MAVS LLPS is disrupted by NP. Finally, K63-linked ubiquitination of MAVS by TRIM31 is blocked by NP, preventing interaction with downstream adaptor proteins[282,283]. This provokes open-ended questions regarding the potential development and applicability of therapeutics targeting mediators of MAVS LLPS and NP acetylation during SARS-CoV-2 infection[283].

1.3 Research Objectives

As discussed in this chapter, the activation of PRRs and their downstream adaptors is a complex and highly regulated system, opening up a plethora of targets for viral antagonism. Alternatively, the malfunction of PRRs as a result of genetic mutations presents an opportunity for viruses to more readily infect cells.

My work builds upon two interesting aspects of PRR research – the viral antagonism of nucleic acid sensors and the susceptibility to infection if receptor pathway proteins are genetically faulty.

Objective 1: Importance of MAVS-SNPs for induction of the IFN response (Chapter 3)

Through a collaboration with Dr. Johnathan Cooper-Knock, we discovered single nucleotide polymorphisms (SNPs) within MAVS that are associated with severe COVID-19 infections in <60-year-old patients. As outlined above, SARS-CoV-2 employs a multitude of evasion and suppression tactics to inhibit RNA sensing pathways and MAVS specifically. The RLR signalling pathways has crucial importance for managing SARS-CoV-2 infection. Therefore, its logical that mutations in any RLR proteins and/or downstream signalling proteins could render patients more susceptible to not only SARS-CoV-2 infection, but any RNA viral infection. Based on our knowledge that MAVS is translationally regulated by producing truncated MAVS isoforms which counteract the anti-viral activity of full-length MAVS we hypothesized that these SNPs could result in pro-viral innate immune suppression. I expressed these MAVS-SNPs *in vitro* to determine the downstream antiviral effect and its inhibition of MAVS aggregation.

Objective 2: Mechanism of VZV-ORF9 inhibition of cGAS (Chapters 4 & 5)

Based on our published work in The EMBO Journal (outlined in Chapter 4), we know that VZV-ORF9 binds and antagonizes cGAS. Yet we do not know the mechanism by which it does this. A common strategy in viruses, briefly highlighted above, is to mimic host protein structures to evade detection or to bind host factors. We hypothesize that ORF9 may be acting as a histone mimic, based on partial sequence homology with H2A, binding to cGAS in a manner analogous to H2A. Aligning the protein-coding sequence for ORF9 and histone H2A revealed numerous regions of sequence similarity in important binding sites. I mutagenized an ORF9 plasmid to alter the amino acids identical to H2A's cGAS binding regions to determine if these residues are critical for cGAS binding. I further validated the ability of mutant ORF9 to bind and activate cGAS.

Chapter 2

Materials & Methods

2. 1 Materials

2.1.1 Cells

All cells were cultured at 37°C and 5% CO_2 with regular mycoplasma contamination testing. Adherent cells were passaged using Trypsin-EDTA (ThermoFisher Scientific) dissociation reagent. Media used to maintain all cells were supplemented with 10% fetal calf serum (FCS) (Gibco) and 2mM L-glutamine (L-G) (Gibco).

HEK293 — HEK cells are derived from female embryonic kidneys exhibiting an epithelial morphology. Cells were maintained in Dulbecco's modified Eagle medium (DMEM) (Gibco). The cells were a kind gift from Caetano Reis e Sousa (The Francis Crick Institute, UK).

HEK293-p125 — HEK293-p125 cells are HEK293 cells stably transduced with a p125-GreenFire construct to express GFP and Firefly luciferase from *IFNβ*-promoter control. Parental and *MAVS*-KO cells were used[284]. Cells were maintained in DMEM (Gibco). The cells were a kind gift from Caetano Reis e Sousa (The Francis Crick Institute, UK).

HEK293T — HEK293T are a modified HEK293 cell line which stably express the polyomavirus SV40 large T antigen, allowing for efficient replication of plasmids carrying the SV40 promoter[285–287]. Cells were maintained in DMEM (Gibco). The cells were a kind gift from Caetano Reis e Sousa (The Francis Crick Institute, UK).

3C11 — 3C11 denotes a plate coordinate for a clone of HEK293s stably transduced with pGreenFire-ISRE reporter construct to express GFP and Luciferase. These cells act as a type I IFN reporter cell line and

were initially described in REF[81]. Cells were maintained in DMEM (Gibco).

THP1

THP1 cells are a monocyte cell line derived from peripheral blood of a patient with acute monocytic leukemia. Cells were differentiated to a macrophage-like cell type by the addition of phorbol 12-myristate 13-acetate (PMA) (Sigma-Aldrich) to the cells Roswell Park Memorial Institute (RPMI) medium (Gibco) media. Cells were a kind gift from Søren Paludan (Aarhus University, Denmark).

THP1 Dual

THP1 Lucia Dual reporter cells (Invivogen) secrete Lucia luciferase under the control of an ISG54 minimal promoter. They also express secreted embryonic alkaline phosphatase (SEAP) driven by an *NF-κB* transcriptional response element. Cells are resistant to Zeocin and blasticidin. Cells were differentiated to a macrophage-like cell type by the addition of PMA (Sigma-Aldrich) to RPMI medium (Gibco). Cells were a kind gift from Søren Paludan (Aarhus University, Denmark).

Huh7

Huh7 cells are an immortalized hepatoma cell line isolated from a 57-year-old Japanese male[288]. Parental and *MAVS*-KO cells were used. Cells were maintained in DMEM (Gibco). Parental cells were a kind gift from Jane McKeating (University of Oxford, UK). *MAVS*-KO cells were generated by Chiara Cursi, who previously worked in the Rehwinkel group as a research assistant (data not shown).

HFFF-TERT

HFFF cells are a fibroblast cell line isolated from human fetal foreskin and immortalized with human telomerase[289]. I will refer to them as simply HFFs throughout. Cells were maintained in DMEM (Gibco). Cells were a kind gift from Micheal Weekes (University of Cambridge, UK). HFF cells are puromycin-sensitive.

MeWo — MeWo cells are a fibroblast cell line isolated from a 78-year-old White male patient with malignant melanoma. MeWo cells are used to propagate VZV and are cultured in Minimal Essential Medium (MEM) (Gibco). Cells were a kind gift from Jeffrey Cohen (NIH, USA).

HaCaT — HaCaT cells are a spontaneously immortalized human epidermal keratinocyte cell line. Cells were maintained in DMEM (Gibco). The cells were a kind gift from Leonie Unterholzner (Lancaster University, UK).

HEKn — HEKn cells are a primary keratinocyte cell line isolated from neonatal foreskin (ThermoFisher Scientific). Cells were maintained in EpiLife™ Medium with 60 µM calcium (ThermoFisher Scientific) and supplemented with 1% Human Keratinocyte Growth Supplement (ThermoFisher Scientific). The cells were dissociated during Trypsin/EDTA Solution (ThermoFisher Scientific) and neutralized using Trypsin Neutralizer Solution (ThermoFisher Scientific).

F8Y/F10Y — Cells are two clones of dermal fibroblast cells isolated from healthy human skin. Cells were maintained in DMEM (Gibco). Cells were a kind gift from Yanick Crow (University of Edinburgh, UK).

2.1.2 Viruses

VZV — VZV rOka (cosmid-derived recombinant pOka) was propagated in a monolayer of MeWo cells that were closely observed for cytopathic effects such as syncytia formation. Cells were then dissociated and mixed with uninfected MeWos in a 1:4 ratio and re-plated. Infected cells were cryopreserved in a freezing medium (10% DMSO, Merck),

90% FCS (Gibco)) and stored in liquid nitrogen. Cells were a kind gift from Jeffrey Cohen (NIH, Bethesda, USA)[290].

VZV-ORF9^{ecDHFR} A recombinant VZV virus, derived from the VZV pOka strain, with a degron motif fused to the ORF9 protein. The virus was propagated in monolayers of MeWo cells and the degron motif was stabilized with trimethoprim (TMP). MeWo cells were cryopreserved in a freezing medium (10% DMSO, Merck), 90% FCS (Gibco)) and stored in liquid nitrogen. The recombinant virus was a gift from Paul R. Kinchington[291] (University of Pittsburgh, USA).

2.1.3 Plasmids

Name	Description	Origin
Gateway Entry and Destination Vectors		
pcDNA3.2/V5/ccdB_CmR	Protein expression construct driven by a cytomegalovirus promoter and contains a C-terminal V5 tag.	Invitrogen Cat #: A11141
pLenti6.3/TO/V5/ccdB_CmR	Lentiviral mammalian expression vector that contains a C-terminal V5 tag. Blasticidin resistance gene.	Invitrogen Cat #: 12489019
pLenti/TO/C-V5_PURO_DEST	Lentiviral mammalian expression vector that contains a C-terminal V5-tg. Blasticidin resistance gene was exchanged for hPGK_puro gene.	Generated by Jonny Hertzog.
Gateway Entry Vector Constructs		
pCR8/VZV-ORF9-STOP	VZV-ORF9 with STOP.	Generated by Jonny Hertzog.
pCR8/VZV-ORF9-E106R/E109R-STOP	VZV-ORF9-E106R/E109R with STOP.	Generated by Gerissa Fowler.
pCR8/VZV-ORF9-N209D-STOP	VZV-ORF9-N209D with STOP.	Generated by Gerissa Fowler.
pCR8/VZV-ORF9-E211R-STOP	VZV-ORF9-E211R with STOP.	Generated by Gerissa Fowler.
pCR8/VZV-ORF9-E106R/E109R/E211R-STOP	VZV-ORF9- E106R/E109R/E211R with STOP.	Generated by Gerissa Fowler.
pCR8/VZV-ORF9-E2227T-STOP	VZV-ORF9-E227T with STOP.	Generated by Gerissa Fowler.
pCR8/hcGAS	hcGAS ORF w/o STOP.	Generated by Lise Chauveau.
pDONR^{TM}221-*MAVS-shRNA-Control Plasmid*	Gateway pDONR221 expression construct for MAVS-WT control. Confers Kanamycin resistance. Synonymous mutations were introduced in shRNA/sgRNA CRISPR	Plasmid insert design by Philip Hublitz & Jan Rehwinkel. Synthesized by GeneArt ThermoFisher Scientific.

	targeting sites to prevent knockout of MAVS plasmids.	
pDONR™221-*MAVS-C5T*	As above with C5T mutation.	See above.
pDONR™221-*MAVS-G409A*	As above with G409A mutation.	See above.
pDONR™221-*MAVS-C421G*	As above with C421G mutation.	See above.
pDONR™221-*MAVS-G580A*	As above with G580A mutation.	See above.
pDONR™221-*MAVS-G1074C*	As above with C1074C mutation.	See above.
pDONR™221-*MAVS-G1186A*	As above with G1186A mutation.	See above.
pDONR™221-*MAVS-G1260C*	As above with G1260C mutation.	See above.
pDONR™221-*MAVS-C1531T*	As above with C1531T mutation.	See above.
Gateway Destination Vectors		
pLenti6.3/N-FLAG/puro/FLAG-VZV-ORF9	Lentiviral mammalian expression plasmid for VZV-ORF9 that contains N-terminal FLAG-tag and confers puromycin resistance.	Generated by Jonny Hertzog[292].
pLenti/TO/N-FLAG_PURO_DEST-ORF9-E106R/E109R	As above with E106R/E109R mutation.	Generated by Gerissa Fowler.
pLenti/TO/N-FLAG_PURO_DEST-ORF9-E211R	As above with E211R mutation.	See above.
pLenti/TO/N-FLAG_PURO_DEST-ORF9-E106R/E109R/E211R	As above with E106R/E109R/E211R mutation.	See above.
pLenti/TO/N-FLAG_PURO_DEST-ORF9-E227T	As above with E227T mutation.	See above.
pLenti/TO/N-FLAG_PURO_DEST-ORF9-E211R-E227T	As abive with E211R/E227T mutation.	See above.
pLenti6/3/V5-DEST-hcGAS-WT	Lentiviral transducing vector for human cGAS WT with V5-tag.	Generated by Lise Chauveau[292].
pLenti6.3/TO/V5/ccdB_CmR (DEST)/cGAS-R255E	Lentiviral transducing vector for human cGAS-R255E with V5-tag. Mutation targets the key arginine anchor residue.	Generated by Gerissa Fowler.
pLenti6.3/TO/V5/MAVS-shRNA-Control Plasmid	Expression plasmid for human MAVS-WT control. A STOP before C-terminal V5-tag prevents its translation. Confers blasticidin resistance.	Generated by Gerissa Fowler.
pLenti6.3/TO/V5/MAVS-C5T	As above with C5T mutation.	See above.
pLenti6.3/TO/V5/MAVS-G409A	As above with G409A mutation.	See above.
pLenti6.3/TO/V5/MAVS-C421G	As above with C421G mutation.	See above.
pLenti6.3/TO/V5/MAVS-G580A	As above with G580A mutation.	See above.
pLenti6.3/TO/V5/MAVS-G1074C	As above with G1074C mutation.	See above.
pLenti6.3/TO/V5/MAVS-G1186A	As above with G1186A mutation.	See above.
pLenti6.3/TO/V5/MAVS-G1260C	As above with G1260C mutation.	See above.
pLenti6.3/TO/V5/MAVS-C1531T	As above with C1531T mutation.	See above.
pcDNA3.2/hSTING-HA	Expression plasmid for human STING with C-terminal HA-tag	Generated by Jonny Hertzog[292].
STING FRET Assay Vectors		
mTurq-mSTING-eYPet	Expression plasmid for mouse STING with an N-terminal mturquoise2 and C-terminal YPet fluorofore. STING transmembrane domain is not present.	A kind gift from Christian Zierhut[293] (The Institute of Cancer Research, UK).
mTurq-blind-mSTING-eYPet	Expression plasmid for mouse STING with an N-terminal mturquoise2 and C-terminal YPet fluorofore. STING binding pocket is mutated to prevent cGAMP binding. STING	A kind gift from Christian Zierhut[293] (The Institute of Cancer Research, UK).

	transmembrane domain is not present.	
Dual Luciferase Assay Vectors		
pRL-TK	Constitutively expresses Renilla luciferase under the control of thymidine kinase promoter.	Progema (Cat #: E2241)
P125-F-Luc	Inducibly expresses Firefly luciferase under the control of the hIFNβ promoter.	Kind gift from Takashi Fujita[294].
pcDNA3.2/V5-hSTING	Constitutively expresses human STING HAQ with V5-tag.	Generated by Lise Chauveau.
pcDNA3.2/V5-hcGAS	Constitutively expresses human cGAS with V5-tag.	Generated by Lise Chauveau.
pLenti6.3/TO/V5/eGFP	Constitutively expresses GFP with C-terminal V5-tag.	Generated by Jonny Hertzog.
pLenti6.3/TO/V5/EV	Constitutively expresses 20bp random sequence in expression cassette (ATCTACCCGCGAGGTCAGAC).	Generated by Jonny Hertzog.
pcDNA3.1/FLAG-EMCV-L Protein	Expresses EMCV Leader (L) protein with FLAG-tag.	Generated by Gregorio Dias[284].
Lentivirus Production		
p8.91	Lentiviral packaging plasmid.	Kind gift from Greg Towers (University College London, UK).
pCMV-VSV-G	Constitutively expresses VSV-G from human cytomegalovirus promoter for lentiviral pseudotyping.	Kind gift from Bob Weinberg (Addgene plasmid #: 8454)
pMD2.G	VSV-G expressing plasmid for lentiviral pseudotyping	Addgene Cat. Number 12259

2.1.4 Oligonucleotides

Name	Forward Primer (5'-3')	Reverse Primer (5'-3')
Site Directed Mutagenesis Primers		
cGAS-R225E	TGAAATTTAAAGAGAATCCGAAAGAAAATC	TCTTTCGGATTCTCTTTAAATTTCACAAAG
ORF9-E106R/E109R	TACAGCATCTCTAACCAGTCTATGTCTCAAACG	GTTTGAGACATAGACTGGTTAGAGATGCTGTATATG
ORF9-N209D	CCCAAGGAATGATGCCGAATTAGAC	TCTAATTCGGCATCATTCCTTGGG
ORF9-E211R	AGGAATAACGCCAGATTAGACCGTT	CAAACGGTCTAATCTGGCGTTATTCCT
ORF9-D213N	AGGAATAACGCCAGATTAGACCGTTTG	GGTTAACAAACGATTTAATTCGGCGTTATT
ORF9-E211R/E227T Overlap PCR	ATGGCATCTTCCGACGGTGACAG GTTAACCGGAGCCGTTATTCGTAT	AATACGAATAACGGCTCCGGTTAAC CTATTTTCGCGCATCAGTTCTTGATG
ORF9-E227T	TACGGTGCATACGGGTTTAAATTTAATAC	TTTAAACCCGTATGCACCGTAATACGAAT
SYBR Green Primers		
VZV-ORF4	CGTGGTCATTGCAGGAGGCG	CGCATCGAACGGGGACATCG
VZV-ORF40	CCGACACGCCAGGGAACCTA	CACACCGTCAACCTGCCGTC
VZV-ORF54	TCCAACCCCTCTTCGGCTCG	GGGGATGGCCGATGGGATGT
GAPDH	CATGGCCTTCCGTGTTCCTA	CCTGCTTCACCACCTTCTTGAT

2.1.5 TaqMan Probes

Gene	Protein	AssayID
ACTB	β-Actin	Hs99999903_m1
DDX58	RIG-I	Hs01061436_m1
GAPDH	GAPDH	*Hs02758991_g1*
IFI44	IFI44	Hs00951349_M1
IFIH1	MDA5	Hs00223420_m1
IFIT1	IFIT1	Hs02758991_g1
IFNA1	IFNα1	Hs00256882_s1
IFNB1	IFNβ1	Hs02621180_s1
IFNL1	IFNλ1	Hs00601677_g1
IL6	IL-6	Hs00174131_m1
IRF3	IRF3	Hs01547283_m1
MAVS	MAVS	Hs00920075_m1
MX1	MX1	Hs00895608_M1
SARS-CoV-2 NP	SARS-CoV-2 nucleocapsid	IDT 2019-nCoV Kit (10006713)
TBK1	TBK1	Hs00179410_m1
TMEM173	STING	Hs00736958_m1
VZV-ORF9	VZV-ORF9	APT2F4Y

2.1.6 Antibodies

Target	Conjugate	Source	Manufacture	Clone/Cat. #	Application	Dilution/ Conc.
αMouse IgG	HRP	Sheep monoclonal	GE Healthcare	NA931V	WB	1:2000
αRabbit IgG	HRP	Goat polyclonal	Cell Signalling	7074	WB	1:2000
β -Actin	HRP	Mouse monoclonal	Sigma-Aldrich	A3854	WB	1:10,000
cGAS	-	Rabbit monoclonal	Cell Signalling	D1D3G/15102	WB	1:1000
FLAG	HRP	Mouse monoclonal	Sigma-Aldrich	M2/A8592-1MG	WB	1:10,000
FLAG	-	Mouse monoclonal	Sigma-Aldrich	M2/F3165	IP	5 µg[1]
GAPDH	HRP	Rabbit	Cell Signalling	3683	WB	1:1000
HA	HRP	Mouse monoclonal	Cell Signalling	2999S	WB	1:1000
HA	-	Mouse monoclonal	SantaCruz	sc-7392	IP	5 µg[1]
IFI44	-	Rabbit polyclonal	ThermoFisher Scientific	PA5-65370	WB	1:1000
IgG	-	Mouse monoclonal	BD Biosciences	557273	IP	5 µg[1]
IRF3	-	Rabbit monoclonal	Cell Signalling	D614C/11904	WB	1:1000
MAVS	-	Rabbit monoclonal	Cell Signalling	D5A9E/24930	WB	1:1000

mcGAS	-	Rabbit monoclonal	Cell Signalling	D3O8O/31659	WB	1:1000
MDA5	-	Mouse monoclonal	In house (Natalia Sampaio)	mAb 17	WB	1:1000
pSTAT1	-	Rabbit monoclonal	Cell Signalling	58D6/9167	WB	1:1000
pSTING	-	Rabbit monoclonal	Cell Signalling	D7C3S/19781	WB	1:1000
RIG-I	-	Mouse monoclonal	AdipoGen	ALME-1	WB	1:1000
SAMHD1	-	Rabbit polyclonal	Cell Signalling	49158S	WB	1:1000
STAT1	-	Rabbit monoclonal	Cell Signalling	9172	WB	1:1000
STING	-	Rabbit monoclonal	Cell Signalling	13647S	WB	1:1000
TBK1	-	Rabbit monoclonal	Cell Signalling	D1B4/3504	WB	1:1000
V5	HRP	Mouse monoclonal	Invitrogen	MA5-15253-HRP	WB	1:5000
V5	-	Mouse monoclonal	Biolegend	680602	IP	5 µg[1]
Vinculin	HRP	Rabbit monoclonal	Cell Signalling	E1E9V/18799	WB	1:5000
Vinculin	-	Mouse monoclonal	Merck	V4505	WB	1:5000
VZV-ORF9	-	Rabbit polyclonal	REF[295]	-	WB	1:2000

2.1.7 General Reagents

Reagent/Resource	Reference or Source	Catalogue Number
0.45µm polyethersulfone filter	Millex	SLHPO33RS
1% Human Keratinocyte Growth Supplement	ThermoFisher Scientific	S0015
1X NuPAGE MOPS-SDS	Invitrogen	NP0001-02
1µm pore transwell insert	Sarsedt	83.3920.101
2-Mercaptoethanol	Sigma Aldrich	63689-100ml
2'3'-cGAMP ELISA Kit	Cayman	501700
4x NuPAGE LDS Sample Buffer	Invitrogen	NP0007
5-alpha competent E. coli	New England Biolabs	C2987H
Blasticidin	ThermoFisher Scientific	A1113903
DDM	Anatrace	D310LA
diABZi	Cambridge Bioscience	28054-500 ug-CAY
Dimethyl sulfoxide (DMSO)	Merck	D8418-100ML
Dual Luciferase assay system	Promega	E1960
Dulbecco's modified Eagle medium	Gibco	41965039
Dynabeads Protein G	Invitrogen	10004D
Epiblastin A	R&D Systems	634015

[1] Concentration of antibody added to 50ul of Dynabeads for co-immunoprecipitation.

(E. coli DNA) dsDNA-EC	Invivogen	tlrl-ecdna
EpiLife™ Medium with 60 µM calcium	ThermoFisher Scientific	MEPI500CA MEPI500CA
Fetal calf serum (FCS)	Gibco	25030081
Gateway LR Recombination Kit	Invitrogen	12538120
GO Taq polymerase	Promega	M7801
HEKn cells	ThermoFisher Scientific	C0015C
Herculase II Fusion DNA polymerase	Agilent Technologies	600677-51
Human CXCL10/IP-10 Kit	R&D Systems	DY266-05
Human IFNβ ELISA Kit	Enzyme Immunoassay	GL02ZA
IGEPAL CA-630	ChemCruz	Sc-280818A
L-glutamine	Gibco	25030081
Lipofectamine 2000	ThermoFisher Scientific	11668030
Minimal Essenetial Medium	Gibco	21090022
Monarch DNA Gel Extraction Kit	New England Biolabs	T1120
Nitrocellulose membrane	BioRad	1620112
NuPAGE Novex 4-12% Bis-TRIS gels	Invitrogen	NP0321
Oligo dT primers	Invitrogen	58862
One Shot TOP10 E. coli	ThermoFisher Scientific	C404003
ONE-Glo Luciferase Assay System	Promega	E6110
pCR™8/GW/TOPO™ TA Cloning Kit	ThermoFisher Scientific	K25002
Phorbol 12-myristate 13-acetate (PMA)	Sigma Aldrich	P1585
Pierce BCA Protein Assay Kit	ThermoFisher Scientific	23227
Poly I:C	Invivogen	tlrl-pic
Polybrene	Sigma Aldrich	H9268-106
Polystyrene flow cytometry test tube	Corning	352235
Ponceau S Solution	Sigma Aldrich	6226-79-5
Protease Inhibitor Cocktail	Cell Signaling Technology	58718
Puromycin	ThermoFisher Scientific	A1113803
Q5 High Fidelity DNA Polymerase Kit	New England Biolabs	E0555S
QIAprep Spin Miniprep kit	Qiagen	27106
QIAshredder spin columns	Qiagen	79656
RNeasy® Plus Mini kit	Qiagen	74136
Roswell Park Memorial Institute medium	Gibco	11875093
SDS	ThermoFisher Scientific	15525017
Skim milk powder	Oxoid	LP0033B
Super Script III Reverse Transcriptase	ThermoFisher Scientific	1806414
SYBR GreenER master mix	Invitrogen	A10315
TaqMan Universal PCR Master Mix	Applied Biosystems	4304437
TBS 0.1% Tween-20	Sigma-Aldrich	P9416-100ml
TC-P 262	R&D Systems	4386/10
THP1 Lucia Dual Cells	Invivogen	thpd-nfis
Triametrene	Merck	T4143-10G
Trimethoprim (TMP)	Sigma-Aldrich	92131-1G
Trypsin Neutralizer Solution	ThermoFisher Scientific	R002100

Trypsin-EDTA	ThermoFisher Scientific	25200056
Trypsin/EDTA Solution	ThermoFisher Scientific	R001100
Ultrapure water	Invitrogen	10977-035
Western Lightning Plus-ECL, Enhanced Chemiluminescence Substrate	PerkinElmer	NEL104001EA
Wet transfer tank	BioRad	1703930
ZymoPURE II Plasmid Midiprep kit	Zymo	D4201

2.2 Methods

2.2.1 Lentiviral Expression Constructs

Primers for polymerase chain reaction (PCR) amplification were designed based on the annotated VZV genome (GenBank accession: GCF_000858285.1) and cGAS (Ensembl: ENSG00000164430) sequences. Primers were designed to reflect complementary bases of the transcript with select bases modified to create missense mutations in ORF9 and cGAS when translated. Amplicons were generated by site-directed mutagenesis with Herculase II Fusion DNA polymerase (Agilent Technologies) using pCR8/VZV-ORF9-STOP and pLenti6/3/V5-DEST-hcGAS-WT plasmids as templates. PCR amplicons were analyzed by agarose gel electrophoresis and bands of the correct size were extracted and purified using Monarch DNA Gel Extraction Kit (NEB). Purified plasmids were propagated in bacterial cultures derived from single colonies of transformed 5-alpha competent *E. coli* (NEB) and then extracted using miniprep (QIAprep Spin Miniprep kit, Qiagen) and midi prep kits (ZymoPURE II Plasmid Midiprep kit). DNA concentration was quantified using a Nanodrop (ThermoFisher Scientific). Plasmid insert sequences were Sanger sequenced (Source Bioscience) to verify the generation of correct mutations. pCR8-ORF9 plasmids were shuttled into pLenti6.3/FLAG (puro) destination vectors using Gateway LR Recombination Kit (Invitrogen). Constructed destination vectors were propagated in *E. coli*, purified and sequenced as outlined above.

The VZV-ORF9-E211R/E227T plasmid was generated via overlap PCR using Q5 High Fidelity DNA Polymerase Kit (NEB). Amplicons were run on an agarose gel and propagated in and purified from *E. coli,* as above. A 3’ A overhang was added to PCR

templates using GO Taq polymerase (Promega) before ligation into TOPO entry vector using pCR™8/GW/TOPO™ TA Cloning Kit (ThermoFisher Scientific). TOPO vectors were transformed into One Shot TOP10 *E. coli* (ThermoFisher Scientific) and extracted using miniprep (QIAprep Spin Miniprep kit, Qiagen). Vector inserts were Sanger sequenced (Source Bioscience) and then shuttled into pLenti6.3/FLAG (puro) destination vectors by Gateway LR recombination (Invitrogen).

MAVS mutant plasmids were designed by Jan Rehwinkel and Philip Hublitz (Genome Engineering Facility, WIMM, UK) and synthesized using ThermoFisher Scientific's GeneArt service. The MAVS-KO cells used in Chapter 3 experiments were generated by CRISPR knockout, therefore the sites targeted by the shRNA/sgRNA were scrambled to prevent knockout of transduced MAVS plasmids in these cells. ThermoFisher Scientific generated pDONR221-MAVS entry plasmids that were shuttled into pLenti6.3/TO/V5 as outlined above.

2.2.2 Lentiviral Production and Transduction

HEK293T cells were seeded in a 10cm dish at $4.5x10^6$ in DMEM (10% FCS, 2mM L-G). Approximately 24 hours later, cells were transfected with 3µg of p8.91 plasmid, 1µg pVSV-G (or pMD2.G) and 3µg lentiviral expression plasmids using Lipofectamine 2000 (ThermoFisher Scientific). 24 hours later, lentiviral medium was replaced with fresh medium. A further 24 hours later lentiviral supernatant was harvested, filtered through a 0.45µm polyethersulfone filter (Millex) and stored at 4°C. Another lot of supernatant was collected after an additional 8 hours, filtered, and pooled with the previous collection. Lentiviral supernatants were stored at 80°C in cryovials.

THP1s cells were spin infected by adding $1x10^6$ cells to a 6-well plate along with 3ml of lentiviral supernatant and 8µg/ml Polybrene (Sigma-Aldrich) and centrifuged at 2600rpm for 90 minutes (with no brakes). HEK293-p125-MAVS-KO cells, Huh7-MAVS-KO cells, and HFFs were seeded in 6 well plates at $5x10^5$, $2.5x10^5$ and $2.5x10^5$ cells/well

respectively, and transduced without centrifugation. 24 hours post-transduction, the lentiviral medium was replaced with fresh medium. The next day, the medium was replaced with medium containing 10 µg/ml blasticidin (ThermoFisher Scientific) or 1µg/ml puromycin (ThermoFisher Scientific). Untransduced cells were treated with antibiotics and used as a control to determine the time point at which all untransduced cells in culture had died. Once transduced cells were selected, cells were used for experimentation.

2.2.3 IFN Bioassay

3C11 cells were seeded at $2x10^4$ in a 96-well plate in DMEM (10% FCS, 2mM L-G). The next day, the cell supernatant to be measured was put onto 3C11 cells that inducibly express firefly luciferase from an ISRE, i.e. respond to type I IFN in the supernatant. After overnight incubation, the expression of luciferase was quantified using the ONE-Glo Luciferase Assay System (Promega) and the GloMax Multi+ Microplate Multimode Reader.

HEK293-p125-MAVS-KO cells were seeded at $2x10^4$ in a 96-well plate in DMEM (10% FCS, 2mM L-G). The next day, the cells were transfected with 5ng MAVS constructs and 3.33ng IVT RNA (5' triphosphate RNA[191]). Approximately 24 hours later, the luciferase produced under IFNβ promoter control was measured using the OneGlo protocol as outlined above.

2.2.4 Dual Luciferase Assay

HEK293T cells were seeded at $2x10^4$ into 96 well plates. The following day, cells were transfected with the following plasmids using Lipofectamine 2000 (ThermoFisher Scientific): 20ng p125-F-Luc, 5ng pRL-TK, 1ng hcGAS, and 10ng hSTING. The cells were also transfected with 50ng of VZV-ORF9 expression plasmids, empty vector (EV) or

EMCV-L. The next day, the expression of Firefly and Renilla luciferase was assessed using Dual Luciferase assay system (Promega). The luminescence of firefly (IFNβ production) was divided by Renilla (constitutively expressed) to normalize the transfection efficiency.

2.2.5 Flow cytometry for STING FRET Assay

HEK293T cells were seeded at $1x10^6$ cell/well in 6 well plates. The next day, cells were transfected with 300ng mTurq-mSTING-eYPet, 30ng pLenti6.3/V5-DEST-human-cGAS WT, and 150ng of either pLenti/N-FLAG/puro/FLAG-VZV-ORF9 constructs or pLenti6.3/TO/V5/EV. Approximately 24 hours later, cells were dissociated, pelleted, and resuspended in phosphate buffered saline (PBS) to remove residual DMEM (10% FCS, 2mM L-G). The cells were pelleted and resuspended in 600µl FACS buffer (0.5mM EDTA, 2.5% FCS, autoclaved PBS). The cells were then strained through a 35µm nylon mesh (Corning) to remove cell clumps and debris, with the flow through collected in a polystyrene flow cytometry test tube (Corning). Activation of STING via FRET shift was determined by flow cytometry using an LSRFortessa™ X-20 Cell Analyzer (BD). Data was analyzed using the software FlowJo. A detailed explanation of mTurq-mSTING-eYPet plasmid design and function can be found in Section 5.5.

2.2.6 Western Blotting

Cells were lysed for western blot using 30µl of RIPA buffer (10mM TRIS-HCl pH8, 140mM NaCl, 1% Triton-X 100, 0.1% SDS, 0.1% sodium deoxycholate, 1mM EDTA, 0.5mM EGTA) for 12 well plates and 90µl for 6 well plates. Cells were scrapped from the plates, on ice, and insoluble cellular debris was removed by centrifugation. Protein concentration of lysates was determined using the Pierce BCA Protein Assay Kit (ThermoFisher Scientific) and normalized to 15ug/µl with (PBS). 4x NuPAGE LDS Sample Buffer (Invitrogen) was added along with 20% of 2-Mercaptoethanol (Sigma-

Aldrich) and samples were boiled at 95°C for 10 minutes. Samples were run on a NuPAGE Novex 4-12% Bis-TRIS gels (Invitrogen) in 1X NuPAGE MOPS-SDS (Invitrogen) running buffer. Proteins were then transferred from the gel onto a nitrocellulose membrane (Bio-Rad) in a solution of 1X transfer buffer (25mM TRIS, 192mM glycine and 10% methanol) via a Trans-Blot Turbo Transfer System (Bio-Rad). Protein transfer was verified using Ponceau S Solution (Sigma-Aldrich). Membranes were blocked for non-specific binding in a solution of 5% skim milk powder (Oxoid) in TBS 0.1% Tween-20 (Sigma-Aldrich) for 1 hour at room temperature. Membranes were incubated with primary antibodies in 5% skim milk TBS-T overnight at 4°C. Primary antibodies used in this project are listed in Section 2.1.6 above. Primary antibodies targeting phosphorylated proteins were diluted in 5% bovine serum albumin (BSA) in TBS-T. Membranes were washed five times for 5 minutes in TBS-T and incubated for 1 hour at room temperature in 5% skim milk powder containing 1:2000 dilution of the appropriate horseradish peroxidase (HRP) coupled secondary antibody. Proteins were then detected using Western Lightning Plus-ECL, Enhanced Chemiluminescence Substrate (PerkinElmer) and imaged using the iBright FL1000 Imaging System (ThermoFisher). Band intensity was quantified using densitometry analysis software on ThermoFisher Connect.

2.2.7 Immunoprecipitation

$1.4x10^7$ HEK293T cells were seeded in a 15cm cell culture dish for each protein interaction condition. The following day plates were transfected with 12.7µg of STING-HA expression plasmid using Lipofectamine® 2000 Transfection Reagent (ThermoFisher Scientific). Each dish was also transfected with 2µg FLAG-ORF9 constructs and 10µg cGAS-V5. 24 hours later the cells were lysed with lysis IP buffer (20mM TRIS-HCl pH 7.4, 100mM NaCl, 1mM EDTA, 0.5% NP-40 (IGEPAL CA-630, ChemCruz) containing 1:100 Protease Inhibitor Cocktail (Cell Signaling Technology). For select experiments, IP buffer contained increasing concentrations of salt (100mM, 200mM, 500mM, 1M NaCl). A small sample of lysate was set aside as the input fraction for immunoprecipitation.

Lysates were pre-cleared by incubating in 200µl of Dynabeads Protein G (Invitrogen) for 30 minutes. The lysates were split into four equal parts, for each antibody of interest, and incubated in 50µl of Dynabeads coated in 5µg of α-V5, α-FLAG, α-HA, or control IgG antibody for 1 hour under rotation at 4°C. The supernatant was removed with an aliquot stored as an unbound fraction from each sample. The beads were washed three times in lysis buffer, boiled and the supernatant removed from the beads, which is the bound fraction. Input, unbound, and bound fractions were subjected to immunoblotting as outlined in Section 2.2.6.

2.2.8 Recombinant Protein Pull-Down Assays

Recombinant proteins were also used as input for pull-down assays. 3µl cGAS-HA was mixed with 1.5µl FLAG-ORF9 or FLAG-GFP in IP lysis buffer (20mM Tris-HCl pH7.4, 100mM NaCl, 1mM EDTA, 0.5% NP-40). Samples were incubated with 25 µl Dynabeads Protein G (Invitrogen) coated in 2.5µg α-FLAG or α-HA. The supernatant was removed with an aliquot stored as an unbound fraction from each sample. The beads were washed three times in lysis buffer, boiled and the supernatant removed from the beads. Input, unbound, and bound fractions were subjected to immunoblotting as outlined in Section 2.2.6.

Histone competition assays were performed by introducing recombinant hH2A-H2B protein to the cGAS-ORF9 lysates. The histone protein was added to the lysates after the unbound fraction had been removed. A reverse experiment was also performed, in which cGAS was incubated with hH2A-H2B, and then ORF9 protein was introduced after the unbound stage to determine if either protein had competitive binding properties/capabilities. hH2A-H2B recombinant protein was kindly gifted by Christian Zierhut (Institute of Cancer Research, UK). cGAS, ORF9 and GFP recombinant protein was generated by Jonny Hertzog[292].

2.2.9 RT-qPCR

Cells from the indicated experiments were washed with PBS and lysed in RLT Plus Buffer (Qiagen) containing a 1% volume of 2-Mercaptoethanol. RNA was extracted using QIAshredder spin columns (Qiagen) and the RNeasy® Plus Mini kit (Qiagen) according to the manufacturer's instructions. The concentration of extracted RNA was measured using a Nanodrop (Thermofisher) and normalized with ultrapure water (Invitrogen). RNA was reverse transcribed using Super Script III Reverse Transcriptase (ThermoFisher Scientific) and oligo dT primers (Invitrogen). The qPCR reaction containing TaqMan Universal PCR Master Mix (Applied Biosystems) and TaqMan Probes (Section 2.1.5) was run on QuantStudio 7 Flex Real-Time PCR System (ThermoFisher Scientific) with standard fast settings. Gene expression was analyzed with the Ct method, normalizing against *GAPDH* expression. Quantitative reverse transcription PCR (RT-qPCR) for VZV transcripts was performed with SYBR GreenER master mix (Invitrogen) using primers pairs listed in Section 2.1.4.

2.2.10 RLR Stimulations

Huh7-MAVS-KO cells transduced with MAVS constructs were seeded at $2x10^5$ cells/well in 6 well plates and left to adhere overnight. The next day, the cells were transfected with 25ng Poly I:C (Invivogen) and lysed for RT-qPCR and WB (as outlined in sections 2.2.9 and 2.2.6) 24 hours post-stimulation. Transfected HEK293-p125-MAVS-KO cells were seeded $5x10^5$ in 6 well plates and 24 hours later, transfected with 50ng MAVS constructs or EV. The next day, cells were transfected with either 5ng Poly I:C (Invivogen) or 100ng IVT RNA[191], depending on the experimental setup. As above, 24 hours post-stimulation, cells were lysed for RT-qPCR or WB.

2.2.11 MAVS Aggregation Assay

HEK293-p125-MAVS-KO cells were seeded in 15cm dishes and transfected with 1µg MAVS constructs. The next day, cells were transfected with 1µg of IVT RNA and left to incubate overnight. Cells were lysed with 3ml of hypotonic buffer (1.5mM $MgCl_2$, 5mM KCl, 10mM Tris 7.5) plus protease inhibitors (Cell Signalling). Cell lysates were spun at 1000g for 5 minutes to remove the nuclei. Supernatants were subjected to another 1000g for 5 minutes and 10,000g for 10 minutes centrifugation steps to isolate mitochondria. Mitochondrial pellets were dissolved in hypotonic buffer and 0.5% DDM (Anatrace) and treated with benzonase. 1x SDS (ThermoFisher Scientific) and loading buffer (0.5X TBE, 10% glycerol, 2% SDS, 0.0025% bromophenol blue, ultrapure H_2O) were added to samples that were thend incubated at room temperature for 10min. Samples were run on a vertical 1.5% agarose gel (1X TBE) in 1X SDS (in TBE solution) at 4°C. Proteins were then transferred from the gel onto a nitrocellulose membrane (Bio-Rad) using a wet tank (BioRad) transfer method and subjected to immunoblotting. MAVS aggregation immunoblotting protocol was adapted from REF[296].

2.2.12 VZV Co-Infection via Co-Culture

$6x10^6$ transduced THP1 cells were seeded into a 6-well plate containing 10ng/ml PMA in RPMI (10% FCS, 2mM L-G) and left overnight to adhere to the plate. The THP1 cells were then co-cultured with $1.5x10^6$ freshly thawed uninfected and VZV-infected MeWo cells in MEM. VZV or mock-infected MeWo cells were added in a 1:2 ratio of infected to uninfected MeWo cells. After 1 hour of co-culture infection cells were washed with 1X PBS three times to remove MeWo cells. Fresh RMPI was added to cells and left to incubate overnight. Cells were lysed with RLT for RT-qPCR as described.

2.2.14 Conditional Degradation of VZV-ORF9

$6x10^6$ THP1 cells treated with PMA were seeded in a 6-well plate (or $2.5x10^6$ in a 12-well) and co-cultured with VZV-ORF9^{ecDHFR} infected MeWo cells in medium containing 25 mM TMP (trimethoprim, Sigma-Aldrich). 10uM of Triametrene (Merck), epiblastin A (R&D Systems), and TC-P 262 (R&D Systems) were tested as TMP alternatives. After a 1-hour incubation, the cells were washed three times in PBS and cultured with TMP for an additional 24 hours. Finally, the cells were washed free of TMP, cultured overnight in the presence or absence of TMP, and harvested for RT-qPCR and immunoblot analysis.

2.2.15 VZV Infection in a Transwell System

A 6-well insert with 1µm pore size (Sarsedt) was placed upside down in a 15cm dish. Cryopreserved infected MeWo cells were thawed and mixed in a 4:1 ratio with uninfected MeWo cells. 500µl of uninfected or infected MeWo cells were carefully pipetted onto the inverted insert, forming a liquid dome and left to adhere overnight. Using forceps, the excess liquid was removed, and inserts were placed in a 6-well plate with RPMI (10% FCS, 2mM L-G). HaCaT, dermal fibroblast, or primary keratinocytes were seeded onto the top side of the insert membrane, creating a barrier between cell lines through which only virus can pass. 24 hours later HaCaT, fibroblast and keratinocyte cells were lysed for RT-qPCR as described in Section 2.2.9. A detailed methodology of this transwell system for VZV infection (Fig. 7) can be found here in reference[297].

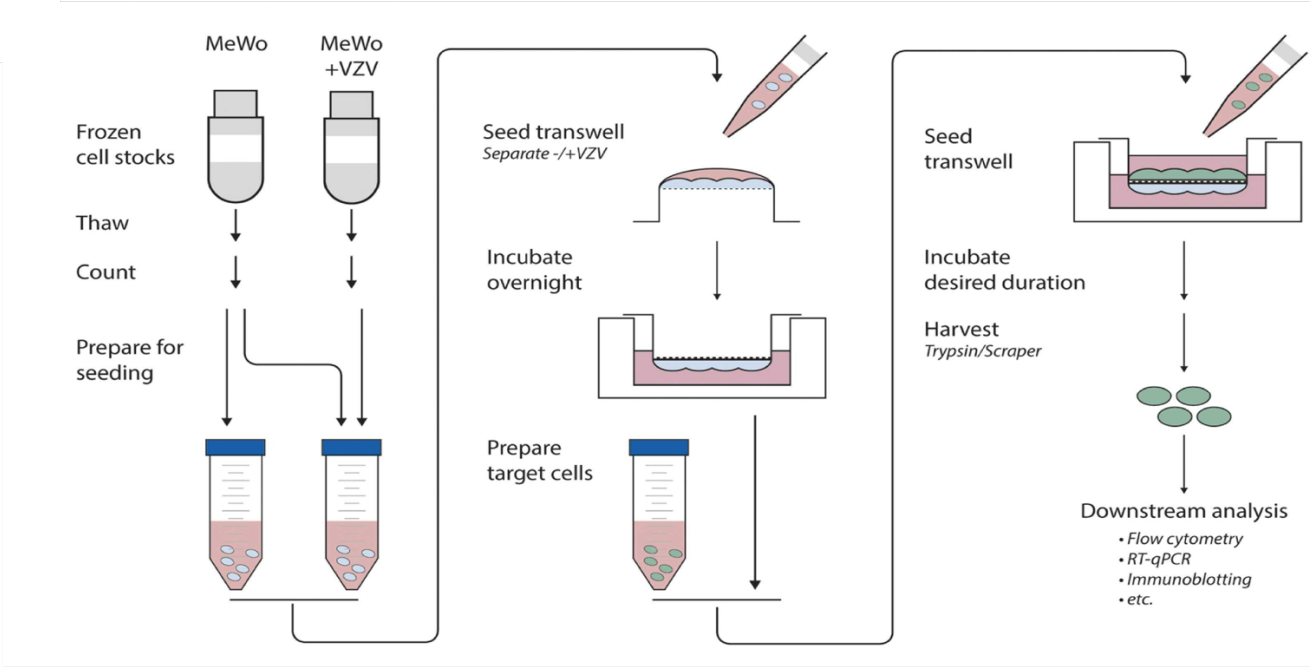


Figure 7: Methodology of transwell co-infection experiments.
A graphical summary of co-infection of infected MeWo cells with differentiated THP1s, separated by a mesh to prevent cell mixing. Figure taken from Hertzog & Rehwinkel 2023. doi: 10.1016/j.jviromet.2022.114661.

2.2.16 DNA Stimulation

Transduced THP1 cells overexpressing FLAG-ORF9 constructs or GFP-V5 were transfected with 200ng of E. coli dsDNA (Invivogen) to stimulate cGAS. Transduced HFF cells overexpressing FLAG-ORF9 constructs or GFP-V5 were transfected with 100ng or 200ng of *E. coli* dsDNA. Cells were lysed 24 hours after transfection and ISG and IFN induction was measured using RT-qPCR.

2.2.17 ELISA

2.2.17.1 IFNβ and IP-10 ELISA

Media from stimulated transduced HFFs (2.2.16) was collected, clarified by centrifugation and stored at -80°C until use. Secreted IFNβ was quantified via Human

IFNβ ELISA Kit (Enzyme Immunoassay) as per manufacturer instructions. Absorbance was measured using Clariostar and concentration was calculated from IFNβ standard curve. Secreted CXCL10 levels were measured using Human CXCL10/IP-10 Kit (R&D Systems) as per manufacturer instructions.

2.2.17.2 cGAMP ELISA

HFF cells transduced to express ORF9 constructs or GFP were seeded into 15cm dishes at $1.5x10^6$ cells/well. The next day, cells were transfected with 2.5µg *E. coli* dsDNA and were incubated overnight. Cells were dissociated, pelleted and washed with PBS. After centrifugation, cells were dry frozen at -80°C for at least overnight. Cell pellets were lysed in 250µl lysis buffer (50mM Tris pH7.5, 150mM NaCl, 0.5% sodium deoxycholate, 0.03% SDS, 0.005% Triton X-100, 0.5mM EDTA, 1mM $MgCl_2$ and 25,000U benzonase). This protocol for lysis was kindly provided by Marie-Therese El-Daher (Yanick Crow Lab, University of Edinburgh, UK). Lysates were quantified in duplicate using 2'3'-cGAMP ELISA Kit (Cayman) as per manufacturer instructions. Absorbance was measured using Clariostar at 450nm and concentration was calculated from cGAMP standard curve.

2.2.18 STING Stimulations

$2x10^6$ THP1 cells transduced with VZV-ORF9 or GFP lentivirus were seeded in a 12-well plate in RPMI growth medium and stimulated with the 0.005mM of the STING agonist diABZi (Cambridge Bioscience). The diABZi compound was left to stimulate the cells overnight. Cells were lysed in RLT lysis buffer (Qiagen) for RNA isolation and RT-qPCR.

2.2.19 Protein Structure Predictions

The secondary structure of VZV-ORF9 was modelled using AlphaFold Colab notebook. This notebook does not use homologous structure templates and instead relies on the BFD database, a collection of 2.5 billion protein sequences. The binding configuration of cGAS and VZV-ORF9 was modelled using AlphaFold2-multimer notebook (v1.5.5) [298,299]. AlphaFold-generated structures represent a predicted model of secondary structure folding and configuration in a 3D space, while the multimer notebook provides a prediction of protein binding. Structures were visualized and coloured using Mol* 3D Viewer (RCSB PDB). Angstrom distance between amino acids was measured using Mol* 3D Viewer (RCSB PDB) and PyMol. Peptide binding predictions were modelled using PepSite2. Root Mean Square Deviation (RSMD) value was calculated using PDBeFold (Protein Data Bank in Europe, EMBL-EBI).

2.2.20 Data Analysis and Software

Data was processed and analyzed using Excel (Microsoft) and GraphPad Prism 10 (GraphPad Software). iBright Image Analysis Software and ThermoFisher Connect Platform were used to process immunoblot images. Flow cytometry was analyzed using FlowJo (v10.10). GraphPad was used to perform statistical analysis and generate graphs. Statistical tests used are further detailed in figure legends. Adobe Illustrator (Adobe Systems) was used to compile figures. Snapgene (v6.1.2 – GSL Biotech) was used to design restriction digest screens, analyze sequences and design primers.

Chapter 3

Polymorphisms Alter Translation and Function of MAVS

3.1 SARS-CoV-2

3.1.1 Origin story

Coronaviruses are a family of positive-sense ssRNA viruses that infect mammals and avian species. Three coronaviruses caused zoonotic spillover into humans: SARS-CoV-1 caused an epidemic in China in 2003, Middle East respiratory syndrome coronavirus (MERS-CoV) has caused intermittent outbreaks since 2012, and SARS-CoV-2 quickly spread into a global pandemic in 2020[300–303]. SARS-CoV-2 infection causes COVID-19 and was first detected in patients exhibiting symptoms of pneumonia in Wuhan, China in late 2019[304–306]. Coronaviruses exhibit wide genetic diversity in humans and bats, which led to the rapid development of divergent SARS-CoV-2 strains during the COVID-19 pandemic[307,308].

A monumental effort has taken place to determine the causative events of SARS-CoV-2's spillover into humans. Early hypotheses situated its origins in the meat sold in wet markets in Wuhan due to the high rate of SARS-CoV-2 infected COVID-19 patients who resided near or worked in the city's Huanan Market[307,309–311]. Additionally, genetic tracing of early infections classified two distinct lineages - lineage A and lineage B. Lineage A is linked to patients that resided near the Huanan market area; while lineage B patients had an epidemiological link to Huanan Market specifically[307,312]. It has been proposed that two progenitor viruses circulating in non-human mammals established zoonotic transmission to humans around the same time, creating these two lineages[307].

Several animals sold at the Huanan market are susceptible to SARS-CoV-2 infection[307,313–315]. Many species sold at Huanan market were farmed in Hubei Province –

this region holds an extensive series of caves housing *Rhinolophus* bats[311,316,317]. Palm civets farmed in Hubei Province were found to be infected with SARS-CoV-1 in 2003 and 2004[318]. *Rhinolophus* bats were presumed to be the progenitor species of SARS-CoV-2 infection and pangolins were thought to be the intermediate spillover species to humans but may have been infected by humans or yet another intermediate species. A key question remains: when did the spike protein evolve a high affinity for hACE2 and in which species? One study using simulations found that an ancestral virus of SARS-CoV-2 and RaTG13, a *Rhinolophus* bat coronavirus, already possessed a spike protein with strong hACE2 affinity[308,319].

The exact zoonotic transmission event to humans is unclear and likely will never be resolved with absolute certainty. However, three probable scenarios have been proposed:

1. Bats are the progenitor species and transmitted the virus to humans directly, likely in the Huanan Market

2. A closely related virus had already infected humans until a mutation that increased virulence evolved in a patient in Wuhan

3. A spillover virus from a bat infected one or multiple intermediate hosts until zoonotic transmission to humans[307,308,312,320,321].

3.1.2 Pathology & Epidemiology

As of writing, COVID-19 has caused >7 million deaths[322], accounting for a ~1% mortality rate. Up to 20% of infected individuals require hospitalizations, of which <30% require intensive care[323–328]. Unsurprisingly, COVID-19 was the leading cause of death in the USA in 2020, ahead of cardiovascular disease and cancer[329,330].

SARS-CoV-2 is spread via respiratory droplets and aerosols from presymptomatic, asymptomatic, or symptomatic individuals[323,329]. Early in the pandemic, it was believed the virus could be fomite transmitted (transmission from contaminated objects) as laboratory experiments found viable virus on a variety of surfaces and objects[331–334]. However, subsequent investigations, including patient studies did not detect viable virus on surfaces unless contained in liquid droplets[333,335–337]. The resulting consensus is that the risk of fomite transmission is low but not insignificant, highlighting the importance of hand hygiene.

The incubation period for symptom onset is 4-5 days[323,329]. The first site of SARS-CoV-2 infection is cells of the upper respiratory tract: specifically, the ciliated cells of the nasopharynx, trachea, and olfactory mucosa[323]. Alternatively, an infection can begin from the lower respiratory tract or spread by gradual dissemination, where it spreads to the alveoli, particularly the alveolar type 2 cells[323].

Infected individuals can remain asymptomatic, although most patients present with mild to moderate respiratory disease with common symptoms of fever, cough, and shortness of breath[323,329]. Less common symptoms include malaise, diarrhea, myalgia, headache and anosmia[323,329,338]. Critical cases of infection that require hospitalization are characterized by progressive respiratory failure (and resultant acute respiratory distress syndrome), septic shock, and multiple organ failure[323,329,339]. Patients with severe cases of SARS-CoV-2 infection typically experience systemic hyperinflammation, caused by increased expression of inflammatory cytokines – aptly called a cytokine storm [323,329,339–341]. The uncontrolled and dysregulated release of IFN causes a positive feedback loop, inducing more IFN, and further exacerbating symptoms. The secretion of inflammatory cytokines (IL-6, IL-8 and TNF) is positively associated with disease severity and can be a predictor of mortality rate[341]. While low levels of viral titres can be detected in many organs of COVID-19 patients, it is still unclear if this is a result of direct infection as is the full extent of the effect on each organ[323]. Notably, the intestine can be directly infected by the virus, as patients experience gastrointestinal symptoms and viral RNA has been found in feces[323,329,342,343].

Indeed, sampling sewage runoff acted as a predictor of geographic outbreaks in the early stages of the pandemic.

Early pandemic studies in Wuhan found hypertension was present in <30% of patients and represented a high risk of comorbidity[344,345]. While those findings are significant, the strongest predictors of severe COVID-19 outcomes are being male, obesity, and the strongest correlating factor being advanced age. Indeed, 50-64-year-olds have a 25x greater risk of death compared to adults aged <30, with this rate increasing to 340x when over 85 years old[329,331,345]. The most common co-morbidities of severe COVID are hypertension, heart failure, diabetes, asthma, cancer, and various respiratory diseases[323,328,329,346–348]. Additionally, racial and ethnic minority groups experienced a higher rate of infection and hospitalizations compared to White patients, however, this phenomenon seems to be primarily driven by socioeconomic factors[329,349,350].

Genome-wide association studies have linked mutations in the chemokine receptors *CXCR6* and *CCR9* to severe COVID-19. Inborn errors of the TLR3 and TLR7-dependent type I IFN response predisposed patients to severe SARS-CoV-2 infection. Indeed at least 3.5% of patients with severe COVID-19 pneumonia had mutations in *IRF3, IRF7*, *IFNAR1, IFNAR2, TLR3, TBK1*, and *TICAM1*, underscoring a genetic predisposition to severe disease[351,352]. Neutralizing antibodies against IFNα are associated with severe COVID-19, contributing to ~20% of deaths and are present in ~4% of uninfected > 70-year-olds[323,353–355]. These data all together highlight the importance of IFN in immune control of SARS-CoV-2 infection.

3.1.3 The SARS-CoV-2 Genome

SARS-CoV-2 shares 79% sequence similarity with SARS-CoV-1[356]. It has a large genome of 29.9kb encoding 9860 amino acids and 29 proteins[357]. ORF1a and ORF1b comprise the majority of the genome, encoding 16 non-structural proteins that mediate viral replication and interactions with the host cell[271]. While translation would normally halt at the C-terminal stop codon of ORF1a, a programmed ribosomal frameshift in this

overlapping region with ORF1b allows some ribosomes to continue translation, generating a much longer protein from ORF1a[271,358,359].

SARS-CoV-2 encodes structural proteins, non-structural proteins and accessory proteins (Fig. 8, B). The structural proteins consist of NP, membrane (M), envelope (E) and spike (S) proteins, which together with the host lipid bilayer, form the virion[271,323]. Accessory proteins are encoded by ORF3a, ORF3c, ORF6, ORF 7a, ORF 7b, ORF 8, and ORF 9b[271,360]. These accessory proteins are not required for viral replication but antagonize immune response mechanisms[323,361–363].

If a cell becomes infected with multiple coronaviral particles, the polymerase can switch templates during replication. This results in the emergences of recombined viruses. These recombination events occur with frequency in the spike protein[271]. The abundance of genomes collected during the pandemic and from suspected reservoir species, allowed for real-time observation of viral evolution[271].

3.1.4 Replication & Life Cycle

The spike glycoprotein, divided into two subunits, mediates entry into host cells via binding to angiotensin-converting enzyme 2 (ACE2) entry receptor via its S1 subunit while S2 mediates membrane fusion[271,323,364] (Fig. 8). The distribution of ACE2 receptors in specific cells and tissues is the primary determinant of coronavirus tropism[271,365,366]. The S1 subunit has an N-terminal domain, the receptor binding domain (RBD), and a C-terminal domain. Components of the RBD are the main targets of neutralizing antibodies and therefore prone to evolve mutations with host immune evasion phenotypes[367–372]. The circulating strains of SARS-CoV-2 (Alpha, Beta, Delta, Gamma and Omicron) were predominantly driven by the evolution of mutations in regions of the RBD that dictate ACE2 binding, and thereby the cell types and species it can infect, and mechanisms of immune evasion[271,373,374]. Upon binding to ACE2, the S protein is cleaved by the transmembrane serine protease TMPRSS2 to catalyze the fusion of viral and host

membranes[271,323,375–378]. Considering *TMPRSS2* is highly expressed in epithelial cells lining of respiratory tract, it gives reason for this being the most highly infected and symptom-stricken area.[271,375,379]. Alternatively, the S protein can enter the cell by endocytosis of the lipid bilayer and cleavage by the proteases cathepsin L or B in the endosome to release viral particles into the cytoplasm[367,375,376,378,380,381]. Considering the low expression of cathepsin L in endosomes of the respiratory tract, it provides reasoning that this is not the primary route of cellular entry in epithelial cells[271,323,378–383].

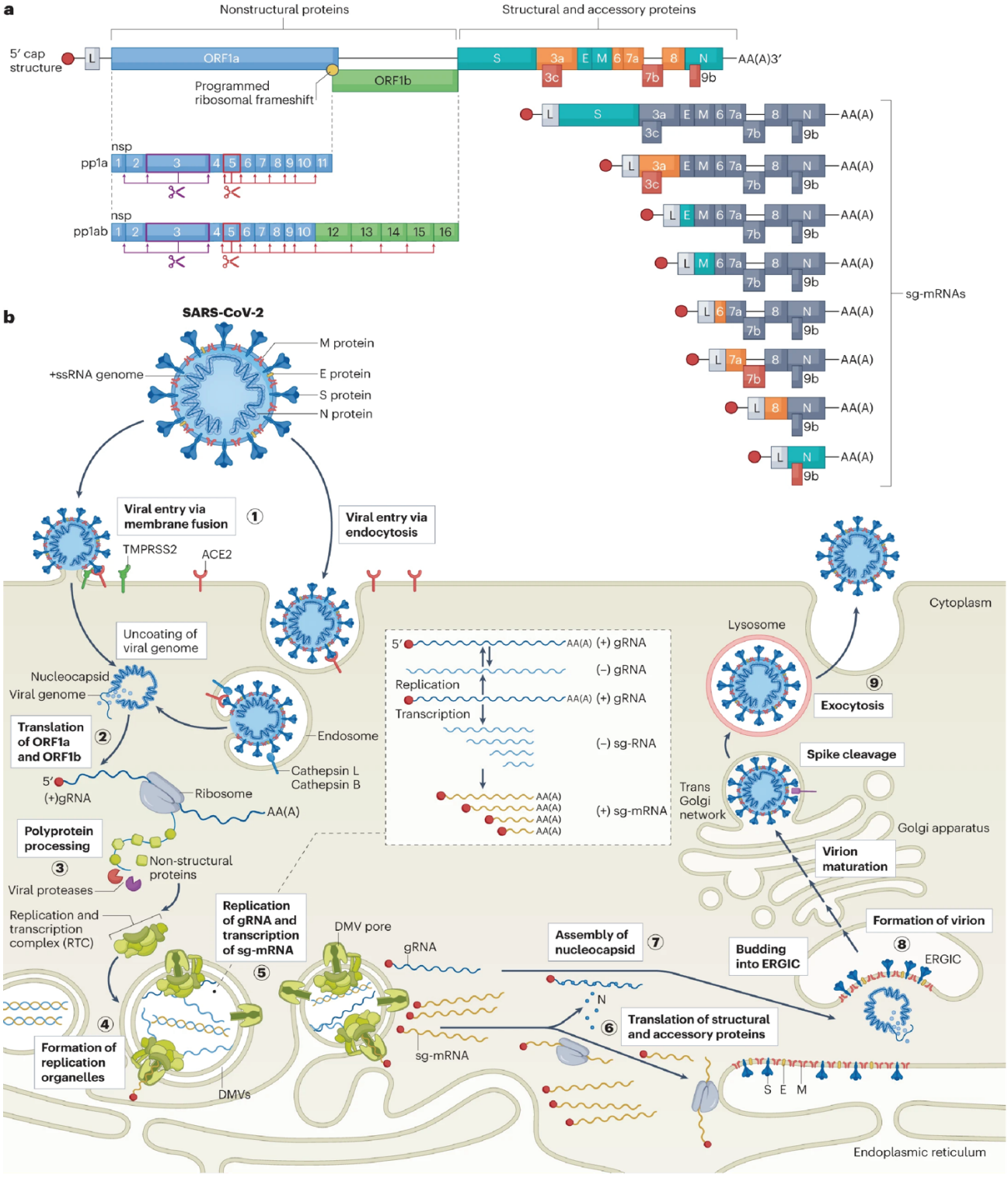


Figure 8: The SARS-CoV-2 genome and viral life cycle.
(**A**) The SARS-CoV-2 genome encodes non-structural proteins, structural proteins and accessory proteins. Structural and accessory proteins are produced from sg-mRNA by discontinuous transcription. (**B**) SARS-CoV-2 virions gain entry into the cell via the ACE2 receptor or membrane fusion mediated by TMPRSS2. Viral replication begins inside ER membranes remodelled by the virus into replication factories. Translated structural and accessory proteins are shuttled to the ERGIC along with the nucleocapsid to form progeny virus which egress from the cell via lysosomal exocytosis. Figure taken from Steiner et al. 2024. doi:10.1038/s41579-023-01003-z.

Upon entry into the cell the viral genome begins production of ORF1a and ORF1b by host ribosomes to generate replication and translation complexes (RTC). During this process, endoplasmic reticulum (ER) membranes are remodelled to form replication factories in which the newly synthesized RTCs will reside[271,323,384–386]. The RTC synthesizes viral RNA inside of double membraned vesicles, hijacked from the ER, thereby shielding viral RNA from detection by cytosolic PRRs. The RTC produce viral gRNA and transcribe sg-mRNA from the negative sense complements of each RNA species[271,360,387]. A subset of sg-mRNA undergo leaky ribosomal scanning during translation to produce further proteins from downstream ORFs [271,360,387]. The positive sense gRNA undergoes LLPS with NP proteins during the assembly of the nucleocapsid[271,274,277,388]. sg-mRNA are translated into S, E, and M proteins at the ER and NP proteins in the cytoplasm[271,388,389]. S, E, and M proteins are membrane-bound in the ER, which are then translocated to the ER-to-Golgi intermediate compartment (ERGIC) and combined with the NP proteins[271,388,389]. The viral particles undergo post-translation modifications and further maturation in the Golgi network until exit from the Golgi in lysosomes as matured virions (Fig. 8) [271,390]. The virions are released from the cell via lysosomal exocytosis at the plasma membrane[271,391].

3.1.5 Experimental Models of SARS-CoV-2

The permissive nature of cell lines to viral infection allows for the study of viral characteristics in isolation, including replication cycles, immune detection receptors and inhibitors of viral replication.

Calu-3 cells are an epithelial cell line that is used to study SARS-CoV-1 and have high expression levels of *ACE2* and *TMPRSS2*[392,393]. Vero E6 epithelial cells, originally isolated from African Green Monkeys, are highly permissive for SARS-CoV-2 and therefore widely used to isolate, propagate and test anti-viral drugs for SARS-CoV-2. These cells express *ACE2* and show increased viral titres if engineered to express

TMPRSS2[392,393,393,394]. Caco-2, a colorectal adenocarcinoma cell line, exhibit lower expression of *ACE2* but higher expression of *TMPRSS2* compared to Calu-3[395,396]. Caco-2 cells have been used to study SARS-CoV-1 and are now one of the main cell lines used in SARS-CoV-2 studies[393,397,398]. Huh7 cells, isolated from a liver carcinoma cell line, are permissive to SARS-CoV-1[393,399]. Despite this, viral replication is moderate, potentially due to abortive infection, and there is little differential global protein expression in Huh7 infected cells compared to control cells left uninfected[393,395,400]. While some reports have shown Huh7 cells to be permissive for SARS-CoV-2 infection[304,364,400–404], expression analysis revealed strong *TMPRSS2* expression but a lack of *ACE2* expression[393,395]. However, a late-stage IFN response at 48hrs in Huh7 cells indicates a delayed IFN response to infection[400,404]. A549 cells have low expression of *ACE2* and no expression of *TMPRSS2*[394,400,405], however overexpression of *ACE2* makes these cells permissive to infection[406,407] and has shown to be a valuable tool for anti-viral drug screening[393,408–410]. HEK293T express low levels of *ACE2* and no *TMPRSS2*, preventing viral entry and propagation[400,411,412]. Similar to studies in Huh7 cells, proteomic analysis revealed no differential protein expression in infected cells[393,395]. No cytopathic effects and low viral production make HEK293T cells a less attractive model than Caco-2 clles; however, when engineered to overexpress *ACE2* they are highly permissive to infection and show a robust IFN and ISG response[393,413].

Organoids are a powerful tool to study the effects of SARS-CoV-2 on whole organs. Organoids are grown from human induced pluripotent stem cells (iPSCs) on an extracellular matrix scaffold and provide a valuable investigation tool as iPSCs can be generated from donors harboring genetic mutations and disease phenotypes[393,414–417]. Respiratory models of SARS-CoV-2 are generated from multipotent adult stem cells to generate human distal lung organoids and can be infected with SARS-CoV-2 using an air-cell interface model to provide a physiologically relevant transmission and pathology[271,418]. Organoids of tonsils, brain, kidney, intestine, and respiratory (alveolar lung, lung airway, and bronchial) models are used to study organ-specific effects of SARS-CoV-2 infection[271,381,414–418].

Several animal models have been developed to study SARS-CoV-2 *in vivo*, however, most have pitfalls, primarily mild disease phenotypes compared with severe COVID-19 cases in humans[323]. Ferrets, Syrian golden hamsters, mice and non-human primates are all used as in vivo models of SARS-CoV-2[271,419]. Hurdles in finding an appropriate *in vivo* model include recapitulating disease phenotypes and severity and low expression of *ACE2* receptors in the respiratory tract with affinities for the spike protein of circulating SARS-CoV-2 strains. This raised issues with mice, dogs and pigs as their ACE2 does not show affinity for human circulating SARS-CoV-2 spike protein[419,420]. To circumvent this, transgenic mouse models expressing human *ACE2* have been developed and show a robust chemokine and inflammatory cytokine response to infection[421–424]. Alternatively, viral adaptation of the spike protein can increase affinity for mouse ACE2 but poses risk for viral clearance by neutralizing antibodies which target the receptor binding domain[419]. Syrian golden hamsters are convenient animal models that are used for infection with MERS, SARS-CoV-1, influenza and adenovirus[419,425–428]. Transmission occurs between inoculated hamsters and naïve cage mates, providing a useful tool for transmission studies[419,429]. Demographic differences in COVID-19 severity are reflected in infected hamsters, i.e. aged male hamsters are the most severely affected, making them an ideal model for comorbidity studies[419,430,431]. Infection in ferrets is predominantly limited to disease presentation in the upper respiratory tract as evident from post-mortem histopathology [419,424]. Ferrets typically display mild disease and can transmit infection to naïve cage mates, providing a useful model for upper respiratory tract infections/phenotypes, mucosal vaccines and transmission studies[419,421]. Non-human primates provide the closest *in vivo* model of human pathology and infection but, of course, pose the greatest hurdle to feasible research due to their expensive nature and husbandry logistics. Rhesus macaques, cynmolgus macaques and African green monkeys show high levels of viral replication in both the upper and lower respiratory tract and exhibit a mild form of disease[419,432–434]. Infection of non-human primates showed viral shedding in both respiratory and gastrointestinal tract and hematological phenotypes including T cell activation and neutrophilia[419]. Many vaccine and drug trials have taken place in rhesus macaques and oncynmolgus macaques [435–439]. Finally, the most accurate model of SARS-CoV-2 infection in humans is to infect humans in a controlled setting. COVID-19 human

challenge studies inoculated young healthy volunteers intranasally with SARS-CoV-2[440–443]. Studies later in the pandemic inoculated young healthy volunteers previously vaccinated for SARS-CoV-2. The majority of patients experienced mild-to-moderate symptoms with the remaining asymptomatic. Following the rollout of COVID-19 vaccines, it became unethical to include unvaccinated patients in the placebo group in vaccine clinical trials[440]. While these challenge studies did not investigate severe COVID, they provided useful insight into vaccine efficiency and provided guidance for optimizing SARS-CoV-2 testing strategies and regimes[440–443].

3.1.6 Immune Evasion by SARS-CoV-2

As with all viruses that infect humans, they evolve a multitude of mechanisms to avoid immune detection. Viral replication includes the addition of an N7-methylguanosine and 2'-O-methylation cap structure onto the viral mRNA which is a characteristic of eukaryotic mRNAs[271,444–446]. This allows SARS-CoV-2 mRNA to mimic endogenous RNAs and avoid detection by RIG-I. The function of this cap does not serve as only anti-viral, but to hijack host machinery for translation of viral mRNA[271,447,448].

Components of SARS-CoV-2 are sensed by TLR2 and some evidence suggests a role for TLR3,4,7 and 8[271,449–453]. Sensing of viral envelope proteins by TLR2 triggers the production of inflammatory cytokines, creating a positive feedback loop that results in cytokine storms[449,450]. RIG-I, MDA5 and LGP2 all sense SARS-CoV-2 viral RNAs, with a specific role for MDA5 (expanded upon in Section 3.1) and LGP2 in mediating IFN production (Fig. 9)[400,454–457]. SARS-CoV-2 harbours a nuclease protein that cleaves viral RNA, thereby preventing the pool of RNAs available for sensing[271,458–460]. SARS-CoV-2 inhibits MAVS through a variety of mechanisms mentioned in Section 1.1.2.2.3 above. Interestingly, cGAS-STING signalling is activated during COVID-19 infection due to mtDNA release after mitochondrial damage[461–464]. However, ORF3a and 3CL bind STING to inhibit PTMs and signalling[465]. Nsp1 protein interferes with the translation of IFN and

interleukins while nsp3 cleaves IRF3[466–468]. NSP13, NSP14, NSP15, and ORF6 have all reported functions of inhibiting RLR pathway components[466,469].

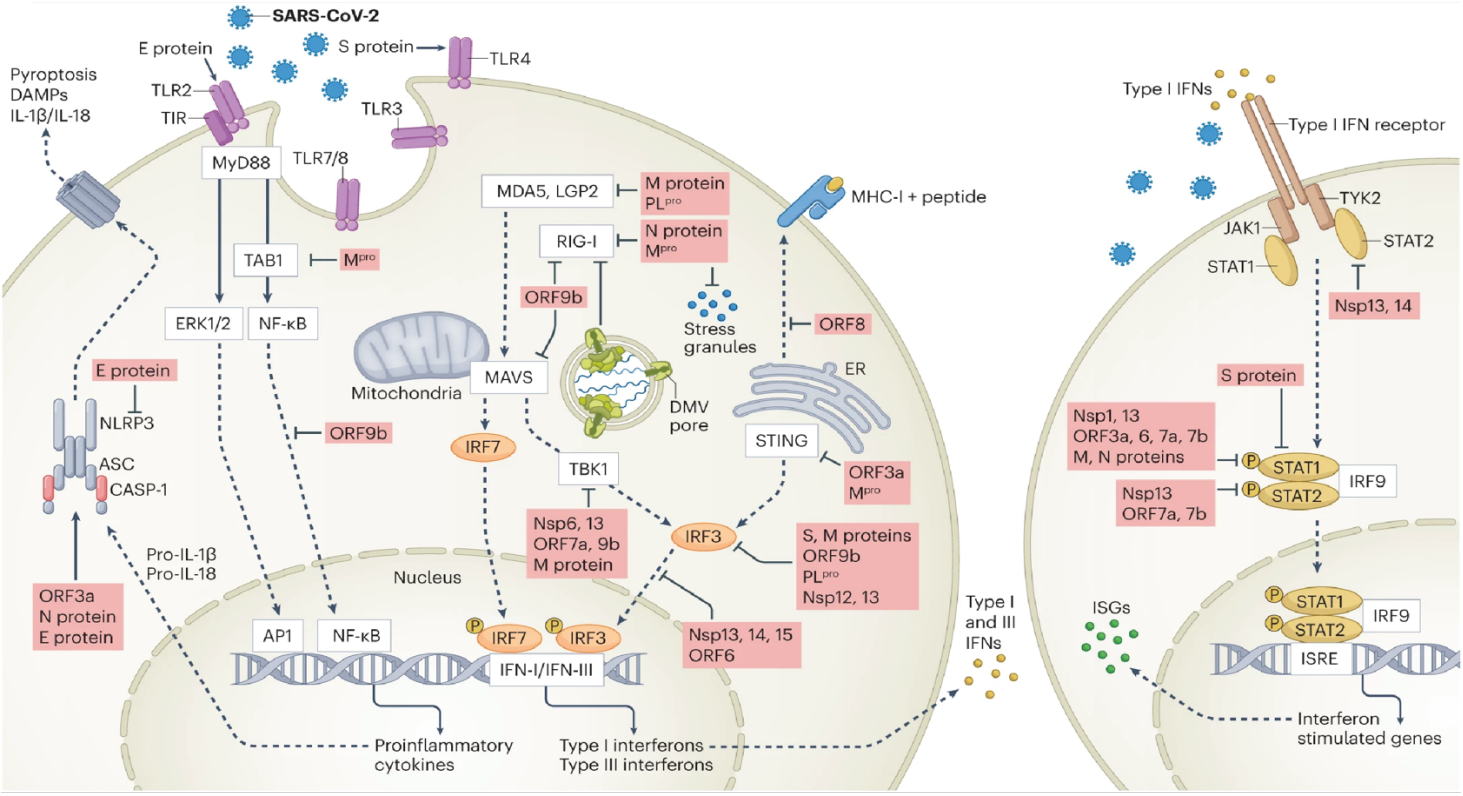


Figure 9: Mechanisms of SARS-CoV-2 innate immune evasion strategies.
During COVID-19 infection, viral particles are sensed by TLR2, and potentially TLR3, TLR4, TLR7 and TLR8. The virus can be sensed by RLRs and the cGAS-STING pathway. SARS-CoV-2 evades the innate immune response by inhibiting a multitude of points along the pathway, from PRR to ISG and IFN expression. Figure taken from Steiner et al. 2024. doi:10.1038/s41579-023-01003-z.

Similar viral mechanisms antagonizing adaptive immunity during MERS infection, SARS-CoV-2's ORF8 protein downregulates the expression of major histocompatibility complex class 1 (MHC-I) in a time and dose-dependent manner[271,470–472]. ORF6 also targets the expression MHC-I, while ORF3a and ORF7a inhibit antigen presentation[271,471,472].

Blocking the recognition and response to the virus during infection is crucial for survival of SARS-CoV-2 within the host. Type I IFNs are expressed early during infection, thereby becoming a prime target for inhibition. SARS-CoV-2 encodes a protease which de-ISGylates MDA5, preventing its oligomerization, and further cleaves IRF3 and ISG15

thereby ablating activation of the innate immune response[271,468,473–475]. The suppression of TBK1 or IRF3 by SARS-CoV-2 is achieved by nsp6, nsp13, nsp14 and nsp15 by preventing nuclear localization and phosphorylation of TBK1/IRF3 [271,466,469,476]. Downstream from PRRs and TBK1, the nsp14 protein targets IFNAR1 for lysosomal degradation[271,477]. ORF3a prevents STAT1 phosphorylation while ORF6 binds nuclear pore complex proteins to prevent STAT1 and STAT2 nuclear localization[271,478–481].

An efficient method employed by viruses to inhibit host proteins is to encode host shutoff proteins, which indiscriminately inhibit host protein synthesis in favour of viral mRNA translation[482]. The nsp1 protein inhibits host translation in three ways; degradation and depletion of host mRNA and binding a nuclear export signal to prevent transport of nuclear RNA[271,482–484].

The COVID-19 pandemic provided a unique environment in which researchers from academia, industry and government agencies united on a collective global front to uncover as much as possible about SARS-CoV-2. From its discovery until the time of writing (July 2024) a keyword search of SARS-CoV-2 yields 232,168 publications on PubMed NCBI records. This unprecedented amount of work in just four years makes it incredibly difficult to summarize the breadth of knowledge gained. However, from just the examples above (and highlighted innate immune antagonism in Fig. 9) it is clear that SARS-CoV-2, like its coronavirus relatives, employs a multitude of anti-viral antagonists creating a redundant system of efficient innate immune inhibition.

The viral replication cycle, the function of each viral ORF, response to the immune system and the pathology of SARS-CoV-2 are extensively reviewed in REF[271,323,485].

3.2 Establishment of MAVS as an Important Component in the Recognition of SARS-Cov-2 Infection

Nucleic acid sensors RIG-I and MDA5 detect cytosolic RNAs, such as viral RNA genomes. Upon activation by RNAs, the CARDs of RIG-I and MDA5 interact with the

CARD domain of the MAVS protein, which goes on to induce ISGs and IFN gene expression[11]. This signalling pathway collectively initiates an antiviral response as a part of the innate immune system.

Early in my program, I took part in a collaborative SARS-CoV-2 project within the Rehwinkel laboratory, which resulted in the Scientific Reports publication "The RNA sensor MDA5 detects SARS-CoV-2 infection", of which I co-author[400] (full publication in Appendix). Below I have highlighted the data I contributed to the publication – where my role was to isolate RNA from lysates and perform RT-qPCR.

After the emergence of the COVID-19 pandemic in Wuhan, China in late 2019, it quickly spread to all areas of the world by March of 2020. This prompted a global effort to uncover information about the virology, epidemiology and pathology of the SARS-CoV-2 virus. As introduced previously, the important role of IFN in mediating infection was highlighted by the association of severe infection with inborn errors in IFN immunity and the production of IFN autoantibodies[351–353,355]. Given our laboratory's focus is innate immunity and specifically nucleic acid sensors that detect infection, we sought to determine the causative RLR responsible for sensing SARS-CoV-2 and inducing innate immunity.

Given that SARS-CoV-2 is a ssRNA coronavirus and members of RLR recognize coronaviruses[211,486], we focused our efforts on RIG-I and MDA5. Calu-3 cells are commonly used to model both SARS-CoV-1 and SARS-CoV-2 as they express *ACE2* and *TMPRSS2*. Our laboratory first validated that our Calu-3 cells were permissive to infection; moreover, we observed a potent induction of IFN, ISGs and inflammatory cytokines[400]. The shRNA depletion of MAVS was used to validate that the virus was sensed through the RLR signalling pathway. Calu-3 cells were transduced with shRNA-MAVS or a control (shRNA-GFP) and infected with SARS-CoV-2 at a multiplicity of infection (MOI) of 0.1. 48 hours after infection, lysates were collected for RNA isolation. I performed RNA extractions from SARS-CoV-2 infected and uninfected Calu-3 cells to analyze expression levels of ISGs and type I and III IFNs by RT-qPCR (Fig. 10, A & B). The cells depleted of MAVS showed a reduced type I and III IFN and ISG response after

infection, while *TNF* and *IL6* expression were not affected by *MAVS* knockdown. These data indicate that SARS-CoV-2 induces an innate immune response through RIG-I and/or MDA5.

Determining the causative RLR in detecting SARS-CoV-2 and producing an IFN response was crucial for researchers and clinicians to understand the pathology of the disease. Calu-3 cells were transduced with lentiviruses expressing Cas9 and sgRNA targeting *MAVS, MDA5, RIG-I, IRF3, MAVS* and a control (*GFP*). To determine if the DNA sensing pathway was activated during infection a sgRNA targeting *STING* was also included. Cells were infected with SARS-CoV-2 (MOI=0.1) and lysates were collected for RNA isolation 48 hours post-infection. I performed RNA extractions to analyze expression levels of ISGs and type I IFNs by RT-qPCR (Fig. 10, C). Infected cells depleted for MDA5 and IRF3 showed minimal induction of type I IFN and ISGs compared to infected control cells. The CRISPR depletion of MAVS was less efficient than shRNA targeting, likely explaining the discrepancy between the ISG/IFN induction potential of cells transduced with shRNA and sgRNA MAVS. The pro-inflammatory response was unaffected as levels of *TNF* and *IL6* mRNAs were not reduced in infected MDA5 or IRF3 knockout cells. The depletion of RIG-I or STING had no effect on response to SARS-CoV-2, suggesting the cGAS-STING pathway and RIG-I are not involved in sensing of the virus. These results were further validated via flow cytometry by other laboratory members (data provided in Appendix).

Collectively, our data showed that the cytosolic RNA sensor MDA5 was necessary for type I and III IFN responses to SARS-CoV-2 in infected Calu-3 cells. In agreement with our findings, two other reports further validated that MDA5 was the nucleic acid sensor responsible for detecting SARS-CoV-2[454,457,487]. One group did report RIG-I-dependent sensing of SARS-CoV-2, however, this relied solely on siRNA knockdown of RIG-I and warrants further investigation[487]. These data highlight the importance of the RLR pathway in mediating SARS-CoV-2 infection and are dependent on the proper functioning of not only the sensors themselves but also the downstream signalling adaptors.

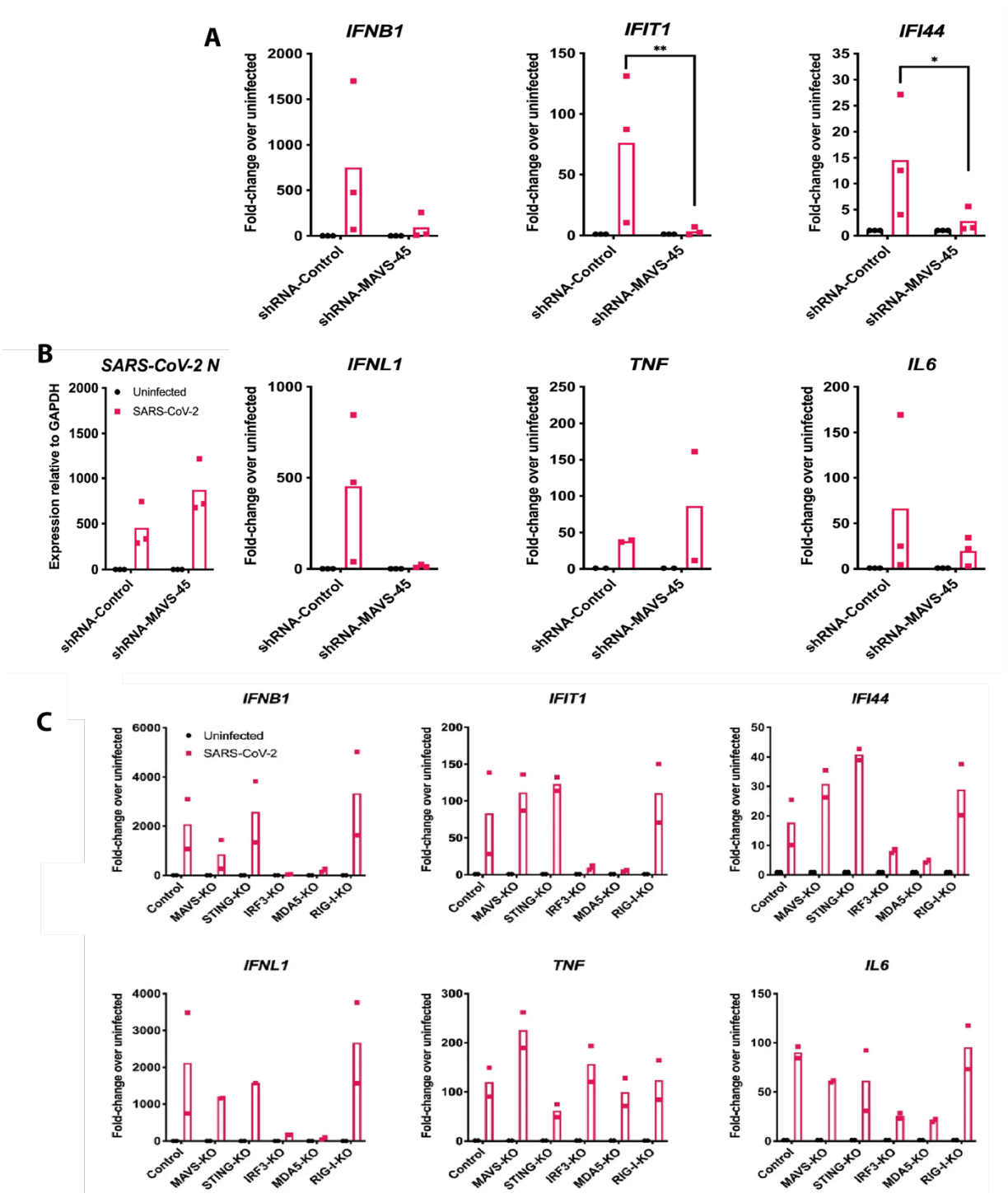


Figure 10: MAVS and MDA5 are required for the type I and III IFN response to SARS-CoV-2.
(**A,B**) Calu-3 cells were depleted of MAVS by lentiviral shRNA delivery using shRNAs (shRNA-MAVS-45). (**B**) SARS-CoV-2 infection efficiency was validated by RT-qPCR. (A,B) Calu-3 cells depleted of MAVS using shRNA-MAVS-45 were infect ed with SARS-CoV-2 (MOI = 0.1) for 48 h, followed by RNA extraction and RT-qPCR for the indicated transcripts. Data are relative to GAPDH expression. (**C**) Calu-3 cells were depleted of MAVS, STING, IRF3, MDA5 or RIG-I using a lenti-CRISPR approach and were infected with SARS-CoV-2 (MOI = 0.1) for 48 h. This was followed by RNA extraction and RT-qPCR for the indicated transcripts. Data are relative to GAPDH expression. Data in Panel A and B are pooled from 3 independent biological repeats, with bars representing the average. Data were analyzed by t-test and significant differences are indicated (**P < 0.01; *P < 0.05). Data in Panel C are pooled from two independent biological repeats, with bars representing the average. My contribution to this data was to isolate RNA from lysates and perform RT-qPCR.

3.3 Translation Initiation by Ribosomes

It is common among viruses and bacteria to generate multiple translational products from the same mRNA – known as polycistronic messages – to create protein diversity without the need for alternative splicing[242]. Viruses have evolved to produce multiple protein products from the same mRNA strand through leaky ribosomal scanning, ribosomal termination-reinitiation, ribosomal shunting, ribosomal hopping and ribosomal frameshifting[488].

The translation of mRNA into proteins in eukaryotes is a multistep process that begins with the initiation step, involving the assembly of ribosomal subunits onto the mRNA, which is then followed by the elongation and termination steps. Marylin Kozak first described this 'scanning mechanism' wherein the first AUG codon is recognized by the preinitiation complex (PIC) consisting of the 40S ribosomal subunit, eukaryotic initiation factors and a Met-tRNA[239,489–493]. The PIC complex begins scanning the 5' untranslated region (UTR) of the mRNA in a 5'-3' direction until it recognizes the first suitable start codon, typically AUG, where the initiation factors dissociate and the 60S ribosomal subunit is recruited[239,491,492,494,495]. The probability of the PIC to initiate translation at an mRNA start codon is largely dependent on the sequence of surrounding nucleotides. In 1987, Marilyn Kozak described the 6 nucleotides preceding the start codon and the first nucleotide after to have the greatest influence on the efficiency of translation initiation. Specifically, an A/G base in the -3 position and G in the +4 position (Fig. 11, C) provide the strongest Kozak sequence, i.e. highest probability of translation initiation[492,496–498]. More recently, a screen of all possible nucleotide compositions surrounding the AUG start codon (-6 to +5) was performed using FACS-seq, which found the strongest Kozak sequence to be RYMRMV<u>AUG</u>GC (M = A or C, R = A or G, V= G, C or A, Y = C or U)[492,499].

Interestingly, thousands of human mRNAs possess weak Kozak sequences flanking their start codon, resulting in leaky scanning of the mRNA[241,500]. If a ribosome

encounters an AUG with a weak Kozak sequence, it is less likely to recognize it and a portion of ribosomes continue scanning for the next downstream AUG[239,241,501]. When downstream start codons are in-frame, translation results in an N-terminally truncated protein which may retain the function of the full-length (FL) protein, have a partial function or a new phenotype altogether. For example, if an N-terminal domain is crucial for localization, and function is dependent on its localization, N-terminal truncation of the protein by leaky scanning will increase the probability of a non-functional protein. Conversely, when downstream start codons are out-of-frame, the synthesis of a new polypeptide ensues; however, these are typically short due to frequent stop codons found out-of-frame. An analysis of over 22,000 human mRNAs revealed that only 37.4% of genes had optimal initiation nucleotides at both the -3 and +4 positions, suggesting that the remaining 62.6% of genes have suboptimal Kozak sequences and may facilitate leaky ribosomal scanning[501].

Ribosomes can also recognize AUG codons in the 5' UTR of an mRNA and initate translation of so called upstream open reading frame (uORF). This initiation of translation at a uORF typically acts as a regulatory gene expression mechanism[502–504]. The initiation of protein synthesis at an AUG of an uORF may reduce the proportion of ribosomes available for initiation at the first coding region AUG, thereby inhibiting the expression of the primary ORF. Thus, uORFs can result in the translation of short polypeptides and/or facilitate skipping of the first AUG to an alternative downstream start codon[492,502]. More than half of human mRNA possess an upstream AUG and uORF and are thus capable of leaky ribosomal initiation at downstream AUG sites[492,500,505,506], although most are unlikely to produce a functioning protein[507,508].

3.4 Leaky Ribosomal Scanning of *MAVS*

MAVS possesses multiple translational start sites along the mRNA transcript that can result in multiple protein isoforms of MAVS translated from one transcript[242,243] (Fig. 11, A). Interestingly, it has an out-of-frame uORF that overlaps with the start site of the

canonical ORF. Ribosomes that begin translation at this uORF therefore bypass the start codon of the canonical ORF and terminate shortly downstream. After termination, the ribosomes can often reinitiate scanning until reaching a downstream start codon[242,243] . MAVS has five downstream in-frame AUG start sites that are translated by leaky ribosomal scanning to produce truncated isoforms of the MAVS protein[242,243]. The six methionines encoded by MAVS produce FL-MAVS (M1 – 72kDa) and the 'mini-MAVS' truncated proteins M2 (M142 – 50kDa), M3 (M303 – ~45kDa), M4 (M358 – ~30kDa), M5 (M367 – ~25kDa), and M6 (M449 – ~18kDa) (Fig. 11, A)[243]. The uORF is thought to regulate the translation ratio of FL to mini-MAVS products. Indeed, artificial strengthening of the uORF Kozak sequence significantly increases downstream AUG initiation[242,509].

The CARD domains of RIG-I and MDA5 interact with the N-terminal CARD of MAVS, prompting its aggregation and downstream signalling[243,296] (Fig. 16, A). The CARD of MAVS alone is sufficient for its aggregation. The shortened isoforms of MAVS (M2-M6) all lack the CARD and are thought to prevent FL-MAVS (herein simply MAVS) from its spontaneous aggregation, thereby inhibiting IFN induction[243]. Indeed, overexpression of MAVS with M2 resulted in significantly reduced expression of *IFNβ*[242,509]. Additionally, all truncated isoforms retain the C-terminal transmembrane domain and localize to the mitochondria and reduce expression of *IFNβ* after viral stimulation[243]. Transmembrane domain (TM) mutants ablate MAVS aggregation and signalling of MAVS, highlighting the importance of the C-terminal region for mitochondrial localization and proper function[243]. Indeed, two highly conserved leucine residues (L530 & L534) in the TM are crucial for inhibition of MAVS aggregation and stunted IFN expression[243].

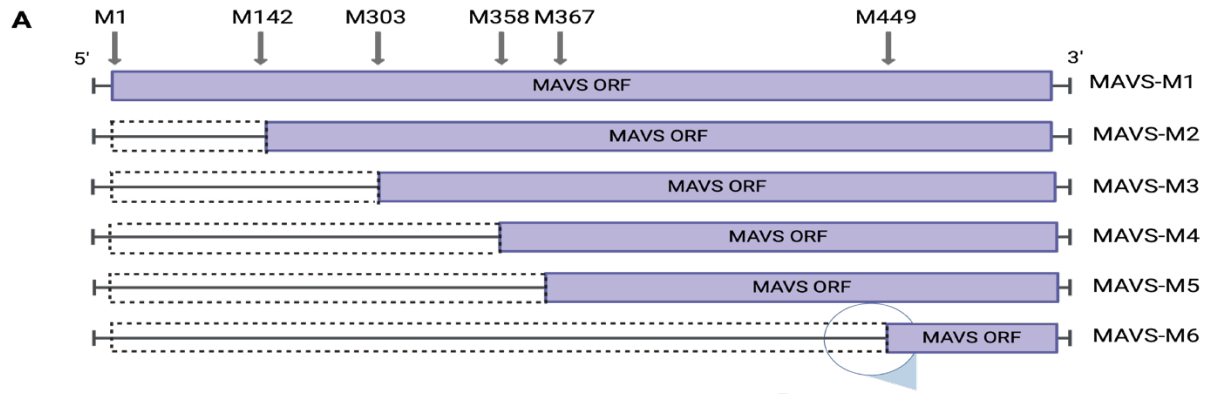
The majority of evidence supports MAVS-M2 as the main isoform with anti-MAVS activity[242,243]. One study speculates that mini-MAVS proteins interact not with MAVS directly, but rather with its downstream adaptors TRAF2 and TRAF6[242,510]. However, another study a few years afterwards showed a transmembrane domain-mediated homotypic interaction between mini-MAVS and MAVS prevented the spontaneous aggregation of canonical MAVS[243]. This mechanism is thought to act as a regulator of antiviral signalling – mainly to prevent inappropriate signalling[242,243,509]. Taken together,

the function(s) of MAVS's N-terminally truncated protein isoforms and their antagonistic mechanism of MAVS-dependent IFN induction are not yet fully understood.

3.5 Single Nucleotide Polymorphism Screen of *MAVS*

Dr. Johnathan Cooper-Knock (University of Sheffield, UK) performed a rare variant analysis on the GEN-COVID cohort[511] of whole exome sequencing from 799 COVID-19 patients, of which 332 had severe COVID-infections* and 467 with non-severe COVID infections. The database was filtered to exclude patients aged >60 and those who had pre-existing diabetes mellitus or significant lung disease. Eight SNPs were found in the coding region of *MAVS* in severely ill SARS-CoV-2 patients from this screen (Fig. 11, D).

* Severe COVID-19 infection was characterized by the need for ICU admission and respiratory support.



D

Cohort	Amino Acid Change	Codon Change	Mutation	Variant	rs Number	CADD	Predicted Phenotype
Italian	P2L	CCG > CTG	C5T	20:3854629		18.65	Reduced MAVS-M1
UK	E137K	GAG > AAG	G409A	20:3861448	rs779903870	17.4	Unknown
Italian	P141A	CCC > GCC	C421G	20:3861460	rs374414172	22	Increased MAVS-M2
Vatican City	G194R	GGG > AGG	G580A	20:3862368	rs76715450	4.6	Unknown[1]
Italian	M358I	ATG > ATC	G1074C	20:3864704	rs202136760	3.65	Increased MAVS-M1 / No MAVS-M4
Italian	G396S	GGC > AGC	G1186A	20:3865710	rs45529136	7.7	Unknown[1]
Italian	K420N	AAG > AAC	G1260C	20:3865784	rs1333615886	24.4	Unknown
Vatican City	P511S	CCC > TCC	C1531T	20:3866055	rs142615910	0.001	Unknown

[1]A study by Xing *et al.* (2016) found that over expression of G194R significantly increased basal *IFNβ* expression but no differential expression was seen after poly I:C stimulation compared to WT MAVS. Based on this study, we expect to see an increase in basal expression but no differential expression after stimulation. The authors found no differential expression in G396S mutants compared to WT-MAVS.

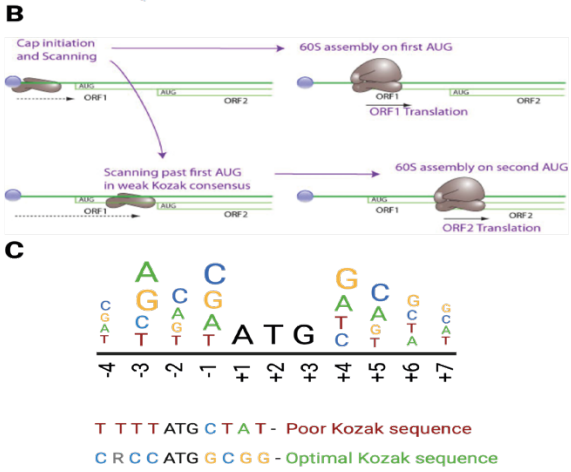


Figure 11: Discovery of MAVS SNPs Within Translation Start Sites.
(**A**) Schematic of the six isoforms of MAVS (M1, M2, M3, M4, M5 & M6) that are translated by leaky ribosomal scanning. The position of each start site along the transcript is listed above with an arrow. (**B**) Ribosomes scan mRNA transcripts until the first ATG, where they initiate translation. (**C**) The sequence of bases flanking ATG sites (Kozak sequence) determines the strength or probability of ribosomal initiation. R= A or G. If a Kozak sequence is weak, the (B) ribosome can continue scanning past the first ATG site to another ATG further downstream in the transcript - this is referred to as leaky ribosomal scanning. (**D**) A rare variant analysis of GEN-COVID database (performed by Dr. Johnathan Cooper-Knock) revealed eight MAVS-SNPs in severely ill COVID-19 patients admitted to the ICU. Patients were excluded if they were >60 years of age, and had lung disease or diabetes mellitus. SNPs within or flanking MAVS isoform start sites are highlighted in pink. Panel B is taken from www.viralzone.expasy.org/1976. Panel D made with BioRender.

Two of these SNPs found in the screen were of particular interest as they were positioned in the translation start sites of truncated MAVS isoforms or in the Kozak sequences – the nucleotides flanking the ATG start site. The C421G SNP is present in the amino acid immediately before the M142 translational start site of the annotated MAVS-M2 protein[243]. The change from CCC to GCC results in a stronger Kozak sequence for this mini-MAVS transcript, likely contributing to a higher ratio of MAVS-M2 to canonical MAVS (MAVS-M1). The G1074C SNP results in a change of the ATG site that initiates translation of MAVS-M4 protein. The change from ATG to ATC will render the start site non-functional, predicted to yield a higher proportion of canonical MAVS translation and likely a more robust IFN response to infection. The C5T mutation will be discussed further below. The remaining five SNPs along the MAVS transcript are not in

any known mini-MAVS ATG start sites or Kozak sequence locations. They may still result in a malfunction of the MAVS protein and warrant investigation to determine if downstream IFN production is altered.

Xing *et al*. (2016) hypothesized that SNPs in innate immune pathway proteins, specifically *MAVS*, may reduce their functionality and increase patient susceptibility to viral RNA infection[512]. They chose 12 SNPs isolated from Japanese patients from the NCBI database within coding regions of MAVS that result in missense mutations. They reconstituted the MAVS SNPs in HeLa cells and assessed their effect on MAVS function[512]. Of the 12 SNPs chosen by the authors, two corresponded with SNPs found in our rare variant analysis – G194R and G396S. HeLa cells overexpressing MAVS-G194R and G396S have a typical morphology of the mitochondria and localization of MAVS. Interestingly, overexpression of G194R resulted in a significant increase in *IFNβ* expression at steady state but not after Poly I:C stimulation[512]; while G396S overexpressing cells responded in a similar manner to WT MAVS expressing cells[512]. In agreement, neither mutant resulted in altered phosphorylation of MAVS[512]. Given this data, I predict that the overexpression of MAVS-G194R in cells will increase only the basal expression of ISGs or IFNs but no increase in response to RNA stimulation. Likewise, I do not expect to see a difference in ISG or IFN expression between MAVS-G396S and MAVS-WT.

While I initially tested all eight SNPs, the majority of experiments will focus on testing the three SNPs predicted to impact the alternative translation of MAVS – C5T, C421G and G1074C. I hypothesize that the C5T and C421G MAVS SNPs result in the translation of truncated MAVS isoforms that antagonize full-length MAVS, thereby counteracting antiviral responses of the MAVS-RIG-I pathway. I hypothesize that the G1074C SNP will result in a decreased proportion of MAVS-M4 and consequently an increase in full-length MAVS, thereby promoting antiviral responses.

3.6 SNPs Within MAVS Alter the Ratio of Translated FL Protein

To investigate the effects of the eight SNPs described in Figure 11 we first started by designing MAVS variant constructs. Philip Hublitz (Genome Engineering Facility, WIMM, UK) and Jan Rehwinkel designed MAVS constructs that were then synthesized by GeneArt ThermoFisher Scientific. In addition to one of the SNPs, Philip Hublitz and Jan Rehwinkel introduced synonymous mutations in the MAVS sequences targeted by shRNAs and sgRNAs used in the group to deplete MAVS. This does not change the amino acid sequence of MAVS but renders these constructs resistant to shRNAs/sgRNAs in MAVS-deficient cells, thus allowing for reconstitution experiments. Moreover, a proportion of the endogenous MAVS 5'UTR containing the uORF was included. I received Entry clones from GeneArt and then used Gateway cloning to generate lentiviral expression constructs using the pLenti6.3 destination vector. This vector allows for both transient transfection and lentivirus production.

HEK293-p125-MAVS-KO cells [513] were transiently transfected with each pLenti-MAVS construct, along with EV and pcDNA3-3FLAG-MAVS control plasmids. 24 hours later lysates were collected for WB, *IFNβ*-luciferase (OneGlo) assay and RNA isolation for use in RT-qPCR (Fig. 12, D). HEK293-p125 express firefly luciferase under an *IFNβ* promoter. Therefore, the measured intensity of luciferase is a readout for induction of *IFNβ*. The transfection of EV acted as a negative control for western blotting to ensure expression of MAVS antibody expression was specific. It also acted as a negative transfection control for RT-qPCR to validate that the transfection reagent was not responsible for any induction of the IFN response. Additionally, pcDNA3-3FLAG-MAVS acted as a positive control for the expression of MAVS protein. It is important to note that the over-expression of *MAVS* induces IFNs independently of RIG-I and MDA5.

Cells transfected with WT MAVS expressed slightly higher levels of M2 compared to FL (Fig. 12, A & B). The pcDNA3-3FLAG-MAVS plasmid has an N-terminal FLAG tag that makes FL MAVS migrate more slowly on western blots, resulting in a slightly elevated FL band compared to other MAVS constructs. Most of the eight SNPs tested showed a

similar expression pattern to that of WT MAVS, except G409A, G1186A and G1260. Cells overexpressing G409A produced similar levels of FL MAVS and M2, suggesting that M2 translation may be slightly downregulated in these cells. The most remarkable reduction was observed in G1260C overexpressing cells, with more than 2-fold and 3-fold reduction of FL and M2 protein levels respectively, compared to WT MAVS. Despite this reduction in protein expression, the SNP had no impact on ISG and IFN production as measured through One Glo (Fig. 12, C) and RT-qPCR (Fig. 12, D). Due to the variability and inconsistent spread of OneGlo data, it is difficult to interpret any functional consequence of MAVS SNPs. This may be due in part to that the assay is not sensitive enough for this application. Alternatively, the transfection of cells is not completely efficient, therefore some untransfected cells can still be stimulated by circulating IFN to produce ISGs. This has the potential to mask results.

As mentioned previously, the G1186A mutation causing a missense mutation of G396S is annotated as a rare variant (MAF <0.01) and tested in a previous study[512]. Xing *et al*. did not find a phenotype associated with this SNP and overexpression of G396S did not result in malfunction of MAVS or altered IFN production[512]. In agreement, no differential expression of ISGs or IFN was observed between G1186A and MAVS-WT in HEK293 cells. RT-qPCR results showed six out of seven SNPs had increased ISG and IFN levels compared to MAVS-WT and warranted further investigation.

The MAVS antibody used throughout this chapter was made by inoculating rabbits with a synthetic peptide targeting residues surrounding MAVS-L202. The M3-M6 isoforms are all translated from methionines downstream from L202 (Fig. 11, A), therefore, the antibody only recognizes FL and MAVS-M2. Due to this, the amount of translated M3-M6 protein by each construct cannot be quantified with this antibody. To circumvent this issue, I attempted to find commercial antibodies with peptides designed against an epitope in the C-terminal domain of MAVS. Unfortunately, all commercially available antibodies were designed against an N-terminal epitope. Therefore, I commissioned Cambridge Research Biochemicals to generate a C-terminal targeted MAVS antibody. Qi et al. (2017) generated a C-terminal MAVS antibody by immunizing rabbits with MAVS-AA460-510 recombinant protein that showed specificity for all MAVS isoforms[243].

With this information, Cambridge Research Biochemicals designed an epitope from the C-terminal of MAVS (AA:487-505, ADPDGGPRPQADRKFQERE) and immunized two rabbits with six boosters over 77 days. Despite promising high antibody titres, no expression of MAVS was detected in THP1, Huh7, or HEK293 cells (data not shown). A wide variety of western blot conditions were tested without success.

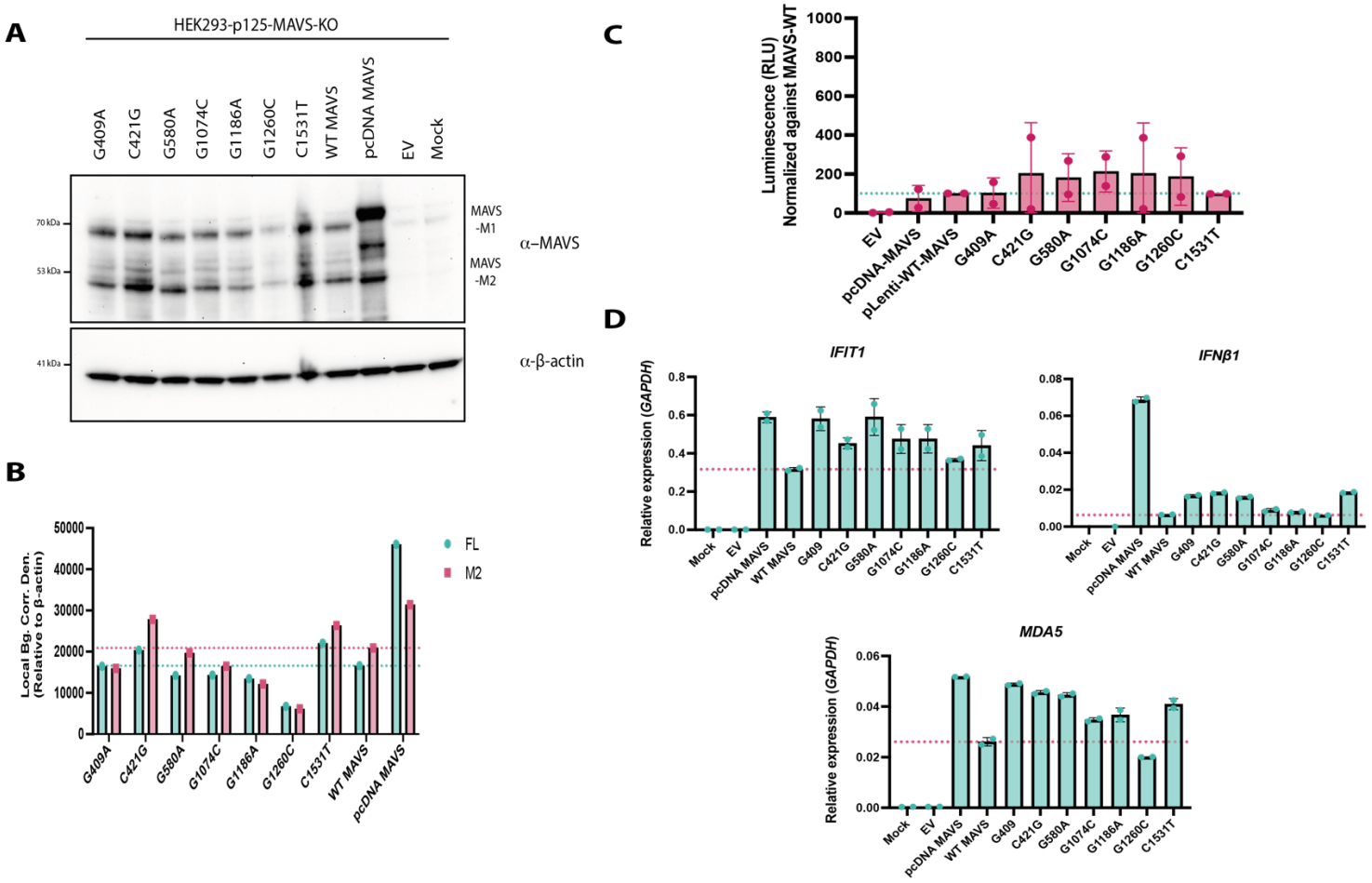


Figure 12: Expression and Function of MAVS Protein Between Mutant Constructs.
(**A**) HEK293-p125-MAVS-KO cells were transfected with pLenti-MAVS-WT and the indicated MAVS mutants. Untransfected cells (mock), and cells transfected with empty vector (EV) or pcDNA-MAVS acted as controls. (**B**) Densitometry was performed on MAVS-FL and MAVS-M2 bands corresponding to 72kDa and 50kDa respectively using ThermoFishers Connect platform (n=1). (**C**) In parallel cells were lysed for OneGlo luminescence assay and (**D**) RNA isolation for RT-qPCR. Results in Panel C are data from two independent biological repeats with three technical replicates in each experiment. Data was averaged and normalized against pLenti-MAVS-WT, with each plotted point representing the normalized biological replicate (average and range, n=2). Results in Panel D are data from one biological experiment with technical duplicates graphed (average and range, n=1). Dotted lines indicate MAVS-WT levels.

3.7 RNA Sensing Ability of *MAVS* Mutants in HEK293 Cells

Given the variability seen in experiments testing all mutants, we decided to streamline further experiments by selecting the SNPs predicted to affect leaky ribosomal scanning. The G1260C mutant was also included as it produced the lowest levels of MAVS expression, potentially impacting downstream signalling and warranting further exploration.

The GEN-COVID database was updated with new sequences throughout the pandemic. A further screen of the GEN-COVID database by Dr. Johnathan Cooper-Knock revealed an interesting SNP in the N-terminal of MAVS^{C5T} corresponding to a P2L missense mutation. The C5T mutation is positioned immediately after the full-length MAVS ATG start site, changing the flanking Kozak sequence from CCG to CTG, and likely resulting in an inferior initiation start site (Fig. 11, C & D).

3.7.1 MAVS-C5T Exhibits Reduced Activity in Transfected HEK293 Cells

I first explored the expression pattern as a result of the C5T mutation. HEK293-p125-MAVS-KO cells transiently transfected with MAVS-C5T had reduced levels of both FL and M2 MAVS at baseline and after IVT RNA stimulation (Fig. 13, B & C). At baseline, C421G, G1074C and G1260C mutants expressed FL MAVS protein at similar levels to the WT MAVS construct. After stimulation, however, the C421G and G1074C overexpressing cells produce more M2 protein compared to WT MAVS. However, this experiment was only performed once and therefore, firm conclusions cannot be stated from this blot alone.

These results indicate that the C5T mutant caused translation of less MAVS overall, while stimulation of cells expressing C421G and G1074C promoted the production of more M2 protein. This finding prompted me to investigate the functional consequence.

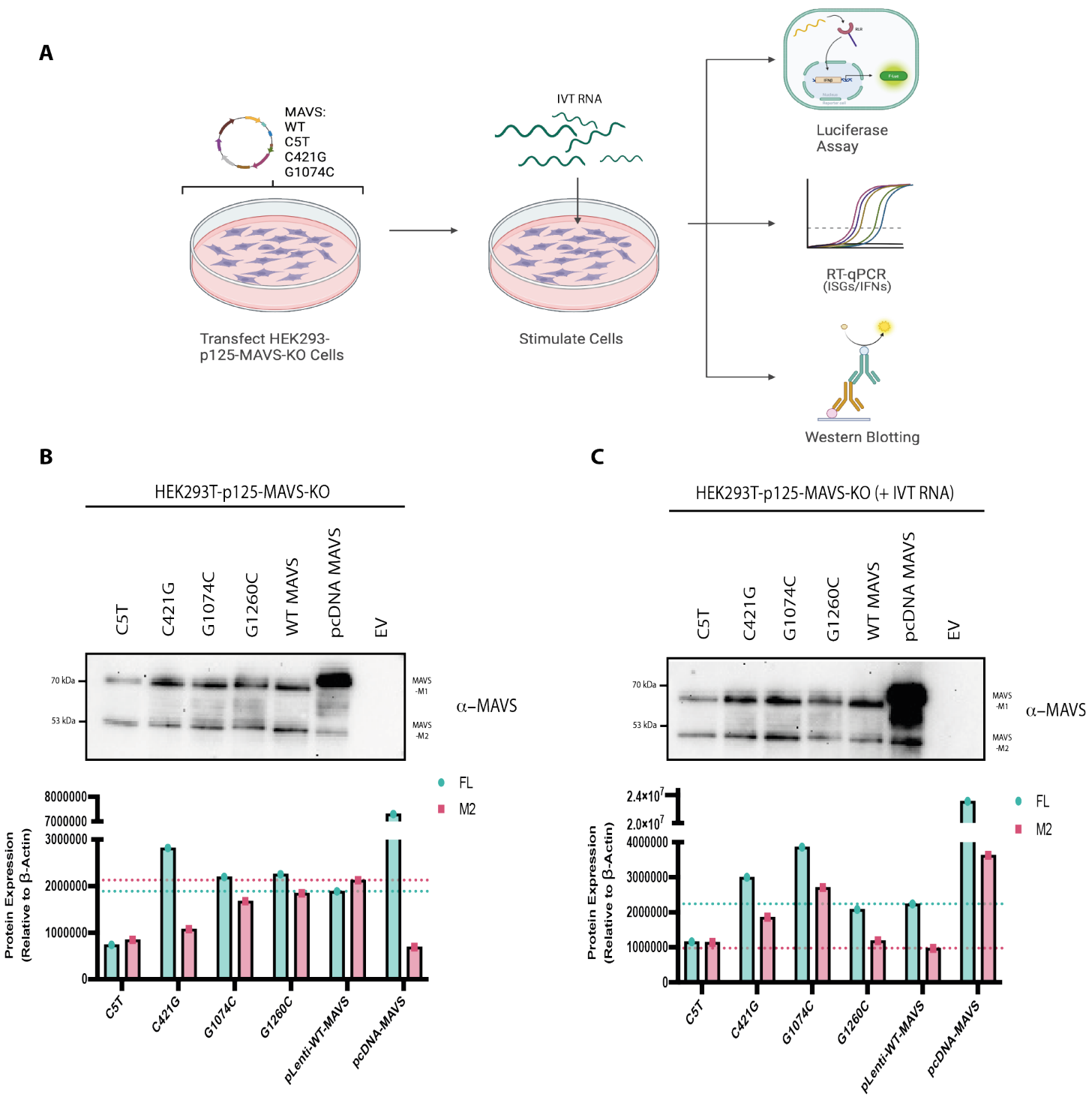


Figure 13: MAVS expression in Transfected HEK293-p125 Cells.
(**A**) Flow chart of the following experiments with MAVS mutants. HEK293-p125-MAVS-KO cells were transiently transfected with MAVS constructs or control plasmids and either (**B**) left to incubate for 48 hours or (**C**) stimulated 24 hours later with 3.3ng IVT RNA. 24 hours after stimulation, lysates were collected for immunoblotting. Densitometry was performed on MAVS-FL and MAVS-M2 bands corresponding to 72kDa and 50kDa respectively. Panel B and C show one independent experiment (n=1). Dotted lines drawn for the MAVS-WT FL and M2 expression profiles. Panel A made with BioRender.

In parallel, cell lysates were collected for *IFNβ*-luciferase assay and RT-qPCR (Fig. 13, A). As expected, *IFNβ* promoter activation was induced by IVT RNA in MAVS-WT expressing cells (Fig. 14, A). Cells harbouring MAVS-C5T showed reduced *IFNβ, IFI44*, and *IFIT1* mRNA expression compared to MAVS-WT (Fig. 14, B). In agreement, luciferase assay results show *IFNβ* levels were reduced in C5T-expressing cells compared to WT (Fig. 14, A). Interestingly, RT-qPCR analysis revealed that G1074C and G1260C promoted the expression of IFNs and ISGs when stimulated with IVT RNA (Fig. 14, B). This is in contrast to the luciferase assay results, which depict *IFNβ* promoter activation as similar between WT, C421G, G1074C and G1260C. It is possible the luciferase assay is not sufficiently sensitive to detect small changes in downstream induction or reduction of IFN activation. This could be exacerbated by the fact that transfection is not completely efficient, therefore the results can be diluted by the bulk effect of non-transfected cells.

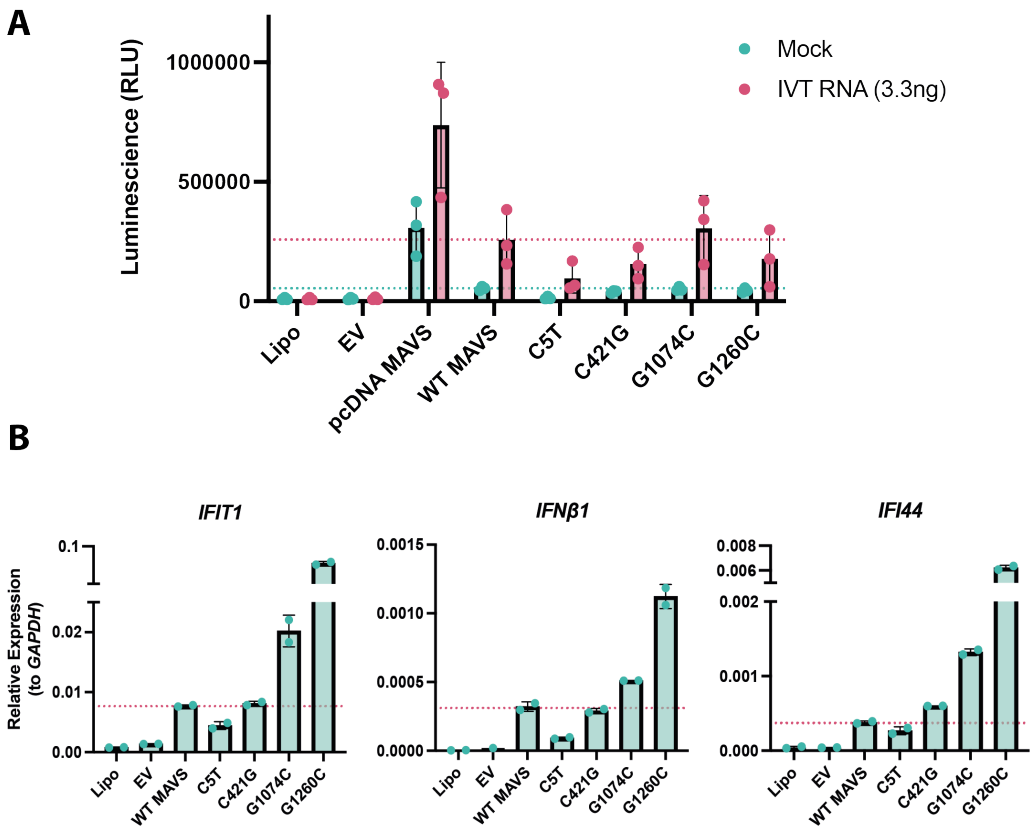


Figure 14: Functional impact of MAVS SNPs in Transfected HEK293-p125 Cells.
HEK293-p125-MAVS-KO cells were transfected with MAVS constructs or control plasmids and stimulated 24 hours later with (A) 3.3ng or (B) 100ng IVT RNA. (**A**) After an overnight incubation, activation of the *IFNβ* promoter was assayed via OneGlo luciferase assay. (**B**) 24 hours after stimulation, RNA was isolated from lysates and RT-qPCR was performed for the indicated genes. Panel A shows averaged data from three independent biological repeats with three technical replicates each (average and range, n=3). Panel B shows data from one biological repeat with technical duplicates. (average and range, n=1). Dotted lines drawn for MAVS-WT expression profiles.

3.7.2 MAVS-C5T Exhibits Reduced Activity in Transduced HEK293 Cells

To validate the phenotypes found in transiently transfected HEK cells, HEK293-p125-MAVS-KO cells were stably transduced to express *MAVS* constructs. Immunoblotting of cells showed a 4.4 fold reduction in expression of FL MAVS protein in C5T expressing cells and a 3-4.4 fold reduction of M2 in C5T, C421G and G1074C compared to WT-MAVS at baseline (Fig. 15, A & B). Additionally, C5T produced roughly equal levels of FL to M2, while C421G and G1074C produced a higher proportion of FL MAVS to M2.

Utilizing the luciferase assay system revealed stimulation of cells with 0.1ng IVT RNA (for 24 hours) induced *IFNβ* promoter activation in WT-MAVS transduced cells, with a significant reduction in activation in all mutant MAVS constructs (Fig. 15, C). As expected, the level of *IFNβ* promoter activation was correlated with the level of FL MAVS protein expression. For example, the C5T mutation caused the translation of a small amount of FL MAVS which significantly reduced its downstream signalling potential. C421G and G1074C resulted in the translation of a higher proportion of FL MAVS and, in agreement, an increased readout of *IFNβ* activation compared to C5T.

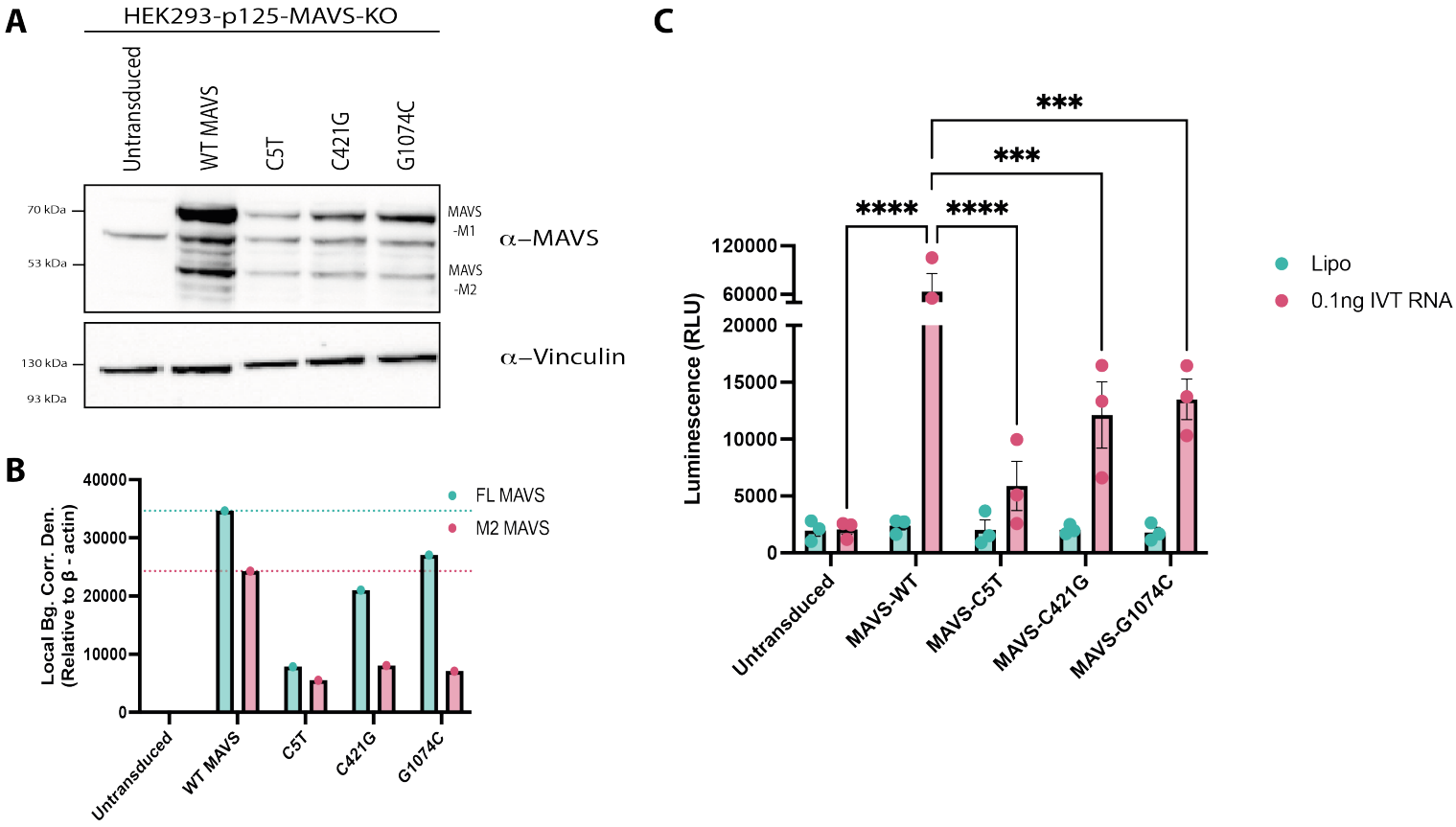


Figure 15: MAVS SNPs Elicit a Reduced IFN Response.
(**A**) HEK293-p125-MAVS-KO cells were transduced with the indicated MAVS constructs and subject to immunoblotting. (**B**) Densitometry was performed on MAVS-FL and MAVS-M2 bands corresponding to 72kDa and 50kDa respectively using ThermoFishers Connect platform (n=3). (**C**) Cells were stimulated with 0.1ng IVT RNA and lysed 24 hours later for OneGlo luminescence assay. Panel A is a representative blot from three independent biological experiments (n=3). Panel B data derived from the blot in Panel A. Dotted lines drawn for MAVS-WT expression profiles. Panel C shows pooled data from three independent biological experiments. Panel C: Multiple comparison two-way ANOVA (ns, not significant=p>0.05, *=p≤0.05, **=p≤0.01, ***=p≤0.001, ****=p≤0.0001) (Mean and SEM, n=3).

It is worth noting, that during the generation of the p125-GreenFire plasmid by Hertzog *et al.*, which was used to generate HEK293-p125-MAVS-KO cells[513], the puromycin N-

acetyl-transferase gene was replaced by the blasticidin-S deaminase gene[284]. The pLenti-MAVS constructs I generated are also blasticidin resistant, thereby preventing the selection of transduced cells. This may contribute some level of confounding bulk effect as experiments likely contained a mix of transduced and untransduced cells. However, I compensated for this by validating equalized protein expression in immunoblotting with a loading control and normalizing total MAVS protein expression against the loading control.

3.8 MAVS Mutants Form Fewer Aggregates Than WT-MAVS

Given the functional impact of MAVS SNPs on downstream activation in HEK293 cells, I postulated that truncated isoforms could reduce canonical MAVS aggregation, thereby preventing IRF3 activation. I tested this by transfecting HEK293-p125-MAVS-KO cells with MAVS constructs and stimulating cells with 1µg IVT RNA. Lysates were collected 24 hours later and subjected to subcellular fractionation to isolate mitochondria from cell lysates. To prevent disassembly of aggregates during immunoblotting, samples were not boiled and run on 1.5% agarose gels instead of Bis-Tris denaturing gels. WT-MAVS aggregated at both baseline and after stimulation, while cells expressing C5T, C421G and G1074C MAVS variants had only marginal expression of MAVS aggregates after IVT RNA stimulation (Fig. 16, B). The appropriate control for an aggregation blot would be to probe for MAVS and a loading control (mitochondrial inner membrane protein such as COX IV) via SDS-PAGE from whole cell lysates and mitochondrial fractions. However, this was not achieved on this occasion and would be required to make definitive conclusions from the aggregation assay.

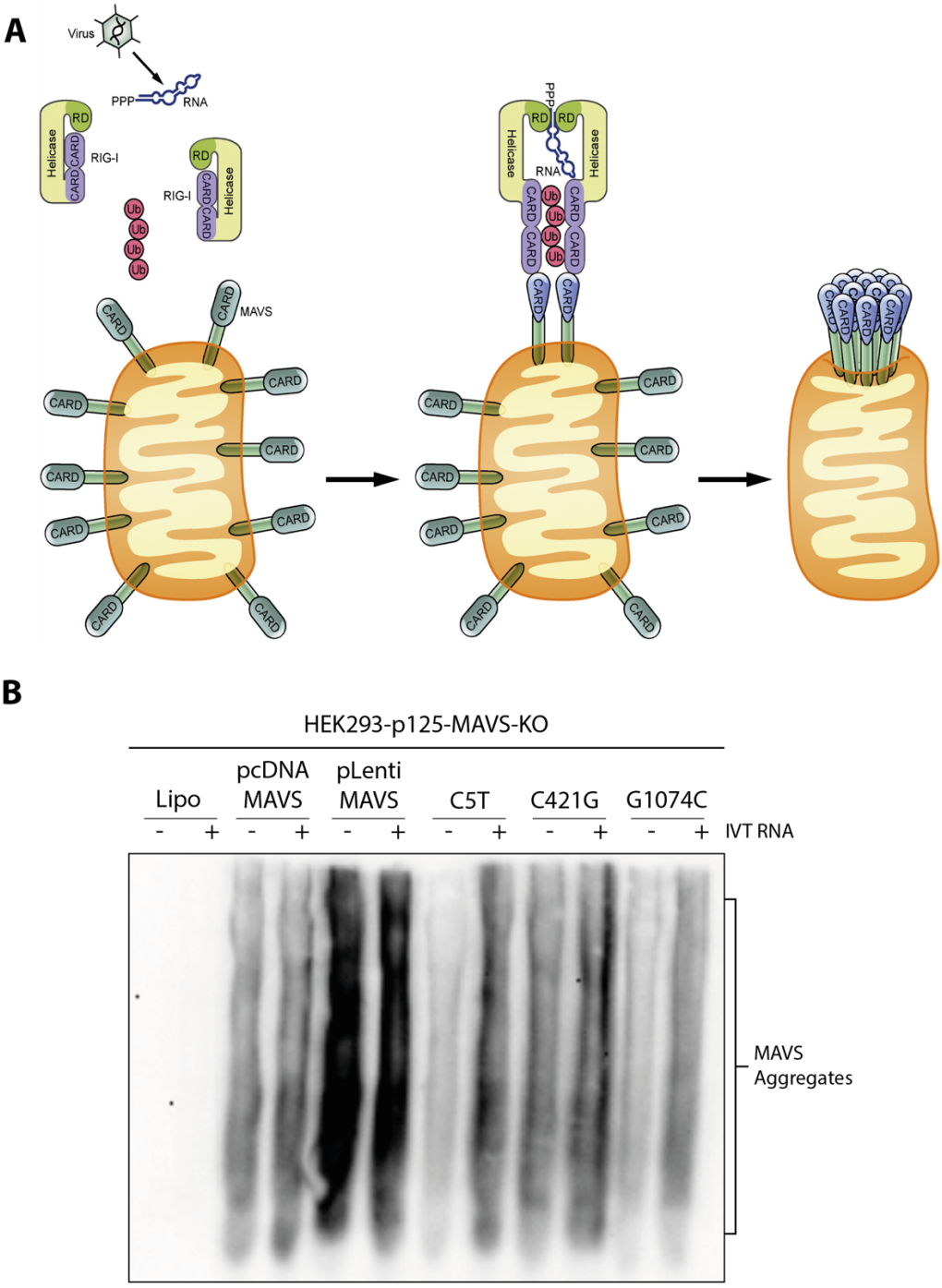


Figure 16: Aggregation of MAVS is depleted in MAVS mutants.
(**A**) Depiction of RIG-I induced MAVS aggregation on the mitochondria. (**B**) HEK293-p125-MAVS-KO cells were transfected with the indicated expression plasmids. The next day cells were stimulated with 1µg IVT RNA. Lysates were collected 24 hours later and subject to subcellular fractionation to isolate mitochondria. Protein was run on a 1.5% agarose gel and membranes were probed with the indicated antibodies. Panel shows representative blot from three independent experiments. Panel A is taken from Hou *et al*. 2011. doi: 10.1016/j.cell.2011.06.041.

Collectively, these results for experiments in HEK293 cells provide convincing evidence for the inhibitory effect of the C5T SNP on WT-MAVS aggregation and function. However, the results for the functional consequence of C421G and G1074C have been contradictory. In transiently transfected cells, C421G and G1074C elicit a stronger stimulatory response than WT-MAVS, compared to a reduced IFN response in stably transduced cells. Perhaps this is an effect of transfection versus transduction. To attempt to clarify this phenotype, I tested the SNPs in a different cell line.

3.9 MAVS-C5T Exhibits Reduced Activity in Transduced Huh7 Cells

Huh7 cells were selected as a secondary cell model to test MAVS SNP phenotypes as our laboratory had already generated Huh7-MAVS-KO cell lines. Additionally, Huh7s have been used as a cell model for SARS-CoV-2 as they express *TMPRSS2*, are permissive to infection and induce a moderate IFN response to infection[393,404]. A long-term proposed experiment for this project included infections of MAVS mutant-expressing cells with SARS-CoV-2. Therefore, the validation of SNP phenotypes in Huh7 was to be conducted first.

Huh7-MAVS-KO cells were stably transduced to express WT-MAVS, C5T-MAVS, C421G and G1074C. Cells were stimulated with 100ng IVT RNA and lysed for western blot analysis 24 hours later. An immunoblot analysis of all SNPs at baseline revealed a similar pattern of expression between WT-MAVS and G1074C (Fig. 17). At baseline, the C421G SNP induced more translation of M2 compared to WT while C5T reduced the proportion of FL MAVS translation. After stimulation, C5T-expressing cells still produce less FL MAVS as compared to WT, while C421G produces more M2.

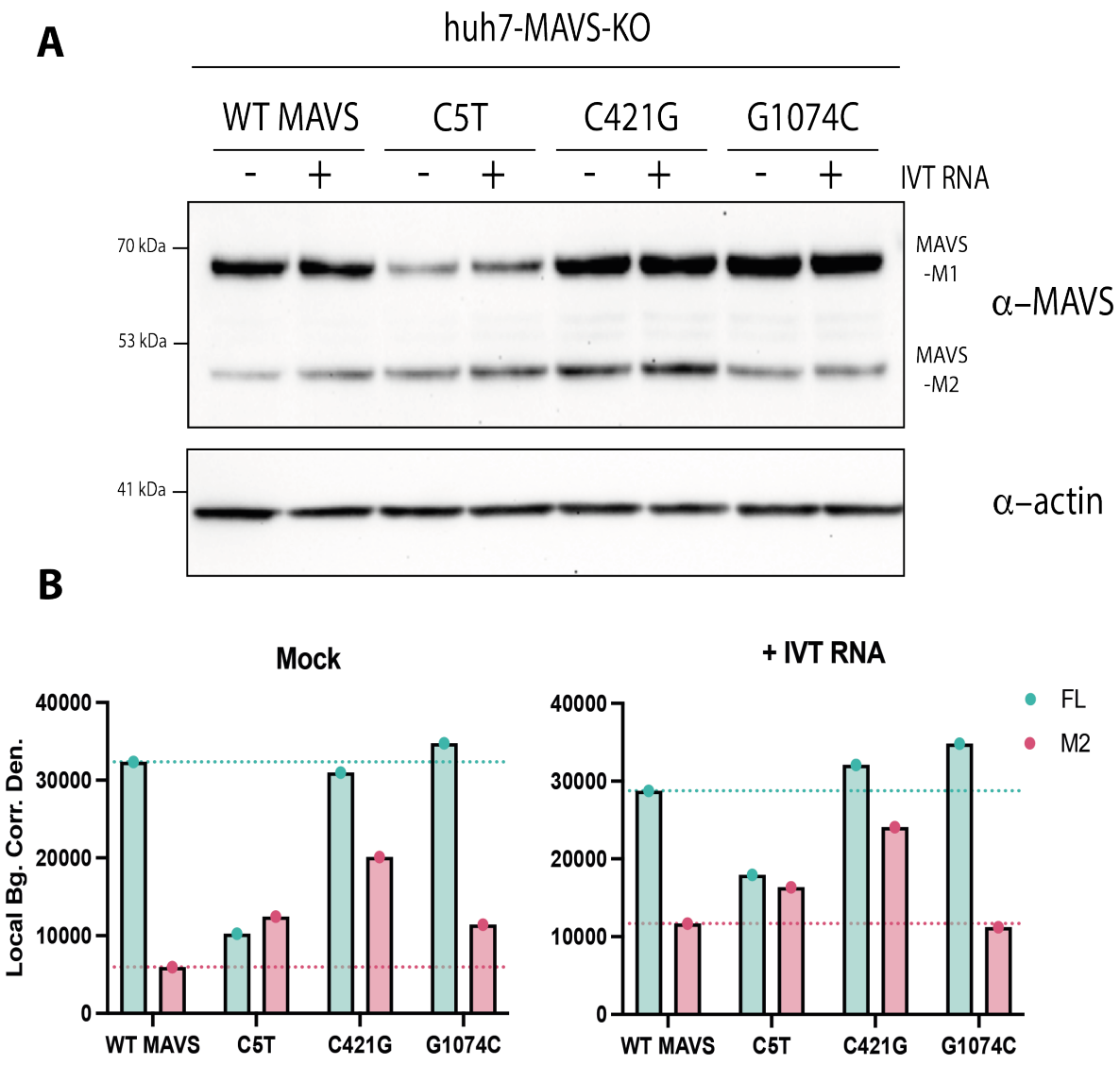


Figure 17: MAVS-C5T Polymorphism Reduces Protein Expression.
(**A**) Huh7-MAVS-KO cells were transduced with indicated expression plasmids and stimulated with 100ng IVT RNA. The next day, lysates were collected for immunoblotting and probed with the indicated antibodies. Panel A is a representative blot from two independent biological experiments (n=2). (**B**) Densitometry was performed (Panel A) on MAVS-FL and MAVS-M2 bands corresponding to 72kDa and 50kDa respectively using ThermoFishers Connect platform (n=1). Dotted lines drawn for MAVS-WT expression profiles.

I then assessed the innate immune activation capacity of each MAVS mutant in stably transduced Huh7 cells. I stimulated transduced Huh7 cells with 25ng of poly I:C, a potent RLR stimulator, and collected lysates for western blotting and RT-qPCR 24 hours post-stimulation. While IVT RNA is sensed by RIG-I, high molecular weight poly I:C is detected by MDA5[196]. Both RIG-I and MDA5 signal through MAVS downstream, and

therefore results should be comparable between IVT RNA and poly I:C stimulation. Western blotting results revealed a moderate reduction of pSTAT1 expression in C5T-expressing cells (Fig. 18, A). In agreement, C5T led to a significant reduction in *IFIT1* and *IL6* expression after poly I:C stimulation (Fig. 18, B). Cells expressing C421G had significantly greater *IFIT1 and IL6* mRNA expression compared to WT-MAVS after stimulation. Similarly, G1074C overexpression significantly increased *IFNβ1, IFI44* and *IL6* expression. From this data, the MAVS SNPs C421G and G1074C appear to promote the IFN response after infection, while C5T inhibits innate immune responses. Additionally, these phenotypes are linked to a pro-inflammatory response as differential expression of *TNF* and *IL6* mRNA was found between constructs.

For future work, it would be crucial to validate the phenotypic effect of each SNP during endogenous viral RNA infection, by infecting cells with Sendai virus, Encephalomyocarditis virus (EMCV), IAV or SARS-CoV-2 and measuring the downstream IFN/ISG production via inflammatory cytokine ELISAs, western blotting, RT-qPCR, and luciferase assays.

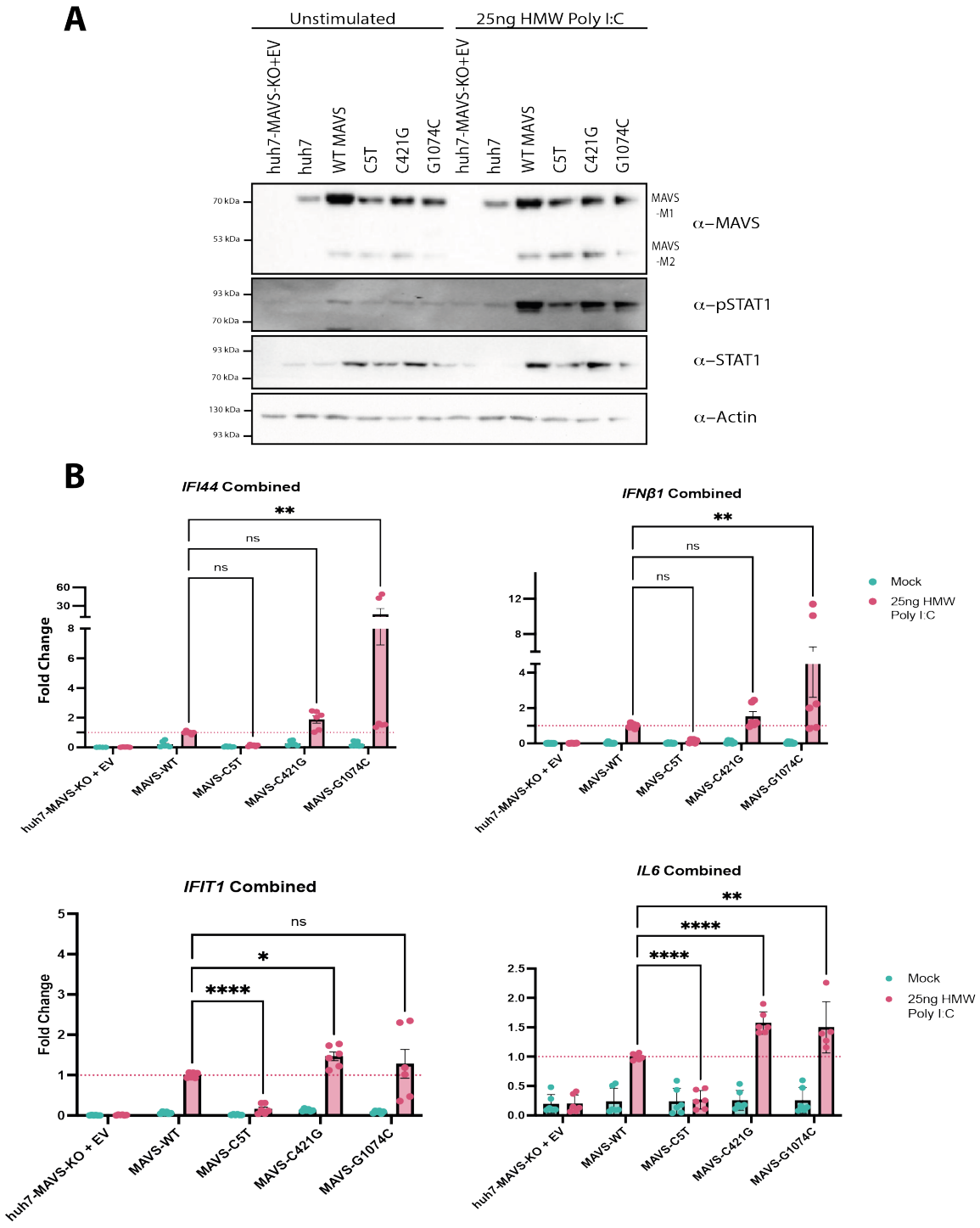


Figure 18: MAVS SNPs Elicit Differential Expression of Cytokines.
Huh7-MAVS-KO cells were transduced with the indicated plasmids and stimulated with 25ng of Poly I:C. The next day, lysates were collected for (**A**) immunoblotting with the indicated antibodies and (**B**) processed for RT-qPCR for the indicated genes. Panel A is a representative blot from four independent biological experiments (n=4). Panel B shows pooled data from three independent biological experiments. Panel B: Multiple comparison two-way ANOVA (ns, not significant=p>0.05, *=p≤ 0.05, **=p≤0.01, ***=p≤0.001, ****=p≤0.0001) (Mean and SEM, n=3).

3.10 Discussion

Despite the technical challenges during this project, I successfully modelled MAVS SNPs found in severe COVID-19 patients. From this, I identified the MAVS-C5T as a significant inhibitor of antiviral signalling. Whether this mutation was causative of severe COVID-19 remains to be determined. Given this mutation is in an RLR pathway protein, one would assume the patient would experience increased susceptibility to any RNA virus infection. It would be intriguing to gain more information regarding the family history of the patient but unfortunately, we do not have access to this information. It would be interesting to determine if the cellular phenotypes are recapitulated in cells infected with RNA viruses such as EMCV, Sendai, or influenza A. Of course, determining the IFN response of MAVS SNPs in SARS-CoV-2 infected cells or *in vivo* would represent the most ideal model of endogenous infection and pathological effects of MAVS mutations.

The ribosomal P-site is responsible for the recognition of AUG by Met-tRNA; however Watson-Crick geometry of base pairing is much less strictly adhered to in the P-site compared to the A-site which decodes codons during the elongation phase[492,514,515]. This presumably explains the ability of Met-tRNA to recognize non-AUG codons as start codons. An AUG with a strong Kozak sequence is recognized with a probability near 1, while weak Kozak AUGs and non-AUG start codons have a range of initiation efficiencies from 0 to 1[239]. Translation from non-AUG start codons still begins with a methionine as the mispairing of Met-tRNA is only tolerated in the P-site[516]. The most efficient non-AUG codon is CUG, with a 2-3 fold efficiency over any other non-AUG codon[492,517]. Similar to the outcome of downstream AUG codons, initiation at non-AUG codons can result in truncated protein isoforms if synthesis is in-frame[492]. However, non-AUG initiation is severely stunted if the +4 position is a non-G nucleotide[492]. In the context of MAVS, a C residing in the +4 position already reduces its Kozak strength. Considering the C5T SNP converts the CCG to CUG, I considered the possibility that the C5T mutant would provide a second non-AUG start codon for FL-MAVS and promote its translation. However, overexpression of C5T significantly reduced FL MAVS expression

in all conditions tested, providing evidence for my initial hypothesis that the canonical AUG of FL MAVS would be skipped in favour of alternative downstream AUG start sites.

From the results in transduced Huh7 cells, it appears the levels of expressed M2 protein have less of an effect on downstream IFN induction: C421G expresses ~2-fold more M2 than WT, yet these cells induce *more* IFN and ISGs after stimulation. I hypothesized that the mutation would result in a stronger Kozak sequence flanking M142 (which translates MAVS-M2) and therefore produce a skewed ratio of FL to M2, favouring M2 translation. Huh7s transduced with C421G and stimulated transiently transfected HEK293 exhibited a higher proportion of M2. However, HEK293 cells transduced with C421G did not express more M2 compared to MAVS. It is difficult to make concrete conclusions about the functional impact of MAVS-C421G as the results were inconsistent between transfected or transduced HEK293 and Huh7 cells.

Across the majority of experiments, with the exception of reduced *IFNβ* promoter activation in transduced HEK293 cells, G1074C promoted the downstream production of ISGs and IFN. The G1074C SNP results in a change of the M4 AUG start site to an AUC, which should prevent the translation of M4. This led me to hypothesize that the translation of M1 may be greater as a result. Indeed, in most experimental setups G1074C expressed similar or higher levels of FL compared to WT-MAVS. Interestingly, however, this mutant exhibited the least amount of aggregated MAVS protein.

Despite our best efforts to locate and/or generate a C-terminal targeting MAVS antibody, I was unsuccessful and could only quantify M1 and M2 protein expression. Quantifying expression levels of M3-M6 in C5T and G1074C mutants would likely provide more clarity on the phenotypic consequence. Brubaker et al. (2014) initially discovered the presence of downstream an ATG site along the MAVS transcript and further described its translation into the M2 protein isoform[242]. The authors validated that leaky ribosomal scanning was responsible for M2 translation by performing ribosomal profiling of MAVS mRNA in cells treated with harringtonine[242]. Harringtonine treatment stalls ribosomes on the mRNA immediately after translation initiation, which are then subject to ribosomal deep sequencing of ribosome-protected mRNA

fragments[242,518–520]. Without harringtonine treatment, ribosomes are found along the transcript, indicating active translation. However, after harringtonine treatment ribosomes stalled at downstream start sites can be quantified to provide information on protein translation dynamics of a particular mRNA[242,518]. Future work could utilize ribosomal profiling as an alternative approach to western blotting, to quantify the proportion of ribosomes on M1-M6 in each MAVS mutant instead of directly measuring protein expression.

Prion aggregates have most commonly been associated as the causative agent for neurodegenerative diseases, however, numerous examples exist of prion-catalyzed conformational switches that have regulatory functions[296,521]. Viral infection induces the formation of prion-like aggregation of MAVS on the mitochondrial membrane, which converts the conformation of native protein of other MAVS proteins to form aggregates, creating a feedback loop of activation[296]. These aggregates interact with TRAFs to facilitate the activation of IKK and TBK1 and act as highly potent activators of IRF3[296]. Interestingly, the CARD domain of MAVS shares little sequence homology with the CARD of RIG-I and MDA5, explaining why only MAVS forms aggregates[296]. Given that only the CARD domain is required for MAVS aggregation[296], it provides some evidence as to why truncated isoforms are auto-inhibitory. Whether this is due to a skewed portion of protein toward M2-M6, leaving insufficient FL MAVS to aggregate and initiate downstream signalling or whether M2-M6 prevent aggregation directly, is not clear. I observed an apparent reduction in the aggregation of MAVS-C5T both at baseline and after stimulation. It would be interesting to determine the protein expression profile and aggregation potential in cells simultaneously expressing both WT-MAVS and C5T.

Interestingly, uORF translation itself is regulated by phosphorylated eukaryotic translation initiation factor 2A (eIF2α)[241,242,501,509,522]. Upon detection of cytoplasmic dsRNA, the protein kinase R (PKR) phosphorylates eIF2α to suppress protein synthesis and induces apoptosis of virally infected cells[523,524]. Indeed, numerous examples exist of viruses (1) preventing phosphorylation of eIF2α to promote translation of viral transcripts or (2) promoting the phosphorylation of eIF2α to block anti-viral gene translation[525–532]. The NP proteins of SARS-CoV-1, MERS-CoV and SARS-CoV-2 inhibit

the phosphorylation of PKR and eIF2α thereby impairing this anti-viral host response[533]. It is still unclear what regulates the proportion of translated protein and whether ribosomal attachment at the uORF of MAVS is promoted by viruses as a means to suppress innate immunity. This prompts me to consider whether viral proteins de-phosphorylate eIF2α to promote ribosomal initiation at the uORF of *MAVS*, thereby potentially promoting the leaky ribosomal scanning and translation of mini-MAVS products, which reduce canonical MAVS signalling. This opens a potentially interesting line of future work in understanding MAVS regulation during viral infection.

The presence of truncated MAVS isoforms raises an interesting question of how the translation of MAVS and mini-*MAVS* isoforms strike a balance within a cell. If translation of MAVS is too high, determinantal inflammation might ensue, whereas a skewed ratio towards translation of mini-MAVS proteins could leave cells susceptible to viral RNA infections. These experiments reveal an exciting phenotype, in which SNPs associated with severe SARS-CoV-2 display higher proportions of mini-MAVS to conical MAVS protein. The functional data indicates the MAVS-C5T mutant had a reduced ability to induce an IFN response, while G1074C boosted innate responses. Given that these MAVS mutations are affecting the host's innate immune response, it will be interesting to investigate whether similar mutations contribute to a predisposition of severe infection to other RNA-based viral infections – both in these patients and other databases.

Our collaborator, Dr. Kenneth Baillie (University of Edinburgh), performed an additional analysis for rare missense *MAVS* variants for associations with severe COVID-19 in the GenOMICC whole genome sequencing dataset[534]. Unfortunately, from this screen two variants were detected at M303 and M358, however these were not associated with severe COVID-19 infection (Data not shown). Given this, larger-scale experiments (which requires specialized category 3 laboratory access training) such as SARS-CoV-2 infections, which I had planned at the beginning of the project, were deprioritized to focus on my VZV project.

Chapter 4

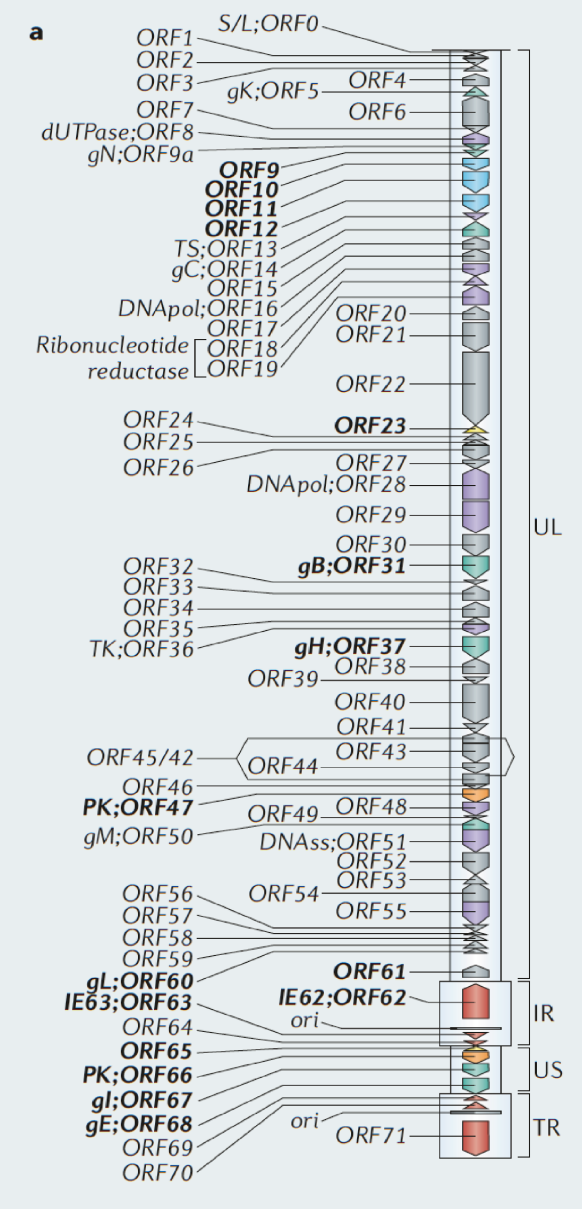
Innate Immune Recognition of Varicella Zoster Virus

4.1 Introduction

4.1.1 Virology & The Genome

Varicella zoster virus (VZV) is a member of the *Orthoherpesviridae* virus family and the alphaherpesvirus subfamily[535]. Two other members of the alphaherpesviruses, herpes simplex virus type 1 (HSV-1) and herpes simplex virus type 2 (HSV-2) are closely related virus to VZV[535]. These three members are the only alphaherpesviruses capable of human infection[536], with no animal reservoir[537]. While VZV can only infect human or guinea pig cells, HSV can infect a variety of species[8].

VZV is a dsDNA virus with a 125kb genome, the smallest genome of the human herpesviruses[537]. All herpesviruses are enveloped, with their DNA packaged inside of the nucleocapsid[8,538]. VZV like many large DNA-based viruses, has a genetically stable genome with minimal nucleotide variation between isolates[535,539]. For example, deep RNA sequencing of the full transcriptome of VZV EMC-1 and pOka strains revealed no specific lytic transcript isoforms existed in ARPE-19 tested[539]. The genome was first sequenced in 1986 and encodes at least 71 open reading frames expressed during lytic infection[539,540] (Fig. 19, A), only one of which contains introns. The genome annotation relies on a mix of sequencing, *in silico* predictions and the characterization of homologous ORFs in HSV-1[539]. The genome consists of two unique regions, a long region (UL, 100kb), a short region (US, 5kb), and internal repeat (IR) and terminal repeat (TR) regions[538,540]. The proteins encoded by ORFs 20, 21, 23, 33, 40 and 41 are structural capsid components or related to genomic structure (i.e. RHIM domains, etc). The tegument is composed of 14 viral proteins encoded by ORFs 4, 9, 10, 11, 12, 22, 38, 47, 53, 57, 62, 63, 64 and 69[8]. The viral envelope is made up of viral glycoproteins gC, gB, gE, gH, gI, gK,gL, and gM[541]. ORFs 62, 63 and 64 were inverted and duplicated to produce ORFs 71, 70 and 69.



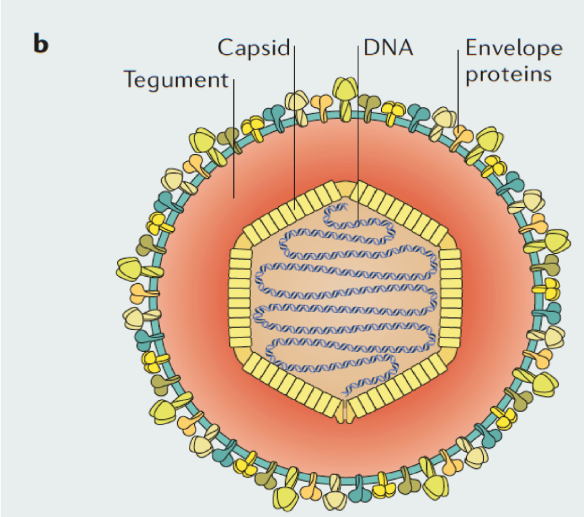


Figure 19: VZV Genome Composition.
(**A**) The VZV dsDNA genome is 125kb and encodes at least 71 unique ORFs. The genome is categorized into unique long region (UL), unique short region (US), internal repeat (IR), and terminal repeat (TR) regions. (**B**) The VZV virion is composed of a linear genome packaged into an icosahedral nucleocapsid core, which is surrounded by a protein tegument layer. The outer virion is made up of a lipid membrane envelope with incorporated glycoproteins. Figure from Zerboni et al. 2014. doi: 10.1073/pnas.0501045102.

VZV encodes ~41 'core genes' that are conserved across the three subfamilies of herpesviruses, alphaherpesvirus, betaherpesvirus, and gammaherpesvirus[542].

4.1.2 Pathology & Epidemiology

Varicella-Zoster virus (VZV) is one of nine herpes viruses that infect humans[8]. Primary VZV infection causes chickenpox (Varicella). VZV then goes on to establish lifelong latency in ganglionic neurons, from which it, can reactivate and cause shingles (Herpes zoster) in immunocompromised individuals or, typically later in life, by waning immunity with age[8,535,537,543]. The reactivation frequency for shingles is approximately 30%[537,544]. VZV, HSV-1 and HSV-2 share the ability to establish life-long latency in the sensory ganglia neurons, from which these viruses can re-activate as a recurrent disease one or more times[8].

VZV is transmitted via liquid aerosolized droplets, by inhalation of vesicular fluid secreted by open sores of varicella or zoster[8,537,545] (Fig. 20). Therefore, the first cells to encounter VZV are those of the respiratory tract. VZV begins replication in the epithelial cells of the upper respiratory mucosa and proliferates to the tonsillar ring, thereby gaining access to highly permissive T cells in the lymphoid tonsillar tissue[8,537,538,543]. Infected T cells transport the virus through the bloodstream to the skin – VZV has the capacity to remodel T cells to facilitate homing to the skin cells where VZV then infects keratinocytes and other specialized skin cells[546]. Alternatively, the virus can infect tissue-resident dendritic cells (DC), which will migrate to lymphoid tissue and can spread the virus to circulating T cells[547]. Viral DNA can be detected in the blood up to 10 days prior to the appearance of a rash[537]. Establishment of infection in the skin tissue causes the characteristic varicella blister rash. These blisters secrete highly infectious fluid that transmits the infection to uninfected individuals[537,548]. Most virus is shed from the skin in highly concentrated vesicles containing cell-free viruses. Infected individuals are contagious ~1-2 days prior to the appearance of the rash[537].

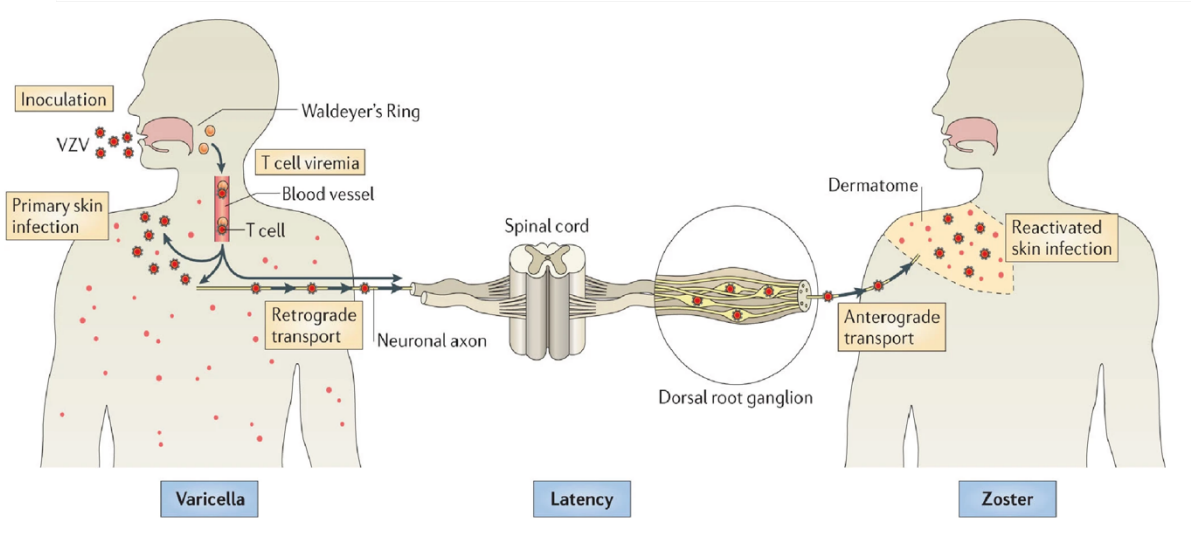


Figure 20: VZV Primary and Latent Pathogenesis.
VZV is transmitted via aerosolized droplets that infect the upper respiratory tract and tonsils. Circulating T cells become infected in the tonsils and transport virus to the skin where varicella blisters form. Latency is established in the sensory ganglia after transport along the neuronal axon or by T cell viremia. Reactivation of the virus, establishes a second phase of viral replication in skin, causing zoster blister formation in the dermatome. Figure is from Zerboni et al. 2014. doi: 10.1073/pnas.0501045102.

During lytic infection, the virus can infect peripheral neurons via their axon endings present in the skin or be transferred to neuronal cells that lack cutaneous projections by infected T cells. The peripheral neurons in the dorsal root or cranial ganglia are the site of VZV latency[8,537]. The mechanism that govern latency are still not understood but it are broadly believed to be linked to insufficient control of the immune system[537]. When viral replication is reactivated, viral particles are transported to the skin via anterograde axonal transport[8,538]. Here the virus creates zoster lesions in the dermatome[538].

4.1.2.1 Epidemiology

As much as 90% of most worldwide populations have been infected with Varicella, typically during childhood, with only 5-10% of adults remaining susceptible[535,537]. After initial exposure, the virus undergoes an incubation period of 10-21 days before the appearance of skin lesions[8,537]. The disease, often mild in children, is characterized by

fever during the same period as the lesions which cover the body[8,537,545]. Both infections and epidemics are self-limiting as the pool of susceptible individuals dwindles[537]. The disease severity is thought to correlate with age as the risk of complications increases[549]. Complications associated with VZV include cerebella ataxia, meningitis, pneumonia, meningoencephalitis, encephalitis, birth defects (if active infection during pregnancy) and bacterial sepsis[8,537,545]. Rare cases of severe VZV infection have been fatal[538].

The vesicular zoster rash affects the dermatome[538]. Replication of the virus in the ganglion damages the neurons and can lead to fibrosis. This damage to the tissue is what is thought to cause severe pain that is commonly associated with zoster rash[538]. The incidence of shingles increases with age, with the probability of a shingles episode reaching 50% once over 85 years old[8]. The rash is characterized by blisters, similar in appearance to varicella, but often accompanied by significant itching and pain[537]. Unlike chickenpox, shingles is usually concentrated in one area, typically the chest or face. If the virus infects the tissue in or around the eye it can cause herpes zoster ophthalmicus, resulting in temporary or permanent vision loss[549,550]. Similarly, Ramsay-Hunt syndrome occurs when VZV infects the geniculate ganglion of the face and carries a risk of up to 85% chance of hearing loss[549,551,552]. Patients have commonly reported the persistence of pain even months after the blisters have resolved. This lingering pain, termed post-herpetic neuralgia, significantly affects their quality of life[8,553]. While the risk of VZV-associated hearing loss can be mitigated by the intervention of antiviral or steroidal therapy[552], the shingles vaccine is the best method of preventative protection.

VZV is the only herpesvirus with a licensed vaccine, however, in the wake of the COVID-19 pandemic, mRNA vaccines have gained momentum and increased popularity. Currently, a phase I clinical trial for HSV-2 is utilizing a mRNA vaccine to deliver three HSV-2 glycoproteins to prevent viral entry, spread, and the formation of genital lesions[554]. Varivax and Varilix are versions of the live attenuated vOka vaccine manufactured by Merck and GlaxoSmithKline. The vOka strain was generated by serial passage of a wild-type clinical isolate of the parental Oka (pOka) strain[555–559]. Only 42 nucleotide changes differ the VZV vaccine strain vOka from its parental pOka stain[560].

The vaccine establishes latency and can reactivate as zoster, however, the incidence rate of this is lower compared to that in naturally infected individuals[555]. The vaccine has been introduced into regular vaccination programs for children in developed countries and some adults with increased risk. The vOka vaccine, prepared in higher titres (Zostavax) was approved for use in elderly individuals to prevent shingles[561,562], as was a subunit based vaccine Shingrix[563]. The Shingrix and Zostavax vaccines are the two vaccines currently recommended in the UK for adults over 65 and immunocompromised adults over 50[564]. Another live attenuated vaccine (MAV/06 - Biopharma), genetically similar to vOka, was approved for use in Korea in 2020 and has been shown to produce similar antibody responses as the vOka vaccines, complemented with increased B cell and Th1 cell responses[565].

4.1.3 Replication & Life Cycle

The VZV virion is composed of a dsDNA genome, capsid, tegument and envelope (Fig. 19, B)[535]. Like other herpesviruses, VZV has a lipid-rich envelope, acquired from cellular membranes, coated in viral glycoproteins[538]. The tegument, a layer of proteins situated between the viral envelope and the nucleocapsid, surrounds an icosahedral nucleocapsid core that holds linear dsDNA genome [8,538].

VZV enters the cell by either direct fusion with the membrane or endocytosis[541] (Fig. 21). While HSV requires gD for membrane fusion and cell entry, VZV utilizes a core fusion complex of gB and gH-gL heterodimer to perform membrane fusion[538,541]. Nucleocapsids are shuttled to nuclear pores via the host cell's machinery, where viral genomes are injected into the nucleus[538]. The genome remains linear in virions and circularizes once the viral DNA is injected into the nucleus. Viral replication of nuclear circular DNA is thought to stop during latent infection, where little to no replication occurs and no production of infectious virions[537,538]. In latently infected neurons, viral DNA is permanently circularized and forms an episome. Genome replication relies on both viral and host transcription factors and translation systems[538]. After entry into the

cell the virions uncoat and allow tegument proteins to enter the nucleus. Tegument proteins IE4 and IE62, encoded by ORF4 and ORF62 respectively, initiate a temporal cascade of gene expression by transactivating immediate early (IE), late and early promoters before *de novo* protein synthesis[538,540,566]. This allows for the early genes required for viral DNA replication to be expressed during early-stage infection[535]. Viral mRNAs are transported to the cytosol for translation and proteins are imported back into the nucleus. After viral replication, structural proteins encoded by late genes are expressed to allow for egress out of the cell[535]. Once newly replicated DNA is packaged into capsids, it egresses from the nucleus by the primary envelopment of the nuclear membrane and then de-envelopment to the cytoplasm[538]. The capsid undergoes secondary envelopment, which coats the naked capsid in tegument protein and glycoprotein-containing membranes in the trans-Golgi network. The newly assembled virions are diverted into late endosomes where a portion are degraded and the remainder are released at the plasma membrane[567].

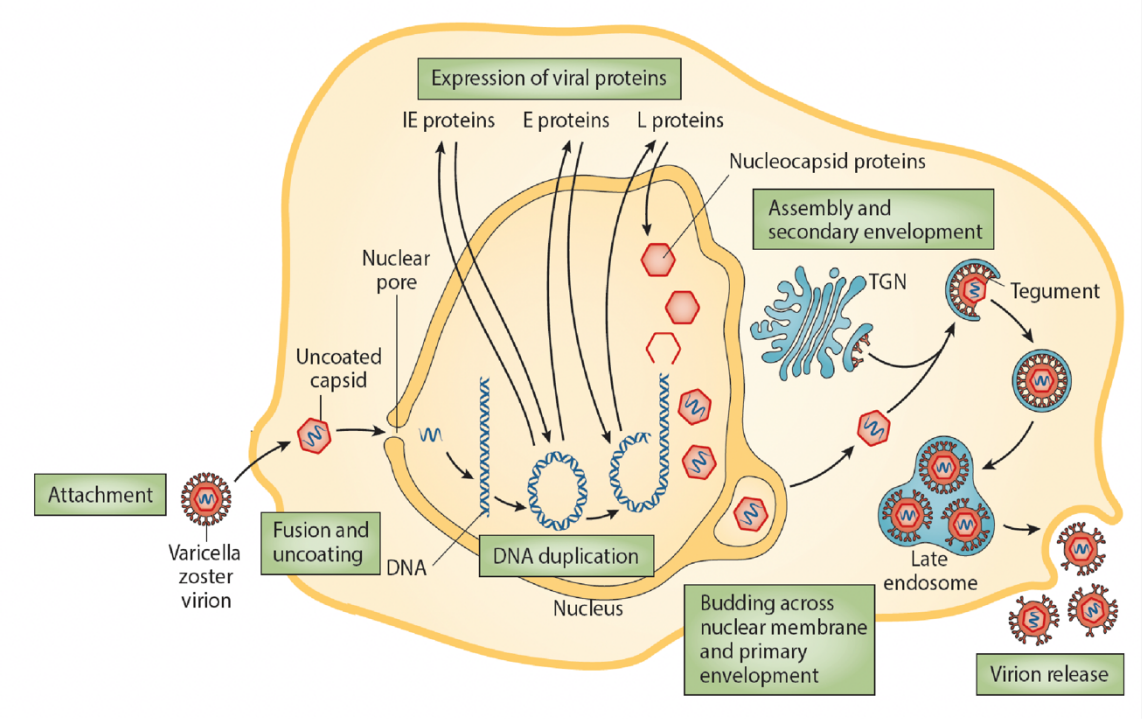


Figure 21: VZV Lytic Replication Cycle.
VZV virions fuse to the membrane where capsids are transported to nuclear pores. The linear dsDNA viral genome is inserted into the nucleus where its circularizes and viral replication occurs. Its thought immediate early genes are transcribed, followed by early and late genes. The newly synthesized DNA is packaged into nucleocapsids, which then bud across the nuclear membrane. In the cytoplasm, a secondary envelopment adds glycoproteins and tegument to the capsid. A portion of virions exit the late endosomes and are released from the plasma membrane. Figure is from Gershon et al. 2015. doi: 10.1038/nrdp.2015.16.

VZV differs from other herpes viruses in that its virions remain highly cell-associated[538]. This distinction introduces an interesting paradox of VZV pathogenesis – *in vivo* VZV generates highly infectious and cell-free particles while *in vitro* virions are predominantly cell-associated. Therefore, virions cannot be collected from the media but exclusively from cell lysates[567]. The highly infectious nature of VZV is evident from the observation that 90% of susceptible individuals in a household will become infected with VZV by the infected household member[568]. Additionally, VZV doesn't overcome the host but rather, slowly spreads over a long incubation period[537].

Its replication cycle is likely cell type dependent, in that infection of skin cells and circulating T-cells have different pathologies[543]. The viral glycoproteins that mediate cell

entry also allow for the fusion of infected and uninfected cells, which facilitates viral spread. This fusion results in syncytia, large multinucleated structures, represents the mode of transmission in skin cells and is the cause of epidermal blister formation[8,538,569].

Ultra-deep RNA sequencing of latently infected ganglia demonstrated consistent expression of spliced VZV mRNA anti-sense to ORF61[570]. The spliced VZV latency-associated transcript (VLT) is expressed in neurons and encodes late kinetic proteins in *in vitro* infected cells and shingles skin lesions[570]. Multiple alternatively spliced VLT isoforms are expressed during lytic infection, however only a single VLT isoform is expressed during latency[570,571]. Fusion transcripts expression of VLT-ORF63 is induced by reactivation stimuli[572]. VLT-ORF63 is postulated to induce viral gene expression during the transition from latency to lytic VZV infection[572,573,573]. These transcripts were also highly enriched in post-mortem samples and should be an important line of future research. The pathology of VZV latency in neurons is still poorly understood and characterized. Whether any viral genes are expressed or proteins are translated during latency is still unclear.

4.1.4 In Vivo Models

VZV was first isolated and propagated in cell culture in 1953[574]. Investigating VZV in an *in vivo* model is challenging as it lacks the capacity to infect other species[538]. Researchers have attempted to establish a VZV rodent model, however, the infections result in seroconversion but do not recapitulate other phenotypes of VZV disease[575]. The immunology of VZV infection is primarily studied in human foetal skin cells, guinea pig models, dorsal root ganglion xenografts transplanted onto severe combined immunodeficient (SCID) mice, and simian varicella virus (SVV) non-human primate models for VZV[543,576–578]. However, no animal model has been generated to recapitulate human disease of both varicella and zoster infections. Conversely, xenografts transplanted onto SCID mice show the characteristic varicella rash and the

immunodeficient mouse allows the study of the innate response to infection[579,580]. However, this method relies on a highly artificial system of studying VZV infection and utilizes an elaborate technique that is prohibitive to most researchers.

4.1.5 Immune Response To VZV

4.1.5.1 Apoptotic Response

Programmed cell death is a method of innate immune response to control viral infection by eliminating damaged or infected cells[535]. These cell death pathways can be triggered during viral infection via sensing by PRRs, damage to host DNA, release of mtDNA, and endoplasmic reticulum stress[124,187,535]. These cell death pathways include necroptosis, apoptosis, and pyroptosis. VZV has been shown to regulate apoptosis in a cell-dependent manner. For example, infection of MeWo cells downregulates the expression of an anti-apoptotic protein, Bcl-2[535]. Studies have shown that infected HFF cells were susceptible to apoptosis while neurons and foetal ganglia remained resistant, potentially relating to their role in latency[535,573,581].

4.1.5.2 Innate Response

Innate and adaptive responses are crucial to limit VZV severity and reactivation[543]. Given the key role of IFNs in controlling viral infections, its unsurprising to find IFNs are important for VZV control[535]. A clinical trial in the 1980s treated VZV infection in children with cancer with IFNα, which successfully disseminated severe skin lesions[582]. Indeed, healthy patients experiencing acute primary varicella infection have elevated IFNα and IFNγ detected in their serum[583]. Analogously, blocking type I IFN receptor in SCID-hu skin mouse model results in a 10-fold increase in virus titre compared to control mice[584]. The type I and III IFN response to VZV infection is found to be mediated by STING in dermal fibroblasts[585]. Otherwise healthy patients with inborn errors in subunit proteins of RNA polymerase III show significantly reduced IFN production during VZV

infection and reduced control of viral replication[586]. Leukocytes isolated from three of these patients recapitulated the phenotypes seen *in vivo*[586].

Cell surface toll-like receptor 2 (TLR2) recognize VZV particles and viral dUTPase. The recognition of VZV glycoproteins by TLR2 leads to an NFκB dependent increase in inflammatory cytokines[587]. Viral dsDNA is recognized by endosomal TLR9[543]. Infected pDCs produce higher levels of IFNα in a TLR9-dependent manner compared to controls[588]. Endosomal TLR3 recognizes dsRNA and is known to be expressed in neurons and peripheral nerve Schwann cells[535,589]. In a case study, a 28-year-old with recurrent herpes zoster opthalmicus, usually only seen in immunocompromised individuals, was found to have a TLR3 mutation[590]. Fibroblasts isolated from this patient do not respond to stimulation by a TLR3 agonist, while antigen-presenting cells do respond[535,590]. This provides some evidence that TLR3, despite being recognized as a dsRNA receptor, may act to control VZV infection in a cell-type dependent manner.

The significance of NK cells in the control of VZV is apparent from the severe nature of infection in NK-deficient patients. Often herpesvirus infections in NK-deficient patients are fatal, especially concerning VZV disease[591–594]. While VZV infection is typically mild in children, a fatal case of infection was observed in a child with NK cell deficiency[595]. *In vitro,* NK cells have been found to show cytotoxic activity against VZV-infected cells[595]. Indeed, a $CD56^{dim}$ subset of NK cells predominates in the blood and is highly permissive to VZV infection with clinical and vOka VZV strains[596]. These circulating infected NK cells can transmit infection to epithelial and fibroblasts in culture, and upregulate skin-homing chemokines[596]. This suggests that NK cells have a role in viral dissemination, but have been overlooked in research focussing often on T cell and B cell tropism[535].

4.1.5.3 Adaptive Response

The adaptive immune response is crucial for the control of both primary and reactivating VZV infection. The time between infection and onset of blistered rash is 10-21 days; despite this, T-cell and antibody responses can be detected only 3 days after

the onset of a rash[583]. Given this, it appears VZV viremia and infiltration into the skin are not inducing an adaptive response, likely due to the abundance of PRR signalling pathway antagonists encoded by VZV (expanded in 4.1.5.4). After rash onset, the production of viral-specific T cells increases over time and correlates with disease severity[583].

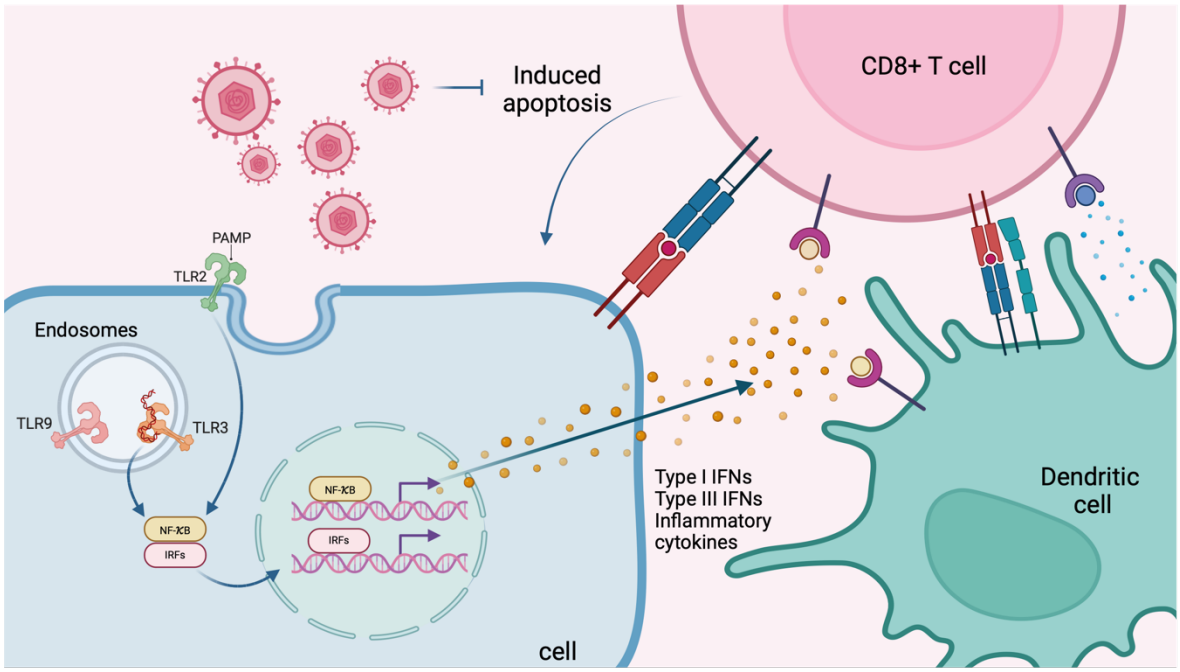


Figure 22: Immune Response to VZV Infection.
VZV-ORF66 can act to delay or prevent T cell mediated apoptosis to promote viral dissemination. Dendritic cells increase secretion of IFNa in an anti-viral response against VZV infection. TLR2, TLR3 and TLR9 have been linked with to a role in VZV recognition and mediating an inflammatory cytokine response. Figure has been adapted from Hakami et al. 2024. doi: 10.1002/rmv.2554. Made with BioRender.

VZV also targets IFN production by infecting immune system cells that have anti-viral roles[535]. Plasmacytoid dendritic cells (pDCs) produce large quantities of IFNα given the appropriate stimulation[535]. VZV significantly hampered the *in vitro* and *in vivo* production of IFNα in pDCs after stimulation with a TLR9 agonist[597].

VZV reconfigures T cells to active memory T cells with a defective immune response and targeted skin-home capacity[543]. The re-exposure to VZV and reactivation acts to maintain the pool of VZV-specific T cells, which are found in the highest proportion in adults aged 30-40[598,599]. Interestingly, from age 55 upwards there are very low titres of VZV-specific T cells[598], which appears to correlate with the probability of VZV

reactivation. VZV pathogenesis involves both CD4+ and CD8+ T cells[600]. A screen of CD4 and CD8 T cell lines from latently VZV-infected healthy adults assayed reactivity to individual VZV-ORFs, identifying ORF9 and ORF62 as the major targets of CD8 T cells[543]. This potentially highlights a function of ORF9 in VZV latency. The pathways, PRRs, and cell types that govern VZV control remain incompletely understood.

4.1.5.4 Immune Modulation

VZV encodes a number of proteins that function to evade innate and adaptive immune responses, which likely enables its ability to persist as a human pathogen[600]. Protection against apoptosis in neuronal and HaCaT cells has been attributed to ORF63[601], which is likely linked to its increased expression and role in latency[572]. Similarly, overexpression of ORF66 inhibited apoptosis in T cells, as evidenced further by an increased rate of cell death in ORF66 deletion cells[535,602].

The regulatory role of IFN in controlling VZV infection is apparent from the range of viral antagonist proteins encoded to regulate the production and response to IFNs[535]. The ORF47 gene encodes a serine/threonine kinase that disrupts normal phosphorylation of IRF3, therefore preventing IRF3 dimerization required for downstream signalling of IFNβ[535]. ORF61 induces the degradation of phosphorylated IRF3 through the ubiquitin-proteosome pathway[603]. Two VZV ORFs cause dysregulated phosphorylation of signalling proteins: firstly, ORF66 protein prevents the phosphorylation of STAT1. Downstream from this, ORF62 protein blocks multiple sites of phosphorylation along IRF3, thereby inhibiting downstream IFN activation[604]. Lastly, the downstream IFN receptor IRF9 is degraded by the ORF63 protein[605].

4.1.6 Societal Impact of VZV

Before the introduction of the VZV vaccine, chickenpox parties were common. Indeed, I believe I may have even attended one as a child. It was understood that chickenpox is much less severe in children compared to acquiring infection as an adult, and therefore parents were strongly encouraged to expose their children to chickenpox to 'get it over with'[606–609]. Indeed, the phenomenon of pox parties was so widespread that The Simpsons produced an entire episode with a plot centred around Maggie's chickenpox party for the neighbourhood children (Fig. 23, A). The popular show South Park also produced an episode with an almost identical plot (Fig. 23, B).

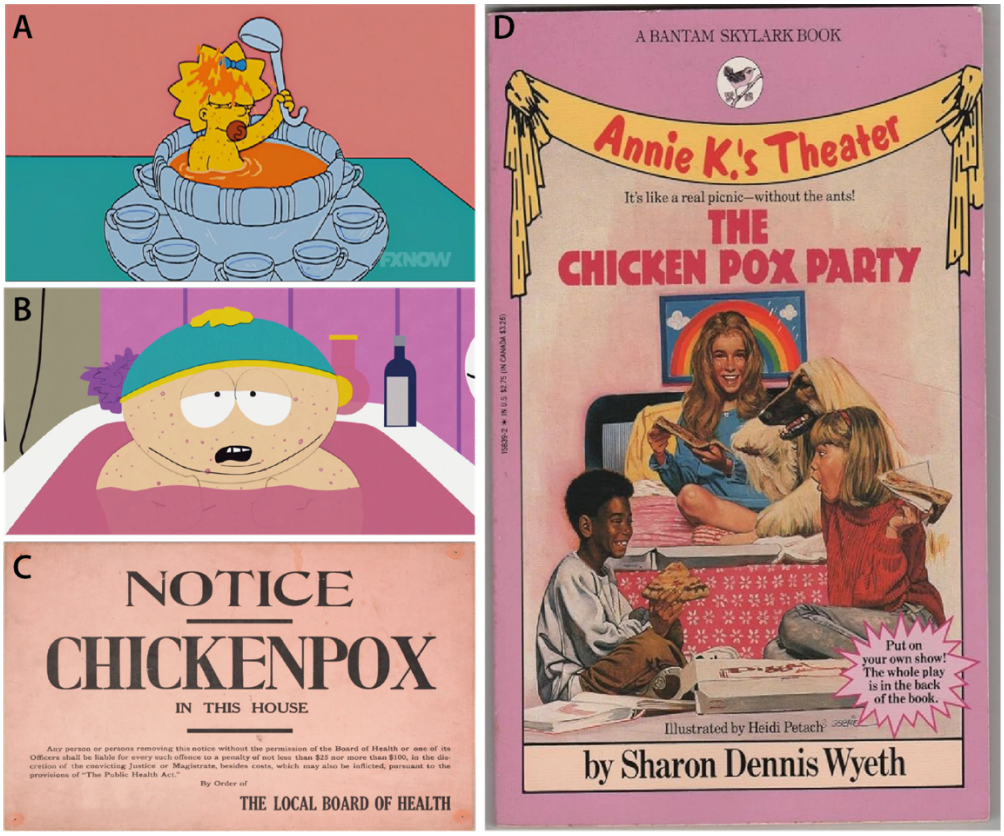


Figure 23: Chickenpox Parties.
(**A**) Maggie bathes in punch to expose the neighbourhood children to chickenpox that is shed from vesicular fluid in her chickenpox lesions. Featured in The Simpsons S17E03. (**B**) Cartman bathes in a tub full of calamine lotion, as it was said to ease the itching of chickenpox rash. Featured in South Park S02E10. (**C**) The Chicken Pox Party is a book published by author Sharon Wyeth about a group of school kids preparing for a play when they realize they're breaking out with chickenpox. (**D**) A public notice by the local health authority warning of chickenpox infection in a household.

VZV being the causative agent of both shingles and chickenpox has been established since 1953 when vesicle fluid derived from a patient with shingles was able to introduce chickenpox in young volunteers[574]. It is interesting that while the public knew about the link between chickenpox and shingles, they still willingly exposed their children to VZV to circumvent a potentially greater risk of severe side effects later in life. After the introduction of the VZV vaccine in the USA, the occurrence of pox parties lessened as parents opted to vaccinate their children instead. While the disease is much milder in children, it still poses complication risks[549,600,609]. The vaccine circumvents these risks while providing a high degree (~85%) of protection[606]. While this may seem like a tangential aside, it highlights the increasing rates of vaccine hesitancy, fuelled by emotion and growing distrust of vaccines – the same fear fuelling vaccine refusal during the COVID-19 pandemic. This presents an interesting psychology behind parents' decision to vaccinate their children and a cost-benefit analysis of vaccine risks, childhood infection complications and late-life infection risks.

4.1.7 Summary

Our findings regarding the inhibition of cGAS via VZV-ORF9 have been published in The EMBO Journal (Ref [292], Full text is attached in Appendix). Dr. Jonny Hertzog completed the majority of the work featured in this paper as part of his DPhil thesis and post-doctoral work. This first Results section (4.2.1) will highlight the main findings from our EMBO paper and solely reflects work completed by Dr. Jonny Hertzog. Chapter 4.2.2 contains a summary of contributions I made to the paper, particularly to the revisions in response to reviewers' comments.

4.2 Results

4.2.1 VZV-ORF9 is Responsible for Inhibition of the cGAS-STING Signalling Axis During Infection

Given what we know about VZV, we hypothesized a role of the cGAS-STING signalling axis in the recognition of VZV given its DNA genome composition[8,537,538] and STING-mediated antiviral response following VZV infection[585]. Immortalized THP1 cells induce type I & III IFN via the cGAS-STING signalling axis after both DNA stimulation[12,24] and VZV infection. Additionally, VZV can infect primary human monocytes and macrophages *in vitro* and *in vivo*[610,611]. THP1 cells are amenable to genetic editing and can be used to investigate the role of individual proteins in pattern recognition. Additionally, VZV can infect and propagate in THP1 cells[612]. Thus, THP1 cells are a suitable cell line for investigating the inhibition of innate immune signalling by VZV infection. To determine the causative PRR responsible for type I IFN induction, a monocytic cell line THP1 was utilized for experiments. THP1 cells were infected with VZV by co-seeding with infected MeWo cells, separated by a transwell membrane. MeWo cells are a melanoma cell line that has been established as optimal for VZV propagation. RT-qPCR results showed that cGAS-KO THP1 cells infected with VZV failed to upregulate ISGs compared to MAVS-KO THP1 cells (Fig. 24, A). This indicates that the innate immune response to VZV infection in THP1 cells is mediated by the DNA sensor cGAS.

To investigate possible antagonists of the cGAS-STING signalling axis, a luciferase-based screening platform was used by Dr. Jonny Hertzog in HEK293T cells. In short, a plasmid expressing Firefly luciferase under *IFNβ1* promoter control and pRL-TK, which expresses Renilla luciferase was transfected into HEK293T cells, resulting in firefly luminescence when *IFNβ1* was induced. As HEK293T cells do not endogenously express cGAS or STING, cGAS and STING plasmids were also transfected into cells along with individual plasmids from a library of VZV-ORFs. The results revealed several VZV-ORFs that blocked *IFNβ1* activation, including the aforementioned previously unknown VZV innate immune antagonists (Section 4.1.5.4). This screen also identified

ORF9, with very low induction of firefly luciferase in ORF9 expressing reporter cells compared to control cells.

To validate that ORF9 inhibits dsDNA activation of cGAS, stably transduced ORF9-THP1 or GFP-THP1 cells were transfected with increasing doses of *E. coli* dsDNA. The expression levels of ISGs and IFNβ1 induction were measured via RT-qPCR (Fig. 24, B). As expected, the GFP-THP1 stimulated cells showed a dsDNA dose-dependent increase in these transcripts. ORF9-expressing cells showed minimal responses to low-dose dsDNA transfection. At higher doses, the response was attenuated when compared to GFP-expressing cells.

As ORF9 was shown to inhibit innate immune sensing in a cGAS-dependent manner, it was hypothesized that the ORF9 protein may perform this antagonist function by directly binding to cGAS. To test this, HEK293T cells were transiently transfected with cGAS-FLAG, STING-HA or ORF9-V5 and interaction was assessed via immunoprecipitation (IP) (Fig. 24, C). ORF9 protein was detected in the bound fraction of the FLAG IP and conversely, in the reverse IP, cGAS protein was present in the V5 IP. Neither protein was pulled down with STING (HA tag). These experiments performed by Dr. Jonny Hertzog indicate that ORF9 binds cGAS in HEK293T cells.

Kaposi sarcoma-associate herpesvirus (KSHV) encodes a protein, ORF52, that has been identified as having DNA binding properties and is a known cGAS antagonist[613]. Given this, we hypothesised that ORF9 may bind to DNA and mediate its interaction with cGAS. To test this, biotinylated dsDNA was incubated with recombinant ORF9 and cGAS or GFP. The DNA was precipitated using streptavidin beads and the bound beads were analyzed using immunoblotting (Fig. 24, D). As expected for a DNA sensor, cGAS bound to DNA. The ORF9 protein was also pulled down with DNA both alone and in the presence of cGAS. The GFP negative control did not pull down with DNA.

To further validate that ORF9 was antagonising cGAS directly, Dr. Jonny Hertzog used an in vitro cGAMP synthesis assay to measure enzymatic activity. Recombinant human cGAS was incubated with radioactivity labelled ATP, GTP and DNA along with ORF9 or

bovine serum albumin (BSA) negative control. Thin-layer chromatography was used to visualize the radioactively labelled 2'3'-cGAMP. ORF9 inhibited the production of cGAMP in a dose-dependent manner, with the highest concentrations of ORF9 protein resulting in the lowest quantity of cGAMP (Fig. 24, E). The production of cGAMP was not affected by any dose of BSA.

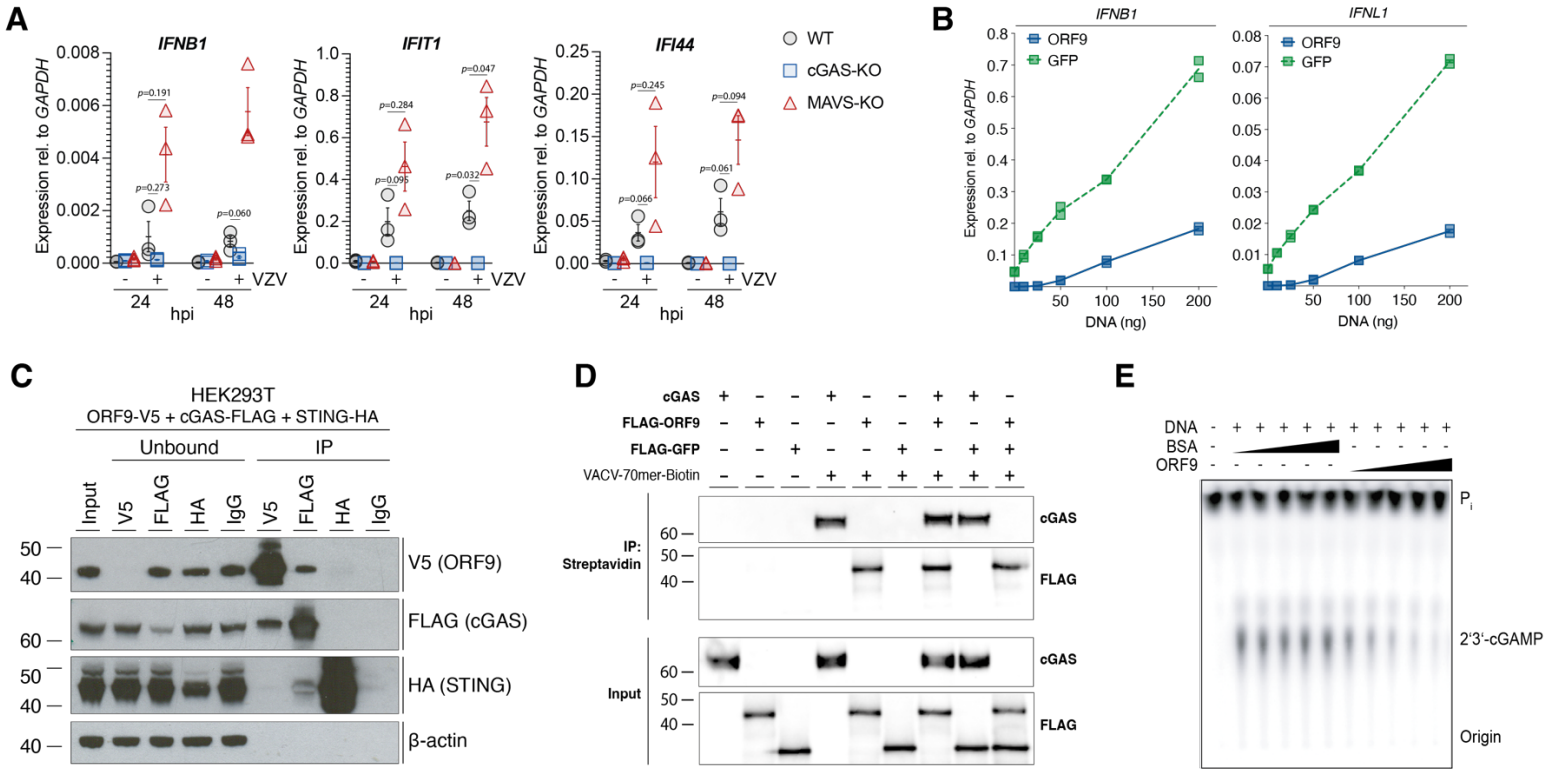


Figure 24: VZV-ORF9 Antagonizes cGAS Through Binding and Inhibition of cGAMP Production.
(**A**) THP1 cells of the indicated genotypes were mock infected or infected with VZV for 24 and 48 h using the transwell assay. RT–qPCR analysis of *IFNβ1*, *IFI44*, and *IFIT1* expression in cells infected as in (C). Graphs show expression relative to GAPDH. (**B**) THP1 monocytes stably transduced with either VZV ORF9 or GFP were PMA-differentiated and transfected with indicated doses of dsDNA. Expression of *IFNβ1* and *IFNL1* was assessed by RT–qPCR. Graphs show expression relative to GAPDH. (**C**) HEK293T cells were transfected with expression plasmids for ORF9-V5, human cGAS-FLAG, and human STING-HA. The next day, cells were lysed, and overexpressed proteins were immunoprecipitated with a-V5, a-FLAG, a-HA, or IgG isotype control antibody. Input, unbound, and IP fractions were subjected to immunoblotting using the indicated antibodies. (**D**) Recombinant cGAS, FLAG-ORF9, FLAG-GFP, and biotinylated VACV70mer dsDNA were incubated in the indicated combinations. Recombinant proteins were precipitated using streptavidin beads. Fractions were analyzed by immunoblotting. (**E**) In vitro cGAS activity assay. Recombinant hcGAS was incubated with ATP, GTP, and radioactive a32P-ATP at 37°C with addition of dsDNA and other proteins as indicated (triangles represent concentrations of 0.5, 1, 2, 4, 6 μM). ORF9-DM was tested only at 0.5, 1, 2 μM. Reactions were treated with calf-intestinal phosphatase, and products were analyzed by thin-layer chromatography and phosphorimaging. Statistical anayalsis in Panel A was a paired ratio t-test. *This figure represents a summary of data from Hertzog et al. 2022. doi: 10.15252/embj.2021109217. All work featured in this figure was completed by Dr. Jonny Hertzog.

4.2.2. Revision Work

In this Chapter, I highlight the results I contributed to this publication that formed the basis of my VZV project featured in Chapter 5.

4.2.2.1 ORF9 Inhibition of IFN Induction Does Not Involve Antagonism of STING

A reviewer requested confirmation that ORF9 inhibition is selective to cGAS and that ORF9 is not blocking STING activation. Therefore, I tested ISG induction levels in ORF9 and GFP THP1 cells after direct STING activation. To test for this, I stimulated stably transduced ORF9-THP1 or GFP-THP1 control cells with diABZi, a potent STING agonist. I first started by performing a dose titration of diABZi in wild-type THP1 cells to determine a sub-maximal response, finding a plateaued maximal response for $\geqq$ 0.01μM diABZi (Fig. 25, A). A dose of 0.005 μM appeared suitable to induce a sub-maximal response for further experiments. The mRNAs of *IFNβ1*, and two common ISGs were induced to similar levels in THP1 cells expressing ORF9 or GFP after treatment with diABZi (Fig. 25, B). These data indicate that STING signalling is unaffected in ORF9-expressing cells and that inhibition of this pathway by ORF9 is likely at the level of cGAS.

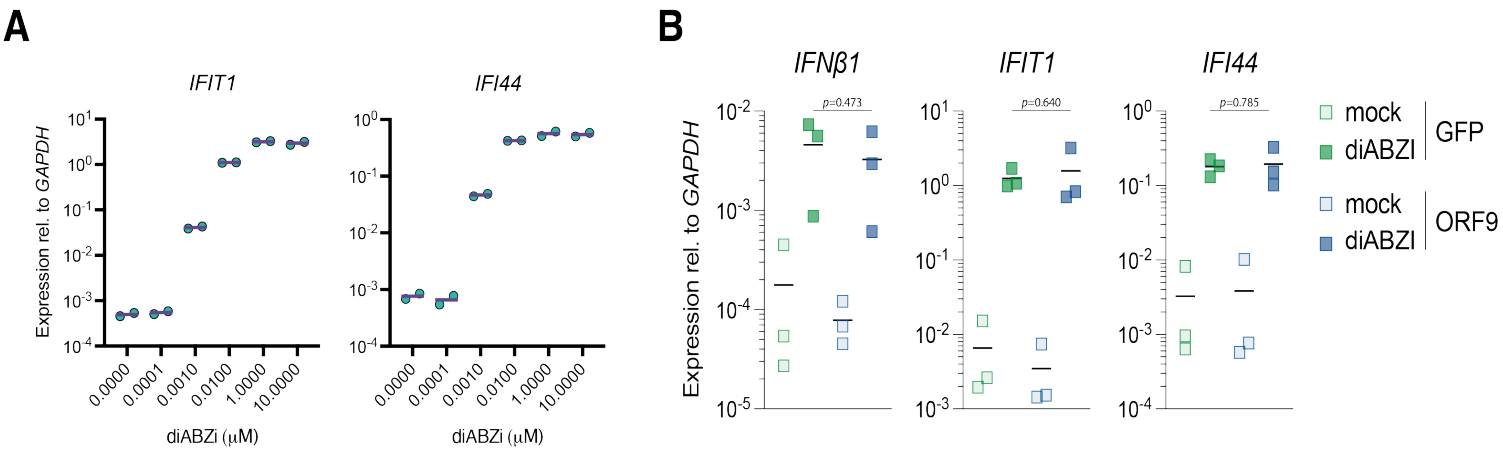


Figure 25: ORF9 Inhibition of IFN Signalling is Not STING Dependent.
(**A**) THP1 monocytes were treated with increasing doses of STING agonist diABZi to determine sub-maximal response. Expression of *IFNβ 1*, *IFIT1*, and *IFI44* was assessed by RT–qPCR (**B**) THP1 monocytes stably transduced with either VZV ORF9 or GFP were treated with diABZi (0.005 μM). Expression of *IFNβ1*, *IFIT1*, and *IFI44* was assessed by RT–qPCR. Graphs show expression relative to *GAPDH*. Panel A shows pooled data from two repeats, where each data point represents technical replicates (horizontal bars show means). Panel B shows pooled data from three repeats, where each data point represents an independent biological experiment (horizontal bars show means). Statistical analysis in Panel B was a paired t-tests.

4.2.2.2 ORF9 Predicted DNA Binding Region is Dispensable for cGAS Binding

Dr. Jonny Hertzog's pulldown experiments showed ORF9 and cGAS proteins binding each other in both a cellular over-expression system and in a complex with DNA in an *in vitro* streptavidin pulldown. To better understand the importance of DNA binding in mediating ORF9's antagonism of cGAS, we first needed to determine DNA binding regions present in ORF9. An alignment of closely related herpesviral proteins revealed several conserved positively charged residues. This alignment revealed two pairs of residues common between VZV-ORF9 and HSV-1's VP22 protein. VZV-ORF9 also shared common residues with MHV68 ORF52 and KSHV ORF52. The ORF9 amino acid residues K178A/R179A aligned with KSHV ORF52 R68/K69 residues that are annotated as crucial for DNA binding[613]. An ORF9 double mutant (K178A/R179A and R186A/R187A) was generated to harbour mutations of the aligned residues. To determine the importance of these residues on cGAS inhibition, stably transduced THP1 cells with GFP, ORF9 or ORF9-DM were stimulated with increasing doses of dsDNA and assessed

for *IFNβ1* induction (Fig. 26, A). The ORF9 and ORF9-DM expressing cells showed a comparable level of reduced *IFNβ1* expression compared to GFP-expressing cells. This indicates that the binding of DNA by ORF9 is not required for cGAS inhibition. The expression of each protein was validated through immunoblotting (Fig. 26, B).

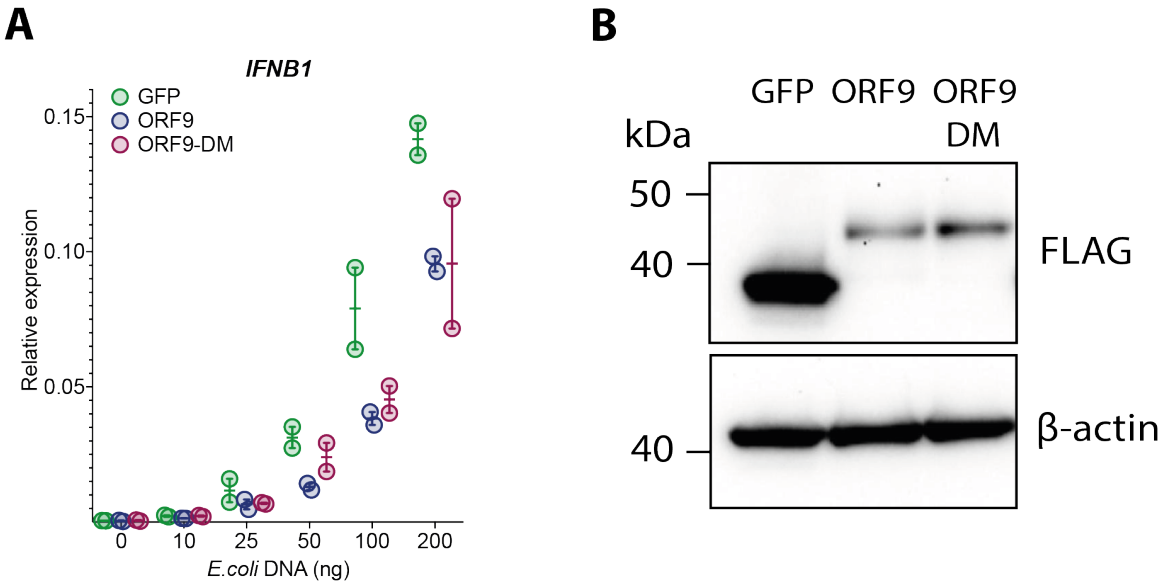


Figure 26: ORF9 Predicted DNA Binding Region is Dispensable for cGAS Inhibition. (**A**) THP1 cells stably transduced with GFP, ORF9, or ORF9-DM were transfected with the indicated amounts of *E. coli* dsDNA. The next day, *IFNB1* expression was assessed by RT–qPCR. Panel (A) shows pooled data from two repeats, where each data point represents an independent biological experiment (n = 2). (**B**) THP1 cells stably transduced with GFP, ORF9, or ORF9-DM cells were lysed and protein abundance was analyzed via immunoblotting using the indicated antibodies. This is a representative blot from three independent biological experiments. (n=3).

4.2.2.3 Conditional Knockout of ORF9 Attenuates cGAS Inhibition

ORF9 is 1 of 14 viral tegument proteins encoded in the VZV genome[8,295] and is essential for the generation of progeny virus[614]. Therefore, a knockout of this protein would render the virus non-viable. To circumvent this we used a recombinant virus with an *E. coli* dihydrofolate reductase degron motif (ecDHFR) fused to the carboxy-terminus of the ORF9 protein (VZV-ORF9^{ecDHFR})[291,615]. This recombinant virus was made and kindly gifted

to us by Ben Warner and Paul Kinchington[291]. The turnover of the degron protein complex is regulated by the stabilization compound, trimethoprim (TMP), that prevents degradation by the proteasome[291,616]. TMP stabilizes the destabilization domain of the degron protein, thereby allowing reversible and dose-dependent knock-down[616]. Once TMP is removed, the unstable degradation domain of the degron and fused protein are rapidly and efficiently targeted for degradation[616,617]. Hulleman et al. did a large chemical compound screen to compare the efficiency and duration required for TMP and other small-molecule pharmacological chaperones (SMPCs) (that were predicted to have an ecDHFR binding pocket) in their ability to stabilize ecDHFR[617–619]. They determined the "on" kinetics, the time required after the addition of SMPCs to bind the ecDHFR complex, and the "off" kinetics, the time required after SMPC removal until the protein is degraded (Fig. 27). Based on Dr. Hulleman's recommendation obtained by email and video call, we tested triamterene (TRI), epiblastin (EPI), TC-P 262 (TCP) and TMP to determine which compound would efficiently stabilize the degron protein and provide a short protein turnover time once the SMPC was removed.

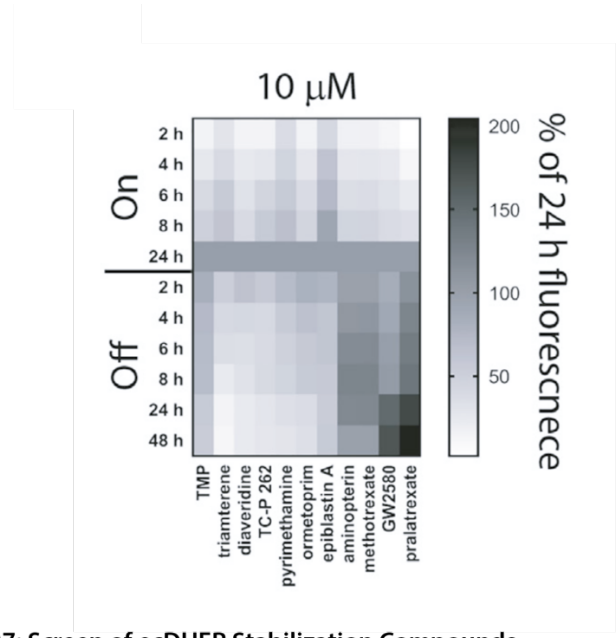


Figure 27: Screen of ecDHFR Stabilization Compounds.
To identify these potential ecDHFR molecules, the authors screened an ARPE-19 cell line that constitutively expresses R12Y/G67S/Y100I ecDHFR fused to yellow fluorescent protein. After validation of hit compound stabilizing effects after 24 h of treatment, the authors next determined how quickly and efficiently select compounds could stabilize ecDHFR-YFP, followed by destabilization after compound withdrawal. Figure taken from Ramadurgum et al. 2020. doi:10.1016/j.chembiol.2020.03.006.

Differentiated THP1 cells were infected by co-culturing with MeWo-VZV-ORF9-ecDHFR for one hour. The cells were washed, to remove residual MeWo cells, and media with the SMPC was added to the cells. 24 hours post-infection the media was changed to include the SMPC as a control or replaced with fresh media to remove the SMPC from the cells. After 48 hours the cells were lysed for immunoblotting and RT-qPCR (Fig. 28, B).

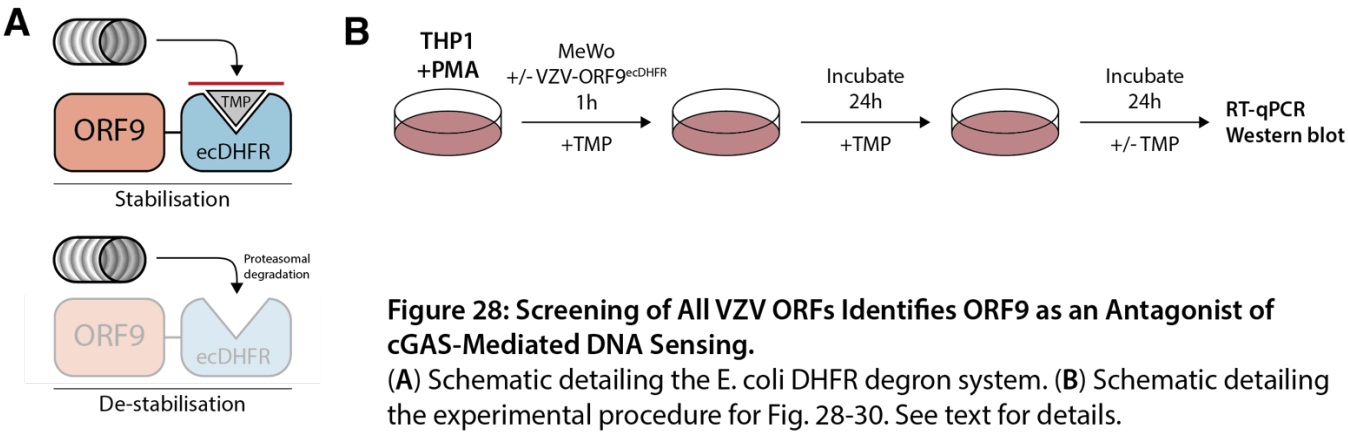


Figure 28: Screening of All VZV ORFs Identifies ORF9 as an Antagonist of cGAS-Mediated DNA Sensing.
(**A**) Schematic detailing the E. coli DHFR degron system. (**B**) Schematic detailing the experimental procedure for Fig. 28-30. See text for details.

At this time point, TMP stabilizes the ORF9 protein when added to the media (Fig. 28, A and Fig. 29, A). When TMP was removed ORF9 expression was significantly depleted indicating that the removal of TMP successfully degrades ORF9 via the proteasome.

An observable increase in ISG expression was present in TMP-depleted samples (Fig. 29, B) compared to TMP-stabilized cells, despite significantly less viral presence (Fig. 29, C). This indicates that despite the lack of strong viral presence, it was sufficient to induce expression above baseline (VZV- TMP+). Likewise, the level of ISG induction was comparable between VZV+TMP+ and VZV-TMP+ cells, indicating that ORF9 was stabilised and blocking cGAS activation to levels seen at baseline.

There was little to no specific ISG induction seen in EPI or TCP-depleted cells. There was a small increase in ISG induction when ORF9 was degraded, however, the results were more variable for this compound compared to TMP. Likewise, Likewise, TRI, EPI,

and TCP were unable to stabilize the ORF9^{ecDHFR} complex at this time point, evidenced by a lack of ORF9 expression in SMPC stabilized conditions (Fig. 29, A). Optimisation of the TRI compound at shorter time points yielded inconsistent results (Data not shown). Given this, the TMP compound was determined to be the most suitable for further degron experiments.

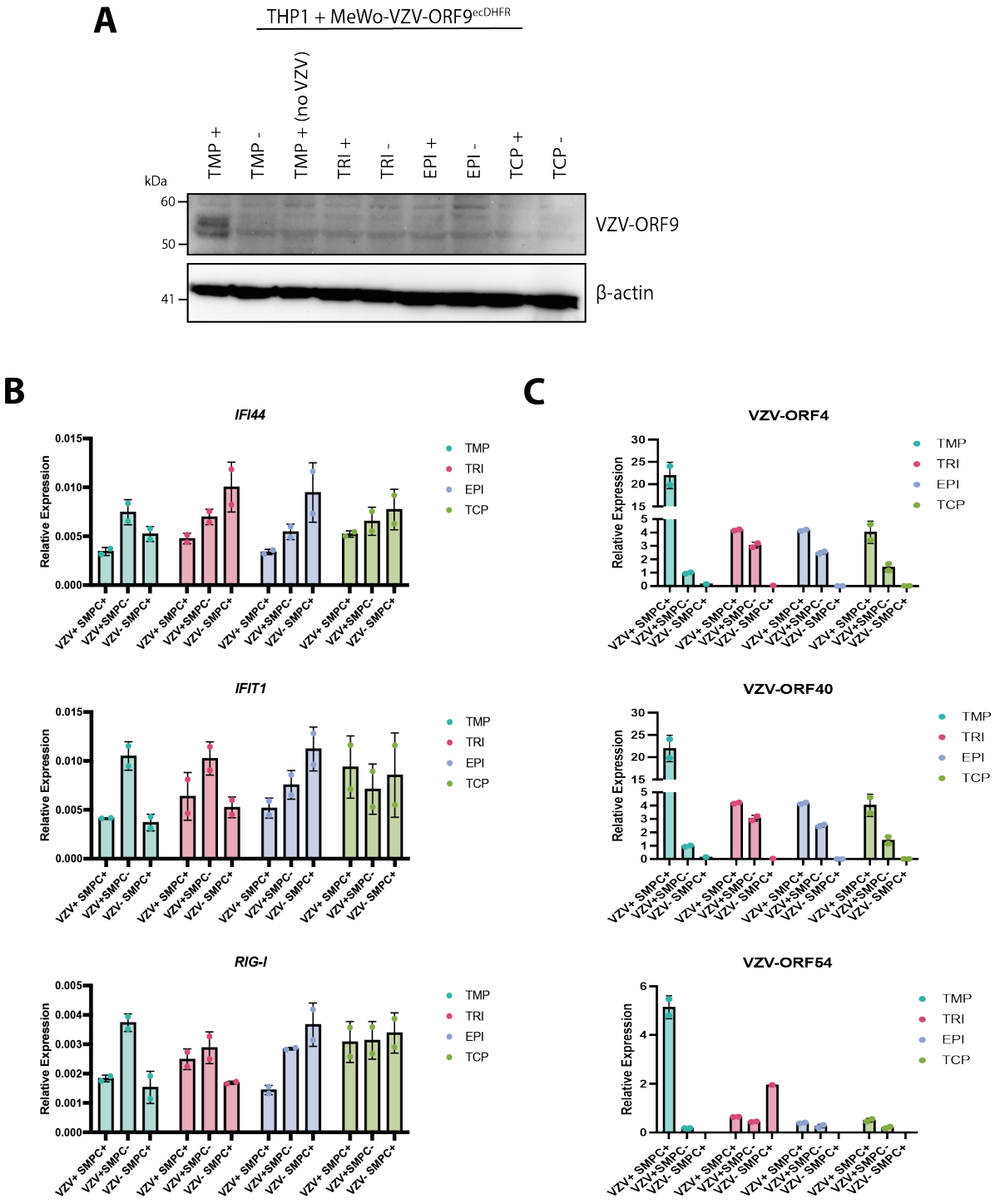


Figure 29: Test Panel of Small Molecular Pharmacological Chaperone Stabilization (SMPC) Efficiency.
(**A**) THP1 cells were co-cultured with infected MeWo-VZV-ORF9-^{ecDHFR} for 1 hour, washed and left to infect overnight in TMP-containing media. Approximately 24 hours later, the cells were washed and replaced with SMPC-containing media for a further 48 hours. Cells were lysed 48 hours post SMPC -/+ and ORF9 protein abundance was assessed via immunoblotting (n=1). (**B**) A set of duplicated experimental cells were lysed to assess ISG induction and viral abundance (**C**) via RT-qPCR (n=1, average of technical duplicates).

From this data, it was clear that the TMP compound was the most suitable. TMP rapidly binds ecDHFR, maintaining the stability of the protein without the need for media changes or re-addition.

A time-course experiment was performed to determine the optimal on and off kinetics of the TMP compound in THP1 cells. This experiment utilized THP-1 Lucia Dual reporter cells which secrete Lucia luciferase into the medium under the control of an ISG54 minimal promotor in conjunction with five IFN-stimulated response elements. They also secrete embryonic alkaline phosphatase (SEAP), controlled by an IFNβ promoter fused to an NF-κB consensus transcriptional response element. This allows for quantification of both IRF and NF-κB activity by measuring secreted luciferase and SEAP. The supernatant from infected THP1 cells was collected at the indicated time points and analyzed for luminescence. IFNβ1 spiked into the media of THP1 cells served as a positive control, and showed a robust IRF3 activation (Fig. 30, A). There were only marginal differences in IRF3 activation between TMP+ and TMP- conditions, indicating that the secreted luciferase may have been too dilute, and therefore this system may not have the sensitivity required to detect small changes in activation.

The stabilization and subsequent degradation efficiency were assessed via western blotting for 21, 48 and 72-hour time points (Fig. 30, B). ORF9 protein was detected at both 21 and 48 hours but was not present at the 72-hour time point. The removal of TMP resulted in degradation of ORF9 after both 21 and 48 hours. Considering ORF9 expression was highest in the TMP+ condition at 21 hours and the corresponding removal of TMP was sufficient for ORF9 degradation, we chose this time point for further experiments.

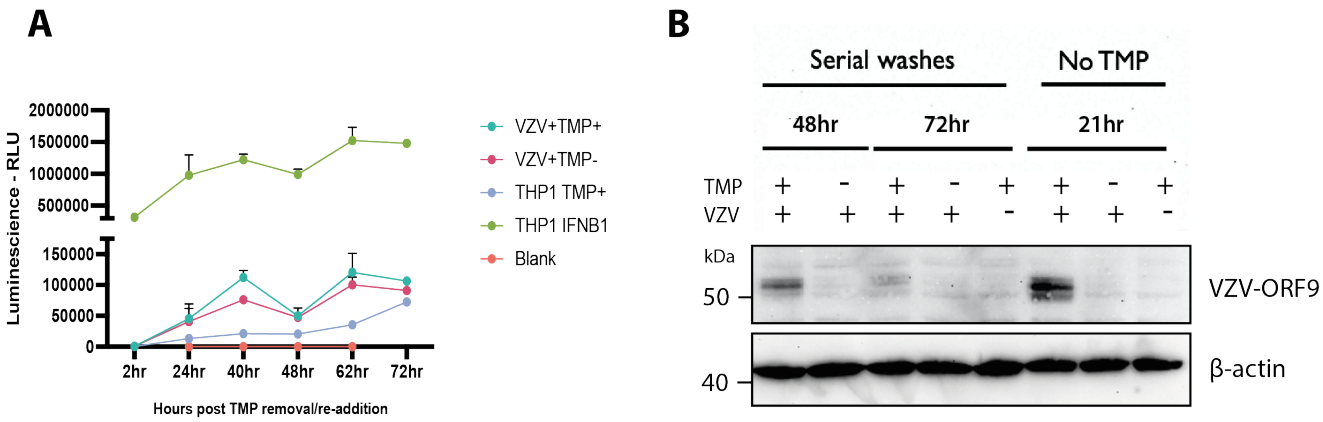


Figure 30: TMP Time Course Experiment.

(A) THP1-Dual IRF3 reporter cells were co-cultured with infected MeWo-VZV-ORF9^{ecDHFR} cells for 1 hour. The TMP was removed by washing and replaced with fresh R10 (-, TMP removal) or R10 with fresh TMP (+, TMP re-addition) until the indicated time points. IFNβ1 or TMP was added to media as a positive and negative control respectively. Luminescence was measured via a microplate reader after the addition of the luciferase reagent Quanti-Luc to the supernatant of cells. **(B)** THP1 cells were co-cultured with infected MeWo-VZV-ORF9^{ecDHFR} cells. In the 'Serial Washes' condition, infected MeWo cells were left to co-infect overnight. The next morning the TMP was removed by washing and replaced with fresh R10 (-, TMP removal) or R10 with fresh TMP (+, TMP re-addition) until the indicated time points. For the 'No TMP' condition the infected MeWo cells were left to co-infect for only 1 hour. Then the TMP was removed by washing and replaced with fresh R10 (-, TMP removal) or R10 with fresh TMP (+, TMP re-addition) until the indicated time points. Cells were analyzed by western blotting with the indicated antibodies. Panel (A) shows pooled data from two independent biological experiments (n=2, average of biological repeats shown). Panel (B) is a representative blot from two independent biological experiments.

Given this data, we used a 24-hour time point for subsequent experiments and RT-qPCR as a more sensitive readout of IFN induction. The TMP compound stabilized the ORF9 protein with the greatest efficiency while observing a nearly complete reduction in protein signal when the compound was removed for 24 hours (Fig. 31, B).

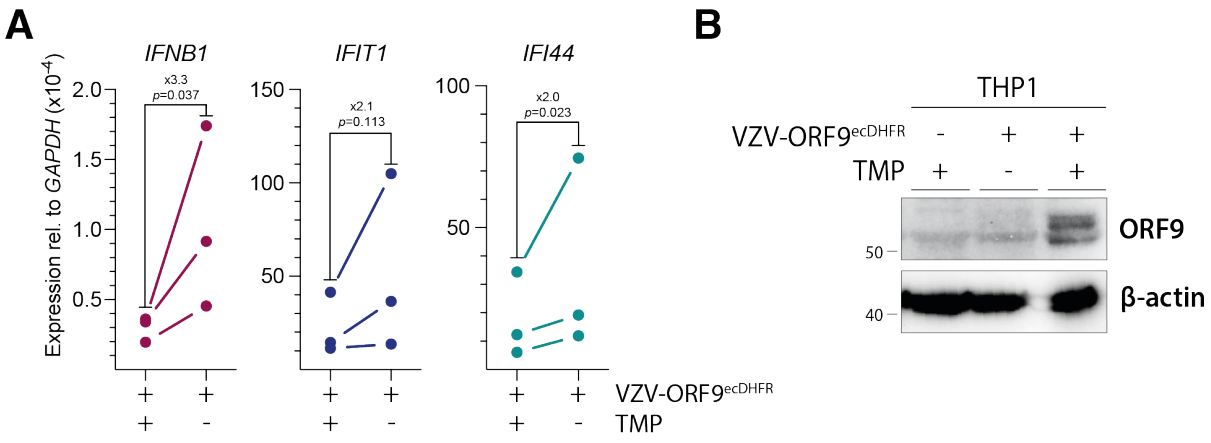


Figure 31: Conditional Knockdown of ORF9 Reduces ISG and IFN Response.
(**A**) PMA-differentiated THP1 cells were co-cultured with VZV-ORF9ecDHFR-infected MeWo cells for 1 h in the presence of TMP, washed, and incubated for another 24 h in the presence of TMP. Cells were then washed extensively, and fresh medium was added that was supplemented or not with TMP. Expression levels of *IFNβ1*, *IFIT1*, and *IFI44* were measured by RT–qPCR after a further 24 h incubation. Graphs show expression relative to *GAPDH*. Mean fold changes are indicated. (**B**) Cells infected and treated as in (A) with the addition of uninfected cells were analyzed by western blotting using the indicated antibodies. Panel (A) shows pooled data from three repeats, where each data point represents an independent biological experiment. Fold change was calculated from the average of repeats. Statistical analysis was a paired t-tests, preformed on the three repeats. Panel (B) is representative of three independent experiments.

RNA was isolated from whole cell lysate for RT-qPCR to determine the effect of ORF9 knockout on the IFN response. The expression of *IFNβ1*, *IFIT1*, and *IFI44* was increased in cells where TMP was withdrawn and ORF9 was absent (Fig 31, A). These data show that in the absence of endogenously expressed ORF9 during VZV infection there was an increased type I IFN response in THP1 cells. The lack of ORF9 expression confirms the role of ORF9-dependent inhibition of the cGAS signalling pathway.

4.2.2.4 VZV Infection Prevents Interferon Production in Keratinocyte and Fibroblast Cells

While THP1 cells make for a well-studied cell model for innate immune sensing, the reviewers of our publication requested some key experiments to be repeated in a cell

type that would facilitate VZV replication. Considering VZV replicates in epithelial cells, keratinocytes, neurons and T cells[538], we decided to select several cell lines that would better represent the virus's tropism, thus bearing more physiological relevance to VZV disease pathogenesis. To address this reviewer's suggestion, I infected a spontaneously immortalized human keratinocyte cell line, HaCaT, with VZV. We chose these cells as they endogenously express cGAS and our laboratory had previously generated HaCaT-cGAS-KO cells. Co-culturing (transwell system) VZV-infected MeWo cells with HaCaT cells did not result in induction of an IFN response when compared to the uninfected MeWo control (Fig 32, A). RT-qPCR of both early and late VZV genes validated that the keratinocytes were infected (Fig 32, B). The same experiment was repeated by co-culturing (transwell system) human primary keratinocytes and dermal fibroblasts with VZV-infected MeWo cells. As was the case with the immortalized keratinocytes, VZV infection did not induce an IFN response in these primary keratinocytes and fibroblasts as compared to the non-infected control condition (co-culture with non-infected MeWo cells) (Fig 32, C and E respectively). The cells were well infected with VZV, indicated by the high level of mRNA expression of early and late VZV genes (Fig 32, D and F). We intended to investigate cGAS dependency by utilizing a cGAS inhibitor in these cells during VZV infection; unfortunately, however, this was not possible given the lack of an IFN response. While these results were negative, these data addressed the reviewer's request for tests in additional cell lines and were included in our point-by-point reply (available online via The EMBO Journal). Thus, my work made an important indirect contribution to the publication, despite not featuring in a main or supplemental figure.

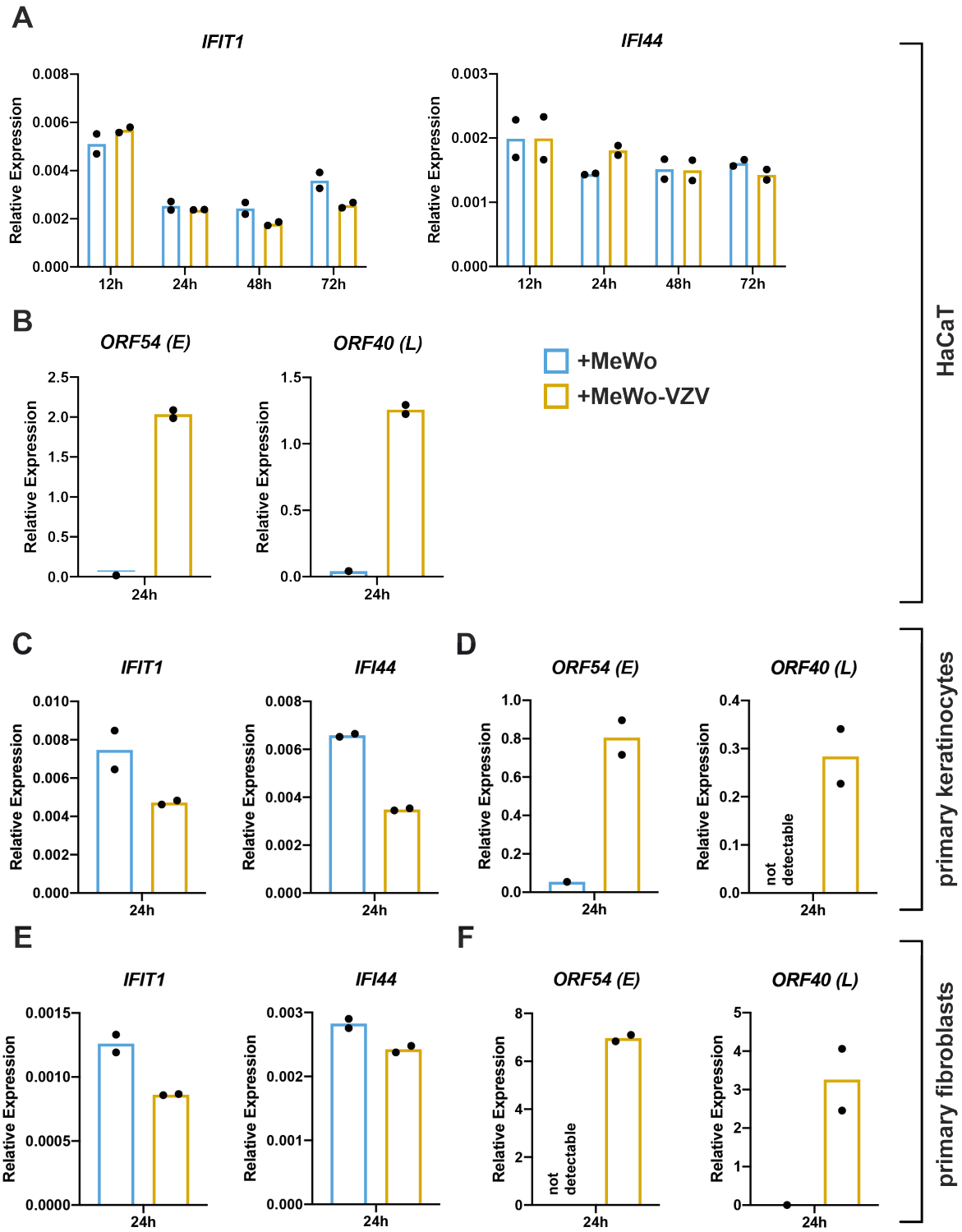


Figure 32: HaCaT Cells, Primary Keratinocytes and Primary Fibroblasts Do Not Detect VZV Infection.
HaCaT cells (**A, B**), primary keratinocytes (**C, D**) and primary fibroblasts (**E, F**) were infected with VZV by co-culture with VZV-infected MeWo cells or as control were co-cultured with uninfected MeWo cells. After 1h, inoculum MeWo cells were washed away. At the indicated time points, RNA was extracted for RT-qPCR analysis. (A,C,E) RT-qPCR analysis of *IFIT1* and *IFI44*. Data are shown relative to *GAPDH*. (B, D, F) RT-qPCR analysis of VZV *ORF54* (early (E) gene) and *ORF40* (late (L) gene) transcripts. Data are shown relative to *GAPDH*. Results shown are from one biological experiment (n=1), data points represent technical duplicates.

4.3 Discussion

It is estimated that as much as >90% of the world's population are seropositive for Varicella and yet little is known about VZV's interaction with the innate immune system and the mechanism of latency reactivation[535,537]. Our EMBO paper reports cGAS-dependent induction of the type I IFN response to VZV infection in THP1 cells. Previous reports implicated STING in the control of VZV viral replication – inhibition of STING by siRNA or shRNA resulted in increased viral replication and reduced phosphorylation of IRF3[585,620,621]. This complements our finding that cGAS and its downstream adaptors STING, IRF3 and TBK1 are necessary for mounting an innate immune response to VZV.

Evidenced from our publication (Appendix) and work presented in this chapter, we identified VZV-ORF9 as a cGAS antagonist in THP1 cells, evidenced by its inhibition of cGAMP production and ablated type I IFN response. ORF9 encodes a tegument protein, making it essential to viral replication and an unviable target for knockout studies. We confirmed ORF9's specific antagonism of cGAS via a conditional knockout mutant degron virus. A screen of SMPCs ruled out four possibilities, as they showed poor stabilization kinetics of the ORF9-degron fusion protein. There are two likely explanations for this result: 1. The concentration of these SMPC in the media was too low. 2. The half-life of the compounds are likely shorter than 48 hours, resulting in destabilization of the ecDHFR complex. Given the short off kinetics, seen in Ramadurgum et al. (Fig. 26), we can speculate that the compounds are only capable of creating a stable bond with the ecDHFR complex for shorter periods.

A limitation of our work is that cGAS's detection of VZV infection may be cell-type specific. While THP1s are a monocyte cell line, VZV typically replicates in skin cells, neurons, and T cells. To address this, we attempted to characterize the response to VZV in different cell types, specifically cell types that are physiologically relevant for VZV disease pathogenesis. Primary epidermal keratinocytes isolated from neonatal foreskin showed no enhanced induction of ISGs despite being adequately infected. The same was the case for an immortalized keratinocyte cell line, HaCaT, and primary dermal

fibroblasts. For our EMBO publication, we were unable to establish a cell model of innate immune signalling to VZV infection and its cGAS dependency, outside of THP1 cells. As is common among large DNA viruses, VZV encodes multiple antagonists of innate immunity, including ORF47, ORF61, ORF62, and ORF63 [603–605,622]. It is therefore likely, that along with inhibition by ORF9, these ORFs act together to repress type I IFN signalling during infection. Given the increased induction of ISGs in response to VZV infection in THP1 cells, it would be interesting to consider whether the aforementioned ORF antagonists are specialized for inhibition in select cell types. Conversely, specialized cell types may have independently adapted antagonistic methods against individual ORFs. Without an increased level of IFN or ISG induction during VZV infection, we would be unable to assess the inhibition capability of the ORF9-degron virus. I have since found success in investigating the innate immune response to VZV in human foreskin fibroblasts (HFFs), which will be further discussed in Chapter 5.

Our finding that cGAS is the causative PRR for VZV infection implies the presence of immunostimulatory DNA in infected cells. However, based on the VZV replication cycle, the viral genome should be protected from detection by its nuclear capsid when in the presence of cytoplasmic cGAS[538]. It is therefore a possibility that cGAS is detecting pools of viral DNA from abortive infections. Alternatively, many viruses have been described to damage mitochondrial membranes, releasing mtDNA that then stimulates cGAS[124]. cGAS is present in high abundance in the nucleus of cells and inhibited by nucleosomes to shield against excessive immunostimulation[28–30,32,33]. It was suggested that cGAS enters the nucleus during mitosis when the nuclear envelope disassembles and is transported out of the nucleus via nuclear pores during interphase[141]. However, recent compelling evidence found a ubiquitin ligase complex forming with nuclear cGAS, targeting it for proteasomal degradation[140]. Given cGAS's presence in the nucleus, it is possible that uncoated viral DNA undergoing replication in the nucleus could bind and activate nuclear cGAS. It would be useful to have a better understanding of the DNA species that activates cGAS during VZV infection; this could be achieved by sequencing DNA that pulls down with the ORF9-cGAS complex. The tegument proteins are contained in the virions and delivered into cells along with viral DNA[538]. ORF9 would likely inhibit DNA sensing during early infection before viral

replication. While the induction of ISGs during endogenous VZV infection and inhibition by ORF9 may seem a contradictory finding, it is common for viral antagonists to limit, but not completely eliminate innate immune responses. This is evident by the array of viruses that encode multiple antagonists of the same host defence pathway[623,624].

We found that ORF9 pulled down with cGAS both alone and in the presence of DNA, indicating its DNA binding ability is not required for inhibition of cGAS. Whether its binding ability provides other functions is yet to be determined. Understanding the mechanism behind cGAS inhibition and reduced enzymatic activity has been the focus of my DPhil project – expanded in Chapter 5.

Chapter 5

VZV-ORF9 Acts as a Histone Mimic to Inhibit cGAS

As introduced in Chapter 4, my project started by contributing to our publication on innate immune sensing of VZV infection[292]. This work discovered VZV-ORF9 as an antagonist of nucleic acid sensing by binding cGAS and inhibiting its enzymatic activity.

5.1 Viral Inhibitors of cGAS

Viruses rely on the host cell's machinery for their replication. Therefore, they must evolve a broad range of anti-viral immunity evasion mechanisms to ensure their successful reproduction. The main categories of offensive measures viruses employ are (#1-8[22]):

1. Hiding their genome, through selective localized replication or capping and methylating 5' ends to mimic host mRNAs[22,625].
2. Inhibiting PRRs of RNA and DNA sensing pathways.
3. Regulation of phosphorylation of these PRRs and/or downstream sensing pathways.
4. Regulating ubiquitination of PRRs such as STING, MAVS, and RIG-I.
5. Interference with host transcription.
6. Translational shut off of IFNs and ISGs.
7. Interference of RNA processing and trafficking.
8. Viral decoy proteins to sequester host proteins from their anti-viral mechanisms.

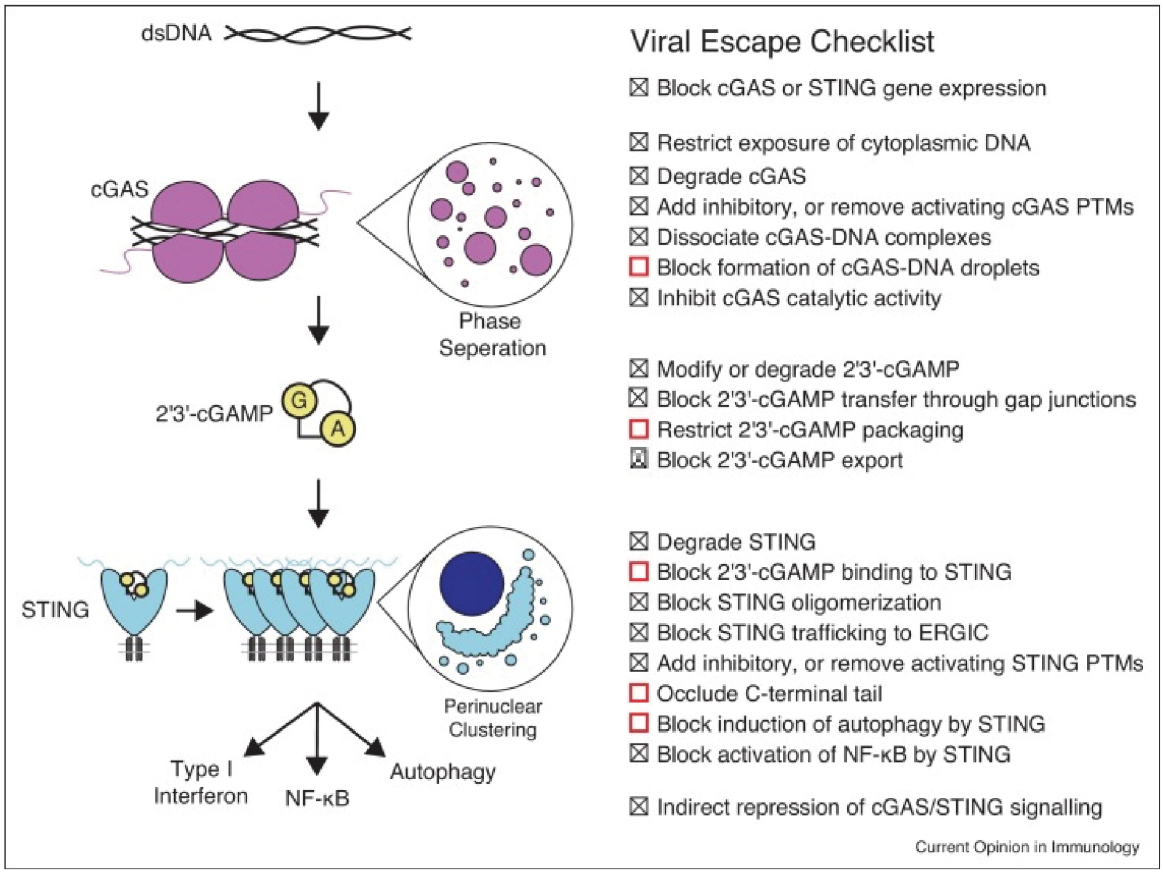


Figure 33: Summary of cGAS-STING Pathway Components Targeted by Pathogens. Parts of the cGAS-STING signalling cascade targeted by viruses are indicated by a checked box. Components suspected to be targeted are annotated with a red box. Figure taken from Eaglesham and Kranzusch 2020. doi: 10.1016/j.coi.2020.04.002.

The multitude of evasion strategies by herpesviruses against DNA sensing pathways (Fig. 33) has been reviewed in-depth in Ref. [624]. These present many strategies that aim to ultimately prevent IFN and ISG induction[16,626–630]; however, I will focus on viral antagonists of cGAS.

Kaposi's sarcoma-associated herpesvirus (KSHV) ORF52 tegument protein (also known as kicGAS) is a cGAS antagonist. KSHV-ORF52 inhibits cGAS by binding both DNA and cGAS, reducing phosphorylation of IRF3 and transcription of *IFNβ*[613,624,631]. This highly oligomerized protein facilitates the formation of phase-separated liquid condensates with DNA, thereby sequestering it from cGAS detection[613,631]. The HSV-1 UL56 protein is

a direct cGAS antagonist and also targets for degradation the cGAMP export channels SLC46A2, P2X7 and VRAC to inhibit intercellular cGAMP transfer[632,633].

HSV-1 encodes two cGAS antagonists, UL37 and VP22, which deamidate or inhibit cGAS's enzymatic activity, respectively[634–638]. HSV-1 VP22 shares 36% amino acid (aa) sequence similarity with VZV-ORF9. In our EMBO paper, Dr. Hertzog found (summarized in Chapter 4 and attached in full in the Appendix) a central core region in ORF9 (AA151-240) to be homologous with HSV-1 VP22's core domain[10]. Both VP22 and ORF9 are herpesvirus tegument proteins and have similar functions of cGAS inhibition. *Murine herpesvirus 68 (*MHV68) is a closely related virus to KSHV, and their ORF52 proteins are homologues of each other[639]. Hew *et al*. describe the structural similarity of HSV-1 VP22 and MHV68 ORF52. While HSV-1 VP22 and VZV ORF9 are evolutionarily unrelated to KSHV ORF52, comparison of crystal structures shows a shared two helix-sheet structure[292]. DNA-induced LLPS is essential for cGAS enzymatic activity, with the abundance and length of DNA mediating the strength of this separation[123,638]. Both HSV-1 VP22 and KSHV ORF52 have been shown to accumulate into cGAS-DNA condensates and disrupt them[631,638].

While previous evidence suggested KSHV ORF52 requires its DNA binding properties to inhibit cGAS[613], newer reports have suggested that modulation of phase separation, rather than direct interaction, is what hampers cGAS activation[638]. In agreement, mutation of predicted DNA binding sites in ORF9 did not ablate cGAS inhibition[292]. This suggested that ORF9 may disrupt DNA-cGAS phase separation; however, evidence from our collaboration with Dr. Wen Zhou showed ORF9 facilitates DNA-cGAS condensate formation in a 250mM salt condition[292]. Interestingly, at 300mM salt, the addition of ORF9 limited cGAS abundance in condensates. Conversely, Xu *et al* ([638]), found ORF9 displaced cGAS from droplets at 200mM. Whether this is due to differences in experimental set-up, such as order of protein addition, or length of DNA added, is yet to be determined. While KSHV ORF52 likely inhibits DNA sensing by disrupting DNA-cGAS droplets, ORF9 may instead facilitate droplet formation to isolate and directly bind cGAS for inhibition. It is possible ORF9 has dual functions, to directly

inhibit cGAS at low osmolarity and disrupt the formation of DNA-cGAS condensates at high osmolarity.

The sheer number of viral antagonists targeting the cGAS-STING pathway highlights the importance of this pathway in anti-viral restriction and alludes to the existence of yet more cGAS antagonists. Viral mimicry of host proteins is a known method of evading host detection – therefore, the inhibition of cGAS by host histones may be a strategy mimicked by viruses to inhibit cGAS.

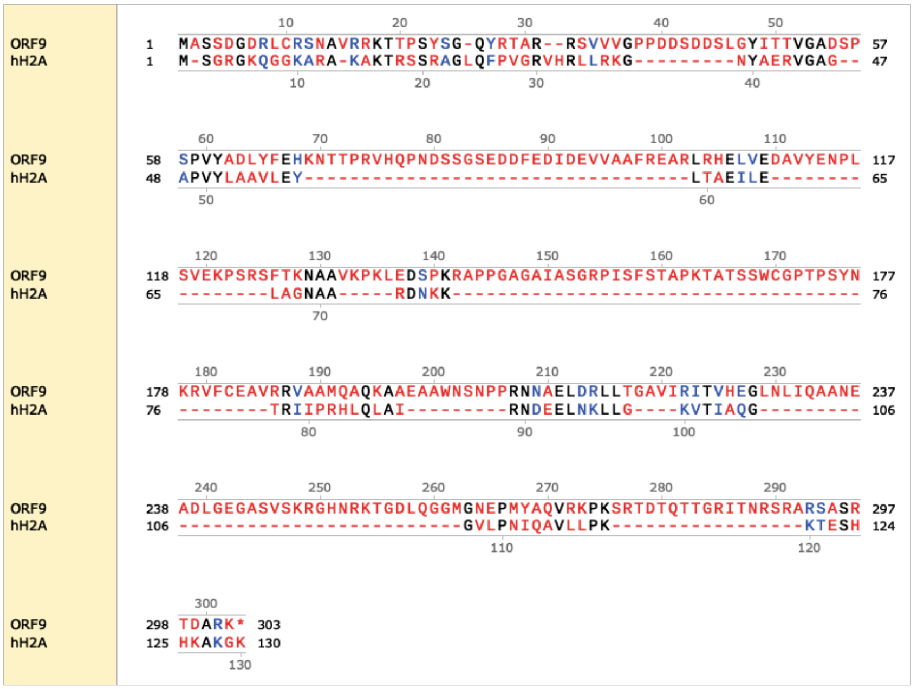
5.2 Investigating Histone and ORF9 Similarities.

Early in my DPhil program, six publications were released describing nucleosome inhibition of nuclear cGAS, specifically by the histone dimer H2A-H2B which forms a part of the nucleosome[28,29,31–33,640] (described in Section 1.1.1.1.3.2).

Dr. Jonny Hertzog performed a semi-global amino acid sequence alignment of human histone H2A with VZV-ORF9 (Fig. 34, A). Aligning the protein-coding sequence for ORF9 and histone H2A revealed numerous regions of sequence similarity in important cGAS binding site locations (Fig. 34, B). In particular, H2A residues annotated to bind to cGAS were shared between H2A and ORF9. H2A binds cGAS through the H2A 'acidic pocket' composed of four residues: E61, E64, D90 and E92 (Fig. 34, B & C). The ORF9 E106 and E109 residues align with H2A E61 and E64 (Fig. 34, D) which make up two of the four residues in the acidic patch pocket. Similarly, ORF9 E211 aligns with the fourth H2A acidic patch residue, E92. ORF9 E227 aligns with the E113 residue of H2B. H2B E105 and E113 have been annotated in select papers as contributing to the H2A-H2B acidic patch[641,642]. In addition, the introduction of a missense mutation at position E113 of H2B (as a combination mutant with other H2A/H2B acidic patch residues) ablated binding to cGAS[29,126]. This led us to hypothesize that VZV-ORF9 mimics the structure of H2A-H2B to inhibit cytoplasmic cGAS. This was based on partial sequence homology with H2A, possibly indicating binding to cGAS in a manner analogous to H2A. ORF9 plasmids were

generated to introduce missense mutations of amino acids predicted to correspond to H2A's cGAS binding residues. The following mutated ORF9 proteins were overexpressed in cells to determine if these residues are critical for cGAS binding: ORF9$^{E106R/E109R}$, ORF9^{E211R}, ORF9^{E227T}, and ORF9$^{E211R/E227T}$ (Fig. 34, D).

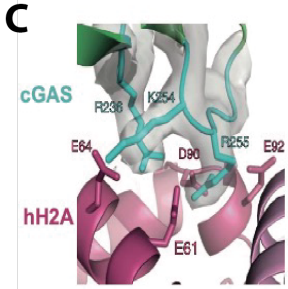
A



B

H2A:	E61	E64	N69	R71	D72	K75	T76	D90	E91	E92
(Zhao et al., 2020)	X	X		X		X	X	X		X
(Pathare et al., 2020)	X	X	X		X			X		
(Michalski et al., 2020)	X	X		X				X	X	X
(Kujirai et al., 2020)	X	X		X				X		X
(Boyer et al., 2020)	X	X		X				X	X	X
semi-global alignment of VZV ORF9 and hH2A amino acid sequences (see below):										
VZV ORF9	E106	E109	N129	E137	D138	K141	R186	N209	A210	E211

C



D

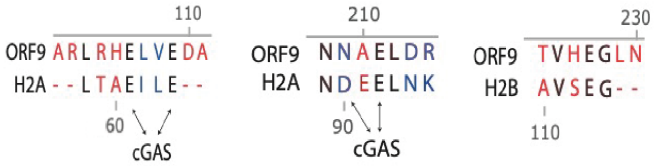


Figure 34: VZV-ORF9 Has Homologous Residues with Human Histone H2A.
(**A**) Semi-global amino acid sequence alignment of VZV-ORF9 and human histone H2A. Black = identical, blue = similar, red = not similar. (**B**) A list of all hH2A residues described to bind cGAS in the nucleus. An X indicates the publication(s) that annotated hH2A residue(s) as binding to cGAS. Green = Alignment with ORF9, red = Does not align with ORF9, yellow = Not aligned, negative to neutral charge (see text for further description). (**C**) Image taken from Kujirai *et al*. 2020. cGAS's (cyan) arginine anchor bound to the acidic patch of hH2A (pink). (**D**) Residues of interest from the semi-global alignment of hH2A and hH2B with ORF9 are highlighted with arrows. VZV-ORF9 mutants of 106, 109, 211, and 227 were generated in this project.

5.3 Mutating ORF9 Residues Homologous to Histones Reduces its Ability to Antagonize cGAS.

To test my hypothesis that VZV ORF9 antagonizes cGAS by acting as a histone mimic, I utilized a luciferase-based screening platform in HEK293T cells. In brief, plasmids expressing firefly luciferase under *IFNβ* promotor control and pRL-TK, which constitutively expresses renilla luciferase, were transiently transfected (Fig. 35). HEK293T cells do not express cGAS and STING endogenously, therefore human cGAS and human STING were transiently transfected into these cells. The transfection of cGAS acts as a self-stimulator, which results in the activation of the *IFNβ* promotor and the production of firefly luciferase. Lastly, WT or mutant ORF9 plasmids were co-expressed. The L protein of EMCV, a previously described IRF3-antagonist[643], and a pLenti6.3 plasmid with a random 20nt insert (EV) served as positive and negative controls, respectively. As expected, WT ORF9 blocked firefly luciferase induction by inhibiting cGAS (Fig. 36, A). In line with our expectations, ORF9$^{E106R/E109R}$ exhibited significantly higher induction of *IFNβ* compared to WT ORF9, lending some evidence to support our hypothesis that these amino acids are crucial to cGAS inhibition. In addition, a mutagenized cGAS plasmid with mutations within its binding site region for histone H2A[29] was transfected to determine if its arginine anchor was required for inhibition by ORF9. No difference was detected between WT and mutant cGAS.

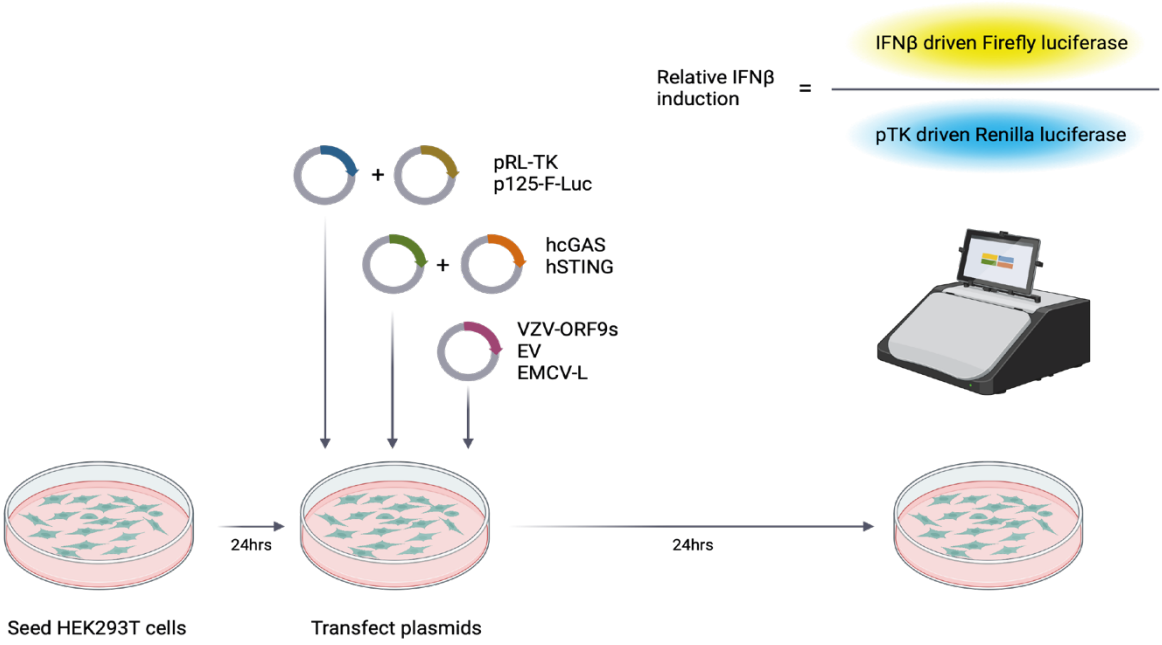


Figure 35: Dual Luciferase Assay Schematic.
HEK293T cells were transfected with pRL-TK which expresses renilla luciferase under a TK promoter and p125-F-Luc to express firefly luciferase under the control of an IFNβ reporter. Cells were also transfected with cGAS and STING, along with ORF9 expression constructs and the control plasmids EV and EMCV-L. 24 hours post-transfection, luminescence was quantified for both renilla and firefly luciferase. Firefly luminescence was divided by renilla luminescence to normalize for transfection efficiency.

The inhibitory potential of ORF9 bearing the E106R/E109R mutation was further validated by assessing mRNA expression levels via RT-qPCR. THP1 cells are a monocyte cell line which endogenously express cGAS/STING and produce a robust IFN response after VZV infection[292]. THP1 cells stably transduced to express GFP and ORF9 constructs were stimulated by transiently transfecting *E. coli* DNA. 24 hours post-stimulation, lysates were collected for RNA isolation and subsequent RT-qPCR. As expected, *IFNβ1 and IFIT1* transcript levels were reduced in WT-ORF9 expressing cells compared to GFP (Fig. 36, B). In agreement with dual luciferase assay results, THP1-ORF9$^{E106R/E109R}$ cells displayed a higher level of *IFNβ1 and IFIT1* induction compared to WT-ORF9.

As outlined in Chapter 4, Dr. Hertzog found ectopically expressed ORF9 bound to cGAS. Next, I investigated whether the introduced mutations would impact binding to cGAS.

HEK293T cells were transiently transfected with FLAG-ORF9, cGAS-V5, and STING-HA. 24 hours later, protein interaction was assessed by collecting lysates for immunoprecipitation (IP). Antibodies against the epitope tags were used to pull down the tagged proteins. A non-specific IgG antibody was used as a control. All proteins were detected in the bound fractions of the antibodies recognizing their respective epitope tags, indicating the pulldown was successful and specific. As expected, ORF9 was present in the cGAS bound fraction – conversely, cGAS was detected in the ORF9 bound fraction (Fig. 36, C). Reversing the charge of the cGAS 'arginine anchor' by replacing it with glutamic acid ablates binding to histone H2A[29,31,32,640]. We hypothesized that if ORF9 mimics the structure of H2A to bind and inhibit cGAS, then mutating the arginine anchor of cGAS should ablate binding to ORF9. However, the binding of ORF9 and cGAS was unaffected by the cGAS^{R255E} mutation (Fig. 36, E). Along the same vein of thought, mutating the acidic patch of H2A ablates binding to cGAS[29], therefore I mutated 'acidic patch' like residues in ORF9 and tested the mutated protein's ability to bind cGAS. ORF9$^{E106R/E109R}$ protein was detected in cGAS IP and vice versa (Fig. 36, F). However, the co-expression of ORF9$^{E106R/E109R}$ and cGAS^{R255E} reduced the proportion of ORF9 expression in the cGAS IP, and conversely cGAS expression in the ORF9 IP (Fig. 36, D). The IgG isotype control antibody did not precipitate any of the proteins. The cGAS-V5 and FLAG-ORF9 signals detected when blotting for HA were likely residual signals from the immunoblotting for FLAG and V5, as these were performed probing with anti-HA antibody of the same membrane.

The most ideal control to ensure accurate comparisons of expression levels between constructs is to run the wildtype and mutant conditions on the same gel. This experiment ran each condition on a separate gel and membrane for protein transfer potentially introducing small discrepancies in transfer efficiencies and protein expression profiles.

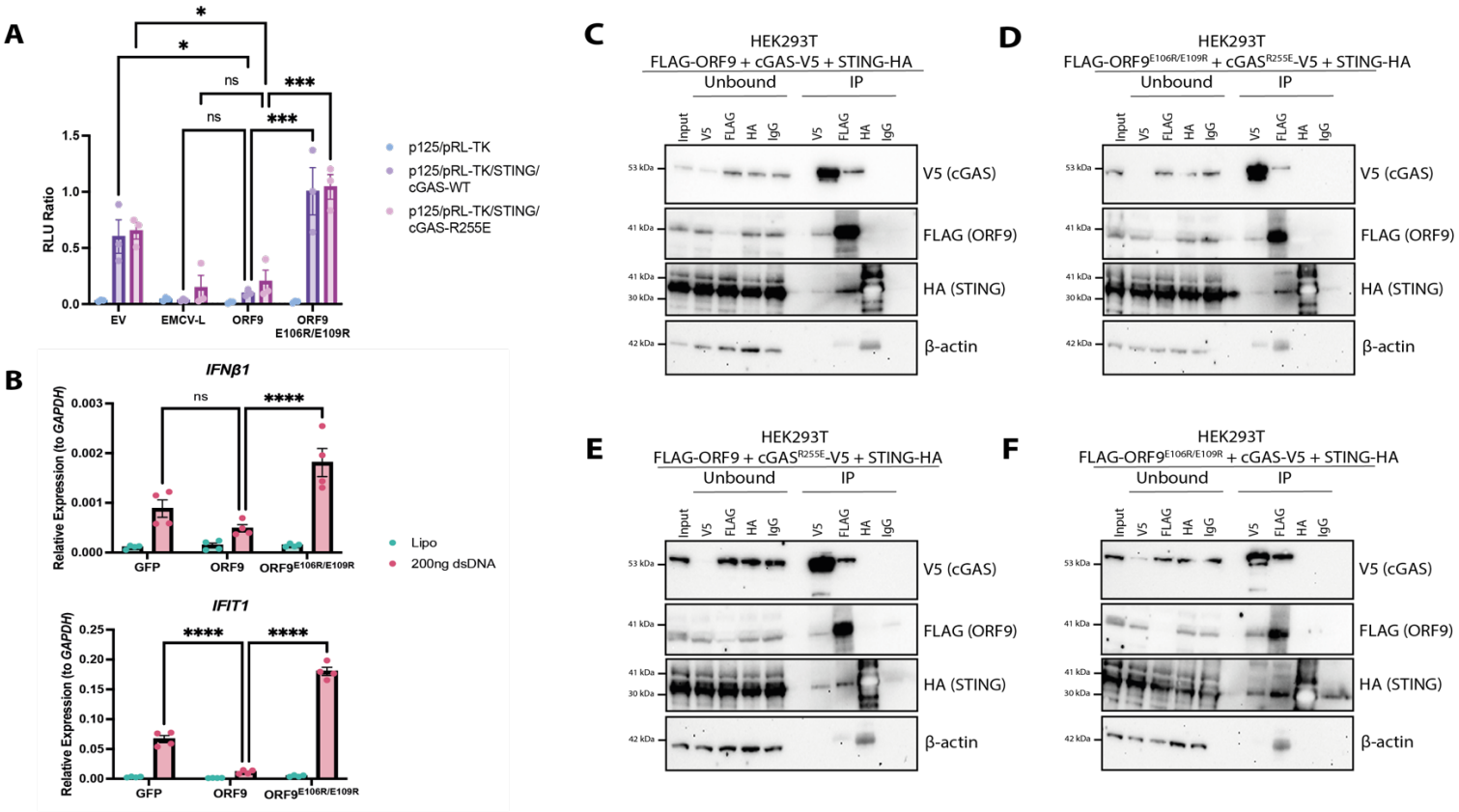


Figure 36: ORF9 Histone Mutant Shows Reduced Ability to Block cGAS Activation.
(**A**) HEK293T cells were transfected with p125-F-Luc, pRL-TK, STING and cGAS-WT or cGAS-R255E plasmids. Cells were also transfected with either control plasmids (EV or EMCV-L) or ORF9 expression plasmids. Luciferase activity was assayed 24 hours post-transfection. (**B**) THP1 cells transduced with GFP or ORF9 constructs were stimulated with 200ng *E. coli* DNA and left to incubate for 24 hours. Cells were lysed for RNA isolation and mRNA expression of the indicated transcripts was assessed for RT-qPCR. (**C-F**) HEK293T cells were transfected with expression plasmids for FLAG-ORF9, cGAS-V5, or STING-HA. 24 hours later, cells were lysed for ectopically expressed proteins were immunoprecipitated using epitope tag antibodies. The input, unbound and bound fractions were subject to immunoblotting using the indicated plasmids. Panel A shows pooled data from two independent biological experiments. Panel B shows pooled data from three independent biological experiments. Panel C & F shows a representative blot from three independent biological experiments (n=3). Panel D & E shows a blot from one independent biological experiment (n=1). Panel A: Multiple comparisons two-way ANOVA (Mean and SEM, n=2). Panel B: Multiple comparisons two-way ANOVA (Mean and SEM, n=3). ns, not significant=p>0.05, *=p≤0.05, **=p≤0.01, ***=p≤0.001, ****=p≤0.0001.

After the promising data generated for ORF9$^{E106R/E109R}$, I began investigations of other ORF9 residues homologous to H2A – ORF9^{E211} and ORF9^{E227}, expanded upon below. While analyzing data from these experiments it became apparent that the reduced cGAS inhibition phenotype exhibited by ORF9$^{E106R/E109R}$, included alongside the new mutants, could not be reproduced. RT-qPCR using RNA from transduced THP1 cells lysates and luciferase assays in HEK293T cells lysates were performed as above. HEK293T cell lysates for luciferase assay were used in parallel for immunoblotting to validate ORF9 expression (Fig. 37, B). This set of experiments found *IFI44, IFIT1* and *IFNβ1* mRNA levels were comparable in cells transduced with ORF9 $^{E106R/E109R}$ and ORF9 (Fig. 37, A). Moreover, ORF9 $^{E106R/E109R}$ transiently transfected cells exhibited similar

levels of *IFNβ* promoter activation as ORF9 (Fig. 37, C). Given, these contradicting phenotypes in experiments using ORF9$^{E106R/E109R}$ I choose to exclude it from most future experiments.

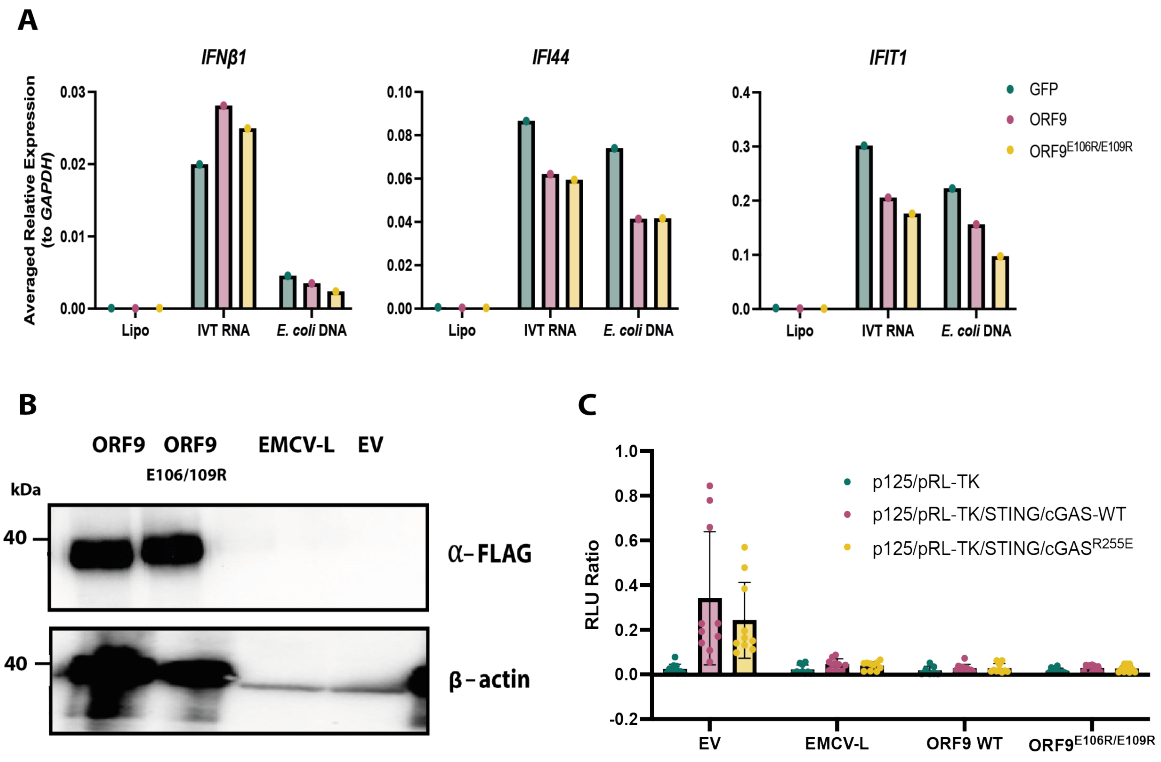


Figure 37: VZV-ORF9E106R/E109R Inhibit cGAS Activation.
(**A**) THP1 cells transduced with GFP or ORF9 constructs were stimulated with 200ng *E. coli* DNA and left to incubate for 24 hours. Cells were lysed for RNA isolation and mRNA expression of the indicated transcripts was assessed for RT-qPCR. (**B**) Remaining cell lysate from (C) were subject to immunoblotting with the indicated antibodies. (**C**) HEK293T cells were transfected with p125-F-Luc, pRL-TK, STING and cGAS-WT or cGAS-R255E plasmids. Cells were also transfected with either control plasmids (EV or EMCV-L) or ORF9 expression plasmids. Luciferase activity was assayed 24 hours post-transfection. Panel A shows pooled data from three independent biological experiments with technical duplicates, averages of the three repeats are graphed (n=3). Panel B shows a blot from one biological experiment (n=1). Panel C shows pooled data from three independent biological experiments each with technical triplicates, all data graphed (Mean and SD, n=3).

5.4 ORF9 Mutants Exhibit Reduced cGAS Inhibition in Transduced HFFs.

To validate the effects of ORF9 mutations with endogenous cGAS in an additional cell line, HFFs were transduced with GFP or ORF9 constructs. Cells were stimulated with

IVT RNA and *E. coli* DNA and left to incubate for 24 hours (Fig. 38). Cells were lysed for cGAMP ELISA, RT-qPCR and western blotting. Mock and *E. coli* DNA-stimulated cells were lysed for western blotting and analyzed for ORF9 expression. Equal expression of ORF9 protein was first assessed to ensure accurate comparisons were made between ORF9 constructs when analyzing the data of functional experiments (Fig. 39, A). All ORF9 constructs were expressed at equal levels both at baseline and after *E. coli* DNA stimulation. However, ORF9^{E211R}-stimulated cells expressed slightly less ORF9. STAT1 phosphorylation was found in all cells stimulated with DNA; however, no difference was detected between GFP or ORF9 constructs (Fig. 39, A). As induction of the cGAS-STING pathway is as early as 3 hours post-stimulation, future work should focus on investigating earlier time points of pathway activation[41,644].

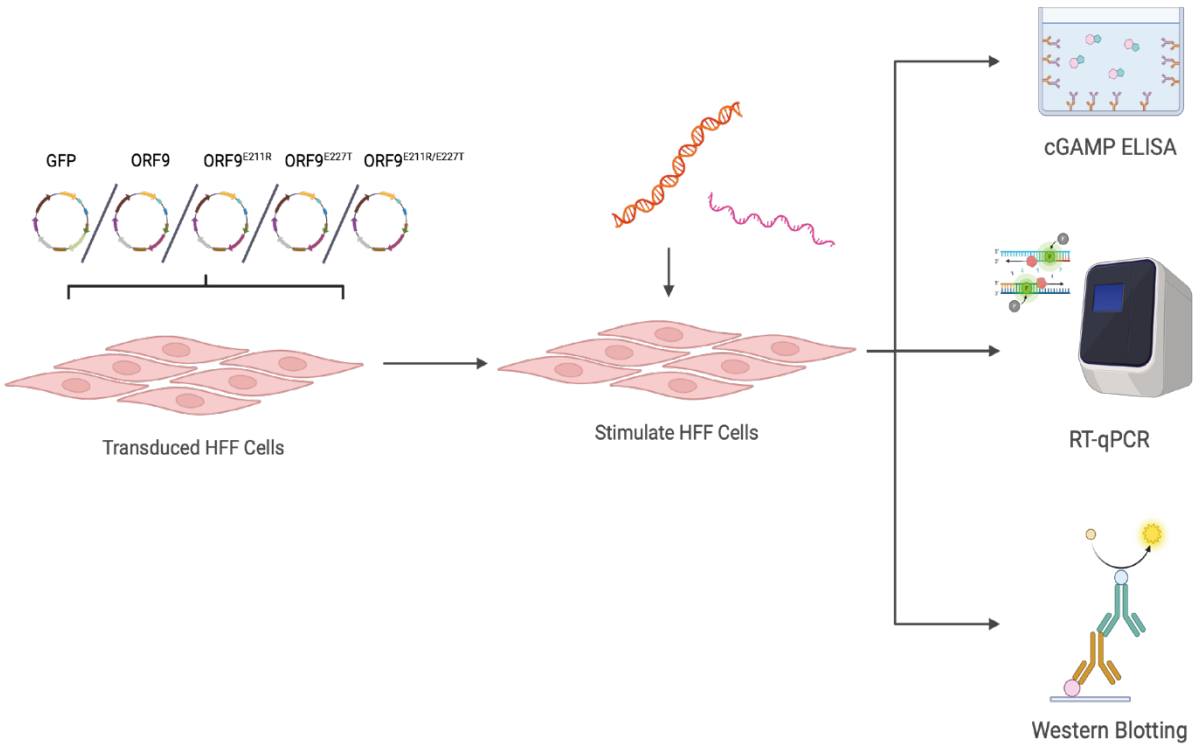


Figure 38: Transduced HFF Experiment Schematic.
HFF transduced with ORF9 and GFP constructs were stimulated with either IVT RNA or *E. coli* DNA and left to incubate for 24 hours. Cells were lysed to quantify cGAMP concentration via cGAMP ELISA. In parallel cells were lysed for immunoblotting and RNA isolation for quantifying mRNA expression levels via RT-qPCR.

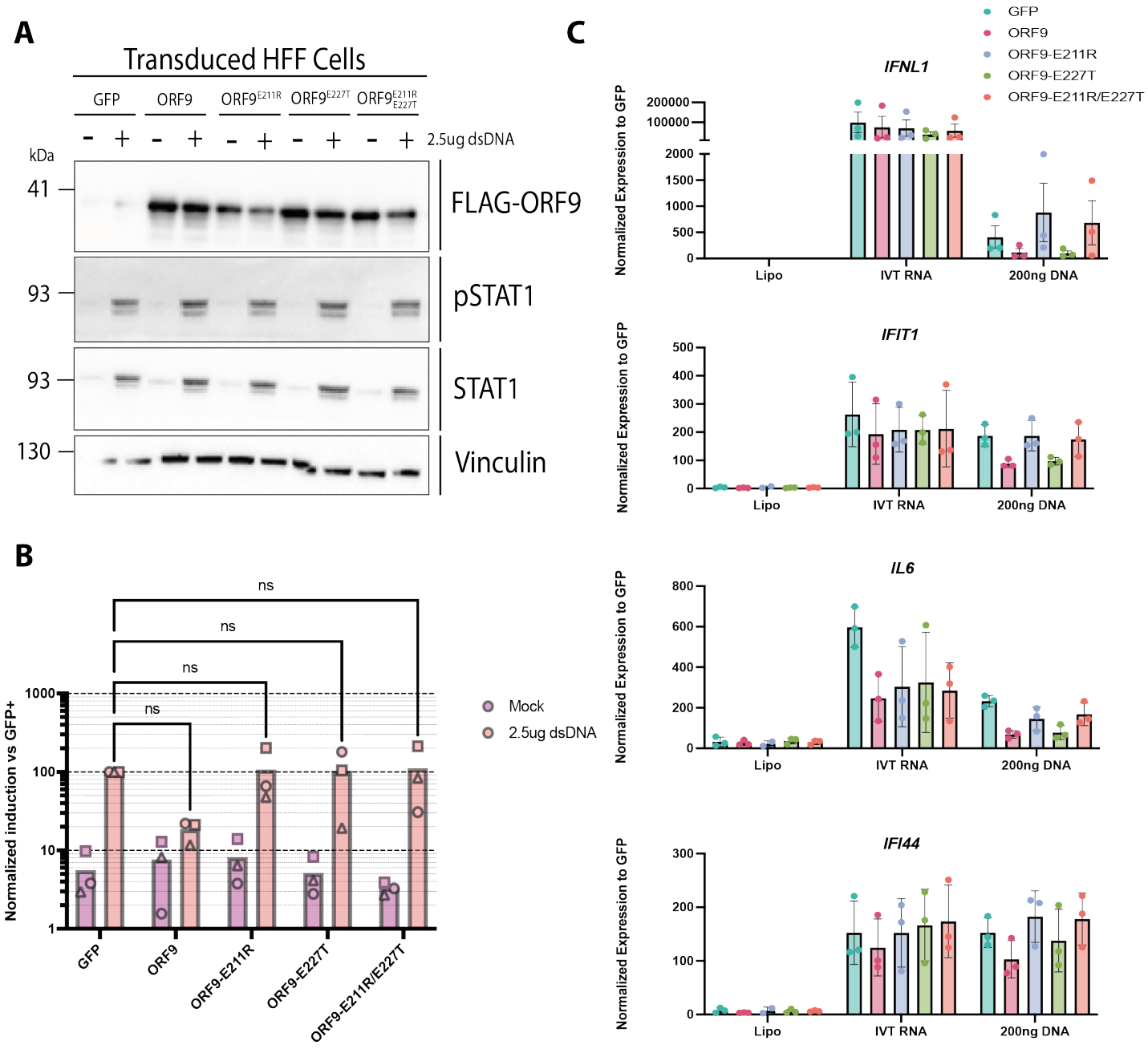


Figure 39. Transduced HFFs Expressing Mutant ORF9 Constructs Have Reduced Ability to Antagonize cGAS. HFF cells stably transduced with either GFP or ORF9 constructs, were stimulated with *E. coli* dsDNA and the induction of ISG and IFN were assessed via cGAMP ELISA 24 hours post transfection. Three independent experiments were conducted in which cells were collected for ELISA, RT-qPCR and western blotting. (**A**) Western blotting was used to assess protein expression levels from whole cell lysates. (**B**) The concentration of cGAMP was calculated against a standard curve, normalized against total cell lysate protein concentration and normalized against the stimulated GFP condition. (**C**) Expression levels for the indicated mRNA transcripts were assessed via RT-qPCR (mean and SEM, n=3). Panel A is a representative blot from three independent biological experiments (n=3). Panel B shows pooled data from three independent biological experiments. Each experiment is denoted with a unique symbol. Panel B: Multiple comparison two-way ANOVA (ns, not significant=p>0.05, *=p≤0.05, **=p≤0.01, ***=p≤0.001, ****=p≤0.0001) (mean, n=3). Panel C shows pooled data from three independent biological experiments where relative expression of each probe was normalized against GAPDH and GFP.

The most direct measure of cGAS activity is the production of cGAMP. Therefore, I measured cGAMP concentrations in lysates from each cell line via cGAMP ELISA (Fig. 39, B). Transduced HFFs (Fig. 38) stimulated with *E. coli* DNA were lysed 24 hours post-stimulation and whole cell lysate was used to determine cGAMP concentrations. At baseline, all cells produced similar levels of cGAMP (Fig. 39, B). As expected, GFP-expressing cells produced more cGAMP after stimulation, compared to wild-type ORF9-expressing cells. Interestingly, all three cell lines expressing ORF9 mutants produced similar levels of cGAMP as GFP-expressing control cells. This indicates that these mutants may have lost their ability to inhibit cGAS. Of note, however, neither condition reached statistical significance. This is likely due to the slight variation of cGAMP concentration between biological replicates (see denoted symbols for each biological replicate Fig. 39, B). All raw cGAMP ELISA results and accompanying western blots can be found in Supplemental Figure S1. Supernatants from stimulated transduced HFFs (cell lysates used for cGAMP ELISA above) were collected for IFNβ ELISA (Supp. Fig. S2). Concentrations of IFNβ were below the limit of detection for some samples in one replicate, which is likely the result of the age of the kit used. However, for at least one experiment, trends of IFNβ concentration mirror the results obtained by cGAMP ELISA, in that, ORF9 mutant constructs failed to inhibit the induction of IFNβ compared to wild-type ORF9. This experiment needs to be repeated with a new IFNβ ELISA kit before making definitive conclusions.

To validate these findings, I next compared ISG and IFN responses in cells stably transduced with ORF9 and GFP. HFF cells transduced with GFP or ORF9 were stimulated with *E. coli* DNA and IVT RNA as a positive control. 24 hours post-transfection, cell lysates were collected for RNA isolation and subsequent RT-qPCR. Induction of all tested transcripts as a result of IVT RNA stimulation was similar across all cell lines. However, IL6 mRNA levels were higher in IVT RNA-stimulated GFP cells (Fig. 39, C). To ensure accurate comparisons could be made for data between ORF9 constructs, I validated that all cell lines had equal *ORF9* mRNA levels using a custom TaqMan probe (Supp. Fig. S3). After DNA stimulation, GFP transduced cells produced higher *IFNL1, IFIT1, IL6* and *IFI44* transcript levels than ORF9 transduced cells.

ORF9^{E227T} transduced cells induced similar transcript levels compared to ORF9 transduced cells. ORF9^{E211R} and ORF9$^{E211R/E227T}$ transduced cells had higher transcript levels than ORF9 transduced cells. Unfortunately, a multiple comparison two-way ANOVA test yielded no significant differences between any conditions tested (statistics not displayed on the graph).

Collectively, these findings showed promising evidence to support my hypothesis that mutations in residues homologous with histones reduced ORF9's ability to inhibit cGAS activity.

5.5 ORF9 Mutants Exhibit Reduced cGAS Inhibition in Transfected HEK293T Cells as Measured by FRET Assay.

To test the functionality of ORF9 mutants in an alternative cell type and readout, I utilized a STING-based FRET assay in HEK293T cells. Dr. Christian Zierhut and Dr. Vicente Lebrec generated a STING-based FRET assay to measure STING activation[293]. They generated a pLEX_306 vector with an N-terminal fluorescent mTurquoise protein and a C-terminal fluorescent YPet protein flanking mouse STING (Fig. 42, A). The STING region was truncated only to include the CDN binding domain that forms the binding pocket for cGAMP[645–647].The transmembrane and TBK1/IRF3 binding domain were removed, thereby producing a STING that can bind cGAMP but cannot signal downstream. At baseline STING forms a dimer, which undergoes a conformational change and oligomerization after binding to cGAMP – both of which are critical for downstream signalling[293,648–650]. The binding of cGAMP to this mTurq-STING-YPet fusion protein induces a conformational change, bringing the bright cyan and yellow proteins within close proximity (Fig. 42, A). The closed distance between donor and acceptor fluorophores causes an excitation energy transfer between fluorophores[293,647], the ratio of which can be measured via flow cytometry. This provides us with a sensitive cell-based biosensor system, which quantifies the ligand occupancy of STING and thus a measure of cellular cGAMP concentration.

HEK293T cells were transfected with mTurquoise-mSTING-YPet, hcGAS and EV or ORF9 constructs. 24 hours later, a subset of cells were collected for western blot analysis; the remaining cells were analyzed for FRET shift via flow cytometry (Fig. 40). Cells set up in duplicate were lysed for cGAMP ELISA.

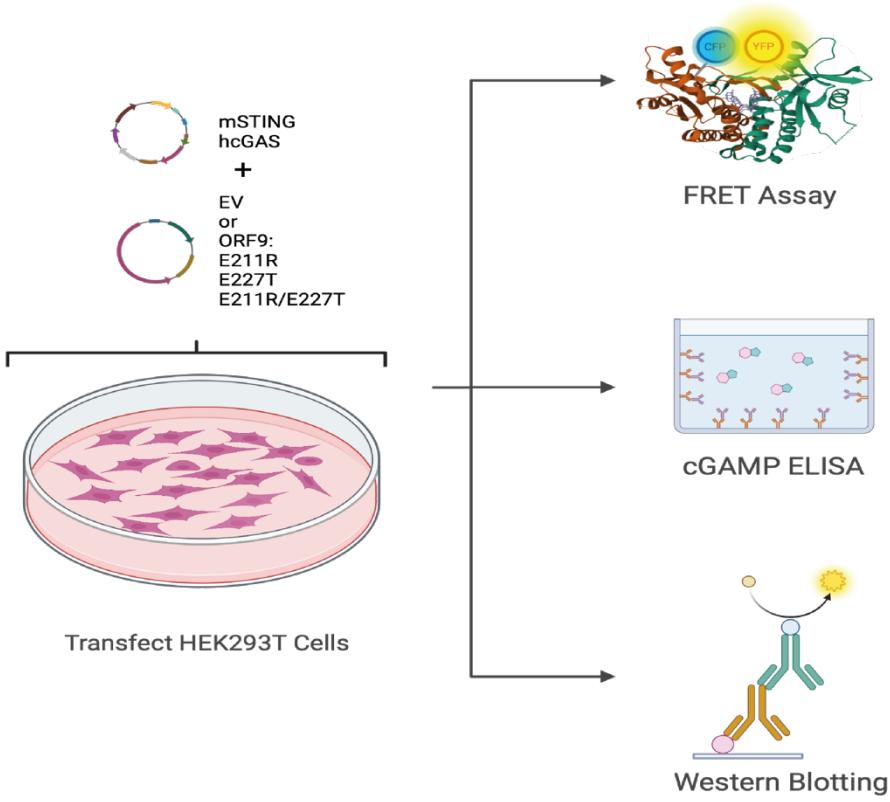


Figure 40: Workflow Schematic of Experiments in HEK293T Cells.
HEK293T Cells were transfected with mSTING-FRET and hcGAS. Cells were also transfected with EV or ORF9 expression constructs. Cells were lysed 24 hours later for immunoblotting and cGAMP ELISA. In parallel cells were collected to assess FRET shift via flow cytometry.

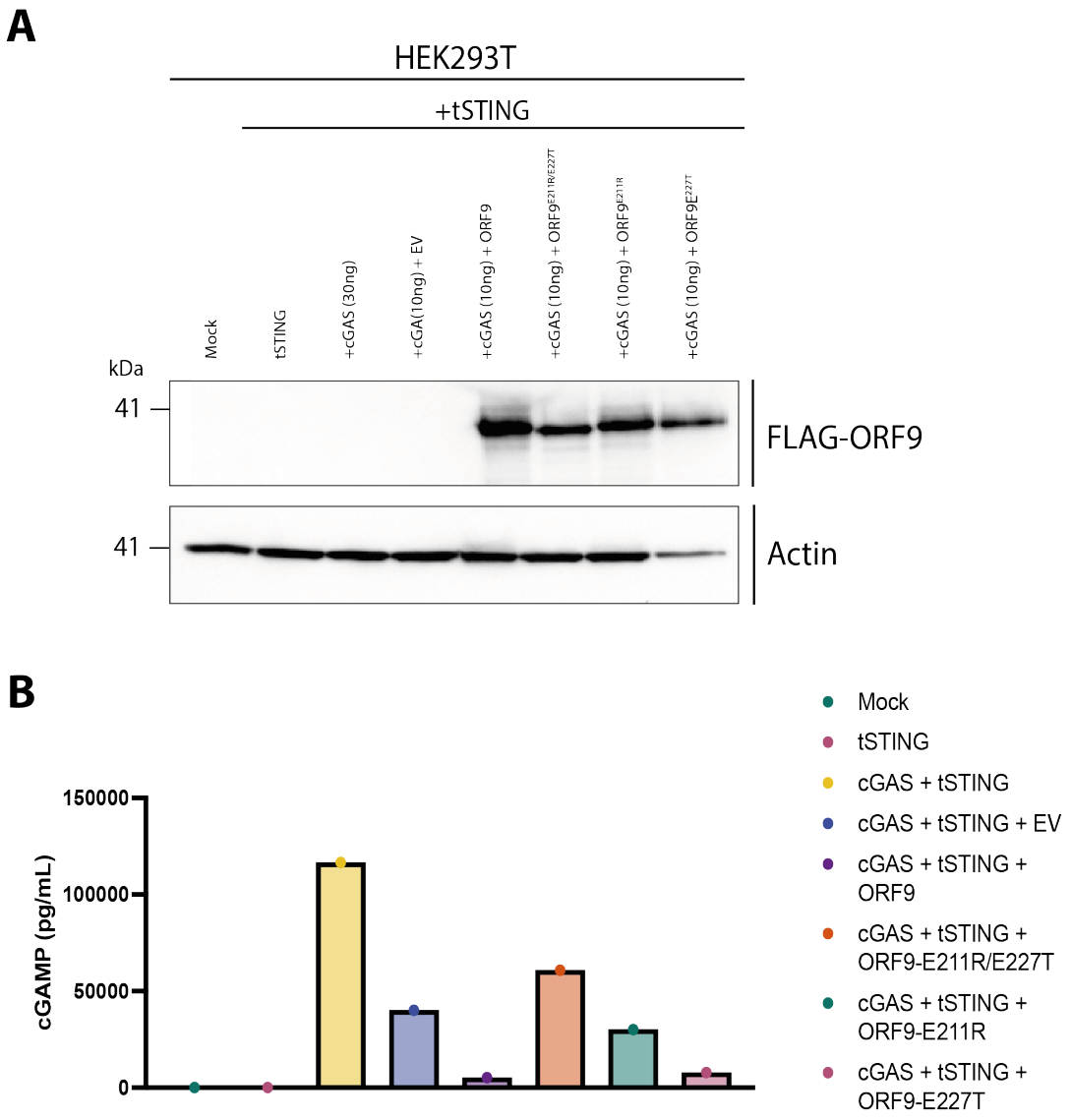


Figure 41: Mutations in ORF9 Promote Increased cGAMP Production.
HEK293T cells were transfected with mTurq-STING-YPet, hcGAS, EV and ORF9 constructs. 24 hours post-transfection, cells were collected for FRET assay (Fig. 28), immunoblotting and cGAMP ELISA. Whole cell lysates were collected for (**A**) and (**B**), while intact cells were used in flow cytometry. Panel A shows a representative blot from three independent biological experiments (n=3). Panel B shows cGAMP concentrations calculated from the analysis of technical duplicates in one biological experiment (n=1).

I first validated that ORF9 protein was expressed in transiently transfected cells that would be used in the FRET assay and cGAMP ELISA experiments. Indeed, ORF9 was detected in all samples transfected with the ORF9 construct (Fig. 41, A), albeit WT-ORF9 was expressed at a higher level than mutants. To determine the functional

consequence of ORF9 mutations on cGAS activity I assessed cGAMP concentration by ELISA. Cells transfected with EV produced over 7-fold more cGAMP than ORF9-expressing cells (Fig. 41, B). Cells transfected with ORF9^{E227T} produced similar levels of cGAMP compared to ORF9 transfected cells, while cells expressing ORF9^{E211R} and ORF9$^{E211R/E227T}$ produced cGAMP levels equal to or above EV transfected cells.

Cells were processed for flow cytometry and data were first gated on live and single-cell populations (Fig. 42, B). Transfected cells were gated by comparing the FRET emission between mock and tSTING conditions (Fig. 42, B). FRET Shift gates were determined by gating populations that shifted between unstimulated (tSTING) and stimulated conditions (tSTING + cGAS). Full gating strategy can be found in Supplementary Figure S4.

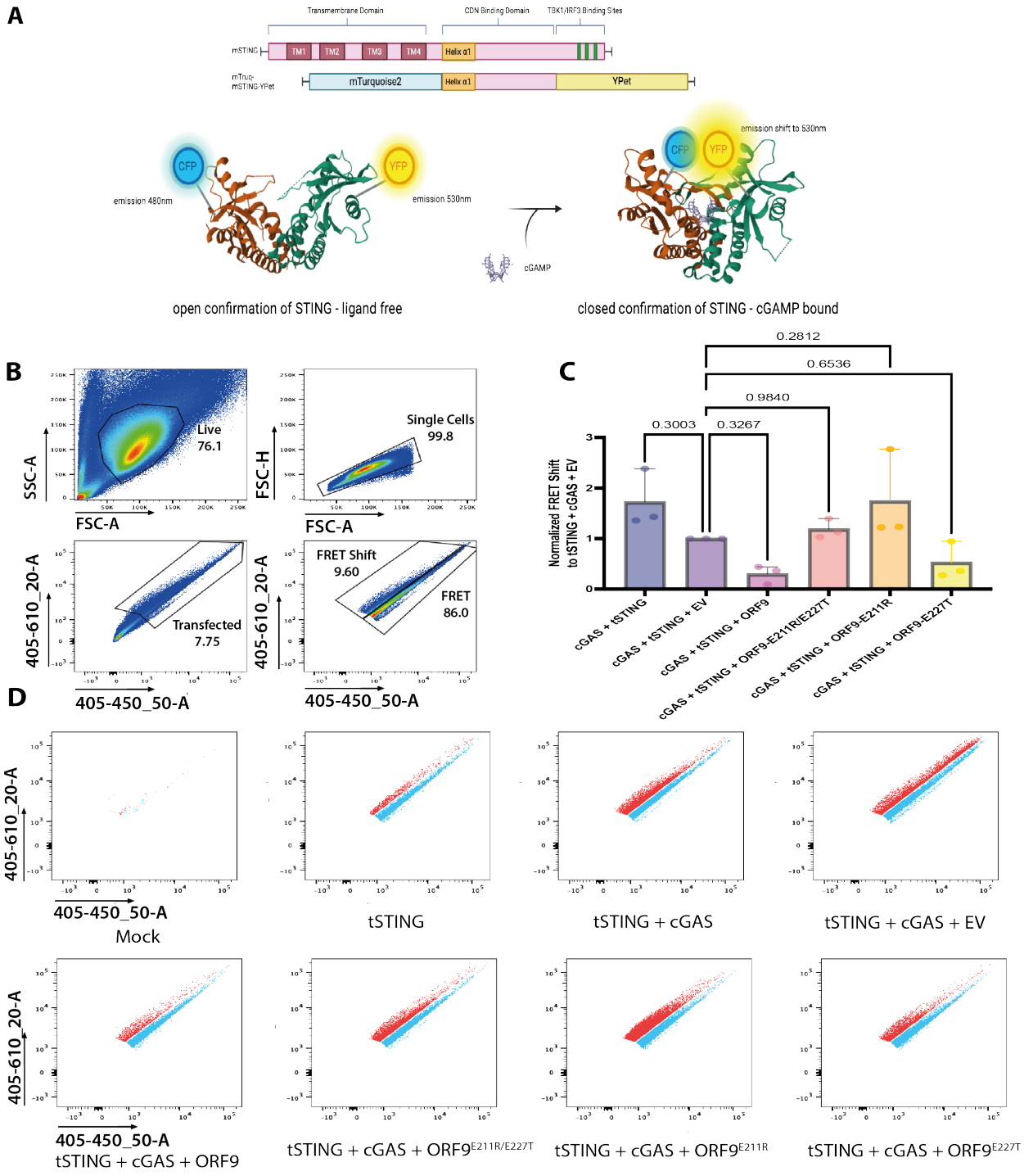


Figure 42: Flow Cytometry Assay to Measure Level of STING Activation.
(**A**) The mTurquoise2-mSTING-YPet plasmid, developed by Zierhut et al., undergoes a conformational change when bound by cGAMP. This brings the two fluorophores within close proximity, shifting the emission wavelength. The mSTING plasmid is truncated to no longer contain the transmembrane section, therefore it is incapable of downstream signalling. PDB: 4EMU and 4KSY. (**B**) Flow cytometry gating strategy. (**C**) Percent FRET shift was pooled and normalized to the tSTING + cGAS + EV condition. Two-way ANOVA with Dunnett's multiple comparisons was used to compare results for each construct. p-values indicated above bars. Panel C shows pooled data from three independent biological experiments (n=3). (**D**) Blue dots represent cells transfected with tSTING plasmid in an unbound state. Red dots indicate transfected tSTING cells that have been activated by cGAMP and have CFP-YFP fluorophores in close proximity to elicit a shift in fluorescence.

STING activation in ORF9-expressing cells was reduced to approximately half compared to EV control cells (Fig. 42, C-D). ORF9^{E227T} expressing cells exhibited similar levels of STING activation to ORF9, while ORF9^{E221R} and ORF9$^{E211R/E227T}$ expressing cells displayed similar levels of STING activation to EV control cells. Flow cytometry plots from all three repeats can be found in Supplemental Figure S5.

The crystal structure of cGAS bound to nucleosomes was modelled using both human and mouse cGAS[28,29,31–33,640]. Mouse cGAS binds to H2A in the same acidic patch as human cGAS, therefore I speculated that ORF9 would also inhibit mcGAS and mutated ORF9 would lose this function. To test this, I replicated the above experiment with mcGAS (Supp. Fig. S6). Similar to hcGAS results, cells expressing ORF9$^{E106R/E109R}$, ORF9^{E211R}, ORF9^{E227T} and ORF9$^{E211R/E227T}$ displayed more STING activation than wild-type ORF9 transfected cells. However, the phenotype was not as strong in cells expressing mcGAS.

Collectively, these results in HEK293T cells agree with data generated in transduced HFFs, in that, ORF9^{E211R} and ORF9$^{E211R/E227T}$ exhibited reduced ability to inhibit cGAS.

5.6 Binding Interactions of ORF9 Mutants with cGAS.

Given the above functional data, I repeated immunoprecipitation experiments with the ORF9 mutants. HEK293T cells were transfected with cGAS-V5 and FLAG-ORF9 constructs. 24 hours later, protein interaction was assessed by collecting lysates for IP. Antibodies against the epitope tags were used to immunoprecipitated cGAS or ORF9. All proteins were detected in the bound fractions when using antibodies against their tags, indicating the pulldown was successful and specific. As expected, ORF9 was present in the cGAS-V5 precipitates – conversely, cGAS was also detected in the ORF9-FLAG precipitates (Fig. 43). Similarly, all ORF9 constructs were detected in the cGAS-V5

precipitates and vice versa cGAS was present in the ORF9-FLAG precipitates. These data indicate that the tested mutations in ORF9 do not ablate binding to cGAS.

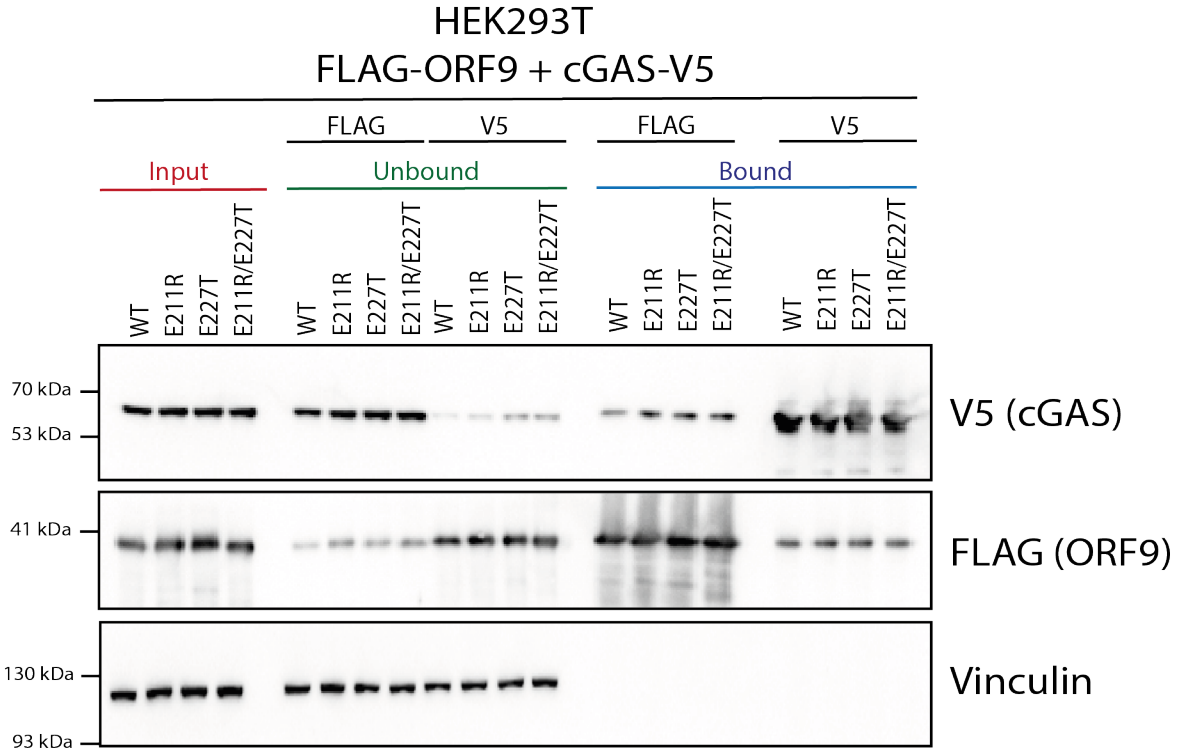


Figure 43: ORF9 Mutants Retain Binding Ability to cGAS.
HEK293T cells were transfected with cGAS and ORF9 expression constructs. 24 hours post-transfection cells were lysed for ectopically expressed proteins and were immuno-precipitated using epitope tag antibodies. The input, unbound and bound fractions were subject to immunoblotting using the indicated plasmids. This figure shows a representative blot from three independent biological experiments (n=3).

5.6.1 cGAS-ORF9 Binding Interactions are Highly Salt Resistant.

cGAS forms a highly salt-resistant bridge between R255 and H2A[125]. I postulated that if the ORF9-cGAS complex resembled cGAS-NCP complexes, then the binding interaction between ORF9 and cGAS would also be highly salt resistant. To test this, I transfected HEK293T cells with FLAG-ORF9 and cGAS-V5. 24 hours later, protein interaction was assessed by collecting lysates for IP. Lysis buffers contained increasing

NaCl concentrations from 100mM to 1M. Antibodies against the epitope tag were used to pull down cGAS-V5 (Fig. 44). ORF9 was detected in cGAS IP fractions at all salt concentrations. Volkman et al. found the cGAS-NCP complex to be salt-resistant up to 750mM[125]. Despite the strong binding of ORF9 and cGAS up to 1M NaCl, the salt solubilized large amounts of DNA making the lysates highly viscous and thus pipetting difficult. Therefore, 500mM NaCl was used to make a lysis buffer for all subsequent IP experiments.

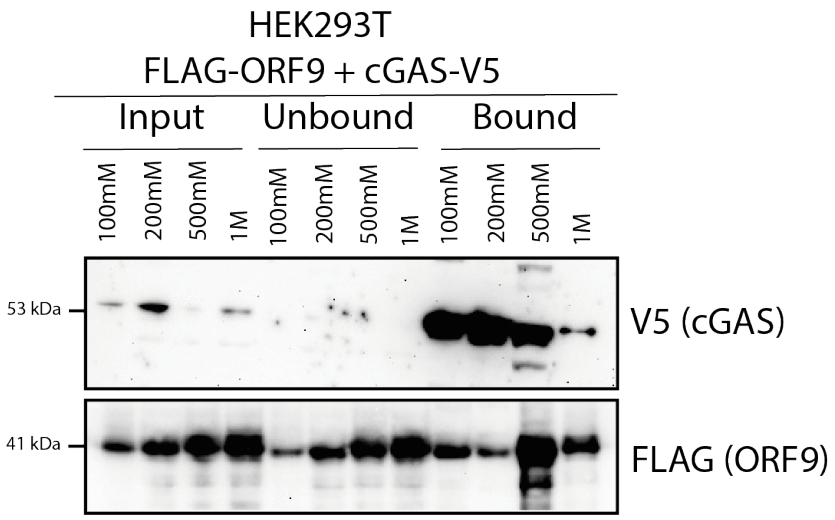
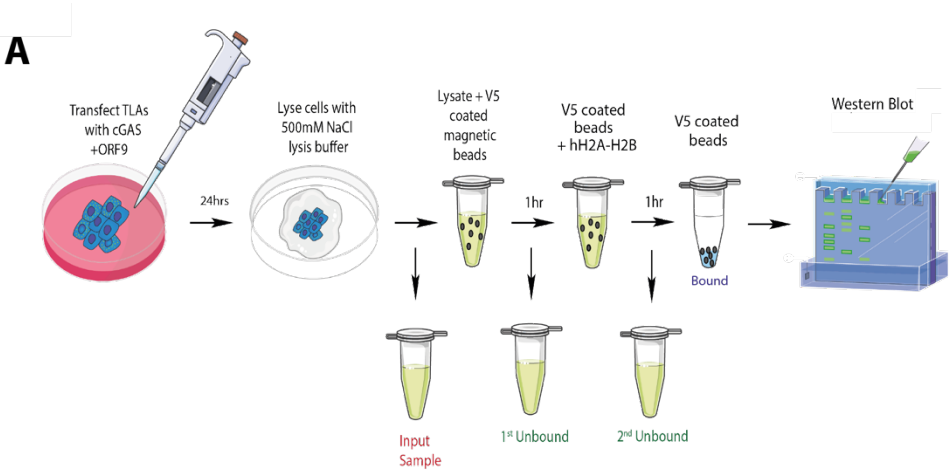


Figure 44: ORF9-cGAS Interaction is Salt Resistant.
HEK293T cells were transfected with expression plasmids for FLAG-ORF9, cGAS-V5, or STING-HA. 24 hours later, cells were lysed with a lysis buffer containing an increasing concentration of salt and ectopically expressed proteins were immunoprecipitated using a V5 epitope tag antibody. The input, unbound and bound fractions were subject to immunoblotting using the indicated plasmids. This data depicts a representative blot from two independent biological experiments (n=2).

5.6.2 VZV-ORF9 Forms a Complex with H2A-H2B and cGAS.

I theorized that if histones and ORF9 bind to cGAS via the same arginine anchor then they may outcompete each other for binding to cGAS. To test this, I added recombinant H2A-H2B dimers to pre-formed cGAS-ORF9 complexes. To obtain the latter, I

transfected HEK293T cells with FLAG-ORF9 and cGAS-V5 as above. 24 hours later, cells were lysed in IP buffer containing 500mM NaCl, as lower salt conditions led to non-specific binding of recombinant histones to the Dynabeads used for IP (data not shown). Antibodies against the epitope tag were used to pull down cGAS-V5 (Fig. 45). Unbound fractions were collected, and then lysates and beads were incubated with recombinant H2A-H2B (kindly gifted by Dr. Christian Zierhut) for one hour. After incubation, a second set of unbound fractions were collected. As expected, hH2B was detected in cGAS-V5 immunoprecipitates by western blot. Surprisingly, ORF9 was also detected in cGAS fractions. hH2B was detected in cGAS-V5 immunoprecipitates. This may indicate the formation of a potential cGAS-ORF9-H2A-H2B complex instead of ORF9 / H2A-H2B competition for cGAS binding. Svea Wupper, a master's student under my supervision, performed IPs to test the ideal salt concentration for efficient ORF9-cGAS and cGAS-H2A/H2B binding. From this experiment she discovered non-specific binding of H2A-H2B to Dynabeads with a lysis buffer containing <150mM NaCl, however non-specific binding was ablated when NaCl concentration was increased to 500mM (data not shown). While a control condition of H2A-H2B with Dynabeads (no cell lysate) was not included in this experiment (Fig. 45), all IP pulldowns were performed using a lysis buffer containing 500mM and should therefore be preventative against non-specific binding of recombinant histone protein to IP beads. This control will need to be included in future experiments to ensure reliable conclusions.



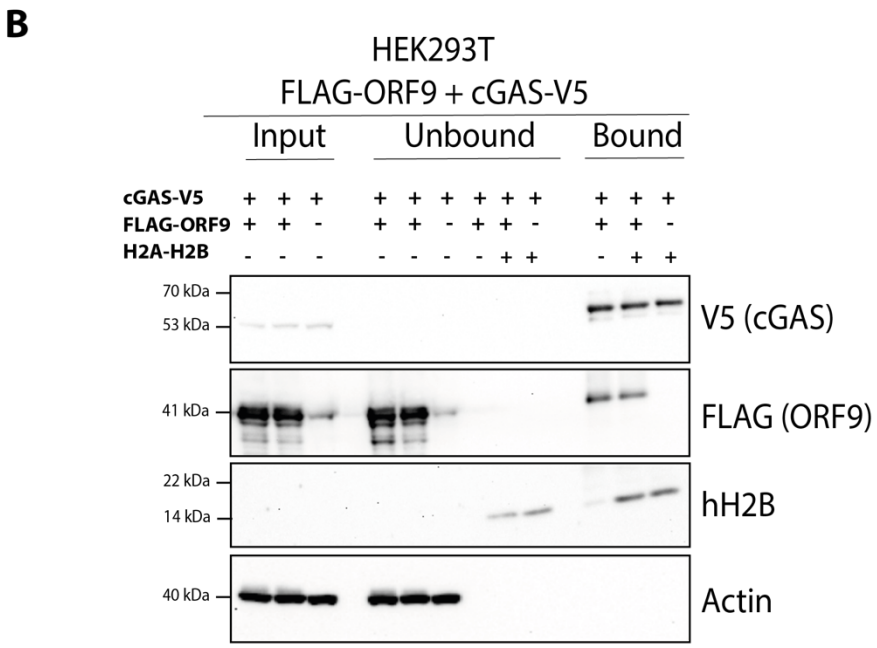


Figure 45: Histones Do Not Disrupt ORF9-cGAS complexes.
(**A**) A schematic of IP methodology. (**B**) HEK293T cells were transfected with expression plasmids for FLAG-ORF9 and cGAS-V5. 24 hours later, cells were lysed with a lysis buffer (500mM NaCl) and ectopically expressed proteins were immunoprecipitated using a V5 epitope tag antibody. The first set of unbound fractions were collected before histones were added to the beads, and the second set of unbound fractions were collected after incubation of histones with beads for 1 hour. The input, unbound and bound fractions were subject to immunoblotting using the indicated plasmids. Panel B shows a representative blot from three independent biological experiments (n=3).

5.7 ORF9 Protein Structure Predictions.

Viruses are known to mimic the secondary or tertiary structure of host proteins to prevent anti-viral mechanisms. The tertiary structure of VZV-ORF9 has not yet been experimentally determined. AlphaFold (developed by Google DeepMind) is an AI system that uses as a training data set the AA sequences of proteins with experimentally resolved structures to predict protein structures simply from AA in a sequence[299,651]. To better understand the tertiary structure of ORF9 I utilized AlphaFold Colab Notebook to generate a predicted model of ORF9 (Fig. 46)[299,651]. This notebook does not use homologous structure templates and instead relies on the BFD database, a collection of 2.5 billion protein sequences. This method is used to generate a predicted protein structure from any input AA sequence. I first modelled full-length ORF9, which generated a structure composed of one central alpha helix with four small adjoining alpha helices and long unstructured tails (data not shown). The AAs corresponding to the unstructured tail regions were removed to generate a more manageable model of the ORF9 protein (Fig. 46, Panel A: ORF9 E89 to G241). The AlphaFold2-multimer Notebook was used to generate a prediction of the putative ORF9-cGAS interaction (Fig. 46, B) as this notebook is more suitable for accurately modelling multimeric interfaces of protein-protein complexes than the standard single chain notebook[652]. A close-up examination of the predicted cGAS-ORF9 complex revealed predicted binding of ORF9 D213 and L216 to cGAS R204 and K198, respectively (Fig. 46, G). The measured ångstrom distance (calculated with Pymol) between these residues was 3.77Å and 3.78 Å, respectively. Angstrom distances of <5 Å indicate a high probability of binding between residues, with most hydrogen bonds forming at a distance of 3.3-4 Å[653]. The structure of H2A-H2B has already been resolved by numerous groups with high resolution. I selected a H2A-H2B heterodimer structure file from the PDB (PDB:2RVQ) (Fig. 46, C) resolved by nuclear magnetic resonance (NMR), for comparison with ORF9 [654]. H2A alone was modelled with cGAS using AlphaFold2-multimer, which showed the binding between the cGAS^{R255} to the acidic patch of H2A (Fig. 46, D).

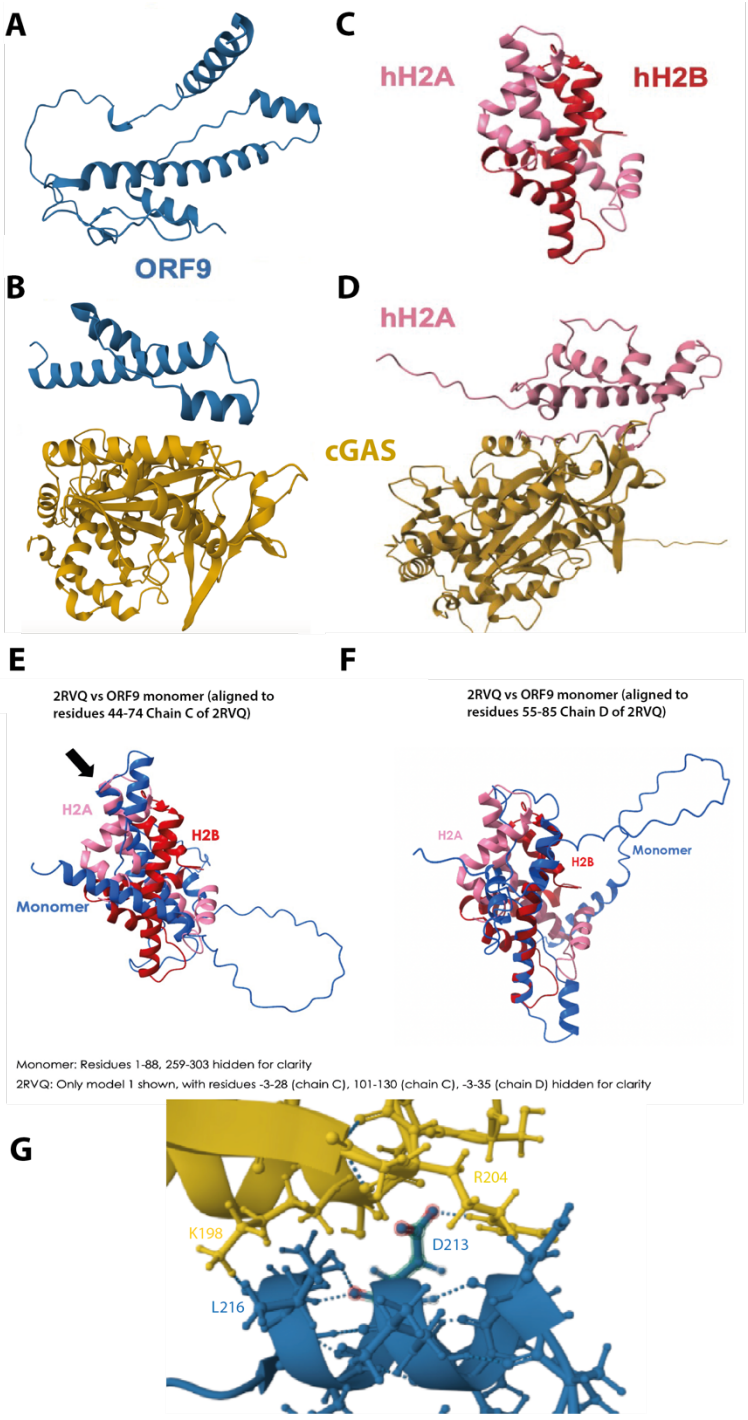


Figure 46: AlphaFold Predictions of VZV-ORF9.
(**A**) AlphaFold protein prediction of VZV-ORF9 (ORF9 E89 to G241, unstructured tail region removed for clarity). (**B**) AlphaFold-multimer prediction of VZV-ORF9 (C170-G241) binding to hcGAS. (**C**) Resolved secondary structure of hH2A-H2B visualized on PDB Mol* 3D Viewer. (**D**) AlphaFold-multimer prediction of hH2A and hcGAS. (**E-F**) Resolved structure of hH2A-H2B (PDB: 2RVQ) superimposed onto ORF9 monomer (blue) using ChimeraX (work done by Kendra Leigh, Cambridge, UK). Chain C refers to H2A, Chain D refers to H2B. (**G**) Predicted cGAS ORF9 binding model showing a close-up of cGAS (orange) residues R204 and K198 binding to ORF9 (green) residues D213 and L216. Visualized using PDB Mol* 3D Viewer.

Kendra Leigh (University of Cambridge) superimposed ORF9 monomer structure predictions with the known H2A-H2B structure using ChimeraX (Fig. 46, E-F), showing the similarities of the central alpha helices between the three proteins. She aligned the ORF9 monomer with H2A (Fig. 46, E) and H2B (Fig. 46, F), which depicted a slightly different orientation of ORF9 when superimposed onto the H2A-H2B dimer. Structural biologists determine the similarity of two proteins by first superimposing the proteins and calculating the room-mean-square-distance (RMSD), which measures the distance between atoms to give an overall average value. This metric is commonly used to calculate the affinity for ligand docking and quantify the similarity between evolutionarily conserved proteins[655,656]. The smaller the RMSD value, the higher the probability the two structures are similar. Identical structures have an RMSD of 0, while homologous proteins typically have an RMSD value of 2-3 Å[657–659]. An RMSD value of <2 Å generally indicates a high degree of similarity between structures. A summary of calculated RMSD values can be found in Table 1 below.

Histones / ORF9		H2A	H2B	H2A-H2B	
				H2A	H2B
ORF9-FL	**RMSD**	3.16	1.06	1.97	1.23
	N_{Align}	46	33	33	35
ORF9 E89-G241	**RMSD**	3.83	0.75	2.54	0.91
	N_{Align}	45	31	40	33
Dimer	**RMSD**	2.15	1.09	2.40	1.64
	N_{Align}	44	32	31	37

Table 1: RMSD Results of Alignment between ORF9 and H2A-H2B.
Calculated RMSD values of ORF9-FL, ORF9 E89-G241 and ORF9-FL dimer against H2A, H2B and H2A-H2B dimer. PDBeFold by EMBL-EBI was used to calculate RMSD.

RMSD values indicated the highest degree of similarity between ORF9 and H2B, however, ORF9 still scored between 1.97 Å and 2.54 Å when modelled against H2A-H2B dimer.

I then considered whether the formation of ORF9-cGAS complex was facilitated by a short peptide. To determine this, I utilized the PepSite2 platform that generates spatial position-specific scoring matrices compiled from a protein/peptide structural database[660]. The matrices are used to find optimal binding sites and orientation of the input peptide[660]. I input the cGAS peptide sequence KFKRNPKE that spans K252 to E259, against hH2A, FL ORF9, and truncated ORF9 (E89 to G241). The ORF9 protein was truncated to remove the unstructured tail domain which often introduces uncertainties in computational modelling. The chosen cGAS peptide had a predicted binding with H2A with KF-RNPK- residues with a p-value = 0.1309. The cGAS peptide had a predicted binding with FL-ORF9 with -F-RNPK- residues with a p-value = 0.06261. The cGAS peptide had a predicted binding with truncated ORF9 with -FKRNPK- residues with a p-value = 0.0084. These data indicate a statistically significant likelihood of the motif surrounding the cGAS arginine anchor binding to ORF9 E89-G241; yielding a higher statistical significance than the same cGAS motif binding to H2A.

5.8 Discussion

Despite the conflicting results for ORF$^{E106R/E109R}$, I successfully generated an array of ORF9 mutants, identifying a 'histone-like' region in ORF9 to be important for cGAS inhibition. The generated AlphaFold predictions, structural similarity and peptide binding calculations indicate commonality between regions of ORF9 and the H2A acidic patch. The ability of ORF9 to bind cGAS^{R255E} indicates that the binding may be mediated by residues other than R255. Alternatively, binding may involve R255 and other complementing amino acids. Interestingly, the co-expression of ORF9$^{E106R/E109R}$ with cGAS^{R255E} reduced the ability of both proteins to bind each other. This indicates that the arginine anchor of cGAS and the proposed 'acidic patch' of ORF9 may facilitate, at least in part, the interaction of these two proteins. Albeit, the experiments utilizing cGAS^{R255E} were only performed once and need to be repeated to come to a definitive conclusion.

It is difficult to determine the cause of the contradicting results with ORF9$^{E106R/E109R}$ (compare Fig. 36 and Fig. 37). I validated the expression of ORF9 at protein level by western blot and re-sequenced the plasmids used, confirming correct plasmids were used in all experiments. At the time these experiments were performed, I did not have the custom VZV-ORF9 TaqMan probe; therefore, inconsistencies may be due to differences in mRNA expression of *ORF9*. However, this scenario is unlikely given that ORF9 WT and mutant proteins were expressed at similar levels as judged by western blot. Considering the phenotype of this mutant reversed in both stably transduced and transiently transfected cell lines it is difficult to explain this inconsistency. Indeed, following numerous discussions with my supervisors, with current and former lab members, and with collaborators, no easy explanation for the inconsistent results with ORF9$^{E106R/E109R}$ emerged. I therefore decided to abandon my investigations of this mutant to avoid working with an artefact.

Work completed by Dr. Jonny Hertzog and featured in our EMBO publication[292] (Appendix), highlighted the regions of ORF9 crucial for cGAS binding (Fig. 47). He tested ORF9 truncation mutations and tested their ability to bind cGAS, finding ORF9 AA151-240 was required for cGAS binding[292]. Given this information, it is unsurprising that mutating residues E106 and E109 did not affect cGAS binding. ORF9^{E211} aligns with E92 of H2A, while ORF9^{E227} aligns with E113 of H2B. Studies which have ablated binding between H2A-H2B and cGAS have introduced missense mutations in all six H2A acidic patch residues and the two additional binding residues in H2B[29,126,641]. Therefore, it may be necessary to introduce missense mutations in all ORF9 residues homologous to H2A-H2B to see a significant depletion of cGAS binding (i.e. E106, E109, N209, E211 and E227).

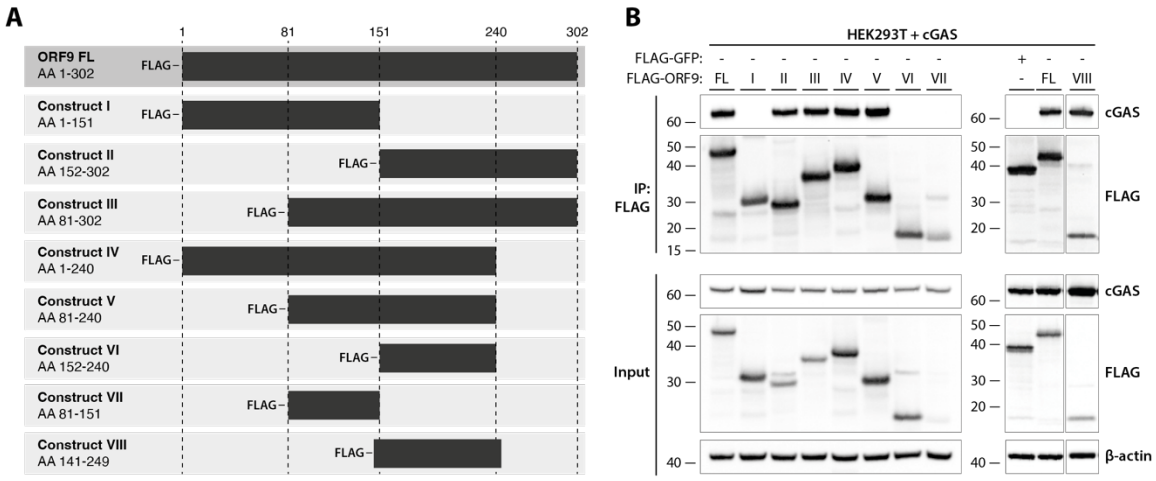


Figure 47: VZV ORF9 Binds cGAS.
(**A**) Schematic detailing ORF9 truncation mutants used in (B). (**B**) HEK293T cells were transfected with expression plasmids for human cGAS and ORF9 truncation mutants. The next day, cells were lysed and ORF9 proteins were immunoprecipitated using a-FLAG antibody. IP fractions were subjected to immunoblotting using the indicated antibodies. This figure and figure description was taken directly from our Hertzog *et al.* 2022. publication and was completed in entirety by Jonny Hertzog.

Our Hertzog *et al.* 2022 publication described ORF9 forming DNA-cGAS phase-separated condensates and pulling down with DNA both alone and with cGAS without displacing cGAS from DNA[292]. ZBP1, a cellular Z-RNA/DNA sensor, binds the N-terminal region of cGAS via its RHIM domain. A secondary interaction is formed via a DNA bridge bound to the two protein's DNA binding interfaces[190]. The knockout of Z-binding domains in ZBP1 significantly ablated binding to cGAS[190]. It is interesting to consider whether ORF9 binds cGAS in a similar manner; perhaps ORF9 binds cGAS via a histone-like 'acidic patch' and is stabilized by a DNA bridge. It is possible that salt and detergent conditions in my IP lysis buffer preserve DNA bridges between cGAS and ORF9. DNA bridges could connect cGAS and ORF9 without direct protein-protein interaction, thereby explaining the presence of ORF9 mutants in cGAS IP fractions. Future experiments should subject lysates to rigorous DNase treatment before addition to beads. It would be interesting to perform pulldowns with streptavidin-labelled DNA with ORF9 and its mutants to determine if ORF9-cGAS complexes pulldowns are facilitated by DNA bridges. Nucleosomal bound cGAS binds NCP complex DNA via its binding site C and is inhibited by histones via site B. Thus, it is possible that cGAS binds ORF9-bound DNA via site C and is directly inhibited by ORF9-bound to site B. A mutant cGAS

protein lacking DNA binding site C for use in IPs with ORF9 would be an interesting line of future research. Alternatively, generating a truncated cGAS protein with only the DNA binding site retained and performing streptavidin DNA pull-down with ORF9 would determine whether this protein complex is mediated by DNA. Creating an ORF9 mutant in the AA151-240 region known to be required for cGAS binding and investigating proteins pulled down with streptavidin would provide insight into whether this interaction if facilitated by DNA binding.

Nuclear cGAS forms a highly salt-resistant tether to histones[125]. cGAS-DNA-ORF9 condensates were formed in high salt conditions (300mM)[292]. cGAS^{R255} forms a salt bridge with H2A residues D91, E93 and E62[640], with the binding between residues highly salt resistent[125]. I found that ORF9-cGAS complexes are highly salt-resistant up to a NaCl concentration of 1M, above the concentration tolerated by cGAS-NCP (0.75 M). The similarities between the binding affinity of the two proteins with cGAS provide some evidence for ORF9 mimicking H2A-H2B.

Histone competition experiments showed ORF9-cGAS complexes were still able to bind H2A-H2B proteins. This potentially indicates that H2A-H2B and ORF9 bind to cGAS via different regions. Alternatively, as postulated above, the complex could be facilitated by the non-specific binding of DNA between these proteins and is not necessarily an indicator of direct binding. As mentioned, future experiments should subject lysates to rigorous DNase treatment before addition to beads. The binding affinity of cGAS-ORF9 is not known, therefore it is difficult to know whether histones would be able to displace ORF9 from cGAS if they are tightly bound. Alternatively, the reverse is true if ORF9 was introduced to cGAS-NCP complexes. Ongoing experiments have investigated differences between adding recombinant histones to ORF9-cGAS lysates or adding ORF9 lysates to cGAS lysates containing recombinant histones. Size exclusion chromatography could provide some clarity on the stoichiometry of ORF9-cGAS complexes. In the nucleus the dominant stoichiometry of cGAS-NCP is 2:2[28,29,32–34,640]. If ORF9 mimics histone structure, it would be reasonable to assume it forms a dimer or an octamer, like the full nucleosome structure. Additionally, if cGAS concentration is too high, cGAS may be bound to histones and ORF9 separately, which

cannot be differentiated in this type of experiment. However, this requires further optimization and experimentation before conclusions can be drawn.

The overexpression of other ORF9 mutants yielded interesting and reproducible results. In HFFs transduced with ORF9^{E221R}, ORF9^{E227T}, or ORF9$^{E211R/E227T}$, DNA transfected induced similar levels of cGAMP compared to GFP transduced control cells, while cGAMP levels were reduced in wild-type ORF9 expressing cells. Similar to these cGAMP ELISA results, DNA transfection induced comparable levels *IFNL1, IFIT1, IL6* and *IFI44* mRNA in cells transduced with GFP, ORF9^{E221R} or ORF9$^{E211R/E227T}$.as GFP. However, both ORF9 and ORF9^{E227T} inhibited the production of these ISG and IFN mRNA transcripts. There was no differential phosphorylation of STAT1 between cells expressing GFP and different ORF9 constructs; however, this may be due to the late time point tested – in that early signalling events may not be apparent at 24 hours. cGAMP ELISA results were very similar in transiently transfected HEK293T cells. However, ORF9^{E227T} inhibited the production of cGAMP, similar to wild-type ORF9. The downstream activation of STING by cGAMP was measured via a FRET assay. The results of the FRET assay replicated the cGAMP ELISA results, in that ORF9^{E221R} and ORF9$^{E211R/E227T}$ expressing cells induced the production of cGAMP and downstream STING activation to levels similar to or above EV transfected cells. Together, these functional results provide exciting evidence to support our hypothesis that these ‘acidic patch’-like residues in ORF9 are crucial for cGAS inhibition.

cGAS is a highly conserved protein in mammals, with its arginine anchor highly conserved between vertebrate cGAS homologs[645,661,662]. mcGAS has a similar structure to hcGAS and is inhibited by H2A-H2B through electrostatic interactions between the same cGAS site B and acidic patch residues of H2A-H2B[28,32,33]. Considering both mcGAS and hcGAS bind to the acidic patch of H2A-H2B through their arginine anchor, I postulated that ORF9 would inhibit mcGAS in a similar manner. Despite robust ORF9 expression in HEK293T cells (Supp. Fig. S7) the inhibition effects of ORF9 seemed less potent against mcGAS. Regardless, the trend of inhibition across ORF9 mutant constructs remained consistent – cells expressing all mutants produced a higher FRET shift compared to ORF9. In addition, ORF9$^{E106R/E109R}$ was also included in this

experiment, and cells expressing this mutant showed higher FRET shift populations than ORF9. As the STING plasmid used in FRET experiments was truncated to remove the transmembrane and TBK1/IRF3 signalling domain, I did not attempt to assess downstream activation of ISGs and IFN by western blotting or RT-qPCR. Collectively, experiments with hcGAS and mcGAS lends exciting evidence in support of our hypothesis that histone-like residues in ORF9 are responsible for cGAS inhibition.

I considered whether the entire tertiary structure of ORF9 would be needed to mimic H2A/H2B or whether a short peptide would be sufficient for cGAS inhibition. Given ORF9's role as a tegument protein, I thought perhaps it is unlikely that the entire protein may mimic a histone, but rather only an acidic patch-like motif is necessary for binding cGAS. Computational modelling indicates similarities between ORF9 and H2A-H2B. To generate a preliminary structure of ORF9, I generated a predicted model using AlphaFold. The unstructured tail of ORF9 displays many AA with low confidence in folding structure. It remains to be seen whether AlphaFold is simply unable to determine the structural composition, or it is an unstructured tail in cells. Indeed, the tail domain of cGAS and histones appear unstructured with low confidence when run through AlphaFold's prediction model. AlphaFold-generated structures represent a predicted model of tertiary structure folding and configuration in a 3D space, while the multimer notebook provides a prediction of protein binding. Quantitative comparison of ORF9 three-dimensional structure by calculating RMSD values found the ORF9 protein with the unstructured tail removed had a high degree of similarity with H2B alone and both proteins when modelled in its H2A-H2B dimer formation. The PepSite2 results show the peptide flanking cGAS arginine anchor had a higher statistical likelihood of binding truncated ORF9 than H2A.

Its important to note that RMSD calculation is limited by the size of the structures. Considering RMSD is a measure of atoms in the structural alignment, it is limited by the length of the structures compared and becomes an inappropriate quantitative model when there's a large discrepancy between structure lengths[659]. While there is a length difference between ORF9 (truncated version: 152AA) and H2A (133AA)-H2B (129AA), the difference is not substantial for the proteins compared as monomers but may be an

inappropriate metric for dimer comparisons. To confidently validate the structural similarities, the ORF9-cGAS complex would have to be experimentally resolved through cryo-EM, NMR or X-ray crystallography. We have recently initiated a collaboration with Dr. Karim Rafie (University of Groningen), who has started to produce recombinant ORF9 and cGAS proteins to experimentally determine the ORF9-cGAS complex using cryo-EM.

Both HSV-1 VP22 and VZV-ORF9 are tegument proteins, which form phase-separated condensates with cGAS, antagonize cGAS function and bind DNA. Interestingly, VP22 interacts with template-activating factor I (TAF-I), which is responsible for adenovirus replication, chromatin remodelling, deposition of histones onto DNA and transcription of ISGs[146,636,663–667]. Specifically, VP22 binds TAF-I to prevent nucleosome deposition on DNA[636]. This is likely a mechanism to prevent host anti-viral immune gene transcription. Considering VP22's role in binding histone chaperone proteins and the similarities with ORF9, it's interesting to consider whether ORF9 also has anti-transcription roles in the nucleus. Perhaps ORF9 inhibits cGAS by mimicking a histone while also preventing the transcription of anti-viral host factors by interacting with histone chaperone proteins, in a manner similar to VP22.

ORF9 possesses three of the four acidic patch residues, with only the D90 residue not aligned with ORF9. H2A possesses an aspartic acid at position 90 and an asparagine at position 94. Conversely, ORF9 possesses an asparagine at position 209 and an aspartic acid at position 213. These AAs between H2A and ORF9 are four AAs apart and both directly align with each other in the semi-global sequence alignment (Fig. 34, A). It is interesting to consider whether ORF9 possesses all four acidic patch residues, but this short segment is flipped within ORF9. The orientation of the peptide is likely less important than the distance between each residue in the sequence.

The acidic patch of H2A-H2B is also composed of two residues from H2B - P50 and D51 which bind to R349 and R353 of cGAS[31,32,640]. ORF9 P73 aligns with H2B P50, highlighting yet another similarity of ORF9 with this histone dimer and another residue to investigate in future work.

In the future, we hope to generate a VZV-ORF9 recombinant virus through a collaboration with Dr. Paul Kinchington (University of Pittsburgh, USA) to test the inhibition of cGAS during endogenous infection.

Chapter 6

Discussion

The innate immune system is the first line of defence against pathogens and therefore, any malfunction of this system leads to increased susceptibility to infection. This was highlighted during the COVID-19 pandemic when seemingly healthy individuals succumbed to severe SARS-CoV-2 infection caused by errors in type I IFN immunity[351]. In the same vein of reasoning, this study aimed to (1) characterize the consequence of SNPs within *MAVS* on activation of IFN responses by upstream nucleic acid sensors. Pathogens have evolved a myriad of mechanisms that evade and antagonize anti-viral immunity to promote their own success. In a clever bid to fool immune recognition systems, many viruses camouflage by evolving host mimicry proteins. This study's second aim was to (2) investigate the mechanism of cGAS inhibition by VZV-ORF9.

6.1 Objective 1: Importance of MAVS SNPs for Induction of the IFN Response (Chapter 3)

This project has several exciting prospects, particularly to further investigate the phenotypic consequence of the MAVS-C5T variant. I have been working to optimize an *in vitro* transcription - translation assay with the intention of testing via western blot the translation of the different MAVS protein isoforms from MAVS constructs with SNPs. With this assay, the translation of each MAVS protein isoform could be quantified in isolation from any confounding or stimulatory factors present in cell culture. However, I decided not to pursue this line of work due to the lack of a MAVS antibody capable of detecting MAVS M1 through M6. A caveat of my work in cells was that MAVS was overexpressed. Future experiments should investigate endogenous MAVS, something

that could be achieved by CRISPR editing the MAVS gene in HEK293T cells to introduce the SNPs of interest. This would allow for testing of MAVS SNPs in a setting of endogenous level of expression, in contrast to overexpressing MAVS via transfection or transduction. Additionally, Calu3 cells depleted of MAVS by lentivirally delivered shRNA or sgRNA (used in our recent publication; Appendix, Sampaio et al. 2021), could be utilized for reconstitution experiments. Of note, my MAVS constructs are resistant to the shRNA and sgRNA sequences targeting the endogenous MAVS mRNA or gene, respectively, due to the introduction of synonymous codons during cloning. Additionally, A549 cells could be an additional exploratory cell line as they can be stably transduced to express the ACE2 receptor. Moreover, pluripotent stem cells could be genome-edited to harbour *MAVS* SNPs of interest and differentiated into pneumocytes to experimentally recapitulate SARS-CoV-2's tropism. With differentiated lung cells, an air-liquid interface can be utilized to infect with SARS-CoV-2 to model an endogenous environment of respiratory infection. Transfected cells can then be infected with SARS-CoV-2 and subjected to subcellular fractionation to isolate pelleted mitochondria. Cellular lysates and an IRF3 dimerization assay could be used to assess MAVS aggregation capacity and activity. Finally, it would be interesting to determine if overexpression of FL MAVS in transduced Calu3 cells would restore the suppressive phenotype seen in C5T mutant cells.

Multiple sclerosis (MS) is an autoimmune disorder caused by neuroinflammation of, and subsequent damage to, myelin sheath and nerve cell bodies[668,669]. MS is caused by a complex interplay of environmental factors and genetics, with most attributed SNPs within non-coding regions[670,671]. However, SNPs in the coding region of tyrosine kinase 2 (*TYK2*) have been linked to increased susceptibility to MS. The binding of type I IFNs to their receptor (IFNAR1/2) activates TYK2 and JAK1, which then recruit STAT1 and STAT2 to initiate the downstream induction of ISGs[16,199] (Fig. 2). While some studies have found the loss of function rs34536443 *TYK2* variant impairs cytokine signalling and confers a protective effect against autoimmunity, including MS[670–672], other studies have found the rs55762744 variant to increase risk of MS[673]. Interestingly, SNPs in the promoter of *TYK2* decreased its promoter activity but increased the risk factor for developing viral induced type I diabetes (T1D)[674–677]. Similarly, rare variants in *IFIH1* (that

encodes MDA5) are protective against T1D, whereas the most common *IFIH1* SNPs associated with T1D found in patients predisposes to disease[678–680]. The *IFIH1* loss of function decreases the risk of developing T1D but likely increases predisposition to infection[678,681]. This suggests that variants protective of T1D have been negatively selected due to the negative impact on viral protection, rather than positively selected for protection against T1D[678].

These examples highlight the importance of a finely tuned balance of innate immune activation – overstimulation leads to autoimmune disorders, while understimulation raises susceptibility risk to severe infection. The necessity to balance innate immune induction highlights the possible importance of truncated MAVS isoforms in mediating MAVS signalling at baseline and during infection. The link between *IFIH1* and T1D, and *TYK2* and MS, alludes to yet more unknown variants in innate immune proteins that modulate autoimmune conditions. We consider expanding the GWAS search to other RNA virus databanks as a future direction; moreover, it may be equally as exciting to investigate *MAVS* SNPs in its various AUG start sites and their Kozak sequences in autoimmune disease databanks. Additionally, as highlighted in Chapter 3, over 50% of human mRNAs contain uORFs[492,500,505,506] , alluding to the possibility that other truncated isoforms of innate immune proteins have important and perhaps non-canonical functions.

In conclusion, I successfully modelled patient-derived MAVS SNPs and characterized their impact on innate immune function (Fig. 48). This identified two SNPs with promising phenotypes – MAVS-C5T dampens cytokine signalling after stimulation, while MAVS-G1074C boosts innate immune responses. C5T is therefore a SNP of interest in susceptibility to infection, while G1074C may increase the risk for autoimmune disorders. Alternatively, it is possible C5T reduces the anti-viral response and thereby allows for increased susceptibility to severe infection, while overactivation by G1074C induces cytokine storms that contribute to acute inflammation found in severe SARS-CoV-2 patients. This may provide genetic markers to consider in clinical settings when evaluating aberrant innate immune signalling.

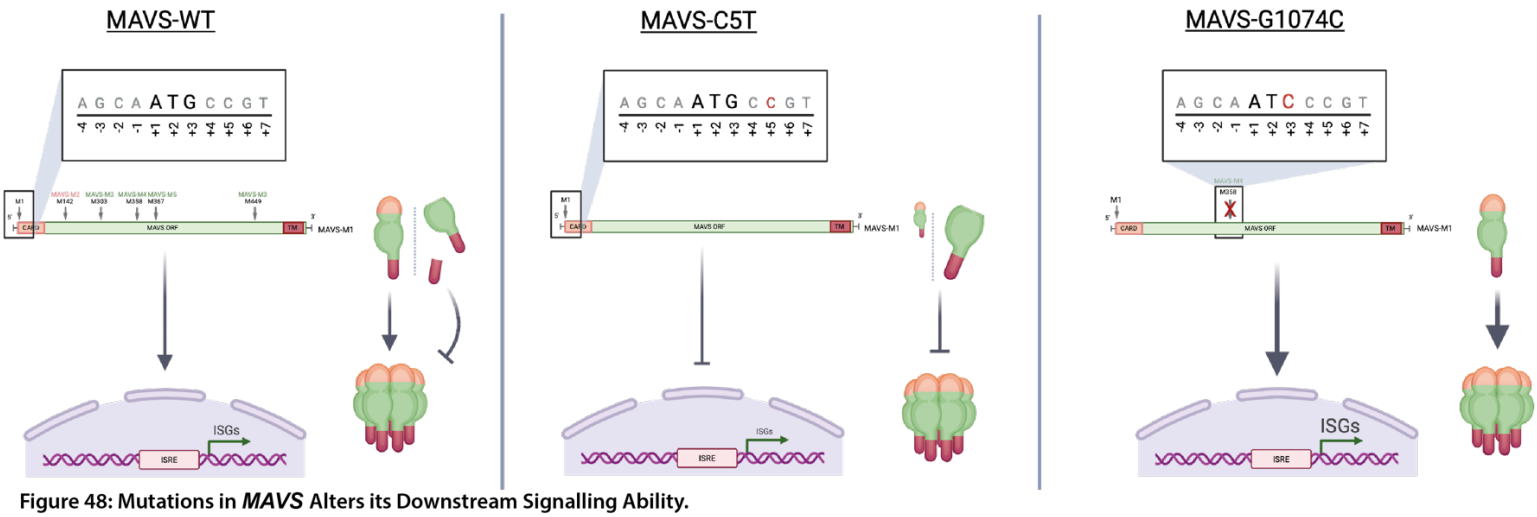


Figure 48: Mutations in *MAVS* Alters its Downstream Signalling Ability.
This schematic summarizes the findings from Chapter 3, comprising data from my MAVS project. The translation of MAVS can result in the production of full-length or five truncated isoforms of MAVS. Full-length MAVS has anti-viral functions, while the truncated isoforms function to counteract the downstream synthesis of ISGs and IFNs. Mutations in Kozak sequences of alternative start sites or the start sites themselves result in skewed production of MAVS truncated isoforms. The MAVS-C5T mutation weakens the Kozak sequence flanking the start site for full-length canonical MAVS and results in reduced ISG/IFN induction and MAVS aggregation *in vitro*. The MAVS-G1074C mutation alters the original MAVS-M4 ATG site to an ATC, thereby preventing MAVS-M4 translation. This results in an increased production of ISGs and larger MAVS aggregates compared to WT MAVS. Graphic made using BioRender.com.

6.2 Objective 2: Mechanism of VZV-ORF9 Inhibition of cGAS (Chapters 4 & 5)

Viruses commonly mimic host proteins to evade viral detection and suppress anti-viral mechanisms to promote viral infection. Perfect mimics adopt host like features to hijack host machinery for viral benefit, while imperfect mimics resemble host factors but perform different functions distinct from canonical host function[682,683]. Numerous examples exist of viruses mimicking nucleosomes, histones, chromatin-interacting or histone chaperone proteins to regulate chromatin-mediated gene expression[684,685]. For example, the non-structural protein 1 (NS1) of influenza A H3N2 strain, the predominant subtype circulating during seasonal influenza, possesses a histone-like sequence that resembles the unstructured tail of histone H3[682,686,687]. Specifically, NS1 contains an ARSK sequence that is homologous to H3's ARTK sequence. The C-terminus of NS1 is non-structured and likely susceptible to post-translational modification, much like H3 tails[682,687,688]. NS1 mimics H3 tails to suppress human PAF1 transcription elongation complex (hPAF1C), which is an important regulator of anti-viral

and proinflammatory responses[687]. NS1 also utilizes its mimicry of H3 to bind CHD1, a chromatin remodelling factor, to promote virus transcription[682,684]. While IAV is an RNA virus, infection can trigger the cGAS-STING-mediated IFN response, which has mainly been attributed to stimulatory mtDNA released from damaged mitochondrial membranes[689–692]. Many chromatin-binding proteins interact with the acidic patch of histones to hijack the regulation of gene expression[684,687]. LANA of KSHV, IE1 of cytomegalovirus (CMV), and Gag of spumaretovirus all bind the acidic patch of nucleosomes by mimicking the arginine anchor motif[143,684,693–696].

Interestingly, some viruses organize their genome using nucleosomes encoded by virally-encoded histone-like proteins or have adopted host histones during infection[684,697–699]. Two members of the *Marseilleviridae* family, *Marseillevirus* and *Melbournevirus* isolated from amoeba encode homologs of histone proteins[684,697,700,701]. The *Marseillevirus* encodes fused histone doublets Hα-Hβ and H*γ*-Hδ that are structurally analogous to human histone dimers H2A-H2B and H3-H4, respectively[697,700,701]. Phylogenic analyses suggest *Marseillevirus* histones genes were acquired from eukaryotic histone genes[700,702]. Cyro-EM structures of both *Marseillevirus* and *Melbournevirus* depict remarkable similarity to human nucleosomes. While these viral nucleosomes wind ~120bp of DNA, compared to 147bp by human nucleosomes, the function of viral nucleosomes resembles canonical eukaryotic chromatin packaging function. Indeed, histone doublet-deficient viruses were less infectious in amoeba cells compared to WT viruses[697]. The low sequence similarity with eukaryotic histones and conservation of viral nucleosomes within the *Marseilleviridae* family suggests additional roles outside of DNA organization[697]. The eukaryotic acidic patch is composed of six H2A residues and two H2B residues – four H2A and two H2B residues are conserved in viral histone doublets, creating a similarly sized and charged acidic patch to the eukaryotic nucleosome acidic patch[700,701]. In addition, the viral Hδ histone tail possesses charged residues that may be sites of post-translation modification[701]. *Marseillevirius* is found in the blood and gut of asymptomatic individuals, however, recent evidence has attributed flu-like symptoms to chronic *Marseillevirus* infection[703–708]. Whether this is directly attributable to *Marseillevirus* or an amoeba infection is unclear. The presence of *Marseillevirus* was detected by RT-qPCR and is therefore likely

indicative of a virally infected amoeba within the patient. *Marseillevirus* is adapted to infect amoeba and, therefore, is unlikely to have adaptions necessary for human infection. However, it is worth considering whether *Marseilleviridae* viral histone doublets bind cGAS in a similar manner to eukaryotic nucleosomes? Additionally, is it possible that 'cases of *Marseillvirdiae'* are actually amoeba infected with *marseillevirus* that remain asymptomatic because the viral nucleosomes bind and inhibit cGAS to avoid eliciting an anti-viral response?

These examples highlight that viruses mimic both entire host proteins and short motifs found in cellular proteins. Short linear motifs (SLiMs) are polypeptides 3-10 aa in length that are recognized by an interacting domain[709]. SLiMs are often located in disordered regions and regulate crucial transient interactions[709]. Viral motifs tend to possess higher binding affinity than host motifs, to outcompete cellular proteins for binding[709,710] – alluding to the possibility that ORF9 may outcompete H2A-H2B for binding to cGAS. It is common for viral proteins to harbour sequences with similarity to specific motifs of a host protein without adopting the entire secondary structure of that host protein[684,709]. This raises the possibility that ORF9 may possess a motif mimic of the H2A-H2B acidic patch rather than mimic the entire protein dimer. While the tertiary structure of ORF9 is not completely homologous to H2A-H2B, which is likely given its primary function as a tegument protein, the aa sequence identity between acidic patch residues, their orientation in space, and distance between residues is likely the key driver of arginine anchor binding.

Viruses must package their DNA into capsids to protect it from detection by nucleic acid sensors, while also making their DNA available for transcription during infection. Interestingly, during VZV infection, tegument proteins enter the nucleus to promote transcription of immediately early viral genes (Fig. 21). It is possible that ORF9 inhibits both nuclear and cytosolic cGAS and the binding of cGAS to nucleosomes acts as a redundant system of cGAS inhibition in favour of VZV pathogenesis. The presence of viral tegument proteins in the nucleus likely also facilitates inhibition of nuclear cGAS while the uncoated viral genome is transcribed.

In conclusion, the work presented here adds another example of viral inhibition of cGAS-STING signalling, specifically a novel mechanistic strategy of cGAS inhibition by viral histone mimicry (Fig. 49). A better understanding of inhibition mechanisms can advance our knowledge of cGAS biology during infection and may be a mechanism employed by other viruses. As numerous RNA viruses induce cGAS-STING-dependent IFN activation, it would be interesting to explore possible viral histone mimicry of cGAS in RNA viruses.

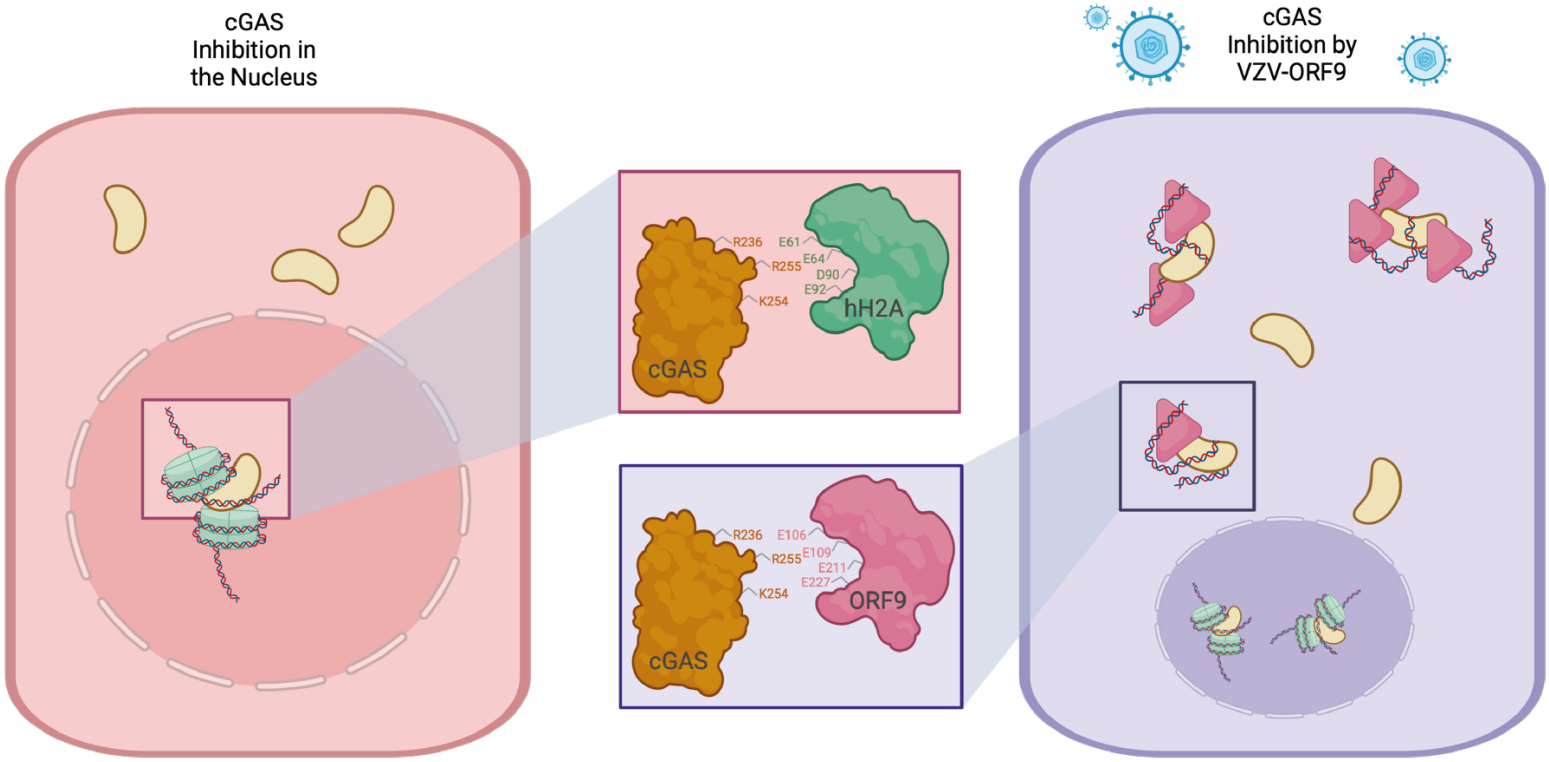


Figure 49: VZV-ORF9 Acts as a Histone Mimic to Bind and Inhibit cGAS.
This schematic summarizes the findings from Chapter 5, comprising data from my VZV project. cGAS is inhibited in the nucleus by human histone H2A-H2B. This interaction is primarily mediated by the R255 residue of cGAS to four residues of hH2A (E61, E64, D90 and E92) that make up its the acidic patch. VZV-ORF9 possesses a similar acidic patch as hH2A. In VZV infected cells, ORF9 binds to cGAS via its own acidic patch to inhibit the production of cGAMP and thereby preventing downstream anti-viral activation. Graphic made using BioRender.com.

Bibliography

1. Janeway, C. A. Approaching the Asymptote? Evolution and Revolution in Immunology. *Cold Spring Harb. Symp. Quant. Biol.* **54**, 1–13 (1989).
2. Murphy, K. M. & Weaver, C. *Janeway's Immunobiology*. (GS, Garland Science, Taylor & Francis Group, New York London, 2017).
3. Iwasaki, A. & Medzhitov, R. Regulation of Adaptive Immunity by the Innate Immune System. *Science* **327**, 291–295 (2010).
4. Tan, X., Sun, L., Chen, J. & Chen, Z. J. Detection of Microbial Infections Through Innate Immune Sensing of Nucleic Acids. *Annu. Rev. Microbiol.* **72**, 447–478 (2018).
5. Wu, J. & Chen, Z. J. Innate Immune Sensing and Signaling of Cytosolic Nucleic Acids. *Annu. Rev. Immunol.* **32**, 461–488 (2014).
6. Carpenter, S. & O'Neill, L. A. J. From periphery to center stage: 50 years of advancements in innate immunity. *Cell* **187**, 2030–2051 (2024).
7. Nawaz, N. *et al.* Lysozyme and Its Application as Antibacterial Agent in Food Industry. *Molecules* **27**, 6305 (2022).
8. *Fields Virology*. (Wolters Kluwer/Lippincott Williams & Wilkins Health, Philadelphia, PA, 2013).
9. Pradeu, T., Thomma, B. P. H. J., Girardin, S. E. & Lemaitre, B. The conceptual foundations of innate immunity: Taking stock 30 years later. *Immunity* **57**, 613–631 (2024).
10. Hertzog, J. & Rehwinkel, J. Regulation and inhibition of the DNA sensor cGAS. *EMBO Rep.* **21**, (2020).
11. Rehwinkel, J. & Gack, M. U. RIG-I-like receptors: their regulation and roles in RNA sensing. *Nat. Rev. Immunol.* **20**, 537–551 (2020).

12. Sun, L., Wu, J., Du, F., Chen, X. & Chen, Z. J. Cyclic GMP-AMP Synthase Is a Cytosolic DNA Sensor That Activates the Type I Interferon Pathway. *Science* **339**, 786–791 (2013).

13. Ablasser, A. *et al.* cGAS produces a 2'-5'-linked cyclic dinucleotide second messenger that activates STING. *Nature* **498**, 380–384 (2013).

14. Civril, F. *et al.* Structural mechanism of cytosolic DNA sensing by cGAS. *Nature* **498**, 332–337 (2013).

15. Isaacs, A., Cox, R. A. & Rotem, Z. FOREIGN NUCLEIC ACIDS AS THE STIMULUS TO MAKE INTERFERON. *The Lancet* **282**, 113–116 (1963).

16. Mesev, E. V., LeDesma, R. A. & Ploss, A. Decoding type I and III interferon signalling during viral infection. *Nat. Microbiol.* **4**, 914–924 (2019).

17. Orzalli, M. H. & Parameswaran, P. Effector-triggered immunity in mammalian antiviral defense. *Trends Immunol.* **43**, 1006–1017 (2022).

18. Stuart, L. M., Paquette, N. & Boyer, L. Effector-triggered versus pattern-triggered immunity: how animals sense pathogens. *Nat. Rev. Immunol.* **13**, 199–206 (2013).

19. Gaidt, M. M. *et al.* Self-guarding of MORC3 enables virulence factor-triggered immunity. *Nature* **600**, 138–142 (2021).

20. Sloan, E., Orr, A. & Everett, R. D. MORC3, a Component of PML Nuclear Bodies, Has a Role in Restricting Herpes Simplex Virus 1 and Human Cytomegalovirus. *J. Virol.* **90**, 8621–8633 (2016).

21. Rodríguez, M. C., Dybas, J. M., Hughes, J., Weitzman, M. D. & Boutell, C. The HSV-1 ubiquitin ligase ICP0: Modifying the cellular proteome to promote infection. *Virus Res.* **285**, 198015 (2020).

22. García-Sastre, A. Ten Strategies of Interferon Evasion by Viruses. *Cell Host Microbe* **22**, 176–184 (2017).

23. Rotem, Z., Cox, R. A. & Isaacs, A. Inhibition of Virus Multiplication by Foreign Nucleic Acid. *Nature* **197**, 564–566 (1963).

24. Wu, J. *et al.* Cyclic GMP-AMP Is an Endogenous Second Messenger in Innate Immune Signaling by Cytosolic DNA. *Science* **339**, 826–830 (2013).

25. Zhang, X. *et al.* Cyclic GMP-AMP Containing Mixed Phosphodiester Linkages Is An Endogenous High-Affinity Ligand for STING. *Mol. Cell* **51**, 226–235 (2013).

26. Diner, E. J. *et al.* The Innate Immune DNA Sensor cGAS Produces a Noncanonical Cyclic Dinucleotide that Activates Human STING. *Cell Rep.* **3**, 1355–1361 (2013).

27. Gao, P. *et al.* Cyclic [G(2',5')pA(3',5')p] Is the Metazoan Second Messenger Produced by DNA-Activated Cyclic GMP-AMP Synthase. *Cell* **153**, 1094–1107 (2013).

28. Boyer, J. A. *et al.* Structural basis of nucleosome-dependent cGAS inhibition. *Science* **370**, 450–454 (2020).

29. Kujirai, T. *et al.* Structural basis for the inhibition of cGAS by nucleosomes. *Science* **370**, 455–458 (2020).

30. Pathare, G. R. *et al.* Structural mechanism of cGAS inhibition by the nucleosome. *Nature* **587**, 668–672 (2020).

31. Cao, D., Han, X., Fan, X., Xu, R.-M. & Zhang, X. Structural basis for nucleosome-mediated inhibition of cGAS activity. *Cell Res.* **30**, 1088–1097 (2020).

32. Zhao, B. *et al.* The molecular basis of tight nuclear tethering and inactivation of cGAS. *Nature* **587**, 673–677 (2020).

33. Michalski, S. *et al.* Structural basis for sequestration and autoinhibition of cGAS by chromatin. *Nature* **587**, 678–682 (2020).

34. De Oliveira Mann, C. C. & Hopfner, K. Nuclear cGAS: guard or prisoner? *EMBO J.* **40**, e108293 (2021).

35. Hopfner, K.-P. & Hornung, V. Molecular mechanisms and cellular functions of cGAS–STING signalling. *Nat. Rev. Mol. Cell Biol.* **21**, 501–521 (2020).

36. Ablasser, A. & Chen, Z. J. cGAS in action: Expanding roles in immunity and inflammation. *Science* **363**, eaat8657 (2019).

37. Mankan, A. K. *et al.* Cytosolic RNA:DNA hybrids activate the cGAS–STING axis. *EMBO J.* **33**, 2937–2946 (2014).

38. Ma, Y. *et al.* Roles of Emerging RNA-Binding Activity of cGAS in Innate Antiviral Response. *Front. Immunol.* **12**, 741599 (2021).

39. Typas, D. Breaking the loop: RNA–DNA hybrids escape to the cytoplasm. *Nat. Struct. Mol. Biol.* **30**, 134–134 (2023).

40. Crossley, M. P. *et al.* R-loop-derived cytoplasmic RNA–DNA hybrids activate an immune response. *Nature* **613**, 187–194 (2023).

41. Ishikawa, H. & Barber, G. N. STING is an endoplasmic reticulum adaptor that facilitates innate immune signalling. *Nature* **455**, 674–678 (2008).

42. Zhong, B. *et al.* The Adaptor Protein MITA Links Virus-Sensing Receptors to IRF3 Transcription Factor Activation. *Immunity* **29**, 538–550 (2008).

43. Decout, A., Katz, J. D., Venkatraman, S. & Ablasser, A. The cGAS–STING pathway as a therapeutic target in inflammatory diseases. *Nat. Rev. Immunol.* **21**, 548–569 (2021).

44. Gui, X. *et al.* Autophagy induction via STING trafficking is a primordial function of the cGAS pathway. *Nature* **567**, 262–266 (2019).

45. Spang, A. & Schekman, R. Reconstitution of Retrograde Transport from the Golgi to the ER In Vitro. *J. Cell Biol.* **143**, 589–599 (1998).

46. Deng, Z. *et al.* A defect in COPI-mediated transport of STING causes immune dysregulation in COPA syndrome. *J. Exp. Med.* **217**, e20201045 (2020).

47. Mukai, K. *et al.* Homeostatic regulation of STING by retrograde membrane traffic to the ER. *Nat. Commun.* **12**, 61 (2021).

48. Kim, J. *et al.* VDAC oligomers form mitochondrial pores to release mtDNA fragments and promote lupus-like disease. *Science* **366**, 1531–1536 (2019).

49. McArthur, K. *et al.* BAK/BAX macropores facilitate mitochondrial herniation and mtDNA efflux during apoptosis. *Science* **359**, eaao6047 (2018).

50. Sorouri, M., Chang, T. & Hancks, D. C. Mitochondria and Viral Infection: Advances and Emerging Battlefronts. *mBio* **13**, e02096-21 (2022).

51. Patrushev, M. *et al.* Mitochondrial permeability transition triggers the release of mtDNA fragments. *Cell. Mol. Life Sci.* **61**, 3100–3103 (2004).

52. Gao, D. *et al.* Cyclic GMP-AMP Synthase Is an Innate Immune Sensor of HIV and Other Retroviruses. *Science* **341**, 903–906 (2013).

53. Lahaye, X. *et al.* NONO Detects the Nuclear HIV Capsid to Promote cGAS-Mediated Innate Immune Activation. *Cell* **175**, 488-501.e22 (2018).

54. Siddiqui, M. A. *et al.* A Novel Phenotype Links HIV-1 Capsid Stability to cGAS-Mediated DNA Sensing. *J. Virol.* **93**, e00706-19 (2019).

55. Kumar, S., Morrison, J. H., Dingli, D. & Poeschla, E. HIV-1 Activation of Innate Immunity Depends Strongly on the Intracellular Level of TREX1 and Sensing of Incomplete Reverse Transcription Products. *J. Virol.* **92**, e00001-18 (2018).

56. Herzner, A.-M. *et al.* Sequence-specific activation of the DNA sensor cGAS by Y-form DNA structures as found in primary HIV-1 cDNA. *Nat. Immunol.* **16**, 1025–1033 (2015).

57. Reinert, L. S. *et al.* Sensing of HSV-1 by the cGAS–STING pathway in microglia orchestrates antiviral defence in the CNS. *Nat. Commun.* **7**, 13348 (2016).

58. Royer, D. J. & Carr, D. J. J. A STING-dependent innate-sensing pathway mediates resistance to corneal HSV-1 infection via upregulation of the antiviral effector tetherin. *Mucosal Immunol.* **9**, 1065–1075 (2016).

59. Parker, Z. M., Murphy, A. A. & Leib, D. A. Role of the DNA Sensor STING in Protection from Lethal Infection following Corneal and Intracerebral Challenge with Herpes Simplex Virus 1. *J. Virol.* **89**, 11080–11091 (2015).

60. Andreeva, L. *et al.* cGAS senses long and HMGB/TFAM-bound U-turn DNA by forming protein–DNA ladders. *Nature* **549**, 394–398 (2017).

61. Hoss, M. A human DNA editing enzyme homologous to the Escherichia coli DnaQ/MutD protein. *EMBO J.* **18**, 3868–3875 (1999).

62. Stetson, D. B., Ko, J. S., Heidmann, T. & Medzhitov, R. Trex1 Prevents Cell-Intrinsic Initiation of Autoimmunity. *Cell* **134**, 587–598 (2008).

63. Gao, D. *et al.* Activation of cyclic GMP-AMP synthase by self-DNA causes autoimmune diseases. *Proc. Natl. Acad. Sci.* **112**, (2015).

64. Crowl, J. T., Gray, E. E., Pestal, K., Volkman, H. E. & Stetson, D. B. Intracellular Nucleic Acid Detection in Autoimmunity. *Annu. Rev. Immunol.* **35**, 313–336 (2017).

65. Crow, Y. J. *et al.* Mutations in the gene encoding the 3'-5' DNA exonuclease TREX1 cause Aicardi-Goutières syndrome at the AGS1 locus. *Nat. Genet.* **38**, 917–920 (2006).

66. Banani, S. F., Lee, H. O., Hyman, A. A. & Rosen, M. K. Biomolecular condensates: organizers of cellular biochemistry. *Nat. Rev. Mol. Cell Biol.* **18**, 285–298 (2017).

67. Alberti, S., Gladfelter, A. & Mittag, T. Considerations and Challenges in Studying Liquid-Liquid Phase Separation and Biomolecular Condensates. *Cell* **176**, 419–434 (2019).

68. Larson, A. G. *et al.* Liquid droplet formation by HP1α suggests a role for phase separation in heterochromatin. *Nature* **547**, 236–240 (2017).

69. Strom, A. R. *et al.* Phase separation drives heterochromatin domain formation. *Nature* **547**, 241–245 (2017).

70. Schmidt, H. B. & Görlich, D. Transport Selectivity of Nuclear Pores, Phase Separation, and Membraneless Organelles. *Trends Biochem. Sci.* **41**, 46–61 (2016).

71. Su, X. *et al.* Phase separation of signaling molecules promotes T cell receptor signal transduction. *Science* **352**, 595–599 (2016).

72. Zhou, W., Mohr, L., Maciejowski, J. & Kranzusch, P. J. cGAS phase separation inhibits TREX1-mediated DNA degradation and enhances cytosolic DNA sensing. *Mol. Cell* **81**, 739-755.e7 (2021).

73. Ahn, J., Gutman, D., Saijo, S. & Barber, G. N. STING manifests self DNA-dependent inflammatory disease. *Proc. Natl. Acad. Sci.* **109**, 19386–19391 (2012).

74. Cordova, A. F., Ritchie, C., Böhnert, V. & Li, L. Human SLC46A2 Is the Dominant cGAMP Importer in Extracellular cGAMP-Sensing Macrophages and Monocytes. *ACS Cent. Sci.* **7**, 1073–1088 (2021).

75. Ritchie, C., Cordova, A. F., Hess, G. T., Bassik, M. C. & Li, L. SLC19A1 Is an Importer of the Immunotransmitter cGAMP. *Mol. Cell* **75**, 372-381.e5 (2019).

76. Luteijn, R. D. *et al.* SLC19A1 transports immunoreactive cyclic dinucleotides. *Nature* **573**, 434–438 (2019).

77. Lahey, L. J. *et al.* LRRC8A:C/E Heteromeric Channels Are Ubiquitous Transporters of cGAMP. *Mol. Cell* **80**, 578-591.e5 (2020).

78. Zhou, C. *et al.* Transfer of cGAMP into Bystander Cells via LRRC8 Volume-Regulated Anion Channels Augments STING-Mediated Interferon Responses and Anti-viral Immunity. *Immunity* **52**, 767-781.e6 (2020).

79. Zhou, Y. *et al.* Blockade of the Phagocytic Receptor MerTK on Tumor-Associated Macrophages Enhances P2X7R-Dependent STING Activation by Tumor-Derived cGAMP. *Immunity* **52**, 357-373.e9 (2020).

80. Maltbaek, J. H., Cambier, S., Snyder, J. M. & Stetson, D. B. ABCC1 transporter exports the immunostimulatory cyclic dinucleotide cGAMP. *Immunity* **55**, 1799-1812.e4 (2022).

81. Bridgeman, A. *et al.* Viruses transfer the antiviral second messenger cGAMP between cells. *Science* **349**, 1228–1232 (2015).

82. Gentili, M. *et al.* Transmission of innate immune signaling by packaging of cGAMP in viral particles. *Science* **349**, 1232–1236 (2015).

83. Carozza, J. A. *et al.* Extracellular cGAMP is a cancer-cell-produced immunotransmitter involved in radiation-induced anticancer immunity. *Nat. Cancer* **1**, 184–196 (2020).

84. Mardjuki, R. *et al.* Identification of the extracellular membrane protein ENPP3 as a major cGAMP hydrolase and innate immune checkpoint. *Cell Rep.* **43**, 114209 (2024).

85. Hou, Y. *et al.* SMPDL3A is a cGAMP-degrading enzyme induced by LXR-mediated lipid metabolism to restrict cGAS-STING DNA sensing. *Immunity* **56**, 2492-2507.e10 (2023).

86. Wang, Q. *et al.* The E3 ubiquitin ligase RNF185 facilitates the cGAS-mediated innate immune response. *PLOS Pathog.* **13**, e1006264 (2017).

87. Zhao, W. *et al.* Tripartite Motif-Containing Protein 38 Negatively Regulates TLR3/4- and RIG-I–Mediated IFN-β Production and Antiviral Response by Targeting NAP1. *J. Immunol.* **188**, 5311–5318 (2012).

88. Tsuchida, T. *et al.* The Ubiquitin Ligase TRIM56 Regulates Innate Immune Responses to Intracellular Double-Stranded DNA. *Immunity* **33**, 765–776 (2010).

89. Chen, M. *et al.* TRIM14 Inhibits cGAS Degradation Mediated by Selective Autophagy Receptor p62 to Promote Innate Immune Responses. *Mol. Cell* **64**, 105–119 (2016).

90. Zhong, B. *et al.* The Ubiquitin Ligase RNF5 Regulates Antiviral Responses by Mediating Degradation of the Adaptor Protein MITA. *Immunity* **30**, 397–407 (2009).

91. Cui, Y. *et al.* SENP7 Potentiates cGAS Activation by Relieving SUMO-Mediated Inhibition of Cytosolic DNA Sensing. *PLOS Pathog.* **13**, e1006156 (2017).

92. Hu, M.-M. *et al.* Sumoylation Promotes the Stability of the DNA Sensor cGAS and the Adaptor STING to Regulate the Kinetics of Response to DNA Virus. *Immunity* **45**, 555–569 (2016).

93. Xia, P. *et al.* Glutamylation of the DNA sensor cGAS regulates its binding and synthase activity in antiviral immunity. *Nat. Immunol.* **17**, 369–378 (2016).

94. Choudhuri, S. & Garg, N. J. PARP1-cGAS-NF-κB pathway of proinflammatory macrophage activation by extracellular vesicles released during Trypanosoma cruzi infection and Chagas disease. *PLOS Pathog.* **16**, e1008474 (2020).

95. Wang, F. *et al.* Cytoplasmic PARP1 links the genome instability to the inhibition of antiviral immunity through PARylating cGAS. *Mol. Cell* **82**, 2032-2049.e7 (2022).

96. Kim, C., Wang, X.-D. & Yu, Y. PARP1 inhibitors trigger innate immunity via PARP1 trapping-induced DNA damage response. *eLife* **9**, e60637 (2020).

97. Uggenti, C. *et al.* cGAS-mediated induction of type I interferon due to inborn errors of histone pre-mRNA processing. *Nat. Genet.* **52**, 1364–1372 (2020).

98. Rice, G. I. *et al.* Mutations in ADAR1 cause Aicardi-Goutières syndrome associated with a type I interferon signature. *Nat. Genet.* **44**, 1243–1248 (2012).

99. Rice, G. I. *et al.* Mutations involved in Aicardi-Goutières syndrome implicate SAMHD1 as regulator of the innate immune response. *Nat. Genet.* **41**, 829–832 (2009).

100. Rice, G. I. *et al.* Gain-of-function mutations in IFIH1 cause a spectrum of human disease phenotypes associated with upregulated type I interferon signaling. *Nat. Genet.* **46**, 503–509 (2014).

101. Crow, Y. J. *et al.* Mutations in genes encoding ribonuclease H2 subunits cause Aicardi-Goutières syndrome and mimic congenital viral brain infection. *Nat. Genet.* **38**, 910–916 (2006).

102. Rodero, M. P. & Crow, Y. J. Type I interferon–mediated monogenic autoinflammation: The type I interferonopathies, a conceptual overview. *J. Exp. Med.* **213**, 2527–2538 (2016).

103. Rahman, A. & Isenberg, D. A. Systemic Lupus Erythematosus. *N. Engl. J. Med.* **358**, 929–939 (2008).

104. Paul, B. D., Snyder, S. H. & Bohr, V. A. Signaling by cGAS–STING in Neurodegeneration, Neuroinflammation, and Aging. *Trends Neurosci.* **44**, 83–96 (2021).

105. Gulen, M. F. *et al.* cGAS–STING drives ageing-related inflammation and neurodegeneration. *Nature* **620**, 374–380 (2023).

106. Beernaert, B. & Parkes, E. E. cGAS–STING signalling in cancer: striking a balance with chromosomal instability. *Biochem. Soc. Trans.* **51**, 539–555 (2023).

107. Larkin, B. *et al.* Cutting Edge: Activation of STING in T Cells Induces Type I IFN Responses and Cell Death. *J. Immunol.* **199**, 397–402 (2017).

108. Concepcion, A. R. *et al.* The volume-regulated anion channel LRRC8C suppresses T cell function by regulating cyclic dinucleotide transport and STING–p53 signaling. *Nat. Immunol.* **23**, 287–302 (2022).

109. Cerboni, S. *et al.* Intrinsic antiproliferative activity of the innate sensor STING in T lymphocytes. *J. Exp. Med.* **214**, 1769–1785 (2017).

110. Imanishi, T. *et al.* Reciprocal regulation of STING and TCR signaling by mTORC1 for T-cell activation and function. *Life Sci. Alliance* **2**, e201800282 (2019).

111. Wu, J., Dobbs, N., Yang, K. & Yan, N. Interferon-Independent Activities of Mammalian STING Mediate Antiviral Response and Tumor Immune Evasion. *Immunity* **53**, 115-126.e5 (2020).

112. Wu, J. *et al*. STING-mediated disruption of calcium homeostasis chronically activates ER stress and primes T cell death. *J. Exp. Med.* **216**, 867–883 (2019).

113. Marcus, A. *et al*. Tumor-Derived cGAMP Triggers a STING-Mediated Interferon Response in Non-tumor Cells to Activate the NK Cell Response. *Immunity* **49**, 754-763.e4 (2018).

114. Zierhut, C. & Funabiki, H. Regulation and Consequences of cGAS Activation by Self-DNA. *Trends Cell Biol.* **30**, 594–605 (2020).

115. Xia, T., Konno, H., Ahn, J. & Barber, G. N. Deregulation of STING Signaling in Colorectal Carcinoma Constrains DNA Damage Responses and Correlates With Tumorigenesis. *Cell Rep.* **14**, 282–297 (2016).

116. Xia, T., Konno, H. & Barber, G. N. Recurrent Loss of STING Signaling in Melanoma Correlates with Susceptibility to Viral Oncolysis. *Cancer Res.* **76**, 6747–6759 (2016).

117. Konno, H. *et al*. Suppression of STING signaling through epigenetic silencing and missense mutation impedes DNA damage mediated cytokine production. *Oncogene* **37**, 2037–2051 (2018).

118. Liu, H. *et al*. Nuclear cGAS suppresses DNA repair and promotes tumorigenesis. *Nature* **563**, 131–136 (2018).

119. Chen, Q. *et al*. Carcinoma–astrocyte gap junctions promote brain metastasis by cGAMP transfer. *Nature* **533**, 493–498 (2016).

120. Bakhoum, S. F. *et al*. Chromosomal instability drives metastasis through a cytosolic DNA response. *Nature* **553**, 467–472 (2018).

121. Zhou, W. *et al*. Structure of the Human cGAS–DNA Complex Reveals Enhanced Control of Immune Surveillance. *Cell* **174**, 300-311.e11 (2018).

122. Luecke, S. *et al*. cGAS is activated by DNA in a length-dependent manner. *EMBO Rep*. **18**, 1707–1715 (2017).

123. Du, M. & Chen, Z. J. DNA-induced liquid phase condensation of cGAS activates innate immune signaling. *Science* **361**, 704–709 (2018).

124. Sun, B. *et al*. Dengue virus activates cGAS through the release of mitochondrial DNA. *Sci. Rep*. **7**, 3594 (2017).

125. Volkman, H. E., Cambier, S., Gray, E. E. & Stetson, D. B. Tight nuclear tethering of cGAS is essential for preventing autoreactivity. *eLife* **8**, e47491 (2019).

126. Zierhut, C. *et al*. The Cytoplasmic DNA Sensor cGAS Promotes Mitotic Cell Death. *Cell* **178**, 302-315.e23 (2019).

127. Gentili, M. *et al*. The N-Terminal Domain of cGAS Determines Preferential Association with Centromeric DNA and Innate Immune Activation in the Nucleus. *Cell Rep*. **26**, 2377-2393.e13 (2019).

128. Cutter, A. R. & Hayes, J. J. A brief review of nucleosome structure. *FEBS Lett*. **589**, 2914–2922 (2015).

129. Bednar, J. *et al*. Nucleosomes, linker DNA, and linker histone form a unique structural motif that directs the higher-order folding and compaction of chromatin. *Proc. Natl. Acad. Sci*. **95**, 14173–14178 (1998).

130. White, C. L., Suto, R. K. & Luger, K. Structure of the yeast nucleosome core particle reveals fundamental changes in internucleosome interactions. *EMBO J*. **20**, 5207–5218 (2001).

131. Luger, K., Mäder, A. W., Richmond, R. K., Sargent, D. F. & Richmond, T. J. Crystal structure of the nucleosome core particle at 2.8 Å resolution. *Nature* **389**, 251–260 (1997).

132. Lorch, Y., LaPointe, J. W. & Kornberg, R. D. Nucleosomes inhibit the initiation of transcription but allow chain elongation with the displacement of histones. *Cell* **49**, 203–210 (1987).

133. Han, M. & Grunstein, M. Nucleosome loss activates yeast downstream promoters in vivo. *Cell* **55**, 1137–1145 (1988).

134. Clark-Adams, C. D., Norris, D., Osley, M. A., Fassler, J. S. & Winston, F. Changes in histone gene dosage alter transcription in yeast. *Genes Dev.* **2**, 150–159 (1988).

135. Orzalli, M. H. *et al.* cGAS-mediated stabilization of IFI16 promotes innate signaling during herpes simplex virus infection. *Proc. Natl. Acad. Sci.* **112**, (2015).

136. Jiang, H. *et al.* Chromatin-bound cGAS is an inhibitor of DNA repair and hence accelerates genome destabilization and cell death. *EMBO J.* **38**, e102718 (2019).

137. Mackenzie, K. J. *et al.* cGAS surveillance of micronuclei links genome instability to innate immunity. *Nature* **548**, 461–465 (2017).

138. Kalashnikova, A. A., Porter-Goff, M. E., Muthurajan, U. M., Luger, K. & Hansen, J. C. The role of the nucleosome acidic patch in modulating higher order chromatin structure. *J. R. Soc. Interface* **10**, 20121022 (2013).

139. McGinty, R. K. & Tan, S. Recognition of the nucleosome by chromatin factors and enzymes. *Curr. Opin. Struct. Biol.* **37**, 54–61 (2016).

140. Xu, P. *et al.* The CRL5–SPSB3 ubiquitin ligase targets nuclear cGAS for degradation. *Nature* **627**, 873–879 (2024).

141. Sun, H. *et al.* A Nuclear Export Signal Is Required for cGAS to Sense Cytosolic DNA. *Cell Rep.* **34**, 108586 (2021).

142. Makde, R. D., England, J. R., Yennawar, H. P. & Tan, S. Structure of RCC1 chromatin factor bound to the nucleosome core particle. *Nature* **467**, 562–566 (2010).

143. Barbera, A. J. *et al.* The Nucleosomal Surface as a Docking Station for Kaposi's Sarcoma Herpesvirus LANA. *Science* **311**, 856–861 (2006).

144. Roussel, L., Erard, M., Cayrol, C. & Girard, J. Molecular mimicry between IL-33 and KSHV for attachment to chromatin through the H2A–H2B acidic pocket. *EMBO Rep.* **9**, 1006–1012 (2008).

145. Armache, K.-J., Garlick, J. D., Canzio, D., Narlikar, G. J. & Kingston, R. E. Structural Basis of Silencing: Sir3 BAH Domain in Complex with a Nucleosome at 3.0 Å Resolution. *Science* **334**, 977–982 (2011).

146. Kato, H. *et al.* Architecture of the high mobility group nucleosomal protein 2-nucleosome complex as revealed by methyl-based NMR. *Proc. Natl. Acad. Sci.* **108**, 12283–12288 (2011).

147. Chiu, Y.-H., MacMillan, J. B. & Chen, Z. J. RNA Polymerase III Detects Cytosolic DNA and Induces Type I Interferons through the RIG-I Pathway. *Cell* **138**, 576–591 (2009).

148. Ablasser, A. *et al.* RIG-I-dependent sensing of poly(dA:dT) through the induction of an RNA polymerase III–transcribed RNA intermediate. *Nat. Immunol.* **10**, 1065–1072 (2009).

149. Ferguson, B. J., Mansur, D. S., Peters, N. E., Ren, H. & Smith, G. L. DNA-PK is a DNA sensor for IRF-3-dependent innate immunity. *eLife* **1**, e00047 (2012).

150. Unterholzner, L. *et al.* IFI16 is an innate immune sensor for intracellular DNA. *Nat. Immunol.* **11**, 997–1004 (2010).

151. Kim, T. *et al.* Aspartate-glutamate-alanine-histidine box motif (DEAH)/RNA helicase A helicases sense microbial DNA in human plasmacytoid dendritic cells. *Proc. Natl. Acad. Sci.* **107**, 15181–15186 (2010).

152. Zhang, Z. *et al.* The helicase DDX41 senses intracellular DNA mediated by the adaptor STING in dendritic cells. *Nat. Immunol.* **12**, 959–965 (2011).

153. Kondo, T. *et al.* DNA damage sensor MRE11 recognizes cytosolic double-stranded DNA and induces type I interferon by regulating STING trafficking. *Proc. Natl. Acad. Sci.* **110**, 2969–2974 (2013).

154. Hornung, V. *et al.* AIM2 recognizes cytosolic dsDNA and forms a caspase-1-activating inflammasome with ASC. *Nature* **458**, 514–518 (2009).

155. Bürckstümmer, T. *et al.* An orthogonal proteomic-genomic screen identifies AIM2 as a cytoplasmic DNA sensor for the inflammasome. *Nat. Immunol.* **10**, 266–272 (2009).

156. Fernandes-Alnemri, T., Yu, J.-W., Datta, P., Wu, J. & Alnemri, E. S. AIM2 activates the inflammasome and cell death in response to cytoplasmic DNA. *Nature* **458**, 509–513 (2009).

157. Vance, R. E. Cytosolic DNA Sensing: The Field Narrows. *Immunity* **45**, 227–228 (2016).

158. Poltorak, A. *et al.* Defective LPS signaling in C3H/HeJ and C57BL/10ScCr mice: mutations in Tlr4 gene. *Science* **282**, 2085–2088 (1998).

159. Akira, S. & Takeda, K. Toll-like receptor signalling. *Nat. Rev. Immunol.* **4**, 499–511 (2004).

160. Kawasaki, T. & Kawai, T. Toll-Like Receptor Signaling Pathways. *Front. Immunol.* **5**, (2014).

161. Fitzgerald, K. A. & Kagan, J. C. Toll-like Receptors and the Control of Immunity. *Cell* **180**, 1044–1066 (2020).

162. Krug, A. *et al.* Herpes simplex virus type 1 activates murine natural interferon-producing cells through toll-like receptor 9. *Blood* **103**, 1433–1437 (2004).

163. Zhang, S.-Y. *et al.* TLR3 Deficiency in Patients with Herpes Simplex Encephalitis. *Science* **317**, 1522–1527 (2007).

164. Han, Y., Yan, C., Fishbain, S., Ivanov, I. & He, Y. Structural visualization of RNA polymerase III transcription machineries. *Cell Discov.* **4**, 40 (2018).

165. Cramer, P. *et al.* Structure of Eukaryotic RNA Polymerases. *Annu. Rev. Biophys.* **37**, 337–352 (2008).

166. Naesens, L., Haerynck, F. & Gack, M. U. The RNA polymerase III–RIG-I axis in antiviral immunity and inflammation. *Trends Immunol.* **44**, 435–449 (2023).

167. Galloway, A. & Cowling, V. H. mRNA cap regulation in mammalian cell function and fate. *Biochim. Biophys. Acta BBA - Gene Regul. Mech.* **1862**, 270–279 (2019).

168. Carter-Timofte, M. E., Paludan, S. R. & Mogensen, T. H. RNA Polymerase III as a Gatekeeper to Prevent Severe VZV Infections. *Trends Mol. Med.* **24**, 904–915 (2018).

169. Jehl, S. P., Nogueira, C. V., Zhang, X. & Starnbach, M. N. IFNγ Inhibits the Cytosolic Replication of Shigella flexneri via the Cytoplasmic RNA Sensor RIG-I. *PLoS Pathog.* **8**, e1002809 (2012).

170. Blackford, A. N. & Jackson, S. P. ATM, ATR, and DNA-PK: The Trinity at the Heart of the DNA Damage Response. *Mol. Cell* **66**, 801–817 (2017).

171. Zhang, X. *et al.* Cutting Edge: Ku70 Is a Novel Cytosolic DNA Sensor That Induces Type III Rather Than Type I IFN. *J. Immunol.* **186**, 4541–4545 (2011).

172. Peters, N. E. *et al.* A Mechanism for the Inhibition of DNA-PK-Mediated DNA Sensing by a Virus. *PLoS Pathog.* **9**, e1003649 (2013).

173. Burleigh, K. *et al.* Human DNA-PK activates a STING-independent DNA sensing pathway. *Sci. Immunol.* **5**, eaba4219 (2020).

174. Jin, T. *et al.* Structures of the HIN Domain:DNA Complexes Reveal Ligand Binding and Activation Mechanisms of the AIM2 Inflammasome and IFI16 Receptor. *Immunity* **36**, 561–571 (2012).

175. Almine, J. F. *et al.* IFI16 and cGAS cooperate in the activation of STING during DNA sensing in human keratinocytes. *Nat. Commun.* **8**, 14392 (2017).

176. Jiang, Z. *et al.* IFI16 directly senses viral RNA and enhances RIG-I transcription and activation to restrict influenza virus infection. *Nat. Microbiol.* **6**, 932–945 (2021).

177. Monroe, K. M. *et al.* IFI16 DNA Sensor Is Required for Death of Lymphoid CD4 T Cells Abortively Infected with HIV. *Science* **343**, 428–432 (2014).

178. Kerur, N. *et al.* IFI16 Acts as a Nuclear Pathogen Sensor to Induce the Inflammasome in Response to Kaposi Sarcoma-Associated Herpesvirus Infection. *Cell Host Microbe* **9**, 363–375 (2011).

179. Doitsh, G. *et al.* Cell death by pyroptosis drives CD4 T-cell depletion in HIV-1 infection. *Nature* **505**, 509–514 (2014).

180. Gray, E. E. *et al.* The AIM2-like Receptors Are Dispensable for the Interferon Response to Intracellular DNA. *Immunity* **45**, 255–266 (2016).

181. Rathinam, V. A. K. *et al.* The AIM2 inflammasome is essential for host defense against cytosolic bacteria and DNA viruses. *Nat. Immunol.* **11**, 395–402 (2010).

182. Wu, J., Fernandes-Alnemri, T. & Alnemri, E. S. Involvement of the AIM2, NLRC4, and NLRP3 Inflammasomes in Caspase-1 Activation by Listeria monocytogenes. *J. Clin. Immunol.* **30**, 693–702 (2010).

183. Karki, R. *et al.* Concerted Activation of the AIM2 and NLRP3 Inflammasomes Orchestrates Host Protection against Aspergillus Infection. *Cell Host Microbe* **17**, 357–368 (2015).

184. Thapa, R. J. *et al.* DAI Senses Influenza A Virus Genomic RNA and Activates RIPK3-Dependent Cell Death. *Cell Host Microbe* **20**, 674–681 (2016).

185. Maelfait, J. & Rehwinkel, J. The Z-nucleic acid sensor ZBP1 in health and disease. *J. Exp. Med.* **220**, e20221156 (2023).

186. Song, Q., Qi, Z., Wang, K. & Wang, N. Z-nucleic acid sensor ZBP1 in sterile inflammation. *Clin. Immunol.* **261**, 109938 (2024).

187. Maelfait, J. *et al.* Sensing of viral and endogenous RNA by ZBP 1/ DAI induces necroptosis. *EMBO J.* **36**, 2529–2543 (2017).

188. Kuriakose, T. *et al.* ZBP1/DAI is an innate sensor of influenza virus triggering the NLRP3 inflammasome and programmed cell death pathways. *Sci. Immunol.* **1**, (2016).

189. Vandenabeele, P., Bultynck, G. & Savvides, S. N. Pore-forming proteins as drivers of membrane permeabilization in cell death pathways. *Nat. Rev. Mol. Cell Biol.* **24**, 312–333 (2023).

190. Lei, Y. *et al.* Cooperative sensing of mitochondrial DNA by ZBP1 and cGAS promotes cardiotoxicity. *Cell* **186**, 3013-3032.e22 (2023).

191. Rehwinkel, J. *et al.* RIG-I Detects Viral Genomic RNA during Negative-Strand RNA Virus Infection. *Cell* **140**, 397–408 (2010).

192. Liu, G. & Gack, M. U. Distinct and Orchestrated Functions of RNA Sensors in Innate Immunity. *Immunity* **53**, 26–42 (2020).

193. Chow, K. T., Gale, M. & Loo, Y.-M. RIG-I and Other RNA Sensors in Antiviral Immunity. *Annu. Rev. Immunol.* **36**, 667–694 (2018).

194. Hornung, V. *et al.* 5'-Triphosphate RNA Is the Ligand for RIG-I. *Science* **314**, 994–997 (2006).

195. Pichlmair, A. *et al.* RIG-I-Mediated Antiviral Responses to Single-Stranded RNA Bearing 5'-Phosphates. *Science* **314**, 997–1001 (2006).

196. Kato, H. *et al.* Length-dependent recognition of double-stranded ribonucleic acids by retinoic acid–inducible gene-I and melanoma differentiation–associated gene 5. *J. Exp. Med.* **205**, 1601–1610 (2008).

197. Pichlmair, A. *et al.* Activation of MDA5 Requires Higher-Order RNA Structures Generated during Virus Infection. *J. Virol.* **83**, 10761–10769 (2009).

198. Horner, S. M., Liu, H. M., Park, H. S., Briley, J. & Gale, M. Mitochondrial-associated endoplasmic reticulum membranes (MAM) form innate immune synapses and are targeted by hepatitis C virus. *Proc. Natl. Acad. Sci.* **108**, 14590–14595 (2011).

199. Platanias, L. C. Mechanisms of type-I- and type-II-interferon-mediated signalling. *Nat. Rev. Immunol.* **5**, 375–386 (2005).

200. Negishi, H., Taniguchi, T. & Yanai, H. The Interferon (IFN) Class of Cytokines and the IFN Regulatory Factor (IRF) Transcription Factor Family. *Cold Spring Harb. Perspect. Biol.* **10**, a028423 (2018).

201. Lee, A. J. & Ashkar, A. A. The Dual Nature of Type I and Type II Interferons. *Front. Immunol.* **9**, 2061 (2018).

202. Hauptmann, R. & Swetly, P. A novel class of human type I interferons. *Nucleic Acids Res.* **13**, 4739–4749 (1985).

203. Fung, K. Y. *et al.* Interferon-ε Protects the Female Reproductive Tract from Viral and Bacterial Infection. *Science* **339**, 1088–1092 (2013).

204. LaFleur, D. W. *et al.* Interferon-κ, a Novel Type I Interferon Expressed in Human Keratinocytes. *J. Biol. Chem.* **276**, 39765–39771 (2001).

205. Green, D. S., Young, H. A. & Valencia, J. C. Current prospects of type II interferon γ signaling and autoimmunity. *J. Biol. Chem.* **292**, 13925–13933 (2017).

206. Schroder, K., Hertzog, P. J., Ravasi, T. & Hume, D. A. Interferon-γ: an overview of signals, mechanisms and functions. *J. Leukoc. Biol.* **75**, 163–189 (2004).

207. Österlund, P. I., Pietilä, T. E., Veckman, V., Kotenko, S. V. & Julkunen, I. IFN Regulatory Factor Family Members Differentially Regulate the Expression of Type III IFN (IFN-λ) Genes. *J. Immunol.* **179**, 3434–3442 (2007).

208. Thomson, S. J. P. *et al.* The role of transposable elements in the regulation of IFN-λ1 gene expression. *Proc. Natl. Acad. Sci.* **106**, 11564–11569 (2009).

209. De Weerd, N. A. *et al.* A hot spot on interferon α/β receptor subunit 1 (IFNAR1) underpins its interaction with interferon-β and dictates signaling. *J. Biol. Chem.* **292**, 7554–7565 (2017).

210. De Weerd, N. A. *et al.* Structural basis of a unique interferon-β signaling axis mediated via the receptor IFNAR1. *Nat. Immunol.* **14**, 901–907 (2013).

211. Park, A. & Iwasaki, A. Type I and Type III Interferons – Induction, Signaling, Evasion, and Application to Combat COVID-19. *Cell Host Microbe* **27**, 870–878 (2020).

212. Sommereyns, C., Paul, S., Staeheli, P. & Michiels, T. IFN-Lambda (IFN-λ) Is Expressed in a Tissue-Dependent Fashion and Primarily Acts on Epithelial Cells In Vivo. *PLoS Pathog.* **4**, e1000017 (2008).

213. Kim, S. *et al.* The Superiority of IFN-λ as a Therapeutic Candidate to Control Acute Influenza Viral Lung Infection. *Am. J. Respir. Cell Mol. Biol.* **56**, 202–212 (2017).

214. Davidson, S. *et al.* IFNλ is a potent anti-influenza therapeutic without the inflammatory side effects of IFNα treatment. *EMBO Mol. Med.* **8**, 1099–1112 (2016).

215. Galani, I. E. *et al.* Interferon-λ Mediates Non-redundant Front-Line Antiviral Protection against Influenza Virus Infection without Compromising Host Fitness. *Immunity* **46**, 875-890.e6 (2017).

216. Schoggins, J. W. & Rice, C. M. Interferon-stimulated genes and their antiviral effector functions. *Curr. Opin. Virol.* **1**, 519–525 (2011).

217. Schoggins, J. W. *et al.* A diverse range of gene products are effectors of the type I interferon antiviral response. *Nature* **472**, 481–485 (2011).

218. Teijaro, J. R. Type I interferons in viral control and immune regulation. *Curr. Opin. Virol.* **16**, 31–40 (2016).

219. Khanna, N. R. & Gerriets, V. Interferon. in *StatPearls* (StatPearls Publishing, Treasure Island (FL), 2024).

220. Chiang, J. J. *et al.* Viral unmasking of cellular 5S rRNA pseudogene transcripts induces RIG-I-mediated immunity. *Nat. Immunol.* **19**, 53–62 (2018).

221. Murali, A. *et al.* Structure and Function of LGP2, a DEX(D/H) Helicase That Regulates the Innate Immunity Response. *J. Biol. Chem.* **283**, 15825–15833 (2008).

222. Rothenfusser, S. *et al*. The RNA Helicase Lgp2 Inhibits TLR-Independent Sensing of Viral Replication by Retinoic Acid-Inducible Gene-I. *J. Immunol.* **175**, 5260–5268 (2005).

223. Yoneyama, M. *et al*. Shared and Unique Functions of the DExD/H-Box Helicases RIG-I, MDA5, and LGP2 in Antiviral Innate Immunity. *J. Immunol.* **175**, 2851–2858 (2005).

224. Komuro, A. & Horvath, C. M. RNA- and Virus-Independent Inhibition of Antiviral Signaling by RNA Helicase LGP2. *J. Virol.* **80**, 12332–12342 (2006).

225. Saito, T. *et al*. Regulation of innate antiviral defenses through a shared repressor domain in RIG-I and LGP2. *Proc. Natl. Acad. Sci.* **104**, 582–587 (2007).

226. Quicke, K. M., Kim, K. Y., Horvath, C. M. & Suthar, M. S. RNA Helicase LGP2 Negatively Regulates RIG-I Signaling by Preventing TRIM25-Mediated Caspase Activation and Recruitment Domain Ubiquitination. *J. Interferon Cytokine Res.* **39**, 669–683 (2019).

227. Venkataraman, T. *et al*. Loss of DExD/H Box RNA Helicase LGP2 Manifests Disparate Antiviral Responses. *J. Immunol.* **178**, 6444–6455 (2007).

228. Satoh, T. *et al*. LGP2 is a positive regulator of RIG-I– and MDA5-mediated antiviral responses. *Proc. Natl. Acad. Sci.* **107**, 1512–1517 (2010).

229. Liddicoat, B. J. *et al*. RNA editing by ADAR1 prevents MDA5 sensing of endogenous dsRNA as nonself. *Science* **349**, 1115–1120 (2015).

230. Pestal, K. *et al*. Isoforms of RNA-Editing Enzyme ADAR1 Independently Control Nucleic Acid Sensor MDA5-Driven Autoimmunity and Multi-organ Development. *Immunity* **43**, 933–944 (2015).

231. Mannion, N. M. *et al.* The RNA-Editing Enzyme ADAR1 Controls Innate Immune Responses to RNA. *Cell Rep.* **9**, 1482–1494 (2014).

232. Dong, H. & Shen, J. MAVS Ubiquitylation: Function, Mechanism, and Beyond. *Front. Biosci.-Landmark* **29**, 72 (2024).

233. Ren, Z. *et al.* Regulation of MAVS Expression and Signaling Function in the Antiviral Innate Immune Response. *Front. Immunol.* **11**, 1030 (2020).

234. Xu, H. *et al.* Correction: Structural basis for the prion-like MAVS filaments in antiviral innate immunity. *eLife* **4**, e07546 (2015).

235. Zeng, W. *et al.* Reconstitution of the RIG-I Pathway Reveals a Signaling Role of Unanchored Polyubiquitin Chains in Innate Immunity. *Cell* **141**, 315–330 (2010).

236. Karginov, T. A., Pastor, D. P. H., Semler, B. L. & Gomez, C. M. Mammalian Polycistronic mRNAs and Disease. *Trends Genet.* **33**, 129–142 (2017).

237. Samuel, C. E. Polycistronic Animal Virus mRNAs. in *Progress in Nucleic Acid Research and Molecular Biology* vol. 37 127–153 (Elsevier, 1989).

238. Sorokin, I. I. *et al.* Non-Canonical Translation Initiation Mechanisms Employed by Eukaryotic Viral mRNAs. *Biochem. Mosc.* **86**, 1060–1094 (2021).

239. Benitez-Cantos, M. S. *et al.* Translation initiation downstream from annotated start codons in human mRNAs coevolves with the Kozak context. *Genome Res.* **30**, 974–984 (2020).

240. Touriol, C. *et al.* Generation of protein isoform diversity by alternative initiation of translation at non-AUG codons. *Biol. Cell* **95**, 169–178 (2003).

241. Ferreira, J. P., Noderer, W. L., Diaz De Arce, A. J. & Wang, C. L. Engineering ribosomal leaky scanning and upstream open reading frames for precise control of protein translation. *Bioengineered* **5**, 186–192 (2014).

242. Brubaker, S. W., Gauthier, A. E., Mills, E. W., Ingolia, N. T. & Kagan, J. C. A Bicistronic MAVS Transcript Highlights a Class of Truncated Variants in Antiviral Immunity. *Cell* **156**, 800–811 (2014).

243. Qi, N. *et al.* Multiple truncated isoforms of MAVS prevent its spontaneous aggregation in antiviral innate immune signalling. *Nat. Commun.* **8**, 15676 (2017).

244. Liu, B. *et al.* The ubiquitin E3 ligase TRIM31 promotes aggregation and activation of the signaling adaptor MAVS through Lys63-linked polyubiquitination. *Nat. Immunol.* **18**, 214–224 (2017).

245. Liu, S. *et al.* MAVS recruits multiple ubiquitin E3 ligases to activate antiviral signaling cascades. *eLife* **2**, e00785 (2013).

246. Xue, B. *et al.* TRIM21 Promotes Innate Immune Response to RNA Viral Infection through Lys27-Linked Polyubiquitination of MAVS. *J. Virol.* **92**, e00321-18 (2018).

247. Castanier, C. *et al.* MAVS ubiquitination by the E3 ligase TRIM25 and degradation by the proteasome is involved in type I interferon production after activation of the antiviral RIG-I-like receptors. *BMC Biol.* **10**, 44 (2012).

248. Flotho, A. & Melchior, F. Sumoylation: A Regulatory Protein Modification in Health and Disease. *Annu. Rev. Biochem.* **82**, 357–385 (2013).

249. Vertegaal, A. C. O. Signalling mechanisms and cellular functions of SUMO. *Nat. Rev. Mol. Cell Biol.* **23**, 715–731 (2022).

250. Dai, T. *et al.* MAVS deSUMOylation by SENP1 inhibits its aggregation and antagonizes IRF3 activation. *Nat. Struct. Mol. Biol.* **30**, 785–799 (2023).

251. Liu, X. *et al.* Dual modifying of MAVS at lysine 7 by SIRT3-catalyzed deacetylation and SIRT5-catalyzed desuccinylation orchestrates antiviral innate immunity. *Proc. Natl. Acad. Sci.* **121**, e2314201121 (2024).

252. You, F. *et al.* PCBP2 mediates degradation of the adaptor MAVS via the HECT ubiquitin ligase AIP4. *Nat. Immunol.* **10**, 1300–1308 (2009).

253. Roberts, D. J. & Miyamoto, S. Hexokinase II integrates energy metabolism and cellular protection: Akting on mitochondria and TORCing to autophagy. *Cell Death Differ.* **22**, 248–257 (2015).

254. Ju, L.-G. *et al.* TTLL12 Inhibits the Activation of Cellular Antiviral Signaling through Interaction with VISA/MAVS. *J. Immunol.* **198**, 1274–1284 (2017).

255. Zhang, W. *et al.* Lactate Is a Natural Suppressor of RLR Signaling by Targeting MAVS. *Cell* **178**, 176-189.e15 (2019).

256. Wang, P. *et al.* UBXN1 Interferes with Rig-I-like Receptor-Mediated Antiviral Immune Response by Targeting MAVS. *Cell Rep.* **3**, 1057–1070 (2013).

257. Uchida, S., Horie, R., Sato, H., Kai, C. & Yoneda, M. Possible role of the Nipah virus V protein in the regulation of the interferon beta induction by interacting with UBX domain-containing protein1. *Sci. Rep.* **8**, 7682 (2018).

258. Matsushima-Miyagi, T. *et al.* TRAIL and Noxa Are Selectively Upregulated in Prostate Cancer Cells Downstream of the RIG-I/MAVS Signaling Pathway by Nonreplicating Sendai Virus Particles. *Clin. Cancer Res.* **18**, 6271–6283 (2012).

259. Kawaguchi, Y., Miyamoto, Y., Inoue, T. & Kaneda, Y. Efficient eradication of hormone-resistant human prostate cancers by inactivated Sendai virus particle. *Int. J. Cancer* **124**, 2478–2487 (2009).

260. Li, X.-D., Sun, L., Seth, R. B., Pineda, G. & Chen, Z. J. Hepatitis C virus protease NS3/4A cleaves mitochondrial antiviral signaling protein off the mitochondria to evade innate immunity. *Proc. Natl. Acad. Sci.* **102**, 17717–17722 (2005).

261. Mukherjee, A. *et al*. The Coxsackievirus B 3Cpro Protease Cleaves MAVS and TRIF to Attenuate Host Type I Interferon and Apoptotic Signaling. *PLoS Pathog*. **7**, e1001311 (2011).

262. Pang, L. *et al*. The suppression of innate immune response by human rhinovirus C. *Biochem*. *Biophys*. *Res*. *Commun*. **490**, 22–28 (2017).

263. Qian, S. *et al*. Seneca Valley Virus Suppresses Host Type I Interferon Production by Targeting Adaptor Proteins MAVS, TRIF, and TANK for Cleavage. *J. Virol*. **91**, e00823-17 (2017).

264. Wei, C. *et al*. The Hepatitis B Virus X Protein Disrupts Innate Immunity by Downregulating Mitochondrial Antiviral Signaling Protein. *J. Immunol*. **185**, 1158–1168 (2010).

265. Ekanayaka, P. *et al*. Inhibition of MAVS Aggregation-Mediated Type-I Interferon Signaling by Foot-and-Mouth Disease Virus VP3. *Viruses* **13**, 1776 (2021).

266. Boergeling, Y. *et al*. Evidence for a Novel Mechanism of Influenza Virus-Induced Type I Interferon Expression by a Defective RNA-Encoded Protein. *PLOS Pathog*. **11**, e1004924 (2015).

267. Varga, Z. T., Grant, A., Manicassamy, B. & Palese, P. Influenza Virus Protein PB1-F2 Inhibits the Induction of Type I Interferon by Binding to MAVS and Decreasing Mitochondrial Membrane Potential. *J. Virol*. **86**, 8359–8366 (2012).

268. Hsu, A. C.-Y. *et al*. MicroRNA-125a and -b inhibit A20 and MAVS to promote inflammation and impair antiviral response in COPD. *JCI Insight* **2**, e90443 (2017).

269. Shi, C.-S. *et al*. SARS-Coronavirus Open Reading Frame-9b Suppresses Innate Immunity by Targeting Mitochondria and the MAVS/TRAF3/TRAF6 Signalosome. *J. Immunol*. **193**, 3080–3089 (2014).

270. Gao, X. *et al*. Crystal structure of SARS-CoV-2 Orf9b in complex with human TOM70 suggests unusual virus-host interactions. *Nat. Commun*. **12**, 2843 (2021).

271. Steiner, S. *et al*. SARS-CoV-2 biology and host interactions. *Nat. Rev. Microbiol*. **22**, 206–225 (2024).

272. Jin, X. *et al*. Structural characterization of SARS-CoV-2 dimeric ORF9b reveals potential fold-switching trigger mechanism. *Sci. China Life Sci*. **66**, 152–164 (2023).

273. Caobi, A. & Saeed, M. Upping the ante: enhanced expression of interferon-antagonizing ORF6 and ORF9b proteins by SARS-CoV-2 variants of concern. *Curr. Opin. Microbiol*. **79**, 102454 (2024).

274. Cubuk, J. *et al*. The SARS-CoV-2 nucleocapsid protein is dynamic, disordered, and phase separates with RNA. *Nat. Commun*. **12**, 1936 (2021).

275. Wu, Y. *et al*. RNA-induced liquid phase separation of SARS-CoV-2 nucleocapsid protein facilitates NF-κB hyper-activation and inflammation. *Signal Transduct. Target. Ther*. **6**, 167 (2021).

276. Zhao, M. *et al*. GCG inhibits SARS-CoV-2 replication by disrupting the liquid phase condensation of its nucleocapsid protein. *Nat. Commun*. **12**, 2114 (2021).

277. Iserman, C. *et al*. Genomic RNA Elements Drive Phase Separation of the SARS-CoV-2 Nucleocapsid. *Mol. Cell* **80**, 1078-1091.e6 (2020).

278. Chen, H. *et al*. Liquid–liquid phase separation by SARS-CoV-2 nucleocapsid protein and RNA. *Cell Res*. **30**, 1143–1145 (2020).

279. Perdikari, T. M. *et al*. SARS-CoV-2 nucleocapsid protein phase-separates with RNA and with human hnRNPs. *EMBO J*. **39**, e106478 (2020).

280. Savastano, A., Ibáñez De Opakua, A., Rankovic, M. & Zweckstetter, M. Nucleocapsid protein of SARS-CoV-2 phase separates into RNA-rich polymerase-containing condensates. *Nat. Commun.* **11**, 6041 (2020).

281. Carlson, C. R. *et al.* Phosphoregulation of Phase Separation by the SARS-CoV-2 N Protein Suggests a Biophysical Basis for its Dual Functions. *Mol. Cell* **80**, 1092-1103.e4 (2020).

282. Wang, S. *et al.* Targeting liquid–liquid phase separation of SARS-CoV-2 nucleocapsid protein promotes innate antiviral immunity by elevating MAVS activity. *Nat. Cell Biol.* **23**, 718–732 (2021).

283. Zotta, A., Hooftman, A. & O'Neill, L. A. J. SARS-CoV-2 targets MAVS for immune evasion. *Nat. Cell Biol.* **23**, 682–683 (2021).

284. Hertzog, J. *et al.* Infection with a Brazilian isolate of Zika virus generates RIG-I stimulatory RNA and the viral NS5 protein blocks type I IFN induction and signaling. *Eur. J. Immunol.* **48**, 1120–1136 (2018).

285. Reus, J. B., Trivino-Soto, G. S., Wu, L. I., Kokott, K. & Lim, E. S. SV40 Large T Antigen Is Not Responsible for the Loss of STING in 293T Cells but Can Inhibit cGAS-STING Interferon Induction. *Viruses* **12**, 137 (2020).

286. Helle, F. *et al.* Biology of the BKPyV: An Update. *Viruses* **9**, 327 (2017).

287. DuBridge, R. B. *et al.* Analysis of Mutation in Human Cells by Using an Epstein-Barr Virus Shuttle System. *Mol. Cell. Biol.* **7**, 379–387 (1987).

288. Kawamoto, M. *et al.* Identification of Characteristic Genomic Markers in Human Hepatoma HuH-7 and Huh7.5.1-8 Cell Lines. *Front. Genet.* **11**, 546106 (2020).

289. Nightingale, K. *et al.* Human cytomegalovirus protein RL1 degrades the antiviral factor SLFN11 via recruitment of the CRL4 E3 ubiquitin ligase complex. Preprint at https://doi.org/10.1101/2021.05.14.444170 (2021).

290. Cohen, J. I. & Seidel, K. E. Generation of varicella-zoster virus (VZV) and viral mutants from cosmid DNAs: VZV thymidylate synthetase is not essential for replication in vitro. *Proc. Natl. Acad. Sci.* **90**, 7376–7380 (1993).

291. Warner, B. E. *et al.* Varicella-zoster virus early infection but not complete replication is required for the induction of chronic hypersensitivity in rat models of postherpetic neuralgia. *PLOS Pathog.* **17**, e1009689 (2021).

292. Hertzog, J. *et al.* Varicella-Zoster virus ORF9 is an antagonist of the DNA sensor cGAS. *EMBO J.* **41**, (2022).

293. Lebrec, V. *et al.* A microscopy reporter for cGAMP reveals rare cGAS activation following DNA damage, and a lack of correlation with micronuclear cGAS enrichment. Preprint at https://doi.org/10.1101/2024.05.13.593978 (2024).

294. Yoneyama, M. *et al.* The RNA helicase RIG-I has an essential function in double-stranded RNA-induced innate antiviral responses. *Nat. Immunol.* **5**, 730–737 (2004).

295. Riva, L. *et al.* ORF9p Phosphorylation by ORF47p Is Crucial for the Formation and Egress of Varicella-Zoster Virus Viral Particles. *J. Virol.* **87**, 2868–2881 (2013).

296. Hou, F. *et al.* MAVS Forms Functional Prion-like Aggregates to Activate and Propagate Antiviral Innate Immune Response. *Cell* **146**, 448–461 (2011).

297. Hertzog, J. & Rehwinkel, J. A simple transwell-based infection system for obtaining pure populations of VZV-infected cells. *J. Virol. Methods* **312**, 114661 (2023).

298. Jumper, J. *et al.* Highly accurate protein structure prediction with AlphaFold. *Nature* **596**, 583–589 (2021).

299. Varadi, M. *et al.* AlphaFold Protein Structure Database: massively expanding the structural coverage of protein-sequence space with high-accuracy models. *Nucleic Acids Res.* **50**, D439–D444 (2022).

300. Drosten, C. *et al.* Identification of a Novel Coronavirus in Patients with Severe Acute Respiratory Syndrome. *N. Engl. J. Med.* **348**, 1967–1976 (2003).

301. Peiris, J. *et al.* Coronavirus as a possible cause of severe acute respiratory syndrome. *The Lancet* **361**, 1319–1325 (2003).

302. Kuiken, T. *et al.* Newly discovered coronavirus as the primary cause of severe acute respiratory syndrome. *The Lancet* **362**, 263–270 (2003).

303. Zaki, A. M., Van Boheemen, S., Bestebroer, T. M., Osterhaus, A. D. M. E. & Fouchier, R. A. M. Isolation of a Novel Coronavirus from a Man with Pneumonia in Saudi Arabia. *N. Engl. J. Med.* **367**, 1814–1820 (2012).

304. Zhu, N. *et al.* A Novel Coronavirus from Patients with Pneumonia in China, 2019. *N. Engl. J. Med.* **382**, 727–733 (2020).

305. Preliminary phylogenetic analysis of 11 nCoV2019 genomes, 2020-01-19 - SARS-CoV-2 coronavirus / nCoV-2019 Genomic Epidemiology. *Virological* https://virological.org/t/preliminary-phylogenetic-analysis-of-11-ncov2019-genomes-2020-01-19/329 (2020).

306. Severe acute respiratory syndrome coronavirus 2 isolate Wuhan-Hu-1, complete genome. (2020).

307. Pekar, J. E. *et al.* The molecular epidemiology of multiple zoonotic origins of SARS-CoV-2. *Science* **377**, 960–966 (2022).

308. Voskarides, K. SARS-CoV-2: tracing the origin, tracking the evolution. *BMC Med. Genomics* **15**, 62 (2022).

309. WHO-Convened Global Study of Origins of SARS-CoV-2: China Part (Text Extract) | Infectious Diseases & Immunity. https://mednexus.org/doi/full/10.1097/ID9.0000000000000017.

310. Holmes, E. C. *et al.* The origins of SARS-CoV-2: A critical review. *Cell* **184**, 4848–4856 (2021).

311. Worobey, M. *et al.* The Huanan Seafood Wholesale Market in Wuhan was the early epicenter of the COVID-19 pandemic. *Science* **377**, 951–959 (2022).

312. Sparrer, M. N. *et al.* Role of Spillover and Spillback in SARS-CoV-2 Transmission and the Importance of One Health in Understanding the Dynamics of the COVID-19 Pandemic. *J. Clin. Microbiol.* **61**, e01610-22 (2023).

313. Xiao, X., Newman, C., Buesching, C. D., Macdonald, D. W. & Zhou, Z.-M. Animal sales from Wuhan wet markets immediately prior to the COVID-19 pandemic. *Sci. Rep.* **11**, 11898 (2021).

314. Freuling, C. M. *et al.* Susceptibility of Raccoon Dogs for Experimental SARS-CoV-2 Infection. *Emerg. Infect. Dis.* **26**, 2982–2985 (2020).

315. Porter, S. M., Hartwig, A. E., Bielefeldt-Ohmann, H., Bosco-Lauth, A. M. & Root, J. J. Susceptibility of wild canids to severe acute respiratory syndrome coronavirus 2 (SARS-CoV-2). Preprint at https://doi.org/10.1101/2022.01.27.478082 (2022).

316. Lin, X.-D. *et al.* Extensive diversity of coronaviruses in bats from China. *Virology* **507**, 1–10 (2017).

317. In coronavirus origins search in China, Enshi caves and wildlife farms draw new scrutiny - The Washington Post.

https://www.washingtonpost.com/world/asia_pacific/china-covid-bats-caves-hubei/2021/10/10/082eb8b6-1c32-11ec-bea8-308ea134594f_story.html.

318. Shi, Z. & Hu, Z. A review of studies on animal reservoirs of the SARS coronavirus. *Virus Res.* **133**, 74–87 (2008).

319. Brintnell, E., Gupta, M. & Anderson, D. W. Phylogenetic and Ancestral Sequence Reconstruction of SARS-CoV-2 Reveals Latent Capacity to Bind Human ACE2 Receptor. *J. Mol. Evol.* **89**, 656–664 (2021).

320. Islam, A. *et al.* Transmission dynamics and susceptibility patterns of SARS-CoV-2 in domestic, farmed and wild animals: Sustainable One Health surveillance for conservation and public health to prevent future epidemics and pandemics. *Transbound. Emerg. Dis.* **69**, 2523–2543 (2022).

321. Sánchez, C. A. *et al.* A strategy to assess spillover risk of bat SARS-related coronaviruses in Southeast Asia. *Nat. Commun.* **13**, 4380 (2022).

322. COVID-19 deaths | WHO COVID-19 dashboard. https://data.who.int/dashboards/covid19/deaths?n=o.

323. Lamers, M. M. & Haagmans, B. L. SARS-CoV-2 pathogenesis. *Nat. Rev. Microbiol.* **20**, 270–284 (2022).

324. Petersen, E. *et al.* Comparing SARS-CoV-2 with SARS-CoV and influenza pandemics. *Lancet Infect. Dis.* **20**, e238–e244 (2020).

325. Mahajan, S. *et al.* SARS-CoV-2 Infection Hospitalization Rate and Infection Fatality Rate Among the Non-Congregate Population in Connecticut. *Am. J. Med.* **134**, 812-816.e2 (2021).

326. Wiersinga, W. J., Rhodes, A., Cheng, A. C., Peacock, S. J. & Prescott, H. C. Pathophysiology, Transmission, Diagnosis, and Treatment of Coronavirus Disease 2019 (COVID-19): A Review. *JAMA* **324**, 782 (2020).

327. Karagiannidis, C., Windisch, W., McAuley, D. F., Welte, T. & Busse, R. Major differences in ICU admissions during the first and second COVID-19 wave in Germany. *Lancet Respir. Med.* **9**, e47–e48 (2021).

328. Karagiannidis, C. *et al.* Case characteristics, resource use, and outcomes of 10 021 patients with COVID-19 admitted to 920 German hospitals: an observational study. *Lancet Respir. Med.* **8**, 853–862 (2020).

329. Features, Evaluation, and Treatment of Coronavirus (COVID-19) - StatPearls - NCBI Bookshelf. https://www.ncbi.nlm.nih.gov/books/NBK554776/.

330. Ahmad, F. B., Cisewski, J. A., Miniño, A. & Anderson, R. N. Provisional Mortality Data — United States, 2020. *MMWR Morb. Mortal. Wkly. Rep.* **70**, 519–522 (2021).

331. Derqui, N. *et al.* Risk factors and vectors for SARS-CoV-2 household transmission: a prospective, longitudinal cohort study. *Lancet Microbe* **4**, e397–e408 (2023).

332. Kwon, T., Gaudreault, N. N. & Richt, J. A. Environmental Stability of SARS-CoV-2 on Different Types of Surfaces under Indoor and Seasonal Climate Conditions. *Pathogens* **10**, 227 (2021).

333. Ratnesar-Shumate, S. *et al.* Simulated Sunlight Rapidly Inactivates SARS-CoV-2 on Surfaces. *J. Infect. Dis.* **222**, 214–222 (2020).

334. Van Doremalen, N. *et al.* Aerosol and Surface Stability of SARS-CoV-2 as Compared with SARS-CoV-1. *N. Engl. J. Med.* **382**, 1564–1567 (2020).

335. Kwon, T., Osterrieder, N., Gaudreault, N. N. & Richt, J. A. Fomite Transmission of SARS-CoV-2 and Its Contributing Factors. *Pathogens* **12**, 364 (2023).

336. Sammartino, J. C. *et al.* Real-life lack of evidence of viable SARS-CoV-2 transmission via inanimate surfaces: The SURFACE study. *J. Infect. Public Health* **16**, 736–740 (2023).

337. Short, K. R. & Cowling, B. J. Assessing the potential for fomite transmission of SARS-CoV-2. *Lancet Microbe* **4**, e380–e381 (2023).

338. Stokes, E. K. *et al.* Coronavirus Disease 2019 Case Surveillance — United States, January 22–May 30, 2020. *MMWR Morb. Mortal. Wkly. Rep.* **69**, 759–765 (2020).

339. Singh, D. D., Han, I., Choi, E.-H. & Yadav, D. K. A Clinical Update on SARS-CoV-2: Pathology and Development of Potential Inhibitors. *Curr. Issues Mol. Biol.* **45**, 400–433 (2023).

340. Liu, Q., Chi, S., Dmytruk, K., Dmytruk, O. & Tan, S. Coronaviral Infection and Interferon Response: The Virus-Host Arms Race and COVID-19. *Viruses* **14**, 1349 (2022).

341. Rabaan, A. A. *et al.* Role of Inflammatory Cytokines in COVID-19 Patients: A Review on Molecular Mechanisms, Immune Functions, Immunopathology and Immunomodulatory Drugs to Counter Cytokine Storm. *Vaccines* **9**, 436 (2021).

342. Chen, Y. *et al.* The presence of SARS-CoV-2 RNA in the feces of COVID-19 patients. *J. Med. Virol.* **92**, 833–840 (2020).

343. Wang, W. *et al.* Detection of SARS-CoV-2 in Different Types of Clinical Specimens. *JAMA* (2020) doi:10.1001/jama.2020.3786.

344. Baba, R. *et al.* Angiotensin-converting enzyme 2 expression is not induced by the renin–angiotensin system in the lung. *ERJ Open Res.* **6**, 00402–02020 (2020).

345. Zhou, F. *et al.* Clinical course and risk factors for mortality of adult inpatients with COVID-19 in Wuhan, China: a retrospective cohort study. *The Lancet* **395**, 1054–1062 (2020).

346. Williamson, E. J. *et al.* Factors associated with COVID-19-related death using OpenSAFELY. *Nature* **584**, 430–436 (2020).

347. Grasselli, G. *et al.* Baseline Characteristics and Outcomes of 1591 Patients Infected With SARS-CoV-2 Admitted to ICUs of the Lombardy Region, Italy. *JAMA* **323**, 1574 (2020).

348. O'Driscoll, M. *et al.* Age-specific mortality and immunity patterns of SARS-CoV-2. *Nature* **590**, 140–145 (2021).

349. Romano, S. D. *et al.* Trends in Racial and Ethnic Disparities in COVID-19 Hospitalizations, by Region — United States, March–December 2020. *MMWR Morb. Mortal. Wkly. Rep.* **70**, 560–565 (2021).

350. Sze, S. *et al.* Ethnicity and clinical outcomes in COVID-19: A systematic review and meta-analysis. *EClinicalMedicine* **29–30**, 100630 (2020).

351. Zhang, Q. *et al.* Inborn errors of type I IFN immunity in patients with life-threatening COVID-19. *Science* **370**, eabd4570 (2020).

352. Asano, T. *et al.* X-linked recessive TLR7 deficiency in ~1% of men under 60 years old with life-threatening COVID-19. *Sci. Immunol.* **6**, eabl4348 (2021).

353. Bastard, P. *et al.* Autoantibodies against type I IFNs in patients with life-threatening COVID-19. *Science* **370**, eabd4585 (2020).

354. Koning, R. *et al*. Autoantibodies against type I interferons are associated with multi-organ failure in COVID-19 patients. *Intensive Care Med*. **47**, 704–706 (2021).

355. Bastard, P. *et al*. Autoantibodies neutralizing type I IFNs are present in ~4% of uninfected individuals over 70 years old and account for ~20% of COVID-19 deaths. *Sci. Immunol*. **6**, eabl4340 (2021).

356. Coronaviridae Study Group of the International Committee on Taxonomy of Viruses *et al*. The species Severe acute respiratory syndrome-related coronavirus: classifying 2019-nCoV and naming it SARS-CoV-2. *Nat. Microbiol*. **5**, 536–544 (2020).

357. Wu, F. *et al*. A new coronavirus associated with human respiratory disease in China. *Nature* **579**, 265–269 (2020).

358. Bhatt, P. R. *et al*. Structural basis of ribosomal frameshifting during translation of the SARS-CoV-2 RNA genome. *Science* **372**, 1306–1313 (2021).

359. Su, M.-C. An atypical RNA pseudoknot stimulator and an upstream attenuation signal for -1 ribosomal frameshifting of SARS coronavirus. *Nucleic Acids Res*. **33**, 4265–4275 (2005).

360. Jungreis, I., Sealfon, R. & Kellis, M. SARS-CoV-2 gene content and COVID-19 mutation impact by comparing 44 Sarbecovirus genomes. *Nat. Commun*. **12**, 2642 (2021).

361. V'kovski, P., Kratzel, A., Steiner, S., Stalder, H. & Thiel, V. Coronavirus biology and replication: implications for SARS-CoV-2. *Nat. Rev. Microbiol*. **19**, 155–170 (2021).

362. Wong, L.-Y. R. & Perlman, S. Immune dysregulation and immunopathology induced by SARS-CoV-2 and related coronaviruses — are we our own worst enemy? *Nat. Rev. Immunol*. **22**, 47–56 (2022).

363. Redondo, N., Zaldívar-López, S., Garrido, J. J. & Montoya, M. SARS-CoV-2 Accessory Proteins in Viral Pathogenesis: Knowns and Unknowns. *Front. Immunol.* **12**, 708264 (2021).

364. Zhou, P. *et al.* A pneumonia outbreak associated with a new coronavirus of probable bat origin. *Nature* **579**, 270–273 (2020).

365. Hulswit, R. J. G., De Haan, C. A. M. & Bosch, B.-J. Coronavirus Spike Protein and Tropism Changes. in *Advances in Virus Research* vol. 96 29–57 (Elsevier, 2016).

366. Jackson, C. B., Farzan, M., Chen, B. & Choe, H. Mechanisms of SARS-CoV-2 entry into cells. *Nat. Rev. Mol. Cell Biol.* **23**, 3–20 (2022).

367. Robbiani, D. F. *et al.* Convergent antibody responses to SARS-CoV-2 in convalescent individuals. *Nature* **584**, 437–442 (2020).

368. Hansen, J. *et al.* Studies in humanized mice and convalescent humans yield a SARS-CoV-2 antibody cocktail. *Science* **369**, 1010–1014 (2020).

369. Pinto, D. *et al.* Cross-neutralization of SARS-CoV-2 by a human monoclonal SARS-CoV antibody. *Nature* **583**, 290–295 (2020).

370. Yuan, M. *et al.* A highly conserved cryptic epitope in the receptor binding domains of SARS-CoV-2 and SARS-CoV. *Science* **368**, 630–633 (2020).

371. Liu, L. *et al.* Potent neutralizing antibodies against multiple epitopes on SARS-CoV-2 spike. *Nature* **584**, 450–456 (2020).

372. Chi, X. *et al.* A neutralizing human antibody binds to the N-terminal domain of the Spike protein of SARS-CoV-2. *Science* **369**, 650–655 (2020).

373. Harvey, W. T. *et al.* SARS-CoV-2 variants, spike mutations and immune escape. *Nat. Rev. Microbiol.* **19**, 409–424 (2021).

374. Meng, B. *et al.* SARS-CoV-2 spike N-terminal domain modulates TMPRSS2-dependent viral entry and fusogenicity. *Cell Rep.* **40**, 111220 (2022).

375. Hoffmann, M. *et al.* SARS-CoV-2 Cell Entry Depends on ACE2 and TMPRSS2 and Is Blocked by a Clinically Proven Protease Inhibitor. *Cell* **181**, 271-280.e8 (2020).

376. Zhao, M.-M. *et al.* Cathepsin L plays a key role in SARS-CoV-2 infection in humans and humanized mice and is a promising target for new drug development. *Signal Transduct. Target. Ther.* **6**, 134 (2021).

377. Li, W. *et al.* Angiotensin-converting enzyme 2 is a functional receptor for the SARS coronavirus. *Nature* **426**, 450–454 (2003).

378. Beumer, J. *et al.* A CRISPR/Cas9 genetically engineered organoid biobank reveals essential host factors for coronaviruses. *Nat. Commun.* **12**, 5498 (2021).

379. Ziegler, C. G. K. *et al.* SARS-CoV-2 Receptor ACE2 Is an Interferon-Stimulated Gene in Human Airway Epithelial Cells and Is Detected in Specific Cell Subsets across Tissues. *Cell* **181**, 1016-1035.e19 (2020).

380. Lamers, M. M. *et al.* Human airway cells prevent SARS-CoV-2 multibasic cleavage site cell culture adaptation. *eLife* **10**, e66815 (2021).

381. Mykytyn, A. Z. *et al.* SARS-CoV-2 entry into human airway organoids is serine protease-mediated and facilitated by the multibasic cleavage site. *eLife* **10**, e64508 (2021).

382. Hoffmann, M., Kleine-Weber, H. & Pöhlmann, S. A Multibasic Cleavage Site in the Spike Protein of SARS-CoV-2 Is Essential for Infection of Human Lung Cells. *Mol. Cell* **78**, 779-784.e5 (2020).

383. Hoffmann, M. *et al.* Chloroquine does not inhibit infection of human lung cells with SARS-CoV-2. *Nature* **585**, 588–590 (2020).

384. Ogando, N. S. *et al.* SARS-coronavirus-2 replication in Vero E6 cells: replication kinetics, rapid adaptation and cytopathology. *J. Gen. Virol.* **101**, 925–940 (2020).

385. Cortese, M. *et al.* Integrative Imaging Reveals SARS-CoV-2-Induced Reshaping of Subcellular Morphologies. *Cell Host Microbe* **28**, 853-866.e5 (2020).

386. Wolff, G., Melia, C. E., Snijder, E. J. & Bárcena, M. Double-Membrane Vesicles as Platforms for Viral Replication. *Trends Microbiol.* **28**, 1022–1033 (2020).

387. Finkel, Y. *et al.* The coding capacity of SARS-CoV-2. *Nature* **589**, 125–130 (2021).

388. Lu, S. *et al.* The SARS-CoV-2 nucleocapsid phosphoprotein forms mutually exclusive condensates with RNA and the membrane-associated M protein. *Nat. Commun.* **12**, 502 (2021).

389. Yao, H. *et al.* Molecular Architecture of the SARS-CoV-2 Virus. *Cell* **183**, 730-738.e13 (2020).

390. Ghosh, S. *et al.* β-Coronaviruses Use Lysosomes for Egress Instead of the Biosynthetic Secretory Pathway. *Cell* **183**, 1520-1535.e14 (2020).

391. Tancini, B. *et al.* Lysosomal Exocytosis: The Extracellular Role of an Intracellular Organelle. *Membranes* **10**, 406 (2020).

392. Caldera-Crespo, L. A. *et al.* Experimental Models of COVID-19. *Front. Cell. Infect. Microbiol.* **11**, 792584 (2022).

393. Pires De Souza, G. A. *et al.* Choosing a cellular model to study SARS-CoV-2. *Front. Cell. Infect. Microbiol.* **12**, 1003608 (2022).

394. Matsuyama, S. *et al.* Enhanced isolation of SARS-CoV-2 by TMPRSS2-expressing cells. *Proc. Natl. Acad. Sci.* **117**, 7001–7003 (2020).

395. Saccon, E. *et al.* Cell-type-resolved quantitative proteomics map of interferon response against SARS-CoV-2. *iScience* **24**, 102420 (2021).

396. Shuai, H. *et al.* Differential immune activation profile of SARS-CoV-2 and SARS-CoV infection in human lung and intestinal cells: Implications for treatment with IFN-β and IFN inducer. *J. Infect.* **81**, e1–e10 (2020).

397. Cinatl, J. *et al.* Infection of cultured intestinal epithelial cells with severe acute respiratory syndrome coronavirus. *Cell. Mol. Life Sci. CMLS* **61**, 2100–2112 (2004).

398. Bojkova, D. *et al.* Proteomics of SARS-CoV-2-infected host cells reveals therapy targets. *Nature* **583**, 469–472 (2020).

399. Freymuth, F. *et al.* Replication of respiratory viruses, particularly influenza virus, rhinovirus, and coronavirus in HuH7 hepatocarcinoma cell line. *J. Med. Virol.* **77**, 295–301 (2005).

400. Sampaio, N. G. *et al.* The RNA sensor MDA5 detects SARS-CoV-2 infection. *Sci. Rep.* **11**, 13638 (2021).

401. Harcourt, J. *et al.* Severe Acute Respiratory Syndrome Coronavirus 2 from Patient with Coronavirus Disease, United States. *Emerg. Infect. Dis.* **26**, 1266–1273 (2020).

402. Ou, X. *et al.* Characterization of spike glycoprotein of SARS-CoV-2 on virus entry and its immune cross-reactivity with SARS-CoV. *Nat. Commun.* **11**, 1620 (2020).

403. Mirabelli, C. *et al.* Morphological Cell Profiling of SARS-CoV-2 Infection Identifies Drug Repurposing Candidates for COVID-19. Preprint at https://doi.org/10.1101/2020.05.27.117184 (2020).

404. Chen, X. *et al.* Type-I interferon signatures in SARS-CoV-2 infected Huh7 cells. *Cell Death Discov.* **7**, 114 (2021).

405. Harcourt, J. *et al.* Isolation and characterization of SARS-CoV-2 from the first US COVID-19 patient. Preprint at https://doi.org/10.1101/2020.03.02.972935 (2020).

406. Xie, X. *et al.* A nanoluciferase SARS-CoV-2 for rapid neutralization testing and screening of anti-infective drugs for COVID-19. *Nat. Commun.* **11**, 5214 (2020).

407. Weston, S. *et al.* Broad Anti-coronavirus Activity of Food and Drug Administration-Approved Drugs against SARS-CoV-2 In Vitro and SARS-CoV In Vivo. *J. Virol.* **94**, e01218-20 (2020).

408. Napolitano, V. *et al.* Acriflavine, a clinically approved drug, inhibits SARS-CoV-2 and other betacoronaviruses. *Cell Chem. Biol.* **29**, 774-784.e8 (2022).

409. Plaze, M. *et al.* Inhibition of the replication of SARS-CoV-2 in human cells by the FDA-approved drug chlorpromazine. *Int. J. Antimicrob. Agents* **57**, 106274 (2021).

410. Pyrć, K. *et al.* SARS-CoV-2 inhibition using a mucoadhesive, amphiphilic chitosan that may serve as an anti-viral nasal spray. *Sci. Rep.* **11**, 20012 (2021).

411. Warner, F. J. *et al.* Angiotensin-converting Enzyme 2 (ACE2), But Not ACE, Is Preferentially Localized to the Apical Surface of Polarized Kidney Cells. *J. Biol. Chem.* **280**, 39353–39362 (2005).

412. Modrof, J. *et al.* SARS-CoV-2 and the safety margins of cell-based biological medicinal products. *Biologicals* **68**, 122–124 (2020).

413. Martin-Sancho, L. *et al.* Functional landscape of SARS-CoV-2 cellular restriction. *Mol. Cell* **81**, 2656-2668.e8 (2021).

414. Ranga, A., Gjorevski, N. & Lutolf, M. P. Drug discovery through stem cell-based organoid models. *Adv. Drug Deliv. Rev.* **69–70**, 19–28 (2014).

415. Clevers, H. Modeling Development and Disease with Organoids. *Cell* **165**, 1586–1597 (2016).

416. Sridhar, A. *et al.* A Perspective on Organoids for Virology Research. *Viruses* **12**, 1341 (2020).

417. Hautefort, I., Poletti, M., Papp, D. & Korcsmaros, T. Everything You Always Wanted to Know About Organoid-Based Models (and Never Dared to Ask). *Cell. Mol. Gastroenterol. Hepatol.* **14**, 311–331 (2022).

418. Han, Y., Yang, L., Lacko, L. A. & Chen, S. Human organoid models to study SARS-CoV-2 infection. *Nat. Methods* **19**, 418–428 (2022).

419. Muñoz-Fontela, C. *et al.* Animal models for COVID-19. *Nature* **586**, 509–515 (2020).

420. Zhai, X. *et al.* Comparison of Severe Acute Respiratory Syndrome Coronavirus 2 Spike Protein Binding to ACE2 Receptors from Human, Pets, Farm Animals, and Putative Intermediate Hosts. *J. Virol.* **94**, e00831-20 (2020).

421. Fan, C. *et al.* Animal models for COVID-19: advances, gaps and perspectives. *Signal Transduct. Target. Ther.* **7**, 220 (2022).

422. Winkler, E. S. *et al.* SARS-CoV-2 infection of human ACE2-transgenic mice causes severe lung inflammation and impaired function. *Nat. Immunol.* **21**, 1327–1335 (2020).

423. Oladunni, F. S. *et al.* Lethality of SARS-CoV-2 infection in K18 human angiotensin-converting enzyme 2 transgenic mice. *Nat. Commun.* **11**, 6122 (2020).

424. Blanco-Melo, D. *et al.* Imbalanced Host Response to SARS-CoV-2 Drives Development of COVID-19. *Cell* **181**, 1036-1045.e9 (2020).

425. Iwatsuki-Horimoto, K. *et al.* Syrian Hamster as an Animal Model for the Study of Human Influenza Virus Infection. *J. Virol.* **92**, e01693-17 (2018).

426. Roberts, A. *et al.* Severe Acute Respiratory Syndrome Coronavirus Infection of Golden Syrian Hamsters. *J. Virol.* **79**, 503–511 (2005).

427. Wold, W. S. M. & Toth, K. Syrian Hamster as an Animal Model to Study Oncolytic Adenoviruses and to Evaluate the Efficacy of Antiviral Compounds. in *Advances in Cancer Research* vol. 115 69–92 (Elsevier, 2012).

428. Miao, J., Chard, L. S., Wang, Z. & Wang, Y. Syrian Hamster as an Animal Model for the Study on Infectious Diseases. *Front. Immunol.* **10**, 2329 (2019).

429. Chan, J. F.-W. *et al.* Simulation of the Clinical and Pathological Manifestations of Coronavirus Disease 2019 (COVID-19) in a Golden Syrian Hamster Model: Implications for Disease Pathogenesis and Transmissibility. *Clin. Infect. Dis.* ciaa325 (2020) doi:10.1093/cid/ciaa325.

430. Osterrieder, N. *et al.* Age-Dependent Progression of SARS-CoV-2 Infection in Syrian Hamsters. *Viruses* **12**, 779 (2020).

431. Imai, M. *et al.* Syrian hamsters as a small animal model for SARS-CoV-2 infection and countermeasure development. *Proc. Natl. Acad. Sci.* **117**, 16587–16595 (2020).

432. Rockx, B. *et al.* Comparative pathogenesis of COVID-19, MERS, and SARS in a nonhuman primate model. *Science* **368**, 1012–1015 (2020).

433. Munster, V. J. *et al.* Respiratory disease in rhesus macaques inoculated with SARS-CoV-2. *Nature* **585**, 268–272 (2020).

434. Chandrashekar, A. *et al.* SARS-CoV-2 infection protects against rechallenge in rhesus macaques. *Science* **369**, 812–817 (2020).

435. Yu, J. *et al.* DNA vaccine protection against SARS-CoV-2 in rhesus macaques. *Science* **369**, 806–811 (2020).

436. Gao, Q. *et al.* Development of an inactivated vaccine candidate for SARS-CoV-2. *Science* **369**, 77–81 (2020).

437. Mercado, N. B. *et al.* Single-shot Ad26 vaccine protects against SARS-CoV-2 in rhesus macaques. *Nature* **586**, 583–588 (2020).

438. Van Doremalen, N. *et al.* ChAdOx1 nCoV-19 vaccine prevents SARS-CoV-2 pneumonia in rhesus macaques. *Nature* **586**, 578–582 (2020).

439. Corbett, K. S. *et al.* Evaluation of the mRNA-1273 Vaccine against SARS-CoV-2 in Nonhuman Primates. *N. Engl. J. Med.* **383**, 1544–1555 (2020).

440. Morrison, H., Jackson, S. & McShane, H. Controlled human infection models in COVID-19 and tuberculosis: current progress and future challenges. *Front. Immunol.* **14**, 1211388 (2023).

441. Jackson, S. *et al.* Safety, tolerability, viral kinetics, and immune correlates of protection in healthy, seropositive UK adults inoculated with SARS-CoV-2: a single-centre, open-label, phase 1 controlled human infection study. *Lancet Microbe* **5**, 655–668 (2024).

442. Williams, E. *et al.* Ethics review of COVID-19 human challenge studies: A joint HRA/WHO workshop. *Vaccine* **40**, 3484–3489 (2022).

443. Killingley, B. *et al.* Safety, tolerability and viral kinetics during SARS-CoV-2 human challenge in young adults. *Nat. Med.* **28**, 1031–1041 (2022).

444. Walker, A. P. *et al.* The SARS-CoV-2 RNA polymerase is a viral RNA capping enzyme. *Nucleic Acids Res.* **49**, 13019–13030 (2021).

445. Pan, R. *et al.* N7-Methylation of the Coronavirus RNA Cap Is Required for Maximal Virulence by Preventing Innate Immune Recognition. *mBio* **13**, e03662-21 (2022).

446. Russ, A. *et al.* Nsp16 shields SARS–CoV-2 from efficient MDA5 sensing and IFIT1-mediated restriction. *EMBO Rep.* **23**, e55648 (2022).

447. Decroly, E., Ferron, F., Lescar, J. & Canard, B. Conventional and unconventional mechanisms for capping viral mRNA. *Nat. Rev. Microbiol.* **10**, 51–65 (2012).

448. Kikkert, M. Innate Immune Evasion by Human Respiratory RNA Viruses. *J. Innate Immun.* **12**, 4–20 (2020).

449. Zheng, M. *et al.* TLR2 senses the SARS-CoV-2 envelope protein to produce inflammatory cytokines. *Nat. Immunol.* **22**, 829–838 (2021).

450. Planès, R., Bert, J.-B., Tairi, S., BenMohamed, L. & Bahraoui, E. SARS-CoV-2 Envelope (E) Protein Binds and Activates TLR2 Pathway: A Novel Molecular Target for COVID-19 Interventions. *Viruses* **14**, 999 (2022).

451. Moreno-Eutimio, M. A., López-Macías, C. & Pastelin-Palacios, R. Bioinformatic analysis and identification of single-stranded RNA sequences recognized by TLR7/8 in the SARS-CoV-2, SARS-CoV, and MERS-CoV genomes. *Microbes Infect.* **22**, 226–229 (2020).

452. Choudhury, A. & Mukherjee, S. In silico studies on the comparative characterization of the interactions of SARS-CoV-2 spike glycoprotein with ACE-2 receptor homologs and human TLRs. *J. Med. Virol.* **92**, 2105–2113 (2020).

453. Bortolotti, D. *et al.* TLR3 and TLR7 RNA Sensor Activation during SARS-CoV-2 Infection. *Microorganisms* **9**, 1820 (2021).

454. Yin, X. *et al.* MDA5 Governs the Innate Immune Response to SARS-CoV-2 in Lung Epithelial Cells. *Cell Rep.* **34**, 108628 (2021).

455. Yang, D.-M., Geng, T.-T., Harrison, A. G. & Wang, P.-H. Differential roles of RIG-I like receptors in SARS-CoV-2 infection. *Mil. Med. Res.* **8**, 49 (2021).

456. Thorne, L. G. *et al.* SARS-CoV-2 sensing by RIG-I and MDA5 links epithelial infection to macrophage inflammation. *EMBO J.* **40**, e107826 (2021).

457. Rebendenne, A. *et al.* SARS-CoV-2 Triggers an MDA-5-Dependent Interferon Response Which Is Unable To Control Replication in Lung Epithelial Cells. *J. Virol.* **95**, e02415-20 (2021).

458. Frazier, M. N. *et al.* Flipped over U: structural basis for dsRNA cleavage by the SARS-CoV-2 endoribonuclease. *Nucleic Acids Res.* **50**, 8290–8301 (2022).

459. Ancar, R. *et al.* Physiologic RNA targets and refined sequence specificity of coronavirus EndoU. *RNA* **26**, 1976–1999 (2020).

460. Hackbart, M., Deng, X. & Baker, S. C. Coronavirus endoribonuclease targets viral polyuridine sequences to evade activating host sensors. *Proc. Natl. Acad. Sci.* **117**, 8094–8103 (2020).

461. Targhetta, V. P., Amaral, M. A. & Camara, N. O. S. Through DNA sensors and hidden mitochondrial effects of SARS-CoV-2. *J. Venom. Anim. Toxins Trop. Dis.* **27**, e20200183 (2021).

462. Kim, J., Kim, H.-S. & Chung, J. H. Molecular mechanisms of mitochondrial DNA release and activation of the cGAS-STING pathway. *Exp. Mol. Med.* **55**, 510–519 (2023).

463. Hu, M.-M. & Shu, H.-B. Mitochondrial DNA-triggered innate immune response: mechanisms and diseases. *Cell. Mol. Immunol.* **20**, 1403–1412 (2023).

464. Mahmoodpoor, A. *et al.* Roles of mitochondrial DNA in dynamics of the immune response to COVID-19. *Gene* **836**, 146681 (2022).

465. Rui, Y. *et al.* Unique and complementary suppression of cGAS-STING and RNA sensing- triggered innate immune responses by SARS-CoV-2 proteins. *Signal Transduct. Target. Ther.* **6**, 123 (2021).

466. Lei, X. *et al*. Activation and evasion of type I interferon responses by SARS-CoV-2. *Nat. Commun*. **11**, 3810 (2020).

467. Thoms, M. *et al*. Structural basis for translational shutdown and immune evasion by the Nsp1 protein of SARS-CoV-2. *Science* **369**, 1249–1255 (2020).

468. Moustaqil, M. *et al*. SARS-CoV-2 proteases PLpro and 3CLpro cleave IRF3 and critical modulators of inflammatory pathways (NLRP12 and TAB1): implications for disease presentation across species. *Emerg. Microbes Infect.* **10**, 178–195 (2021).

469. Yuen, C.-K. *et al*. SARS-CoV-2 nsp13, nsp14, nsp15 and orf6 function as potent interferon antagonists. *Emerg. Microbes Infect.* **9**, 1418–1428 (2020).

470. Zhang, Y. *et al*. The ORF8 protein of SARS-CoV-2 mediates immune evasion through down-regulating MHC-I. *Proc. Natl. Acad. Sci.* **118**, e2024202118 (2021).

471. Arshad, N. *et al*. SARS-CoV-2 accessory proteins ORF7a and ORF3a use distinct mechanisms to down-regulate MHC-I surface expression. *Proc. Natl. Acad. Sci.* **120**, e2208525120 (2023).

472. Yoo, J.-S. *et al*. SARS-CoV-2 inhibits induction of the MHC class I pathway by targeting the STAT1-IRF1-NLRC5 axis. *Nat. Commun*. **12**, 6602 (2021).

473. Liu, G. *et al*. ISG15-dependent activation of the sensor MDA5 is antagonized by the SARS-CoV-2 papain-like protease to evade host innate immunity. *Nat. Microbiol.* **6**, 467–478 (2021).

474. Shin, D. *et al*. Papain-like protease regulates SARS-CoV-2 viral spread and innate immunity. *Nature* **587**, 657–662 (2020).

475. Kang, J. A., Kim, Y. J. & Jeon, Y. J. The diverse repertoire of ISG15: more intricate than initially thought. *Exp. Mol. Med.* **54**, 1779–1792 (2022).

476. Xia, H. *et al*. Evasion of Type I Interferon by SARS-CoV-2. *Cell Rep*. **33**, 108234 (2020).

477. Hayn, M. *et al*. Systematic functional analysis of SARS-CoV-2 proteins uncovers viral innate immune antagonists and remaining vulnerabilities. *Cell Rep*. **35**, 109126 (2021).

478. Addetia, A. *et al*. SARS-CoV-2 ORF6 Disrupts Bidirectional Nucleocytoplasmic Transport through Interactions with Rae1 and Nup98. *mBio* **12**, e00065-21 (2021).

479. Kato, K. *et al*. Overexpression of SARS-CoV-2 protein ORF6 dislocates RAE1 and NUP98 from the nuclear pore complex. *Biochem. Biophys. Res. Commun*. **536**, 59–66 (2021).

480. Kimura, I. *et al*. Sarbecovirus ORF6 proteins hamper induction of interferon signaling. *Cell Rep*. **34**, 108916 (2021).

481. Miorin, L. *et al*. SARS-CoV-2 Orf6 hijacks Nup98 to block STAT nuclear import and antagonize interferon signaling. *Proc. Natl. Acad. Sci.* **117**, 28344–28354 (2020).

482. Fisher, T. *et al*. Parsing the role of NSP1 in SARS-CoV-2 infection. *Cell Rep*. **39**, 110954 (2022).

483. Mendez, A. S. *et al*. The N-terminal domain of SARS-CoV-2 nsp1 plays key roles in suppression of cellular gene expression and preservation of viral gene expression. *Cell Rep*. **37**, 109841 (2021).

484. Finkel, Y. *et al*. SARS-CoV-2 uses a multipronged strategy to impede host protein synthesis. *Nature* **594**, 240–245 (2021).

485. Minkoff, J. M. & tenOever, B. Innate immune evasion strategies of SARS-CoV-2. *Nat. Rev. Microbiol*. (2023) doi:10.1038/s41579-022-00839-1.

486. De Wit, E., Van Doremalen, N., Falzarano, D. & Munster, V. J. SARS and MERS: recent insights into emerging coronaviruses. *Nat. Rev. Microbiol.* **14**, 523–534 (2016).

487. Thorne, L. G. *et al.* SARS-CoV-2 sensing by RIG-I and MDA5 links epithelial infection to macrophage inflammation. *EMBO J.* **40**, e107826 (2021).

488. Wang, X., Zhu, J., Zhang, D. & Liu, G. Ribosomal control in RNA virus-infected cells. *Front. Microbiol.* **13**, 1026887 (2022).

489. Kozak, M. Evaluation of the “scanning model” for initiation of protein synthesis in eucaryotes. *Cell* **22**, 7–8 (1980).

490. Kozak, M. How do eucaryotic ribosomes select initiation regions in messenger RNA? *Cell* **15**, 1109–1123 (1978).

491. Hinnebusch, A. G. The Scanning Mechanism of Eukaryotic Translation Initiation. *Annu. Rev. Biochem.* **83**, 779–812 (2014).

492. Andreev, D. E. *et al.* Non-AUG translation initiation in mammals. *Genome Biol.* **23**, 111 (2022).

493. Hinnebusch, A. G. Molecular Mechanism of Scanning and Start Codon Selection in Eukaryotes. *Microbiol. Mol. Biol. Rev.* **75**, 434–467 (2011).

494. Jackson, R. J., Hellen, C. U. T. & Pestova, T. V. The mechanism of eukaryotic translation initiation and principles of its regulation. *Nat. Rev. Mol. Cell Biol.* **11**, 113–127 (2010).

495. Kozak, M. Initiation of translation in prokaryotes and eukaryotes. *Gene* **234**, 187–208 (1999).

496. Kozak, M. Point mutations define a sequence flanking the AUG initiator codon that modulates translation by eukaryotic ribosomes. *Cell* **44**, 283–292 (1986).

497. Kozak, M. An analysis of 5’-noncoding sequences from 699 vertebrate messenger RNAs. *Nucleic Acids Res.* **15**, 8125–8148 (1987).

498. Kozak, M. At least six nucleotides preceding the AUG initiator codon enhance translation in mammalian cells. *J. Mol. Biol.* **196**, 947–950 (1987).

499. Noderer, W. L. *et al.* Quantitative analysis of mammalian translation initiation sites by FACS -seq. *Mol. Syst. Biol.* **10**, 748 (2014).

500. Michel, A. M., Andreev, D. E. & Baranov, P. V. Computational approach for calculating the probability of eukaryotic translation initiation from ribo-seq data that takes into account leaky scanning. *BMC Bioinformatics* **15**, 380 (2014).

501. Smith, E. Leaky ribosomal scanning in mammalian genomes: significance of histone H4 alternative translation in vivo. *Nucleic Acids Res.* **33**, 1298–1308 (2005).

502. Barbosa, C., Peixeiro, I. & Romão, L. Gene Expression Regulation by Upstream Open Reading Frames and Human Disease. *PLoS Genet.* **9**, e1003529 (2013).

503. Morris, D. R. & Geballe, A. P. Upstream Open Reading Frames as Regulators of mRNA Translation. *Mol. Cell. Biol.* **20**, 8635–8642 (2000).

504. Calvo, S. E., Pagliarini, D. J. & Mootha, V. K. Upstream open reading frames cause widespread reduction of protein expression and are polymorphic among humans. *Proc. Natl. Acad. Sci.* **106**, 7507–7512 (2009).

505. Rogozin, I. B., Kochetov, A. V., Kondrashov, F. A., Koonin, E. V. & Milanesi, L. Presence of ATG triplets in 5' untranslated regions of eukaryotic cDNAs correlates with a ‘weak’ context of the start codon. *Bioinformatics* **17**, 890–900 (2001).

506. Lee, S. *et al.* Global mapping of translation initiation sites in mammalian cells at single-nucleotide resolution. *Proc. Natl. Acad. Sci.* **109**, (2012).

507. Andrews, S. J. & Rothnagel, J. A. Emerging evidence for functional peptides encoded by short open reading frames. *Nat. Rev. Genet.* **15**, 193–204 (2014).

508. Shi, Y. *et al.* Upstream ORFs Prevent MAVS Spontaneous Aggregation and Regulate Innate Immune Homeostasis. *iScience* **23**, 101059 (2020).

509. Rayamajhi, M., Miao, E. A. & Moorman, N. J. miniMAVS, You Complete Me! *Cell* **156**, 629–630 (2014).

510. Minassian, A. *et al.* An Internally Translated MAVS Variant Exposes Its Amino-terminal TRAF-Binding Motifs to Deregulate Interferon Induction. *PLOS Pathog.* **11**, e1005060 (2015).

511. GEN-COVID. https://sites.google.com/dbm.unisi.it/gen-covid.

512. Xing, F. *et al.* Alteration of Antiviral Signalling by Single Nucleotide Polymorphisms (SNPs) of Mitochondrial Antiviral Signalling Protein (MAVS). *PLOS ONE* **11**, e0151173 (2016).

513. Hertzog, J. *et al.* Infection with a Brazilian isolate of Zika virus generates RIG-I stimulatory RNA and the viral NS5 protein blocks type I IFN induction and signaling. *Eur. J. Immunol.* **48**, 1120–1136 (2018).

514. Ogle, J. M. *et al.* Recognition of Cognate Transfer RNA by the 30 *S* Ribosomal Subunit. *Science* **292**, 897–902 (2001).

515. Demeshkina, N., Jenner, L., Westhof, E., Yusupov, M. & Yusupova, G. A new understanding of the decoding principle on the ribosome. *Nature* **484**, 256–259 (2012).

516. Fedorova, A. D., Kiniry, S. J., Andreev, D. E., Mudge, J. M. & Baranov, P. V. Thousands of human non-AUG extended proteoforms lack evidence of evolutionary selection among mammals. *Nat. Commun.* **13**, 7910 (2022).

517. Kameda, T., Asano, K. & Togashi, Y. Free energy landscape of RNA binding dynamics in start codon recognition by eukaryotic ribosomal pre-initiation complex. *PLOS Comput. Biol.* **17**, e1009068 (2021).

518. Ingolia, N. T., Brar, G. A., Rouskin, S., McGeachy, A. M. & Weissman, J. S. The ribosome profiling strategy for monitoring translation in vivo by deep sequencing of ribosome-protected mRNA fragments. *Nat. Protoc.* **7**, 1534–1550 (2012).

519. Ingolia, N. T., Lareau, L. F. & Weissman, J. S. Ribosome Profiling of Mouse Embryonic Stem Cells Reveals the Complexity and Dynamics of Mammalian Proteomes. *Cell* **147**, 789–802 (2011).

520. Ingolia, N. T., Brar, G. A., Rouskin, S., McGeachy, A. M. & Weissman, J. S. Genome-Wide Annotation and Quantitation of Translation by Ribosome Profiling. *Curr. Protoc. Mol. Biol.* **103**, (2013).

521. Prusiner, S. B. Prions. *Proc. Natl. Acad. Sci.* **95**, 13363–13383 (1998).

522. Ventoso, I. *et al.* Translational resistance of late alphavirus mRNA to eIF2α phosphorylation: a strategy to overcome the antiviral effect of protein kinase PKR. *Genes Dev.* **20**, 87–100 (2006).

523. Feng, G. S., Chong, K., Kumar, A. & Williams, B. R. Identification of double-stranded RNA-binding domains in the interferon-induced double-stranded RNA-activated p68 kinase. *Proc. Natl. Acad. Sci.* **89**, 5447–5451 (1992).

524. Lee, Y. S., Kunkeaw, N. & Lee, Y. Protein kinase R and its cellular regulators in cancer: An active player or a surveillant? *WIREs RNA* **11**, e1558 (2020).

525. Liu, Y. *et al.* The role of host eIF2α in viral infection. *Virol. J.* **17**, 112 (2020).

526. Kobayashi, M., Arias, C., Garabedian, A., Palmenberg, A. C. & Mohr, I. Site-Specific Cleavage of the Host Poly(A) Binding Protein by the Encephalomyocarditis Virus 3C Proteinase Stimulates Viral Replication. *J. Virol.* **86**, 10686–10694 (2012).

527. Sun, D. *et al.* Cleavage of poly(A)-binding protein by duck hepatitis A virus 3C protease. *Sci. Rep.* **7**, 16261 (2017).

528. Castelló, A. *et al.* HIV- 1 Protease Inhibits Cap- and Poly(A)-Dependent Translation upon eIF4GI and PABP Cleavage. *PLoS ONE* **4**, e7997 (2009).

529. Gingras, A. C., Svitkin, Y., Belsham, G. J., Pause, A. & Sonenberg, N. Activation of the translational suppressor 4E-BP1 following infection with encephalomyocarditis virus and poliovirus. *Proc. Natl. Acad. Sci.* **93**, 5578–5583 (1996).

530. Rabouw, H. H. *et al.* Middle East Respiratory Coronavirus Accessory Protein 4a Inhibits PKR-Mediated Antiviral Stress Responses. *PLOS Pathog.* **12**, e1005982 (2016).

531. Li, S., Min, J.-Y., Krug, R. M. & Sen, G. C. Binding of the influenza A virus NS1 protein to PKR mediates the inhibition of its activation by either PACT or double-stranded RNA. *Virology* **349**, 13–21 (2006).

532. Schierhorn, K. L. *et al.* Influenza A Virus Virulence Depends on Two Amino Acids in the N-Terminal Domain of Its NS1 Protein To Facilitate Inhibition of the RNA-Dependent Protein Kinase PKR. *J. Virol.* **91**, e00198-17 (2017).

533. Zheng, Z.-Q., Wang, S.-Y., Xu, Z.-S., Fu, Y.-Z. & Wang, Y.-Y. SARS-CoV-2 nucleocapsid protein impairs stress granule formation to promote viral replication. *Cell Discov.* **7**, 38 (2021).

534. GenOMICC. *GenOMICC* https://genomicc.org//.

535. Gerada, C. *et al.* Manipulation of the Innate Immune Response by Varicella Zoster Virus. *Front. Immunol.* **11**, 1 (2020).

536. Norberg, P. *et al.* Recombination of Globally Circulating Varicella-Zoster Virus. *J. Virol.* **89**, 7133–7146 (2015).

537. Gershon, A. A. *et al.* Varicella zoster virus infection. *Nat. Rev. Dis. Primer* **1**, 15016 (2015).

538. Zerboni, L., Sen, N., Oliver, S. L. & Arvin, A. M. Molecular mechanisms of varicella zoster virus pathogenesis. *Nat. Rev. Microbiol.* **12**, 197–210 (2014).

539. Braspenning, S. E. *et al.* Decoding the Architecture of the Varicella-Zoster Virus Transcriptome. *mBio* **11**, e01568-20 (2020).

540. Cohen, J. I. The Varicella-Zoster Virus Genome. in *Varicella-zoster Virus* (eds. Abendroth, A., Arvin, A. M. & Moffat, J. F.) vol. 342 1–14 (Springer Berlin Heidelberg, Berlin, Heidelberg, 2010).

541. Oliver, S. L., Yang, E. & Arvin, A. M. Varicella-Zoster Virus Glycoproteins: Entry, Replication, and Pathogenesis. *Curr. Clin. Microbiol. Rep.* **3**, 204–215 (2016).

542. Davison, A. J. Herpesvirus Genes. *Rev. Med. Virol.* **3**, 237–244 (1993).

543. Laing, K. J., Ouwendijk, W. J. D., Koelle, D. M. & Verjans, G. M. G. M. Immunobiology of Varicella-Zoster Virus Infection. *J. Infect. Dis.* **218**, S68–S74 (2018).

544. Chapman, R. S., Cross, K. W. & Fleming, D. M. The incidence of shingles and its implications for vaccination policy. *Vaccine* **21**, 2541–2547 (2003).

545. Varicella / Chickenpox | CDC Yellow Book 2024. https://wwwnc.cdc.gov/travel/yellowbook/2024/infections-diseases/varicella-chickenpox.

546. Sen, N. *et al*. Single-Cell Mass Cytometry Analysis of Human Tonsil T Cell Remodeling by Varicella Zoster Virus. *Cell Rep*. **8**, 633–645 (2014).

547. Abendroth, A., Morrow, G., Cunningham, A. L. & Slobedman, B. Varicella-Zoster Virus Infection of Human Dendritic Cells and Transmission to T Cells: Implications for Virus Dissemination in the Host. *J. Virol*. **75**, 6183–6192 (2001).

548. Tsolia, M., Gershon, A. A., Steiberg, S. P. & Gelb, L. Live attenuated varicella vaccine: Evidence that the virus is attenuated and the importance of skin lesions in transmission of varicella-zoster virus. *J. Pediatr*. **116**, 184–189 (1990).

549. Gnann, Jr., J. W. Varicella-Zoster Virus: Atypical Presentations and Unusual Complications. *J. Infect. Dis*. **186**, S91–S98 (2002).

550. Opstelten, W. & Zaal, M. J. W. Managing ophthalmic herpes zoster in primary care. *BMJ* **331**, 147–151 (2005).

551. Cohen, B. E., Durstenfeld, A. & Roehm, P. C. Viral Causes of Hearing Loss: A Review for Hearing Health Professionals. *Trends Hear*. **18**, 233121651454136 (2014).

552. Son, H. J., Choi, E.-J., Jeong, U. & Choi, Y. J. Effect of Herpes Zoster Treatment and Sudden Sensorineural Hearing Loss Using National Health Insurance Claims Data of South Korea. *Medicina (Mex.)* **59**, 808 (2023).

553. Dworkin, RobertH. & Portenoy, RussellK. Proposed classification of herpes zoster pain. *The Lancet* **343**, 1648 (1994).

554. BioNTech Starts Phase 1 Clinical Trial for Prophylactic Herpes Simplex Virus-2 Vaccine Candidate BNT163.

555. Quinlivan, M. & Breuer, J. Clinical and molecular aspects of the live attenuated Oka varicella vaccine. *Rev. Med. Virol*. **24**, 254–273 (2014).

556. Takahashi, M. *et al.* LIVE VACCINE USED TO PREVENT THE SPREAD OF VARICELLA IN CHILDREN IN HOSPITAL. *The Lancet* **304**, 1288–1290 (1974).

557. Papaloukas, O., Giannouli, G. & Papaevangelou, V. Successes and challenges in varicella vaccine. *Ther. Adv. Vaccines* **2**, 39–55 (2014).

558. Tillieux, S. L. *et al.* Complete DNA Sequences of Two Oka Strain Varicella-Zoster Virus Genomes. *J. Virol.* **82**, 11023–11044 (2008).

559. *Human Herpesviruses*. vol. 1045 (Springer Singapore, Singapore, 2018).

560. Gomi, Y. *et al.* Comparison of the Complete DNA Sequences of the Oka Varicella Vaccine and Its Parental Virus. *J. Virol.* **76**, 11447–11459 (2002).

561. Gagliardi, A. M. *et al.* Vaccines for preventing herpes zoster in older adults. *Cochrane Database Syst. Rev.* **2019**, (2019).

562. Lal, H. *et al.* Efficacy of an Adjuvanted Herpes Zoster Subunit Vaccine in Older Adults. *N. Engl. J. Med.* **372**, 2087–2096 (2015).

563. James, S. F., Chahine, E. B., Sucher, A. J. & Hanna, C. Shingrix: The New Adjuvanted Recombinant Herpes Zoster Vaccine. *Ann. Pharmacother.* **52**, 673–680 (2018).

564. Shingles vaccine. *nhs.uk* https://www.nhs.uk/vaccinations/shingles-vaccine/ (2024).

565. Shin, D. *et al.* Immunological characteristics of MAV/06 strain of varicella-zoster virus vaccine in an animal model. *BMC Immunol.* **23**, 27 (2022).

566. Kinchington, P. R., Fite, K., Seman, A. & Turse, S. E. Virion Association of IE62, the Varicella-Zoster Virus (VZV) Major Transcriptional Regulatory Protein, Requires Expression of the VZV Open Reading Frame 66 Protein Kinase. *J. Virol.* **75**, 9106–9113 (2001).

567. Chen, J. J., Zhu, Z., Gershon, A. A. & Gershon, M. D. Mannose 6-Phosphate Receptor Dependence of Varicella Zoster Virus Infection In Vitro and in the Epidermis during Varicella and Zoster. *Cell* **119**, 915–926 (2004).

568. Ross, A. H., Lenchner, E. & Reitman, G. Modification of Chicken Pox in Family Contacts by Administration of Gamma Globulin. *N. Engl. J. Med.* **267**, 369–376 (1962).

569. Yang, E., Arvin, A. M. & Oliver, S. L. The Cytoplasmic Domain of Varicella-Zoster Virus Glycoprotein H Regulates Syncytia Formation and Skin Pathogenesis. *PLoS Pathog.* **10**, e1004173 (2014).

570. Depledge, D. P. *et al.* A spliced latency-associated VZV transcript maps antisense to the viral transactivator gene 61. *Nat. Commun.* **9**, 1167 (2018).

571. Kennedy, P., Mogensen, T. & Cohrs, R. Recent Issues in Varicella-Zoster Virus Latency. *Viruses* **13**, 2018 (2021).

572. Ouwendijk, W. J. D. *et al.* Varicella-zoster virus VLT-ORF63 fusion transcript induces broad viral gene expression during reactivation from neuronal latency. *Nat. Commun.* **11**, 6324 (2020).

573. Kennedy, P. G. E. & Montague, P. Variable Gene Expression in Human Ganglia Latently Infected with Varicella-Zoster Virus. *Viruses* **14**, 1250 (2022).

574. Weller, T. H. Serial Propagation in vitro of Agents Producing Inclusion Bodies Derived from Varicella and Herpes Zoster. *Exp. Biol. Med.* **83**, 340–346 (1953).

575. Wroblewska, Z. *et al.* The production of varicella zoster virus antiserum in laboratory animals. *Arch. Virol.* **74**, 233–238 (1982).

576. Zerboni, L. & Arvin, A. Investigation of varicella-zoster virus neurotropism and neurovirulence using SCID mouse–human DRG xenografts. *J. Neurovirol.* **17**, 570–577 (2011).

577. Laemmle, L., Goldstein, R. S. & Kinchington, P. R. Modeling Varicella Zoster Virus Persistence and Reactivation – Closer to Resolving a Perplexing Persistent State. *Front. Microbiol.* **10**, 1634 (2019).

578. Sorel, O. & Messaoudi, I. Varicella Virus-Host Interactions During Latency and Reactivation: Lessons From Simian Varicella Virus. *Front. Microbiol.* **9**, 3170 (2018).

579. Zerboni, L., Ku, C.-C., Jones, C. D., Zehnder, J. L. & Arvin, A. M. Varicella-zoster virus infection of human dorsal root ganglia *in vivo*. *Proc. Natl. Acad. Sci.* **102**, 6490–6495 (2005).

580. Mahalingam, R. *et al.* Current In Vivo Models of Varicella-Zoster Virus Neurotropism. *Viruses* **11**, 502 (2019).

581. Gowrishankar, K. *et al.* Productive Varicella-Zoster Virus Infection of Cultured Intact Human Ganglia. *J. Virol.* **81**, 6752–6756 (2007).

582. Arvin, A. M. *et al.* Human Leukocyte Interferon for the Treatment of Varicella in Children with Cancer. *N. Engl. J. Med.* **306**, 761–765 (1982).

583. Arvin, A. M., Koropchak, C. M., Williams, B. R. G., Grumet, F. C. & Foung, S. K. H. Early Immune Response in Healthy and Immunocompromised Subjects with Primary Varicella-Zoster Virus Infection. *J. Infect. Dis.* **154**, 422–429 (1986).

584. Ku, C.-C. *et al.* Varicella-Zoster Virus Transfer to Skin by T Cells and Modulation of Viral Replication by Epidermal Cell Interferon-α. *J. Exp. Med.* **200**, 917–925 (2004).

585. Kim, J.-A., Park, S.-K., Seo, S.-W., Lee, C.-H. & Shin, O. S. STING Is Involved in Antiviral Immune Response against VZV Infection via the Induction of Type I and III IFN Pathways. *J. Invest. Dermatol.* **137**, 2101–2109 (2017).

586. Ogunjimi, B. *et al.* Inborn errors in RNA polymerase III underlie severe varicella zoster virus infections. *J. Clin. Invest.* **127**, 3543–3556 (2017).

587. Wang, J. P. *et al.* Varicella-Zoster Virus Activates Inflammatory Cytokines in Human Monocytes and Macrophages via Toll-Like Receptor 2. *J. Virol.* **79**, 12658–12666 (2005).

588. Yu, H.-R. *et al.* IFN-α production by human mononuclear cells infected with varicella-zoster virus through TLR9-dependent and -independent pathways. *Cell. Mol. Immunol.* **8**, 181–188 (2011).

589. Préhaud, C., Mégret, F., Lafage, M. & Lafon, M. Virus Infection Switches TLR-3-Positive Human Neurons To Become Strong Producers of Beta Interferon. *J. Virol.* **79**, 12893–12904 (2005).

590. Liang, F. *et al.* Recurrent Herpes Zoster Ophthalmicus in a Patient With a Novel Toll-Like Receptor 3 Variant Linked to Compromised Activation Capacity in Fibroblasts. *J. Infect. Dis.* jiz229 (2019) doi:10.1093/infdis/jiz229.

591. Biron, C. A., Byron, K. S. & Sullivan, J. L. Severe Herpesvirus Infections in an Adolescent without Natural Killer Cells. *N. Engl. J. Med.* **320**, 1731–1735 (1989).

592. Wendland, T., Herren, S., Yawalkar, N., Cerny, A. & Pichler, W. J. Strong αβ and γδ TCR response in a patient with disseminated Mycobacterium avium infection and lack of NK cells and monocytopenia. *Immunol. Lett.* **72**, 75–82 (2000).

593. Etzioni, A. *et al.* Fatal varicella associated with selective natural killer cell deficiency. *J. Pediatr.* **146**, 423–425 (2005).

594. Notarangelo, L. D. & Mazzolari, E. Natural killer cell deficiencies and severe varicella infection. *J. Pediatr.* **148**, 563–564 (2006).

595. Ihara, T., Kamiya, H., Starr, S. E., Arbeter, A. M. & Lange, B. Natural Killing of Varicella-Zoster Virus (VZV)-Infected Fibroblasts in Normal Children, Children with VZV Infections, and Children with Hodgkin's Disease. *Pediatr. Int.* **31**, 523–528 (1989).

596. Campbell, T. M. *et al.* Varicella zoster virus productively infects human natural killer cells and manipulates phenotype. *PLOS Pathog.* **14**, e1006999 (2018).

597. Huch, J. H. *et al.* Impact of Varicella-Zoster Virus on Dendritic Cell Subsets in Human Skin during Natural Infection. *J. Virol.* **84**, 4060–4072 (2010).

598. Weinberg, A. *et al.* Influence of Age and Nature of Primary Infection on Varicella-Zoster Virus–Specific Cell-Mediated Immune Responses. *J. Infect. Dis.* **201**, 1024–1030 (2010).

599. Steain, M., Slobedman, B. & Abendroth, A. The host Immune Response to Varicella Zoster Virus. *Future Virol.* **7**, 1205–1220 (2012).

600. Hakami, M. A. *et al.* Varicella-zoster virus-related neurological complications: From infection to immunomodulatory therapies. *Rev. Med. Virol.* **34**, e2554 (2024).

601. Gerada, C., Steain, M., McSharry, B. P., Slobedman, B. & Abendroth, A. Varicella-Zoster Virus ORF63 Protects Human Neuronal and Keratinocyte Cell Lines from Apoptosis and Changes Its Localization upon Apoptosis Induction. *J. Virol.* **92**, e00338-18 (2018).

602. Schaap, A. *et al.* T-Cell Tropism and the Role of ORF66 Protein in Pathogenesis of Varicella-Zoster Virus Infection. *J. Virol.* **79**, 12921–12933 (2005).

603. Zhu, H. *et al*. Varicella-Zoster Virus Immediate-Early Protein ORF61 Abrogates the IRF3-Mediated Innate Immune Response through Degradation of Activated IRF3. *J. Virol.* **85**, 11079–11089 (2011).

604. Sen, N. *et al*. Varicella-Zoster Virus Immediate-Early Protein 62 Blocks Interferon Regulatory Factor 3 (IRF3) Phosphorylation at Key Serine Residues: a Novel Mechanism of IRF3 Inhibition among Herpesviruses. *J. Virol.* **84**, 9240–9253 (2010).

605. Verweij, M. C. *et al*. Varicella Viruses Inhibit Interferon-Stimulated JAK-STAT Signaling through Multiple Mechanisms. *PLOS Pathog.* **11**, e1004901 (2015).

606. Parad, J. E. A Psychological Critique of the Public Health Response to Chicken Pox Parties. *Society* **49**, 495–499 (2012).

607. Hambleton, S. & Arvin, A. M. Chickenpox Party or Varicella Vaccine? in *Hot Topics in Infection and Immunity in Children II* (eds. Pollard, A. J. & Finn, A.) vol. 568 11–24 (Springer US, Boston, MA, 2005).

608. Lanphier, E. & Harris, K. W. The Strawman at the Pox Party. *Am. J. Bioeth.* **20**, 73–75 (2020).

609. Rotem, C. E. Complications of Chicken-pox. *BMJ* **1**, 944–947 (1961).

610. Mainka, C., Fuß, B., Geiger, H., Höfelmayr, H. & Wolff, M. H. Characterization of viremia at different stages of varicella-zoster virus infection. *J. Med. Virol.* **56**, 91–98 (1998).

611. Kennedy, J. J., Steain, M., Slobedman, B. & Abendroth, A. Infection and Functional Modulation of Human Monocytes and Macrophages by Varicella-Zoster Virus. *J. Virol.* **93**, e01887-18 (2019).

612. Nour, A. M. *et al.* Varicella-Zoster Virus Infection Triggers Formation of an Interleukin-1β (IL-1β)-processing Inflammasome Complex. *J. Biol. Chem.* **286**, 17921–17933 (2011).

613. Wu, J. *et al.* Inhibition of cGAS DNA Sensing by a Herpesvirus Virion Protein. *Cell Host Microbe* **18**, 333–344 (2015).

614. Tischer, B. K. *et al.* A Self-Excisable Infectious Bacterial Artificial Chromosome Clone of Varicella-Zoster Virus Allows Analysis of the Essential Tegument Protein Encoded by *ORF9*. *J. Virol.* **81**, 13200–13208 (2007).

615. Warner, B. E., Goins, W. F., Kramer, P. R. & Kinchington, P. R. A Guide to Preclinical Models of Zoster-Associated Pain and Postherpetic Neuralgia. in *Varicella-zoster Virus* (eds. Arvin, A. M., Moffat, J. F., Abendroth, A. & Oliver, S. L.) vol. 438 189–221 (Springer International Publishing, Cham, 2021).

616. Iwamoto, M., Björklund, T., Lundberg, C., Kirik, D. & Wandless, T. J. A General Chemical Method to Regulate Protein Stability in the Mammalian Central Nervous System. *Chem. Biol.* **17**, 981–988 (2010).

617. Ramadurgum, P. & Hulleman, J. D. Protocol for Designing Small-Molecule-Regulated Destabilizing Domains for In Vitro Use. *STAR Protoc.* **1**, 100069 (2020).

618. Ramadurgum, P. *et al.* Simultaneous Control of Endogenous and User-Defined Genetic Pathways Using Unique ecDHFR Pharmacological Chaperones. *Cell Chem. Biol.* **27**, 622-634.e6 (2020).

619. Peng, H. *et al.* Non-antibiotic Small-Molecule Regulation of DHFR-Based Destabilizing Domains In Vivo. *Mol. Ther. - Methods Clin. Dev.* **15**, 27–39 (2019).

620. Jin, X. *et al.* The battle between the innate immune cGAS-STING signaling pathway and human herpesvirus infection. *Front. Immunol.* **14**, 1235590 (2023).

621. Kim, J.-A., Park, S.-K., Kumar, M., Lee, C.-H. & Shin, O. S. Insights into the role of immunosenescence during varicella zoster virus infection (shingles) in the aging cell model. *Oncotarget* **6**, 35324–35343 (2015).

622. Vandevenne, P. *et al*. The Varicella-Zoster Virus ORF47 Kinase Interferes with Host Innate Immune Response by Inhibiting the Activation of IRF3. *PLoS ONE* **6**, e16870 (2011).

623. Smith, G. L., Talbot-Cooper, C. & Lu, Y. How Does Vaccinia Virus Interfere With Interferon? in *Advances in Virus Research* vol. 100 355–378 (Elsevier, 2018).

624. Stempel, M., Chan, B. & Brinkmann, M. M. Coevolution pays off: Herpesviruses have the license to escape the DNA sensing pathway. *Med. Microbiol. Immunol. (Berl.)* **208**, 495–512 (2019).

625. Daffis, S. *et al*. 2'-O methylation of the viral mRNA cap evades host restriction by IFIT family members. *Nature* **468**, 452–456 (2010).

626. Lei, J. & Hilgenfeld, R. RNA-virus proteases counteracting host innate immunity. *FEBS Lett.* **591**, 3190–3210 (2017).

627. Miorin, L., Maestre, A. M., Fernandez-Sesma, A. & García-Sastre, A. Antagonism of type I interferon by flaviviruses. *Biochem. Biophys. Res. Commun.* **492**, 587–596 (2017).

628. Best, S. M. The Many Faces of the Flavivirus NS5 Protein in Antagonism of Type I Interferon Signaling. *J. Virol.* **91**, e01970-16 (2017).

629. Chambers, R. & Takimoto, T. Antagonism of Innate Immunity by Paramyxovirus Accessory Proteins. *Viruses* **1**, 574–593 (2009).

630. Chowdhury, F. Z. & Farrar, J. D. STAT2: A shape-shifting anti-viral super STAT. *JAK-STAT* **2**, e23633 (2013).

631. Bhowmik, D., Tian, Y., Wang, B., Zhu, F. & Yin, Q. Structural basis of higher order oligomerization of KSHV inhibitor of cGAS. *Proc. Natl. Acad. Sci.* **119**, e2200285119 (2022).

632. Blest, H. T. W. *et al.* HSV-1 employs UL56 to antagonize expression and function of cGAMP channels. *Cell Rep.* **43**, 114122 (2024).

633. Zheng, Z.-Q. *et al.* Herpes simplex virus protein UL56 inhibits cGAS-Mediated DNA sensing to evade antiviral immunity. *Cell Insight* **1**, 100014 (2022).

634. Zhang, J. *et al.* Species-Specific Deamidation of cGAS by Herpes Simplex Virus UL37 Protein Facilitates Viral Replication. *Cell Host Microbe* **24**, 234-248.e5 (2018).

635. Maruzuru, Y., Koyanagi, N., Kato, A. & Kawaguchi, Y. Role of the DNA Binding Activity of Herpes Simplex Virus 1 VP22 in Evading AIM2-Dependent Inflammasome Activation Induced by the Virus. *J. Virol.* **95**, e02172-20 (2021).

636. van Leeuwen, H. *et al.* Herpes simplex virus type 1 tegument protein VP22 interacts with TAF-I proteins and inhibits nucleosome assembly but not regulation of histone acetylation by INHAT. *J. Gen. Virol.* **84**, 2501–2510 (2003).

637. Huang, J. *et al.* Herpes Simplex Virus 1 Tegument Protein VP22 Abrogates cGAS/STING-Mediated Antiviral Innate Immunity. *J. Virol.* **92**, (2018).

638. Xu, G. *et al.* Viral tegument proteins restrict cGAS-DNA phase separation to mediate immune evasion. *Mol. Cell* **81**, 2823-2837.e9 (2021).

639. Hew, K., Dahlroth, S.-L., Pan, L. X., Cornvik, T. & Nordlund, P. VP22 core domain from Herpes simplex virus 1 reveals a surprising structural conservation in both the Alpha- and Gammaherpesvirinae subfamilies. *J. Gen. Virol.* **96**, 1436–1445 (2015).

640. Pathare, G. R. *et al.* Structural mechanism of cGAS inhibition by the nucleosome. *Nature* **587**, 668–672 (2020).

641. McGinty, R. K. & Tan, S. Principles of nucleosome recognition by chromatin factors and enzymes. *Curr. Opin. Struct. Biol.* **71**, 16–26 (2021).

642. Michalski, S. Structural studies on autoimmunity regulation by the nucleic acid sensors cGAS and RIG-I.

643. Freundt, E. C., Drappier, M. & Michiels, T. Innate Immune Detection of Cardioviruses and Viral Disruption of Interferon Signaling. *Front. Microbiol.* **9**, 2448 (2018).

644. Liu, S. *et al.* Phosphorylation of innate immune adaptor proteins MAVS, STING, and TRIF induces IRF3 activation. *Science* **347**, aaa2630 (2015).

645. Kranzusch, P. J. *et al.* Ancient Origin of cGAS-STING Reveals Mechanism of Universal 2',3' cGAMP Signaling. *Mol. Cell* **59**, 891–903 (2015).

646. Hong, Z. *et al.* STING inhibitors target the cyclic dinucleotide binding pocket. *Proc. Natl. Acad. Sci.* **118**, e2105465118 (2021).

647. Pollock, A. J., Zaver, S. A. & Woodward, J. J. A STING-based biosensor affords broad cyclic dinucleotide detection within single living eukaryotic cells. *Nat. Commun.* **11**, 3533 (2020).

648. Shang, G., Zhang, C., Chen, Z. J., Bai, X. & Zhang, X. Cryo-EM structures of STING reveal its mechanism of activation by cyclic GMP–AMP. *Nature* **567**, 389–393 (2019).

649. Ergun, S. L., Fernandez, D., Weiss, T. M. & Li, L. STING Polymer Structure Reveals Mechanisms for Activation, Hyperactivation, and Inhibition. *Cell* **178**, 290-301.e10 (2019).

650. Ergun, S. L. & Li, L. Structural Insights into STING Signaling. *Trends Cell Biol.* **30**, 399–407 (2020).

651. Jumper, J. *et al*. Highly accurate protein structure prediction with AlphaFold. *Nature* **596**, 583–589 (2021).

652. Evans, R. *et al*. Protein complex prediction with AlphaFold-Multimer. Preprint at https://doi.org/10.1101/2021.10.04.463034 (2021).

653. Salamanca Viloria, J., Allega, M. F., Lambrughi, M. & Papaleo, E. An optimal distance cutoff for contact-based Protein Structure Networks using side-chain centers of mass. *Sci. Rep.* **7**, 2838 (2017).

654. Moriwaki, Y. *et al*. Solution structure of the isolated histone H2A-H2B heterodimer. *Sci. Rep.* **6**, 24999 (2016).

655. Armougom, F., Moretti, S., Keduas, V. & Notredame, C. The iRMSD: a local measure of sequence alignment accuracy using structural information. *Bioinformatics* **22**, e35–e39 (2006).

656. Jewett, A. I., Huang, C. C. & Ferrin, T. E. MINRMS: an efficient algorithm for determining protein structuresimilarity using root-mean-squared-distance. *Bioinformatics* **19**, 625–634 (2003).

657. Reva, B. A., Finkelstein, A. V. & Skolnick, J. What is the probability of a chance prediction of a protein structure with an rmsd of 6 å? *Fold. Des.* **3**, 141–147 (1998).

658. Chothia, C. & Lesk, A. M. The relation between the divergence of sequence and structure in proteins. *EMBO J.* **5**, 823–826 (1986).

659. Carugo, O. & Pongor, S. A normalized root-mean-spuare distance for comparing protein three-dimensional structures. *Protein Sci.* **10**, 1470–1473 (2001).

660. Trabuco, L. G., Lise, S., Petsalaki, E. & Russell, R. B. PepSite: prediction of peptide-binding sites from protein surfaces. *Nucleic Acids Res.* **40**, W423–W427 (2012).

661. Wischnewski, M. & Ablasser, A. Interplay of cGAS with chromatin. *Trends Biochem. Sci.* **46**, 822–831 (2021).

662. Kranzusch, P. J., Lee, A. S.-Y., Berger, J. M. & Doudna, J. A. Structure of Human cGAS Reveals a Conserved Family of Second-Messenger Enzymes in Innate Immunity. *Cell Rep.* **3**, 1362–1368 (2013).

663. Kato, K., Kawaguchi, A. & Nagata, K. Template activating factor-I epigenetically regulates the TERT transcription in human cancer cells. *Sci. Rep.* **11**, 17726 (2021).

664. Matsumoto, K., Nagata, K., Ui, M. & Hanaoka, F. Template activating factor I, a novel host factor required to stimulate the adenovirus core DNA replication. *J. Biol. Chem.* **268**, 10582–10587 (1993).

665. Okuwaki, M. & Nagata, K. Template Activating Factor-I Remodels the Chromatin Structure and Stimulates Transcription from the Chromatin Template. *J. Biol. Chem.* **273**, 34511–34518 (1998).

666. Miyaji-Yamaguchi, M., Okuwaki, M. & Nagata, K. Coiled-coil structure-mediated dimerization of template activating factor-I is critical for its chromatin remodeling activity. *J. Mol. Biol.* **290**, 547–557 (1999).

667. Kajitani, K., Kato, K. & Nagata, K. Histone H1 chaperone activity of TAF -I is regulated by its subtype-dependent intramolecular interaction. *Genes Cells* **22**, 334–347 (2017).

668. Nakahara, J., Maeda, M., Aiso, S. & Suzuki, N. Current Concepts in Multiple Sclerosis: Autoimmunity Versus Oligodendrogliopathy. *Clin. Rev. Allergy Immunol.* **42**, 26–34 (2012).

669. Berer, K. & Krishnamoorthy, G. Microbial view of central nervous system autoimmunity. *FEBS Lett.* **588**, 4207–4213 (2014).

670. Attfield, K. E., Jensen, L. T., Kaufmann, M., Friese, M. A. & Fugger, L. The immunology of multiple sclerosis. *Nat. Rev. Immunol.* **22**, 734–750 (2022).

671. The Wellcome Trust Case–Control Consortium (WTCCC) and Alastair Compston *et al.* Replication analysis identifies TYK2 as a multiple sclerosis susceptibility factor. *Eur. J. Hum. Genet.* **17**, 1309–1313 (2009).

672. Dendrou, C. A. *et al.* Resolving TYK2 locus genotype-to-phenotype differences in autoimmunity. *Sci. Transl. Med.* **8**, (2016).

673. Dyment, D. A. *et al.* Exome sequencing identifies a novel multiple sclerosis susceptibility variant in the *TYK2* gene. *Neurology* **79**, 406–411 (2012).

674. Mine, K. *et al.* TYK2 signaling promotes the development of autoreactive CD8+ cytotoxic T lymphocytes and type 1 diabetes. *Nat. Commun.* **15**, 1337 (2024).

675. Izumi, K. *et al.* Reduced Tyk2 gene expression in β-cells due to natural mutation determines susceptibility to virus-induced diabetes. *Nat. Commun.* **6**, 6748 (2015).

676. Mine, K. *et al.* Subtyping of Type 1 Diabetes as Classified by Anti-GAD Antibody, IgE Levels, and Tyrosine kinase 2 (TYK2) Promoter Variant in the Japanese. *EBioMedicine* **23**, 46–51 (2017).

677. Nagafuchi, S. *et al.* TYK2 Promoter Variant and Diabetes Mellitus in the Japanese. *EBioMedicine* **2**, 744–749 (2015).

678. Nejentsev, S., Walker, N., Riches, D., Egholm, M. & Todd, J. A. Rare Variants of IFIH1, a Gene Implicated in Antiviral Responses, Protect Against Type 1 Diabetes. *Science* **324**, 387–389 (2009).

679. Lincez, P. J., Shanina, I. & Horwitz, M. S. Reduced Expression of the MDA5 Gene IFIH1 Prevents Autoimmune Diabetes. *Diabetes* **64**, 2184–2193 (2015).

680. Smyth, D. J. *et al*. A genome-wide association study of nonsynonymous SNPs identifies a type 1 diabetes locus in the interferon-induced helicase (IFIH1) region. *Nat. Genet.* **38**, 617–619 (2006).

681. Knip, M. *et al*. Environmental Triggers and Determinants of Type 1 Diabetes. *Diabetes* **54**, S125–S136 (2005).

682. Qin, S. *et al*. Structural basis for histone mimicry and hijacking of host proteins by influenza virus protein NS1. *Nat. Commun.* **5**, 3952 (2014).

683. Elde, N. C. & Malik, H. S. The evolutionary conundrum of pathogen mimicry. *Nat. Rev. Microbiol.* **7**, 787–797 (2009).

684. Xiao, S., Wang, Y., Shan, S. & Zhou, Z. The interplay between viral molecular mimicry and host chromatin dynamics. *Nucleus* **14**, 2216560 (2023).

685. Wei, H. & Zhou, M.-M. Viral-encoded enzymes that target host chromatin functions. *Biochim. Biophys. Acta BBA - Gene Regul. Mech.* **1799**, 296–301 (2010).

686. Influenza (Seasonal). https://www.who.int/news-room/fact-sheets/detail/influenza-(seasonal).

687. Marazzi, I. *et al*. Suppression of the antiviral response by an influenza histone mimic. *Nature* **483**, 428–433 (2012).

688. Bornholdt, Z. A. & Prasad, B. V. V. X-ray structure of NS1 from a highly pathogenic H5N1 influenza virus. *Nature* **456**, 985–988 (2008).

689. Webb, L. G. & Fernandez-Sesma, A. RNA viruses and the cGAS-STING pathway: reframing our understanding of innate immune sensing. *Curr. Opin. Virol.* **53**, 101206 (2022).

690. Sun, F., Xu, Y., Deng, Z. & Yang, P. A recombinant oncolytic influenza virus expressing a PD-L1 antibody induces CD8+ T-cell activation via the cGas-STING

pathway in mice with hepatocellular carcinoma. *Int. Immunopharmacol.* **120**, 110323 (2023).

691. Tang, L., Liu, X., Wang, C. & Shu, C. USP18 promotes innate immune responses and apoptosis in influenza A virus-infected A549 cells via cGAS-STING pathway. *Virology* **585**, 240–247 (2023).

692. Moriyama, M., Koshiba, T. & Ichinohe, T. Influenza A virus M2 protein triggers mitochondrial DNA-mediated antiviral immune responses. *Nat. Commun.* **10**, 4624 (2019).

693. Mücke, K. *et al.* Human Cytomegalovirus Major Immediate Early 1 Protein Targets Host Chromosomes by Docking to the Acidic Pocket on the Nucleosome Surface. *J. Virol.* **88**, 1228–1248 (2014).

694. Fang, Q. *et al.* Human cytomegalovirus IE1 protein alters the higher-order chromatin structure by targeting the acidic patch of the nucleosome. *eLife* **5**, e11911 (2016).

695. Kotlar, R. M. *et al.* Retroviral prototype foamy virus intasome binding to a nucleosome target does not determine integration efficiency. *J. Biol. Chem.* **296**, 100550 (2021).

696. Lesbats, P. *et al.* Structural basis for spumavirus GAG tethering to chromatin. *Proc. Natl. Acad. Sci.* **114**, 5509–5514 (2017).

697. Liu, Y. *et al.* Virus-encoded histone doublets are essential and form nucleosome-like structures. *Cell* **184**, 4237-4250.e19 (2021).

698. Lieberman, P. M. Chromatin organization and virus gene expression. *J. Cell. Physiol.* **216**, 295–302 (2008).

699. Oh, J. *et al.* Genome Wide Nucleosome Mapping for HSV-1 Shows Nucleosomes Are Deposited at Preferred Positions during Lytic Infection. *PLOS ONE* **10**, e0117471 (2015).

700. Sato, S., Dacher, M. & Kurumizaka, H. Nucleosome Structures Built from Highly Divergent Histones: Parasites and Giant DNA Viruses. *Epigenomes* **6**, 22 (2022).

701. Valencia-Sánchez, M. I. *et al.* The structure of a virus-encoded nucleosome. *Nat. Struct. Mol. Biol.* **28**, 413–417 (2021).

702. Erives, A. J. Phylogenetic analysis of the core histone doublet and DNA topo II genes of Marseilleviridae: evidence of proto-eukaryotic provenance. *Epigenetics Chromatin* **10**, 55 (2017).

703. Goodman, J. L. Marseillevirus, Blood Safety, and the Human Virome. *J. Infect. Dis.* **208**, 1039–1041 (2013).

704. Sahmi-Bounsiar, D. *et al.* Marseilleviruses: An Update in 2021. *Front. Microbiol.* **12**, 648731 (2021).

705. Aherfi, S., La Scola, B., Pagnier, I., Raoult, D. & Colson, P. The expanding family Marseilleviridae. *Virology* **466–467**, 27–37 (2014).

706. Lagier, J.-C. *et al.* Microbial culturomics: paradigm shift in the human gut microbiome study. *Clin. Microbiol. Infect.* **18**, 1185–1193 (2012).

707. Popgeorgiev, N., Michel, G., Lepidi, H., Raoult, D. & Desnues, C. Marseillevirus Adenitis in an 11-Month-Old Child. *J. Clin. Microbiol.* **51**, 4102–4105 (2013).

708. Popgeorgiev, N. *et al.* Marseillevirus-Like Virus Recovered From Blood Donated by Asymptomatic Humans. *J. Infect. Dis.* **208**, 1042–1050 (2013).

709. Wadie, B., Kleshchevnikov, V., Sandaltzopoulou, E., Benz, C. & Petsalaki, E. Use of viral motif mimicry improves the proteome-wide discovery of human linear motifs. *Cell Rep*. **39**, 110764 (2022).

710. Sheng, Y. *et al*. Molecular recognition of p53 and MDM2 by USP7/HAUSP. *Nat. Struct. Mol. Biol*. **13**, 285–291 (2006).

List of Figures

Figure 1: Pathogen Triggered Immunity.
(**A**) PAMP-triggered immune response is triggered by the detection of viral DNA or RNA by pattern recognition receptors (PRRs) in the cytoplasm. The detection by PRRs initiates the transcription of type I interferons (IFNs) which induce bystander cells to transcribe interferon stimulated genes (ISGs). (**B**) HSV-1 encodes an E3- ubiquitin ligase ICP0, which degrades host MORC3. MORC3 regulates IFNβ1 expression by inhibiting its transcription. MORC3 is targeted for degradation by ICP0 as it has anti-viral functions during HSV-1 infections, however the loss of MORC3 increases IFNβ1 expression. This system is an example of effector triggered immunity (ETI) as IFNβ1 production is independent of direct HSV-1 detection by PRRs. Panel A is from Rehwinkel & Gack 2020. doi: 10.1038/ s41577-020-0288-3. Panel B is from Orzalli & Parameswaran 2022. doi: 10.1016/j.it.2022.10.004.

Figure 2: The cGAS-STING Signalling Pathway.
The presence of dsDNA in the cytoplasm binds and activates cGAS, which catalyzes the production of cGAMP. cGAMP binds to STING, which initiates a downstream signalling cascade to ultimately produce IFNs and inflammatory cytokines. These cytokines stimulate the production of ISGs within the cell and bystander cells. Made with BioRender.

Figure 3: Post-Translational Modification of cGAS.
Numbers indicate amino acids along the cGAS transcript. Residues that contribute to DNA binding are indicated with star, diamond or circle symbols. All post-translational modification sites along cGAS are indicated with a circle - the circles with a border indicate residues with annotated function in human cGAS. Residues with a (m) are post-translational modifications described in mouse cGAS that are predicted at these homologous positions along human cGAS. Figure taken from Hertzog & Rehwinkel 2020. doi: 10.15252/embr.202051345.

Figure 4: Interaction of cGAS and histones in the nucleus.
(**A**) cGAS binds dsDNA at sites A & B, while site-C mediates cGAS-DNA higher-order ladder-like assemblies. (**B**) cGAS bound to NCP. NCP inhibits DNA binding at the A-site by inducing sterical clashes, at the B-site by binding to the arginine anchor and C-site residues are bound to prevent higher-order structures. (**C**) Cyro-EM structure of cGAS bound to NCP. (**D**) Close-up views of cGAS and the acidic patch of H2A. (E) cGAS residues in the B-site bound to H2A. (F) KRKR loop of cGAS bound to DNA in the distal NCP. (D-E) hcGAS DNA binding site B residues are depicted in cyan, hH2A residues are pink. (F) distal nucleosomal DNA is yellow, cGAS binding site C residues are purple. Panel A & B from Wischnewski & Ablasser 2021. doi:10.1016/j.tibs.2021.05.011
Panel C-F from Kujirai et al. 2020. doi: 10.1126/science.abd0237.

Figure 5: Domain architecture of RLRs and their signalling.
(**A**) RIG-I, MDA5, and LGP2 have a helicase, and CTD domain, while LGP2 lacks a CARD domain. The downstream signalling adaptor MAVS possesses a CARD and TM domain.

(**B**) RLR signalling begins with activation of RIG-I or MDA5 via dsRNA that induces interaction of their CARD domains with the CARD of MAVS. MAVS activates IRF3 and NF-kB pathways to induce transcription of type I IFN and inflammatory cytokines. Panel (A) is taken from Rehwinkel & Gack 2020 doi: 10.1038/ s41577-020-0288-3. Panel (B) is taken from Ren et al. 2020 doi: 10.3389/fimmu.2020.01030.

Figure 6: Post-translation modification of MAVS.
MAVS is regulated through the K27, K48 and K63-linked ubiquitylation. The ubiquitylation is mediated by a number of co-factors listed in yellow blobs above the MAVS transcript. Ubiquitin chains are added to the indicated lysine residues. K63-linked ubiquitylation promotes MAVS aggregation and signalling, while K27 and K48-linked ubiquitylation promotes degradation of MAVS. Figure taken from Dong & Shen 2024. doi:10.31083/j.fbl2902072.

Figure 7: Methodology of transwell co-infection experiments.
A graphical summary of co-infection of infected MeWo cells with differentiated THP1s, separated by a mesh to prevent cell mixing. Figure taken from Hertzog & Rehwinkel 2023. doi: 10.1016/j.jviromet.2022.114661.

Figure 8: The SARS-CoV-2 genome and viral life cycle.
(**A**) The SARS-CoV-2 genome encodes non-structural proteins, structural proteins and accessory proteins. Structural and accessory proteins are produced from sg-mRNA by discontinuous transcription. (**B**) SARS-CoV-2 virions gain entry into the cell via the ACE2 receptor or membrane fusion mediated by TMPRSS2. Viral replication begins inside ER membranes remodelled by the virus into replication factories. Translated structural and accessory proteins are shuttled to the ERGIC along with the nucleocapsid to form progeny virus which egress from the cell via lysosomal exocytosis. Figure taken from Steiner et al. 2024. doi:10.1038/s41579-023-01003-z.

Figure 9: Mechanisms of SARS-CoV-2 innate immune evasion strategies.
During COVID-19 infection, viral particles are sensed by TLR2, and potentially TLR3, TLR4, TLR7 and TLR8. The virus can be sensed by RLRs and the cGAS-STING pathway. SARS-CoV-2 evades the innate immune response by inhibiting a multitude of points along the pathway, from PRR to ISG and IFN expression. Figure taken from Steiner et al. 2024. doi:10.1038/s41579-023-01003-z.

Figure 10: MAVS and MDA5 are required for the type I and III IFN response to SARS-CoV-2.
(**A,B**) Calu-3 cells were depleted of MAVS by lentiviral shRNA delivery using shRNAs (shRNA-MAVS-45). (**B**) SARS-CoV-2 infection efficiency was validated by RT-qPCR . (A,B) Calu-3 cells depleted of MAVS using shRNA-MAVS-45 were infected with SARS-CoV-2 (MOI = 0.1) for 48 h, followed by RNA extraction and RT-qPCR for the indicated transcripts. Data are relative to GAPDH expression. (**C**) Calu-3 cells were depleted of MAVS, STING, IRF3, MDA5 or RIG-I using a lenti-CRISPR approach and were infected with SARS-CoV-2 (MOI = 0.1) for 48 h. This was followed by RNA extraction and RT-qPCR for the indicated transcripts. Data are relative to GAPDH expression. Data in Panel A and B are pooled from 3 independent biological repeats, with bars representing the average. Data were analyzed by t-test and significant differences are indicated (**P

< 0.01; *P < 0.05). Data in Panel C are pooled from two independent biological repeats, with bars representing the average. My contribution to this data was to isolate RNA from lysates and perform RT-qPCR.

Figure 11: Discovery of MAVS SNPs Within Translation Start Sites.
(**A**) Schematic of the six isoforms of MAVS (M1, M2, M3, M4, M5 & M6) that are translated by leaky ribosomal scanning. The position of each start site along the transcript is listed above with an arrow. (**B**) Ribosomes scan mRNA transcripts until the first ATG, where they initiate translation. (**C**) The sequence of bases flanking ATG sites (Kozak sequence) determines the strength or probability of ribosomal initiation. R= A or G. If a Kozak sequence is weak, the (B) ribosome can continue scanning past the first ATG site to another ATG further downstream in the transcript - this is referred to as leaky ribosomal scanning. (**D**) A rare variant analysis of GEN-COVID database (performed by Dr. Johnathan Cooper-Knock) revealed eight MAVS-SNPs in severely ill COVID-19 patients admitted to the ICU. Patients were excluded if they were >60 years of age, and had lung disease or diabetes mellitus. SNPs within or flanking MAVS isoform start sites are highlighted in pink. Panel B is taken from www.viralzone.expasy.org/1976. Panel D made with BioRender.

Figure 12: Expression and Function of MAVS Protein Between Mutant Constructs.
(A) HEK293-p125-MAVS-KO cells were transfected with pLenti-MAVS-WT and the indicated MAVS mutants. Untransfected cells (mock), and cells transfected with empty vector (EV) or pcDNA-MAVS acted as controls. (B) Densitometry was performed on MAVS-FL and MAVS-M2 bands corresponding to 72kDa and 50kDa respectively using ThermoFishers Connect platform (n=1). (C) In parallel cells were lysed for OneGlo luminescence assay and (D) RNA isolation for RT-qPCR. Results in Panel C are data from two independent biological repeats with three technical replicates in each experiment. Data was averaged and normalized against pLenti-MAVS-WT, with each plotted point representing the normalized biological replicate (average and range, n=2). Results in Panel D are data from one biological experiment with technical duplicates graphed (average and range, n=1). Dotted lines indicate MAVS-WT levels.

Figure 13: MAVS expression in Transfected HEK293-p125 Cells.
(**A**) Flow chart of the following experiments with MAVS mutants. HEK293-p125-MAVS-KO cells were transiently transfected with MAVS constructs or control plasmids and either (**B**) left to incubate for 48 hours or (**C**) stimulated 24 hours later with 3.3ng IVT RNA. 24 hours after stimulation, lysates were collected for immunoblotting. Densitometry was performed on MAVS-FL and MAVS-M2 bands corresponding to 72kDa and 50kDa respectively. Panel B and C show one independent experiment (n=1). Dotted lines drawn for the MAVS-WT FL and M2 expression profiles.

Figure 14: Functional impact of MAVS SNPs in Transfected HEK293-p125 Cells.
HEK293-p125-MAVS-KO cells were transfected with MAVS constructs or control plasmids and stimulated 24 hours later with (**A**) 3.3ng or (**B**) 100ng IVT RNA. (**A**) After an overnight incubation, activation of the IFNβ promoter was assayed via OneGlo luciferase assay. (**B**) 24 hours after stimulation, RNA was isolated from lysates and RT-qPCR was performed for the indicated genes. Panel A shows averaged data from three independent biological repeats with three technical replicates each (average and

range, n=3). Panel B shows data from one biological repeat with technical duplicates. (average and range, n=1). Dotted lines drawn for MAVS-WT expression profiles.

Figure 15: MAVS SNPs Elicit a Reduced IFN Response.
(**A**) HEK293-p125-MAVS-KO cells were transduced with the indicated MAVS constructs and subject to immunoblotting. (**B**) Densitometry was performed on MAVS-FL and MAVS-M2 bands corresponding to 72kDa and 50kDa respectively using ThermoFishers Connect platform (n=3). (**C**) Cells were stimulated with 0.1ng IVT RNA and lysed 24 hours later for OneGlo luminescence assay. Panel A is a representative blot from three independent biological experiments (n=3). Panel B data derived from the blot in Panel A. Dotted lines drawn for MAVS-WT expression profiles. Panel C shows pooled data from three independent biological experiments. Panel C: Multiple comparison two-way ANOVA (ns, not significant=p>0.05, *=p≤0.05, **=p≤0.01, ***=p≤0.001, ****=p≤0.0001) (Mean and SEM, n=3).

Figure 16: Aggregation of MAVS is depleted in MAVS mutants.
(**A**) Depiction of RIG-I-induced MAVS aggregation on the mitochondria. (**B**) HEK293-p125-MAVS-KO cells were transfected with the indicated expression plasmids. The next day cells were stimulated with 1µg IVT RNA. Lysates were collected 24 hours later and subject to subcellular fractionation to isolate mitochondria. Protein was run on a 1.5% agarose gel and membranes were probed with the indicated antibodies. Panel A shows representative blot from three independent experiments. Panel A is taken from Hou et al. 2011. doi: 10.1016/j.cell.2011.06.041.

Figure 17: MAVS-C5T Polymorphism Reduces Protein Expression.
(**A**) Huh7-MAVS-KO cells were transduced with indicated expression plasmids and stimulated with 100ng IVT RNA. The next day, lysates were collected for immunoblotting and probed with the indicated antibodies. Panel A is a representative blot from two independent biological experiments (n=2). (**B**) Densitometry was performed (Panel A) on MAVS-FL and MAVS-M2 bands corresponding to 72kDa and 50kDa respectively using ThermoFishers Connect platform (n=1). Dotted lines drawn for MAVS-WT expression profiles.

Figure 18: MAVS SNPs Elicit Differential Expression of Cytokines.
Huh7-MAVS-KO cells were transduced with the indicated plasmids and stimulated with 25ng of Poly I:C. The next day, lysates were collected for (**A**) immunoblotting with the indicated antibodies and (**B**) processed for RT-qPCR for the indicated genes. Panel A is a representative blot from four independent biological experiments (n=4). Panel B shows pooled data from three independent biological experiments. Panel B: Multiple comparison two-way ANOVA (ns, not significant=p>0.05, *=p≤0.05, **=p≤0.01, ***=p≤0.001, ****=p≤0.0001) (Mean and SEM, n=3).

Figure 19: VZV Genome Composition.
(**A**) The VZV dsDNA genome is 125kb and encodes at least 71 unique ORFs. The genome is categorized into unique long region (UL), unique short region (US), internal repeat (IR), and terminal repeat (TR) regions. (**B**) The VZV virion is composed of a linear genome packaged into an icosahedral nucleocapsid core, which is surrounded by a protein tegument layer. The outer virion is made up of a lipid membrane envelope with

incorporated glycoproteins. Figure from Zerboni et al. 2014. doi: 10.1073/pnas.0501045102.

Figure 20: VZV Primary and Latent Pathogenesis.
VZV is transmitted via aerosolized droplets that infect the upper respiratory tract and tonsils. Circulating T cells become infected in the tonsils and transport virus to the skin where varicella blisters form. Latency is established in the sensory ganglia after transport along the neuronal axon or by T-cell viremia. Reactivation of the virus, establishes a second phase of viral replication in skin, causing zoster blister formation in the dermatome. Figure is from Zerboni et al. 2014. doi: 10.1073/pnas.0501045102.

Figure 21: VZV Lytic Replication Cycle.
VZV virions fuse to the membrane where capsids are transported to nuclear pores. The linear dsDNA viral genome is inserted into the nucleus where its circularizes and viral replication occurs. Its thought immediate early genes are transcribed, followed by early and late genes. The newly synthesized DNA is packaged into nucleocapsids, which then bud across the nuclear membrane. In the cytoplasm, a secondary envelopment adds glycoproteins and tegument to the capsid. A portion of virions exit the late endosomes and are released from the plasma membrane. Figure is from Gershon et al. 2015. doi: 10.1038/nrdp.2015.16.

Figure 22: Immune Response to VZV Infection.
VZV-ORF66 can act to delay or prevent T cell mediated apoptosis to promote viral dissemination. Dendritic cells increase secretion of IFNa in an anti-viral response against VZV infection. TLR2, TLR3 and TLR9 have been linked with to a role in VZV recognition and mediating an inflammatory cytokine response. Figure has been adapted from Hakami et al. 2024. doi: 10.1002/rmv.2554. Made with BioRender.

Figure 23: Chickenpox Parties.
(**A**) Maggie bathes in punch to expose the neighbourhood children to chickenpox that is shed from vesicular fluid in her chickenpox lesions. Featured in The Simpsons S17E03. (**B**) Cartman bathes in a tub full of calamine lotion, as it was said to ease the itching of chickenpox rash. Featured in South Park S02E10. (C) The Chicken Pox Party is a book published by author Sharon Wyeth about a group of school kids preparing for a play when they realize they're breaking out with chickenpox. (D) A public notice by the local health authority warning of chickenpox infection in a household.

Figure 24: VZV-ORF9 Antagonizes cGAS Through Binding and Inhibition of cGAMP Production.
(**A**) THP1 cells of the indicated genotypes were mock infected or infected with VZV for 24 and 48hr using the transwell assay. RT–qPCR analysis of *IFNβ1, IFI44*, and *IFIT1* expression in cells infected as in (C). Graphs show expression relative to GAPDH. (**B**) THP1 monocytes stably transduced with either VZV ORF9 or GFP were PMA-differentiated and transfected with indicated doses of dsDNA. Expression of *IFNβ1* and *IFNL1* was assessed by RT–qPCR. Graphs show expression relative to GAPDH. (**C**) HEK293T cells were transfected with expression plasmids for ORF9-V5, human cGAS-FLAG, and human STING-HA. The next day, cells were lysed, and overexpressed proteins were immunoprecipitated with a-V5, a-FLAG, a-HA, or IgG isotype control

antibody. Input, unbound, and IP fractions were subjected to immunoblotting using the indicated antibodies. (**D**) Recombinant cGAS, FLAG-ORF9, FLAG-GFP, and biotinylated VACV70mer dsDNA were incubated in the indicated combinations. Recombinant proteins were precipitated using streptavidin beads. Fractions were analyzed by immunoblotting. (**E**) In vitro cGAS activity assay. Recombinant hcGAS was incubated with ATP, GTP, and radioactive a32P-ATP at 37°C with addition of dsDNA and other proteins as indicated (triangles represent concentrations of 0.5, 1, 2, 4, 6 μM). ORF9-DM was tested only at 0.5, 1, 2 μM. Reactions were treated with calf-intestinal phosphatase, and products were analyzed by thin-layer chromatography and phosphorimaging. Statistical anayalsis in Panel A was a paired ratio t-test. *This figure represents a summary of data from Hertzog et al. 2022. doi: 10.15252/embj.2021109217. All work featured in this figure was completed by Dr. Jonny Hertzog.

Figure 25: ORF9 inhibition of IFN signalling is not STING dependent.
(**A**) THP1 monocytes were treated with increasing doses of STING agonist diABZi to determine sub-maximal response. Expression of IFNβ1, IFIT1, and IFI44 was assessed by RT–qPCR (**B**) THP1 monocytes stably transduced with either VZV ORF9 or GFP were treated with diABZi (0.005 μM). Expression of IFNβ1, IFIT1, and IFI44 was assessed by RT–qPCR. Graphs show expression relative to GAPDH. Panel A shows pooled data from two repeats, where each data point represents technical replicates (horizontal bars show means). Panel B shows pooled data from three repeats, where each data point represents an independent biological experiment (horizontal bars show means). Statistical analysis in Panel B was a paired t-test.

Figure 26: ORF9 Predicted DNA Binding Region is Dispensable for cGAS Inhibition.
(**A**) THP1 cells stably transduced with GFP, ORF9, or ORF9-DM were transfected with the indicated amounts of E. coli dsDNA. The next day, IFNB1 expression was assessed by RT–qPCR. Panel (A) shows pooled data from two repeats, where each data point represents an independent biological experiment (n = 2). (**B**) THP1 cells stably transduced with GFP, ORF9, or ORF9-DM cells were lysed and protein abundance was analyzed via immunoblotting using the indicated antibodies. This is a representative blot from three independent biological experiments. (n=3).

Figure 27: Screen of ecDHFR stabilization compounds.
To identify these potential ecDHFR molecules, the authors screened an ARPE-19 cell line that constitutively expresses R12Y/G67S/Y100I ecDHFR fused to yellow fluorescent protein. After validation of hit compound stabilizing effects after 24 h of treatment, the authors next determined how quickly and efficiently select compounds could stabilize ecDHFR-YFP, followed by destabilization after compound withdrawal. Figure taken from Ramadurgum et al. 2020. doi:10.1016/j.chembiol.2020.03.006.

Figure 28: Screening of All VZV ORFs Identifies ORF9 as an Antagonist of cGAS-Mediated DNA Sensing.
(**A**)Schematic detailing the E. coli DHFR degron system. (**B**)Schematic detailing the experimental procedure for Fig. 28-30. See text for details.

Figure 29: Test Panel of Small Molecular Pharmacological Chaperone Stabilization (SMPC) Efficiency.
(**A**) THP1 cells were co-cultured with infected MeWo-VZV-ORF9-ecDHFR for 1 hour, washed and left to infect overnight in TMP-containing media. Approximately 24 hours later, the cells were washed and replaced with SMPC-containing media for a further 48 hours. Cells were lysed 48 hours post SMPC -/+ and ORF9 protein abundance was assessed via immunoblotting (n=1). (**B**) A set of duplicated experimental cells were lysed to assess ISG induction and viral abundance (**C**) via RT-qPCR (n=1, average of technical duplicates).

Figure 30: TMP Time Course Experiment.
(**A**) THP1-Dual IRF3 reporter cells were co-cultured with infected MeWo-VZV-ORF9ecDHFR cells for 1 hour. The TMP was removed by washing and replaced with fresh R10 (-, TMP removal) or R10 with fresh TMP (+, TMP re-addition) until the indicated time points. IFNβ1 or TMP was added to media as a positive and negative control respectively. Luminescence was measured via a microplate reader after the addition of the luciferase reagent Quanti-Luc to the supernatant of cells. (**B**) THP1 cells were co-cultured with infected MeWo-VZV-ORF9ecDHFR cells. In the 'Serial Washes' condition, infected MeWo cells were left to co-infect overnight. The next morning the TMP was removed by washing and replaced with fresh R10 (-, TMP removal) or R10 with fresh TMP (+, TMP re-addition) until the indicated time points. For the 'No TMP' condition the infected MeWo cells were left to co-infect for only 1 hour. Then the TMP was removed by washing and replaced with fresh R10 (-, TMP removal) or R10 with fresh TMP (+, TMP re-addition) until the indicated time points. Cells were analyzed by western blotting with the indicated antibodies. Panel (A) shows pooled data from two independent biological experiments (n=2, average of biological repeats shown). Panel (B) is a representative blot from two independent biological experiments.

Figure 31: Conditional Knockdown of ORF9 Reduces ISG and IFN Response.
(**A**) PMA-differentiated THP1 cells were co-cultured with VZV-ORF9ecDHFR-infected MeWo cells for 1 h in the presence of TMP, washed, and incubated for another 24 h in the presence of TMP. Cells were then washed extensively, and fresh medium was added that was supplemented or not with TMP. Expression levels of IFNβ1, IFIT1, and IFI44 were measured by RT–qPCR after a further 24 h incubation. Graphs show expression relative to GAPDH. Mean fold changes are indicated. (**B**) Cells infected and treated as in (A) with the addition of uninfected cells were analyzed by western blotting using the indicated antibodies. Panel (A) shows pooled data from three repeats, where each data point represents an independent biological experiment. Fold change was calculated from the average of repeats. Statistical analysis was a paired t-tests, preformed on the three repeats. Panel (B) is representative of three independent experiments.

Figure 32: HaCaT Cells, Primary Keratinocytes and Primary Fibroblasts Do Not Detect VZV Infection.
HaCaT cells (**A, B**), primary keratinocytes (**C, D**) and primary fibroblasts (**E, F**) were infected with VZV by co-culture with VZV-infected MeWo cells or as control were co-cultured with uninfected MeWo cells. After 1h, inoculum MeWo cells were washed away. At the indicated time points, RNA was extracted for RT-qPCR analysis. (A, C, E)

RT-qPCR analysis of IFIT1 and IFI44. Data are shown relative to GAPDH. (B, D, F) RT-qPCR analysis of VZV ORF54 (early (E) gene) and ORF40 (late (L) gene) transcripts. Data are shown relative to GAPDH. Results shown are from one biological experiment (n=1), data points represent technical duplicates.

Figure 33: Summary of cGAS-STING Pathway Components Targeted by Pathogens.
Parts of the cGAS-STING signalling cascade targeted by viruses are indicated by a checked box. Components suspected to be targeted are annotated with a red box. Figure taken from Eaglesham and Kranzusch 2020. doi: 10.1016/j.coi.2020.04.002.

Figure 34: VZV-ORF9 Has Homologous Residues with Human Histone H2A.
(**A**) Semi-global amino acid sequence alignment of VZV-ORF9 and human histone H2A. Black = identical, blue = similar, red = not similar. (**B**) A list of all hH2A residues described to bind cGAS in the nucleus. An X indicates the publication(s) that annotated hH2A residue(s) as binding to cGAS. Green = Alignment with ORF9, red = Does not align with ORF9, yellow = Not aligned, negative to neutral charge (see text for further description). (**C**) Image taken from Kujirai et al. 2020. cGAS's (cyan) arginine anchor bound to the acidic patch of hH2A (pink). (D) Residues of interest from the semi-global alignment of hH2A and hH2B with ORF9 are highlighted with arrows. VZV-ORF9 mutants of 106, 109, 211, and 227 were generated in this project.

Figure 35: Dual Luciferase Assay Schematic.
HEK293T cells were transfected with pRL-TK which expresses renilla luciferase under a TK promoter and p125-F-Luc to express firefly luciferase under the control of an IFNβ reporter. Cells were also transfected with cGAS and STING, along with ORF9 expression constructs and the control plasmids EV and EMCV-L. 24 hours post-transfection, luminescence was quantified for both renilla and firefly luciferase. Firefly luminescence was divided by renilla luminescence to normalize for transfection efficiency.

Figure 36: ORF9 Histone Mutant Shows Reduced Ability to Block cGAS Activation.
(**A**) HEK293T cells were transfected with p125-F-Luc, pRL-TK, STING and cGAS-WT or cGAS-R255E plasmids. Cells were also transfected with either control plasmids (EV or EMCV-L) or ORF9 expression plasmids. Luciferase activity was assayed 24 hours post-transfection. (**B**) THP1 cells transduced with GFP or ORF9 constructs were stimulated with 200ng E. coli DNA and left to incubate for 24 hours. Cells were lysed for RNA isolation and mRNA expression of the indicated transcripts was assessed for RT-qPCR. (**C-F**) HEK293T cells were transfected with expression plasmids for FLAG-ORF9, cGAS-V5, or STING-HA. 24 hours later, cells were lysed for ectopically expressed proteins were immunoprecipitated using epitope tag antibodies. The input, unbound and bound fractions were subject to immunoblotting using the indicated plasmids. Panel A shows pooled data from two independent biological experiments. Panel B shows pooled data from three independent biological experiments. Panel C & F shows a representative blot from three independent biological experiments (n=3). Panel D & E shows a blot from one independent biological experiment (n=1). Panel A: Multiple comparisons two-way ANOVA (Mean and SEM, n=2). Panel B: Multiple comparisons two-way ANOVA (Mean and SEM, n=3). ns, not significant=$p>0.05$, *=$p\leq0.05$, **=$p\leq0.01$, ***=$p\leq0.001$, ****=$p\leq0.0001$.

Figure 37: VZV-ORF9E106R/E109R Inhibit cGAS Activation.
(**A**) THP1 cells transduced with GFP or ORF9 constructs were stimulated with 200ng E. coli DNA and left to incubate for 24 hours. Cells were lysed for RNA isolation and mRNA expression of the indicated transcripts was assessed for RT-qPCR. (**B**) Remaining cell lysate from (C) were subject to immunoblotting with the indicated antibodies. (**C**) HEK293T cells were transfected with p125-F-Luc, pRL-TK, STING and cGAS-WT or cGAS-R255E plasmids. Cells were also transfected with either control plasmids (EV or EMCV-L) or ORF9 expression plasmids. Luciferase activity was assayed 24 hours post-transfection. Panel A shows pooled data from three independent biological experiments with technical duplicates, averages of the three repeats are graphed (n=3). Panel B shows a blot from one biological experiment (n=1). Panel C shows pooled data from three independent biological experiments each with technical triplicates, all data graphed (Mean and SD, n=3).

Figure 38: Transduced HFF Experiment Schematic.
HFF transduced with ORF9 and GFP constructs were stimulated with either IVT RNA or E. coli DNA and left to incubate for 24 hours. Cells were lysed to quantify cGAMP concentration via cGAMP ELISA. In parallel cells were lysed for immunoblotting and RNA isolation for quantifying mRNA expression levels via RT-qPCR.

Figure 39. Transduced HFFs Expressing Mutant ORF9 Constructs Have Reduced Ability to Antagonize cGAS.
HFF cells stably transduced with either GFP or ORF9 constructs, were stimulated with E. coli dsDNA and the induction of ISG and IFN were assessed via cGAMP ELISA 24 hours post transfection. Three independent experiments were conducted in which cells were collected for ELISA, RT-qPCR and western blotting. (**A**) Western blotting was used to assess protein expression levels from whole cell lysates. (**B**) The concentration of cGAMP was calculated against a standard curve, normalized against total cell lysate protein concentration and normalized against the stimulated GFP condition. (**C**) Expression levels for the indicated mRNA transcripts were assessed via RT-qPCR (mean and SEM, n=3). Panel A is a representative blot from three independent biological experiments (n=3). Panel B shows pooled data from three independent biological experiments. Each experiment is denoted with a unique symbol. Panel B: Multiple comparison two-way ANOVA (ns, not significant=$p>0.05$, *=$p\leq0.05$, **=$p\leq0.01$, ***=$p\leq0.001$, ****=$p\leq0.0001$) (mean, n=3). Panel C shows pooled data from three independent biological experiments where relative expression of each probe was normalized against GAPDH and GFP.

Figure 40: Workflow Schematic of Experiments in HEK293T Cells.
HEK293T Cells were transfected with mSTING-FRET and hcGAS. Cells were also transfected with EV or ORF9 expression constructs. Cells were lysed 24 hours later for immunoblotting and cGAMP ELISA. In parallel cells were collected to assess FRET shift via flow cytometry.

Figure 41: Mutations in ORF9 Promote Increased cGAMP Production.
HEK293T cells were transfected with mTurq-STING-YPet, hcGAS, EV and ORF9 constructs. 24 hours post-transfection, cells were collected for FRET assay (Fig. 28), immunoblotting and cGAMP ELISA. Whole cell lysates were collected for (**A**) and (**B**),

while intact cells were used in flow cytometry. Panel A shows a representative blot from three independent biological experiments (n=3). Panel B shows cGAMP concentrations calculated from the analysis of technical duplicates in one biological experiment (n=1).

Figure 42: Flow cytometry assay to measure level of STING activation.
(**A**) The mTurquoise2-mSTING-YPet plasmid, developed by Zierhut et al., undergoes a conformational change when bound by cGAMP. This brings the two fluorophores within close proximity, shifting the emission wavelength. The mSTING plasmid is truncated to no longer contain the transmembrane section, therefore it is incapable of downstream signalling. PDB: 4EMU and 4KSY. (**B**) Flow cytometry gating strategy. (**C**) Percent FRET shift was pooled and normalized to the tSTING + cGAS + EV condition. Two-way ANOVA with Dunnett's multiple comparisons was used to compare results for each construct. p-values indicated above bars. Panel C shows pooled data from three independent biological experiments (n=3). (**D**) Blue dots represent cells transfected with tSTING plasmid in an unbound state. Red dots indicate transfected tSTING cells that have been activated by cGAMP and have CFP-YFP fluorophores in close proximity to elicit a shift in fluorescence.

Figure 43: ORF9 Mutants Retain Binding Ability to cGAS.
HEK293T cells were transfected with cGAS and ORF9 expression constructs. 24 hours post-transfection cells were lysed for ectopically expressed proteins and were immunoprecipitated using epitope tag antibodies. The input, unbound and bound fractions were subject to immunoblotting using the indicated plasmids. This figure shows a representative blot from three independent biological experiments (n=3).

Figure 44: ORF9-cGAS Interaction is Salt Resistant.
HEK293T cells were transfected with expression plasmids for FLAG-ORF9, cGAS-V5, or STING-HA. 24 hours later, cells were lysed with a lysis buffer containing an increasing concentration of salt and ectopically expressed proteins were immunoprecipitated using a V5 epitope tag antibody. The input, unbound and bound fractions were subject to immunoblotting using the indicated plasmids. This data depicts a representative blot from two independent biological experiments (n=2).

Figure 45: Histones do not disrupt ORF9-cGAS complexes.
(**A**) A schematic of IP methodology. (**B**) HEK293T cells were transfected with expression plasmids for FLAG-ORF9 and cGAS-V5. 24 hours later, cells were lysed with a lysis buffer (500mM NaCl) and ectopically expressed proteins were immunoprecipitated using a V5 epitope tag antibody. The first set of unbound fractions were collected before histones were added to the beads, and the second set of unbound fractions were collected after incubation of histones with beads for 1 hour. The input, unbound and bound fractions were subject to immunoblotting using the indicated plasmids. Panel B shows a representative blot from three independent biological experiments (n=3).

Figure 46: AlphaFold Predictions of VZV-ORF9.
(**A**) AlphaFold protein prediction of VZV-ORF9 (ORF9 E89 to G241, unstructured tail region removed for clarity). (**B**) AlphaFold-multimer prediction of VZV-ORF9 (C170-G241) binding to hcGAS. (**C**) Resolved secondary structure of hH2A-H2B visualized on

PDB Mol* 3D Viewer. (**D**) AlphaFold-multimer prediction of hH2A and hcGAS. (**E-F**) Resolved structure of hH2A-H2B (PDB: 2RVQ) superimposed onto ORF9 monomer (blue) using ChimeraX (work done by Kendra Leigh, Cambridge, UK). Chain C refers to H2A, Chain D refers to H2B. (**G**) Predicted cGAS ORF9 binding model showing a close-up of cGAS (orange) residues R204 and K198 binding to ORF9 (green) residues D213 and L216. Visualized using PDB Mol* 3D Viewer.

Figure 47: VZV ORF9 Binds cGAS.
(**A**) Schematic detailing ORF9 truncation mutants used in (B). (**B**) HEK293T cells were transfected with expression plasmids for human cGAS and ORF9 truncation mutants. The next day, cells were lysed and ORF9 proteins were immunoprecipitated using a-FLAG antibody. IP fractions were subjected to immunoblotting using the indicated antibodies. This figure and figure description were taken directly from our Hertzog et al. 2022. publication and was completed in its entirety by Jonny Hertzog. doi: 10.15252/embj.2021109217.

Figure 48: Mutations in MAVS Alters its Downstream Signalling Ability.
This schematic summarizes the findings from Chapter 3, comprising data from my MAVS project. The translation of MAVS can result in the production of full-length or five truncated isoforms of MAVS. Full-length MAVS has anti-viral functions, while the truncated isoforms function to counteract the downstream synthesis of ISGs and IFNs. Mutations in Kozak sequences of alternative start sites or the start sites themselves result in skewed production of MAVS truncated isoforms. The MAVS-C5T mutation weakens the Kozak sequence flanking the start site for full-length canonical MAVS and results in reduced ISG/IFN induction and MAVS aggregation in vitro. The MAVS-G1074C mutation alters the original MAVS-M4 ATG site to an ATC, thereby preventing MAVS-M4 translation. This results in an increased production of ISGs and larger MAVS aggregates compared to WT MAVS. Graphic made using BioRender.com.

Figure 49: VZV-ORF9 Acts as a Histone Mimic to Bind and Inhibit cGAS.
This schematic summarizes the findings from Chapter 5, comprising data from my VZV project. cGAS is inhibited in the nucleus by human histone H2A-H2B. This interaction is primarily mediated by the R255 residue of cGAS to four residues of hH2A (E61, E64, D90 and E92) that make up its the acidic patch. VZV-ORF9 possesses a similar acidic patch as hH2A. In VZV infected cells, ORF9 binds to cGAS via its own acidic patch to inhibit the production of cGAMP and thereby preventing downstream anti-viral activation. Graphic made using BioRender.com.

Supplemental Figure S1: cGAMP ELISA Experiments.
HFF cells stably transduced with either GFP or ORF9 constructs, were stimulated with *E. coli* dsDNA and the induction of ISG and IFN were assessed via cGAMP ELISA. Three independent experiments were conducted in which cells were collected for ELISA and western blotting. The concentration of cGAMP was calculated against a standard curve and normalized against total cell lysate protein concentration.

Supplemental Figure S2: **ORF9 Transduced Cells Secrete Reduced Levels of IFNβ.**
HFF cells were transduced with GFP and ORF9 constructs and stimulated with E. coli DNA. Cells were used for cGAMP ELISA (Fig. 39) while supernatants from stimulated

cells were collected 24 hours post-stimulation to assess IFNβ concentration via ELISA (n=2). Limit of detection was determined from IFNβ standards.

Supplementary Figure S3: mRNA Expression of ORF9 is Stable Between Constructs.
HFF cells transduced with ORF9 constructs were stimulated with IVT RNA (not shown) and E. coli DNA. 24 hours later cells were lysed for immunoblotting, cGAMP ELISA and RT-qPCR (results in Figure 39). The mRNA expression levels for VZV-ORF9 was determined by RT-qPCR using a custom TaqMan probe from ThermoFisher Scientific. Data shows pooled data from three independent biological experiments each with technical duplicates (mean and SEM, n=3). Each biological experiment is denoted with a unique symbol.

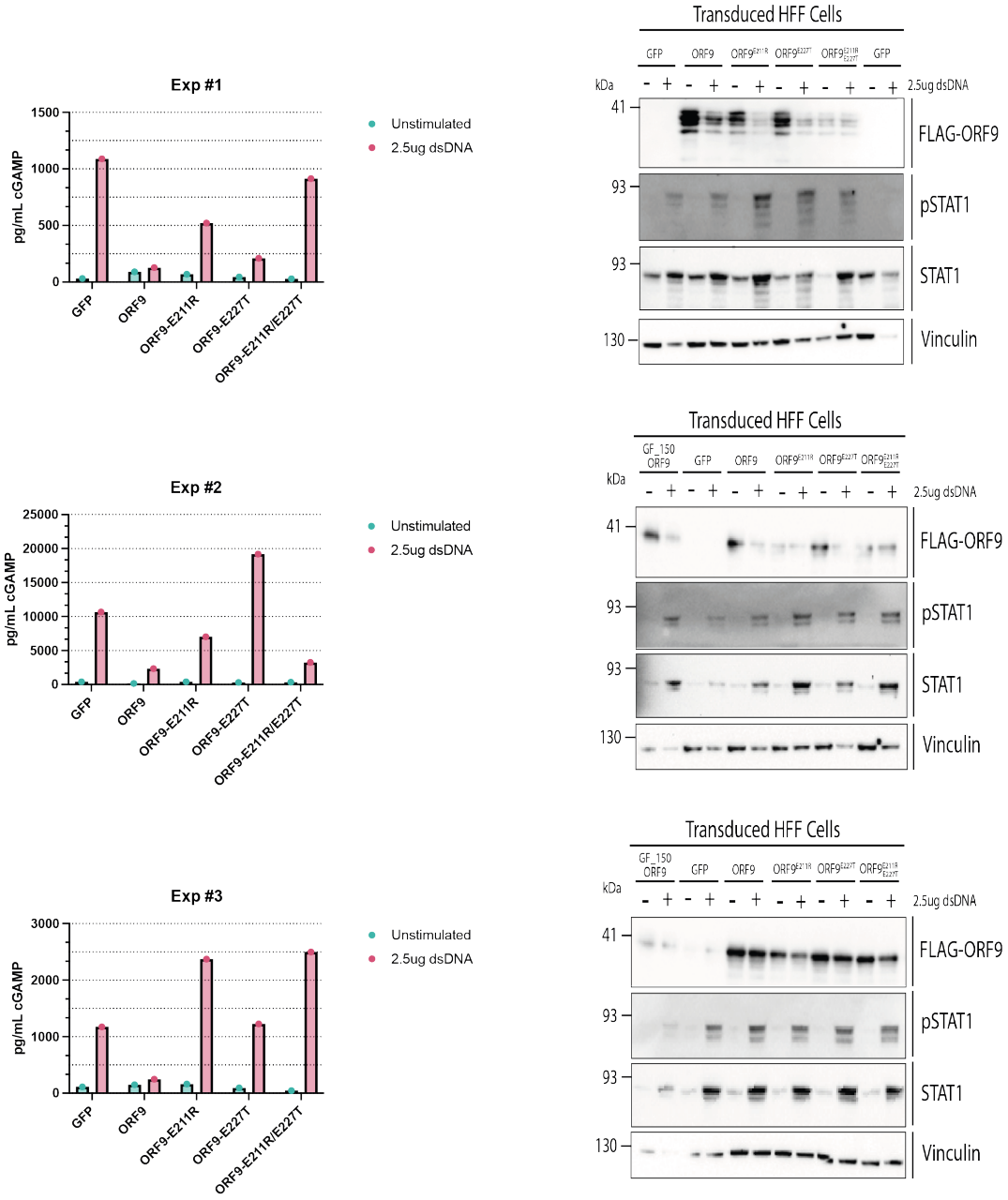
Supplementary Figure S4: Gating strategy.
Corresponds to results summarised in Figure 42 and discussed in section 5.5. HEK293-TLA cells transiently expressing the indicated genes were assessed for STING activation via FRET shift by flow cytometry (n=3).

Supplemental Figure S5: Flow Cytometry Assay to Measure Level of STING Activation.
(**A-C**) FRET gates represent cells transfected with tSTING plasmid in an unbound state. FRET Shift gates indicate transfected tSTING cells that have been activated by cGAMP and have CFP-YFP fluorophores in close proximity to elicit a shift in fluorescence. Three independent biological experiments depicted (n=3).

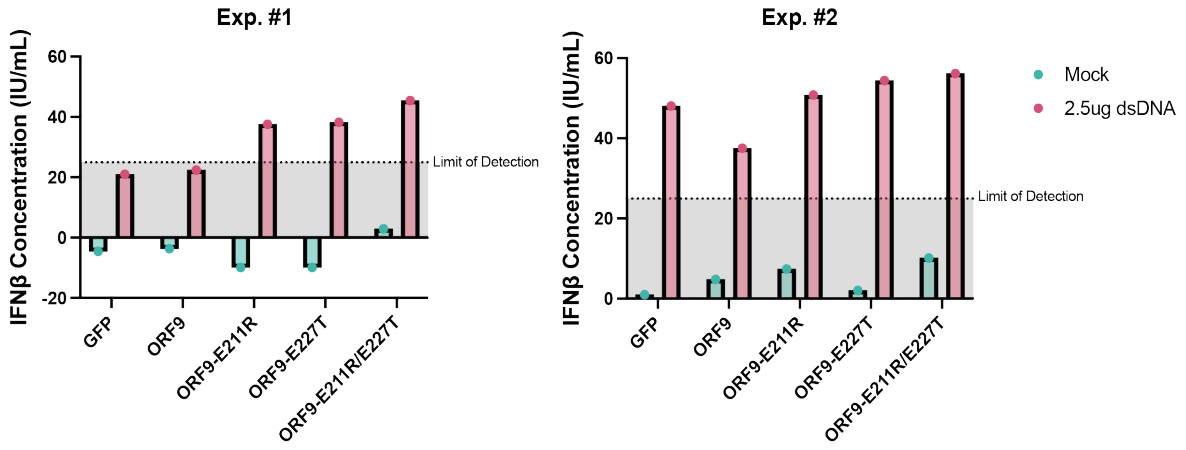
Supplemental Figure S6: Flow Cytometry Assay To Measure the Level of STING Activation via mcGAS.
(**A**) Flow cytometry gating strategy. (**B**) Percent FRET shift was pooled (n=3) and normalized to the tSTING + cGAS + EV condition. Two-way ANOVA with Dunnett's multiple comparisons was used to compare results for each construct. (**C**) Cells within the 'FRET' gate represent cells transfected with tSTING plasmid in an unbound state. Cells present in the 'FRET Shift' gate indicate transfected tSTING cells that have been activated by cGAMP and have CFP-YFP fluorophores in close proximity to elicit a shift in fluorescence.

Supplementary Figure S7: Expression of mcGAS and ORF9 in HEK293T Cells.
HEK293T cells were transfected with tSTING, mcGAS or hcGAS, EV and ORF9 constructs. 24 hours later, a fraction of cells were collected for immunoblotting. The remaining cells were subject to flow cytometry to quantify FRET shift (Supp. Fig. S6). Data in this figure is a representative blot from three independent biological experiments (n=3).

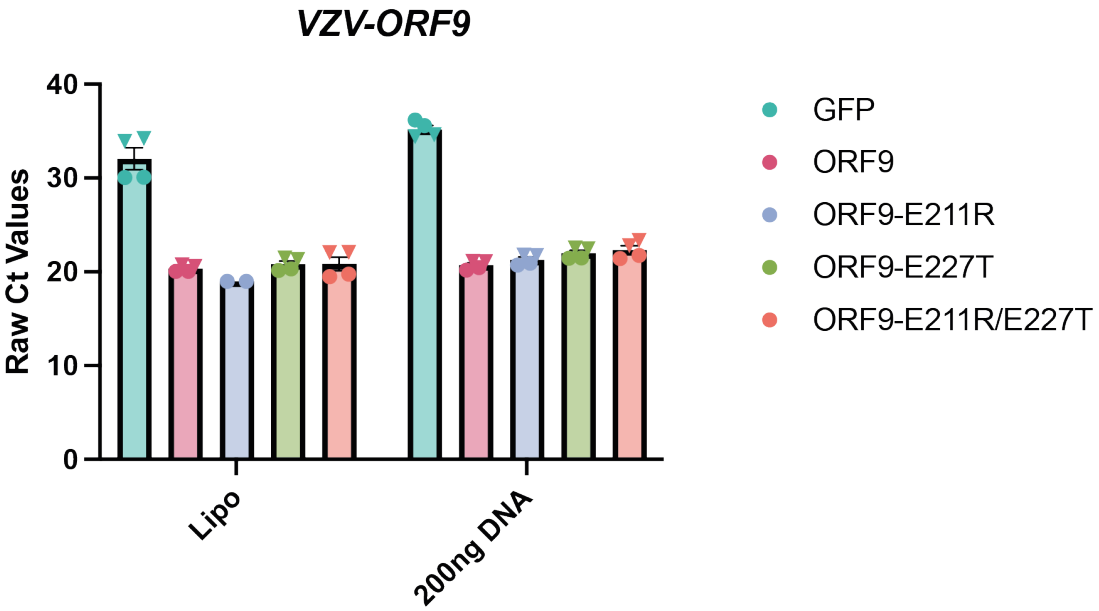
Supplemental Figures



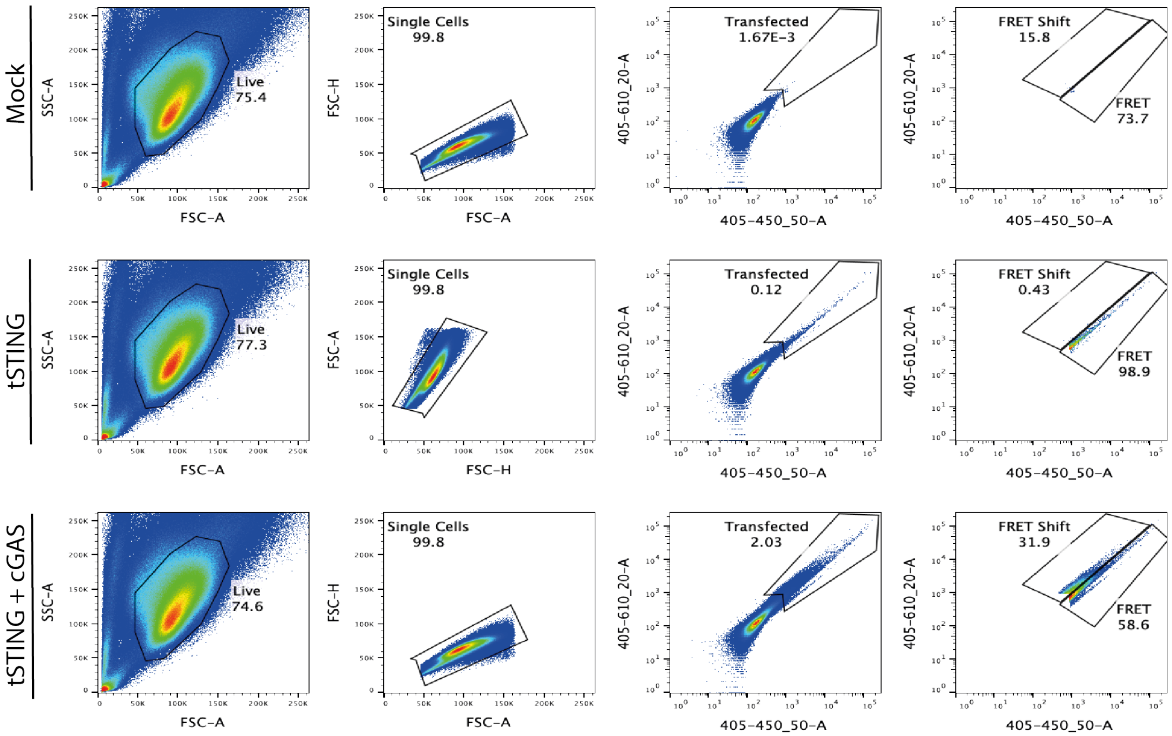
Supplemental Figure S1: cGAMP ELISA Experiments.
HFF cells stably transduced with either GFP or ORF9 constructs, were stimulated with *E. coli* dsDNA and the induction of ISG and IFN were assessed via cGAMP ELISA. Three independent experiments were conducted in which cells were collected for ELISA and western blotting. The concentration of cGAMP was calculated against a standard curve and normalized against total cell lysate protein concentration.



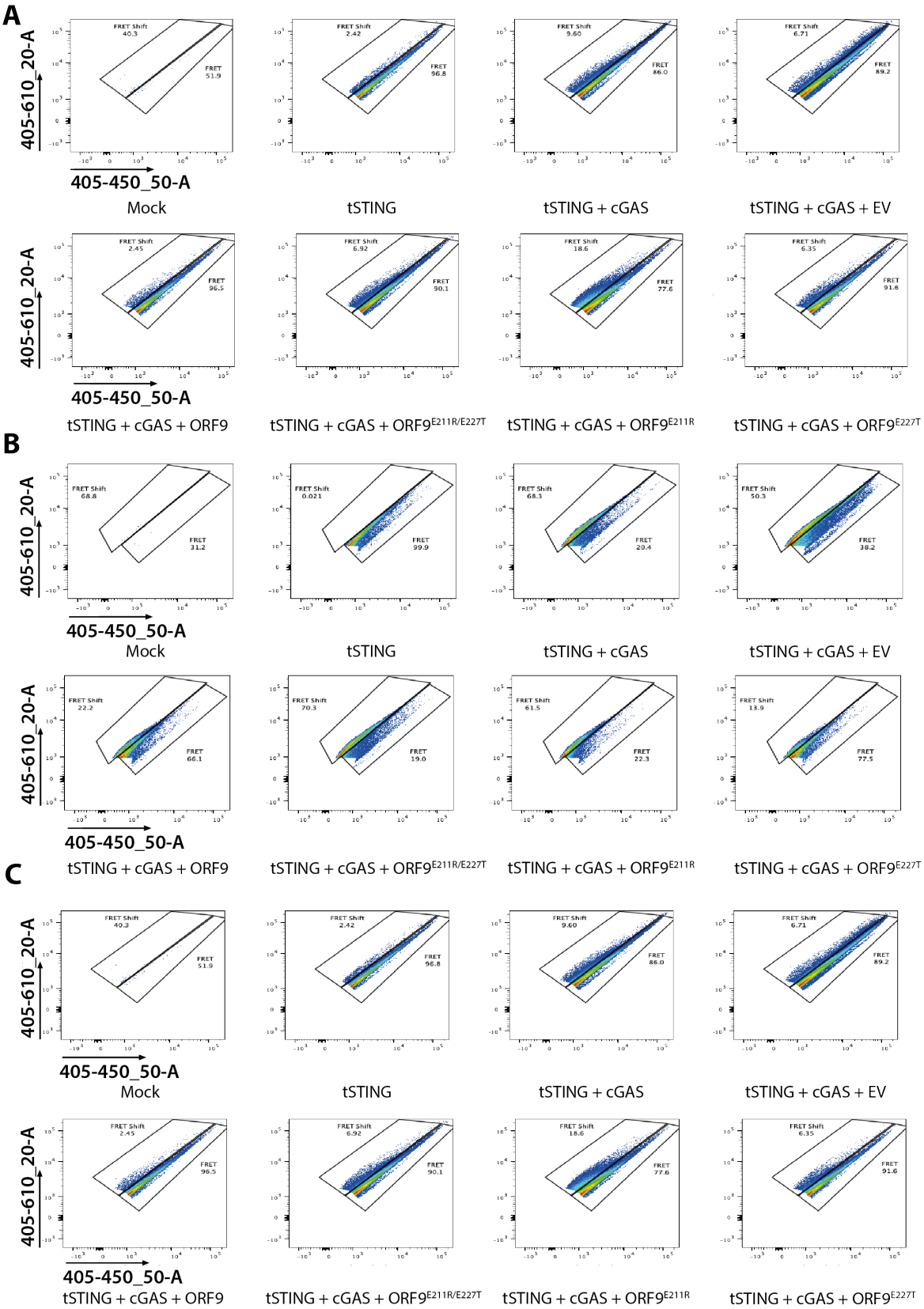
Supplemental Figure S2: ORF9 Transduced Cells Secrete Reduced Levels of IFNβ.
HFF cells were transduced with GFP and ORF9 constructs and stimulated with *E. coli* DNA. Cells were used for cGAMP ELISA (Fig. 39) while supernatants from stimulated cells were collected 24 hours post stimulation to assess IFNβ concentration via ELISA (n=2). Limit of detection was determined from IFNβ standards.



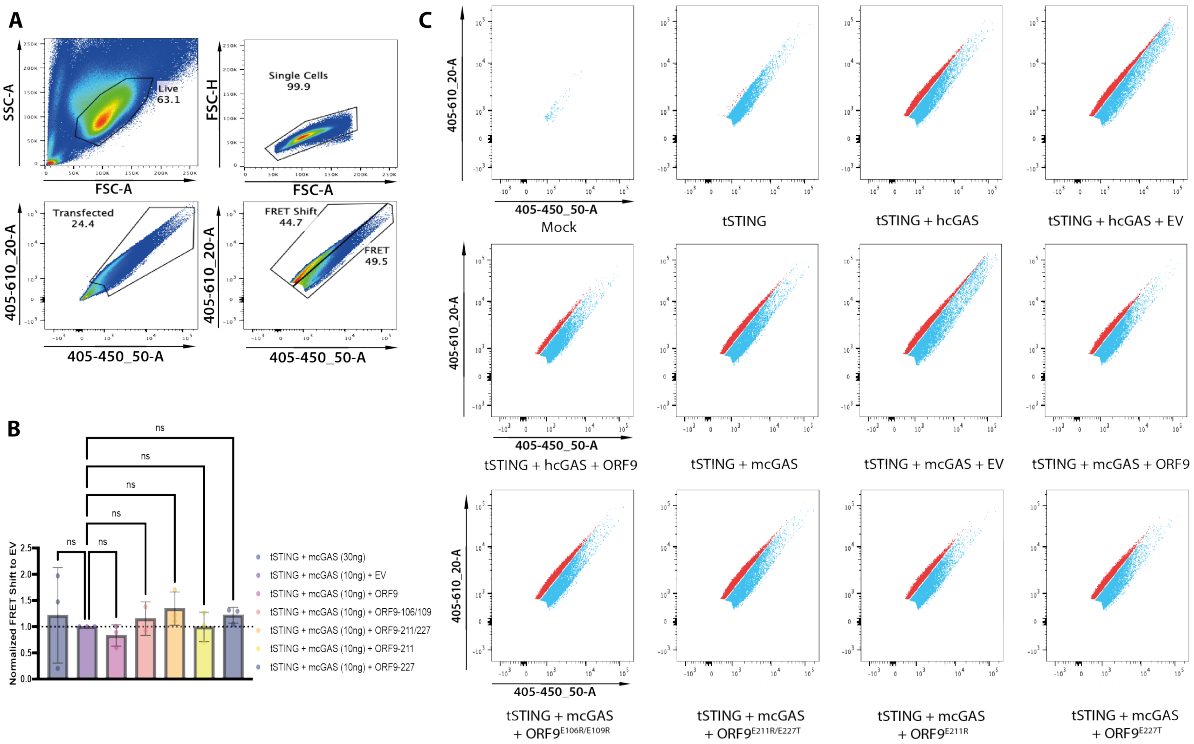
Supplementary Figure S3: mRNA Expression of ORF9 is Stable Between Constructs.
HFF cells transduced with ORF9 constructs were stimulated with IVT RNA (not shown) and *E. coli* DNA. 24 hours later cells were lysed for immunoblotting, cGAMP ELISA and RT-qPCR (results in Figure 39). The mRNA expression levels for VZV-ORF9 was determined by RT-qPCR using a custom TaqMan probe from ThermoFisher Scientific. Data shows pooled data from two independent biological experiments each with technical duplicates (mean and SEM, n=2). Each biological experiment is denoted with a unique symbol.



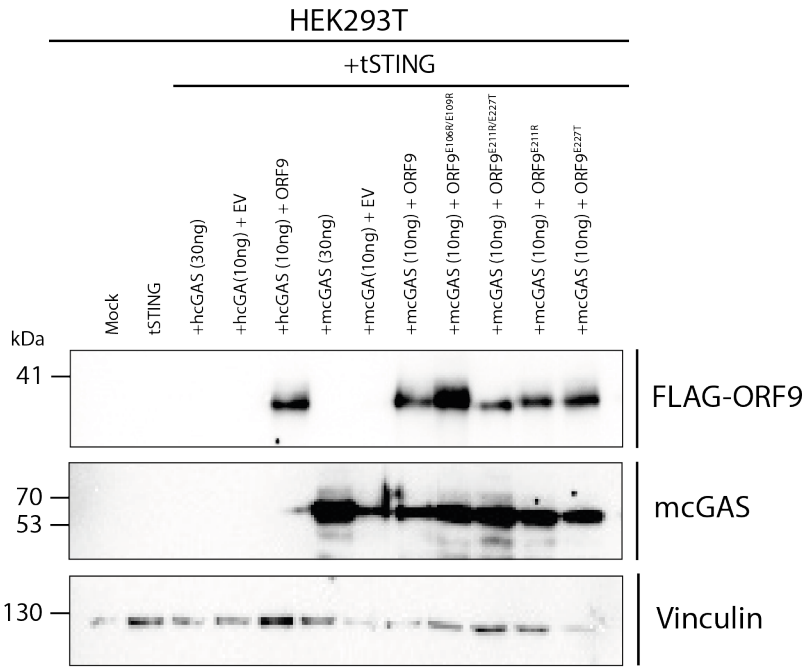
Supplementary Figure S4: Gating Strategy.
Corresponds to results summarised in Figure 42 and discussed in section 5.5. HEK293-TLA cells transiently expressing the indicated genes were assessed for STING activation via FRET shift by flow cytometry (n=3).



Supplemental Figure S5: Flow Cytometry Assay to Measure Level of STING activation.
(**A-C**) FRET gates represent cells transfected with tSTING plasmid in an unbound state. FRET Shift gates indicate transfected tSTING cells that have been activated by cGAMP and have CFP-YFP fluorophores in close proximity to elicit a shift in fluorescence. Three independent biological experiments depicted (n=3).



Supplemental Figure S6: Flow Cytometry Assay to Measure Level of STING Activation via mcGAS.
(**A**) Flow cytometry gating strategy. (**B**) Percent FRET shift was pooled (n=3) and normalized to the tSTING + cGAS + EV condition. Two-way ANOVA with Dunnett's multiple comparisons was used to compare results for each construct. (**C**) Cells within the 'FRET' gate represent cells transfected with tSTING plasmid in an unbound state. Cells present in the 'FRET Shift' gate indicate transfected tSTING cells that have been activated by cGAMP and have CFP-YFP fluorophores in close proximity to elicit a shift in fluorescence.



Supplementary Figure S7: Expression of mcGAS and ORF9 in HEK293T Cells.
HEK293T cells were transfected with tSTING, mcGAS or hcGAS, EV and ORF9 constructs. 24 hours later, a fraction of cells were collected for immunoblotting. The remaining cells were subject to flow cytometry to quantify FRET shift (Supp. Fig. S6). Data in this figure is a representative blot from three independent biological experiments (n=3).

Appendix

Hertzog, J. *et al*. Varicella-Zoster virus ORF9 is an antagonist of the DNA sensor cGAS. *The EMBO Journal* **41**, (2022).

Sampaio, N. G. *et al*. The RNA sensor MDA5 detects SARS-CoV-2 infection. *Sci Rep* **11**, 13638 (2021).

Article

SOURCE DATA | TRANSPARENT PROCESS | OPEN ACCESS

THE EMBO JOURNAL

Varicella-Zoster virus ORF9 is an antagonist of the DNA sensor cGAS

Jonny Hertzog[1,†], Wen Zhou[2,3,‡], Gerissa Fowler[1], Rachel E Rigby[1], Anne Bridgeman[1], Henry TW Blest[1], Chiara Cursi[1], Lise Chauveau[1], Tamara Davenne[1], Benjamin E Warner[4], Paul R Kinchington[4,5], Philip J Kranzusch[2,3,6] & Jan Rehwinkel[1,*]

Abstract

Varicella-Zoster virus (VZV) causes chickenpox and shingles. Although the infection is associated with severe morbidity in some individuals, molecular mechanisms that determine innate immune responses remain poorly defined. We found that the cGAS/STING DNA sensing pathway was required for type I interferon (IFN) induction during VZV infection and that recognition of VZV by cGAS restricted its replication. Screening of a VZV ORF expression library identified the essential VZV tegument protein ORF9 as a cGAS antagonist. Ectopically or virally expressed ORF9 bound to endogenous cGAS leading to reduced type I IFN responses to transfected DNA. Confocal microscopy revealed co-localisation of cGAS and ORF9. ORF9 and cGAS also interacted directly in a cell-free system and phase-separated together with DNA. Furthermore, ORF9 inhibited cGAMP production by cGAS. Taken together, these results reveal the importance of the cGAS/STING DNA sensing pathway for VZV recognition and identify a VZV immune antagonist that partially but directly interferes with DNA sensing via cGAS.

Keywords cGAS; DNA sensing; ORF9; phase separation; Varicella-Zoster virus
Subject Categories Immunology; Microbiology, Virology & Host Pathogen Interaction
DOI 10.15252/embj.2021109217 | Received 15 July 2021 | Revised 4 May 2022 | Accepted 9 May 2022 | Published online 7 June 2022
The EMBO Journal (2022) 41: e109217

Introduction

Varicella-Zoster virus (VZV) is one of nine herpes viruses that infect humans (Arvin & Gilden, 2013). VZV is an alpha-herpesvirus, closely related to herpes simplex virus (HSV) 1 and 2. It has a 125 kb dsDNA genome, the smallest of the human herpesviruses. The genome includes at least 70 open reading frames (ORFs). Primary infection causes chickenpox (*Varicella*). Like all human herpes viruses, VZV establishes life-long latency in an infected host, and VZV can reactivate as shingles (*Zoster*). Shingles is a debilitating disease with significant associated morbidity. During both primary infection and reactivation, the virus can gain access to the central nervous system and cause severe complications such as encephalitis and vasculitis (Nagel & Gilden, 2014). Despite the introduction of the live-attenuated chickenpox vaccine in the early 1990s, the virus remains highly prevalent worldwide (WHO, 2014).

The type I interferon (IFN) system lies at the forefront of host defence against infectious pathogens and is indispensable for the successful control of viral infections (McNab *et al*, 2015). The expression of type I IFNs is induced following pattern recognition receptor (PRR) activation. PRRs are a heterogenous group of proteins that can respond to a diverse array of pathogen-associated molecular patterns (PAMPs; Brubaker *et al*, 2015). The recognition of viral pathogens relies to a large extent on the sensing of nucleic acids (Barrat *et al*, 2016; Hartmann, 2017). Both endosomal toll-like receptors and dedicated cytosolic sensors are potently activated by viral RNA and DNA. The DNA sensor cyclic GMP-AMP synthase (cGAS) synthesises the second messenger 2′3′-cyclic GMP-AMP (hereafter simply cGAMP), a cyclic dinucleotide, upon direct binding to dsDNA (Ablasser & Chen, 2019). Binding of cGAMP to stimulator of IFN genes (STING) results in the activation of the transcription factors IRF3 and NF-κB via the kinases TBK1 and IKKε (Hopfner & Hornung, 2020). IRF3 and NF-κB induce the expression of type I IFNs, type III IFNs, and inflammatory cytokines.

Type I IFNs, including IFNα and IFNβ, are secreted cytokines that act in an autocrine, paracrine, or systemic manner by binding to the type I IFN receptor (IFNAR; McNab *et al*, 2015). Canonical IFNAR signalling results in the phosphorylation and heterodimerisation of the transcription factors STAT1 and STAT2. After recruitment of IRF9, this protein complex drives expression of hundreds of genes,

1 MRC Human Immunology Unit, MRC Weatherall Institute of Molecular Medicine, Radcliffe Department of Medicine, University of Oxford, Oxford, UK
2 Department of Microbiology, Harvard Medical School, Boston, MA, USA
3 Department of Cancer Immunology and Virology, Dana-Farber Cancer Institute, Boston, MA, USA
4 Department of Ophthalmology, University of Pittsburgh, Pittsburgh, PA, USA
5 Department of Microbiology and Molecular Genetics, University of Pittsburgh, Pittsburgh, PA, USA
6 Parker Institute for Cancer Immunotherapy, Dana-Farber Cancer Institute, Boston, MA, USA
*Corresponding author. Tel: +44 1865 222362; E-mail: jan.rehwinkel@imm.ox.ac.uk
†Present address: Clinical Cooperation Unit Virotherapy, German Cancer Research Center (DKFZ), Heidelberg, Germany
‡Present address: School of Life Sciences, Southern University of Science and Technology, Shenzhen, China

© 2022 The Authors. Published under the terms of the CC BY 4.0 license

termed interferon-stimulated genes (ISGs). Among others, ISGs include genes that encode PRRs, proteins involved in type I IFN induction and signalling, negative and positive feedback regulators, restriction factors acting directly on viruses, and proteins that are involved in adaptive immune responses (Schoggins, 2019).

Despite the fact that VZV is a highly prevalent and important human pathogen, its pathogenesis is still poorly understood. The lack of suitable small animal models that recapitulate primary infection and latency establishment has hindered the molecular characterisation of its life cycle *in vivo* (Haberthur & Messaoudi, 2013). During its dissemination in the human host, the virus infects a multitude of different cells. Infection of T cells, keratinocytes, neurons, and epithelial cells is indispensable for VZV's life cycle (Zerboni *et al*, 2014). In addition, immune cells including dendritic cells (DCs), monocytes, and NK cells are capable of supporting VZV replication *in vitro* and are potentially relevant for *in vivo* spread (Abendroth *et al*, 2001; Morrow *et al*, 2003; Wang *et al*, 2005; Campbell *et al*, 2018; Kennedy *et al*, 2019). Current evidence suggests that type I IFNs are critical for the control of VZV infection. Increased IFNα levels can be detected in the serum of patients with primary VZV infection (Arvin *et al*, 1986; Zerboni *et al*, 2014). In addition, type I IFNs limit VZV replication *in vitro* (Torigo *et al*, 2000; Ku *et al*, 2016; Kim *et al*, 2017; Shakya *et al*, 2019). However, the events that govern the cell-intrinsic recognition of the virus in the various cell types it infects and induction of the antiviral cytokine response have only begun to be elucidated *in vitro*. The DNA sensor TLR9 is partly responsible for IFNα secretion after infection of plasmacytoid DCs (Yu *et al*, 2011). In dermal fibroblasts, STING is required for type I and type III IFN production (Kim *et al*, 2017). An interesting genetic link between DNA sensing via RNA polymerase III and infection of the central nervous system by VZV has been uncovered recently (Carter-Timofte *et al*, 2018). However, a comprehensive characterisation of the role of DNA sensing during VZV infection is still lacking.

In this study, we tested which nucleic acid sensors induce type I IFN expression in response to VZV infection. We show that the cGAS–STING–TBK1–IRF3 signalling axis was responsible for antiviral cytokine expression after VZV infection. We further report the generation of a VZV open reading frame (ORF) expression library and identification of a viral cGAS antagonist. The tegument protein encoded by ORF9 curtailed the activation of cGAS and subsequent synthesis of cGAMP. Mechanistically, we show that ORF9 interacted with cGAS and DNA. This resulted in decreased cGAMP and IFN production. We propose a model in which cGAS activation upon VZV infection is limited immediately after viral entry through the tegument protein ORF9.

Results

Induction of the type I IFN response to VZV infection in THP1 cells requires the DNA sensor cGAS

To identify PRRs that induce type I IFNs in response to VZV infection, we used the monocytic cell line THP1. We hypothesised a role of DNA sensors in VZV infection, particularly given its identity as a DNA virus and the previously shown role of STING in recognition of VZV (Kim *et al*, 2017). THP1 cells, unlike many other immortalised cell lines, induce type I and type III IFNs *via* cGAS in response to DNA (Sun *et al*, 2013; Wu *et al*, 2013). Furthermore, THP1 cells are amenable to genome editing and can be used to genetically dissect the role of individual proteins involved in pattern recognition. THP1 cells are permissive for VZV infection and propagation (Nour *et al*, 2011), and VZV infects primary human monocytes and macrophages *in vitro* and *in vivo* (Mainka *et al*, 1998; Kennedy *et al*, 2019). In addition to wild-type (WT) THP1 cells, we tested previously described knockout (KO) lines lacking STING, TBK1, MyD88, or IFNAR2. We further generated cGAS-KO, MAVS-KO, and IRF3-KO cells using CRISPR/Cas9 technology (see Materials and Methods and Appendix Fig S1 and S2). All THP1-KO cells were validated by immunoblotting for the absence of protein and functionally by stimulation with DNA, RNA, and type I IFN (Appendix Fig S1 and S2). These cells contained a secreted luciferase reporter construct under control of an IRF3-responsive promoter.

Upon treatment with PMA, THP1 cells adopt a macrophage-like, adherent, and highly responsive phenotype. Given the difficulties of working with cell-free VZV (Chen *et al*, 2004; Caunt & Taylor-Robinson, 2009), we used co-culture with VZV-infected (+VZV) MeWo cells to infect PMA-treated THP1 cells; co-culture with uninfected MeWo cells served as a control (Fig EV1A). MeWo cells are a melanoma cell line that is well-established for VZV propagation. After 48 h of co-culture, cells were harvested for RT–qPCR and immunoblotting. For all experiments, uninfected MeWo cells were additionally used as target cells. MeWo cells do not induce type I IFNs in response to VZV (Fig EV1B).

To investigate whether THP1 cells induce type I IFNs in response to VZV, we analysed mRNA expression levels of *IFNB1* (encodes IFNβ) and *IFI44*, an ISG. In WT THP1 cells, both transcripts were robustly induced after VZV infection (Fig EV1B). Similar results were obtained using MyD88-KO and MAVS-KO cells. In contrast, no transcriptional upregulation of *IFNB1* or *IFI44* was observed in THP1 cells lacking cGAS, STING, TBK1, IRF3, or IFNAR2. Moreover, immunoblot analysis showed that the transcription factors STAT1 and STAT2 were only phosphorylated in WT, MyD88-KO, and MAVS-KO cells (Fig EV1C). No p-STAT1 and p-STAT2 signals were observed in cells lacking cGAS, STING, TBK1, IRF3, or IFNAR2. This indicated that only WT, MyD88 KO, and MAVS-KO cells secreted type I IFNs in response to VZV infection. Consistently, STAT1 and RIG-I, which are both encoded by ISGs, were upregulated at protein level only in the cells showing STAT1/2 activation (Fig EV1C). Importantly, we could not observe phosphorylation of STAT1/2 or increased abundance of STAT1 and RIG-I in infected MeWo cells. Western blotting with antibodies against VZV-glycoprotein E (gE)/glycoprotein I (gI) and VZV ORF62 confirmed that all cell lines became infected (Fig EV1C). Determination of CXCL10 (IP-10) levels in co-culture supernatants confirmed the findings of our RT–qPCR and immunoblot analyses. WT, MyD88 KO, and MAVS-KO THP1 cells produced low levels of CXCL10 at baseline, and these were increased after infection with VZV (Fig EV1D). No CXCL10 was detected in supernatants from uninfected cells and in samples from infected cGAS-KO, STING-KO, TBK1-KO, and IFNAR2-KO THP1 cells; similarly, MeWo cells did not secrete CXCL10. We could detect low levels of CXCL10 in supernatants from IRF3-KO cells, but there was no increase above baseline after infection. Analysis of co-cultured cells by flow cytometry (cell-surface staining for the VZV-gE/gI complex (Mo *et al*, 2003)) showed that the proportion of inoculum MeWo cells and THP1 target cells differed between

 © 2022 The Authors

samples, in particular for uninfected conditions (Fig EV1E and F). Within the population of THP1 target cells, the percentage of VZV-infected cells was variable and no clear differences between THP1-KO cell lines could be observed (Fig EV1E and G). It is likely that this variability is partly because the different THP1-KO cells were obtained from various sources. Collectively, these results suggest that in THP1 cells, the induction of the type I IFN in response to VZV infection required the DNA sensor cGAS and the STING–TBK1–IRF3 signalling axis. It is therefore likely that dsDNA is a PAMP recognised in VZV-infected cells.

To further dissect the role of the DNA sensor cGAS in the recognition of VZV, we developed a transwell-based infection system (Fig 1A). In this setup, infected MeWo cells are first seeded on the bottom side of the transwell membrane. After adherence, THP1 target cells are seeded on the opposite side of the membrane. The membrane contains 1 μm pores through which cell–cell contacts can be established and VZV can spread. Importantly, the inoculum and target cells do not mix, and a homogenous target cell population can be harvested for analysis. We anticipate that this new infection protocol (see Materials and Methods for details) will be widely applicable to many VZV research projects.

WT, cGAS-KO, and MAVS-KO THP1 (Fig 1B) cells were infected for 24 and 48 h using this transwell assay. Of note, the cGAS-KO and MAVS-KO cells were both generated as part of this study to ensure consistency (Appendix Fig S1). Flow cytometry analysis revealed significantly higher levels of infection in cGAS-KO cells compared to WT and MAVS-KO cells at both time points (Fig 1C and Appendix Fig S3). Additionally, the mean fluorescence intensity (MFI) of VZV-gE/gI staining was significantly higher in cGAS-KO cells compared to WT and MAVS-KO cells (Fig 1C). We further found increased expression of immediate early (IE), early (E), and late (L) viral gene products in cells lacking cGAS (Fig 1D). In line with our previous results, THP1 cells failed to upregulate *IFNB1* and ISG expression after VZV infection in the absence of cGAS (Fig 1E). In WT and MAVS-KO cells, VZV infection robustly induced secretion of the IRF3-controlled luciferase reporter and CXCL10 (Fig 1F and G). This response was undetectable in cGAS-KO cells.

These results confirm our previous observations from the co-culture system and establish that the induction of the type I IFN response to VZV infection in THP1 cells was mediated by the DNA sensor cGAS. Significantly more cells became infected with VZV in the absence of cGAS, indicating that recognition by cGAS was required for restriction of VZV infection.

A VZV ORF expression library

Type I IFNs inhibit VZV infection (Ku *et al*, 2016; Kim *et al*, 2017). VZV, like many other viruses, employs immune evasion strategies that target the type I IFN system. For example, both ORF61 and ORF62 limit IRF3 activation through distinct mechanisms (Sen *et al*, 2010; Zhu *et al*, 2011). In light of our finding that cGAS was crucial for type I IFN induction in response to VZV, we hypothesised that the virus expresses a direct antagonist of cGAS and/or STING. Indeed, other large DNA viruses often encode multiple antagonists of the same innate immune pathway (Smith *et al*, 2018; Stempel *et al*, 2019). In order to test the role of individual viral gene products in immune evasion, we generated an expression library for all canonical VZV ORFs. All coding sequences were PCR-amplified and cloned into a gateway entry vector. Using recombination, these sequences were then shuttled into a lentiviral vector (pLenti6.3/TO/V5). This vector allows expression with a C-terminal V5 epitope tag either after transient transfection or *via* lentiviral transduction. To validate these constructs, we transiently transfected HEK293T cells and analysed expression of VZV proteins by immunoblot using an antibody against the V5 tag (Fig EV2). Fifty-nine of 72 constructs (82%) were expressed, and bands at the expected molecular weights were detected. An additional five constructs were expressed but not at the expected size, and eight were not expressed at detectable levels. This VZV ORF library is a resource for the scientific community and is available to all interested scientists.

VZV ORF9 is an antagonist of DNA sensing

To investigate whether VZV ORFs block cGAS/STING activation, we utilised a luciferase-based screening platform in HEK293T cells. In brief, a plasmid expressing Firefly luciferase under *IFNB1* promoter control and pRL-TK, which constitutively expresses Renilla luciferase, were transiently transfected. HEK293T cells do not express cGAS and STING naturally. We therefore reconstituted human cGAS and human STING by transient transfection, which results in activation of the *IFNB1* promoter and firefly luciferase expression. Lastly, individual viral ORFs (or controls) were co-expressed. Firefly luciferase expression was normalised to Renilla luciferase expression, and we calculated for each ORF a luciferase fold change to an empty vector control condition without cGAS and STING expression constructs. The mean and standard deviation of all data points was then used to calculate Z-values, which represent the number of standard deviations an individual data point is diverging from the mean. We used these Z-scores to rank ORFs in their ability to block IFN activation downstream of cGAS/STING (Fig 2A). KSHV ORF52, a previously described cGAS antagonist (Wu *et al*, 2015), and the L protein of EMCV, a previously described IRF3-antagonist (Freundt *et al*, 2018), served as positive controls. As expected, we found these with the lowest ranks (i.e. smallest fold change) in our assay, and both potently blocked firefly luciferase induction. In addition, we identified a number of VZV ORFs that showed similar behaviour. The two aforementioned IRF3 antagonists expressed by VZV, ORF61 and ORF62, were among them, which further validated our approach.

We performed this screening experiment three times; Fig 2B displays the results as a heatmap. We identified a number of ORFs that reproducibly ranked very low, including ORF9. To test if ORF9 specifically blocked cGAS and/or STING, and not downstream signalling proteins such as IRF3 that are also activated by other PRRs, we compared this hit from the primary screen in its ability to block reporter activation by overexpression of cGAS/STING or RIG-I-CARD. RIG-I-CARD is a constitutively active fragment of RIG-I that activates the *IFNB1* promoter *via* MAVS. A direct cGAS/STING antagonist is therefore unable to block this stimulation. ORF9 selectively blocked reporter activation by cGAS/STING but not RIG-I-CARD when compared to empty vector (Fig 2C).

We then aimed to verify that VZV ORF9 antagonises activation of cGAS by dsDNA in an endogenous setting. THP1 monocytes were stably transduced with ORF9-V5 or GFP-V5 as a negative control (Fig 2D). We stimulated cGAS in these cells by transfection of increasing doses of dsDNA and measured expression levels of *IFNB1* mRNA and *IFNL1* mRNA (encoding a type III IFN) by RT–qPCR

© 2022 The Authors

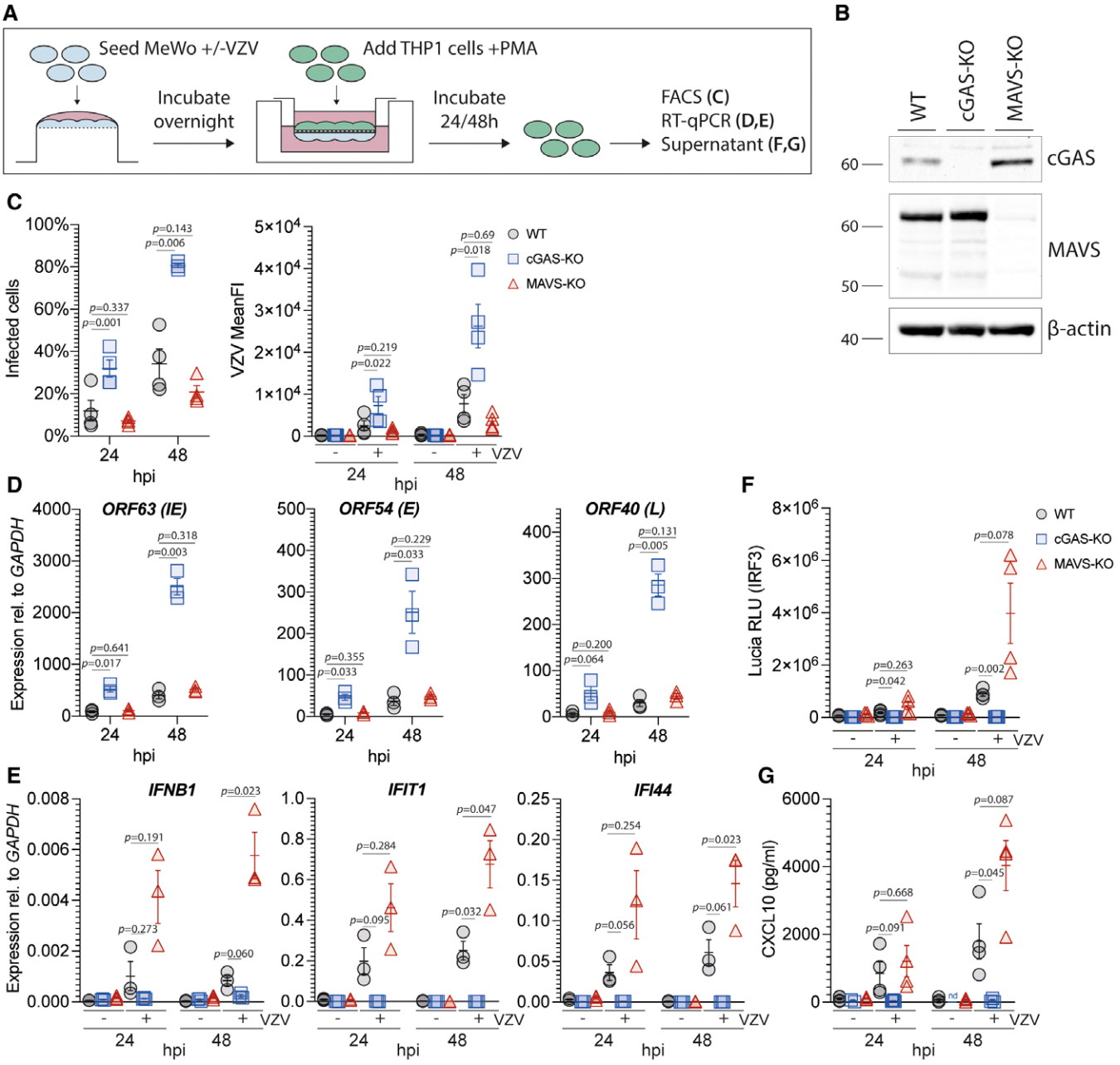


Figure 1. cGAS induces type I IFNs in response to VZV infection.

A Schematic detailing the experimental procedure for infection of PMA-differentiated THP1 cells with VZV by transwell assay. See text for details.

B Immunoblot of WT, cGAS-KO, and MAVS-KO THP1 cells used in (C–G).

C THP1 cells of the indicated genotypes were mock infected or infected with VZV for 24 and 48 h using the transwell assay described in (A). Infected cells were quantified by surface staining for VZV-gE/gI and flow cytometry analysis. See Appendix Fig S3 for gating.

D RT–qPCR analysis of VZV ORF63 (immediate early (IE) gene), ORF54 (early (E) gene), and ORF40 (late (L) gene) transcripts in cells infected as in (C). Graphs show expression relative to *GAPDH*.

E RT–qPCR analysis of *IFNB1*, *IFI44*, and *IFIT1* expression in cells infected as in (C). Graphs show expression relative to *GAPDH*.

F Activity of Lucia luciferase (secreted under an IRF3-dependent promoter) was determined in supernatants of cells infected as in (C) by QUANTI-Luc assay.

G Concentrations of CXCL10 in supernatants of cells infected as in (C) were determined by ELISA.

Data information: Panel (B) is representative of two independent biological experiments. Panels (C), (F), and (G) show pooled data from four repeats, where each data point represents an independent biological experiment ($n = 4 \pm$ SEM). Panels (D) and (E) show pooled data from three repeats, where each data point represents an independent biological experiment ($n = 3 \pm$ SEM). Statistical analysis in panels (C), (D), (F), and (G) was paired *t*-tests and in panel (E) paired ratio *t*-tests. hpi: hours post infection, WT: wild type, KO: knockout.

See also Fig EV1 and Appendix Fig S1, Fig S2, and Fig S3.

Source data are available online for this figure.

© 2022 The Authors

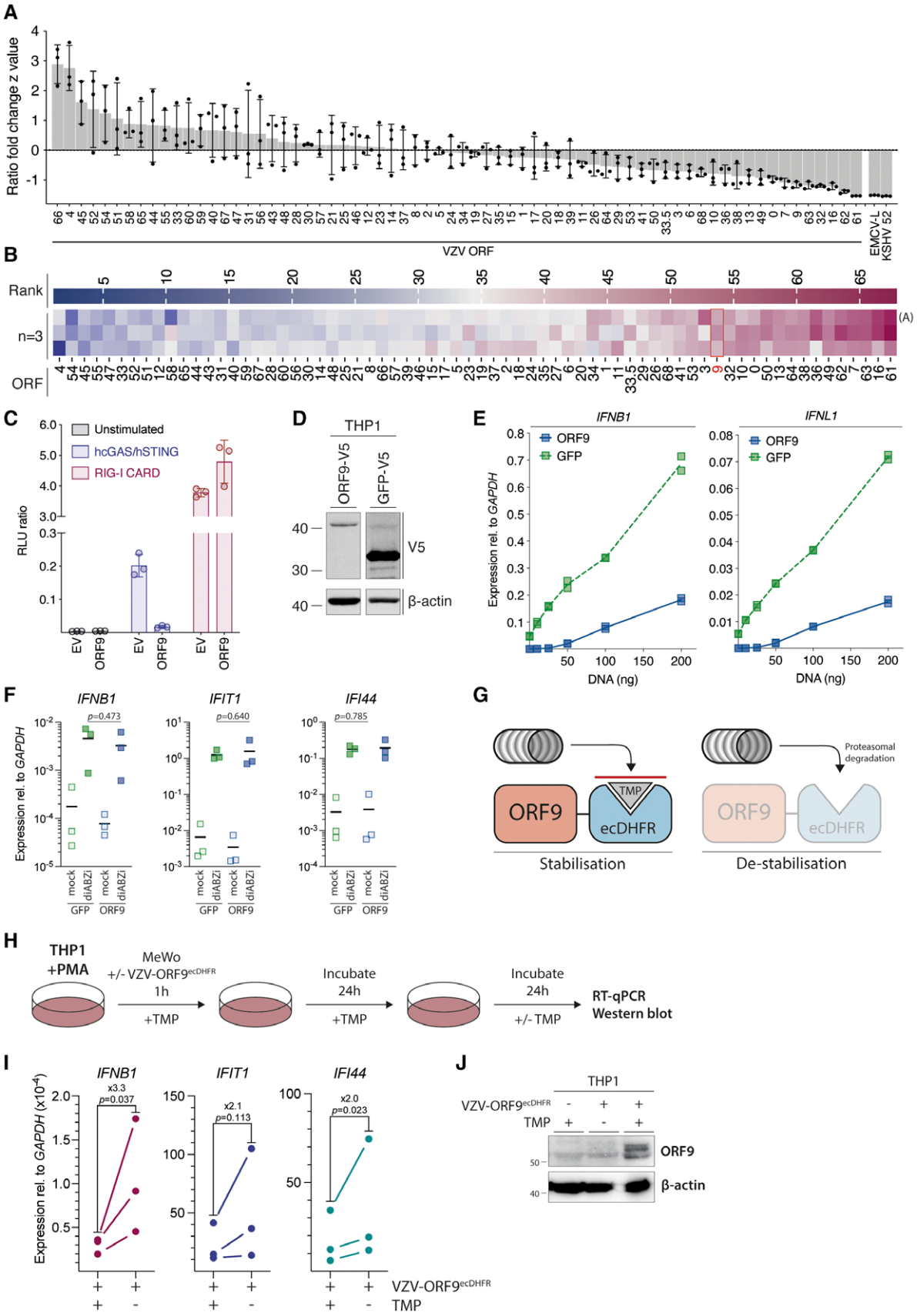

A
Ratio fold change z value
VZV ORF
EMCV-L
KSHV 52
B
Rank
n=3
ORF
C
Unstimulated
hcGAS/hSTING
RIG-I CARD
RLU ratio
EV
ORF9
D
THP1
ORF9-V5
GFP-V5
V5
β-actin
E
IFNB1
IFNL1
ORF9
GFP
Expression rel. to GAPDH
DNA (ng)
F
IFNB1
IFIT1
IFI44
p=0.473
p=0.640
p=0.785
mock
diABZi
GFP
ORF9
G
ORF9
ecDHFR
TMP
Stabilisation
Proteasomal degradation
De-stabilisation
H
THP1
+PMA
MeWo
+/- VZV-ORF9ecDHFR
1h
+TMP
Incubate
24h
+TMP
Incubate
24h
+/- TMP
RT-qPCR
Western blot
I
IFNB1
IFIT1
IFI44
x3.3
p=0.037
x2.1
p=0.113
x2.0
p=0.023
Expression rel. to GAPDH (x10-4)
VZV-ORF9ecDHFR
TMP
J
THP1
VZV-ORF9ecDHFR
TMP
ORF9
β-actin

Figure 2.

Figure 2. Screening of all VZV ORFs identifies ORF9 as an antagonist of cGAS-mediated DNA sensing.

A HEK293T cells were transfected with pRL-TK, p125-F-Luc, expression plasmids for human cGAS and human STING, as well as expression plasmids for individual ORFs. The next day, luciferase activity was determined. For each ORF, a z-value was calculated and ORFs sorted by descending values.

B The experiment shown in panel (A) was repeated three times, and for each ORF in each experiment, a rank was determined according to *z*-value (highest *z*-value = rank 1). Ranks are displayed as a heatmap. The first row shows results displayed in panel (A).

C HEK293T cells were transfected as in (A, B) with expression constructs for VZV ORF9 or empty vector. In parallel, reporter expression was stimulated by co-transfection of the RIG-I-CARD plasmid instead of hcGAS and hSTING.

D Western blot analysis of PMA-differentiated THP1 monocytes stably transduced with either V5-tagged VZV ORF9 or GFP using the indicated antibodies.

E THP1 monocytes stably transduced with either VZV ORF9 or GFP were PMA-differentiated and transfected with indicated doses of dsDNA. Expression of *IFNB1* and *IFNL1* was assessed by RT–qPCR. Graphs show expression relative to *GAPDH*.

F THP1 monocytes stably transduced with either VZV ORF9 or GFP were treated with the STING agonist diABZi (0.005 μM). Expression of *IFNB1*, *IFIT1*, and *IFI44* was assessed by RT–qPCR. Graphs show expression relative to *GAPDH*. See also Fig EV2A.

G Schematic detailing the *E. coli* DHFR degron system.

H Schematic detailing the experimental procedure for (I) and (J). See text for details.

I PMA-differentiated THP1 cells were co-cultured with VZV-ORF9^{ecDHFR}-infected MeWo cells for 1 h in the presence of TMP, washed, and incubated for another 24 h in the presence of TMP. Cells were then washed extensively, and fresh medium was added that was supplemented or not with TMP. Expression levels of *IFNB1*, *IFIT1*, and *IFI44* were measured by RT–qPCR after a further 24 h incubation. Graphs show expression relative to *GAPDH*. Mean fold changes are indicated.

J Cells infected and treated as in (I) with the addition of uninfected cells were analysed by western blotting using the indicated antibodies.

Data information: Panel (A) is representative of three independent biological experiments, where each data point represents a technical replicate (mean ± SD). The three independent experiments are summarised in panel (B), where the data from (A) forms the first row. Panel (C) is representing two independent biological experiments, where each data point represents a technical replicate (mean ± SD). Panels (D) and (E) are representing two independent biological experiments. In (E), each data point represents a technical replicate. Panel (F) shows pooled data from three repeats, where each data point represents an independent biological experiment (horizontal bars show means). Panel (I) shows pooled data from three repeats, where each data point represents an independent biological experiment. Panel (J) is representative of three independent experiments. Statistical analysis in (F) and (I) were paired *t*-tests.

See also Figs EV2 and EV3.
Source data are available online for this figure.

(Fig 2E). As expected, THP1 cells expressing GFP showed a dose-dependent increase in expression of both transcripts. In contrast, cells expressing ORF9 did not respond to low doses of DNA. At higher doses, their response was attenuated when compared to GFP-expressing cells. To test whether ORF9 inhibits cGAS or STING, we used the small molecule STING agonist diABZi to stimulate STING signalling independently of cGAS (Ramanjulu *et al*, 2018). Based on a dose titration (Fig EV3A), we added a non-saturating dose (0.005 μM) of diABZi to THP1 cells transduced with ORF9 or GFP as control. The expression of *IFNB1* and two ISGs was stimulated to a similar degree in cells expressing ORF9 or GFP (Fig 2F). These data show that STING signalling is unaffected in ORF9-expressing cells, indicating that ORF9 acts on cGAS directly. We further investigated how ORF9 affects the type I IFN response in THP1 cells upon VZV infection. THP1 cells expressing ORF9 or GFP were infected by co-culture with VZV-infected MeWo cells, and the type I IFN response was measured by RT–qPCR. The presence of ectopically expressed ORF9 attenuated the upregulation of *IFNB1* and ISGs (Fig EV3B). This effect was not simply due to a soluble factor released by VZV-infected MeWo cells: the response of THP1 cells to transfected immunostimulatory nucleic acids was largely unaffected by supernatant samples from VZV-infected cells (Fig EV3C).

Lastly, we aimed to investigate the antagonist function of endogenous ORF9 expressed during viral infection. Since ORF9 is essential for viral replication, we used a recombinant virus in which a degron motif is fused to the ORF9 protein (VZV-ORF9^{ecDHFR}; Warner *et al*, 2021). In this setting, the stability of the degron (and the ORF9 protein fused to it) in cells can be regulated with the degron ligand trimethoprim (TMP) (Fig 2G). Withdrawal of TMP leads to destabilisation of the degron and subsequent proteasomal degradation of the ORF9-degron protein. We hypothesised that upon TMP withdrawal, ORF9 degradation leads to an increased type I IFN response in VZV-ORF9^{ecDHFR}-infected THP1 cells. To test this, PMA-differentiated THP1 cells were co-cultured in the presence of TMP with VZV-ORF9^{ecDHFR}-infected MeWo cells for 1 h (Fig 2H). The cells were then washed of inoculum and cultured with TMP for an additional 24 h. Finally, the cells were washed free of TMP, cultured overnight in the presence or absence of TMP, and harvested for RT–qPCR and immunoblot analysis. Expression of *IFNB1* and ISGs was increased in cells where TMP was withdrawn (Fig 2I). The absence of ORF9 protein in cells cultured without TMP was confirmed by immunoblotting (Fig 2J). These data show that the absence of endogenously expressed ORF9 during VZV infection leads to an increased type I IFN response in THP1 cells. This confirms a role of ORF9 in inhibiting the cGAS-dependent response to VZV infection in these cells. Collectively, the data presented in Fig 2 revealed that ectopically and endogenously expressed VZV ORF9 protein prevented cGAS activation.

ORF9 interacts with cGAS

We hypothesised that VZV ORF9 exerts its antagonistic function by directly interacting with cGAS. To test this, HEK293T cells were transiently transfected with expression constructs for cGAS-FLAG, STING-HA, and ORF9-V5, and protein interaction was analysed by immunoprecipitation (IP). We used antibodies against the epitope tags and analysed IP fractions by immunoblotting (Fig 3A). All ectopically expressed proteins were precipitated efficiently, and an IgG isotype control antibody did not precipitate any of the proteins tested. Interestingly, ORF9 was detected in the bound fraction after cGAS IP. The reverse IP confirmed this result: we found cGAS in the ORF9 IP. In contrast, ORF9 did not interact with STING in this assay (Fig 3A). To verify that this interaction occurred with endogenous cGAS, we used THP1 cells stably transduced to express FLAG-ORF9, which was precipitated from cell lysates with α-FLAG antibody. Indeed, endogenous cGAS was present in the IP fraction; IP of FLAG-GFP served as a negative control (Fig 3B).

 © 2022 The Authors

Next, we asked whether ORF9 expressed from its endogenous promoter during viral infection had the ability to interact with cGAS. We used a recombinant VZV that expressed C-terminally V5-tagged ORF9 from its endogenous genomic locus. We infected THP1 cells and HaCaT cells (a keratinocyte cell line that expresses cGAS) with WT VZV or VZV$^{ORF9\text{-}V5}$ and performed α-V5 IP (Fig 3C). In both THP1 and HaCaT cells infected with VZV$^{ORF9\text{-}V5}$, endogenous cGAS co-precipitated with ORF9. These data showed that endogenous ORF9 protein expressed by the virus in infected cells interacted with cGAS.

To investigate whether the two proteins co-localise in cells, we overexpressed tagged ORF9 and cGAS in HEK293T cells and performed immunofluorescence analysis (Fig 3D). Expression of ORF9 alone resulted in cytoplasmic staining. Similarly, cGAS was detected in the cytoplasm. We further observed cGAS foci co-

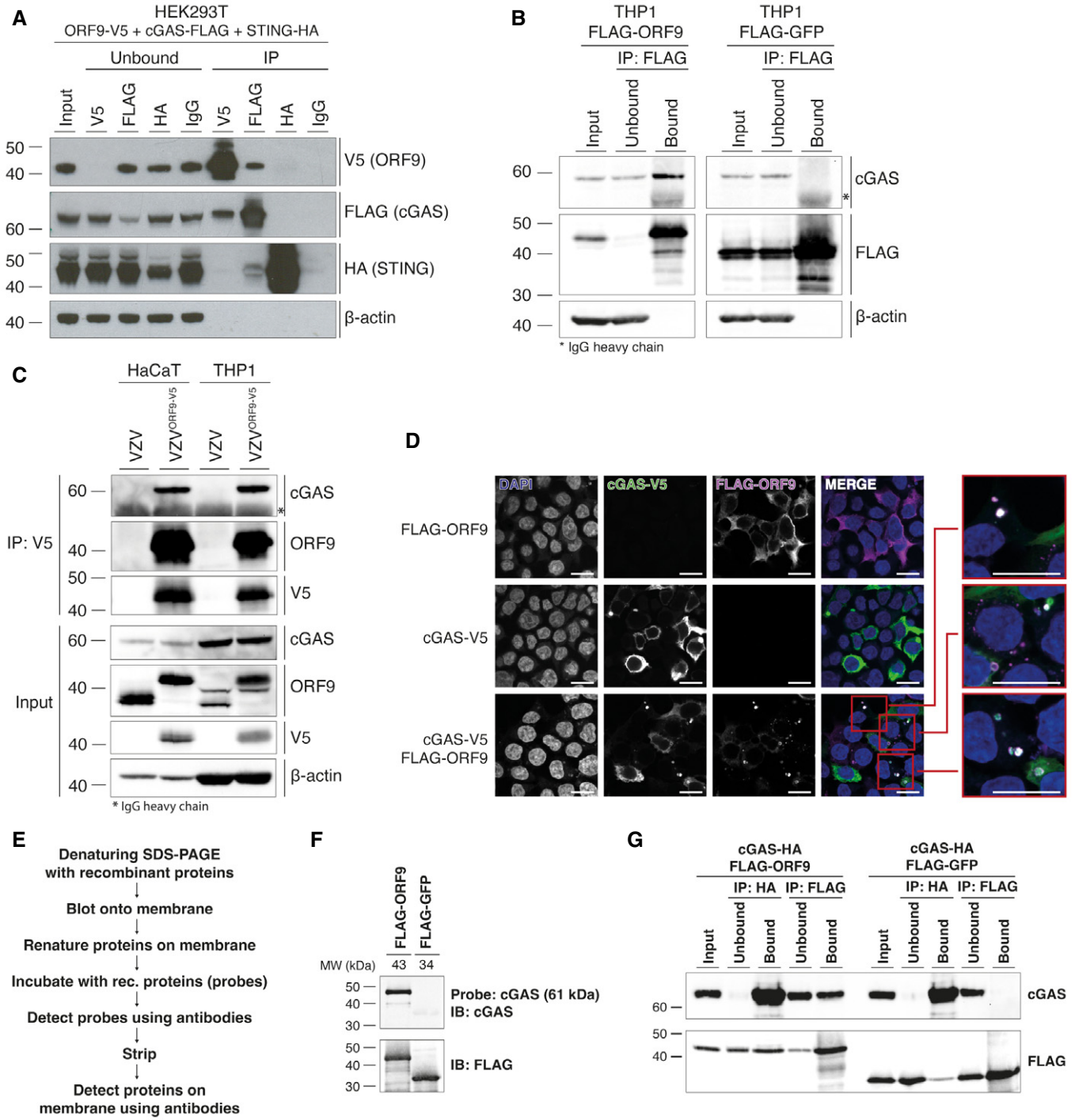


Figure 3.

Figure 3. ORF9 interacts with cGAS.

A HEK293T cells were transfected with expression plasmids for ORF9-V5, human cGAS-FLAG, and human STING-HA. The next day, cells were lysed, and overexpressed proteins were immunoprecipitated with α-V5, α-FLAG, α-HA, or IgG isotype control antibody. Input, unbound, and IP fractions were subjected to immunoblotting using the indicated antibodies.

B THP1 monocytes stably transduced with either VZV FLAG-ORF9 or FLAG-GFP were PMA-differentiated overnight. The next day, cells were lysed and ectopically expressed proteins were immunoprecipitated using α-FLAG antibody. Input, unbound, and IP fractions were subjected to immunoblotting using the indicated antibodies.

C HaCaT cells and PMA-differentiated THP1 cells were infected with WT VZV or $VZV^{ORF9\text{-}V5}$ through co-culture with infected MeWo cells for 48 h. Cells were lysed and ORF9 was immunoprecipitated using α-V5 antibody. Input and IP fractions were subjected to immunoblotting using the indicated antibodies.

D HEK293T cells were seeded onto glass coverslips and were transfected with human cGAS-V5, FLAG-ORF9, or both together. The next day, cells were fixed, permeabilised and stained using α-V5-FITC, rabbit-α-FLAG, and goat-α-rabbit-AF647 antibodies, and DAPI. Mounted coverslips were imaged using confocal microscopy. Scale bars: 15 μm.

E Outline of the far western protocol.

F Far western analysis of cGAS-ORF9 interaction. Recombinant FLAG-ORF9 and FLAG-GFP protein were run on an SDS–PAGE gel and transferred to a membrane. After renaturation of proteins, the membrane was incubated with recombinant human cGAS as a probe, which was detected using α-cGAS antibody. After stripping, the proteins on the membrane were detected using α-FLAG antibody.

G Recombinant human cGAS-HA was mixed with recombinant FLAG-ORF9 or FLAG-GFP. Proteins were immunoprecipitated using α-HA and α-FLAG antibodies. Input, unbound, and IP fractions were analysed by immunoblotting.

Data information: Recombinant proteins used in (F) and (G) are shown in Appendix Fig S4A. Panels (A) and (G) are representative of two independent experiments. Panels (B), (D), and (F) are representative of three independent experiments. Panel (C) is representative of two (HaCaT) and three (THP1) independent experiments.
Source data are available online for this figure.

localising with extranuclear DNA. Extranuclear DNA foci, sometimes in the form of micronuclei, can be observed in some cancer cells and have been shown to bind cGAS (Harding *et al*, 2017; Mackenzie *et al*, 2017; Hu *et al*, 2019). Interestingly, when ORF9 and cGAS were expressed together, both proteins co-localised in DAPI-positive, extranuclear regions (Fig 3D). This indicated that ORF9 interacted with cGAS in cells and localised together with cGAS in DNA-positive areas.

In order to biochemically characterise the interaction between ORF9 and cGAS in more detail, we performed experiments in a cell-free system. We expressed cGAS, cGAS-HA, FLAG-ORF9, and FLAG-GFP in *Escherichia coli* and performed single-step purification (Appendix Fig S4A). First, we tested whether ORF9 and cGAS interacted directly using the far western protocol (Fig 3E). FLAG-ORF9 or FLAG-GFP protein were separated on a denaturing SDS–PAGE gel and transferred to a membrane. The proteins on the membrane were then re-natured and incubated with recombinant cGAS as a probe. Binding of cGAS to proteins on the membrane was then tested using α-cGAS antibody. Indeed, we found that probing for cGAS resulted in a signal at the size of ORF9 (Fig 3F). Importantly, cGAS did not bind to GFP.

We then tested interaction of the two recombinant proteins using immunoprecipitation. FLAG-ORF9 or FLAG-GFP was incubated with cGAS-HA in the test tube. The proteins were then precipitated using antibodies against the epitope tags. Immunoblot analysis of the IP fractions showed that cGAS was co-immunoprecipitated with ORF9 but not GFP (Fig 3G). The reverse IP of cGAS resulted in binding of both ORF9 and GFP; however, the signal was stronger for ORF9. Taken together, these data indicate that VZV ORF9 and cGAS interacted without the requirement for another cellular or viral protein.

To characterise the interaction of ORF9 and cGAS mechanistically, we constructed ORF9 truncation mutants (Fig 4A). We tested their ability to interact with cGAS by co-IP after overexpression in HEK293T cells (Fig 4B). Consistent with our earlier observation, full-length ORF9 co-immunoprecipitated cGAS. The C-terminal half of ORF9 (construct II) behaved the same, whilst the N-terminal half (construct I) failed to interact with cGAS. ORF9 constructs III, IV, and V also pulled down cGAS. All ORF9 constructs that interacted with cGAS shared amino acids (AA) 151 to 240. However, the IP of this region in isolation ($ORF9^{151\text{-}240}$, construct VI) did not co-precipitate cGAS (Fig 4B). Extension of this construct at both ends by about 10 amino acids to generate construct VIII (AA 141–249) restored robust interaction with cGAS (Fig 4B).

ORF9 binds DNA

To gain insight into possible structural features of ORF9 in this region, we used the PSIPRED 4.0 algorithm to predict its secondary

Figure 4. VZV ORF9 binds DNA.

A Schematic detailing ORF9 truncation mutants used in (B).

B HEK293T cells were transfected with expression plasmids for human cGAS and ORF9 truncation mutants. The next day, cells were lysed and ORF9 proteins were immunoprecipitated using α-FLAG antibody. IP fractions were subjected to immunoblotting using the indicated antibodies.

C Schematic detailing predicted structural features of VZV ORF9 in relation to predicted and crystal structure-derived features in HSV-1 VP22, KSHV ORF52, and MHV68 ORF52. See text for details.

D Recombinant cGAS, FLAG-ORF9, FLAG-GFP, and biotinylated VACV70mer dsDNA were incubated in the indicated combinations. Recombinant proteins were precipitated using streptavidin beads. Fractions were analysed by immunoblotting.

E HEK293T cells were transfected with expression plasmids for FLAG-GFP or FLAG-ORF9. The next day, cells were lysed and the lysate was spiked with biotinylated VACV70mer dsDNA. DNA was precipitated using streptavidin beads and fractions were subjected to immunoblotting using the indicated antibodies.

F VACV70mer dsDNA was incubated with indicated proteins and analysed by agarose gel EMSA. Triangles indicate concentrations of ORF9 (0.7, 1.4, 2.9, 5.7, 8.6 μM), cGAS (0.6, 1.1, 2.2, 4.5, 6.7 μM), and ORF9 (as before) in the presence of 4.5 μM cGAS.

Data information: Recombinant proteins used in (D) and (F) are described in Appendix Fig S4A and B, respectively. Results shown in panels (B) and (D–F) are representative of two independent experiments.
Source data are available online for this figure.

© 2022 The Authors

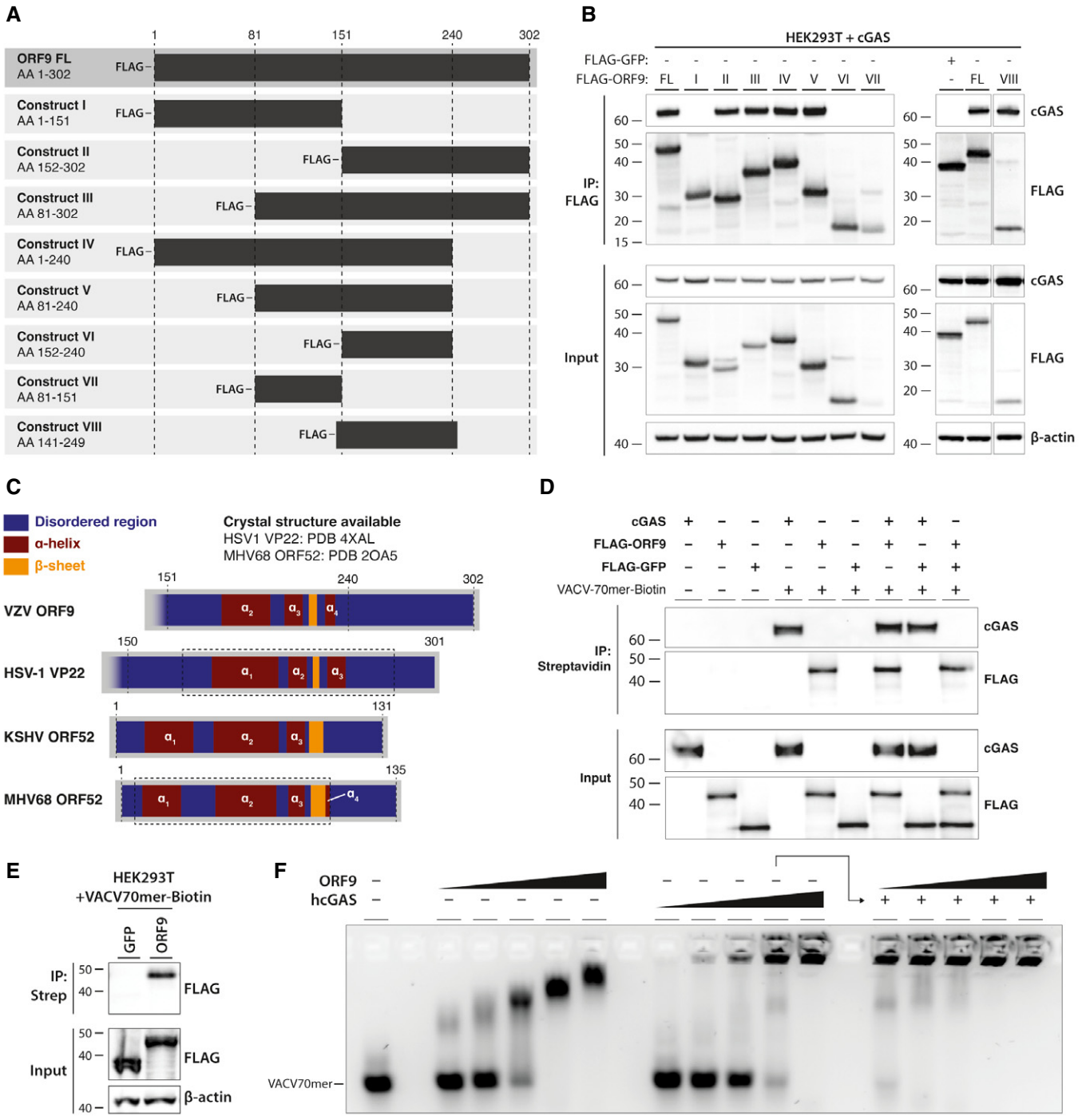


Figure 4.

structure based on the AA sequence (Buchan & Jones, 2019). This analysis predicted a two helix–sheet–helix motif in the C-terminal region of ORF9 (Fig 4C). We obtained a similar secondary structure prediction for the C-terminal half of VP22, the HSV-1 homologue of VZV ORF9. A crystal structure is available for this region of VP22 (Hew *et al*, 2015) and confirms the presence of the predicted two helix–sheet–helix motif. Hew *et al* further identified a structural similarity of VP22 with the unrelated ORF52 protein of murine herpesvirus 68 (MHV68). MHV68 is closely related to human herpesvirus 8, also known as Kaposi sarcoma-associated herpesvirus (KSHV). KSHV ORF52 has been identified as a cGAS antagonist and has DNA-binding properties (Wu *et al*, 2015). This led us to hypothesise that ORF9 interacts with DNA. To test this, we incubated biotinylated VACV-70mer dsDNA with recombinant ORF9; recombinant cGAS and GFP served as positive and negative controls, respectively. The VACV-70mer is a well-established immunostimulatory dsDNA that binds cGAS (Unterholzner *et al*, 2010; Almine *et al*, 2017; Lum *et al*, 2018). The DNA was then

© 2022 The Authors

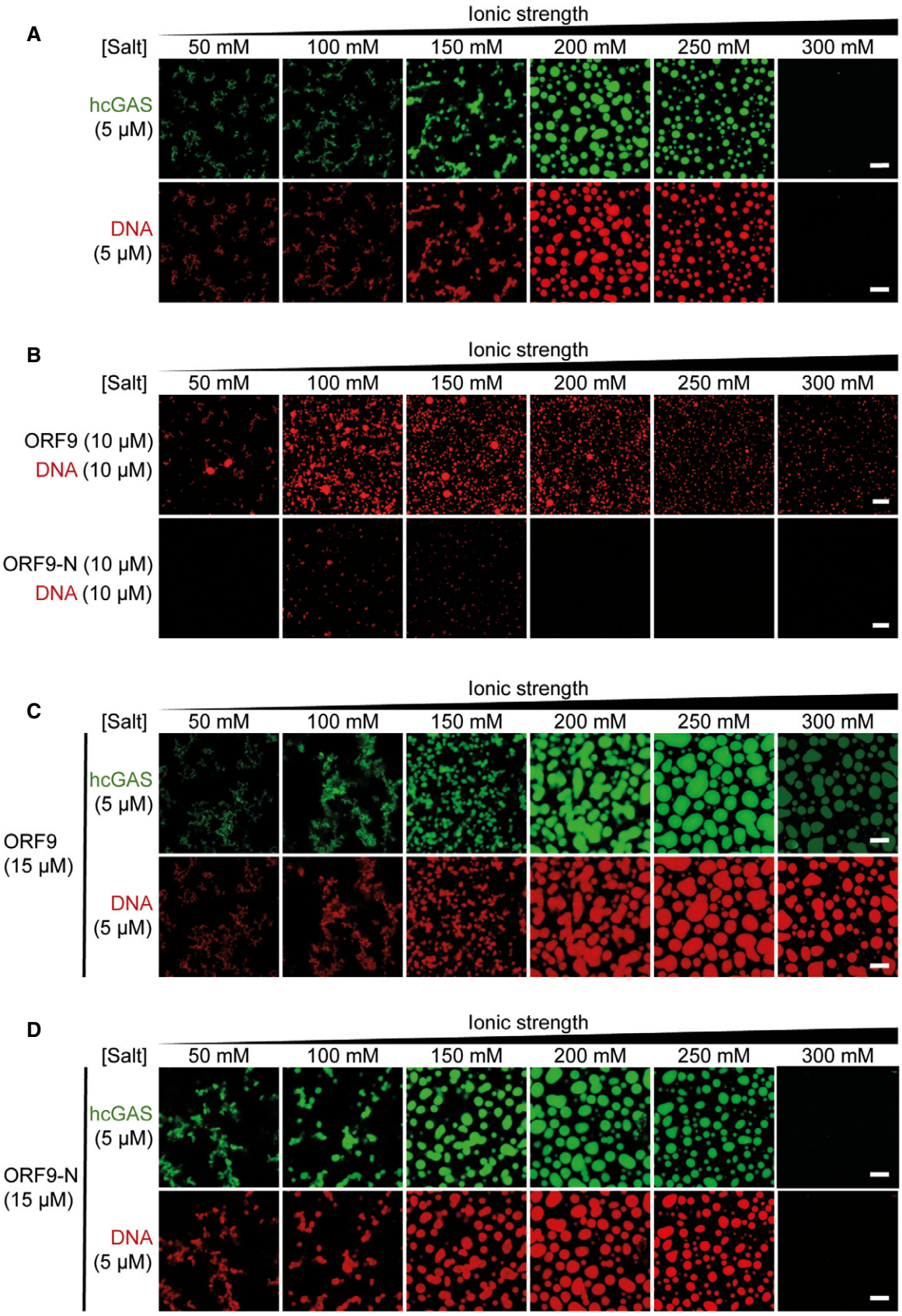


Figure 5.

© 2022 The Authors

Figure 5. ORF9 phase-separates with DNA.

A 5 μM hcGAS (with 10% AlexaFluor-488-labelled) was incubated with 5 μM dsDNA-100 (with 10% of DNA Cy3-labelled) with increasing salt concentrations (total NaCl and KCl) and imaged by confocal microscopy.

B 10 μM ORF9 or ORF9-N were incubated with 10 μM dsDNA-100 (with 10% of DNA Cy3-labelled) and analysed as in (A).

C, D 5 μM hcGAS (with 10% AlexaFluor-488-labelled) was incubated with 5 μM dsDNA-100 (with 10% of DNA Cy3-labelled) and 15 μM ORF9 (C) or ORF9-N (D) and analysed as in (A).

Data information: Recombinant proteins used in are described in Appendix Fig S4C. Scale bar, 10 μm. Data are representative of 3 experiments. See also Fig EV4.

precipitated using streptavidin beads, and the presence of bound proteins was analysed by immunoblotting (Fig 4D and Appendix Fig S4A). In the absence of DNA, none of the proteins were precipitated. As expected, cGAS bound to DNA. Interestingly, ORF9 was also pulled down by DNA, both alone and in the presence of cGAS. GFP did not bind DNA under any conditions (Fig 4D). We further overexpressed either FLAG-ORF9 or FLAG-GFP in HEK293T cells and performed a similar precipitation experiment after spiking the lysates from these cells with VACV70mer-Biotin (Fig 4E). As expected, ORF9, but not GFP, was pulled down with DNA. To characterise the interaction of ORF9 and DNA in more detail, we performed agarose gel electromobility shift assays (EMSA; Fig 4F and Appendix Fig S4B). Recombinant ORF9 protein impaired the mobility of VACV70mer dsDNA, indicating the formation of ORF9-DNA complexes. These increased in size with higher doses of ORF9, suggesting multivalent protein–protein/protein–DNA interactions. We performed similar experiments with full-length human cGAS protein. As previously described (Zhou *et al*, 2018), hcGAS and DNA form high-molecular-weight (HMW) complexes, which are unable to migrate out of the gel pocket. Next, we tested incubation of VACV70mer and cGAS with increasing doses of ORF9 protein. Addition of ORF9 to cGAS and DNA increased the size of protein/DNA complexes observed at this concentration of cGAS alone (Fig 4F). Taken together, these data show that ORF9 interacted with both DNA and cGAS, without displacing cGAS from DNA.

ORF9 phase-separates with DNA

Liquid–liquid phase separation contributes to cGAS activation by dsDNA (Du & Chen, 2018; Xie *et al*, 2019; Zhou *et al*, 2021). This is driven by multivalent interactions between cGAS and DNA. In light of our results that ORF9 bound cGAS and DNA, we investigated the effect of ORF9 on cGAS–DNA phase separation. As reported previously, we observed droplet formation by human cGAS and labelled dsDNA, which was sensitive to increasing salt concentration > 250 mM (Fig 5A and Appendix Fig S4C). Similarly, ORF9 and labelled dsDNA formed liquid droplets in the absence of cGAS (Fig 5B and Appendix Fig S4C). ORF9-DNA droplets were smaller than cGAS-DNA droplets, which may indicate a lower propensity of ORF9 to phase-separate with DNA compared to cGAS. A C-terminally truncated version of ORF9 (ORF9-N, AA 1–244) had much reduced ability to form liquid droplets (Fig 5B and Appendix Fig S4C). Next, we formed cGAS–DNA droplets in the presence of ORF9. Larger droplets were formed by cGAS and DNA when a three-fold molar excess of full-length ORF9, but not ORF9-N, was added (Fig 5C and D). This was consistent with our EMSA data (Fig 4F). Interestingly, at 300 mM NaCl/KCl, DNA and cGAS alone did not phase-separate, but droplets containing DNA and cGAS were formed at this salt concentration in the presence of ORF9 (Fig 5A and C). Furthermore, at 300 mM NaCl/KCl, the intensity of the cGAS signal, but not of the DNA signal, was diminished compared to lower salt concentrations. These observations were reproducible using lower ORF9:cGAS molar ratios (Fig EV4). One of the multiple possible interpretations is that ORF9 displaces cGAS from DNA under these conditions, which is consistent with a recent report (Xu *et al*, 2021).

VZV ORF9 Inhibits cGAMP synthesis

We next sought to establish the importance of DNA binding for ORF9's function as a cGAS antagonist. Alignment of ORF9 with related herpesvirus proteins (Fig 4C) revealed multiple conserved, positively charged residues (Fig 6A). This included ORF9 K178/R179 and ORF9 R186/R187. The latter is aligned with KSHV ORF52 R68/K69 that are required for DNA binding (Wu *et al*, 2015). We therefore generated three ORF9 mutants: K178A/R179A (construct A), R186A/R187A (construct B), and a double mutant (DM), in which all four residues were mutated to alanine. The mutation sites A and B are located at the beginning and in the middle, respectively, of the first alpha helix in the predicted two helix–sheet–helix of ORF9 (Fig 6B). In the HSV-1 VP22 crystal structure, the corresponding helix forms part of a large, positively charged groove, consistent with a possible role in DNA binding (Hew *et al*, 2015). To test the effect of these mutations experimentally, we performed DNA pull-down experiments. As observed before (Fig 4E), WT ORF9 robustly precipitated with DNA (Fig 6C). In contrast, both the A and B mutants were impaired in their ability to bind DNA, with a stronger effect for the B site. The double mutant did not detectably interact with DNA. Next, we investigated whether the mutant ORF9 proteins interacted with cGAS (Fig 6D). Mutation of either the A or B site alone had no effect on cGAS binding, but ORF9-DM showed attenuated cGAS binding.

To test the ORF9-DM protein functionally, we generated THP1 cell lines that stably overexpressed GFP, ORF9, or ORF9-DM and stimulated these cells with increasing doses of dsDNA (Fig 6E). Compared to GFP-expressing cells, we found equally reduced *IFNB1* induction in cells expressing either WT or mutant ORF9. Taken together, these results indicate that the interaction of ORF9 and cGAS was partially dependent on ORF9's ability to bind DNA. Intriguingly, however, DNA binding by ORF9 was not required for its ability to inhibit DNA sensing.

Lastly, we used a cell-free cGAMP synthesis assay (Kranzusch *et al*, 2013) to test whether ORF9 inhibits cGAS enzymatic activity directly. For this, recombinant human cGAS was incubated with radioactively labelled ATP, GTP, DNA, and recombinant ORF9 or bovine serum albumin (BSA) as control. The radioactively labelled 2′3′-cGAMP produced in these reactions was visualised by thin-layer chromatography and phosphorimaging (Fig 6F and Appendix Fig S4B). Whilst addition of BSA did not affect cGAMP production at any dose, ORF9 inhibited cGAS activity in a dose-dependent manner

© 2022 The Authors

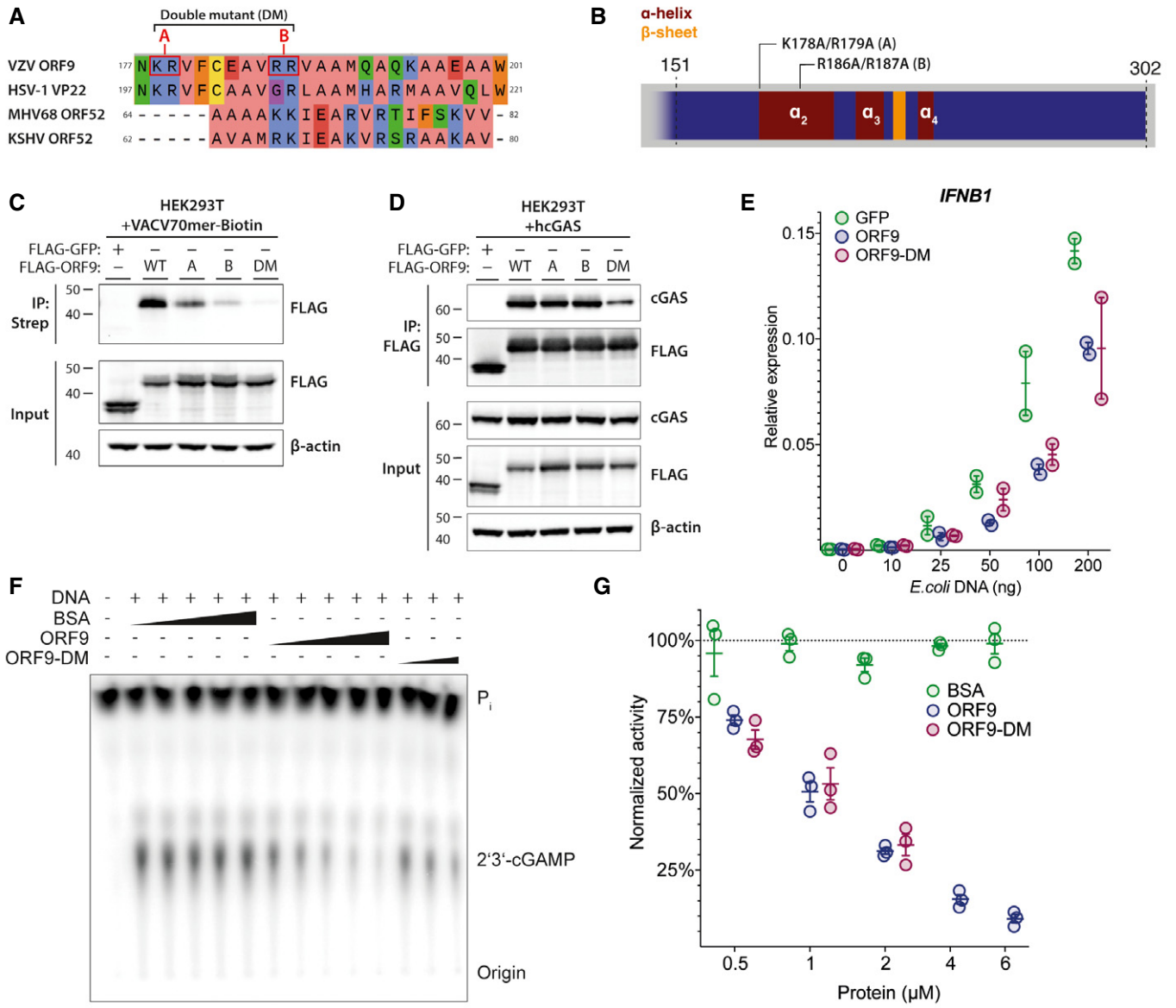


Figure 6. ORF9 inhibits cGAS' catalytic activity.

A Protein sequence alignment of VZV ORF9, HSV-1 VP22, KSHV ORF52, and MHV68 ORF52. Residues selected for mutagenesis in ORF9 are highlighted in red. Residue colouring represents physico-chemical properties (green: hydrophilic, blue: positive, coral: aliphatic/hydrophilic, orange: aromatic, yellow: cysteine, red: negative, purple: conformationally special). See text for details.

B Schematic detailing position and identity of residues mutated in (C–G).

C HEK293T cells were transfected with expression plasmids for FLAG-GFP or FLAG-ORF9 as indicated. The next day, cells were lysed and the lysate was spiked with biotinylated VACV70mer dsDNA. DNA was precipitated using streptavidin beads and proteins were analysed by immunoblotting using the indicated antibodies.

D HEK293T cells were transfected with expression plasmids for human cGAS and FLAG-GFP or FLAG-ORF9. The next day, cells were lysed and proteins were immunoprecipitated using α-FLAG antibody and analysed by immunoblotting using the indicated antibodies.

E THP1 cells stably transduced with GFP, ORF9, or ORF9-DM were transfected with the indicated amounts of *E. coli* dsDNA. The next day, *IFNB1* expression was assessed by RT–qPCR.

F *In vitro* cGAS activity assay. Recombinant hcGAS was incubated with ATP, GTP, and radioactive α32P-ATP at 37°C with addition of dsDNA and other proteins as indicated (triangles represent concentrations of 0.5, 1, 2, 4, 6 μM). ORF9-DM was tested only at 0.5, 1, 2 μM. Reactions were treated with calf-intestinal phosphatase, and products were analysed by thin-layer chromatography and phosphorimaging.

G Signal intensities from (F) were determined by densitometry analysis and normalised to the average BSA signal.

Data information: Recombinant proteins used in (F) and (G) are described in Appendix Fig S4B. Data shown in panels (C) and (D) are representative of two independent experiments. Panel (E) shows pooled data from two repeats, where each data point represents an independent biological experiment ($n = 2 \pm$ range). Panel (F) is representative of three independent experiments. Panel (G) shows pooled data from three repeats, where each data point represents an independent biological experiment ($n = 3 \pm$ SEM).
Source data are available online for this figure.

© 2022 The Authors

(Fig 6F and G). At the doses tested, ORF9-DM was equally potent in inhibiting cGAS compared to WT ORF9. In sum, these results showed that ORF9 directly inhibited the enzymatic activity of cGAS by a mechanism that did not require DNA binding by ORF9.

Discussion

Varicella-Zoster virus is a highly prevalent human virus, yet little is known about its host–pathogen interactions and innate immunity. Here we report that cGAS and its downstream signalling pathway consisting of STING, TBK1, and IRF3 were required for type I IFN induction after VZV infection in THP1 cells. An earlier study using RNA interference had implicated STING in innate recognition of VZV (Kim *et al*, 2017). Our results confirm this observation by complete genetic ablation, and—importantly—identify cGAS as the DNA sensor for VZV. It is possible that innate sensing pathways that detect VZV differ between cell types. Indeed, a study using inhibitory synthetic oligonucleotides found that plasmacytoid DCs produce type I IFN in a partially TLR9-dependent manner (Yu *et al*, 2011). In contrast, we found that the essential TLR9 adaptor protein MyD88 was dispensable for type I IFN induction in VZV-infected THP1 cells. Of note, the inhibitory ODN used in the aforementioned study was later shown to exert inhibitory activity on cGAS as well (Steinhagen *et al*, 2018), thus complicating interpretation of those results. It will be interesting to characterise innate sensing pathways in different cell types relevant to *in vivo* infection, including neuronal cells, T cells, and skin cells. This is important because the viral life cycle and effects of viral replication on host cells can differ between cell types (Zerboni *et al*, 2014). For example, VZV shows cytopathic effects in fibroblast and some immune cells but does not induce cell death in neurons (Gerada *et al*, 2020). Future investigation should therefore address the role of PRRs not only in the induction of cytokines such as type I IFNs but also in the induction of cell death (Maelfait *et al*, 2020).

Our identification of cGAS as a sensor of VZV infection implicates recognition of an immunostimulatory DNA in infected cells. Studies of herpesvirus entry suggest that the viral DNA remains within the viral capsid during nuclear targeting and may therefore be unavailable for binding to the cytosolic pool of cGAS (Radtke *et al*, 2006). Single-cell analysis of HSV-1 infection showed that only cells undergoing abortive infection respond by production of type I IFNs (Drayman *et al*, 2019). It is therefore possible that viral particles with defective capsids are responsible for the type I IFN response observed in bulk populations of cells. Furthermore, cellular restriction mechanisms may make viral DNA from capsids accessible for cGAS binding. Indeed, degradation of herpesviral capsids *via* the ubiquitin–proteasome system has been suggested to release viral DNA for recognition (Horan *et al*, 2013). Alternatively, cellular DNA may induce type I IFN. Indeed, infections with multiple different viruses result in the accumulation of extranuclear DNA and in mitochondrial damage (Ablasser & Chen, 2019). Host DNA has been shown to stimulate cGAS in the context of HSV-1 infection (West *et al*, 2015). Whether viral and/or cellular DNA species activate cGAS in VZV-infected cells should be tested in the future by deep sequencing of cGAS-bound DNA. However, this approach has thus far been hampered by the lack of suitable antibodies for specific cGAS IP.

We further describe the identification of ORF9 as a cGAS antagonist. ORF9 interacted with cGAS in a variety of assays, and inhibited cGAMP production and DNA-triggered type I IFN induction. ORF9 is a tegument protein, making it an attractive candidate for antagonising innate immunity. Tegument proteins are contained within viral particles and are delivered into cells at the same time as viral DNA. ORF9 may therefore limit DNA sensing during early infection before viral gene expression. At first glance, our findings that cGAS recognises VZV infection and that ORF9 inhibits cGAS activation might appear contradictory. However, viral immune evasion mechanisms typically limit but not entirely suppress innate immune responses. This notion is supported by the observation that in some cases multiple viral antagonists target the same host defence pathway (Smith *et al*, 2018; Stempel *et al*, 2019). In addition, cGAS activation may occur partly in cells infected with defective virions (Drayman *et al*, 2019) that are likely to contain and/or express reduced amounts of ORF9.

What is the molecular mechanism by which ORF9 inhibits cGAS? Formation of multimeric complexes and higher order structures of cGAS and DNA facilitate cGAS activation (Li *et al*, 2013; Zhang *et al*, 2014; Andreeva *et al*, 2017; Du & Chen, 2018; Zhou *et al*, 2018). We found that ORF9 binds DNA and phase-separated with DNA. We therefore speculated that ORF9 might disrupt cGAS–DNA oligomers. However, further gel shift and phase separation experiments revealed a more nuanced situation. At salt concentrations up to 250 mM NaCl/KCl, ORF9-facilitated phase separation and DNA–cGAS complexes migrated more slowly in EMSA when ORF9 was added. Nonetheless, at 300 mM salt, ORF9 appeared to limit the presence cGAS in condensates. Similarly, Xu *et al* (2021) recently reported that ORF9 displaces cGAS from cGAS–DNA droplets. It is noteworthy that these experiments were performed at ~200 mM NaCl, a salt concentration at which we did not observe cGAS displacement by ORF9. It is likely that these differences can be explained by the experimental setup, which involved simultaneous mixing of DNA, cGAS, and ORF9 in our experiments and preformed DNA–cGAS complexes with subsequent addition of ORF9 in Xu *et al* (2021). Other parameters such as DNA length are likely important, too. An ORF9 mutant with abrogated DNA binding retained the ability to bind cGAS and to inhibit cGAMP production *in vitro* and IFNβ induction *in cellulo*. Although we cannot exclude that this mutant retained weak DNA binding below the sensitivity of our assays, we prefer a model in which direct protein–protein interactions between ORF9 and cGAS are important for inhibition of cGAMP production. DNA binding of ORF9 may have unrelated functions and/or may facilitate cGAS interaction and inhibition in specific settings. Future experiments are required to decipher in detail the relationships between ORF9, cGAS, DNA binding, and cGAMP production. This could include testing DNA length requirements as cGAS oligomer formation is dependent on DNA length (Li *et al*, 2013; Andreeva *et al*, 2017; Luecke *et al*, 2017; Zhou *et al*, 2018).

ORF9 is essential for viral replication and is a member of the α-herpesvirus UL49 gene family (Tischer *et al*, 2007; Che *et al*, 2008). With its closest relative, HSV-1 VP22, it shares 36% AA sequence similarity (Hew *et al*, 2015). ORF9 has well-established roles in VZV nuclear egress and secondary envelopment (Che *et al*, 2013; Riva *et al*, 2013, 2015; Lebrun *et al*, 2018). Mutational analyses have attributed these functions to AAs or regions either in the N-terminal half or the extreme C-terminus of the protein, whilst we describe a central region (AA151–240) to be required for the interaction of ORF9 with cGAS. A crystal structure is available for the core domain of

© 2022 The Authors

HSV-1 VP22 that is homologous to this region of ORF9 (Hew *et al*, 2015). The HSV-1 VP22 core folds into a two helix–sheet–helix motif. Hew *et al* further describe the structural similarity between HSV1 VP22 and the unrelated MHV68 ORF52 (Hew *et al*, 2015). MHV68 ORF52 is the homologue of KSHV ORF52. Secondary structure prediction and examination of the published crystal structures revealed that VZV ORF9, HSV1 VP22, KSHV ORF52, and MHV68 ORF52 all potentially share a two helix–sheet structural feature (Fig 4C). Interestingly, both HSV-1 VP22 and KSHV ORF52 have been described previously to inhibit cGAS activation (Wu *et al*, 2015; Huang *et al*, 2018). Antagonism of cGAS by KSHV ORF52 requires its DNA-binding properties (Wu *et al*, 2015). In contrast, we found that ORF9's DNA-binding ability was not required for inhibition of cGAS. This indicates that whilst structural similarity between the aforementioned proteins could confer cGAS inhibitory properties, the precise molecular mechanisms might differ. In addition, VZV ORF9 and KSHV ORF52 are essential viral gene products whilst HSV-1 VP22 is not required for viral replication (Li *et al*, 2016; Huang *et al*, 2018). Future experiment will be required to shed light on the precise relationship between these viral proteins.

Collectively, our observations lead us to propose a model in which distantly related herpesviruses have retained within unrelated proteins a structural feature that confers cGAS antagonist properties. Alpha, beta, and gamma-herpesviruses have been estimated to have evolutionarily diverged hundreds of millions of years ago (McGeoch *et al*, 1995; Davison, 2002; preprint: Brito & Pinney, 2018). Anemone species that have diverged from humans more than 500 million years ago harbour cGAS-like enzymes (Kranzusch *et al*, 2015). This indicates that a common ancestral organism expressed such proteins. It further opens up the possibility that ancient herpes viruses evolved the relevant evasion strategies. We hypothesise that antagonism of cGAS by herpesviruses constitutes an ancient molecular mechanism that evolved long before the advent of antiviral cytokines and IRF3 during evolution.

Materials and Methods

Reagents and Tools table

Reagent/Resource	Reference or Source	Identifier or Catalog Number
Experimental Models		
HaCaT	Gift from Leonie Unterholzner (Lancaster University, UK)	RRID:CVCL_0038
HEK293	Gift from Caetano Reis e Sousa (The Francis Crick Institute, UK)	RRID:CVCL_0045
HEK293-ISRE-Fluc	Generated previously in our laboratory (Bridgeman *et al*, 2015)	N/A
HEK293T	Gift from Caetano Reis e Sousa (The Francis Crick Institute, UK)	RRID:CVCL_0063
MeWo	Gift from Graham Ogg (University of Oxford, UK)	RRID:CVCL_0445
THP1 cGAS KO	This study	N/A
THP1 Dual IFNAR2-KO	Invivogen	Cat. #thpd-koifnar2
THP1 Dual MyD88-KO	Invivogen	Cat. #thpd-komyd
THP1 Dual WT	Invivogen	Cat. #thpd-nfis
THP1 IRF3 KO	This study	N/A
THP1 MAVS KO	This study	N/A
THP1 STING KO	Gift from Soren Paludan (Aarhus University, Denmark) (Holm *et al*, 2016)	N/A
THP1 TBK1 KO	Gift from Soren Paludan (Aarhus University, Denmark) (Holm *et al*, 2016)	N/A
VZV rOka	Gift from Jeffrey Cohen (NIH, Bethesda, USA) (Cohen & Seidel, 1993)	N/A
VZV-ORF9^{ecDHFR}	Gift from Paul R. Kinchington (University of Pittsburgh, USA) (Warner *et al*, 2021)	N/A
VZV$^{ORF9\text{-}V5}$	Gift from Catherine Sadzot (University of Liege, Belgium) (Riva *et al*, 2013)	N/A
Recombinant DNA		
hRIG-I-CARD	Gift from Andreas Pichlmair (Technical University Munich, Germany)	N/A
p125-Luc	Gift from T. Fujita (Kyoto University, Japan) (Yoneyama *et al*, 2004)	N/A
p8.91	Gift from Greg Towers (University College London)	N/A
pcDNA/FLAG/hcGAS	This study	N/A

© 2022 The Authors

Reagents and Tools table (continued)

Reagent/Resource	Reference or Source	Identifier or Catalog Number
pcDNA/HA/hSTING	This study	N/A
pCMV-3tag-KSHV-ORF52	Gift from Fanxiu Zhu (Florida State University, USA) (Wu *et al*, 2015)	N/A
pCMV-VSV-G	Gift from Bob Weinberg	Addgene_8454
pDONR/ORF22A	Gift from Jurgen Haas (University of Edinburgh, UK) (Uetz *et al*, 2006)	N/A
pDONR/ORF22B	Gift from Jurgen Haas (University of Edinburgh, UK) (Uetz *et al*, 2006)	N/A
pET-6xHis-SUMO2/hcGAS	Generated in previous study (Zhou *et al*, 2019)	N/A
pET-6xHis-SUMO2/ORF9	This study	N/A
pET-6xHis-SUMO2/ORF9-N	This study	N/A
pET28a/FLAG-GFP	This study	N/A
pET28a/FLAG-ORF9	This study	N/A
pET28a/FLAG-ORF9-DM	This study	N/A
pGag-eGFP	NIH AIDS reagent programme	#11468
pGEX6P1	Gift from Martin Reijns (University of Edinburgh, UK)	GE Healthcare
pGEX6P1/FLAG-GFP	This study	N/A
pGEX6P1/FLAG-ORF9	This study	N/A
pGEX6P1/hcGAS	Gift from Martin Reijns (University of Edinburgh, UK)	N/A
pGEX6P1/hcGAS-HA	This study	N/A
pLenti/FLAG/GFP	This study	N/A
pLenti/FLAG/ORF9	This study	N/A
pLenti/FLAG/ORF9-DM	This study	N/A
pLenti/FLAG/ORF9-truncation-I	This study	N/A
pLenti/FLAG/ORF9-truncation-II	This study	N/A
pLenti/FLAG/ORF9-truncation-III	This study	N/A
pLenti/FLAG/ORF9-truncation-IV	This study	N/A
pLenti/FLAG/ORF9-truncation-V	This study	N/A
pLenti/FLAG/ORF9-truncation-VI	This study	N/A
pLenti/FLAG/ORF9-truncation-VII	This study	N/A
pLenti/FLAG/ORF9-truncation-VIII	This study	N/A
pLenti6.3/V5/EMCV-L	Generated in previous study (Hertzog *et al*, 2018)	N/A
pLenti6.3/V5/hcGAS	This study	N/A
pLenti6.3/V5/hSTING	This study	N/A
pLenti6.3/V5/VZV-ORF	This study. Expression library for all VZV ORFs (see Figure EV2)	N/A
pRL-TK	Promega	N/A
pX458/Ruby/hcGAS	This study	N/A
pX458/Ruby/hIRF3	This study	N/A
pX458/Ruby/hMAVS	Generated in previous study (Hertzog *et al*, 2018)	N/A
Antibodies		
Donkey-anti-mouse-HRP (WB, 1:2,000)	GE Healthcare	Cat. #NA931, RRID:AB_772210
Donkey-anti-rabbit-HRP (WB, 1:2,000)	GE Healthcare	Cat. #NA934, RRID:AB_772206
Goat-anti-rabbit-AlexaFluor647 (IF, 1:500)	Invitrogen	Cat. #A21246, RRID:AB_1500778
Mouse monoclonal beta-actin-HRP (WB, 1:10,000)	Sigma Aldrich	clone AC-15, RRID:AB_262011
Mouse monoclonal FLAG (IP, 5 µg/sample)	Sigma Aldrich	clone M2, RRID:AB_262044
Mouse monoclonal FLAG-HRP (WB, 1:10,000)	Sigma Aldrich	clone M2, RRID:AB_439702

© 2022 The Authors

Reagents and Tools table (continued)

Reagent/Resource	Reference or Source	Identifier or Catalog Number
Mouse monoclonal HA (IP, 5 µg/sample)	Invitrogen	clone 2-2.2.14, RRID:AB_10978021
Mouse monoclonal RIG-I (WB, 1:2,000)	Calteg Medsystems	clone Alme-1, RRID:AB_2490189
Mouse monoclonal V5 (IP, 5 µg/sample)	Biolegend	Cat. #680602, RRID:AB_2566387
Mouse monoclonal V5-FITC (IF, 1:400)	Invitrogen	Cat. #R963-25, RRID:AB_2556567
Mouse monoclonal V5-HRP (WB, 1:5,000)	Invitrogen	Cat. #R961-25, RRID:AB_2556565
Mouse monoclonal VZV gE/GI (WB, 1:1,000)	GE Healthcare	Cat. #MAB8612, RRID:AB_2158042
Mouse monoclonal VZV gE/GI-FITC (Flow cytometry, 1:500)	GE Healthcare, coupled in-house to FITC	Cat. #MAB8612, RRID:AB_2158042
Mouse monoclonal VZV ORF62 (WB, 1:1,000)	Meridian Life Science	Cat. #C05107MA, RRID:AB_1772162
Rabbit monoclonal FLAG (IF, 1:800)	CellSignaling Technology	clone D6W5B, RRID:AB_2572291
Rabbit monoclonal hcGAS (WB, 1:1,000)	CellSignaling Technology	clone D1D3G, RRID:AB_2799712
Rabbit monoclonal hSTING (WB, 1:1,000)	CellSignaling Technology	clone D2P2F, RRID:AB_2732796
Rabbit monoclonal IRF3 (WB, 1:1,000)	CellSignaling Technology	clone D6I4C, RRID:AB_2722521
Rabbit monoclonal MyD88 (WB, 1:1,000)	CellSignaling Technology	clone D80F5, RRID:AB_10547882
Rabbit monoclonal pSTAT1 (Y701) (WB, 1:1,000)	CellSignaling Technology	clone 58D6, RRID:AB_561284
Rabbit monoclonal pSTAT2 (WB, 1:1,000)	CellSignaling Technology	clone D3P2P, RRID:AB_2800123
Rabbit monoclonal STAT1 (WB, 1:1,000)	CellSignaling Technology	clone 42H3, RRID:AB_2197984
Rabbit monoclonal STAT2 (WB, 1:1,000)	CellSignaling Technology	clone D9J7L, RRID:AB_2799824
Rabbit monoclonal TBK1 (WB, 1:1,000)	CellSignaling Technology	clone D1B4, RRID:AB_2255663
Rabbit polyclonal MAVS (WB, 1:1,000)	ENZO Life Science	Cat. #ALX-210-929-C100, RRID:AB_2050916
Rabbit polyclonal VZV ORF9 (WB, 1:2,000)	Gift from Catherine Sadzot (University of Liege, Belgium) (Riva *et al*, 2013)	N/A
Oligonucleotides and sequence-based reagents		
VZV ORF library cloning PCR primers	This study	Appendix Table S1
Further cloning PCR primer	This study	Appendix Table S2
RT-qPCR primers	This study	Appendix Table S3
VACV70mer F 5'-ccatcagaaagag gtttaatatttttgtgagaccatcgaagag agaaagagataaaactttttacgact-3'	This study. Sequence described previously (Unterholzner *et al*, 2010)	N/A
VACV70mer R 5'-agtcgtaaaaaag ttttatctctttctctcttcgatggtctcaca aaaa-tattaaacctctttctgatgg-3'	This study. Sequence described previously (Unterholzner *et al*, 2010)	N/A
100 bp ISD F 5'-ACATCTAGTACA TGTCTAGTCAGTATCTAGTGATTAT CTAGACATACATCTAGTACATGTCT AGTCAGTATCTAGTGATTATCTAGA CATGGACTCATCC-3'	This study. Sequence described previously (Zhou *et al*, 2021)	N/A
100 bp ISD R 5'-GGATGAGTCCAT GTCTAGATAATCACTAGATACTGAC TAGACATGTACTAGATGTATGTCTA GATAATCACTAGATACTGACTAGAC ATGTACTAGATGT-3'	This study. Sequence described previously (Zhou *et al*, 2021)	N/A
Chemicals, enzymes and other reagents		
AlexaFluor-488 (AF488) carboxylic acid (succinimidyl ester)	Thermo Fisher	Cat. #A20000
Antibody FITC Labeling Kit	abcam	Cat. #ab288100
BL21-pLysS-Rosetta	Novagene	Cat. #70954-3
BL21-RIL DE3 *E. coli*	Agilent	Cat. #230240
Blasticidin	gibco	Cat. #A1113903

© 2022 The Authors

Reagents and Tools table (continued)

Reagent/Resource	Reference or Source	Identifier or Catalog Number
CellTrace Yellow	Invitrogen	Cat. #C34567
DAPI	Invitrogen	Cat. #D1306
diABZi	Cambridge Bioscience	Cat #28054-500 ug-CAY
Dual Luciferase assay system	Promega	Cat. #E1910
Dynabeads Protein G	Invitrogen	Cat. #10004D
E. coli DNA	Invivogen	Cat. #tlrl-ecdna
EZBlue Gel Staining Reagent	Sigma Aldrich	Cat. #G1041-500ML
Gateway LR Clonase II Enzyme mix	Invitrogen	Cat. #11791020
Lipofectamine 2000	Invitrogen	Cat. #11668019
Lipofectamine LTX	Invitrogen	Cat. #15338100
LIVE/DEAD Fixable Violet Dead Cell Stain	Invitrogen	Cat. #L34955
Normal goat serum	Invitrogen	Cat. #10000C
oligo-dT primers	Invitrogen	Cat. #18418012
PMA	Sigma Aldrich	Cat. #P1585-1MG
Polybrene	Sigma Aldrich	Cat. #TR-1003-G
PreScission Protease	GE Healthcare	Cat. #GE27-0843-01
Protease Inhibitor Cocktail	CellSignaling Technology	Cat. #5871
Puyomycin	gibco	Cat. #A1113803
QuantiLuc substrate	Invivogen	Cat. #rep-qlc1
SuperScript IV Reverse Transcriptase	Invitrogen	Cat. #18090050
SYBR GreenER master mix	Invitrogen	Cat. #11762100
TaqMan Universal PCR Master Mix	Invitrogen	Cat. #4304437
Trimethoprim	Sigma Aldrich	Cat. #46984-250MG
α32P-ATP	Perkin Elmer	Cat. #NEG003X250UC
Software		
Web-based iBright Image Analysis software	Thermo Fisher	
FlowJo	FlowJo, LLC	
SnapGene	GSL Biotech	
ApE	M. Wayne Davis, The University of Utah	
Fiji 2.0.0	Schindelin *et al* (2012)	

Methods and Protocols

Cells

All cells were cultured at 37°C and 5% CO_2 and checked regularly for mycoplasma contamination. Adherent cells were passaged using Trypsin-EDTA (0.25%) dissociation reagent (Gibco) at appropriate confluence. FCS was obtained from Sigma-Aldrich. HEK293 and HEK293T cells (gifts from Caetano Reis e Sousa, The Francis Crick Institute, UK) were maintained in DMEM (Sigma-Aldrich) containing 4.5 g/l glucose, supplemented with 10% (v/v) FCS and 2 mM L-glutamine (Gibco) (DMEM complete). HEK293-ISRE-Firefly luciferase reporter cells (clone 3C11) were described previously (Bridgeman *et al*, 2015). HaCaT cells were a gift from Leonie Unterholzner (Lancaster University, UK) and were maintained in DMEM complete medium. MeWo cells were a gift from Graham Ogg (University of Oxford, UK) and were maintained in MEM supplemented with 10% (v/v) FCS, 2 mM L-glutamine (Gibco), 1× non-essential amino acids (Gibco), and 1 mM sodium pyruvate (Gibco). THP1 Dual cells (WT, MyD88-KO, and IFNAR2-KO) were from Invivogen. STING-KO and TBK1-KO THP1 cells were a gift from Soren Paludan (Aarhus University, Denmark) (Holm *et al*, 2016). MAVS-KO, cGAS-KO, and IRF3-KO cells were generated as described below. All THP1 cell lines were maintained in RPMI (Sigma-Aldrich) supplemented with 10% (v/v) FCS and 2 mM L-glutamine (Gibco).

Viruses

Varicella-Zoster virus ROka was a gift from Jeffrey Cohen (NIH, Bethesda, USA; Cohen & Seidel, 1993). The virus was maintained in monolayers of MeWo cells. In brief, monolayers of infected cells were monitored microscopically for cytopathic effect. Cells that showed high level of infection were detached, and infected cells were mixed at appropriate ratios (1:2–1:4) with uninfected cells and re-plated. Aliquots of infected cells were cryopreserved in freezing medium (90% FCS, 10% DMSO), stored in liquid nitrogen, and

© 2022 The Authors

thawed for experiments. VZV$^{ORF9\text{-}V5}$ is a recombinant virus, in which a C-terminal V5 tag was added to the coding sequence of ORF9. The virus was a kind gift from Catherine Sadzot (University of Liege, Belgium; Riva *et al*, 2013). VZV-ORF9^{ecDHFR} is a recombinant virus, in which an *E. coli* dihydrofolate reductase degron motif was fused C-terminally to the coding sequence of ORF9 (University of Pittsburgh, USA; Warner *et al*, 2021).

Plasmids

The p125-Luc plasmid (*hIFNB1* promoter firefly luciferase) was a gift from T. Fujita (Kyoto University, Japan; Yoneyama *et al*, 2004). pRL-TK was from Promega. RIG-I-CARD was a gift from Andreas Pichlmair (Technical University Munich, Germany). pCMV-VSV-G was a gift from Bob Weinberg (Addgene number 8454). The lentiviral packaging plasmid p8.91 was a gift from Greg Towers (University College London). pGag-eGFP was from the NIH AIDS reagent programme (number 11468). pX458/Ruby/hMAVS was described previously (Hertzog *et al*, 2018). pX458/Ruby/hIRF3 and pX458/Ruby/hcGAS were created as described for the MAVS-targeting plasmid. sgRNAs targeting exon 3 of the IRF3 locus and exon 2 of the cGAS locus were designed using the MIT algorithm (crispr.mit.edu) and cloned into the pX458 vector. pCMV-3tag-KSHV-ORF52 was a kind gift from Fanxiu Zhu (Florida State University, USA; Wu *et al*, 2015). The pLenti6.3/EMCV-L-V5 plasmid was described previously (Hertzog *et al*, 2018).

Cloning

Mammalian expression plasmids for hcGAS and hSTING were created by PCR amplification using THP1 cDNA and ligation into the gateway entry vector pCR8. Coding sequences were shuttled into expression vectors (pLenti6.3/C-V5, pcDNA3.2/C-FLAG, pcDNA3.2/C-HA) via Gateway recombination. Mammalian expression plasmids for eGFP (pLenti6.3/puro/N-FLAG, pDEST31/N-FLAG) were created in a similar way by PCR amplification from pGag-eGFP introducing a stop codon. VZV ORF9 expression plasmids (pLenti6.3/puro/N-FLAG, pDEST31/N-FLAG) were created by amplification of ORF9 with a stop codon and gateway recombination. Expression plasmids for ORF9 truncation mutants (pLenti6.3/puro/N-FLAG) were created by PCR amplification of the respective coding sequence with a start and stop codon. ORF9 mutant plasmids were generated using site-directed mutagenesis (QuikChange II Site-Directed Mutagenesis Kit, Agilent). GST-fusion bacterial expression vectors for FLAG-ORF9, FLAG-GFP, and hcGAS-HA were created by PCR amplification of the coding sequences from existing plasmids and restriction enzyme cloning into pGEX6P1. pGEX6P1 and pGEX6P1-hcGAS were a kind gift from Martin Reijns (University of Edinburgh, UK). Further bacterial expression vectors for FLAG-ORF9 and FLAG-ORF9-DM were created by restriction enzyme cloning of coding sequences into the pET28a bacterial expression vector (kind gift from Simon Davis, University of Oxford). Bacterial expression vectors for ORF9 and ORF9-N were created by restriction enzyme cloning of coding sequences into a custom 6xHis-SUMO bacterial expression vector (Zhou *et al*, 2018). All primer sequences are listed in Appendix Table S1.

Immunostimulatory dsDNA

Escherichia coli dsDNA was from Invivogen. A 70 bp immunostimulatory dsDNA fragment from VACV was described previously (Unterholzner *et al*, 2010). Two complementary oligos were synthesised (Sigma-Aldrich) and combined at an equal molar ratio. The solution was heated to 95°C and allowed to anneal by cooling to RT.

Forward sequence: 5′-CCATCAGAAAGAGGTTTAATATTTTTGTGAGACCATCGAAGAGAGAAAGAGA-TAAAACTTTTTTACGACT-3′-TEG-Biotin.
Reverse sequence: 5′-AGTCGTAAAAAAGTTTTATCTCTTTCTCTCTTCGATGGTCTCACAAAAA-TATTAAACCTCTTTCTGATGG-3′

The 100 bp dsDNA used for the phase separation assay was described previously (Zhou *et al*, 2021). DNA oligos were synthesised (Integrated DNA Technologies) and double-stranded DNA was prepared by annealing two complementary oligos.

Forward sequence: 5′-ACATCTAGTACATGTCTAGTCAGTATCTAGTGATTATCTAGACATACATCTA-GTACATGTCTAGTCAGTATCTAGTGATTATCTAGACATGGACTCATCC-3′

Reverse sequence: 5′-GGATGAGTCCATGTCTAGATAATCACTAGATACTGACTAGACATGTACTAGAT-GTATGTCTAGATAATCACTAGATACTGACTAGACATGTACTAGATGT-3′

Antibodies

For immunoblot

beta-actin-HRP (AC-15, Sigma-Aldrich), FLAG-HRP (clone M2, Sigma-Aldrich), V5-HRP (R961-25, Invitrogen), RIG-I (Alme1, Calteg Medsystems), VZV-gE/GI (MAB8612, GE Healthcare), VZV ORF62 (C05107MA, Meridian Life Science), pSTAT1 (Y701) (58D6, CellSignaling Technology), STAT1 (42H3, CellSignaling Technology), pSTAT2 (D3P2P, CellSignaling Technology), STAT2 (D9J7L, CellSignaling Technology), hcGAS (D1D3G, CellSignaling Technology), hSTING (D2P2F, CellSignaling Technology), MyD88 (D80F5, CellSignaling Technology), TBK1 (D1B4, CellSignaling Technology), MAVS (ALX-210-929-C100, ENZO Life Science), IRF3 (D6I4C, CellSignaling Technology), VZV ORF9 (polyclonal rabbit serum, kind gift from Catherine Sadzot (University of Liege, Belgium) (Riva *et al*, 2013), donkey-anti-mouse-HRP (NA931, GE Healthcare), donkey-anti-rabbit-HRP (NA934, GE Healthcare).

For IP

FLAG (clone M2, Sigma-Aldrich, V5 (680602, Biolegend), HA (2-2.2.14, Invitrogen).

For IF

V5-FITC (R963-25, Invitrogen), FLAG (D6W5B, CellSignaling Technology), goat-anti-rabbit-AF647 (A21246, Invitrogen).

For FACS

VZV-gE/gI (see above) was conjugated to FITC using FITC Conjugation Kit (Abcam).

VZV ORF Library

Primers for PCR amplification of individual VZV ORF sequences were designed based on an annotated VZV genome sequence (GenBank accession: AB097933.1). Forward primers included a Kozak sequence (GCCGCC), added before the start codon of an ORF. Reverse primers excluded the Stop codon to allow for the

 © 2022 The Authors

addition of a C-terminal tag through the vector (see below). Primer sequences are listed in Appendix Table S2. The PCR template was generated by extracting RNA from VZV-infected MeWo cells using QIAshredder (Qiagen) and RNeasy Mini Kit (Qiagen). The RNA was reverse transcribed into cDNA using SuperScript II Reverse Transcriptase (Invitrogen). For some ORFs, DNA from infected MeWo cells extracted with DNeasy Blood and Tissue Kit (Qiagen) served as the PCR template. PCR products were generated using Phusion High-Fidelity DNA Polymerase (New England Biolabs) or Herculase II Fusion DNA Polymerase (Agilent Technologies). PCR reactions were analysed by agarose gel electrophoresis, and PCR products of the predicted size were extracted from the gel using QIAquick Gel Extraction Kit (Qiagen). Fragments were ligated into the pCR8/TOPO Gateway entry vector (Invitrogen). Plasmid DNA from single clones of transformed *E. coli* (New England Biolabs) was analysed for correct orientation of the insert by Sanger sequencing. Inserts were then shuttled into pLenti6.3/TO/V5-DEST (Invitrogen) using LR Clonase II Enzyme Mix (Invitrogen) for Gateway recombination. All clones with the pLenti6.3/TO/V5 backbone were propagated in recombination-deficient Stbl3 bacteria (Invitrogen).

Cloning of the entire coding sequence of ORF22 (8,256 bp) was unsuccessful using various amplification and cloning technologies. Therefore, two Gateway entry vectors encoding individual segments within the ORF22 coding sequence (ORF22A: nt 2219-4029, ORF22B: nt 4,012–6,114, described previously (Uetz *et al*, 2006)) were used (kind gift from Jurgen Haas, University of Edinburgh, UK). Expression vectors with the pLenti6.3/TO/V5 backbone were generated as described above.

To validate expression, HEK293T were seeded at 5×10^5 cells per well in 12-well plates. The next day, cells were transfected with 600 ng VZV ORF or control expression plasmids using 3 µl Lipofectamine 3000 (Invitrogen) per well. Twenty-four hours later, cells were lysed in RIPA buffer (10 mM TRIS–HCl pH8, 140 mM NaCl, 1% Triton-X 100, 0.1% SDS, 0.1% sodium deoxycholate, 1 mM EDTA, 0.5 mM EGTA). Lysates were clarified by centrifugation and 30 µg protein was subjected to immunoblotting.

Luciferase reporter assays

HEK293T cells were seeded at 3.5×10^4 cells per well in 96-well plates. On the following day, cells were transfected with the following plasmids using Lipofectamine 2000 (Invitrogen): 20 ng p125-F-Luc, 5 ng pRL-TK, 1 ng hcGAS, 25 ng hSTING, and 50 ng of a VZV ORF. Alternatively, cells were transfected with 5 ng RIG-I-CARD plasmid instead of cGAS and STING plasmids. The next day, expression of firefly and renilla luciferases was assessed using Dual Luciferase assay system (Promega).

Activity of the secreted Lucia luciferase under IRF3 promoter control (THP1 Dual cells) was assessed using QuantiLuc substrate (Invivogen) according to manufacturer's instructions.

Lentivirus production and transduction

1.2×10^7 HEK293T cells were seeded in 15 cm cell culture dishes. The next day, cells were transfected with 9 µg lentiviral expression plasmids harbouring the gene of interest, 9 µg p8.91 plasmid, and 3 µg pVSV-G using Lipofectamine 2000. Sixteen hours later, the medium was replaced with fresh growth medium. Twenty-four hours later, lentivirus containing supernatant was harvested, clarified by centrifugation, and stored at 4°C. Cells were overlaid with fresh growth medium. Eight hours later, supernatants were harvested again and pooled with previous supernatants. After 16 h, lentivirus containing supernatants were harvested for the third time. Pooled supernatants from all three harvests were filtered through a 0.45 µm filter, aliquoted into cryovials and stored at −80°C. For transduction of cells, polybrene (Sigma-Aldrich) was added to lentiviral supernatants to a final concentration of 8 µg/ml. THP1 cells were pelleted and resuspended in lentiviral supernatant containing polybrene. The next day, cells were pelleted and resuspended in fresh growth medium. After overnight incubation, cells were once again pelleted and resuspended in growth medium containing 10 µg/ml blasticidin or 1 µg/ml puromycin (both Gibco) depending on which vector was used. Surviving cells were used for experiments.

THP1 knockout cell generation

For generation of knockout cells using CRISPR/Cas9 technology, the pX458-mRuby plasmid encoding the Cas9 protein, the sgRNA, and mRuby was used (Hertzog *et al*, 2018). The sgRNA sequences were "GAAGTAATATGCACGAGTG" for *cGAS*, "GGCCACCATCTGGATTCCTT" for *MAVS*, and "GGTGGTGCATATGTTCCCGGG" for *IRF3*. 1×10^7 THP1 cells were transiently transfected with 50 µg of respective pX458 plasmids using Lipofectamine LTX (Invitrogen) and incubated overnight. The next day, cells were stained with 10 µg/ml DAPI in PBS for 10 min. After resuspension of cells in growth medium, live, mRuby-positive cells were FACS-sorted into Eppendorf tubes containing growth medium with 20% FCS. The suspension of sorted cells was diluted with special growth medium (50% conditioned THP1 medium, 40% fresh RPMI with 10% FCS, 10% additional FCS) to one or three cells per 200 µl. Two hundred microlitre cell suspension were then dispensed into each well of a 96-well plate (one or three cells per well). The cells were incubated for several weeks until clones grew out.

The absence of the targeted protein in each clone was assessed by immunoblot analysis. For functional validation of MAVS and IRF3 knockout cells, 1.5×10^5 cells were seeded per well into 96-well plates in growth medium containing 10 ng/ml PMA (Sigma-Aldrich). The next day, cells were transfected with 5 ng IVT-RNA (Rehwinkel *et al*, 2010) or 15 ng *E. coli* DNA (Invivogen) using Lipofectamine 2000 (Invitrogen). Twenty-four hours later, IFN in supernatants was measured using the type I IFN bioassay. For functional validation of cGAS knockout cells, cells were stimulated in the same way and activity of Lucia luciferase (under IRF3 promoter control) was assessed in supernatants. Knockout clones were further analysed for insertions and deletions in their genomic loci. *MAVS* and *IRF3* target regions were PCR-amplified using Herculase II Fusion DNA Polymerase. PCR amplicons were gel extracted (QIAquick Gel Extraction Kit) and sequenced by Sanger sequencing. Sequencing traces were analysed using the TIDE software (https://tide.nki.nl; Brinkman *et al*, 2014).

VZV flow cytometry infection assay

Cells were washed in FACS tubes with PBS and incubated with LIVE/DEAD Fixable Violet Dead Cell Stain (Invitrogen) diluted 1:1,000 in PBS for 30 min at 4°C. Cells were washed in PBS and resuspended in 100 µl FACS buffer (1% FCS, 2 mM EDTA in PBS) containing 1:500 FITC-coupled antibody against VZV-gE/gI complex. Cells were incubated 30 min at 4°C. After washing with PBS, cells were resuspended in PBS and an equal volume of 8%

© 2022 The Authors

methanol-free formaldehyde in PBS was added. Cells were fixed for 15 min at room temperature. Cells were washed with PBS, resuspended in FACS buffer, and analysed on a Attune NxT Acoustic Focusing Cytometer (Thermo Fisher).

THP1 VZV co-culture infections

6.125×10^6 THP1 cells (WT, KOs, or stably transduced with ORF9/GFP) were seeded per well in six-well plates in growth medium containing 10 ng/ml PMA (Sigma-Aldrich). As a control, 1.625×10^6 MeWo cells were seeded in MEM. In some experiments, cells were labelled on the next day with a tracer dye (CellTrace Yellow, Invitrogen) before infection. Aliquots of uninfected and VZV-infected MeWo cells were thawed, washed, and resuspended in MEM. Cells were counted and their concentration was adjusted to 6.25×10^5 live cells per ml (for THP1 cells) or 1.25×10^5 live cells per ml (for MeWo cells) with MEM. Medium was removed from labelled cells, and cells were overlaid with 2 ml MeWo ±VZV cell suspension. Cells were incubated at 37°C for 1 h. The cell suspension was removed, adherent cells were washed with PBS, overlaid with their respective growth medium, and incubated for 48 h. Supernatants were removed from cells, clarified by centrifugation, and stored at −80°C. CXCL10 levels were determined using Human CXCL10/IP-10 Quantikine ELISA Kit (R&D Systems) according to manufacturer's instructions. Cells were washed with PBS and incubated with Trypsin-EDTA until they started to detach. Growth medium was added, cells were resuspended by gentle pipetting, and transferred to tubes. Forty percent of the cell suspension were transferred to Eppendorf tubes on ice for extraction of RNA and generation of protein lysates, respectively. The cells in those Eppendorf tubes were pelleted, washed with PBS, and then lysed either in RLT buffer and processed for RT–qPCR or lysed in RIPA buffer and processed for immunoblot analysis. The remaining 20% of cells were processed for flow cytometry analysis.

THP1 transwell VZV infections

PET membrane 1 μm transwell inserts (Sarstedt 83.3930.101) were placed with the bottom membrane facing upwards into 15 cm dishes. Aliquots of uninfected and VZV-infected MeWo cells were thawed, washed, and resuspended in MEM. Cells were counted and their concentration was adjusted to 3×10^6 live cells per ml with MEM. Five hundred microlitre cell suspension (1.5×10^6 cells) was pipetted onto the transwell membrane, and cells were let to adhere in the incubator overnight. Six-well plates were filled with RPMI media and prepared transwells were placed cell-side downwards into the plates, so that the MeWo cells were submerged. 2×10^6 THP1 cells were seeded onto the upward facing side of the transwell membrane in RPMI medium containing 10 ng/ml PMA. Cells were harvested by trypsinisation after 24 h and 48 h and used for downstream analysis. A publication describing this method in more detail is in preparation.

VZV-ORF9^{ecDHFR} infections

THP1 cells were seeded in six-well plates in growth medium containing 10 ng/ml PMA. The next day, cells were co-cultured with uninfected or VZV-ORF9^{ecDHFR}-infected MeWo cells for 1 h in MEM containing 25 μM TMP (trimethoprim, Sigma-Aldrich). Cells were washed and incubated overnight in THP1 growth medium containing 25 μM TMP. Cells were washed extensively with PBS and then cultured for another 24 h in THP1 growth medium containing 25 μM TMP or not. Cells were harvested and subjected to RNA extraction and RT–qPCR for ISGs and immunoblotting.

diABZi stimulations

THP1 cells stably transduced with either ORF9 or GFP were seeded in 12-well plates in growth medium and were treated with the STING agonist diABZi (Cambridge Bioscience, 28054–500 μg-CAY) at the concentrations indicated in the figure legends. After 24 h, cells were harvested and expression of IFNs and ISG was assessed by RT–qPCR.

Pulldowns

1.4×10^7 HEK293T cells were seeded in 15 cm cell culture dishes. The next day, cells were transfected with 12.7 μg of ORF9-V5, cGAS-FLAG, and STING-HA expression plasmids using Lipofectamine 2000. Sixteen hours later, cells were lysed in IP buffer (20 mM TRIS–HCl pH7.4, 100 mM NaCl, 1 mM EDTA, 0.5% NP-40, Protease Inhibitor Cocktail; CellSignaling Technology). After clarification, an aliquot was removed as input sample and the lysate was split into four equal volumes. Each aliquot was incubated with 50 μl Dynabeads Protein G (Invitrogen) that were coated with 5 μg α-V5, α-FLAG, α-HA, or control IgG antibody for 1 h under rotation at 4°C. The supernatant was removed, an aliquot was stored as unbound fraction from each sample, and beads were washed three times in lysis buffer. Input, unbound, and bound fractions were subjected to immunoblotting. For pulldowns from stably transduced THP1 cells, cells were seeded at 2×10^7 per dish in 15 cm cell culture dishes in growth medium containing 10 ng/ml PMA. Lysates were generated the next day and processed as described above. For pulldowns of recombinant proteins, 3 μl recombinant cGAS-HA protein was mixed with 1.5 μl FLAG-ORF9 or FLAG-GFP in IP buffer. IP was performed as described above. For pulldowns from VZV-infected cells, 2.2×10^7 THP1 cells and 4×10^6 HaCaT cells were seeded in 10 cm dishes (in the presence of 10 ng/ml PMA for THP1 cells). The next day, cells were overlaid with 1.25×10^7 MeWo cells infected with VZV or VZV$^{ORF9\text{-}V5}$ for 1 h and afterwards washed with PBS. Lysates were generated 48 h later as described above.

Far western

The experimental procedure for far western was based on a protocol previously described (Wu *et al*, 2007). 1.5 μl FLAG-ORF9 protein or 1.5 μl FLAG-GFP protein was subjected to SDS–PAGE and blotting as described for regular immunoblotting (see below). After transfer, the membrane was incubated for 30 min at RT temperature in AC buffer (6 M Guanidine HCl, 100 mM NaCl, 20 mM TRIS–HCl pH 7.6, 0.5 mM EDTA, 10% glycerol, 0.1% Tween-20, 2% skim milk powder, 1 mM DTT). The membrane was then incubated in AC buffers with decreasing concentrations of Guanidine HCl (3 M, 1 M, 0.1 M) for 30 min each. For the last incubation, the membrane was transferred to 4°C and thereafter incubated in AC buffer free of Guanidine HCl overnight. The membrane was blocked for 1 h in 5% milk powder in PBST (PBS with 0.05% Tween-20) and then incubated with 10 μl recombinant cGAS per 5 ml buffer as probe in 3% milk powder in PBST for 1 h. Membranes were washed for 10 min with PBST thrice and then incubated with α-cGAS antibody for 1 h. After washing, membranes were incubated with appropriate secondary antibodies, washed again, and imaged. Thereafter, membranes

 © 2022 The Authors

were stripped and re-probed with α-FLAG antibody as described for conventional immunoblot.

Immunofluorescence

1.75×10^5 HEK293T cells were seeded onto-glass coverslips. The next day, cells were transfected with 250 ng of cGAS-V5 or FLAG-ORF9 expression plasmid using 1.5 µl Lipofectamine 3000 per well. Additional coverslips were co-transfected with both plasmids. Twenty-four hours later, cells were washed with PBS and fixed with 4% formaldehyde in cytoskeleton stabilisation buffer (CSB; 10 mM KCl, 274 mM NaCl, 8 mM $NaHCO_3$, 0.8 mM KH_2PO_4, 2.2 mM Na_2HPO_4, 4 mM $MgCl_2$, 10 mM PIPES, 4 mM EGTA, 11 mM glucose) for 15 min. Cells were washed and permeabilised with 0.1% Triton X-100 in CSB for 20 min and incubated with 100 mM glycine in CSB for 10 min afterwards. Cells were washed with PBS four times and blocked using 1% BSA and 5% normal goat serum (Invitrogen) in PBS for 1 h. Coverslips were incubated with primary antibodies in blocking solution for 3 h at room temperature. Cells were washed three times with PBS and incubated with secondary antibodies in blocking solution for 1 h. Coverslips were washed with PBS three times and mounted onto glass slides using ProLong Diamond Antifade Mountant with DAPI (Invitrogen). Images were acquired using a Zeiss LSM780 confocal microscopy system (Zeiss).

Recombinant protein expression

Single-step purification of GST-fusion proteins (see Appendix Fig S4A)

BL21-pLysS-Rosetta *E. coli* (Novagene) were transformed with bacterial expression vectors. A single colony or a glycerol stock from a single colony were used to inoculate a starter culture of 25 ml LB-medium containing 34 µg/ml Chloramphenicol and 100 µg/ml Carbenicillin. A large 400 ml LB culture was inoculated using the starter culture. OD600 was measured in intervals and, for VZV ORF9 and GFP, recombinant protein expression was induced by adding 0.1 mM IPTG once OD reached 0.6. Bacteria were grown 3 h at 37°C. For expression of recombinant cGAS and cGAS-HA, bacteria were grown to OD 0.8 and chilled to 18°C. Protein expression was induced by adding 0.4 mM IPTG, and bacteria were incubated for 16 h at 18°C. For all proteins, bacteria were pelleted at 6,000 g for 7 min and the pellet was resuspended in 12 ml lysis buffer (20 mM TRIS pH7.4, 500 mM NaCl, 0.5 mM EDTA, 0.5 mM EGTA, 0.5% NP40, 1:100 Protease Inhibitor Cocktail; CellSignaling Technology). The suspension was sonicated on ice three times at 20% amplitude with 15 s ON and 30 s OFF (Branson Sonifier). Insoluble material was removed by centrifugation for 15 min at 24,000 *g*. In the meantime, 150 µl Glutathione Sepharose beads (GE Healthcare) were prepared according to manufacturer's instructions. The beads were added to the clarified lysate and incubated under rotation for 4 h at 4°C. The beads were pelleted by centrifugation at 500 g and washed five times with lysis buffer. The beads were washed once in PreScission Cleavage buffer (50 mM TRIS pH 7.5, 150 mM, 1 mM freshly added DTT) and resuspended in 500 µl PreScission Cleavage buffer. After addition of 12 µl PreScission Protease (GE Healthcare), the suspension was incubated under rotation for 3 h at 4°C. The supernatant containing the recombinant protein was separated from beads and stored at −80°C. Aliquots from the various purification steps were analysed by SDS–PAGE and subsequent staining of the gel with EZBlue Gel Staining Reagent (Sigma-Aldrich). Based on band intensities, the protein concentrations were estimated to be ca. 1 µg/µl for FLAG-ORF9 and FLAG-GFP, and ca. 0.5 µg/µl for cGAS and cGAS-HA.

ORF9 purifications for EMSA and cGAS activity assay (Appendix Fig S4B)

BL21-pLysS-Rosetta *E. coli* were transformed with bacterial expression vectors. Three fresh, single colonies were used to inoculate a starter culture of 150 ml LB-medium containing 34 µg/ml chloramphenicol and 50 µg/ml kanamycin and grown overnight at 16°C. Two large 1 L LB cultures were then inoculated using the starter culture. Bacteria were grown to OD 0.8 and chilled to 16°C. Protein expression was induced by adding 0.5 mM IPTG and bacteria were incubated for 16 h at 16°C. Bacteria were pelleted at 6,000 g for 15 min and the pellet was resuspended in 120 ml lysis buffer (20 mM HEPES-KOH pH 8, 400 mM NaCl, 0.5% NP40, 10% glycerol, 30 mM imidazole, 1 mM PMSF, 5 mM beta-mercaptoethanol). The suspension was sonicated on ice at 70% amplitude with 15 s ON and 15 s OFF for 8 min total sonication time (Branson Sonifier). Insoluble material was removed by centrifugation for 25 min at 25,000 *g*. In the meantime, 5 ml packed Ni-NTA resin (Qiagen) were equilibrated in lysis buffer. The beads were added to the clarified lysate and incubated under rotation for 30 min at 4°C. The bead suspension was added to a gravity flow column and the flow through was collected. Beads were washed with 40 ml lysis buffer, 120 ml wash buffer (20 mM HEPES-KOH pH8, 1 M NaCl, 0.5% NP40, 10% glycerol, 30 mM imidazole), and 80 ml lysis buffer. Proteins were eluted twice with 30 ml elution buffer (20 mM TRIS–HCl pH 7.5, 300 mM NaCl, 300 mM imidazole). Two HiTrap Heparin 5 ml columns (GE Healthcare) were installed in tandem on an Äkta chromatography system (GE Healthcare) and equilibrated with 10 column volumes of HIEX buffer A (20 mM TRIS–HCl pH 7.5, 300 mM NaCl). The Ni-NTA eluate was applied to the columns, which were subsequently washed with 10 column volumes of HIEX buffer A. Bound proteins were eluted into fractions with a linear salt gradient of HIEX buffer A and HIEX buffer B (20 mM TRIS–HCl pH 7.5, 2 M NaCl). Fractions were analysed by SDS–PAGE, and the desired ones were pooled. After concentration (Amicon Ultra-15 10 kD Spin Filters, EMD Millipore), proteins were applied to a Superdex 75 increase 10/300 GI column and eluted with the final storage buffer (HEPES-KOH pH 7.5, 250 mM KCl, 1 mM TCEP). Fractions were analysed by SDS–PAGE, and the desired ones were pooled, concentrated, and stored at −80°C.

ORF9 purifications for phase separation assay (Appendix Fig S4C)

Recombinant ORF9 was purified using a protocol previously optimised for expression in MDG and M9ZB media (Zhou *et al*, 2019). Briefly, BL21-RIL DE3 *E. coli* (Agilent) were transformed with pET-6xHis-SUMO bacterial expression vectors for full-length ORF9 or C-terminally truncated ORF9 1–244 (ORF9-N). A starter culture of 30 ml grown in MDG-medium was used to inoculate 2×1 L M9ZB-media cultures. Cultures were grown to an OD of ~2.5, chilled to 16°C, and protein expression was induced with 0.5 mM IPTG before incubation at 16°C for ~16 h. Pelleted bacteria were lysed in lysis buffer (20 mM HEPES-KOH pH 7.5, 400 mM NaCl, 10% glycerol, 30 mM imidazole, 1 mM DTT) by sonication. Insoluble material was removed by centrifugation, and 6xHis-tagged protein was purified using Ni-NTA (Qiagen) and gravity chromatography. Proteins were eluted with 30 ml elution buffer (20 mM

© 2022 The Authors

HEPES-KOH pH7.5, 400 mM NaCl, 10% glycerol, 300 mM imidazole, 1 mM DTT), dialysed against low salt buffer (150 mM NaCl) overnight in the presence of 250 μg hSENP2 protease for cleave of the 6xHis-SUMO tag. Cleaved protein was further purified by HiTrap SP ion-exchange for full-length ORF9 and a combination of HiTrap Q ion-exchange and Superdex 75 size-exclusion chromatography for ORF9 1–244. Final purified fractions were pooled, concentrated, and flash-frozen in liquid nitrogen for storage at −80°C.

cGAS

Recombinant human cGAS protein used for EMSA and cell-free cGAS activity assays was purified as described previously (Zhou *et al*, 2019).

Immunoblotting

Protein concentrations in lysates were determined using Pierce BCA Protein Assay Kit (Thermo Scientific) and equalised by dilution of samples with lysis buffer. Subsequently, 4× NuPAGE LDS Sample Buffer (Invitrogen) was added and samples were incubated at 95°C for 10 min. Samples were run on NuPAGE Novex 4–12% Bis-TRIS gels (Invitrogen) using NuPage MOPS-SDS running buffer (Invitrogen). Proteins were subsequently blotted onto PROTRAN Pure nitrocellulose membrane (PerkinElmer) using transfer buffer (25 mM TRIS, 192 mM glycine). Membranes were blocked with 5% skim milk powder (Sigma-Aldrich) in TBS containing 0.1% Tween-20 (5% milk TBS-T) for 1 h at room temperature and were then incubated with primary antibodies in 5% milk TBS-T overnight at 4°C. Primary antibodies that bind to phosphorylated residues were diluted in 5% BSA in TBS-T. Membranes were washed thrice with TBS-T and incubated with HRP-coupled secondary antibodies in 5% milk TBS-T for 1 h at room temperature. After three further washes with TBS-T, proteins were detected using Western Lightning Plus-ECL (PerkinElmer) and the iBright FL1000 Imaging System (Thermo Fisher) or Amersham Hyperfilm MP (GE Healthcare). If needed, antibodies were stripped from the membrane with stripping buffer (200 mM glycine, 0.1% SDS, 1% Tween-20, pH 2.2) for 20 min at room temperature. Membranes were washed with TBS-T, blocked as described above, and re-probed.

RT–qPCR

Cells were lysed in RLT Plus buffer and RNA was extracted using RNeasy Plus Mini Kit (Qiagen). The RNA was reverse transcribed using SuperScript IV Reverse Transcriptase (Invitrogen) and oligo-dT primers (Invitrogen). The qPCR reaction containing TaqMan Universal PCR Master Mix (Applied Biosystems) and TaqMan Primer/Probes was run on QuantStudio 7 Flex Real-Time PCR System (Thermo Fisher) with standard settings. Gene expression was analysed with the Ct method using *GAPDH* expression for normalisation. Taqman primer/probes used were: *GAPDH* (Hs02758991_g1), *IFNB1* (Hs02621180_s1), *IFI44* (Hs00951349_m1), *IFIT1* (Hs03027069_s1), and *IFNL1* (Hs00601677_g1). RT–qPCR for VZV transcripts was performed with SYBR GreenER master mix (Invitrogen) using primer pairs indicated in Appendix Table S3.

Cell-free cGAS activity assay

Cell-free cGAS activity assays were performed according to a previously described procedure (Kranzusch *et al*, 2013). Full-length recombinant human cGAS protein (1 μM) and VACV70mer DNA (1 μM) were incubated in 20 μl reaction buffer (50 mM TRIS–HCl pH 7.5, 10 mM $Mg(OAc)_2$, 10 mM KCl, 1 mM DTT, 25 μM ATP, 25 μM GTP, 1 μCi α32P-ATP; PerkinElmer) for 90 min at 37°C. Reactions were terminated for 5 min at 95°C. Leftover ATP was converted to inorganic phosphate by addition of 10 U calf-intestinal phosphatase and incubation for 20 min at 37°C. Two microlitres of each reaction were spotted onto a PEI Cellulose F thin-layer chromatography plate (EMD Millipore) and run in 1.5 M KH_2PO_4. Plates were dried at room temperature and exposed to a phosphorscreen overnight. Screens were imaged using a Typhoon FLA 9500 imager (GE Healthcare). Signal intensities were quantified using Fiji 2.0.0 software (Schindelin *et al*, 2012) and normalised to the average signal in conditions with BSA.

Phase separation assays

In vitro phase separation was performed as previously described (Du & Chen, 2018; Zhou *et al*, 2021). Briefly, human cGAS was labelled with AlexaFluor-488 (AF488) carboxylic acid (succinimidyl ester) (Thermo Fisher Scientific) according to manufacturer's manuals using a molar ratio of 1:10 at 4°C for 4 h. Excess free dye was removed by dialysis against buffer (20 mM HEPES-KOH pH 7.5, 250 mM KCl, 1 mM DTT) at 4°C overnight, and then human cGAS was further purified on a PD-10 desalting column (GE Healthcare) eluted with storage buffer (20 mM HEPES-KOH pH 7.5, 250 mM KCl, 1 mM TCEP) as previously described (Zhou *et al*, 2021).

To induce phase separation, human cGAS, ORF9, or ORF9 truncation (5–15 μM each) was incubated with 100 bp dsDNA (5–10 μM, containing 10% Cy3-labelled DNA) in the presence of various salt concentrations at 25°C in a total reaction volume of 20 μl. The details of proteins, nucleic acids, and salt concentrations are provided in figure legends. Reactions were placed in 384-well non-binding microplates (Greiner Bio-One) and incubated at 25°C for 30 min prior to imaging to allow condensates to settle. Fluorescence microscopy images were acquired at 25°C using a Leica TCS SP5 X (Leica Microsystems) mounted on an inverted microscope (DMI6000; Leica Microsystems) with an oil immersion 63×/numerical aperture 1.4 objective lens (HCX PL APO; Leica Microsystems). Labelled proteins were detected with excitation at 488 nm (emission at 500–530 nm), and DNA was detected with excitation at 550 nm (emission at 560–590 nm). Microscopy images were processed with Fiji (Schindelin *et al*, 2012) and contrast adjusted with a uniform threshold setup for each enzyme.

Protein sequence analysis

The HSV-1 VP22 (PDB: 4XAL) and MHV68 ORF52 (PDB: 2OA5) crystal structures were used to graphically represent secondary structure features. For VZV ORF9 (UniProt accession Q4JQW6) and KSHV ORF52 (UniProt accession F5HBL8), structural features and sequence disorder was predicted by the PROFphd secondary structure prediction algorithm through submission of protein sequences to the predictprotein.org web interface (Yachdav *et al*, 2014).

Data analysis and software

Data were analysed using Excel for Mac (Microsoft) and GraphPad Prism 8 (GraphPad Software). SnapGene (GSL Biotech) and ApE (M. Wayne Davis, The University of Utah) were utilised for DNA sequence analysis to assist cloning. Statistical analysis is detailed in the figure

 © 2022 The Authors

legends and was performed using GraphPad Prism 8. Sample sizes were estimated based on prior experience and the literature. Randomisation and blinding were not performed. Graphs and figures were created using GraphPad Prism 8 and Adobe Illustrator CC (Adobe Systems). Immunoblot images were processed using web-based iBright Image Analysis software (Thermo Fisher). Flow cytometry data was analysed using FlowJo (FlowJo, LLC). Fiji 2.0.0 software was used to process confocal microscopy images (Schindelin *et al*, 2012).

Data availability

This study includes no data deposited in external repositories.

Expanded View for this article is available online.

Acknowledgments
The authors thank J Cohen, C Sadzot, and S Paludan for VZV stocks, antibodies, and cell lines, and P Hublitz and Z Holloway (MRC WIMM Genome Engineering Facility) for their help with CRISPR plasmid generation. The authors further thank C Reis e Sousa, F Zhu, G Ogg, L Unterholzner, A Pichlmair, G Towers, T Fujita, J Haas, and M Reijns for reagents and advice. The authors thank M Brinkmann, J McKeating, and members of the Rehwinkel lab for critical discussion. This work was funded by the UK Medical Research Council [MRC core funding of the MRC Human Immunology Unit], the Wellcome Trust [grant number 100954], and the Concern Foundation. JH was supported by the European Commission under the Horizon2020 programme H2020 MSCA-ITN GA 675278 EDGE. WZ was supported through a Charles A. King Trust Postdoctoral fellowship. GF was supported by the Rothermere Fellowship and was also supported by Indspire's Building Brighter Futures: Bursaries, Scholarships, and Awards programme. BEW was supported by training grant T32 EY017272. PRK acknowledges support from NIH grants NS064022, EY08098, and unrestricted funds from Research to Prevent Blindness and the Eye and Ear Foundation of Pittsburgh. The MRC WIMM Genome Engineering Facility is supported by grants from the MRC/MHU (MC_UU_12009), the John Fell Fund (123/737), and by MRC WIMM Strategic Alliance awards G0902418 and MC_UU_12025. The funders had no role in study design, data collection and analysis, decision to publish, or preparation of the manuscript.

Author contributions
Jonny Hertzog: Conceptualization; Data curation; Formal analysis; Validation; Investigation; Visualization; Methodology; Writing—original draft; Project administration; Writing—review and editing. **Wen Zhou:** Resources; Investigation; Visualization; Methodology; Writing—review and editing. **Gerissa Fowler:** Investigation; Visualization; Methodology; Writing—review and editing. **Rachel E Rigby:** Conceptualization; Investigation; Methodology; Writing—review and editing. **Anne Bridgeman:** Investigation; Writing—review and editing. **Henry TW Blest:** Investigation; Writing—review and editing. **Chiara Cursi:** Investigation; Methodology; Writing—review and editing. **Lise Chauveau:** Resources; Writing—review and editing. **Tamara Davenne:** Methodology; Writing—review and editing. **Benjamin E Warner:** Resources; Writing—review and editing. **Paul R Kinchington:** Resources; Writing—review and editing. **Philip J Kranzusch:** Supervision; Writing—review and editing. **Jan Rehwinkel:** Conceptualization; Formal analysis; Supervision; Funding acquisition; Validation; Visualization; Writing—original draft; Project administration; Writing—review and editing.

In addition to the CRediT author contributions listed above, the contributions in detail are:

JH, RER, and JR conceived the study. JH, WZ, GF, RER, and JR designed the experiments and analysed the data. JH, WZ, GF, AB, HTWB, CC, LC, and TD performed the experiments. JH, WZ, RER, and PJK developed the methodology. BEW and PRK developed and provided the reagents. JH and JR wrote the manuscript with help from all authors. All authors read and approved the final manuscript.

Disclosure and competing interests statement
The authors declare that they have no conflict of interest.

References

Abendroth A, Morrow G, Cunningham AL, Slobedman B (2001) Varicella-zoster virus infection of human dendritic cells and transmission to T cells: implications for virus dissemination in the host. *J Virol* 75: 6183 – 6192

Ablasser A, Chen ZJ (2019) cGAS in action: Expanding roles in immunity and inflammation. *Science* 363: eaat8657

Almine JF, O'Hare CAJ, Dunphy G, Haga IR, Naik RJ, Atrih A, Connolly DJ, Taylor J, Kelsall IR, Bowie AG *et al* (2017) IFI16 and cGAS cooperate in the activation of STING during DNA sensing in human keratinocytes. *Nat Commun* 8: 14392

Andreeva L, Hiller B, Kostrewa D, Lässig C, de Oliveira Mann CC, Jan Drexler D, Maiser A, Gaidt M, Leonhardt H, Hornung V *et al* (2017) cGAS senses long and HMGB/TFAM-bound U-turn DNA by forming protein-DNA ladders. *Nature* 549: 394 – 398

Arvin AM, Gilden D (2013) Varicella-Zoster Virus. In *Virology*, Fields BN, Knipe DM, Howley PM (eds), pp 2015 – 2057. Philadelphia, PA: Wolters Kluwer Health/Lippincott Williams & Wilkins

Arvin AM, Koropchak CM, Williams BRG, Grumet FC, Foung SKH (1986) Early immune response in healthy and immunocompromised subjects with primary Varicella-Zoster virus infection. *J Infect Dis* 154: 422 – 429

Barrat FJ, Elkon KB, Fitzgerald KA (2016) Importance of nucleic acid recognition in inflammation and autoimmunity. *Annu Rev Med* 67: 323 – 336

Bridgeman A, Maelfait J, Davenne T, Partridge T, Peng Y, Mayer A, Dong T, Kaever V, Borrow P, Rehwinkel J (2015) Viruses transfer the antiviral second messenger cGAMP between cells. *Science* 349: 1228 – 1232

Brinkman EK, Chen T, Amendola M, van Steensel B (2014) Easy quantitative assessment of genome editing by sequence trace decomposition. *Nucleic Acids Res* 42: e168

Brito AF, Pinney JW (2018) Time-calibrated tree reconciliations reveal frequent losses, intrahost speciations, and host switches in the evolution of herpesviruses. *Biorxiv* https://doi.org/10.1101/418111 [PREPRINT]

Brubaker SW, Bonham KS, Zanoni I, Kagan JC (2015) Innate immune pattern recognition: a cell biological perspective. *Annu Rev Immunol* 33: 257 – 290

Buchan DWA, Jones DT (2019) The PSIPRED protein analysis workbench: 20 years on. *Nucleic Acids Res* 47: W402 – W407

Campbell TM, McSharry BP, Steain M, Ashhurst TM, Slobedman B, Abendroth A (2018) Varicella zoster virus productively infects human natural killer cells and manipulates phenotype. *PLoS Pathog* 14: e1006999

Carter-Timofte ME, Paludan SR, Mogensen TH (2018) RNA polymerase III as a gatekeeper to prevent severe VZV infections. *Trends Mol Med* 24: 904 – 915

Caunt AE, Taylor-Robinson D (2009) Cell-free varicella-zoster virus in tissue culture. *Epidemiol Infect* 62: 413 – 424

Che X, Oliver SL, Reichelt M, Sommer MH, Haas J, Rovis TL, Arvin AM (2013) ORF11 protein interacts with the ORF9 essential tegument protein in Varicella-Zoster virus infection. *J Virol* 87: 5106 – 5117

© 2022 The Authors

Che X, Reichelt M, Sommer MH, Rajamani J, Zerboni L, Arvin AM (2008) Functions of the ORF9-to-ORF12 gene cluster in Varicella-Zoster virus replication and in the pathogenesis of skin infection. *J Virol* 82: 5825 – 5834

Chen JJ, Zhu Z, Gershon AA, Gershon MD (2004) Mannose 6-phosphate receptor dependence of varicella zoster virus infection *in vitro* and in the epidermis during varicella and zoster. *Cell* 119: 915 – 926

Cohen JI, Seidel KE (1993) Generation of varicella-zoster virus (VZV) and viral mutants from cosmid DNAs: VZV thymidylate synthetase is not essential for replication *in vitro*. *Proc Natl Acad Sci USA* 90: 7376 – 7380

Davison AJ (2002) Evolution of the herpesviruses. *Vet Microbiol* 86: 69 – 88

Drayman N, Patel P, Vistain L, Tay S (2019) HSV-1 single-cell analysis reveals the activation of anti-viral and developmental programs in distinct sub-populations. *Elife* 8: 2503

Du M, Chen ZJ (2018) DNA-induced liquid phase condensation of cGAS activates innate immune signaling. *Science* 361: 704 – 709

Freundt EC, Drappier M, Michiels T (2018) Innate immune detection of cardioviruses and viral disruption of interferon signaling. *Front Microbiol* 9: 867

Gerada C, Campbell TM, Kennedy JJ, McSharry BP, Steain M, Slobedman B, Abendroth A (2020) Manipulation of the innate immune response by varicella zoster virus. *Front Immunol* 11: 1

Haberthur K, Messaoudi I (2013) Animal models of varicella zoster virus infection. *Pathogens* 2: 364 – 382

Harding SM, Benci JL, Irianto J, Discher DE, Minn AJ, Greenberg RA (2017) Mitotic progression following DNA damage enables pattern recognition within micronuclei. *Nature* 548: 466 – 470

Hartmann G (2017) Nucleic acid immunity. *Adv Immunol* 133: 121 – 169

Hertzog J, Dias Junior AG, Rigby RE, Donald CL, Mayer A, Sezgin E, Song C, Jin B, Hublitz P, Eggeling C *et al* (2018) Infection with a Brazilian isolate of Zika virus generates RIG-I stimulatory RNA and the viral NS5 protein blocks type I IFN induction and signaling. *Eur J Immunol* 48: 1120 – 1136

Hew K, Dahlroth SL, Pan LX, Cornvik T, Nordlund P (2015) VP22 core domain from Herpes simplex virus 1 reveals a surprising structural conservation in both the Alpha- and Gammaherpesvirinae subfamilies. *J Gen Virol* 96: 1436 – 1445

Holm CK, Rahbek SH, Gad HH, Bak RO, Jakobsen MR, Jiang Z, Hansen AL, Jensen SK, Sun C, Thomsen MK *et al* (2016) Influenza A virus targets a cGAS-independent STING pathway that controls enveloped RNA viruses. *Nat Commun* 7: 10680

Hopfner KP, Hornung V (2020) Molecular mechanisms and cellular functions of cGAS-STING signalling. *Nat Rev Mol Cell Biol* 21: 501 – 521

Horan KA, Hansen K, Jakobsen MR, Holm CK, Søby S, Unterholzner L, Thompson M, West JA, Iversen MB, Rasmussen SB *et al* (2013) Proteasomal degradation of herpes simplex virus capsids in macrophages releases DNA to the cytosol for recognition by DNA sensors. *J Immunol* 190: 2311 – 2319

Hu S, Sun H, Yin L, Li J, Mei S, Xu F, Wu C, Liu X, Zhao F, Zhang DI *et al* (2019) PKR-dependent cytosolic cGAS foci are necessary for intracellular DNA sensing. *Sci Signal* 12: eaav7934

Huang J, You H, Su C, Li Y, Chen S, Zheng C (2018) Herpes simplex virus 1 tegument protein VP22 abrogates cGAS/STING-mediated antiviral innate immunity. *J Virol* 92: 783

Kennedy JJ, Steain M, Slobedman B, Abendroth A (2019) Infection and functional modulation of human monocytes and macrophages by Varicella-Zoster virus. *J Virol* 93: 10980

Kim J-A, Park S-K, Seo S-W, Lee CH, Shin OS (2017) STING is involved in antiviral immune response against VZV infection via the induction of type I and III IFN pathways. *J Invest Dermatol* 137: 2101 – 2109

Kranzusch PJ, Lee AS, Berger JM, Doudna JA (2013) Structure of human cGAS reveals a conserved family of second-messenger enzymes in innate immunity. *Cell Rep* 3: 1362 – 1368

Kranzusch PJ, Wilson SC, Lee AS, Berger JM, Doudna JA, Vance RE (2015) Ancient origin of cGAS-STING reveals mechanism of universal 2',3' cGAMP signaling. *Mol Cell* 59: 891 – 903

Ku C-C, Chang Y-H, Chien Y, Lee T-L (2016) Type I interferon inhibits varicella-zoster virus replication by interfering with the dynamic interaction between mediator and IE62 within replication compartments. *Cell Biosci* 6: 519

Lebrun M, Lambert J, Riva L, Thelen N, Rambout X, Blondeau C, Thiry M, Snoeck R, Twizere J-C, Dequiedt F *et al* (2018) Varicella-Zoster virus ORF9p binding to cellular adaptor protein complex 1 is important for viral infectivity. *J Virol* 92: 222

Li W, Avey D, Fu B, Wu JJ, Ma S, Liu X, Zhu F (2016) Kaposi's sarcoma-associated herpesvirus inhibitor of cGAS (KicGAS), encoded by ORF52, is an abundant tegument protein and is required for production of infectious progeny viruses. *J Virol* 90: 5329 – 5342

Li X, Shu C, Yi G, Chaton CT, Shelton CL, Diao J, Zuo X, Kao CC, Herr AB, Li P (2013) Cyclic GMP-AMP synthase is activated by double-stranded DNA-induced oligomerization. *Immunity* 39: 1019 – 1031

Luecke S, Holleufer A, Christensen MH, Jonsson KL, Boni GA, Sorensen LK, Johannsen M, Jakobsen MR, Hartmann R, Paludan SR (2017) cGAS is activated by DNA in a length-dependent manner. *EMBO Rep* 18: 1707 – 1715

Lum KK, Song B, Federspiel JD, Diner BA, Howard T, Cristea IM (2018) Interactome and proteome dynamics uncover immune modulatory associations of the pathogen sensing factor cGAS. *Cell Syst* 7: 627 – 642

Mackenzie KJ, Carroll P, Martin C-A, Murina O, Fluteau A, Simpson DJ, Olova N, Sutcliffe H, Rainger JK, Leitch A *et al* (2017) cGAS surveillance of micronuclei links genome instability to innate immunity. *Nature* 548: 461 – 465

Maelfait J, Liverpool L, Rehwinkel J (2020) Nucleic acid sensors and programmed cell death. *J Mol Biol* 432: 552 – 568

Mainka C, Fuss B, Geiger H, Höfelmayr H, Wolff MH (1998) Characterization of viremia at different stages of varicella-zoster virus infection. *J Med Virol* 56: 91 – 98

McGeoch DJ, Cook S, Dolan A, Jamieson FE, Telford EAR (1995) Molecular phylogeny and evolutionary timescale for the family of mammalian herpesviruses. *J Mol Biol* 247: 443 – 458

McNab F, Mayer-Barber K, Sher A, Wack A, O'Garra A (2015) Type I interferons in infectious disease. *Nat Rev Immunol* 15: 87 – 103

Mo C, Lee J, Sommer MH, Arvin AM (2003) Varicella-zoster virus infection facilitates VZV glycoprotein E trafficking to the membrane surface of melanoma cells. *J Med Virol* 70: S56 – S58

Morrow G, Slobedman B, Cunningham AL, Abendroth A (2003) Varicella-Zoster virus productively infects mature dendritic cells and alters their immune function. *J Virol* 77: 4950 – 4959

Nagel MA, Gilden D (2014) Neurological complications of varicella zoster virus reactivation. *Curr Opin Neurol* 27: 356 – 360

Nour AM, Reichelt M, Ku C-C, Ho MY, Heineman TC, Arvin AM (2011) Varicella-Zoster virus infection triggers formation of an interleukin-1β (IL-1β)-processing inflammasome complex. *J Biol Chem* 286: 17921 – 17933

Radtke K, Döhner K, Sodeik B (2006) Viral interactions with the cytoskeleton: a hitchhiker's guide to the cell. *Cell Microbiol* 8: 387 – 400

Ramanjulu JM, Pesiridis GS, Yang J, Concha N, Singhaus R, Zhang S-Y, Tran J-L, Moore P, Lehmann S, Eberl HC *et al* (2018) Design of

 © 2022 The Authors

amidobenzimidazole STING receptor agonists with systemic activity. *Nature* 564: 439 – 443

Rehwinkel J, Tan CP, Goubau D, Schulz O, Pichlmair A, Bier K, Robb N, Vreede F, Barclay W, Fodor E *et al* (2010) RIG-I detects viral genomic RNA during negative-strand RNA virus infection. *Cell* 140: 397 – 408

Riva L, Thiry M, Bontems S, Joris A, Piette J, Lebrun M, Sadzot-Delvaux C (2013) ORF9p phosphorylation by ORF47p is crucial for the formation and egress of Varicella-Zoster virus viral particles. *J Virol* 87: 2868 – 2881

Riva L, Thiry M, Lebrun M, L'Homme L, Piette J, Sadzot-Delvaux C (2015) Deletion of the ORF9p acidic cluster impairs the nuclear egress of Varicella-Zoster virus capsids. *J Virol* 89: 2436 – 2441

Schindelin J, Arganda-Carreras I, Frise E, Kaynig V, Longair M, Pietzsch T, Preibisch S, Rueden C, Saalfeld S, Schmid B *et al* (2012) Fiji: an open-source platform for biological-image analysis. *Nat Methods* 9: 676 – 682

Schoggins JW (2019) Interferon-stimulated genes: what do they all do? *Annu Rev Virol* 6: 567 – 584

Sen N, Sommer M, Che X, White K, Ruyechan WT, Arvin AM (2010) Varicella-Zoster virus immediate-early protein 62 blocks interferon regulatory factor 3 (IRF3) phosphorylation at key serine residues: a novel mechanism of IRF3 inhibition among herpesviruses. *J Virol* 84: 9240 – 9253

Shakya AK, O'Callaghan DJ, Kim SK (2019) Interferon gamma inhibits Varicella-Zoster virus replication in a cell line-dependent manner. *J Virol* 93: 3904

Smith GL, Talbot-Cooper C, Lu Y (2018) How does vaccinia virus interfere with interferon? *Adv Virus Res* 100: 355 – 378

Steinhagen F, Zillinger T, Peukert K, Fox M, Thudium M, Barchet W, Putensen C, Klinman D, Latz E, Bode C (2018) Suppressive oligodeoxynucleotides containing TTAGGG motifs inhibit cGAS activation in human monocytes. *Eur J Immunol* 48: 605 – 611

Stempel M, Chan B, Brinkmann MM (2019) Coevolution pays off: herpesviruses have the license to escape the DNA sensing pathway. *Med Microbiol Immunol* 208: 495 – 512

Sun L, Wu J, Du F, Chen X, Chen ZJ (2013) Cyclic GMP-AMP synthase is a cytosolic DNA sensor that activates the type I interferon pathway. *Science* 339: 786 – 791

Tischer BK, Kaufer BB, Sommer M, Wussow F, Arvin AM, Osterrieder N (2007) A self-excisable infectious bacterial artificial chromosome clone of Varicella-Zoster virus allows analysis of the essential tegument protein encoded by ORF9. *J Virol* 81: 13200 – 13208

Torigo S, Ihara T, Kamiya H (2000) IL-12, IFN-gamma, and TNF-alpha released from mononuclear cells inhibit the spread of varicella-zoster virus at an early stage of varicella. *Microbiol Immunol* 44: 1027 – 1031

Uetz P, Dong Y-A, Zeretzke C, Atzler C, Baiker A, Berger B, Rajagopala SV, Roupelieva M, Rose D, Fossum E *et al* (2006) Herpesviral protein networks and their interaction with the human proteome. *Science* 311: 239

Unterholzner L, Keating SE, Baran M, Horan KA, Jensen SB, Sharma S, Sirois CM, Jin T, Latz E, Xiao TS *et al* (2010) IFI16 is an innate immune sensor for intracellular DNA. *Nat Immunol* 11: 997 – 1004

Wang JP, Kurt-Jones EA, Shin OS, Manchak MD, Levin MJ, Finberg RW (2005) Varicella-zoster virus activates inflammatory cytokines in human monocytes and macrophages via toll-like receptor 2. *J Virol* 79: 12658 – 12666

Warner BE, Yee MB, Zhang M, Hornung RS, Kaufer BB, Visalli RJ, Kramer PR, Goins WF, Kinchington PR (2021) Varicella-zoster virus early infection but not complete replication is required for the induction of chronic hypersensitivity in rat models of postherpetic neuralgia. *PLoS Pathog* 17: e1009689

West AP, Khoury-Hanold W, Staron M, Tal MC, Pineda CM, Lang SM, Bestwick M, Duguay BA, Raimundo N, MacDuff DA *et al* (2015) Mitochondrial DNA stress primes the antiviral innate immune response. *Nature* 520: 553 – 557

WHO (2014) Varicella and herpes zoster vaccines: WHO position paper, June 2014. *Wkly Epidemiol Rec* 25: 265 – 288

Wu J-J, Li W, Shao Y, Avey D, Fu B, Gillen J, Hand T, Ma S, Liu X, Miley W *et al* (2015) Inhibition of cGAS DNA sensing by a herpesvirus virion protein. *Cell Host Microbe* 18: 333 – 344

Wu J, Sun L, Chen X, Du F, Shi H, Chen C, Chen ZJ (2013) Cyclic GMP-AMP is an endogenous second messenger in innate immune signaling by cytosolic DNA. *Science* 339: 826 – 830

Wu Y, Li Q, Chen X-Z (2007) Detecting protein–protein interactions by far western blotting. *Nat Protoc* 2: 3278 – 3284

Xie W, Lama L, Adura C, Tomita D, Glickman JF, Tuschl T, Patel DJ (2019) Human cGAS catalytic domain has an additional DNA-binding interface that enhances enzymatic activity and liquid-phase condensation. *Proc Natl Acad Sci USA* 116: 11946 – 11955

Xu G, Liu C, Zhou S, Li Q, Feng Y, Sun P, Feng H, Gao Y, Zhu J, Luo X *et al* (2021) Viral tegument proteins restrict cGAS-DNA phase separation to mediate immune evasion. *Mol Cell* 81: 2823 – 2837

Yachdav G, Kloppmann E, Kajan L, Hecht M, Goldberg T, Hamp T, Hönigschmid P, Schafferhans A, Roos M, Bernhofer M *et al* (2014) PredictProtein-an open resource for online prediction of protein structural and functional features. *Nucleic Acids Res* 42: W337 – W343

Yoneyama M, Kikuchi M, Natsukawa T, Shinobu N, Imaizumi T, Miyagishi M, Taira K, Akira S, Fujita T (2004) The RNA helicase RIG-I has an essential function in double-stranded RNA-induced innate antiviral responses. *Nat Immunol* 5: 730 – 737

Yu H-R, Huang H-C, Kuo H-C, Sheen J-M, Ou C-Y, Hsu T-Y, Yang KD (2011) IFN-α production by human mononuclear cells infected with varicella-zoster virus through TLR9-dependent and -independent pathways. *Cell Mol Immunol* 8: 181 – 188

Zerboni L, Sen N, Oliver SL, Arvin AM (2014) Molecular mechanisms of varicella zoster virus pathogenesis. *Nat Rev Microbiol* 12: 197 – 210

Zhang X, Wu J, Du F, Xu H, Sun L, Chen Z, Brautigam CA, Zhang X, Chen ZJ (2014) The cytosolic DNA sensor cGAS forms an oligomeric complex with DNA and undergoes switch-like conformational changes in the activation loop. *Cell Rep* 6: 421 – 430

Zhou W, Mohr L, Maciejowski J, Kranzusch PJ (2021) cGAS phase separation inhibits TREX1-mediated DNA degradation and enhances cytosolic DNA sensing. *Mol Cell* 81: 739 – 755

Zhou W, Whiteley AT, de Oliveira Mann CC, Morehouse BR, Nowak RP, Fischer ES, Gray NS, Mekalanos JJ, Kranzusch PJ (2018) Structure of the human cGAS-DNA complex reveals enhanced control of immune surveillance. *Cell* 174: 300 – 311

Zhou W, Whiteley AT, Kranzusch PJ (2019) Analysis of human cGAS activity and structure. *Methods Enzymol* 625: 13 – 40

Zhu H, Zheng C, Xing J, Wang S, Li S, Lin R, Mossman KL (2011) Varicella-Zoster virus immediate-early protein ORF61 abrogates the IRF3-mediated innate immune response through degradation of activated IRF3. *J Virol* 85: 11079 – 11089

License: This is an open access article under the terms of the Creative Commons Attribution License, which permits use, distribution and reproduction in any medium, provided the original work is properly cited.

scientific reports

Check for updates

OPEN

The RNA sensor MDA5 detects SARS-CoV-2 infection

Natalia G. Sampaio[1,4], Lise Chauveau[1,4], Jonny Hertzog[1,4], Anne Bridgeman[1,4], Gerissa Fowler[1], Jurgen P. Moonen[1], Maeva Dupont[2], Rebecca A. Russell[2], Marko Noerenberg[3] & Jan Rehwinkel[1]✉

Human cells respond to infection by SARS-CoV-2, the virus that causes COVID-19, by producing cytokines including type I and III interferons (IFNs) and proinflammatory factors such as IL6 and TNF. IFNs can limit SARS-CoV-2 replication but cytokine imbalance contributes to severe COVID-19. We studied how cells detect SARS-CoV-2 infection. We report that the cytosolic RNA sensor MDA5 was required for type I and III IFN induction in the lung cancer cell line Calu-3 upon SARS-CoV-2 infection. Type I and III IFN induction further required MAVS and IRF3. In contrast, induction of IL6 and TNF was independent of the MDA5-MAVS-IRF3 axis in this setting. We further found that SARS-CoV-2 infection inhibited the ability of cells to respond to IFNs. In sum, we identified MDA5 as a cellular sensor for SARS-CoV-2 infection that induced type I and III IFNs.

Severe acute respiratory syndrome coronavirus 2 (SARS-CoV-2) emerged at the end of 2019 and is causing an ongoing global pandemic. As of June 7th, 2021, it has infected 173,005,553 and killed 3,727,605 patients worldwide (https://covid19.who.int/). SARS-CoV-2 causes Coronavirus Disease 2019 (COVID-19), a respiratory disease that in some patients results in severe pneumonia and acute respiratory distress syndrome leading to death. Severe disease is linked to exacerbated inflammation with increased production of pro-inflammatory cytokines such as TNF and IL6, and delayed type I and type III interferon (IFN) responses[1–4]. Although serum levels of type I and III IFNs are low or undetectable in many patients, the increased expression of genes known to be induced by IFN (called interferon stimulated genes; ISGs) suggests that production of IFN occurs. The importance of the IFN system in controlling disease was confirmed by the discovery of an association between severe disease and inborn errors in IFN immunity as well as autoantibodies against type I IFNs[2,5]. Moreover, recent studies show that intranasal, but not intravenous, administration of type I IFN improves disease outcome in an in vivo hamster model as well as in a phase 2 clinical trial, supporting a crucial role for the type I IFN response in COVID-19[6–8]. Similarly, pegylated IFNλ1, a type III IFN, shows prophylactic and therapeutic benefits in a mouse model of SARS-CoV-2, and is currently being tested in clinical trials[9,10]. The main replication sites of SARS-CoV-2 in patients are the upper and lower respiratory tract, where the virus infects airway and alveolar epithelial cells, vascular endothelial cells, and alveolar macrophages[11]. Uncovering how these cells detect SARS-CoV-2 infection to produce type I and III IFNs and other pro-inflammatory cytokines is therefore of great importance to understanding the pathology of COVID-19.

SARS-CoV-2 is a member of the beta-coronavirus family and is closely related to other viruses that have caused outbreaks in the last two decades: SARS-CoV in 2003 and MERS-CoV in 2013. Its genome is a ~ 30 kb positive-sense single-stranded RNA that shares ~ 80% sequence identity with SARS-CoV and ~ 50% sequence identity with MERS-CoV[11]. Nucleic acid sensors mediate the early detection and host response to virus infections. These sensors recognise either viral nucleic acids or 'unusual' cellular nucleic acids present upon infection[12]. Cytosolic nucleic acid sensors from the RIG-I-Like Receptor (RLR) family have been identified as important pattern recognition receptors (PRRs) that sense coronaviruses[9,13]. The two signalling receptors in this family are retinoic acid-inducible gene I (RIG-I) and melanoma differentiation-associated protein 5 (MDA5). RIG-I detects RNAs with specific structures such as 5′-triphosphate or 5′-diphosphate ends[14], while the precise properties of MDA5-stimulatory RNAs remain under investigation[15]. Once activated, RIG-I and MDA5 interact with the adaptor mitochondrial antiviral-signalling protein (MAVS), triggering a signalling cascade involving TANK-binding kinase 1 (TBK1) and interferon regulatory factor 3 (IRF3) that ultimately induces the expression of type I IFNs (including IFNα and IFNβ), type III IFNs (also known as IFNλ) and other antiviral genes. Secreted type I and III

[1]Medical Research Council Human Immunology Unit, Medical Research Council Weatherall Institute of Molecular Medicine, Radcliffe Department of Medicine, University of Oxford, Oxford OX3 9DS, UK. [2]The Sir William Dunn School of Pathology, University of Oxford, Oxford OX1 3RE, UK. [3]Department of Biochemistry, University of Oxford, Oxford, UK. [4]These authors contributed equally: Natalia G. Sampaio, Lise Chauveau, Jonny Hertzog and Anne Bridgeman. ✉email: jan.rehwinkel@imm.ox.ac.uk

IFNs signal in a paracrine and autocrine manner through their receptors IFNAR and IFNLR, respectively. Both receptors activate the JAK/STAT signalling pathway, leading to the expression of ISGs, some of which encode anti-viral proteins such as MxA[16]. In some infections with RNA viruses such as Dengue virus, the cytosolic DNA sensing pathway involving cGAMP synthase (cGAS) and stimulator of interferon genes (STING) detects mitochondrial DNA leaked from damaged mitochondria and thereby contributes to IFN induction[17,18]. Whether this also happens during coronavirus infection is unknown.

In this study, we identified Calu-3 cells as a suitable model to study innate immune responses to SARS-CoV-2 infection. Using shRNA depletion and CRISPR-Cas9 knockout, we found that MDA5 was an important cytosolic sensor for SARS-CoV-2 in these cells. The MDA5-MAVS-IRF3 signalling axis was necessary for production of type I and III IFNs, but not pro-inflammatory cytokines, in response to SARS-CoV-2 infection. We further show that expression of the ISG MxA is mainly induced in bystander non-infected cells in this system.

Results

In order to identify innate immune sensors that detect SARS-CoV-2, we screened a number of cell lines for permissiveness to infection and immune response. Calu-3, HEK293 and Huh7 cells were permissive to infection, with expression of SARS-CoV-2 nucleocapsid (N) RNA detectable in these cells 24 h after infection (Fig. 1A). However, only Calu-3 cells showed both visible signs of infection by microscopy (Fig. S1) and an innate immune response to the virus (Fig. 1A). Upon SARS-CoV-2 infection, Calu-3 cells upregulated expression of type I and III IFNs (*IFNB1*, *IFNL1*), pro-inflammatory cytokines (*IL6*, *TNF*) and ISGs (*IFIT1*, *IFIH1, MX1*). Calu-3 are adenocarcinoma-derived lung epithelial cells and as such are related to one of the cell types infected by SARS-CoV-2 in the respiratory tract. In addition, Calu-3 cells expressed many of the proteins required for the major signalling pathways activated during viral infection: cGAS and STING (DNA sensing); RIG-I, MDA5 and MAVS (RNA sensing); the Toll-like receptor (TLR) adaptor MyD88; the kinase TBK1; and the transcription factors IRF3 and STAT1/2 (Fig. 1B). These cells further responded to type I IFN stimulation by phosphorylation of STAT1 and STAT2 (Fig. 1B). Together, these data established that Calu-3 cells were a good model for investigating innate immune responses to SARS-CoV-2 infection.

To investigate if RIG-I-like receptors (RLRs) were involved in virus sensing, we first utilised a lentiviral shRNA knockdown approach targeting MAVS, the downstream signalling adaptor for both RIG-I and MDA5. Two independent shRNAs were tested: both reduced MAVS protein and mRNA levels, with shRNA-MAVS-45 having the more potent effect (Fig. 2A,B). We therefore chose shRNA-MAVS-45 for further experiments and infected Calu-3 cells transduced with this shRNA with SARS-CoV-2 using a multiplicity of infection (MOI) of 0.1. 48 h after infection, RNA was extracted from cells and viral and cellular RNAs were analysed by RT-qPCR. The levels of SARS-CoV-2-N RNA were slightly but not significantly increased in MAVS-depleted cells (Fig. 2C). Importantly, induction of type I and III IFN mRNAs and ISGs in response to SARS-CoV-2 was reduced in cells depleted of MAVS (Fig. 2D). However, expression of the mRNAs encoding the pro-inflammatory cytokines TNF and IL6 was not affected by knockdown of MAVS (Fig. 2D). Taken together, these data suggest that RLRs are necessary for the IFN response to SARS-CoV-2 in Calu-3 cells.

Next, we studied the roles of the two signalling RLRs, MDA5 and RIG-I, in the sensing of SARS-CoV-2 using a knock-out approach. We found that Calu-3 cells were not amenable to selection of clones from single cells and therefore opted to use a lenti-CRISPR approach. We transduced Calu-3 cells with lentiviruses expressing Cas9, an sgRNA and the puromycin resistance gene. Using puromycin selection, we generated polyclonal cell lines. We included sgRNAs targeting MAVS, MDA5 and RIG-I. To determine if the cytosolic DNA sensing pathway was activated during SARS-CoV-2 infection, we also targeted STING. IRF3 is activated downstream of both STING and MAVS; therefore, we included an IRF3 sgRNA. Protein levels of MDA5, RIG-I, STING and IRF3 were notably reduced by this approach, whereas the targeting of MAVS was less efficient (Fig. 3A). Next, we infected these cells with SARS-CoV-2 (MOI = 0.1) and analysed their response by RT-qPCR after 48 h. Cells lacking MDA5 or IRF3 showed minimal induction of type I IFN mRNAs and ISGs in response to SARS-CoV-2 infection (Fig. 3B). This effect was uncoupled from the pro-inflammatory response, as lack of MDA5 and IRF3 did not affect the expression of *TNF*, and minimally affected expression of *IL6*, in response to infection (Fig. 3B). Lack of RIG-I or STING had no effect on the cellular response to SARS-CoV-2, suggesting that neither RIG-I nor the cGAS-STING pathway were involved in sensing SARS-CoV-2 in this setting. It is likely that partial depletion of MAVS (Fig. 3A) explains why cells transduced with MAVS sgRNA responded comparably to control cells.

To confirm these observations with a different readout, we used intracellular staining and flow cytometry to measure protein levels of MxA, which is encoded by the ISG *MX1*, and SARS-CoV-2N (Fig. 3C). We analysed cells infected for 48 h with SARS-CoV-2 (MOI = 0.1). In this setting, ~ 40–60% of cells stained positive for N and there was little difference in infection levels between the knockout cells (Fig. 3D). Consistent with our RT-qPCR data, targeting of MDA5 and IRF3 largely prevented upregulation of MxA in response to SARS-CoV-2 infection (Fig. 3E). Targeting of STING and RIG-I partially reduced MxA induction. Intermediate effects were also observed with the inefficient MAVS sgRNA. Further exploration of the upregulation of MxA upon SARS-CoV-2-infection showed different responses in N+ and N− cells. In the uninfected N− cell population, MxA was upregulated to a greater extent compared with infected N+ cells (Fig. 3F). This shows that SARS-CoV-2 infection inhibited the autocrine response of the same cell to released IFNs, whereas uninfected bystander cells were able to respond to IFNs more strongly, implicating viral antagonism of IFNAR and/or IFNLR signalling.

Discussion

In this study, consistent with several recent reports[19–21], we identified Calu-3 cells as a suitable model system for the study of innate immune responses to SARS-CoV-2 infection in vitro. These adenocarcinoma-derived lung epithelial cells expressed key proteins of RNA- and DNA-sensing pathways, responded to stimulation with type

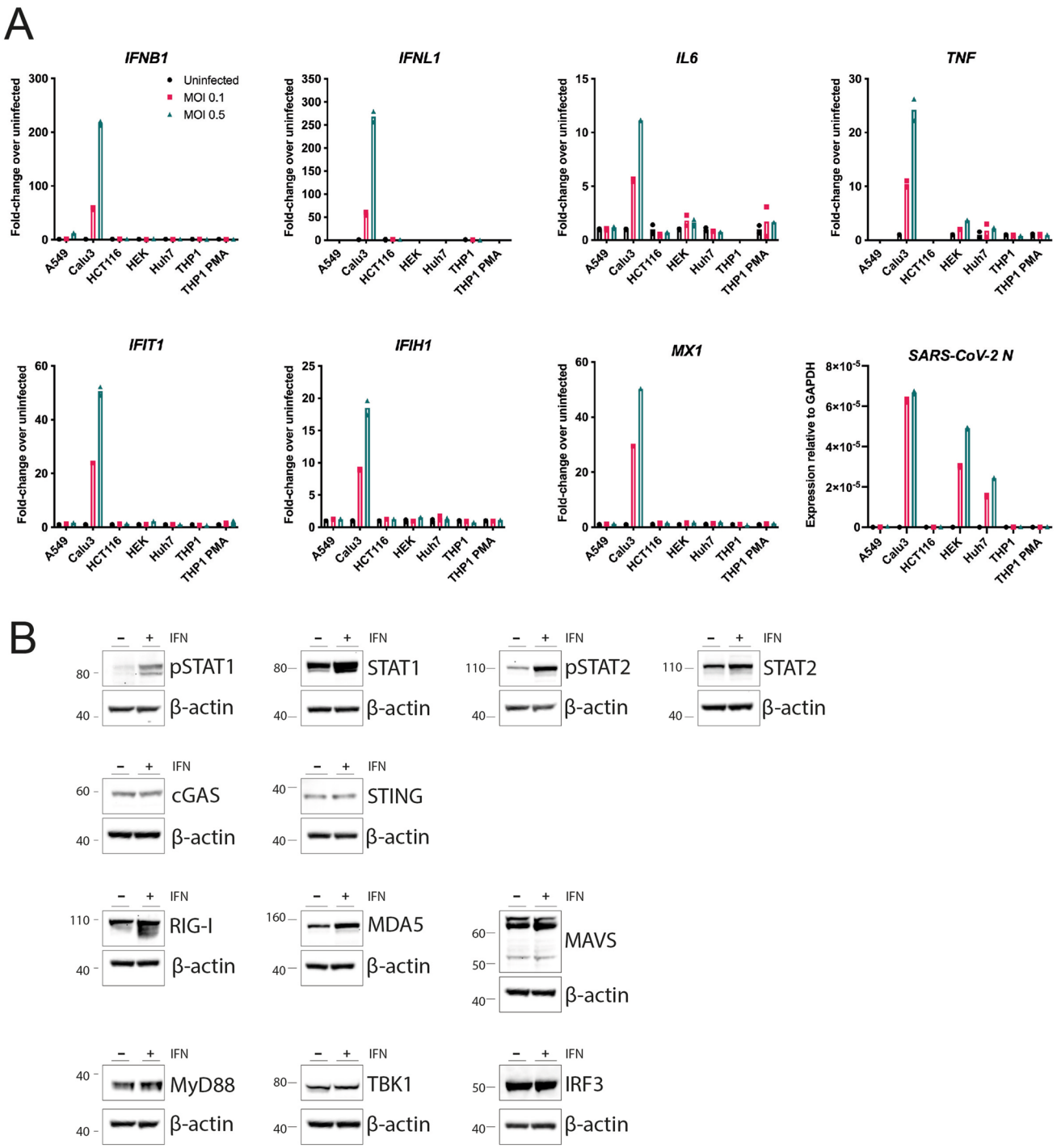


Figure 1. Calu-3 cells respond to SARS-CoV-2 infection by upregulating type I and III IFNs, ISGs and cytokines. (**A**) The indicated cell lines were mock-infected or infected with SARS-CoV-2 (MOI = 0.1 or 0.5) for 24 h prior to RNA extraction and RT-qPCR for the indicated transcripts. Data are relative to *GAPDH* expression. (**B**) Calu-3 cells were stimulated with 100 U/ml IFN-A/D for 16 h. Cell lysates were analysed by western blot using the indicated antibodies. Individual membranes were probed for each protein. Membranes were subsequently re-probed for β-actin. See Supplementary Figure 2 for full blots. Data are from a single experiment. Data points in (**A**) are from technical duplicates and bars indicate the average.

I IFN, and were highly infected by SARS-CoV-2. Importantly, SARS-CoV-2 induced transcription of the genes encoding type I and III IFNs, as well as pro-inflammatory cytokines in these cells. Of the other cell lines tested, A549, HCT116 and THP1 cells were not permissive to SARS-CoV-2 infection and did not upregulate antiviral cytokines in response to the virus. Other reports have established that A549 and THP1 cells do not support viral

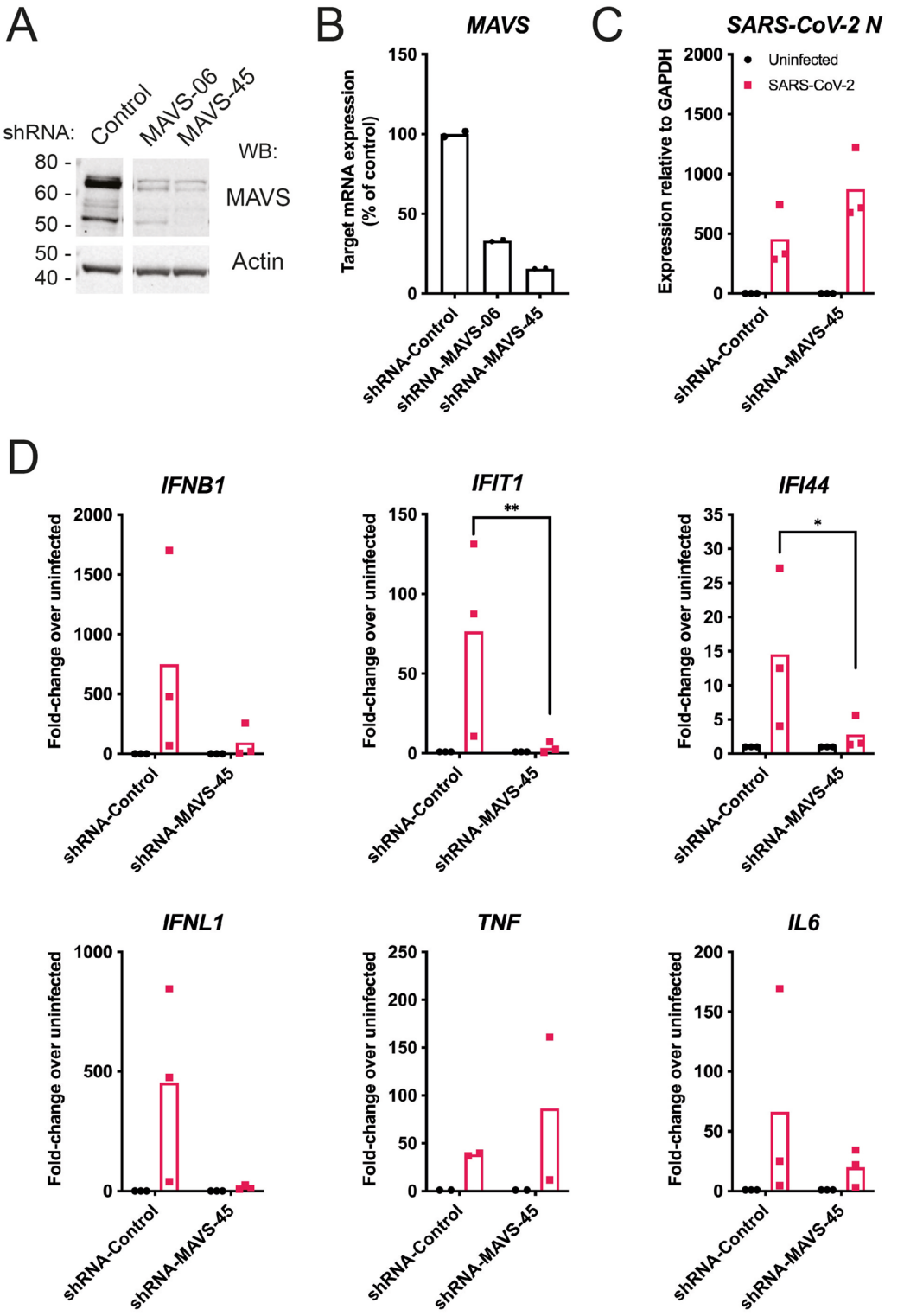


Figure 2. MAVS is required for the type I and III IFN response to SARS-CoV-2. (**A**,**B**) Calu-3 cells were depleted of MAVS by lentiviral shRNA delivery using two independent shRNAs (shRNA-MAVS-06 and shRNA-MAVS-45). Knockdown efficiency was assessed by western blot (**A**) and RT-qPCR (**B**). The control shRNA targeted GFP, which is absent in Calu-3 cells. See Supplementary Figure 3 for full blots. (**C**,**D**) Calu-3 cells depleted of MAVS using shRNA-MAVS-45 were infected with SARS-CoV-2 (MOI = 0.1) for 48 h, followed by RNA extraction and RT-qPCR for the indicated transcripts. Data are relative to *GAPDH* expression. Data in (**A**,**B**) are representative of two independent biological repeats. Data in (**C**,**D**) are pooled from 3 independent biological repeats, with bars representing the average. Data were analysed by t-test and significant differences are indicated (**$P < 0.01$; *$P < 0.05$).

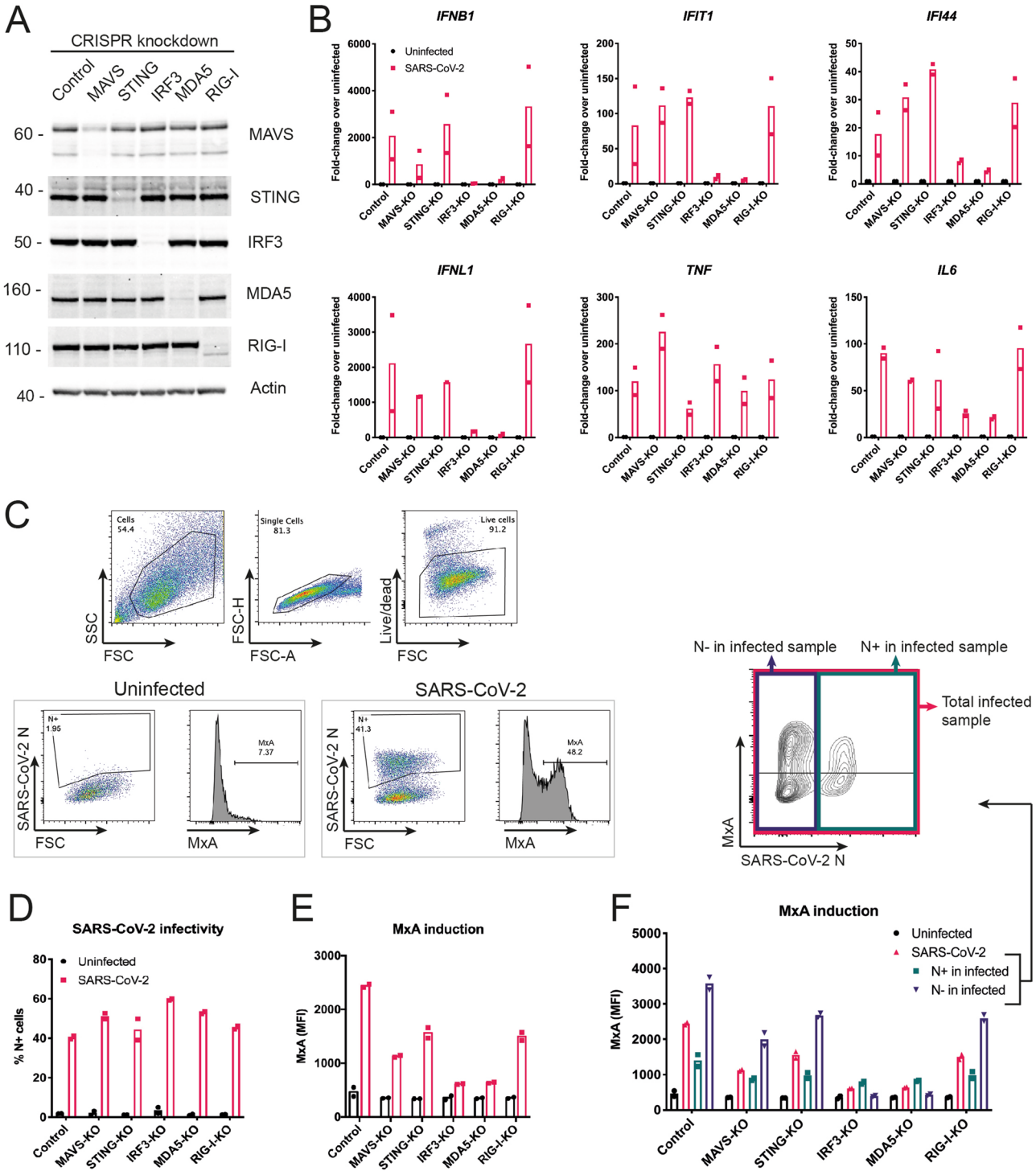


Figure 3. SARS-CoV-2 activates type I and III IFN responses via MDA5 and IRF3, and inhibits ISG induction in infected Calu-3 cells. (**A**) Calu-3 cells were depleted of MAVS, STING, IRF3, MDA5 or RIG-I using a lenti-CRISPR approach. Depletion of the targeted proteins was assessed by western blot. Control cells were targeted for GFP, which is absent in Calu-3 cells. See Supplementary Figure 4 for full blots. (**B**) Cells from (**A**) were infected and analysed as described in Fig. 2C. (**C**–**F**) Cells from (**A**) were infected as in Fig. 2C, stained for live cells, SARS-CoV-2N protein and MxA, and analysed by flow cytometry. Live cells were assessed for SARS-CoV-2 N protein expression (**D**) and MxA induction, shown as mean fluorescence intensity (MFI; **E**). (**F**) Cells in the SARS-CoV-2-infected samples were further subdivided into SARS-CoV-2 N positive (N+) and SARS-CoV-2 N negative (N−) cells, and MxA MFI was determined within these subpopulations. Data in (**A**,**C**) are representative of two independent biological repeats. Data in (**B**,**D**–**F**) are pooled from two independent biological repeats, with bars representing the average.

entry and/or replication, likely due to insufficient expression of the viral entry receptor ACE2[22,23]. In addition, it has recently been suggested that high baseline levels of RIG-I present in cells such as A549 prevent SARS-CoV-2 replication[24]. Mechanistically, this may be independent of IFN induction but instead involve reduced binding of the viral polymerase to viral RNA occupied by RIG-I[24]. Intriguingly, we could detect high levels of viral RNA but no induction of an IFN or cytokine response in HEK293 and Huh7 cells. HEK293 cells have been suggested to express sufficient ACE2 for viral entry, and allow for initial replication of the virus[25,26]. However, the infection appears to be abortive limiting production of substantial progeny virus[26]. Why do HEK293 cells fail to respond to the initial SARS-CoV-2 replication with transcriptional induction of antiviral cytokines? We found that MDA5 protein is undetectable in HEK293 cells at baseline (data not shown) and speculate that this is the reason why SARS-CoV-2 is not detected in these cells. Huh7 cells have been reported to be permissive to viral replication[4,23,27–31]. Recently, a proteomics-based approach found activation of the type I IFN system in Huh7 cells at 48 h but not 24 h post-infection[32]. This indicates a delayed IFN induction in Huh7 cells, potentially explaining our results obtained at the 24h timepoint.

Other coronaviruses induce MDA5-dependent type I IFN responses, as was first shown for mouse hepatitis virus[33]. We now show, using both shRNA-mediated knockdown and CRISPR/Cas9 genetic ablation, that the type I and III IFN response to SARS-CoV-2 was dependent on the RNA sensor MDA5, its downstream adapter MAVS and the transcription factor IRF3. In Calu-3 cells, RIG-I was largely dispensable for the antiviral cytokine response to infection. While our study was in preparation, other manuscripts reported that MDA5 and its adaptor MAVS recognise SARS-CoV-2 infection[19,20,24,34]. Three of these reports[19,20,24] included siRNA-mediated knockdown and/or genetic ablation in Calu-3 cells. In contrast to these three studies and to our work, another study found that both MDA5 and RIG-I sense SARS-CoV-2 infection in Calu-3 cells, and that upregulation of the pro-inflammatory cytokine IL6 was uncoupled from MDA5, but dependent on RIG-I and MAVS[21]. This study utilised an siRNA knockdown approach; whether this or other technical differences explain the disparity between these findings and what we and others report remains to be determined. Another research group reported that total RNA extracted from SARS-CoV-2-infected Vero E6 cells activated MDA5, but not RIG-I, after transfection into human lung fibroblasts[35]. Interestingly, a similar experimental approach in a different study obtained opposing results: here, type I IFN transcriptional upregulation after transfection of RNA from infected cells was dependent on RIG-I and not MDA5[36]. It would be interesting to compare side-by-side the different reporter cells used for RNA transfection by Liu et al. and Wu et al..

Intriguingly, our experiments showed that transcriptional upregulation of the inflammatory cytokines TNF and IL6 was not dependent on the MDA5-MAVS signalling axis. These cytokines are typically induced by the transcription factor NF-κB, which can be activated downstream of MAVS[37], but is also stimulated by other PRRs, such as TLRs[38]. TLR3, a transmembrane receptor located in endosomes and at the cell surface, detects dsRNA and induces both an IRF3-mediated type I IFN response and an NF-κB-mediated pro-inflammatory response. Mutations in *TLR3* are associated with disease severity in patients, suggesting a role for TLR3 in response to SARS-CoV-2[5]. Furthermore, pro-inflammatory cytokines can also be induced when PRRs detect damage-associated molecular patterns released during infection[39]. cGAS and STING have been shown to be activated in this manner by sensing of mitochondrial DNA released into the cytosol in Dengue virus-infected cells. Indeed, it has been proposed that the STING pathway mediates NF-κB activation and TNF induction in response to SARS-CoV-2[40]. In our work, loss of STING reduced but did not abolish the TNF response to SARS-CoV-2 (Fig. 3B). However, it is important to note that some residual STING protein was still present in the targeted cells (Fig. 3A), so it is possible that cytosolic DNA sensing by cGAS/STING induces the expression of TNF in response to SARS-CoV-2. Moreover, the study by Yin et al. reported that, in addition to MDA5-MAVS, the receptors LGP2 and NOD1 are also required for the type I IFN response to SARS-CoV-2 in Calu-3 cells[19]. LGP2 is an RLR and may function to amplify MDA5-mediated responses[41], whereas NOD1 was recently found to play a role in facilitating RLR activation[42]. Canonically, NOD1 recognises bacterial peptidoglycans and signals via NF-κB to induce inflammatory cytokines[43]. In addition, peptidoglycan-free pathogens, such as viruses, as well as ER stress can lead to the activation of NOD proteins[44]. It is conceivable that NOD signalling and/or other pathways were responsible for the inflammatory cytokine response we observed in Calu-3 cells. Taken together, it is likely that the non-IFN pro-inflammatory cytokine responses we observed here resulted from the activation of PRRs other than MDA5.

Lastly, using flow cytometry, we observed upregulation of MxA protein, which is encoded by an ISG, in infected cell populations. This confirmed our RT-qPCR results showing induction of multiple ISG mRNAs upon infection. Staining for the viral nucleocapsid protein (N) allowed us to identify infected cells and uninfected bystander cells contained in the same sample. Interestingly, compared to infected cells, we observed more pronounced induction of MxA in bystander cells. This suggests that viral infection antagonised IFN receptor signalling. Indeed, other studies identified proteins in the IFNAR signalling cascade as targets of specific SARS-CoV-2 proteins. This includes the viral ORF6, which prevents STAT1 nuclear translocation and activation of ISG promoters[45,46]. Additionally, SARS-CoV-2 has been shown to downregulate protein expression of IFNAR1, JAK1 and TYK2, which are all involved in IFN receptor signalling[47]. Like SARS-CoV-2, SARS-CoV encodes viral proteins that interfere with the type I IFN system. For example, ORF3a from SARS-CoV targets IFNAR directly, and NSP1 inhibits STAT1 phosphorylation and IFNAR signalling by supressing host gene expression[48–50]. Therefore, it is likely that SARS-CoV-2 has additional proteins that block IFN receptor signalling[51]. Our work supports the idea that SARS-CoV-2 inhibits the response to type I IFNs, likely reducing host immunity and increasing virus propagation.

In sum, we show that SARS-CoV-2 infection activates MDA5, which—together with its downstream signalling partners MAVS and IRF3—was essential for type I and III IFN production in response to SARS-CoV-2 in Calu-3 cells. MDA5 was dispensable for the pro-inflammatory cytokine response that accompanied infection. In the future, it will be important to pinpoint molecular pathways that drive induction of pro-inflammatory responses, as they are highly relevant to COVID-19 disease progression and clinical outcome[52–56].

Materials and methods

Cell culture and virus infection. Cells were cultured at 37 °C and 5% CO_2 and routinely screened for mycoplasma contamination. Calu-3 cells (ATCC) were maintained in MEM (Gibco) supplemented with 10% v/v foetal calf serum (FCS, Gibco), 2 mM L-glutamine (Gibco), 1 × sodium pyruvate (Gibco) and 1 × non-essential amino acids (Gibco). Where indicated, cells were stimulated with IFN-A/D (R&D Systems) at 100 U/ml overnight. THP1 cells (kind gift from V Cerundolo) were maintained in RPMI (Sigma Aldrich) supplemented with 10% v/v (FCS) and 2 mM L-glutamine (Gibco). Where indicated, THP1 cells were treated with phorbol 12-myristate 13-acetate (PMA, 10 ng/ml; Invivogen) overnight prior to infection. All other cells (A549, kind gift from G Kochs; HEK293T, HEK293 and VERO E6, kind gifts from C Reis E Sousa; Huh7, kind gift from J McKeating) were maintained in DMEM (Sigma Aldrich) supplemented with 10% v/v FCS and 2 mM L-glutamine.

SARS-CoV-2 Victoria/02/2020 (passage 5) was produced by infecting Vero E6 cells at an MOI of 0.01 in DMEM supplemented with 1% FCS for 3–4 days. When cytopathic effects were visible, virus was harvested, aliquoted and frozen at − 80 °C. Virus stock was titrated by plaque assay. Briefly, virus was serially diluted tenfold in DMEM with 1% FCS, and 100 µl of dilutions were added in quadruplicates to 24 well plates containing 2.5×10^5 Vero E6 cells in 500 µl of medium. After incubation for 2 h at 37 °C, 500 µl of a semi-solid overlay (DMEM, 1% FCS, 3% carboxymethylcellulose) was added per well and the cells were incubated for 4 days. After removing the overlay and the medium, cells were washed in PBS, and fixed and stained using Amido Black stain for at least 30 min at room temperature. Plates were rinsed with water and dried before counting the plaques and calculating the titre.

To select the cell line to be used in our study, indicated cell lines were seeded in 25-cm^2 flasks (1×10^6 cells per flask) and infected the next day with SARS-CoV-2 at MOIs of 0.1 and 0.5. 2 h post-infection, the medium was changed, and cells were returned to the incubator for 22 h before analysis. For further experiments, cells were grown in 12-well plates (5.5×10^5 cells per well) for 24 h and infected with SARS-CoV-2 at an MOI 0.1 for 48 h prior to processing.

Lentiviral shRNA knockdown. Lentiviral plasmids encoding shRNAs targeting *GFP* (control; SHC005) and *MAVS* (06: TRCN0000149206; 45: TRCN0000148945) were obtained from the Sigma Mission library (Merck Darmstadt). Lentiviral particles for transduction were generated as follows: HEK293T cells were seeded in 6-well plates and the next day transfected with 1 µg psPAX2 packaging plasmid (Addgene 12260), 500 ng pMD2.G VSV-G envelope plasmid (Addgene 12259) and 1 µg shRNA plasmid using Fugene 6 (Promega). The next day, the medium was replaced. After another 24 h, lentivirus-containing supernatant was harvested three times every 8–16 h. Pooled supernatants were filtered through 0.45 µm filters and stored at − 80 °C. Calu-3 cells were transduced by addition of lentiviral supernatants containing 8 µg/ml polybrene (Merck Darmstadt). 48 h after transduction, cells were selected by addition of media containing 5 µg/ml puromycin (Gibco). Surviving cells were used for experiments.

CRISPR/Cas9 knockdown. The lentiCRISPRv2 plasmid backbone (Addgene #52,961) was used for generation of bulk knockout cell populations[57]. Constructs targeting *GFP* (control, gctcgaactccacgccgttc), *MAVS* (ggccaccatctggattcctt), *IRF3* (ggtggtgcatatgttcccggg), *TMEM173* (STING) (gggtaccggagagtgtgctc), *DDX58* (RIG-I) (gaacaacaagggcccaatgg)[58] and *IFIH1* (MDA5) (gtagcggaaattctcgtctg)[58] were generated by restriction enzyme cloning using a published procedure[57] with modifications. Complimentary oligonucleotides encoding the sgRNAs with suitable overhangs for ligation were annealed and phosphorylated using T4 Polynucleotide Kinase (NEB) with the T4 DNA Ligase Reaction buffer (NEB). The lentiCRISPRv2 vector was linearized by BmsBI (NEB) digestion, gel purified and ligated with prepared oligos using Instant Sticky-end Ligase Master Mix (NEB). After bacterial transformation, suitable clones were identified by Sanger sequencing. Lentiviral particle production and cell transduction was identical to shRNA lentiviruses but using pR8.91 packaging plasmid (kind gift from G Towers), pCMV-VSV-G (Addgene #8454) and Lipofectamine 2000 (Life Technologies).

Immunoblotting. Cells were lysed with RIPA buffer (10 mM TRIS–HCl pH 8, 140 mM NaCl, 1% Triton-X100, 0.1% SDS, 0.1% sodium deoxycholate, 1 mM EDTA, 1 mM EGTA) and protein was quantified by BCA assay (Pierce). NuPAGE LDS sample loading buffer (Life Technologies) and 10% 2-mercaptoethanol were added to samples, which were then denatured by incubation at 95 °C for 5 min. Samples were resolved by electrophoresis on 4–12% Bis–Tris gels with MOPS Running Buffer (Life Technologies NuPAGE system) and transferred to nitrocellulose membrane by electrophoresis at 100 V for 1 h in cold transfer buffer (Life Technologies) with 20% methanol. Membranes were blocked with 0.05% NP-40 (IGEPAL) in Tris-buffered saline (TBS-N; 50 mM NaCl, 50 mM Tris–HCl, pH 7.6) containing 5% non-fat milk (5% milk TBS-N) for 1 h and probed with primary and HRP-conjugated secondary antibodies (GE Healthcare, 1:3000) diluted in 5% milk TBS-N for 1 h at room temperature or overnight at 4 °C, with rotation. Membranes were washed four times in TBS-N (5 min for each wash) after each antibody incubation. Proteins were visualised on an iBright (ThermoFisher) after exposure to Western LightningPlus-ECL chemiluminescent reagent (PerkinElmer). Primary antibodies included: beta-actin-HRP (AC-15, Sigma Aldrich), pSTAT1 (Y701) (58D6, Cell Signaling Technology), STAT1 (42H3, Cell Signaling Technology), pSTAT2 (D3P2P, Cell Signaling Technology), STAT2 (D9J7L, Cell Signaling Technology), hcGAS (D1D3G, Cell Signaling Technology), hSTING (D2P2F, Cell Signaling Technology), MyD88 (D80F5, Cell Signaling Technology), TBK1 (D1B4, Cell Signaling Technology), MAVS (ALX-210-929-C100, ENZO Life Science), IRF3 (D6I4C, Cell Signaling Technology), MDA5 (generated in house[58]) and RIG-I (clone ALME-I, ProSci #PSI-36-102).

RT-qPCR. RNA was extracted from cells using RNeasy Plus Mini Kit (Qiagen, 74136) according to manufacturer's instructions, quantified by Nanodrop, and stored at − 80 °C. RNA (1 µg) was converted into cDNA using SuperScript III Reverse Transcriptase (Thermo Fisher Scientific) and random hexamer primers (Qiagen, 79236) according to manufacturer's instructions. cDNA was diluted to 100 ng/µl and quantitative PCR (qPCR) was performed using TaqMan Real-Time PCR Assays for designated genes and TaqMan Fast Advanced Master Mix (Thermo Fisher Scientific) according to manufacturer's instructions. Assays were performed on QuantStudio 6 Flex Real-Time PCR machines (Thermo Fisher Scientific).

Flow cytometry. Cells were dislodged by washing in PBS and treatment with 0.05% trypsin (Gibco) for 20 min, followed by pipetting and centrifugation. For all subsequent steps, reagents were diluted in FACS buffer (PBS, 1% FCS, 2 mM EDTA) unless stated otherwise, and washed twice with FACS buffer between steps. Cells were stained with Live/Dead Fixable Aqua Cell Stain (1:200 in PBS, Life Technologies, L34957) combined with FcR block (1:200 in PBS, eBioscience), fixed in 4% formaldehyde (10 min at room temperature), and permeabilised in PBS containing 0.1% Triton-X (20 min at room temperature). Cells were incubated with antibodies against human MxA (clone M143, kind gift from G Kochs) and SARS-CoV-2 N protein (clone EY-2A, kind gift from Alain Townsend[59]; 1:200, 30 min, 4 °C), and goat anti-mouse AlexaFluor 488 (Life Technologies, A11029) and anti-human AlexaFluor 647 (1:500, 30 min, 4 °C; Life Technologies, A21445), and resuspended in CellFix (1:10 in water; BD, 340181). Cells were analysed by flow cytometry on an Attune NxT Flow Cytometer (Thermo Fisher Scientific) and data were analysed using FlowJo software (BD).

Data availability

All data generated or analysed during this study are included in this published article (and its Supplementary Information files).

Received: 16 April 2021; Accepted: 16 June 2021
Published online: 01 July 2021

References

1. Blanco-Melo, D. *et al.* Imbalanced host response to SARS-CoV-2 drives development of COVID-19. *Cell* **181**, 1036–1045. https://doi.org/10.1016/j.cell.2020.04.026 (2020) (**e1039**).
2. Bastard, P. *et al.* Autoantibodies against type I IFNs in patients with life-threatening COVID-19. *Science* **370**, eabd4585. https://doi.org/10.1126/science.abd4585 (2020).
3. Lucas, C. *et al.* Longitudinal analyses reveal immunological misfiring in severe COVID-19. *Nature* **584**, 463–469. https://doi.org/10.1038/s41586-020-2588-y (2020).
4. Chu, H. *et al.* Comparative tropism, replication kinetics, and cell damage profiling of SARS-CoV-2 and SARS-CoV with implications for clinical manifestations, transmissibility, and laboratory studies of COVID-19: an observational study. *Lancet Microbe* **1**, e14–e23. https://doi.org/10.1016/S2666-5247(20)30004-5 (2020).
5. Zhang, Q. *et al.* Inborn errors of type I IFN immunity in patients with life-threatening COVID-19. *Science* **370**, eabd4570. https://doi.org/10.1126/science.abd4570 (2020).
6. Monk, P. D. *et al.* Safety and efficacy of inhaled nebulised interferon beta-1a (SNG001) for treatment of SARS-CoV-2 infection: a randomised, double-blind, placebo-controlled, phase 2 trial. *Lancet Respir. Med.* **9**, 196–206. https://doi.org/10.1016/S2213-2600(20)30511-7 (2021).
7. Consortium, W. H. O. S. T. *et al.* Repurposed Antiviral Drugs for Covid-19—Interim WHO Solidarity Trial Results. *N. Engl. J. Med.* **384**, 497–511. https://doi.org/10.1056/NEJMoa2023184 (2021).
8. Hoagland, D. A. *et al.* Leveraging the antiviral type I interferon system as a first line of defense against SARS-CoV-2 pathogenicity. *Immunity* https://doi.org/10.1016/j.immuni.2021.01.017 (2021).
9. Park, A. & Iwasaki, A. Type I and Type III interferons—induction, signaling, evasion, and application to combat COVID-19. *Cell Host Microbe* **27**, 870–878. https://doi.org/10.1016/j.chom.2020.05.008 (2020).
10. Dinnon, K. H. 3rd. *et al.* A mouse-adapted model of SARS-CoV-2 to test COVID-19 countermeasures. *Nature* **586**, 560–566. https://doi.org/10.1038/s41586-020-2708-8 (2020).
11. Harrison, A. G., Lin, T. & Wang, P. Mechanisms of SARS-CoV-2 transmission and pathogenesis. *Trends Immunol.* **41**, 1100–1115. https://doi.org/10.1016/j.it.2020.10.004 (2020).
12. Bartok, E. & Hartmann, G. Immune sensing mechanisms that discriminate self from altered self and foreign nucleic acids. *Immunity* **53**, 54–77. https://doi.org/10.1016/j.immuni.2020.06.014 (2020).
13. de Wit, E., van Doremalen, N., Falzarano, D. & Munster, V. J. SARS and MERS: recent insights into emerging coronaviruses. *Nat. Rev. Microbiol.* **14**, 523–534. https://doi.org/10.1038/nrmicro.2016.81 (2016).
14. Rehwinkel, J. & Gack, M. U. RIG-I-like receptors: their regulation and roles in RNA sensing. *Nat. Rev. Immunol.* **20**, 537–551. https://doi.org/10.1038/s41577-020-0288-3 (2020).
15. Dias Junior, A. G., Sampaio, N. G. & Rehwinkel, J. A balancing act: MDA5 in antiviral immunity and autoinflammation. *Trends Microbiol.* **27**, 75–85. https://doi.org/10.1016/j.tim.2018.08.007 (2019).
16. Schoggins, J. W. Interferon-stimulated genes: what do they all do?. *Annu. Rev. Virol.* **6**, 567–584. https://doi.org/10.1146/annurev-virology-092818-015756 (2019).
17. Sun, B. *et al.* Dengue virus activates cGAS through the release of mitochondrial DNA. *Sci. Rep.* **7**, 3594. https://doi.org/10.1038/s41598-017-03932-1 (2017).
18. Aguirre, S. *et al.* Dengue virus NS2B protein targets cGAS for degradation and prevents mitochondrial DNA sensing during infection. *Nat. Microbiol.* **2**, 17037. https://doi.org/10.1038/nmicrobiol.2017.37 (2017).
19. Yin, X. *et al.* MDA5 governs the innate immune response to SARS-CoV-2 in lung epithelial cells. *Cell. Rep.* **34**, 108628. https://doi.org/10.1016/j.celrep.2020.108628 (2021).
20. Rebendenne, A. *et al.* SARS-CoV-2 triggers an MDA-5-dependent interferon response which is unable to control replication in lung epithelial cells. *J. Virol.* https://doi.org/10.1128/jvi.02415-20 (2021).
21. Thorne, L. G. *et al.* SARS-CoV-2 sensing by RIG-I and MDA5 links epithelial infection to macrophage inflammation. *EMBO J.* e107826. https://doi.org/10.15252/embj.2021107826 (2021).
22. Matsuyama, S. *et al.* Enhanced isolation of SARS-CoV-2 by TMPRSS2-expressing cells. *Proc. Natl. Acad. Sci. USA* **117**, 7001–7003. https://doi.org/10.1073/pnas.2002589117 (2020).

23. Harcourt, J. *et al.* Isolation and characterization of SARS-CoV-2 from the first US COVID-19 patient. *Biorxiv* https://doi.org/10.1101/2020.03.02.972935 (2020).
24. Yamada, T. *et al.* RIG-I triggers a signaling-abortive anti-SARS-CoV-2 defense in human lung cells. *Nat. Immunol.* https://doi.org/10.1038/s41590-021-00942-0 (2021).
25. Warner, F. J. *et al.* Angiotensin-converting enzyme 2 (ACE2), but not ACE, is preferentially localized to the apical surface of polarized kidney cells. *J. Biol. Chem.* **280**, 39353–39362. https://doi.org/10.1074/jbc.M508914200 (2005).
26. Modrof, J. *et al.* SARS-CoV-2 and the safety margins of cell-based biological medicinal products. *Biologicals* **68**, 122–124. https://doi.org/10.1016/j.biologicals.2020.08.010 (2020).
27. Ou, X. *et al.* Characterization of spike glycoprotein of SARS-CoV-2 on virus entry and its immune cross-reactivity with SARS-CoV. *Nat. Commun.* **11**, 1620. https://doi.org/10.1038/s41467-020-15562-9 (2020).
28. Zhu, N. *et al.* A novel coronavirus from patients with pneumonia in China, 2019. *N. Engl. J. Med.* **382**, 727–733. https://doi.org/10.1056/NEJMoa2001017 (2020).
29. Harcourt, J. *et al.* Severe acute respiratory syndrome coronavirus 2 from patient with coronavirus disease, United States. *Emerg. Infect. Dis.* **26**, 1266–1273. https://doi.org/10.3201/eid2606.200516 (2020).
30. Mirabelli, C. *et al.* Morphological cell profiling of SARS-CoV-2 infection identifies drug repurposing candidates for COVID-19. *Biorxiv* https://doi.org/10.1101/2020.05.27.117184 (2020).
31. Zhou, P. *et al.* A pneumonia outbreak associated with a new coronavirus of probable bat origin. *Nature* **579**, 270–273. https://doi.org/10.1038/s41586-020-2012-7 (2020).
32. Chen, X. *et al.* Type-I interferon signatures in SARS-CoV-2 infected Huh7 cells. *Biorxiv*, 2021.2002.2004.429738. https://doi.org/10.1101/2021.02.04.429738 (2021).
33. Roth-Cross, J. K., Bender, S. J. & Weiss, S. R. Murine coronavirus mouse hepatitis virus is recognized by MDA5 and induces type I interferon in brain macrophages/microglia. *J. Virol.* **82**, 9829–9838. https://doi.org/10.1128/JVI.01199-08 (2008).
34. Li, Y. *et al.* SARS-CoV-2 induces double-stranded RNA-mediated innate immune responses in respiratory epithelial-derived cells and cardiomyocytes. *Proc. Natl. Acad. Sci. USA* https://doi.org/10.1073/pnas.2022643118 (2021).
35. Liu, G. *et al.* ISG15-dependent activation of the sensor MDA5 is antagonized by the SARS-CoV-2 papain-like protease to evade host innate immunity. *Nat. Microbiol.* https://doi.org/10.1038/s41564-021-00884-1 (2021).
36. Wu, J. *et al.* SARS-CoV-2 ORF9b inhibits RIG-I-MAVS antiviral signaling by interrupting K63-linked ubiquitination of NEMO. *Cell. Rep.* **34**, 108761. https://doi.org/10.1016/j.celrep.2021.108761 (2021).
37. Seth, R. B., Sun, L., Ea, C. K. & Chen, Z. J. Identification and characterization of MAVS, a mitochondrial antiviral signaling protein that activates NF-kappaB and IRF 3. *Cell* **122**, 669–682. https://doi.org/10.1016/j.cell.2005.08.012 (2005).
38. Kawasaki, T. & Kawai, T. Toll-like receptor signaling pathways. *Front. Immunol.* **5**, 461. https://doi.org/10.3389/fimmu.2014.00461 (2014).
39. Venereau, E., Ceriotti, C. & Bianchi, M. E. DAMPs from cell death to new life. *Front. Immunol.* **6**, 422. https://doi.org/10.3389/fimmu.2015.00422 (2015).
40. Neufeldt, C. J. *et al.* SARS-CoV-2 infection induces a pro-inflammatory cytokine response through cGAS-STING and NF-κB. *bioRxiv*, 2020.2007.2021.212639. https://doi.org/10.1101/2020.07.21.212639 (2020).
41. Sanchez David, R. Y. *et al.* LGP2 binds to PACT to regulate RIG-I- and MDA5-mediated antiviral responses. *Sci. Signal.* https://doi.org/10.1126/scisignal.aar3993 (2019).
42. Wu, X. M. *et al.* NOD1 promotes antiviral signaling by binding viral RNA and regulating the interaction of MDA5 and MAVS. *J. Immunol.* **204**, 2216–2231. https://doi.org/10.4049/jimmunol.1900667 (2020).
43. Caruso, R., Warner, N., Inohara, N. & Nunez, G. NOD1 and NOD2: signaling, host defense, and inflammatory disease. *Immunity* **41**, 898–908. https://doi.org/10.1016/j.immuni.2014.12.010 (2014).
44. Keestra-Gounder, A. M. & Tsolis, R. M. NOD1 and NOD2: Beyond peptidoglycan sensing. *Trends Immunol.* **38**, 758–767. https://doi.org/10.1016/j.it.2017.07.004 (2017).
45. Lei, X. *et al.* Activation and evasion of type I interferon responses by SARS-CoV-2. *Nat. Commun.* **11**, 3810. https://doi.org/10.1038/s41467-020-17665-9 (2020).
46. Miorin, L. *et al.* SARS-CoV-2 Orf6 hijacks Nup98 to block STAT nuclear import and antagonize interferon signaling. *Proc. Natl. Acad. Sci. USA* **117**, 28344–28354. https://doi.org/10.1073/pnas.2016650117 (2020).
47. Chen, D. Y. *et al.* SARS-CoV-2 desensitizes host cells to interferon through inhibition of the JAK-STAT pathway. *Biorxiv*, 2020.2010.2027.358259. https://doi.org/10.1101/2020.10.27.358259 (2020).
48. Minakshi, R. *et al.* The SARS Coronavirus 3a protein causes endoplasmic reticulum stress and induces ligand-independent downregulation of the type 1 interferon receptor. *PLoS ONE* **4**, e8342. https://doi.org/10.1371/journal.pone.0008342 (2009).
49. Wathelet, M. G., Orr, M., Frieman, M. B. & Baric, R. S. Severe acute respiratory syndrome coronavirus evades antiviral signaling: role of nsp1 and rational design of an attenuated strain. *J. Virol.* **81**, 11620–11633. https://doi.org/10.1128/JVI.00702-07 (2007).
50. Narayanan, K. *et al.* Severe acute respiratory syndrome coronavirus nsp1 suppresses host gene expression, including that of type I interferon, infected cells. *J. Virol.* **82**, 4471–4479. https://doi.org/10.1128/jvi.02472-07 (2008).
51. Sa Ribero, M., Jouvenet, N., Dreux, M. & Nisole, S. Interplay between SARS-CoV-2 and the type I interferon response. *PLoS Pathog.* **16**, e1008737. https://doi.org/10.1371/journal.ppat.1008737 (2020).
52. Karki, R. *et al.* Synergism of TNF-alpha and IFN-gamma triggers inflammatory cell death, tissue damage, and mortality in SARS-CoV-2 infection and cytokine shock syndromes. *Cell* **184**, 149–168. https://doi.org/10.1016/j.cell.2020.11.025 (2021) (**e117**).
53. Zhou, F. *et al.* Clinical course and risk factors for mortality of adult inpatients with COVID-19 in Wuhan, China: a retrospective cohort study. *Lancet* **395**, 1054–1062. https://doi.org/10.1016/S0140-6736(20)30566-3 (2020).
54. Del Valle, D. M. *et al.* An inflammatory cytokine signature predicts COVID-19 severity and survival. *Nat. Med.* **26**, 1636–1643. https://doi.org/10.1038/s41591-020-1051-9 (2020).
55. Mudd, P. A. *et al.* Distinct inflammatory profiles distinguish COVID-19 from influenza with limited contributions from cytokine storm. *Sci. Adv.* https://doi.org/10.1126/sciadv.abe3024 (2020).
56. Giamarellos-Bourboulis, E. J. *et al.* Complex immune dysregulation in COVID-19 patients with severe respiratory failure. *Cell Host Microbe* **27**, 992–1000. https://doi.org/10.1016/j.chom.2020.04.009 (2020) (**e1003**).
57. Sanjana, N. E., Shalem, O. & Zhang, F. Improved vectors and genome-wide libraries for CRISPR screening. *Nat. Methods* **11**, 783–784. https://doi.org/10.1038/nmeth.3047 (2014).
58. Hertzog, J. *et al.* Infection with a Brazilian isolate of Zika virus generates RIG-I stimulatory RNA and the viral NS5 protein blocks type I IFN induction and signaling. *Eur. J. Immunol.* **48**, 1120–1136. https://doi.org/10.1002/eji.201847483 (2018).
59. Huang, K.-Y. A. *et al.* Breadth and function of antibody response to acute SARS-CoV-2 infection in humans. *PLoS Pathogens.* **17**(2), e1009352. https://doi.org/10.1371/journal.ppat.1009352 (2021).

Acknowledgements

The authors thank William James for providing access to the BSL3 facility. The authors thank Arthur Huang, Pramila Rijal, Lisa Schimanski, Tiong Kit Tan and Alain Townsend for providing the anti-SARS-CoV-2 N antibody. This work was funded by the UK Medical Research Council (MRC core funding of the MRC Human Immunology Unit; JR) and the Wellcome Trust (Grant No. 100954; JR). JH was supported by the European

Commission under the Horizon2020 program H2020 MSCA-ITN GA 675278 EDGE. GF was supported by the Rothermere Fellowship and was also supported by Indspire's Building Brighter Futures: Bursaries, Scholarships, and Awards program. RAR acknowledges the generous support of philanthropic donors that allowed funding from the University of Oxford's COVID-19 Research Response Fund, which also supported the SARS-CoV-2 BSL3 facility. The funders had no role in study design, data collection and analysis, decision to publish, or preparation of the manuscript.

Author contributions

Conceptualization: N.G.S., L.C., J.H., A.B. and J.R.; Methodology: N.G.S., L.C., J.H. and A.B.; Software: n.a.; Validation: N.G.S., L.C., J.H., A.B. and J.R.; Formal analysis: N.G.S., L.C., J.H., A.B. and J.R.; Investigation: N.G.S., L.C., J.H., A.B., G.F. and J.M.; Resources: M.D., R.A.R. and M.N.; Data curation: N.G.S., L.C., J.H., A.B. and J.R.; Writing—Original Draft: N.G.S., L.C., J.H. and J.R.; Writing—Review & Editing: all authors; Visualization: N.G.S., L.C. and J.H.; Supervision: J.R.; Project administration: J.R.; Funding acquisition: J.R.

Competing interests

The authors declare no competing interests.

Additional information

Supplementary Information The online version contains supplementary material available at https://doi.org/10.1038/s41598-021-92940-3.

Correspondence and requests for materials should be addressed to J.R.

Reprints and permissions information is available at www.nature.com/reprints.

Publisher's note Springer Nature remains neutral with regard to jurisdictional claims in published maps and institutional affiliations.

Open Access This article is licensed under a Creative Commons Attribution 4.0 International License, which permits use, sharing, adaptation, distribution and reproduction in any medium or format, as long as you give appropriate credit to the original author(s) and the source, provide a link to the Creative Commons licence, and indicate if changes were made. The images or other third party material in this article are included in the article's Creative Commons licence, unless indicated otherwise in a credit line to the material. If material is not included in the article's Creative Commons licence and your intended use is not permitted by statutory regulation or exceeds the permitted use, you will need to obtain permission directly from the copyright holder. To view a copy of this licence, visit http://creativecommons.org/licenses/by/4.0/.

© The Author(s) 2021